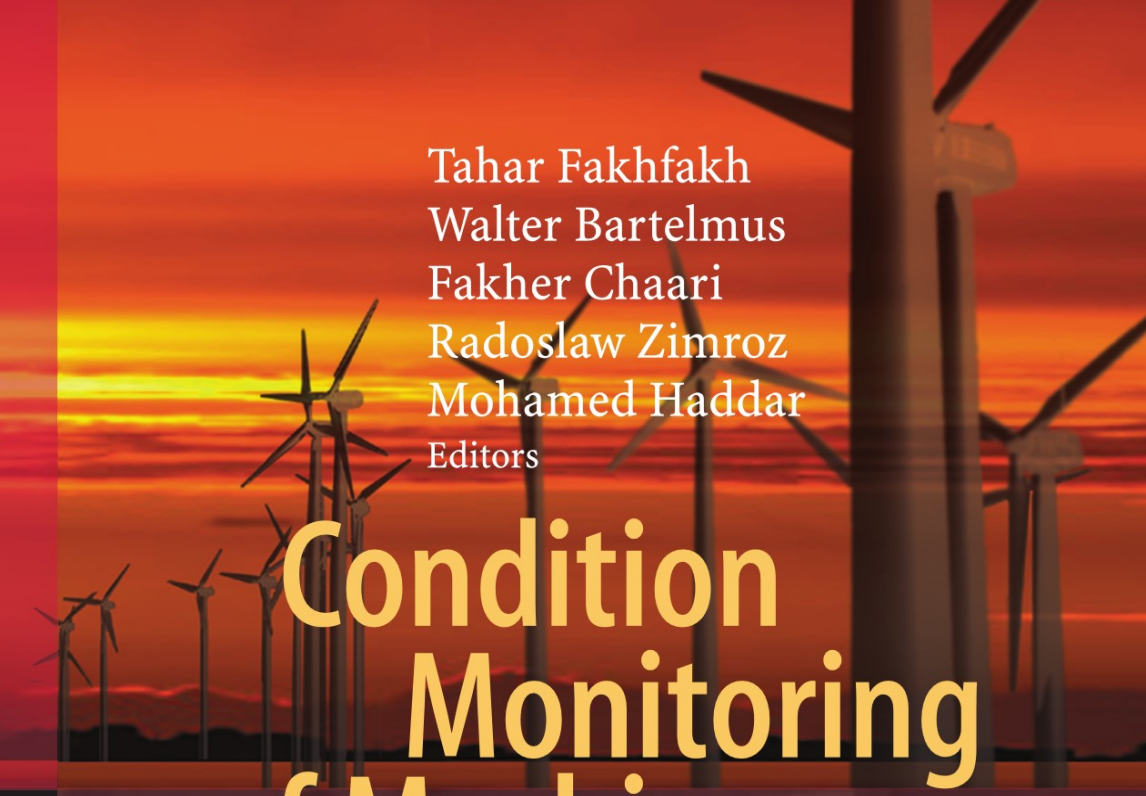

Tahar Fakhfakh
Walter Bartelmus
Fakher Chaari
Radoslaw Zimroz
Mohamed Haddar
Editors

Condition Monitoring of Machinery in Non-Stationary Operations

Proceedings of the Second International Conference **Condition Monitoring of Machinery in Non-Stationary Operations**

CMMNO'2012

Springer

Condition Monitoring of Machinery in Non-Stationary Operations

Tahar Fakhfakh, Walter Bartelmus, Fakher Chaari,
Radoslaw Zimroz, and Mohamed Haddar (Eds.)

Condition Monitoring of Machinery in Non-Stationary Operations

Proceedings of the Second International Conference "Condition Monitoring of Machinery in Non-Stationnary Operations" CMMNO'2012

Springer

Editors
Prof. Tahar Fakhfakh
National School of Engineers of Sfax
Dynamics of Mechanical Systems
Research Unit
Sfax
Tunisia

Dr. Radoslaw Zimroz
Diagnostics and Vibro-Acoustics
Science Laboratory
Wrocław University of Technology
Wrocław
Poland

Prof. Walter Bartelmus
Diagnostics and Vibro-Acoustics
Science Laboratory
Wrocław University of Technology
Wrocław
Poland

Prof. Mohamed Haddar
National School of Engineers of Sfax
Dynamics of Mechanical Systems
Research Unit
Sfax
Tunisia

Prof. Fakher Chaari
National School of Engineers of Sfax
Dynamics of Mechanical Systems
Research Unit
Sfax
Tunisia

ISBN 978-3-642-28767-1 e-ISBN 978-3-642-28768-8
DOI 10.1007/978-3-642-28768-8
Springer Heidelberg New York Dordrecht London

Library of Congress Control Number: 2012933125

Printed on acid-free paper

Springer is part of Springer Science+Business Media (www.springer.com)

Introduction

Condition monitoring of machines in non-stationary operations (CMMNO) can be seen as the major challenge for research in the field of machinery diagnostics.

Condition Monitoring of Machines in Non-stationary Operations is the title of the presented book and the title of the Conference held in Hammamet - Tunisia March 26–28, 2012. It is the second conference under this title, first took place in Wroclaw - Poland, March 2011.

The subject CMMNO comes directly from industry needs and observation of real objects. Most monitored and diagnosed objects used in industry works in non-stationary operations condition. The non-stationary operations come from fulfillment of machinery tasks, for which they are designed for. All machinery used in different kind of mines, transport systems, vehicles like: cars, buses etc, helicopters, ships and battleships and so on work in non-stationary operations.

The papers included in the book are shaped by the organizing board of the conference and authors of the papers.

The papers are divided into five sections, namely:

Condition monitoring of machines in non-stationary operations
Modeling of dynamics and fault in systems
Signal processing and Pattern recognition for condition monitoring
Monitoring and diagnostic systems
Noise and vibration of machines

The presented book gives the background to the main objective of the CMMNO 2012 conference that is to bring together scientific community to discuss the major advances in the field of machinery condition monitoring in non-stationary conditions.

In the first chapter, the main subject of the conference book is discussed. This subject comes directly from industry needs and industry observation of real objects. Most monitored machines used in industry works in non stationary operations condition. The non-stationary operations come from fulfillment of machinery tasks, for which they are designed for. The papers presented in this chapter try to generalize the solution and give individual response for individual applications of monitoring and diagnosing when object works in stationary operations.

Second section discusses the vibration based faults detection in machinery such as misalignment, unbalance, local damages etc.; it is widely developed and extensively used in practice. However, the quantification and the location of defects is still a research subject for many years. In the last decades, an increase of interest

was observed for model based approaches to provide mathematical explanation of the dynamics of machinery especially in presence of faults and in non-stationary operations.

Third chapter shows that modern condition monitoring extensively exploits signal processing and pattern recognition techniques. Signal processing is used for both signal enhancement (de-noising, separation, reconstruction, filtering…etc) and feature extraction (parametric models, two dimensional plane representation).

In some cases, damage detection can be performed using simple rules. However, when considering complex mechanical systems, especially in time varying conditions, problem of classification of features becomes complicated. In such a case, feature selection procedures are proposed and advanced data classifiers are used.

Fourth chapter emphasizes that despite the fact that condition monitoring is well established as a scientific discipline, there is still a great need to implement results of research into the practice, as monitoring and diagnostic system. In this chapter, several good examples of problem complexity is provided in the context of marine gas turbine, mining industry, wind turbine generator or even wind turbines farms. In such practical implementation, as multi-channel online systems, even signal quality assessment seems to be serious data-mining task.

Fifth section, where noise and vibration is discussed, different theoretical and practical methods are presented. The damping phenomenon is used for noise and vibration reduction. There are also given papers on more advanced techniques like: dynamic absorbers, floating supports, damper modeling and so on.

The presented book gives the background to the main objective of the CMMNO 2012 conference that is to bring together scientific community to discuss the major advances in the field of machinery condition monitoring in non-stationary conditions.

Contents

Chapter 1: Condition Monitoring in Non-stationary Operations

Chapter 3: Signal Processing and Pattern Recognition

Chapter 4: Monitoring and Diagnostic Systems

Chapter 5: Noise and Vibration of Machines

Chapter 1
Condition Monitoring in Non-stationary Operations

Condition monitoring in non-stationary operations is the main subject of the conference. The subject comes directly from industry needs and observations of real objects. Most monitored machines used in industry work in non-stationary operations condition. The non-stationary operations are due to the fulfillment of machinery tasks, for which they are designed for. All machinery used in different kind mines, transport systems, the private or public vehicles like: cars, buses, helicopters, ships and battleships and so on work in non-stationary operations. The papers presented in this chapter try to generalize the solution and to give individual response for individual applications of monitoring and diagnosing when the machine works in stationary operations.

Separation of Gear and Bearing Fault Signals from a Wind Turbine Transmission under Varying Speed and Load

Robert B. Randall[1], Nader Sawalhi[2], and Michael Coats[1]

[1] School of Mechanical and Manufacturing Engineering,
University of New South Wales, Sydney 2052, Australia
b.randall@unsw.edu.au, m.coats@yahoo.com.au
[2] Mechanical Engineering Department, Prince Mohammad Bin Fahd University (PMU)
P.O. Box 1664, AlKhobar 31952, Saudi Arabia
nadersaw@hotmail.com

Abstract. Wind turbine transmissions are quite complex, with a multitude of gears and bearings. It is imperative that the different signals are separated from each other in order to locate the source of a problem. They differ from many other gearboxes by operating with a widely varying load over time periods corresponding to individual analysis records, and this gives particular problems with gear vibrations, where the effects of load have to be separated from those of condition. The most efficient turbines operate with widely varying speed as well, and this also has to be compensated for in the analysis procedures.

This paper discusses a number of ways of compensating for speed and load variation, using signals obtained from a round robin study of naturally occurring faults in a wind turbine transmission. The gearbox was mounted on a test rig for the measurements, and so the speed variation was less than can occur in practice, but the way in which larger speed and load variations can be accounted for is demonstrated using signals from a simpler gearbox on another test rig, and another wind turbine.

Keywords: gear diagnostics, bearing diagnostics, speed variation, load variation, order tracking.

1 Introduction

Wind turbine transmissions are quite complex, with a large ratio from input to output, and many different gears and shafts supported in bearings. They usually consist of a planetary section at the input, followed by one or two stages of parallel gears. The arrangement is not unlike that of helicopter gearboxes, with which much experience has been gained over the years, but they differ in a number of ways that introduce new problems. Firstly, they are speedup gearboxes rather than reducers, though this does not appear to give great problems with the diagnostics.

They operate at a much lower speed, by a factor of ten or more, so that record lengths required for analysis of the low speed sections are typically of the order of minutes, and considerable load variation can occur over such time periods. Classical gear diagnostic techniques are usually based on the assumption of roughly constant load, since gear vibrations vary considerably with load as dynamic transmission error (TE) changes with tooth deflection. Bearing vibrations also vary with load, though not as much as for gears, and it is also a mitigating factor that initial faults tend to make the signal more impulsive, and therefore detectable independent of load, which is not always the case with gears.

In any case, the characteristics of the signals can only be determined if the signal from each component can be separated from all others, and in particular bearing signals are often masked by gear signals, even with no faults in the latter. A first separation is often into deterministic and random constituents, as gears fall into the first category, and bearings into the second. A number of methods are available for this [Randall '11], but a new method based on the cepstrum has some advantages [Randall, Sawalhi '11]. Extracting deterministic components usually involves resampling in the angular domain, to make the signals truly periodic, which they will not be in the case of speed variation, even when this is minor. The method, also known as order tracking, can also compensate for large speed variations, such as can be experienced with wind turbines, but other problems then arise. The method usually requires a speed reference signal (tacho or shaft encoder), but methods are described here for extracting a "pseudo-encoder" signal from the vibration signal. Other methods for enhancing and diagnosing the gear and bearing signals are described in the following.

2 Typical Diagnosis of Wind Turbine Transmission Faults

Much of the following is based on the results of our analysis of signals provided by the NREL (National Renewable Energy Labs) of the U.S. Department of Energy, in a round robin study. The signals were taken from a transmission which had experienced oil leakage and overheating in practice, and had then been installed on a test rig where the measurements were made. Initially, no information was given as to the faults, and the analysis was blind, but later an inspection report was provided and the initial predictions could be tested. At about the time of the inspection report, vibration spectra were also provided for the gearbox in healthy condition, so further diagnostic analysis could be done, in particular with respect to the gear condition, for which spectrum comparison is a very valuable technique. Signals were provided for several loads and nominal speeds, but the latter did not vary as much as can happen in practice. Full results of the round robin study will be published in the journal Wind Energy in mid 2012.

The turbine studied had a fixed synchronous speed induction generator (nominally 1800 or 1200 rpm), so the speed variation was not great. The speed signal supplied was not suitable for order tracking so the instantaneous speed was extracted from the high speed gearmesh signal by the method illustrated in Fig. 1 [Urbanek et al '11].

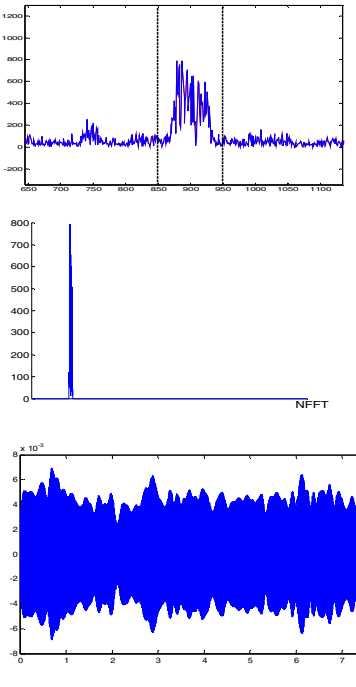

(a) Step 1: Identifying the band of interest. The plot shows the amplitude of the spectrum. Frequency axis scaled in lines rather than Hz

(b) Step 2: Band of interest moved into a buffer filled with zeros

(c) Step 3: real part of the IFFT (Inverse Fast Fourier Transform) of the buffer obtained in step 2.

Fig. 1 Reference (speed) signal extraction stages (a) Identifying a separable band (b) Extracting the band into a new buffer (c) inverse transform signal b into the time domain

If as in this case the speed variation is not large, the correction can be made in one step, but if it is greater the correction can be done iteratively, starting if necessary at a lower harmonic, using an alternative phase demodulation method described below. As the extracted band is progressively narrowed in the angle domain at each iteration, less noise is included in the inverse transformation to the time domain, making the time/angle mapping more accurate. The lowest harmonic that can be used is the fundamental, but this is well separated from the second harmonic, and it is possible to correct for variations up to nearly 30%. An example is shown later in the paper. Note that the zero crossings of the extracted signal represent phase increments of 180°, and amplitude modulation by any non-zero modulating function has no effect on this.

The detected instantaneous shaft speeds for two of the signals are shown in Fig. 2, for the high speed shaft at nominal 1800 and 1200 rpm, respectively.

As discussed in [Urbanek et al ‘11], an alternative method for angular resampling is to phase demodulate the prominent signal used as a pseudo-encoder, and use this as a “map” between time and rotation angle. In [Urbanek et al ‘11], the results were virtually identical, but in a multi-stage iterative procedure the phase demodulation method is probably easier to use since the map is continually updated.

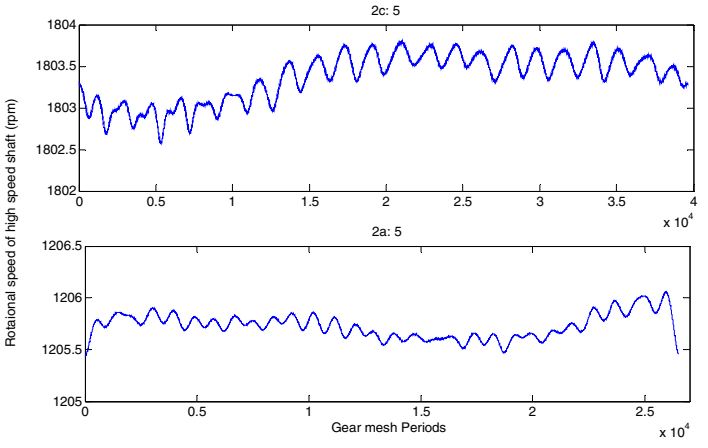

Fig. 2 High speed shaft estimates (upper) 1800 rpm (lower) 1200 rpm

As mentioned above, the amount of correction for speed variation that can be made based on the signal itself is limited by Bedrosian's condition that sidebands around different carrier harmonics should not overlap. This gives a limit of about 30% for the first harmonic and for example 10% for the third harmonic [Coats et al '10]. Fig. 3 shows an example from a simple gear test rig with a faulty bearing, where the speed was varied ± 10% sinusoidally around 6 Hz, with a period of 5s. Note that the amplitude modulation of the acceleration signal, with 5s period, is due to the fact that certain harmonics pass through fixed resonances every speed cycle. The spectrum of the tacho signal shows that the third harmonic is the highest that is separated from adjacent harmonics, and can still be used for speed correction. The spectrum of the acceleration signal shows that the first two harmonics are too weak to use, but the third has a similar spread to that of the tacho signal.

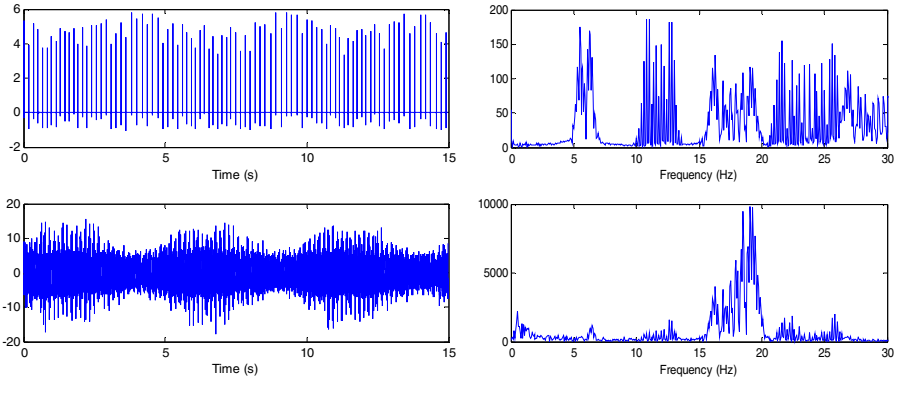

Fig. 3 Signal with ±10% speed variation (upper) tacho (lower) acceleration (left) time signals (right) spectra

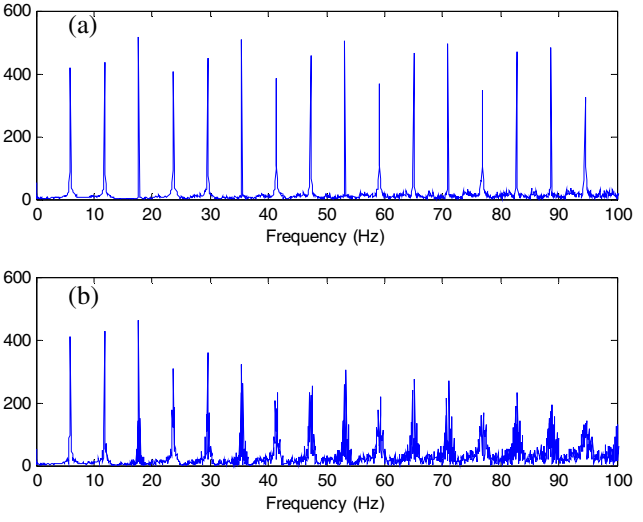

Fig. 4 Spectra of order tracked tacho signal (a) using 3rd harmonic of tacho signal (b) using 3rd harmonic of acceleration signal

Figure 4 shows the results of using the third harmonic of the two signals to perform order tracking. In both cases, the spectrum of the corrected tacho signal is shown (cf Fig. 3 upper right). The frequency axis is scaled in terms of mean speed, but it is actually an order axis. It is seen that even though the tacho signal does a better job, the correction of 4(b) is still sufficient to allow envelope analysis of

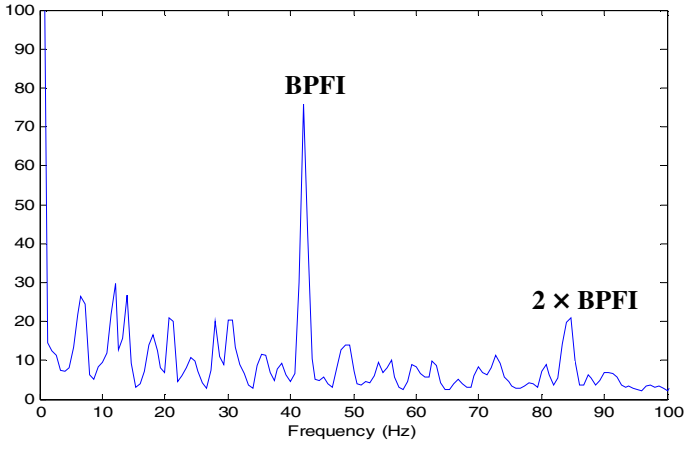

Fig. 5 Spectrum of the squared envelope of the order tracked signal showing harmonics of BPFI as well as harmonics and sidebands spaced at shaft speed 6 Hz

bearing faults, where only the first few harmonics are required. A second iteration using say the 9th harmonic of Fig. 4(b) could have been used to greatly improve the correction, and this (and further iterations) would be required for gear analysis.

Finally, Fig. 5 shows the averaged spectrum of the squared envelope of the acceleration signal, demodulated in a high frequency band which maximised the kurtosis of the transmitted signal. The frequency axis is once again based on mean rotational speed. The first two harmonics of BPFI (ballpass frequency, inner race) are seen, along with low harmonics of shaft speed 6 Hz, and sidebands spaced at this frequency around BPFI. It should be noted that in the direct FFT spectrum of the envelope, there were modulation sidebands spaced at 0.2 Hz because of the amplitude modulation seen in Fig.3.

This brings up an important point about compensating signals for changes in speed over a large range. If amplitude modulation occurs as in Fig. 3, it means that the "deterministic" components are no longer periodic in the angular domain. A synchronous average will produce a sinusoid with the average amplitude and if this is subtracted from the total signal a residual will be left. One thing that can be done to get around this problem is to make a series of averages over shorter lengths where the amplitude does not vary greatly, but this limits the number of averages in each section and thus the enhancement that can be achieved. It is the equivalent of removing the "discrete frequency" components by a sliding filter such as linear prediction or SANC (self adaptive noise cancellation) [Randall '11], where the notch filter is equally broad (with synchronous averaging the width of the notch filter is inversely proportional to the number of averages).

Before leaving the discussion of pseudo-encoder signals based on a gearmesh frequency, it is instructive to view the results in Fig. 6, based on a blind analysis of another wind turbine with squirrel cage induction generator, and synchronous speed 30 Hz [Randall et al '11]. It shows the pseudo-encoder signal corresponding to the final gearmesh frequency at about 590 Hz. It also shows the corresponding

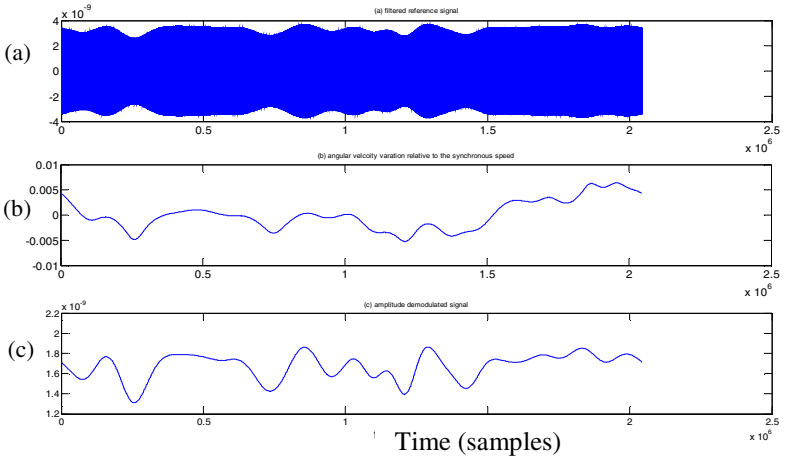

Fig. 6 Frequency and amplitude demodulation of the toothmesh signal (a) Pseudo-encoder signal (b) Frequency modulation signal (c) Amplitude modulation signal

frequency modulation signal (derivative of the phase modulation signal used for order tracking) and amplitude modulation signal. It is interesting that both amplitude and frequency modulation follow approximately the same pattern, and is explained by the fact that both give a measure of the instantaneous torque load. As mentioned above, the amplitude at gearmesh frequency is approximately proportional to tooth load because of increasing tooth deflection, while the instantaneous speed (minus synchronous speed) gives a measure of slip frequency in the generator, which is a more linear measure of torque load. It is suggested that it may be possible to use such a measure of slip frequency as a measure of load, and consequently use it to account for the effects of load on gear vibrations. This has not yet been tested. For variable speed turbines, with a doubly fed (wound rotor) generator, it would be much more difficult to measure the slip frequency, as it then depends also on the supply frequency fed to the rotor to control the speed, but it may be possible to extract this also from the vibration signal. In such a case it would no longer be possible to use the amplitude modulation as a measure of load, as it is also affected by running through resonances (see Fig. 3).

Returning to the NREL round robin data, after order tracking based on the pseudo-encoder signals, the gear signals through the whole gear train were extracted by synchronous averaging, and an example for the 1800 rpm case is shown in Fig. 7. The highest frequency signal shown is for the intermediate speed shaft (ISS), because in this case the gear ratio to the high speed shaft (HSS) was exactly 4:1 (88:22). An estimate for the vibrations of the ISS was thus obtained by averaging the four sectors of the total signal (each corresponding to one revolution of the HSS) and subtracting the repeated average from the total. The residual is shown in Fig. 8 where it is compared with the total signal, apparently dominated by the HSS

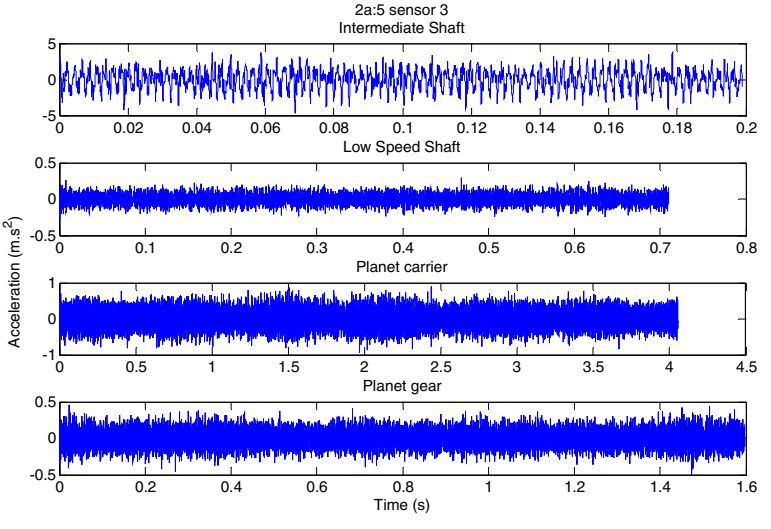

Fig. 7 Synchronously averaged signals for various gears

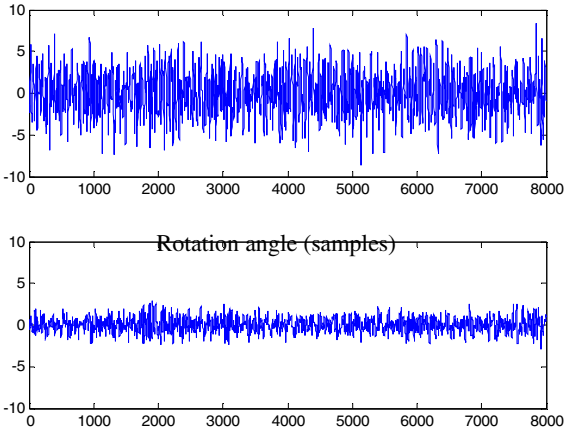

Fig. 8 Averaged signals for ISS (Upper) Original (Lower) Residual

signal. The corresponding spectra are shown in Fig. 9, where it is apparent that the HSS dominates the total signal. It is interesting that there are strong harmonics of the high speed gearmesh surrounded by sidebands from modulation at the HSS frequency, and this agrees [Randall '11] with the fact that both wear and localised faults were found on the HS pinion. On the other hand, the spectrum of the ISS had prominent components at harmonics of the secondary mesh, but without modulation sidebands, which is consistent [Randall '11] with the wear being distributed because this mesh is a "hunting tooth" ratio (23:82), one of the few in the gearbox.

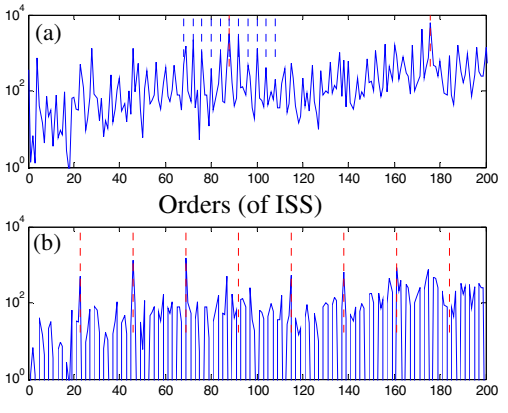

Fig. 9 Spectra of signals in Fig. 8. (a) Original, harmonic cursor at order 88 (HS mesh), sideband cursor at order 4 (HSS) (b) Residual, harmonic cursor at order 23 (IS mesh)

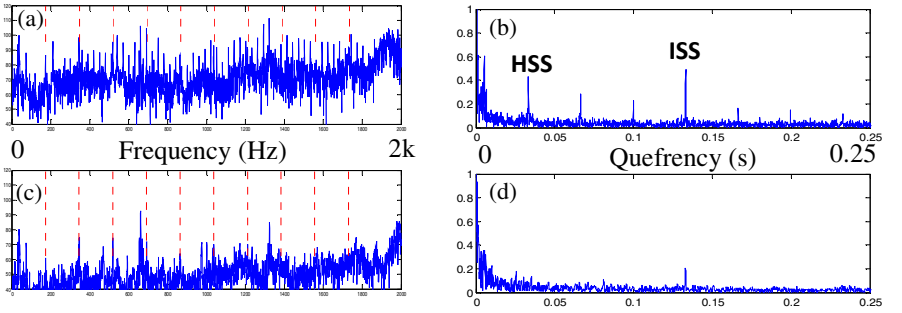

Fig. 10 Comparison of spectra and cepstra in faulty and healthy condition (a,b) Faulty (c,d) Healthy (a,c) Spectra, harmonic cursor at IS mesh (b,d) Cepstra

It is also interesting to compare the spectra in the high frequency range and the corresponding cepstra, for faulty and normal condition, which is done in Fig. 10. The increase in the harmonics of both gearmesh frequencies shows distributed wear of both gears, while the prominent sidebands in the faulty spectrum again testify to the growth of local faults on the HS pinion. Note that the corresponding rahmonics in the cepstrum are only for the faulty case. There has been some growth of harmonics/sidebands at the ISS, as testified by the corresponding rahmonics in the cepstra, but these are not so prominent in the spectra, and probably explained by non-uniformity of the wear since local faults were not discovered.

A couple of bearing faults were also successfully detected and diagnosed, although one was not. The only indication for the undetected fault was the appearance of the second harmonic of the ballpass frequency in the envelope spectrum, but this coincided with the 7th harmonic of another shaft speed, so was not considered definitive enough.

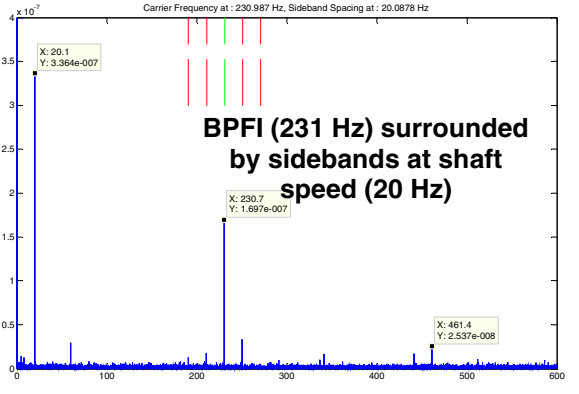

Fig. 11 Envelope spectrum for an inner race fault in a gearbox HSS bearing

Figure 11 shows the envelope spectrum of one of the detected faults, obtained from the residual signal after removing the averages for all gears, and applying cepstral pre-whitening [Randall, Sawalhi '11]. It is for one of the gearbox HSS bearings with the shaft running at 1200 rpm (20 Hz), but the fault was also detected with the shaft running at 1800 rpm. The fault in this case was presumably due to thermal distortion of the race (indicated by discolouration from overheating), since local spalls were not found by inspection.

3 Conclusion

The paper discusses a number of solutions to the problems associated with the diagnostics of wind turbine transmissions, which are subject to large variations in load and speed over relatively short periods. Ways of extracting both the speed and load information from the acceleration signal are demonstrated for certain cases. Potential but untested improvements are also suggested.

Acknowledgements. This work is partially supported by the Australian Research Council under Discovery grant DP0771204, and by Australia's Defence Science and Technology Organisation (DSTO) through the Centre of Expertise in Helicopter Structures and Diagnostics at UNSW. The authors also gratefully acknowledge the provision of signals by NREL and Mechanical Solutions Inc., NJ.

References

Coats, M.D., Randall, R.B.: Single record order-tracking. In: CM-MFPT Conference, Stratford upon Avon (June 2010)

Randall, R.B.: Vibration-based condition monitoring: industrial, aerospace and automotive applications. Wiley, Chichester (2010)

Randall, R.B., Sawalhi, N.: Editing Time Signals using the Real Cepstrum. In: MFPT Conference, Virginia Beach (May 2011)

Randall, R.B., Sawalhi, N., Marscher, W., Walter, T., Weiss, J.: Decomposition of structural vibration for wind turbine diagnosis. In: MFPT Conference, Virginia Beach (May 2011)

Urbanek, J., Barszcz, T., Sawalhi, N., Randall, R.B.: Comparison of amplitude based and phase based methods for speed tracking in application to wind turbines. Metrol. Meas Syst. XVIII 2, 295–304 (2011)

Object and Operation Factor Oriented Diagnostics

Walter Bartelmus

Wroclaw University of Technology, Vibration and Diagnostic Scientific Laboratory
<walter.bartelmus@pwr.wroc.pl>

Abstract. In the paper is presented the object and operation factors oriented diagnostic. This idea is developed by the author in resent times. In the idea detailed machine/object design properties are taken into consideration. Four groups of factors are taken into consideration namely: design, production technology, operation, and change of condition. The system is treated as a unit or divided into subunits and degradation process is included into consideration. The further interpretations of the concept of load susceptibility of machine systems is explored. The paper is a kind of shortened summary on the use of the concept of load susceptibility for machinery condition monitoring.

Keywords: diagnostic, machine, operation, load susceptibility, gearbox, wind turbine.

1 Introduction

The object and operation factor orientated diagnostics is based on factor analysis, which have influence on vibration signals. These factors are divided into four groups namely: design, production technology, operation and change of condition as it is given in Fig.1.

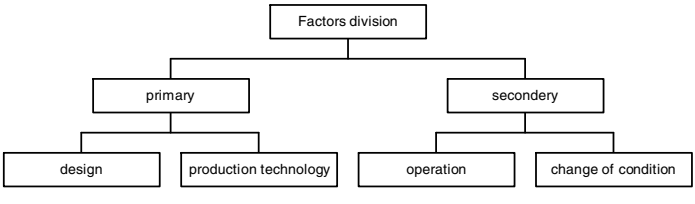

Fig. 1 Introductory division of factors influencing vibration signals

As one can see from the Fig.1 the factors can be also classified as primary and secondary. The object and operation factors orientated diagnostic should give the

solution how to make diagnostic when machines work under non-stationary operations. Such machines would include: wind turbines, helicopters, mining and civil engineering machinery. Many established machine condition monitoring methods are geared to stationary operations. Considering the influence of real fast varying load and rotation to generation of vibration signals there is a need to develop ways of signal analysis which take into consideration that machine is a unity of elements not a system of separated elements (bearings, gears, shafts) and not degradation of a specific element or fault. The developed method should solve the problem of condition monitoring of machinery under varying operation and under the degradation process. As an example, the gear tooth cracking could be a last agent in gear degradation process, and treating it as the first agent in the gear degradation process is only a special case of such process. The interferences existing in real industrial conditions will affect the signal quality. Needed are appropriate condition monitoring and diagnostic systems applicable to the automated diagnostic process.

The issue of the influence of varying load on vibration signals the author has presented for the first time in (Bartelmus 1992) broader description is given in (Bartelmus 2006).

The issues of influence varying load to vibration signals is also noticed by the others authors in papers (Bonnardot et al. 2005); (Baydar and Ball 2000); (Zhan et al 2005); (Stander et al. 2002); (Stander and Heyns 2005). However the issue is not seen in broader contacts as influence of mutual interaction between machine elements, and treating the machine or its subsystem as a unity of elements. The scenario or scenarios of degradation process are not considered or is presumed that only one element of the system change its condition - degrades. To solve the problem of influence of load to vibration signal the author is presented several publications on gearbox mathematical modeling and computer simulations (Bartelmus 1999); (Bartelmus 2000); (Bartelmus 2001); (Bartelmus 2008); and on the new term as the load susceptibility (Bartelmus and Zimroz 2009); (Bartelmus and Zimroz 2009 a); (Bartelmus and Zimroz 2009 b); (Bartelmus and Zimroz 2009 c); (Bartelmus and Zimroz d) which is the new measure of machine condition.

2 Factors Influencing Vibration Signal

Better understanding of machine vibration signals is connected with deeper division of factors, which have influence to vibration signals as it is given in Fig.2 and 3. It obvious that more detailed division factors influencing vibration signals and better understanding of their influence to the signals gives better diagnostic that means better fault identification, understanding of fault influence to the other elements of the diagnosed system, better prognosis would be obtained.

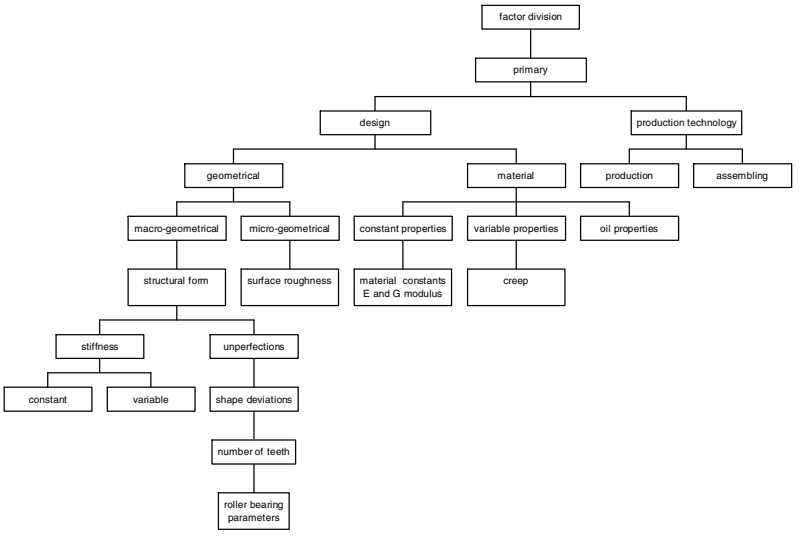

Fig. 2 Division of design and production technology factors having influence to vibration signal

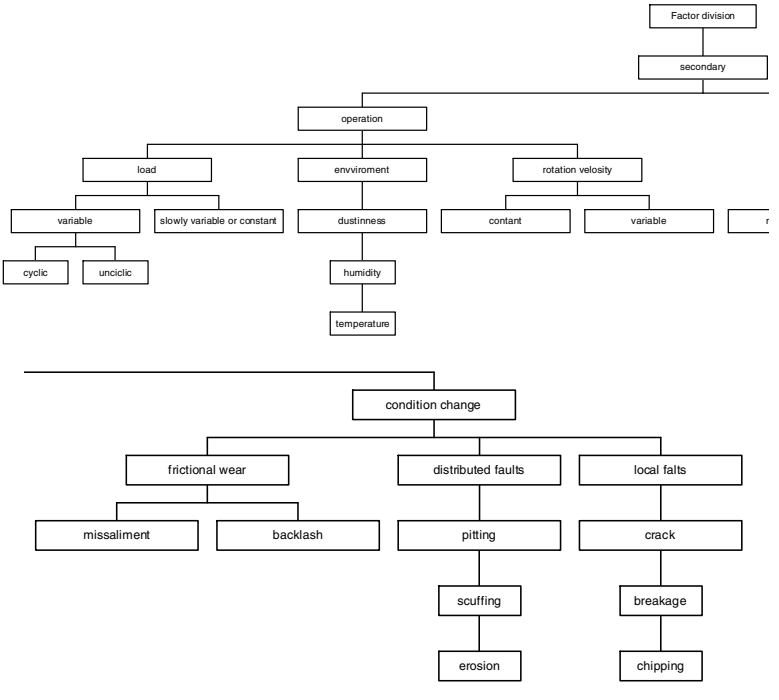

Fig. 3 Division of operation and change of condition factors influencing vibration signal

3 Influence of Design Factors – Object Orientation

According to (Bartelmus and Zimroz 2011) the gearbox systems can be divided as: compound and complex gearboxes, and multifunction gearboxes. Fig.4 a) and b) shows the schemes of complex system gearboxes which can be reduced into compound gear systems.

a) b)

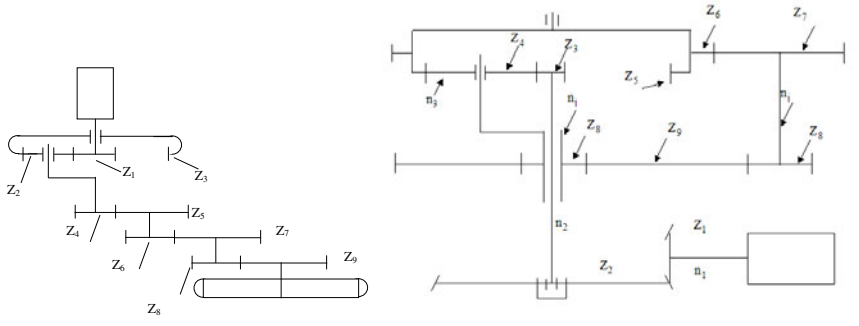

Fig. 4 a) and b) Schemes of complex system of gearboxes which can be reduced into compound gear systems

Using the principals of mechanics as it is given in (Bartelmus and Zimroz 2011) the ratio of planetary gearbox Fig.4a) can be presented by the statement

$$u_p = 1 + \frac{z_3}{z_1} \tag{1}$$

Now the system Fig.4 can be treated as compound system with a ratio

$$u_c = u_p u_{c1} u_{c2} u_{c3} \tag{2}$$

The system presented in Fig.4b may be noticed as a "more complex", for which the ratio of a planetary gearbox (Bartelmus and Zimroz 2011) is given

$$u_p = 1 + \frac{z_5}{z_3} + \frac{z_5 z_7}{z_3 z_6} \tag{3}$$

and its ratio for compound system is

$$u_c = u_b u_p u_c \tag{4}$$

There are also multifunction gearboxes (Bartelmus 2011) with complex gearboxes as it is in Fig.5.

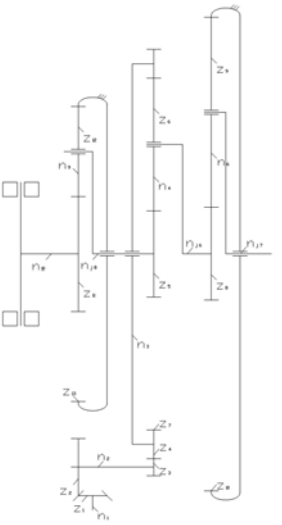

Fig. 5 Scheme of driving system with multifuction gearbox for driving bucked wheel of bucked wheel excavator with overload mechanism

The planetary gearboxes with ratios at a first function are as follow

$$u_{p1} = 1 + \frac{z_5}{z_7} \qquad u_{p2} = 1 + \frac{z_{10}}{z_8} \ , \tag{5}$$

and the total ratio for the compound system is

$$u_t = u_b u_{cy} u_{p1} u_{p2} = \frac{z_2}{z_1}\frac{z_4}{z_3}(1 + \frac{z_5}{z_7})(1 + \frac{z_{10}}{z_8}) \tag{6}.$$

Second function

In the case of overloading, where the bucket wheel is stopped and $n_{j5} = 0$ so the planetary gearbox is redused to the cylindrical stage with an idle gear or third wheel z_6 and the ratio of the fomer planetary gear (gears z_5, z_6, z_7) is now

$$u_{cy2} = \frac{z_5}{z_7} \tag{7}$$

and transmited moment from the electric motor equels to M_b ,which is a fixed friction moment of the overload mechanism; a brake.

In this case power is transmited by a planetary gearbox with (gears z_{11}, z_{12}, z_{13}), which works as multiplier with a ratio

$$u_{p3} = \frac{z_{11}}{z_{11} + z_{13}}. \tag{8}$$

And now one may treat the system as a compound gearbox where the total ratio of the gearbox from the motor to the brake is

$$u_t = u_b u_{cy} u_{cy2} u_{p3}. \tag{9}$$

4 Interaction of Gearbox Elements

Next step in the object and operation factor orientated diagnostics is take in consideration mutual interaction between drive system elements as it is given in Fig.6 and 7.

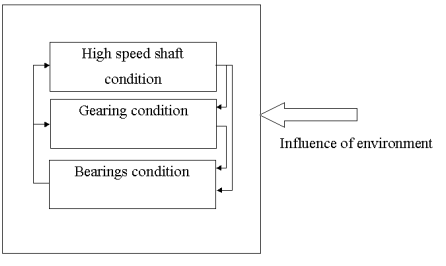

Fig. 6 Interaction of gearbox elements and influence of environment (Bartelmus 1992)

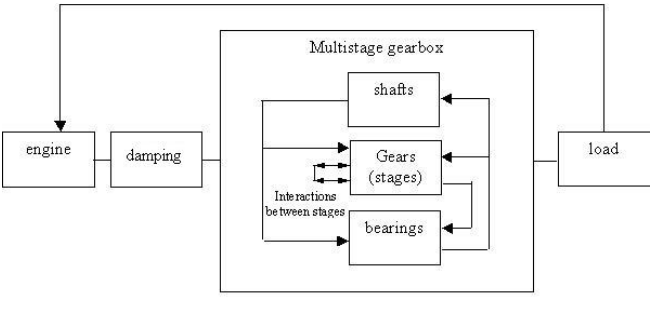

Fig. 7 The interaction of the elements of the whole system (Bartelmus and Zimroz 2009b)

5 Planetary Gearbox Condition Monitoring

In a paper (Bartelmus and Zimroz 2009c) the term load susceptibility is introduced. The load susceptibility is given by the regression characteristics in

Fig.8b) as diagnostic features for planetary gearbox as a function of rotation speed RPM; for a gearbox in good ("o" dots) and bad condition ("x" dots) (Bartelmus and Zimroz 2009c). In this case presentation of susceptibility characteristics an electric motor a linear relationship between the transmitted moment a rotation speed is used. It means that one may use the load susceptibility characteristics as the function of a load or function of a rotation speed RPM as it is given in Fig.8b). In the presented cases of the load susceptibilities the characteristics are interpreted as follows. The case for a good condition of gearbox shows that planetary gearbox behaves as a linear system under increasing load, that means with increasing load, the system deflection increases. In the case of bad condition as result of frictional wear of bearings the gear mesh under the condition of a shaft misalignment what gives a linear increase of the gear cooperation error and linear increase of inter teeth force, which cause linear increase of a vibration acceleration signal as it is presented by linear regression line Fig.8b in a case of the bad gear condition. Fig.8b) also shows very good separation of data for the good and bad condition. Better than is given in Fig.8a when the data distribution functions overlap each other. In (Bartelmus and Zimroz 2010) robust mechatronic condition monitoring and diagnostic method for gearboxes is given.

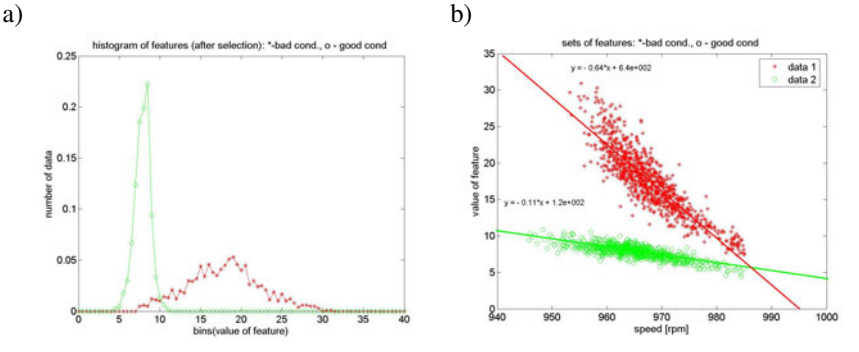

Fig. 8a) Data distribution of measured diagnostic parameters b) Load susceptibility/yielding characteristic as diagnostic features for planetary gearbox as a function of rotation speed RPM; for a gearbox in good ("o" dots) and bad condition ("x" dots) (Bartelmus and Zimroz 2009c)

6 Load Susceptibility - Computer Simulations

For better understanding of the load susceptibilities characteristics computer simulations have been done. Fig.9 shows influence of increase meshing errors to load susceptibility/yielding characteristics. Fig.9 shows linear relations. Fig.9 also shows that with increase of cooperation errors with equal steps of 5 μm there is also an equal step increase of a vibration signal with equal steps of 30 m/s^2. It proves the linear increase of gear cooperation error as it is given in Fig.8b); bad condition. Further interpretations are given in (Bartelmus et al. 2010).

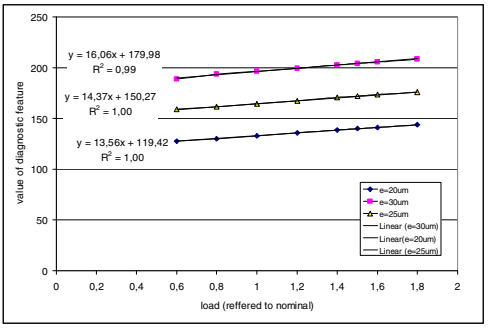

Fig. 9 Influence of increased gear errors to load susceptibility/yielding characteristics

Taking into consideration another diagnostic parameter for condition monitoring and diagnostics, namely kurtosis, further computer simulations has been done. The kurtosis has been used for gear cracked tooth identification and influence of load on susceptibility/yielding characteristics, the results are given in Fig.10.

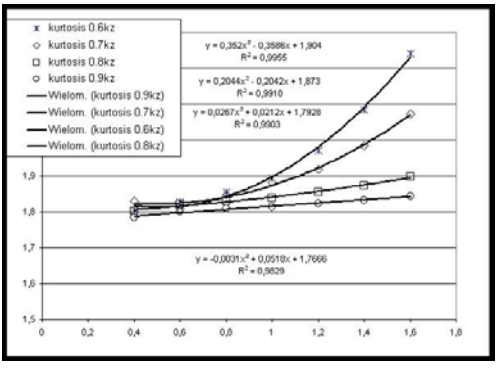

Fig. 10 Influence of increased gear cracked tooth to load susceptibility/yielding characteristics (Bartelmus and Zimroz 2009a)

The load susceptibility characteristics can be used for the robust mechatronic condition monitoring and diagnostic method for gearboxes as is given in (Bartelmus and Zimroz 2010).

7 Wind Turbine Condition Monitoring

In papers (Zimroz et al. 2011a); (Zimroz et al. 2011b) data analysis. which comes from vibration measurements of wind turbines are processed. For data processing

data distributions and load susceptibility characteristics are given as it is shown in Fig.11. If one compares that two ways of presentation. The way of data separation by the load susceptibility characteristic gives better data separation.

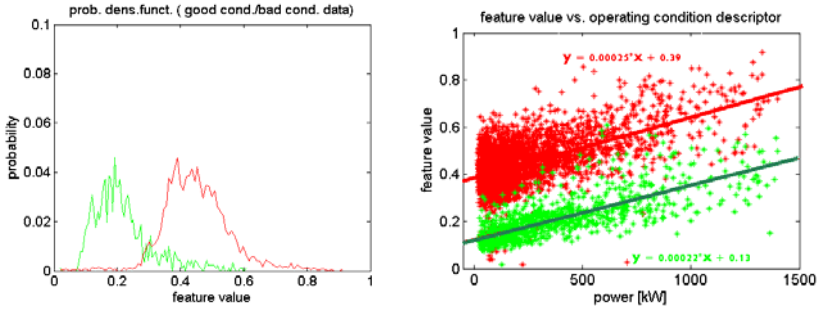

Fig. 11 a) Data distributions b) load susceptibility for data from wind turbine main bearing for good and bad condition

8 Conclusions

The paper gives a discussion on a new way of a diagnostic data processing. The presented way of data processing is the part of new way of diagnostic which is based on the object and operation factors oriented analysis. The new way of data processing leads to presentation of data in the form of load susceptibility characteristics. The presented paper shows two types of susceptibility characteristics connected with type of a fault. The linear system shows its linearity properties that with increase in the load the mean value of generated vibration given by acceleration signals increases linearly. It is given in figures: 8b) (when object is in good condition), 9, 11b (object in good condition). In Figs. 9 and 11b if object condition is changed one can noticed almost parallel shift of a susceptibility characteristic. The shift is proportional to the value of a fault. As it is given in Fig.8b, 9, 11b using the load susceptibility characteristic gives better separation in comparing with presenting them in terms of data distributions. Second type of a susceptibility characteristic is presented in Fig.8b (when object is in bad condition) but with increase of the load the value of the fault increase linearly. The load susceptibility characteristic when for condition assessment is used kurtosis shows no linearity as is given in Fig.10. The use of susceptibility characteristics and its interpretation comes from the result of a study on influence: design, production technology, operation and change of condition factors. Further examples of using the susceptibility characteristics are given in the cited papers and will be also given during the paper presentation.

Acknowledgment. This paper was financially supported by Polish State Committee for Scientific Research 2010-2013 as research project NN 504147838.

References

Bartelmus, W.: Vibration condition monitoring of gearboxes. Machine Vibration, s.178–s.189 (1992)

Bonnardot, F., El Badaoui, M., Randall, R.B., Daniere, J., Guillet, F.: Use of The Acceleration Signal of A Gearbox In Order To Perform Angular Resampling (With Limited Speed Fluctuation). Mechanical Systems and Signal Processing 19, 766–785 (2005)

Baydar, N., Ball, A.: Detection of gear deterioration under varying load conditions by using the instantaneous power spectrum. Mechanical Systems and Signal Processing 14, 907–921 (2000)

Zhan, Y., Makis, Y., Jardine, A.K.S.: Adaptive State Detection of Gearboxes Under Varying Load Conditions Based On Parametric Modelling Mechanical. Systems and Signal Processing (2004)

Stander, C.J., Heyns, P.S., Schoombie, W.: Using Vibration Monitoring For Local Fault Detection on Gears Operating Under Fluctuating Load Conditions. Mechanical Systems and Signal Processing 16(6), 1005–1024 (2002)

Stander, C.J., Heyns, P.S.: Instantaneous Angular Speed Monitoring Of Gearboxes Under Non-Cyclic Stationary Load Conditions. Mechanical Systems and Signal Processing 19, 817–835 (2005)

Bartelmus, W.: Transformation of gear inter teeth forces into acceleration and velocity. International Journal of Rotating Machinery 5(3), s.203–s.218 (1999)

Bartelmus, W.: Mathematical Modelling of Gearbox Vibration for Fault Diagnosis. International Journal of COMADEM 3(4) (2000)

Bartelmus, W.: Mathematical Modelling and Computer Simulations as an Aid to Gearbox Diagnostics. Mechanical Systems and Signal Processing 15(5), s.855–s.871 (2001)

Bartelmus, W.: Root cause and vibration signal analysis for gearbox condition monitoring. Insight 50(4) (April 2008)

Bartelmus, W., Zimroz, R.: Mathematical modelling and computer simulation for local fault detection using new diagnostic feature. In: 80" Annual Meeting of the International Association of Applied Mathematics (GAMM), Gdańsk, February 9-13 (2009a)

Bartelmus, W., Zimroz, R.: Vibration condition monitoring of planetary gearbox under varying external load. Mechanical Systems and Signal Processing 23, 246–257 (2009b)

Bartelmus, W., Zimroz, R.: A new feature for monitoring the condition of gearboxes in non-stationary operation conditions. Mechanical Systems and Signal Processing 23, 1528–1534 (2009c)

Zimroz, R., Bartelmus, W.: Gearbox condition estimation using cyclo-stationary properties of vibration signal. Key Engineering Materials 413-414, 471–478 (2009d)

Bartelmus, W., Chaari, F., Zimroz, R., Haddar, M.: Modelling of gearbox dynamics under time varying non-stationary operation for distributed fault detection and diagnosis. European Journal of Mechanics - A/Solids 29, 637–646 (2010)

Bartelmus, W., Zimroz, R.: Vibration spectra characteristics frequencies for condition monitoring of mine machinery compound and complex gearboxes. In: Scientific Papers of the Institute of Mining of the Wroclaw University of Technology, Mining and geology XVI, Wroclaw, pp. 17–34 (2011a)

Bartelmus, W.: Fundamentals for condition monitoring and diagnostics for driving bucket wheel system with overload mechanism of bucket wheel excavator. In: Scientific Papers of the Institute of Mining of the Wroclaw University of Technology, Mining and Geology XVI, Wroclaw, pp. 5–16 (2011b)

Bartelmus, W., Zimroz, R.: Robust mechatronic condition monitoring and diagnostic method for gearboxes. In: Prace Naukowe Instytutu Górnictwa Politechniki Wrocławskiej Górnictwo i geologia XIV Wrocław, pp. 5–14 (2010)

Zimroz, R., Bartelmus, W., Barszcz, T., Urbanek, J.: Wind turbine main bearing diagnosis - a proposal of data processing and decision making procedure under non stationary load condition. Key Engineering Materials (2011a) (in print)

Zimroz, R., Bartelmus, W., Barszcz, T., Urbanek, J.: Statistical data processing for wind turbine generator bearing diagnostics. Key Engineering Materials (2011b) (in print)

Bartelmus, W.: Condition monitoring of open cast mining machinery. Oficyna Wydawnicza Politechniki Wrocławskiej Wrocław (2006)

Rényi Entropy Based Statistical Complexity Analysis for Gear Fault Prognostics under Variable Load

Pavle Boškoski and Đani Juričić

Jožef Stefan Institute
Jamova 39, 1000 Ljubljana Slovenia
pavle.boskoski@ijs.si

Abstract. In this paper we propose an approach for gear fault prognostics in presumably non-stationary and unknown operating conditions. The approach monitors the evolution of the statistical complexity of the generated vibrations envelope vis-à-vis its Rényi entropy. The statistical complexity is obtained through the wavelet coefficients calculated from the generated vibrations. Such an approach allows seamless estimation of the remaining useful life of the monitored drive without any prior information about the operating conditions and no a priori data regarding the physical characteristics of the monitored drive. The effectiveness of the approach was evaluated on experiments monitoring natural gear fault progress under variable load.

1 Introduction

Majority of the condition monitoring approaches for mechanical drives are based on analysis of vibration signals generated under stationary and known operating conditions. For such cases any change in the vibrational patterns can be unambiguously associated with a change in the condition of the monitored drive. However, such conditions are rarely met and in most cases mechanical drives are subjected to variable load and speed. Consequently, the link between the condition of the mechanical drive and the changes in the generated vibrational patterns becomes obscured. Therefore, reliable condition monitoring and prognostics methods are of significant practical merit.

Usually, condition monitoring of mechanical drives under variable operating conditions is performed by incorporating precise information about the operating conditions in the calculated feature set [18, 23, 21] as well as modelling links between the feature values and the operating conditions [3]. Additionally, there are methods that exploit some statistical properties of the acquired vibrations like instantaneous power spectrum [5, 8, 22].

Conversely, the problems of estimation of the remaining useful life of mechanical drives under variable operating conditions are left largely neglected. There are a

few examples addressing the problems of prognostics under such conditions [9,7]. Although the proposed approaches for condition monitoring and prognostics and health management give satisfactory results they heavily depend on accurate measurements of the current operating conditions.

For the purpose of prognostics, in this paper we propose an approach based on the analysis of the statistical complexity of signals [16,20], a concept readily applied in the analysis of EEG signals [14]. The idea exploits the fact that the presence of faults is directly reflected as an increase of the number of random components comprising the overall vibrations, hence increasing its statistical complexity. Therefore by tracking the the evolution of the statistical complexity of the envelope of the generated vibrations in respect with the changes of its Rényi entropy, one can seamlessly perform an estimation of the remaining useful life of the monitored drive.

We show that such an approach is robust to changes in the operating conditions and in the same time sufficiently sensitive to changes in the drive's condition. Additionally, the calculation process requires no prior information about the operating conditions and no previous knowledge about the physical characteristics of the monitored drive. The effectiveness of the proposed approach was evaluated on two experiments monitoring natural gear fault evolution on a one-stage gearbox.

2 Statistical Complexity

The definitions of the statistical complexity of a signal vary depending of the context, such as data compression, computational algorithms and predictability. Generally, the statistical complexity of a signal is linked with the complexity of the patterns that occur in it. There are two classes of signals with minimal complexity: periodic and purely random signals [1]. The former one, has simple pattern that reoccurs with specified period. The latter, has no recognisable patterns at all, and despite the erratic nature it has practically no complexity. Consequently, the "complex" signals should be located somewhere in between. A typical candidates are signals generated by a system with chaotic behaviour. Despite the deterministic nature, the generated signals contain sufficiently complicated patterns that are difficult to predict.

In this paper the statistical complexity is assessed through the information carried by the signal [16,12]. This approach provides a link between the entropy of the random source that generates the signal and the distance of the probability distribution of the generating source p to the uniform distribution p_e. Therefore, we will first revisit the concepts of entropy and the concept of distance between two probability distributions.

In our analysis we selected the Rényi entropy for discrete probability distribution p defined on a finite set $\mathscr{D}$ [19]:

$$H_\alpha(P) = \frac{1}{1-\alpha} \ln \sum_{x \in \mathscr{D}} p^\alpha(x), \tag{1}$$

and the Jensen-Rényi divergence [4]:

$$D_{H_\alpha^w}(p_1,\cdots,p_n) = H_\alpha\left(\sum_{i=1}^{n} w_i p_i\right) - \sum_{i=1}^{n} w_i H_\alpha(p_i), \tag{2}$$

where $w_i \geq 0$ and $\sum_{i=1}^{n} w_i = 1$. The values of the exponent α governs the sensitivity of these two quantifiers to particular segments of the PDF, i.e. it specifies the relative importance of small values versus large values of the probability mass [10].

Based on (1) and (2), the statistical complexity of a signal with PDF p is defined as [16]:

$$C(p) = Q_0 D_{H_\alpha^w}(p, p_e) H_\alpha(p), \tag{3}$$

where p_e is the uniform distribution and Q_0 is a normalisation constant so that $Q_0 D_{H_\alpha^w}(p, p_e) \in [0,1]$. The product (3) is in accordance with the initial idea that signals with perfect order $H(p) = 0$ and maximal disorder $D(p, p_e) = 0$ have the lowest complexity.

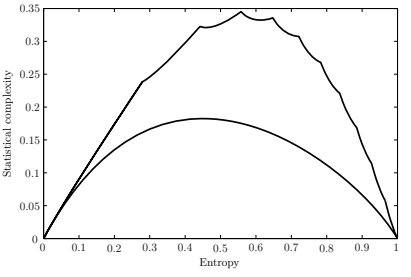

Fig. 1 Signal's statistical complexity area

For the concept of prognostics, the time evolution of the statistical complexity (3) is of great importance. The concept of time is present in (3) indirectly through the entropy $H(p)$ by using the fact that the system's entropy increases in time. Therefore, the statistical complexity $C(p)$ is usually plotted versus the entropy $H(p)$ [16]. This plot always covers a specific area depending on the number of bins used for the calculation of the probability p, as shown in Figure 1. The pre-defined shape of the plot outlines the possible time evolution of the signal's complexity. By trending its evolution, one can easily estimate the time moment when the complexity will reach the apex of the plot.

3 Complexity of Gear Vibrations

Vibrations produced by healthy gears are dominated by components caused by the alteration of the mesh contact stiffness as the number of gear teeth in contact varies [11]. The effect of gear faults is expressed as localised change in the tooth stiffness profile, which leads to the occurrence of additional modulation components around

the mesh frequency and its higher harmonics. These modulations contain all the necessary diagnostic information [17].

In cases when mechanical drive operates under variable operating conditions, the generated vibration signals can be elegantly analysed using the concept of non-stationary evolutionary processes [15]. Such a random process can be expressed in the generalised form:

$$y(t) = \int_{-\infty}^{\infty} A(\omega,t)e^{j\omega t}dZ(\omega), \tag{4}$$

where $A(\omega,t)$ is a slow varying time and frequency dependent modulating function, and $Z(\omega)$ is a complex random process. For the case of gear vibrations, variations in the operating conditions as well as presence of faults will alter the shape and, in the same time, the statistical properties of the envelope $A(\omega,t)$. However, the changes caused by faults are shown to be far more significant than the ones caused by variations in the operating conditions [5]. Herewith, we can conclude that by analysing the statistical complexity of the envelope $A(\omega,t)$ one can estimate the remaining useful life of the monitored drive.

4 Wavelet Based Calculation of the Statistical Complexity

According to (3), the first step in the calculation of the statistical complexity is the estimation of the PDF of the envelope $A(\omega,t)$ from (4). Due to the link between the signal's envelope $A(\omega,t)$ and its instantaneous power [2], in this approach we estimated the underlying PDF through the energy distribution of the wavelet packet coefficients.

Therefore, we used the so-called wavelet packet transform (WPT) [13]. The structure of WPT is usually described by a binary tree structure, as shown in Figure 2. WPT allows arbitrary partition of the time-frequency plane. The wavelet coefficients in the set of terminal nodes contain all information regarding the analysed signal. The analysis of the envelope $A(\omega,t)$ was performed by analysing the signal's energy within each terminal node.

Each terminal node (d,n) contains N_d wavelet coefficients $P_d^n(k)$, where $k = 0,\ldots,N_d-1$ and the number N_d depends on the length of the signal and the depth d of the WPT tree. Using these coeficients, the portion of the signal's energy $E_{d,n}$ contained within one node (d,n) reads [6]:

$$E_{d,n} = \sum_{k=0}^{N_d-1} \|P_d^n(k)\|^2 \tag{5}$$

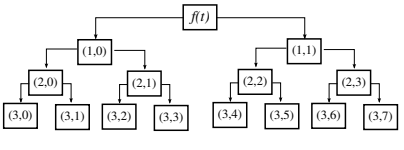

Fig. 2 Example of a full WPT tree with depth $D_0 = 3$

The relative energy that each wavelet coefficient carries, for each terminal node (d,n) is:

$$p_{d,n}(k) = \frac{\left\|P_d^n(k)\right\|^2}{E_{d,n}}, k = 0, \cdots, N_d - 1. \tag{6}$$

The probability distribution (6) is directly related to the PDF of the signal's envelope. Therefore, by introducing (6) into (3) one can calculate the statistical complexity of the signals envelope.

5 Monitoring the Natural Gear Surface Fault Progress in One-Stage Gearbox

The concept of statistical complexity was applied on two experimental runs using same type of gears in a one-stage gearbox. The first experiment was conducted under constant operating conditions, solely for the purpose of obtaining a reference behaviour. The second experiment was conducted under variable load. For the calculation of the probability density (6) we used $db10$ mother wavelet and wavelet packet tree with depth 5. For the purpose of prognostics the statistical complexity (3) was plotted vis-à-vis the Rényi entropy (1) as in Figure 1.

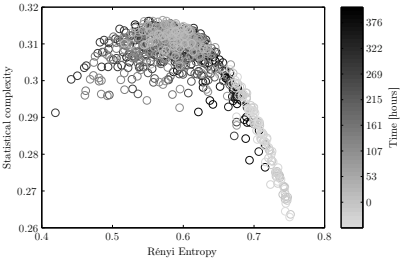

Fig. 3 α-Jensen divergence vs. Rényi Entropy

Experiment #1: Constant operating conditions

The evolution of the statistical complexity for vibration signals from the first experiment is shown in Figure 3. Several observations can be made. Firstly, the shape of the plot, as expected, is quite similar to the one shown in Figure 1. Furthermore, at the beginning of the experiment, the statistical complexity is the lowest and the entropy is the highest. This is a result of the almost periodic patterns present in the vibration signal. Namely, as the gears are fault-free, the generated vibrations contain only components of the meshing frequencies. As the time evolves, the complexity of the signal increases. However after reaching the apex point, the values of the statistical complexity tend to "oscillate" around the maximal point. The decrease of

the statistical complexity occurs when the surface gear faults spread across multiple teeth. Consequently, the modulation components decrease. From the complexity point of view, such a signal is "similar" with the vibration signals from the beginning of the experiment, hence the decrease of the statistical complexity.

Experiment #2: Variable load

The second experiment was performed by using the variable load profile shown in Figure 4. Besides the direct and immediate effect of load variations on the machine vibration, load variations also cause changes in the operating temperature, as shown with the second line in Figure 4. Despite the obvious temperature influence on the generated vibrations, the information about the temperature is rarely taken into account when performing fault detection.

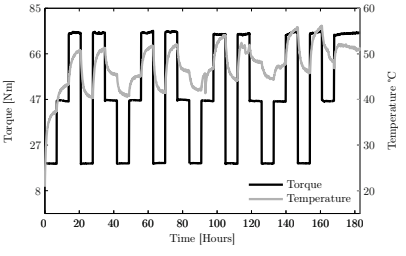

Fig. 4 Torque profile for Experiment #2

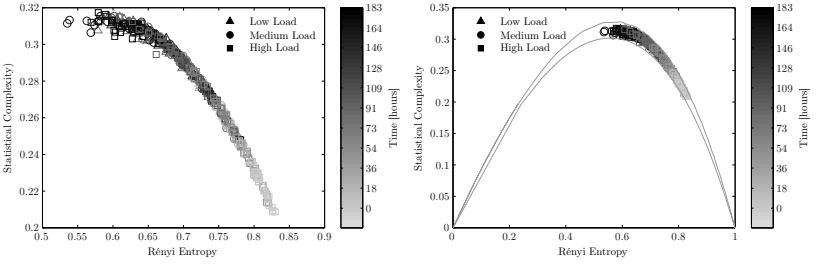

Fig. 5 α-Jensen divergence vs. Rényi Entropy

The statistical complexity plot is shown in Figure 5a. Similarly like in the first experiment, at the beginning the vibration signals exhibit the lowest complexity. As the time progresses the complexity gradually increases regardless of the variations in the load. Unlike the first experiment, the second experiment was stopped around the time moment when the complexity reached its maximum. At this point, pitting fault was clearly visible on several teeth.

The calculation the the PDF (6) was done using 20 bins. The theoretical limits for the statistical complexity of a PDF with 20 bins is shown in Figure 5b. In can be noticed that the experimental results are fully contained within these limits.

6 Conclusions

The calculation of the statistical complexity of the vibrations envelope can serve as an indicator of the overall health of a mechanical drive. In addition, we showed that the plot of the statistical complexity vs. entropy provides a way of estimating the remaining useful life of the monitored drive regardless of the operating conditions.

The application of the statistical complexity has two main advantages. Firstly, the statistical complexity vs. entropy plots have theoretically pre-defined trajectory of evolution. Consequently, the prognostics algorithm reduces to a simple fitting problem, thus the estimation of the remaining useful life is directly connected to the estimation when the statistical complexity values will reach the maximal point in this plot. Secondly, the calculation and the behaviour of the statistical complexity does not depend on the variations in the operating conditions and it required no a priori information regarding the physical characteristics of the monitored drive.

Acknowledgements. We like to acknowledge the support of the Slovenian Research Agency through Research Programme P2-0001 and the Competence Centre for Advanced Control Technologies. The Competence Centre for Advanced Control Technologies is partly financed by the Republic of Slovenia, Ministry of Higher Education, Science and Technology and European Union (EU)-European Regional Development Fund.

References

1. Adami, C.: What is complexity? Bio Essays 24(12), 1085–1094 (2002)
2. Antoni, J.: Cyclostationarity by examples. Mechanical Systems and Signal Processing 23, 987–1036 (2009)
3. Bartelmus, W., Zimroz, R.: A new feature for monitoring the condition of gearboxes in non–stationary operating conditions. Mechanical Systems and Signal Processing 23(5), 1528–1534 (2009)
4. Basseville, M.: Divergence measures for statistical data processing. Tech. rep., IRISA (2010)
5. Baydar, N., Ball, A.: Detection of gear deterioration under variying load conditions using the instantaneous power spectrum. Mechanical Systems and Signal Processing 14(6), 907–921 (2000)
6. Blanco, S., Figliola, A., Quiroga, R.Q., Rosso, O.A., Serrano, E.: Time-frequency analysis of electroencephalogram series. iii. wavelet packets and information cost function. Phys. Rev. E 57(1), 932–940 (1998)
7. Bole, B.M., Brown, D.W., Pei, H., Goebel, K., Vachtsevanos, L.T.G.: Fault adaptive control of overactuated systems using prognostic estimation. In: Annual Conference of the Prognostics and Health Management Society, Portland OR, USA (2010)
8. Chen, P., Taniguchi, M., Toyota, T., He, Z.: Fault diagnosis method for machinery in unsteady operating condition by instantaneous power spectrum and genetic programming. Mechanical Systems and Signal Processing 19(1), 175–194 (2005)

9. Gašperin, M., Boškoski, P., Juričić, Đ.: Model-based prognostics under non-stationary operating conditions. In: Annual Conference of the Prognostics and Health Management Society (2011)
10. Hero, A.O., Ma, B., Michel, O., Gorman, J.: Alpha-divergence for classification, indexing and retrieval. Tech. Rep. CSPL-328, Communications and Signal Processing Laboratory. The University of Michigan (2002)
11. Howard, I., Jia, S., Wang, J.: The dynamic modelling of a spur gear in mesh including friction and crack. Mechanical Systems and Signal Processing 15, 831–853 (2001)
12. Kowalski, A.M., Martin, M.T., Plastino, A., Rosso, O.A., Casas, M.: Distances in probability space and the statistical complexity setup. Entropy 13(6), 1055–1075 (2011)
13. Mallat, S.: A Wavelet Tour of Signal Processing, 3rd edn. Academic Press, Burlington (2008)
14. Martin, M., Plastino, A., Rosso, O.: Generalized statistical complexity measures: Geometrical and analytical properties. Physica A 369(2), 439–462 (2006)
15. Priestley, M.: Spectral Analyses and Time Series. Academic Press, London (1981)
16. López-Ruiz, R., Mancini, H.L., X.C.: A statistical measure of complexity. Physics Letters A 209, 321–326 (1995)
17. Randall, R.: A new method of modeling gear faults. Journal of Mechanical Design 104, 259–267 (1982)
18. Randall, R.B.: Vibration-based condition monitoring: industrial, aerospace and automotive applications. John Wiley & Sons, West Sussex (2011)
19. Rényi, A.: On measures of information and entropy. In: 4th Berkeley Symposium on Mathematics, Statistics and Probability (1960)
20. Rosso, O., Martin, M., Figliola, A., Keller, K., Plastino, A.: EEG analysis using wavelet-based information tools. Journal of Neuroscience Methods 153, 163–182 (2006)
21. Stander, C., Heyns, P.: Instantaneous angular speed monitoring of gearboxes under non-cyclic stationary load conditions. Mechanical Systems and Signal Processing 19(4), 817–835 (2005)
22. Wang, X., Makis, V., Yang, M.: A wavelet approach to fault diagnosis of a gearbox under varying load conditions. Journal of Sound and Vibration 329(9), 1570–1585 (2010)
23. Zhan, Y., Makis, V., Jardine, A.K.: Adaptive state detection of gearboxes under varying load conditions based on parametric modelling. Mechanical Systems and Signal Processing 20(1), 188–221 (2006)

Non Linear Transient Response of a Flexible Shaft Controlled by Electro-rheological Hydrostatic Squeeze Film Dampers

Ahmed Bouzidane[1] and Marc Thomas[2]

[1] Research Laboratory of Industrial Technologies,
Department of Mechanical Engineering,
Ibn Khaldun's University of Tiaret, BP 78 City/ Province: Tiaret,(14000), Algeria
ahmed_bouzidane@mail.univ-tiaret.dz
[2] Department of Mechanical Engineering, École de technologie supérieure,
1100, Notre-Dame Street West, Montreal, Quebec, (H3C 1K3), Canada
marc.thomas@etsmtl.ca

Abstract. The aim of this research is to study the non-linear dynamic behaviour of a flexible shaft supported by hydrostatic squeeze film dampers which are filled with a Negative Electro-Rheological fluid (NERF). In order to study the effect of the electro-rheological fluid on the dynamic behaviour of a flexible shaft, a non linear model of a hydrostatic squeeze film damper has been developed and the results are discussed and compared with the linear model which is restricted to only small vibrations around the equilibrium position. A new control system is proposed to reduce the transient response of the shaft, by applying an electric field in order to modify the viscosity of the NER fluid in the hydrostatic journal, and thus control its damping. The results of this control show that it is possible to effectively monitor the electric field and the viscosity of the fluid inside the hydrostatic squeeze film dampers (HSFD) for controlling flexible shaft vibration.

Keywords: Electro-rheological fluid, journal hydrostatic bearing, vibration control, Squeeze film dampers.

1 Introduction

The tendency towards higher speeds in turbo machinery has necessitated the creation of more flexible shafts, which run at angular speeds above several of their natural frequencies (Baaklini et al, 2002). For this reason, passive squeeze film dampers (SFD) are often used in high speed rotors for aircraft engines. As an effective vibration attenuation device, controllable SFDs working in an active or semi-active manner were recently studied and related research works are still in progress, including those focusing on semi-active-type SFDs using a controllable fluid as the working fluid. An ER fluid is a suspension of micron-sized polarizable particles dispersed in a dielectric liquid. Its rheological properties change when an

electric field is applied. The apparent viscosity of this controllable fluid varies in response to the applied field. Unfortunately, such industrial devices are not yet available on a large scale. In recent years, a few research reports have been published presenting an approach for controlling SFDs using the viscosity change of an ER fluid. Lee et al (2000) presented the vibration attenuation capacities of a pressurized, sealed, ER-SFD supported rotor. Guozhi et al (2000) designed a multi-layer ER fluid SFD, derived the Reynolds equation for the fluid film and studied both theoretically and experimentally the unbalance properties of a single-disk mounted on a flexible rotor that is supported by the multi-layer ER fluid SFD. In order to suppress flexural vibrations of high-speed rotor systems, a compact damper incorporating ER fluid was designed by Seungchul et al (2005). Pecheux et al (1997) numerically investigated the application of squeeze film dampers for active control of flexible rotor dynamics using viscosity change of a negative ER fluid to control the dynamic behavior of the shaft. Bouzidane and Thomas (2008) have numerically simulated the effect of a negative electro-rheological fluid (NERF) within a four-pad hydrostatic bearing by using a linear method. The objective of this research is to adapt ER technology to hydrostatic squeeze film damper in order to control the vibration of high speed flexible shafts. A non-linear model of the ER fluid hydrostatic squeeze film damper has been developed. The transient amplitude–speed responses are calculated for a flexible shaft supported partly by an NER fluid hydrostatic squeeze film damper. A control strategy is proposed for an NER hydrostatic squeeze film damper based on the application of an electric field with a trapezoidal variation according to the rotational speed.

1.1 Negative Electro-Rheological Fluids

An ER fluid is a suspension of micron-sized polarizable particles dispersed in a dielectric liquid. Negative electro-rheological (NER) fluids are suspensions of insulating particles in a high dielectric constant liquid. They are Newtonian fluids with a viscosity which decreases when an electric field is applied, and which is restored to its original value when the field is removed (Boissy et al 1995). The relationship between viscosity and electric field for the NER studied is presented in Figure 1. Figure 2 shows a hydrostatic squeeze film damper made of four identical plane hydrostatic bearing pads with indices 1, 2, 3 and 4 respectively indicating the lower, right, upper and left characteristics of the thrusts. The hydrostatic journal is fed with the negative electro-rheological (NER) fluid through recesses in the bearing, which are themselves supplied with external pressure P_S through capillary restrictor-type hydraulic resistances.

2 Mathematical Modeling

The Reynolds equation allows for the computation of the pressure distribution P_i (x_i, z_i, t). If we consider that the fluid flow is incompressible, laminar, isoviscous,

and inertialess fluid, the Reynolds equation may be written as (Bouzidane and Tomas 2008):

$$\frac{\partial}{\partial x_i}\left(\frac{\partial P_i(x_i,z_i,t)}{\partial x_i}\right)+\frac{\partial}{\partial z_i}\left(\frac{\partial P_i(x_i,z_i,t)}{\partial z_i}\right)= 12\frac{\mu}{h_i^3}\dot{h}_i \tag{1}$$

where: $P_i(x_i,z_i,t)$ is the hydrostatic pressure field of the ith hydrostatic bearing pad; h_i is the film thickness of the ith hydrostatic bearing pad ($h_i \neq f(x_i,z_i)$), (x_i, z_i, y_i) is the coordinate system used in the Reynolds equation, i=1, 2,3 and 4.

2.1 *Shaft Mode*

The rotor is modeled with typical beam finite elements including gyroscopic effects. Each element has four degree of freedom per node (Chen and Gunter, 2005). The governing equations of motion become:

$$[[M_t]+[J_r]]\{\ddot{\delta}\}+\dot{\varphi}[G]\{\dot{\delta}\}+[[K]+\ddot{\varphi}[G]]\{\delta\}=\{F_{imb}\}+\{F_{gr}\}+\{F_{nl}\} \tag{2}$$

where $[M_t]$ and $[J_r]$ are the translational and rotary mass matrices of the shaft, $[G]$ is the gyroscopic matrix, $[K]$ is the stiffness matrix of the shaft and rolling bearings, { δ } is the node displacement vector, $\{F_{imb}\}$ are the imbalance forces, $\{F_{gr}\}$ are the gravity forces, and $\{F_{nl}\}$ are the non-linear hydrostatic bearing forces.

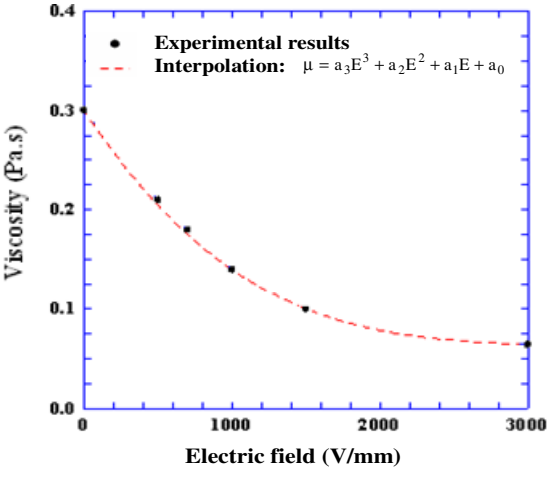

Fig. 1 Variation of the viscosity of the suspension with an NER fluid

($a_3 = -8.410^{-12}; a_2 = 7.410^{-8}; a_1 = -2.2610^{-4}; a_0 = 0.3$)

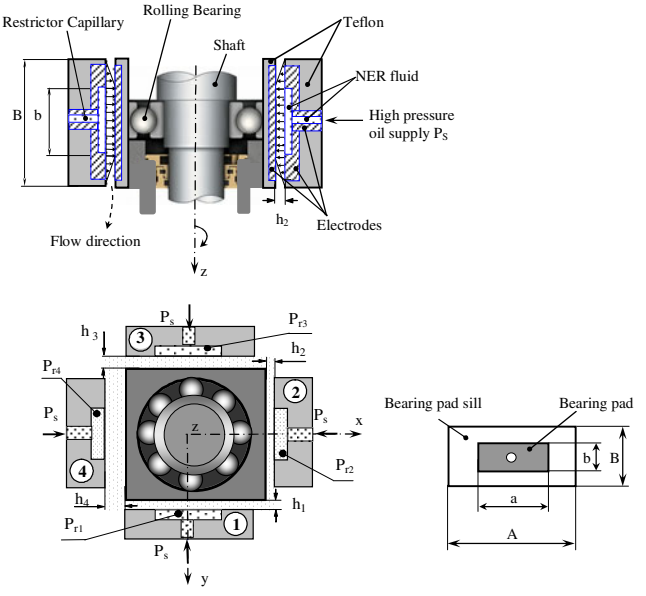

Fig. 2 NER Hydrostatic Squeeze Film Damper Geometry

2.2 *Forces Hydrostatics Bearings*

• **Nonlinear model**: The nonlinear hydrostatic force of the i^{th} hydrostatic bearing pad can be obtained by integrating the pressure over the bearing area:

$$F_{pi} = \int_{S_i} P_i \, ds_i = \iint P_i \, dx_i \, dz_i \tag{3}$$

where s_i and ds_i are the contact surface and element on the surface of the i^{th} bearing pad, respectively. The fluid film forces on the hydrostatic squeeze film damper in Cartesian coordinates (O_j, x, y) are determined as follows (Fig. 2):

$$\begin{cases} F_x = -(F_{P1} - F_{P3}) \\ F_y = -(F_{P2} - F_{P4}) \end{cases} \tag{4}$$

• **Linear model**: The linear model is based on a small displacement and small velocity hypothesis (Bouzidane and Thomas 2008). Therefore, the linear hydrostatic force of the i^{th} hydrostatic bearing (F_{pi}) can be expressed as follows:

$$F_{Pi} = -K_{pi} h_i - C_{pi} \dot{h}_i \tag{5}$$

where K_{pi} and C_{pi} represent the stiffness and damping of the i^{th} hydrostatic bearing pad, and F_{pi} is the hydrostatic force of the i^{th} hydrostatic bearing pad.

3 Numerical Results

The non-linear dynamic behavior of the flexible rotor is simulated step by step on a modal basis. At each step the Reynolds equation (Eq.1) is solved to evaluate the film forces, and then the equations of motion (Eq.2) are integrated using the Newmark method with a step variable to obtain speeds and the position for the next step. Computation of the pressure distribution was done through resolution of the Reynolds equation by applying the centered finite difference method. The linear systems of the equation were solved using Gauss-Seidel methods including an over relaxation factor. The shaft under investigation is a rotating flexible shaft supported at one end by two rolling bearings and at the other end by an NER Journal Hydrostatic Bearing (Figure 2). The model of the shaft is presented in Figure 3. The shaft is divided into 11 beam elements and 12 nodes. Every node has four degrees of freedom including two translations and two rotations. The bearing characteristics are the following: bearing pad length A is 0.09 m; bearing pad width B is 0.015; dimension ratio a/A=b/B is 0.5; film thickness h_0 is 0.07 mm. The capillary diameter d_c is 1.2 mm; l_c the capillary length is 58 mm; the pressure supply is 2.5 MPa. The rotor system is subjected to an imbalance value $\|F_{imb}\|=80.10^{-6}$ kg.m located at the middle of the shaft (node 7). A linear variation of rotation speed between 5000 and 60 000 rpm over a 20 second interval was made. All the amplitudes of transient responses given in this paper are non-dimensional (amplitude/film thickness).

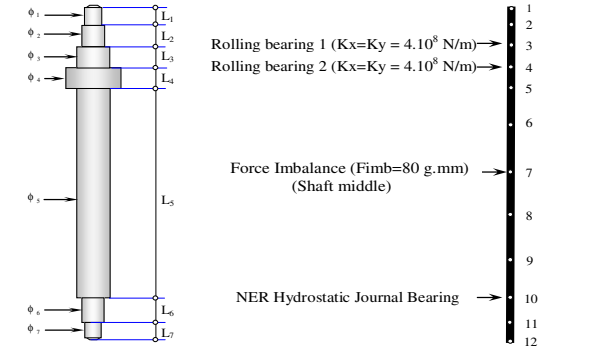

Fig. 3 Schematic diagram of the model of shaft-bearings system

As mentioned above, Figure 4 shows the comparison of linear and nonlinear results for computing the dimensionless vibration amplitudes (at the middle of the shaft and inside the NER-HSFD) for small vibrations around the static equilibrium position. The results obtained by using the non-linear method present a very good agreement and are validated since they are almost identical to those predicted by

the linear method. Note that the values of stiffness and damping (K_{HJB} =3.026 10^7 N/m; C_{HJB} =86281.13 N.s/m) were determined numerically (Bouzidane and Thomas 2007/2008)

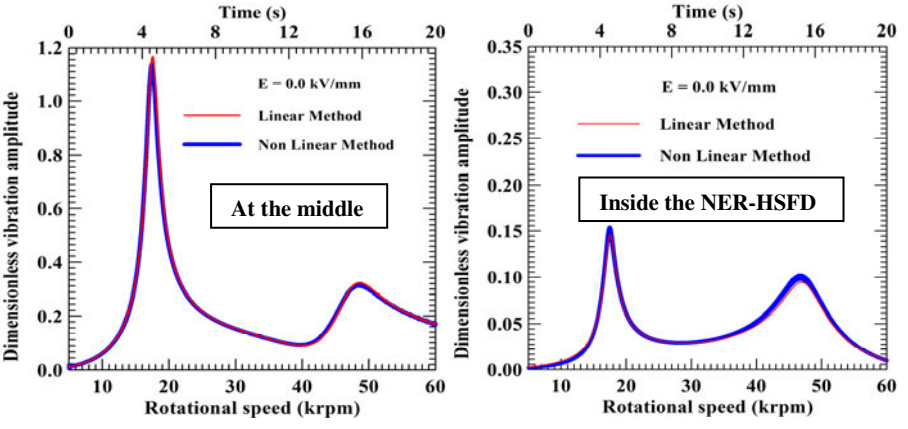

Fig. 4 Transient response of the shaft at the middle and inside the NER-HSFD vs. speed and time

3.1 Control Method for an NER Hydrostatic Journal Bearing

A semi-active control system based on use of an NER-HSFD can be developed to control flexible shaft vibration, reduce excessively high amplitudes of forced vibration. This control system functions by applying an electric field according to the operating speed of the shaft in relation to its critical speeds. A trapezoidal variation of the electric field up to 3kV/mm is proposed (Figure 5a). When the electric field is applied (3kV/mm), the NER fluid viscosity decreases from 0.3 Pa.s to 0.0609 Pa.s, the amplitude of shaft movement in the HSFD increases and consequently the amplitude at the middle of the shaft decreases. Figure 5b shows the variation of viscosity according to rotational speed and time as the electric field is applied. This viscosity variation has been determined by interpolation of the experimental results presented in Figure 1. Figure 6 demonstrates the use of the control system and the corresponding vibratory response. One can observe the effect of variations in the applied electric field on vibratory response versus speed and time at the middle of the shaft, the end of the shaft in the HSFD. It can be seen from these results that the application of an electric field to control the viscosity of a NER-HSFD is an effective way to reduce the vibration of a flexible shaft when operating close to critical speeds. As speeds get further away from these critical frequencies, the same approach reduces vibration of the shaft inside the HSFD.

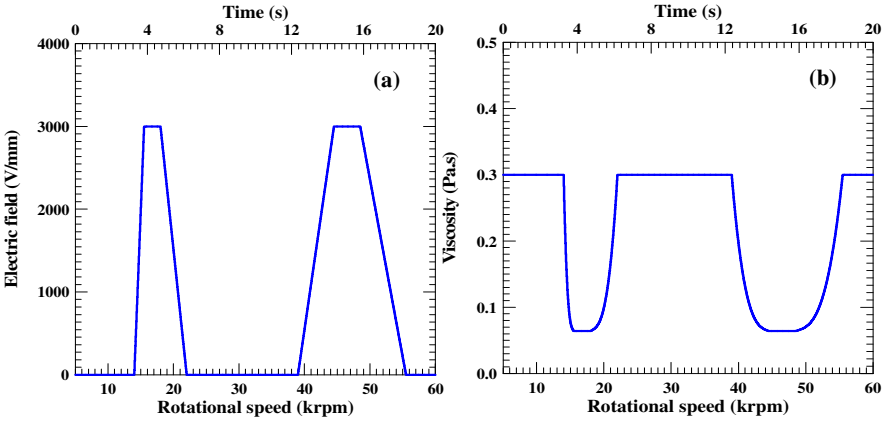

Fig. 5 Electric field and fluid viscosity variation vs. speed and time

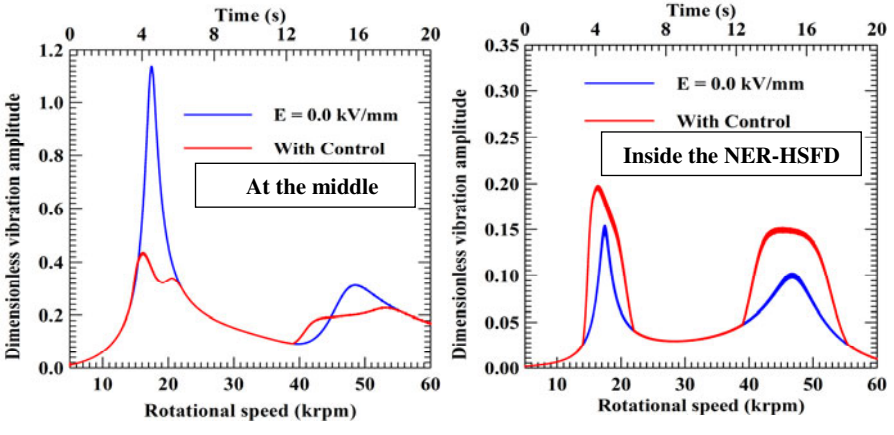

Fig. 6 Control of vibration of the shaft vs. speed and time

4 Conclusion

Non-linear modeling of a hydrostatic squeeze film damper has been presented and applied in a control system to limit the vibration of high speed flexible shafts partly supported by a NER-HSFD. The following conclusions can be obtained.

(a) To reduce the vibration of a flexible shaft, the results have revealed that the vibration inside the journal bearing must be kept large when operating close to critical speeds. This can be achieved by using a negative electro-rheological fluid inside the HSFD. Note that the large vibration inside NER-HSFD dissipates a lot of energy, by means of reducing the viscosity (damping in the HSFD decreases). In the other hand, a high viscosity is required for reducing rotor vibration at

speeds very different from the critical speeds. Results obtained with this kind of NER-HSFD are close to those of Electro-rheological SFD (Pecheux et al. 1997).
(b) Using the negative ER fluid inside NER-HSFD allows for achieving the objective to control the rotor vibration across the critical speeds. This effect is due to the fact that the viscosity of a negative electro-rheological fluid decreases when an electric field is applied. Consequently the command law asked for increasing the electric field in order to reduce the fluid viscosity inside the HSFD when crossing the critical speeds. When the speed is different from the critical speeds, the electric field is kept null.
(c) The results of experiments done during this study demonstrate that the viscosity of the fluid inside the HSFD can be controlled using an electric field and that this approach can effectively reduce rotor vibration. The research shows that the NER-HSFD has a promising potential future in vibration control of flexible shaft.

References

Baaklini, G., Gyekenyesi, A.L., Smith, K.D., Sawicki, J.T., Brasche, L.: Tools for engine diagnostics under the NASA aviation safety program. Materials Evaluation, J. of the American Society for Nondestructive Testing 60, 878–883 (2002)

Boissy, C., Atten, P., Foulc, J.N.: On a negative electro - rheological effect. J. of Electrostatics 35, 13–20 (1995)

Bouzidane, A., Thomas, M.: An electro-rheological hydrostatic journal bearing for controlling rotor vibration. Computers and Structures 86, 463–472 (2008)

Bouzidane, A., Thomas, M., Lakis, A.: Non linear dynamic behaviour of a rigid rotor supported by hydrostatic squeeze film dampers. J. of Tribology, Transactions of the ASME 130, 041102–041102-9 (2008)

Bouzidane, A., Thomas, M.: Equivalent Stiffness and damping investigation of a hydrostatic journal bearing. Tribology Transactions 50, 257–267 (2007)

Chen, W.J., Gunter, E.J.: Introduction Dynamics of Rotor-Bearing Systems. Trafford, Victoria, Canada (2005)

Guozhi, Y., Fah, Y.F., Guang, C., Guang, M., Tong, F., Yang, Q.: Electro-rheological multi-layer squeeze film damper and Its application to vibration control of rotor system. ASME Transactions J. of Vibration and Acoustics 122, 7–11 (2000)

Lee, N.S., Choi, D.H., Seok, K.Y., Lee, Y.B., Kim, C.H.: Vibration control of a flexible rotor with a slotted-ring sealed electro-Rheological squeeze film damper. In: Proceedings of IMECH 7th International Conference, pp. 499–506 (2000)

Pecheux, B., Bonneau, O., Frêne, J.: Investigation about electro-rheological squeeze film damper applied to active control of rotor dynamic. International J. of Rotating Machinery 3, 53–60 (1997)

Seungchul, L., Sang, M.P., Kab, -I.K.: AI vibration control of high-speed rotor systems using electro-rheological fluid. J. of Sound and Vibration 284, 685–703 (2005)

STFT Based Approach for Ball Bearing Fault Detection in a Varying Speed Motor

Marco Cocconcelli[1], Radoslaw Zimroz[2],
Riccardo Rubini[1], and Walter Bartelmus[2]

[1] University of Modena and Reggio Emilia, Reggio Emilia, 42122, Italy
{marco.cocconcelli,riccardo.rubini}@unimore.it
[2] Diagnostics and Vibro-Acoustics Science Laboratory,
Pl Teatralny 2, Wroclaw, 50-051, Poland
{radoslaw.zimroz,walter.bartelmus}@pwr.wroc.pl

Abstract. This paper focuses on the diagnostics of ball bearings in direct-drive motors. These specific AC brushless motors are increasing their importance in automation machineries because they can work with a built-in flexibility. In particular the angular displacement of the shaft is continuously monitored by an embedded encoder while the control system allows to perform complex motion profiles such as polynomial ones, even with the inversion of the rotating direction. Direct-drive motors avoid the presence of a mechanical cams or gearboxes between the motor and the load with a subsequent money-saving. On the other side, unfortunately, the diagnostics of ball bearing in those motors is not trivial. In fact most of the solutions proposed in the literature require a constant frequency rotation of the shaft since the characteristic fault frequencies are directly proportional to speed of the motor. It follows that in a varying speed application the fault characteristic frequencies change instantaneously as the rotational frequency does. In this paper an industrial application is considered, where the direct drive motors are used in the kinematic chain of an automated packaging machine performing a cyclic polynomial profile. The basic idea is to focus on signal segmentation using the position profile of the shaft – directly measured by the encoder – as trigger. Next the single cycles of the machine is analysed in time domain, again using encoder signal machine contribution is deleted. Feature extraction for damage detection is done by applying the Short Time Fourier Transform (STFT), the STFT for each cycle is averaged in time-frequency domain in order to enhance fault signature. Finally, the sum of STFT coefficients is used as a simple indicators of damage.

Keywords: Condition monitoring, time frequency, STFT, Spectral Kurtosis, non-stationary speed conditions, bearings, damage detection.

1 Introduction

Ensuring continuity of production in the enterprise on a global scale is one of the key requirements. Modern production lines are automated, highly efficient, but

unfortunately they are not devoid of common problems in maintaining the machines. To avoid unexpected failures they apply monitoring and diagnostics [Sidahmed2001, Niemkiewicz2001, Martin1994, Randall2011]. The existing condition monitoring procedures have been successfully used for years in the petrochemical, paper manufacturing, etc… industry, mainly focusing on specific components like rotating machinery [El-Shafei2003], gears [Dalpiaz2000] and bearings [Jardine2006, Randall2011]. In most of the cases condition monitoring used to diagnose mechanical systems working in steady conditions, e.g. usually at a constant speed, while only few techniques analysed load/speed variation [Potter1990, Fyfe1997, Baydar2000, Stander2002, Zhan2004, Coconcelli2008, Cocconcelli2012, Curcuru2010, Chaari2010, Makowski2011, Zimroz2012].

This paper focuses on diagnostics of ball-bearing in motors operating in non-stationary conditions. The non-stationary operating conditions influence the vibration signal, masking the presence of incipient faults or hiding fault impacts due to an higher energy of the machine impacts, i.e. those impacts related to the normal working activity of the machine. These motors are called servomotors.

In particular the paper is focused but not limited to a recent class of motors called direct-drive motors. They are usually AC brushless motors controlled by a drive thanks to an embedded encoder that measure the displacement of the shaft at high frequency (e.g. 8 kHz). Servomotors tend to appear more and more often in recent machine designs, as their performances are more flexible than the mechanical solutions for machine motion with respect to the time required to reconfigure the motion profile, since the absence of mechanical cams or gear reduction.

It makes a difference from the problem defined in the literature for “classical” damage detection. Recovery of impulsive, cyclic signal from the noisy observation is well known in the literature. It can be done by simple bandpass filter around resonance, advanced adaptive filters, wavelet decomposition, blind cyclic Wiener filter etc. [[Antoni2002,2003,2006, Sawalhi2007, Boustany2008, Wang2008, Combet2009, Immovilli 2009, Barszcz 2009, Zimroz 2009] Unfortunately, none of these techniques fixed the problem due to wideband, cyclic, high energy contribution from the working environment and serious variation of shaft speed.

This paper proposes a new procedure based on the segmentation of vibration signal guided by the speed profile of the control system. It should be noted that due to modulation phenomena in machinery systems [Chaari2012] it can be possible even if tachometer signal is not available [Combet2009, Zimroz2011]. The segmentation allows to remove the strong contribution of machine impacts. The residual signals are then analysed by the Short Time Fourier Transform (STFT) to highlight the presence of damage impacts in time-frequency domain. At last spectrograms for each segments are averaged to improve the signal-to-noise ratio. Finally, the sum of STFT coefficients is used as a simple indicator of damage. Detection of the status of the bearing can be performed automatically for single cycle or for averaged data using a simple decision scheme (if **value of feature >threshold** then *damage* else *healthy*).

2 Test Machine and Signal Presentation

The system under observation is a machine for the packaging of liquid products with a so-called roll-feed vertical filling and forming process: the monitored bearings support the actuators of a module composed by two cinematic chains moved by servomotors via a belt-pulley. Brushless AC motors MPL-B680B by Rockwell Automation mounting a NSK 6309 single-raw bearing are used as actuators. The angular velocity signal of the motor was retrieved using one of the analogue outputs available in the motor drive, a Kinetix 6000 series BM-01.

As mentioned in the introduction, the general working condition for a servomotor provides for a cyclic polynomial speed profile of the shaft. An example is reported in Fig. 1 where the lower plots show the speed profile performed by the motors in the specific cases analysed in the paper. The comparison between faulty and sound bearings clearly shows the contribution of two components: a strong contribution due to cyclic impacts which is present in both cases, and a small contribution which must be present only on the faulty case and represents the characteristic firm of the damage. The strong contribution in vibration data is a consequence of the variable load forward the motor. In fact the comparison with the speed profile reveals the impacts happen when the motor quickly changes the rotational speed at its maximum (absolute value) – from 0 to 500 to 0 rpm in less than 0.3 seconds – with an instantaneous change of the resisting moment of the load. It must be noted that the machine impacts are non-stationary, non-Gaussian signals and their amplitude covers the damage impacts making their detection difficult. The complexity of the machine and the serious influence of interference of the cyclic signal source make the condition monitoring non-trivial.

3 Condition Monitoring Procedure

The condition monitoring procedure proposed is made of four steps and requires as input the vibration data collected nearby the bearing and the synchronous speed profile of the motor. The speed profile is easily accessible in servomotors since it is however measured for control purpose and can be saved as output from the drive.

3.1 Segmentation of Vibration Signal According to Machine Cycle

In order to reject the influence of machine impacts, the vibration signal is segmented according to speed profile. As noticed in Fig. 1 the machine impacts are related to the quick variation of speed from 100 rpm to -500 rpm (the sign of the speed has no influence on procedure, it's just an example from a real application where the cyclic speed profile has its maximum – as absolute value – in the opposite direction with respect to the assumed positive rotation). This part of the signal can be removed introducing a software trigger threshold in post processing of the data.

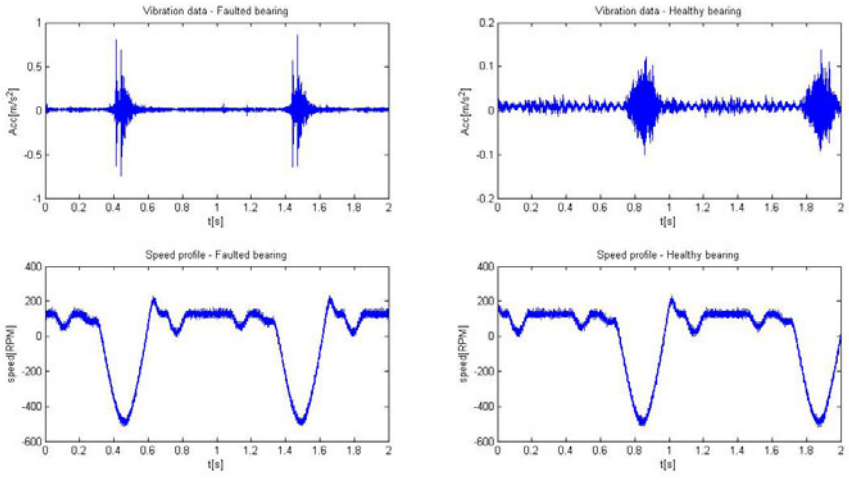

Fig. 1 Vibration data and speed profile for faulty and healthy bearings

Low-pass filtering of the speed profile is recommended to reduce the noise (to smooth speed profile signal) and improve the segmentation of the vibration data. Figure 2 shows in details the extraction of segmentation indices from the speed profile. As requested the impacts related to the machines cycles are removed and only the residual part will be analysed.

3.2 STFT of Every Residual Signal

As the residual signal is very non-stationary (cycles between impulses are not equal, signal is highly impulsive) it has to be analysed in time-frequency domain to highlight the presence of impacts related to incipient faults. The choice of a time-frequency technique is need to overcome the variation of speed which is still present in the speed profile corresponding to the residual signal. Time-frequency domain allows to appreciates the frequency content of the signal as the time varying, independently of the periodicity of incidental impulses. In particular the Short Time Fourier Transform (STFT) answers to the need of a relatively simple techniques with a clear interpretation of the output.

The second step of the procedure consists in the computation of the STFT for each segment of residual signal obtained at the previous step.

3.3 Average of the STFT Spectrograms

In order to enhance indicators of local damage, STFT spectrograms are averaged in time-frequency domain. This step highlights the energy flow related to the impacts between faulty elements of the bearing and increase the signal-to-noise ratio.

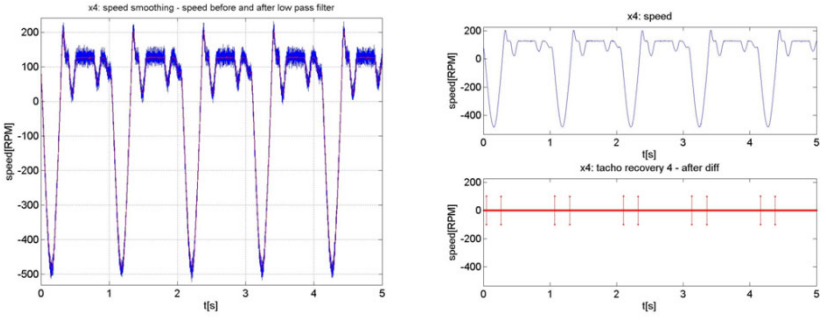

Fig. 2 Extraction of segmentation indices from the speed profile

3.4 Marginal Time Integration

Usually two quantities could be calculated from the STFT spectrogram, integrating the map along the time axis or the frequency axis. The integration along time is called marginal time integration (MTI) and it can be considered as the mean instantaneous power of the signal. The MTI is used as a simple indicators of damage. Detection of the status of the bearing can be done automatically just monitoring the overcoming of an appropriate threshold.

4 Results

The procedure has been tested on 13 bearings, 7 of them are healthy and 6 are faulty (in the paper they will be generally named **"x#"**, where # is the reference number of the bearing during the experiment setup). In particular, the healthy bearings are classified in two sets: 3 are brand-new healthy bearings, 4 are bearings which ran for 1000 hours, then opened without any evidence of fault and classified as healthy. The faulty bearings are also divided in two sets: 2 bearings have been artificially damaged in the lab of the University and 5 come from the field, that is from other industries that claimed the motors as damaged. The vibration signal has been acquired by means of an accelerometer MTN 1100 CQ mounted on the motor in the load direction of the belt. The signal was connected to a NATIONAL INSTRUMENTS acquisition board, made by a CDAQ-9172 back plane upon which a NI-9233 module collected the accelerometer output. The data from acquisition board was stored on a laptop via its USB interface and later post-processed with MATLAB. The sampling frequency used is 10kHz and the single acquisition lasted 50 seconds.

For clearness of exposition this paper reports the graphical results (Figs. 3-4 respectively) for just two significant cases: a sound bearing, an artificially damaged bearing (on the outer ring). Each figure shows the first three steps of the procedure: the vibration data after the removal of machine impacts (only a single segment as example), the spectrogram of a single segment and averaged spectrogram

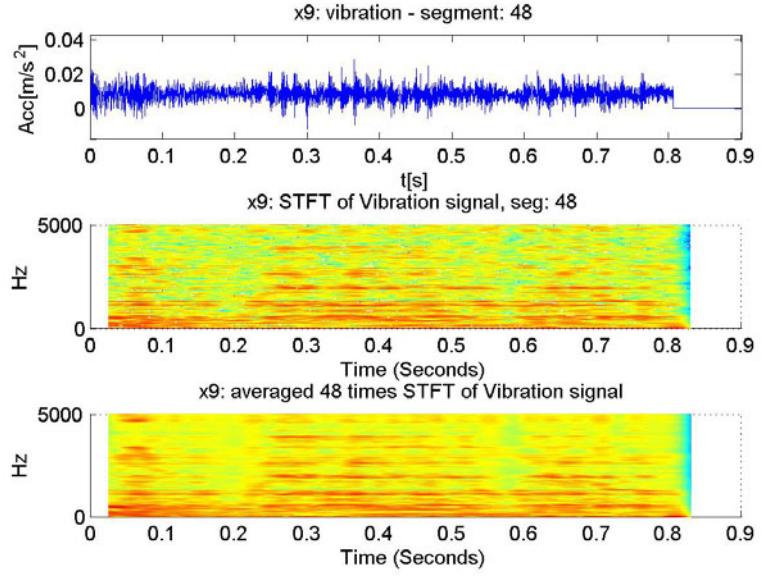

Fig. 3 Condition monitoring procedure for a healthy bearing

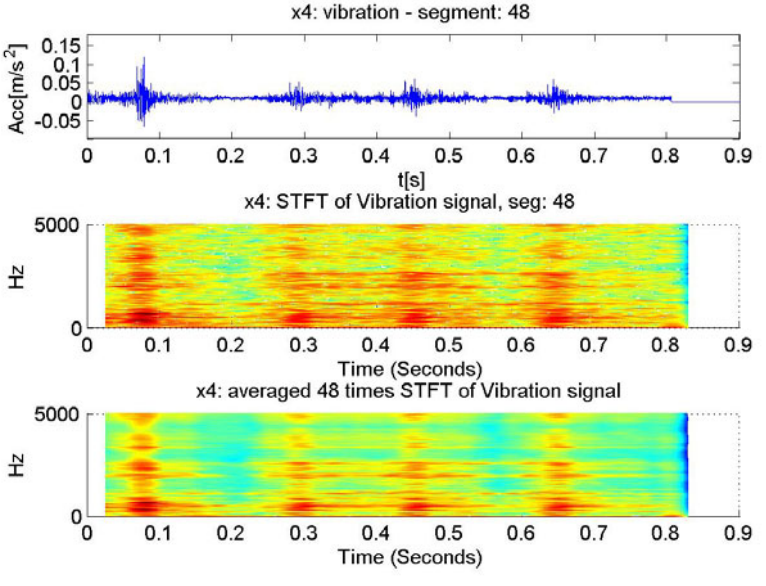

Fig. 4 Condition monitoring procedure for an incipient faulty bearing

over all the segments available. The acquisition of data for 50 seconds allows 48 complete cycles of the machine.

In Fig. 3 the averaged spectrogram of a sound bearing doesn't show any relevant peaks and the frequency content of the signal is the same all along the time axis.

In Fig. 4, the spectrogram of incipient faulty bearing clearly shows four impacts along the time axis with an excitation of the amplitude in all the frequency range. These four impacts (T={0.1 0.3 0.45 0.65}s) are related to the damage on the outer ring of the bearing and the comparison between the spectrogram of a single signal segment and the averaged spectrogram justifies the third step of the procedure since the peaks are highlighted by the average process.

Figure 5 shows the marginal time integration of the STFT spectrogram for the faulty (left) and healthy (right) bearings. The two pictures are plotted in the same scale and the faulty bearing exhibits four severe peaks related to the damage condition, while the healthy bearing doesn't show any relevant peak. The introduction of an appropriate threshold allows an automatic detection of the bearing status. In particular Fig.5 shows the level of the mean value for the both healthy and faulty bearings.

A suggested alarm-threshold and stop-threshold for the machinery may be set adding to the mean value of faulty bearings, respectively, half time the standard deviation, and one time the standard deviation. Both these two thresholds are reported in Fig. 5.

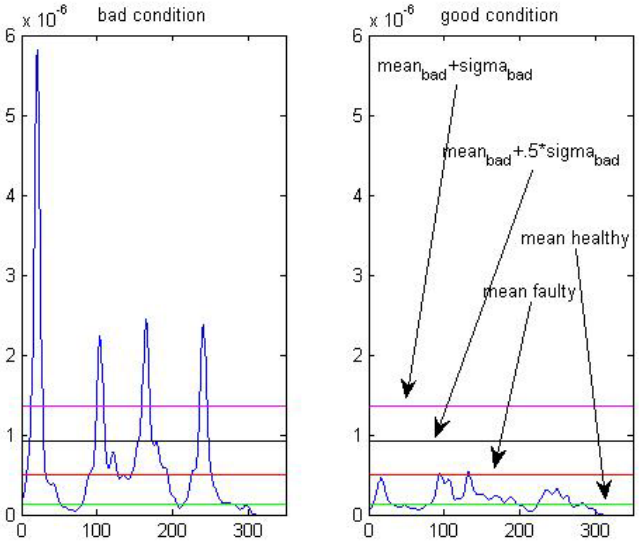

Fig. 5 Marginal time integration of the STFT spetrograms and definition of damage thresholds (mean+0.5 sigma, mean + sigma)

The MTI of the averaged spectrogram produces a bi-dimensional representation of the results that proves the effectiveness of the procedure as diagnostics tool and its improvement in spikes detection. The peaks related to the fault are relevant, while the effect of machine impacts has been removed.

5 Conclusions

In this paper a new procedure for the condition monitoring of ball bearing in non-stationary conditions is presented. The paper focuses on an industrial application, where a servomotor is used as actuator in a kinematic chain for packaging process. The speed profile of the motor is cyclic and follows a polynomial profile with continuously variation of speed and inversion of the motion. The main consequence in the vibration monitoring is the presence of a strong contribution from non-stationary, non-Gaussian, impulsive, cyclic signal source which is strictly related with the variable load of the motor a part from the presence of damage in the bearing. This machine contribution makes hard the condition monitoring with techniques based on kurtosis indicator or simply the envelope analysis due to its strong influence on the rest of the signal. The suggested procedure starts with the removal of machine contribution thanks to the instantaneous speed profile synchronous measured with the vibration data. The speed profile is low-pass filtered to reduce the noise and then a software trigger is used to determine the segmentation indices. Each single residual vibration segment is processed by the STFT in time-frequency domain. The spectrograms are averaged to enhance the indicators of local. Finally, the marginal time integration of the averaged STFT spectrogram is used as a simple indicators of damage.

Acknowledgements. The authors wish to thank the Inter Departmental Research Center INTERMECH MoRE of the University of Modena and Reggio Emilia for the financial support (M. Cocconcelli, R. Rubini).

This paper was also financially supported by State Committee for Scientific Research 2010–2013 as research project (W. Bartelmus, R. Zimroz).

References

Sidahmed, M.: Diagnostics and Condition Monitoring. Basic Concepts. In: Encyclopedia of Vibration, pp. 376–380. Academic Press (2001); ISBN: 978-0-12-227085-7

Niemkiewicz, J.: Standards For Vibrations of Machines and Measurement Procedures. In: Encyclopedia of Vibration, pp. 1224–1238. Academic Press (2001); ISBN: 978-0-12-227085-7

Martin, K.F.: A Review by Discussion of Condition Monitoring and Fault-Diagnosis in Machine-Tools. Int. J. Mach. Tool Manu. 34, 527–551 (1994)

Randall, R.B.: Vibration-based Condition Monitoring. John Wiley & Sons, Chichester (2011); ISBN: 978-0-470-74785-8

El-Shafei, A., Rieger, N.: Automated Diagnostics of Rotating Machinery. In: Proceedings of 2003 ASME Turbo Expo., Atlanta, GA, USA, vol. 4, pp. 491–498 (2003)

Dalpiaz, G., Rivola, A., Rubini, R.: Effectiveness and Sensitivity of Vibration Processing Techniques for Local Fault Detection in Gears. Mech. Syst. Signal Pr. 14, 387–412 (2000)

Jardine, A.K.S., Lin, D., Banjevic, D.: A Review on Machinery Diagnostics and Prognostics Implementing Condition-Based Maintenance. Mech. Syst. Signal Pr. 20, 1483–1510 (2006)

Randall, R.B., Antoni, J.: Rolling Element Bearing Diagnostics—A Tutorial. Mech. Syst. Signal Pr. 25, 485–520 (2011)

Potter, R.: A new order tracking method for rotating machinery. Sound Vib. 24, 30–34 (1990)

Fyfe, K., Munck, E.: Analysis of computed order tracking. Mech. Syst. Signal Pr. 11(2), 187–205 (1997)

Antoni, J., Randall, R.B.: Differential diagnosis of gear and bearing faults. ASME J. Vib. Acoust. 124(2), 165–171 (2002)

Antoni, J., Randall, R.B.: Unsupervised noise cancellation for vibration signals. Part I—Evaluation of Adaptive Algorithms. Mech. Syst. Signal Pr. 18(1), 89–101 (2003)

Zimroz, R., Bartelmus, W.: Gearbox condition estimation using cyclo-stationary properties of vibration signal. Key Eng. Mat. 413-414, 471–478 (2009)

Boustany, R., Antoni, J.: Blind extraction of a cyclostationary signal using reduced rank cyclic regression - A unifying approach. Mech. Syst. Signal Pr. 22, 520–541 (2008)

Barszcz, T., Randall, R.B.: Application of spectral kurtosis for detection of a tooth crack in the planetary gear of a wind turbine. Mech. Syst. Signal Pr. 23(2), 1352–1365 (2009)

Antoni, J.: The spectral kurtosis: a useful tool for characterising non-stationary signals. Mech. Syst. Signal Pr. 20(2), 282–307 (2006)

Bartelmus, W., Chaari, F., Zimroz, R., Haddar, M.: Modelling of gearbox dynamics under time varying non-stationary operation for distributed fault detection and diagnosis. Eur. J. Mech. A-Solid 29, 637–646 (2010)

Stander, C., Heyns, P., Schoombie, W.: Using vibration monitoring for local fault detection on gears operating under fluctuating load conditions. Mech. Syst. Signal Pr. 16(6), 1005–1024 (2002)

Baydar, N., Ball, A.: Detection of gear deterioration under varying load conditions by using the instantaneous power spectrum. Mech. Syst. Signal Pr. 14, 907–921 (2000)

Zhan, Y., Makis, Y., Jardine, A.: Adaptive state detection of gearboxes under varying load conditions based on parametric modelling. Mech. Syst. Signal Pr. 20(1), 188–221 (2004)

Cocconcelli, Bassi, L., M., Secchi, C., Rubini, R., Fantuzzi, C.: An algorithm to diagnose ball bearing faults in servomotors running arbitrary motion profiles. Mech. Syst. Signal Pr. 27 (2), 667-682 (2012), http://dx.doi.org/10.1016/j.ymssp.2011.09.003

Curcurù, G., Cocconcelli, M., Rubini, R.: Wavelet decomposition and energy distribution as ball-bearing diagnostics tools in direct-drive motors. In: Proceedings of 17th International Congress on Sound and Vibration, Cairo, Egypt (2010)

Cocconcelli, M., Secchi, C., Rubini, R., Fantuzzi, C., Bassi, L.: Comparison Between Time-Frequency Techniques to Predict Ball Bearing Fault in Drives Executing Arbitrary Motion Profiles. In: Proceedings of the ASME 2008 International Mechanical Engineering Congress and Exposition, Boston, Massachusetts, USA, pp. 249–255 (2008)

Makowski, R.A., Zimroz, R.: Adaptive Bearings Vibration Modelling for Diagnosis. Lect. Notes Artif. Int., vol. 943, pp. 248–259 (2011)

Zimroz, R., Bartelmus, W.: Application of adaptive filtering for weak impulsive signal recovery for bearings local damage detection in complex mining mechanical systems working under condition of varying load. Solid State Phenom. 180, 250–257 (2012); doi:10.4028/www.scientific.net/SSP.180.250

Wang, Y., Liang, M.: An adaptive SK technique and its application for fault detection of rolling element bearings. Mech. Syst. Signal Pr. 25(5), 1750–1764 (2008)

Sawalhi, N., Randall, R.B., Endo, H.: The enhancement of fault detection and diagnosis in rolling element bearings using minimum entropy deconvolution combined with spectral kurtosis. Mech. Syst. Signal Pr. 21(6), 2616–2633 (2007)

Combet, F., Gelman, L.: Optimal filtering of gear signals for early damage detection based on the spectral kurtosis. Mech. Syst. Signal Pr. 23(3), 652–668 (2009)

Immovilli, F., Cocconcelli, M., Bellini, A., Rubini, R.: Detection of Generalized-Roughness Bearing Fault by Spectral-Kurtosis Energy of Vibration or Current Signals. IEEE T. Ind. Electron 56(11), 4710–4717 (2009)

Zimroz, R., Urbanek, J., Barszcz, T., Bartelmus, W., Millioz, F., Martin, N.: Measurement of Instantaneous Shaft Speed By Advanced Vibration Signal Processing - Application To Wind Turbine Gearbox. Metrology and Measurement Systems XVIII(4), 701–712 (2011)

Chaari, F., Bartelmus, W., Zimroz, R., Fakhfakh, T., Haddar, M.: Gearbox vibration signal amplitude and frequency modulation. Shock Vib (in Press); DOI: 10.3233/SAV-2011-0656

Combet, F., Zimroz, R.: A new method for the estimation of the instantaneous speed relative fluctuation in a vibration signal based on the short time scale transform. Mech. Syst. Signal Pr. 23, s.1382–s.1397 (2009)

Kurtosis over Energy Distribution Approach for STFT Enhancement in Ball Bearing Diagnostics

Marco Cocconcelli[1], Radoslaw Zimroz[2],
Riccardo Rubini[1], and Walter Bartelmus[2]

[1] University of Modena and Reggio Emilia, Reggio Emilia, 42122, Italy
{marco.cocconcelli,riccardo.rubini}@unimore.it
[2] Diagnostics and Vibro-Acoustics Science Laboratory,
Pl Teatralny 2, Wroclaw, 50-051, Poland
{radoslaw.zimroz,walter.bartelmus}@pwr.wroc.pl

Abstract. This paper focuses on the diagnostics of ball bearings under time varying speed conditions. Compared to classical demodulation techniques, time-frequency approach allows to take into account transient occurrence or non-stationary phenomena along the timeline. Among the different time-frequency approaches available the simplest is the Short Time Fourier Transform (STFT). From a practical point of view, its implementation in an industrial environment has a main drawback: the industry usually needs a scalar value as output (like a semaphore: green, yellow and red light) to assess the bearing condition, while time-frequency approaches produce a bi-dimensional map that needs to be interpreted. The authors suggest to combine the information gathered by spectral kurtosis and energy distribution for the automatic selection of a filtering band that could extract from the STFT map the most informative component in time domain, reducing the complexity of the output to a mono-dimensional vector. A simple check if the output exceed a given threshold can then be used to obtain a scalar value.

Keywords: Condition monitoring, time frequency, STFT, Spectral Kurtosis, Energy distribution, bearings, damage detection.

1 Introduction

Predictive maintenance consists of estimating the remaining life of a mechanical component based on data acquisitions and analysis. Among all the possible mechanical components of a generic machine, the predictive maintenance proved its effectiveness in rotating machinery [El-Shafei2003], especially for gears [Dalpiaz2000] and bearings [Jardine2006, Randall2011]. In most of the cases condition monitoring used to diagnose mechanical systems working in steady conditions, e.g. usually at a constant speed, while only few techniques analysed load/speed variation [Potter1990, Fyfe1997, Baydar2000, Stander2002, Zhan2004, Coconcelli2008, Combet2009,

Bassi2010, Curcurù2010, Bartelmus2010, Makowaki2011, Cocconcelli2012, Chaari2010, Zimroz2012a, Zimroz2012b].

In particular the paper is focused but not limited to a recent class of motors called direct-drive motors. They are usually AC brushless motors controlled by a drive thanks to an embedded encoder that measures the angular displacement of the shaft at high frequency (e.g. 8 kHz).

It makes a difference from the problem defined in the literature for "classical" damage detection. Recovery of impulsive, cyclic signal from the noisy observation is well known in the literature. It can be done by simple bandpass filtering around resonance, advanced adaptive filters, wavelet decomposition, blind cyclic Wiener filter etc. [Antoni2002,2003,2006, Sawalhi2007, Boustany2008,Wang2008, Combet2009, Immovili 2009, Barszcz 2009, Zimroz 2009] Unfortunately, none of these techniques is able to solve the problem due to wideband, cyclic, high energy contribution from the working environment and serious variation of shaft speed.

This paper moves from a previous work of the authors that proposed a diagnostic procedure based on the segmentation of vibration signal to highlight the vibration signal for each machine cycle. Each cyclic vibration data was analysed by the Short Time Fourier Transform (STFT) to highlight the presence of damage impacts in time-frequency domain and then they are averaged to improve the signal-to-noise ratio. Averaged STFT still may contain some high energy contributions that would mask fault signature.

In order to eliminate high energy interference, this paper proposes a procedure for the optimal frequency band selection. This topics is of great interest in the literature, and several authors proposed a specific procedure to automatically identify the most informative band of the signal. Among the others Spectral Kurtosis (SK) proposed by Antoni and Randall (see Randall 2011 for rewiev) for bearing and gear diagnostics is the most promising. So far different application of SK have been developed and applied to real data (Barszcz 2009, Wang 2011, Wang 2012).

In this paper frequency band is selected joining together the Spectral Kurtosis and Energy Distribution (ED) approaches. In particular they are normalized with respect their mean value along all the STFT map and then the ratio between them is computed. The highest value of this ratio highlights the optimal filtering band. Detection of the status of the bearing can be performed automatically for single cycle or for averaged data using a simple decision scheme (if **value of feature >threshold** then *damage* else *healthy*).

2 Short Time Fourier Transform Enhancement

As mentioned in the introduction there are a wide range of applications which use the direct-drive motors. Especially the industries which produce machinery with a high level of automation, e.g. the packaging industry, they experience similar working conditions. These conditions can be summarized as cyclic motion of the motor, varying speed, motion inversion and the presence of non-stationary phenomena related to the dynamics of the processes after the motor (the kinematic chain moved by the motor, the presence of packaging material, etc…). Since the signal is very non-stationary (cycles between impulses are not equal, signal is

highly impulsive) it has to be analysed in time-frequency domain to highlight the presence of impacts related to incipient faults. The choice of a time-frequency technique is also needed to overcome the variation of speed. Time-frequency domain allows to appreciate the frequency content of the signal as the time varying, independently of the periodicity of incidental impulses. In particular the Short Time Fourier Transform (STFT) answers to the need of a relatively simple techniques with a clear interpretation of the output.

2.1 STFT Spectrogram

The STFT could be seen as a series of filter banks in time domain. In particular the vibration signal is filtered by a fixed bandwidth window and the spectrum is computed. Then the window is shifted in time domain and the procedure repeated until the complete span of the signal. For a continuous-time data the mathematical expression of the STFT is reported in Eq.1.

$$\mathrm{STFT}\{x(t)\} = \mathrm{STFT}(t, f) = X(\tau, w) = \int_{-\infty}^{+\infty} x(t) w(t-\tau) e^{-jwt} dt \qquad (1)$$

where w(t) is the window function and x(t) the acquired data.

The output of the STFT is then a map in time-frequency domain called spectrogram which is defined as the squared magnitude of the STFT as reported in Eq.2.

$$\mathrm{spectrogram}\{x(t)\} = |X(\tau, w)|^2 \qquad (2)$$

Two other quantities could be calculated from the spectrogram, integrating the map along the time axis or the frequency axis. The integration along time is called marginal time integration and it can be considered as the mean instantaneous power of the signal. The integration along frequency is called marginal frequency integration and it can be considered as the mean power spectrum.

2.2 Spectral Kurtosis

The spectral kurtosis (SK) is a methodology used to select the most suitable frequency band to highlight the presence of impacts due to incipient fault. Antoni and Randall (Antoni 2006, Randall2011) proved its effectiveness in bearing diagnostics. The kurtosis is statistical parameter defined as the ratio between the fourth moment about the mean and the fourth power of the standard deviation as reported in Eq. 3.

$$\mathrm{kurtosis}\{x(t)\} = \frac{E\left[\left(x(t) - E[x(t)]\right)^4\right]}{\sigma^4} \qquad (3)$$

where E is the expectation operator and σ is the standard deviation.

The main idea is clear: a random mechanical noise follows a Gaussian distribution, that is the kurtosis of the signal is almost equal to 3, while the presence of

impacts, hidden in the vibration signal, change the value of kurtosis to higher values than 3. In order to select the most informative bandwidth, the signal is filtered using a series of filter banks (usually with different central frequency and different bandwidth) and the kurtosis of the filtered signal is computed. The frequency band corresponding to the higher kurtosis is selected as optimal filtering band.

2.3 Energy Distribution

It could happen in the SK that there are more than a unique frequency band where the kurtosis is high. Consequently the choice of the proper frequency band is not trivial. In this case the choice could be guided by a consideration on the energy distribution along the signal spectrum. A high level of energy around a frequency band may refer to the energy provided by the impacts caused by an incipient fault, but also to the energy coming from different sources, e.g. mechanical noise, other impacts after the motor, etc… A corresponding high level of kurtosis would be caused by both these reasons, that is may be a component not directly related with an incipient fault in the bearing. On the other hand a high level of kurtosis in correspondence of a low level of energy may indicate the presence of short-duration phenomena like impacts, that they cannot change significantly the overall mean energy but they can increase the level of kurtosis.

The Parseval's theorem states that the total energy contained in a time domain waveform is equal to the total energy of the waveform's Fourier Transform along the frequency domain. The equality is reported in Eq. 4.

$$\int_{-\infty}^{+\infty} |x(t)|^2 \, dt = \int_{-\infty}^{+\infty} |X(f)|^2 \, df \tag{4}$$

Referring to Eq. 2, the marginal frequency integration yields to a spectrum (let's call it simply energy distribution (ED)) quite similar to the Eq. 4 – the STFT could imply an overlap between two subsequent shift of the window – that can be used to select the frequency band together with the spectral kurtosis.

2.4 Kurtosis over Energy

In order to collect together the information gathered by the spectral kurtosis and the energy distribution the authors propose to make the ratio between them. Indeed a normalization is required in order to compare the SK and the ED.

To increase the effect of a high level of kurtosis and a low level of the energy the normalization is made with reference to the mean value of the parameter computed over the spectrum. Equations 5 and 6 shows the normalization process for the kurtosis and energy respectively, and Eq. 7 defines the kurtosis over energy (KoE) distribution.

$$SK_{norm}(f_0)\{x(t)\} = \frac{\int_{-\infty}^{+\infty} \text{kurtosis}\{\hat{x}(t, f_0)\}dt}{E\left[\int_{-\infty}^{+\infty} \text{kurtosis}\{\hat{x}(t, f)\}dt\right]} \tag{5}$$

$$ED_{norm}(f_0)\{x(t)\} = \frac{\int_{-\infty}^{+\infty} \text{STFT}\{\hat{x}(t, f_0)\}dt}{E\left[\int_{-\infty}^{+\infty} \text{STFT}\{\hat{x}(t, f)\}dt\right]} \tag{6}$$

$$KoE\{x(t)\} = \frac{SK_{norm}(f_0)\{x(t)\}}{ED_{norm}(f_0)\{x(t)\}} \tag{7}$$

where $\hat{x}(t, f_0)$ indicates the filtering of waveform *x(t)* around the frequency f_0.

3 Results

The system under observation is a machine for the packaging of liquid products with a so-called roll-feed vertical filling and forming process: the monitored bearings support the actuators of a module composed by two cinematic chains moved by servomotors via a belt-pulley, opportunely synchronized for the packaging forming, transversal sealing and cutting. Brushless AC motors MPL-B680B by Rockwell Automation mounting a NSK 6309 single-raw bearing are used as actuators. The angular velocity signal of the motor was retrieved using one of the analogue outputs available in the motor drive, a Kinetix 6000 series BM-01 by Rockwell Automation. The vibration signal has been acquired by means of an accelerometer MTN 1100 CQ mounted on the motor in the load direction of the belt. The signal was connected to a NATIONAL INSTRUMENTS acquisition board, made by a CDAQ-9172 back plane upon which a NI-9233 module collected the accelerometer output. The data from acquisition board was stored on a laptop via its USB interface and later post-processed with MATLAB. The sampling frequency used is 10kHz and the single acquisition lasted 50 seconds.

Different bearings in different conditions have been tested (in both healthy and faulty conditions), but for a lack of space just the case of a generalized roughness bearing is reported in Fig. 1 and 2. This particular case refer to an inner race faulted bearing. The acquired vibration data have been processed as described in [Cocconcelli2011] and the averaged STFT spectrogram obtained.

In the upper part of Fig. 1 are reported the normalized spectral kurtosis (on the left) and the energy distribution (on the right) along the frequency domain. The frequency axis starts at 500 Hz to remove high energy peak at low frequency for the energy distribution plot. In the bottom of the figure is shown the kurtosis over energy distribution and it is evident the effect of energy distribution that decreases the importance of the kurtosis peak at 2650 Hz but increase the peak at 3950 Hz. Figure 2 shows the selected spectra of the STFT based on the kurtosis over energy distribution and the maximum spectral kurtosis value.

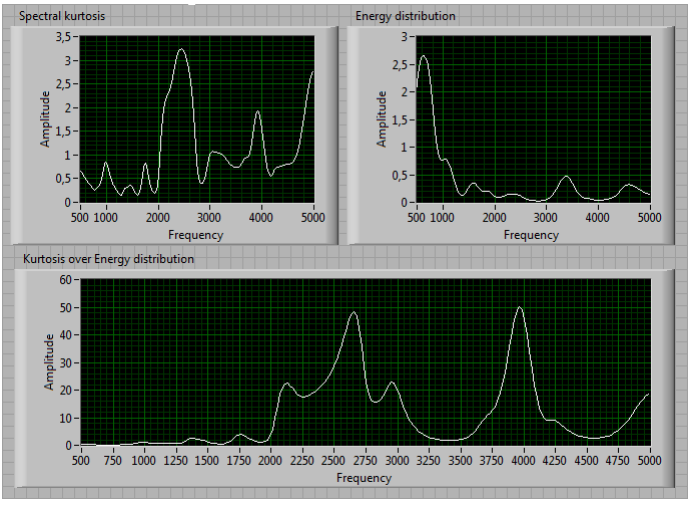

Fig. 1 Normalized spectral kurtosis and energy distribution and the resulting kurtosis over energy distribution along frequency domain

The filtering band has been chosen taking the maximum peak as central frequency and -3db of amplitude reduction as bandwidth, resulting in [2226.57; 2656,25] Hz and [3886.71; 4042,97] Hz for maximum spectral kurtosis and kurtosis over energy criterion respectively.

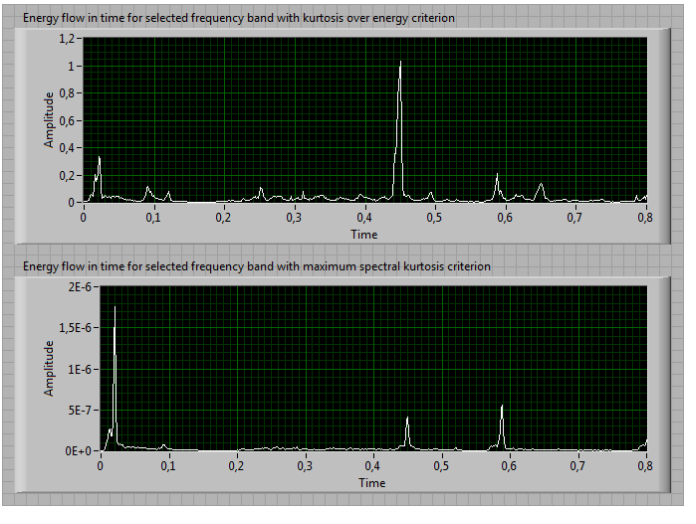

Fig. 2 Comparison of energy flow in time for selected frequency band with Kurtosis over energy and maximum spectral kurtosis used as criterion

The comparison of the two energy flows in Fig. 2 shows that they both report the main peaks, but the kurtosis over energy spectrum allows to appreciate also minor impacts that happen subsequent the main ones. The first of this secondary impacts is also present in the maximum spectral kurtosis spectra but is not appreciable. Among the specific peaks detected, it must be noted that the proposed distribution allows to take into account an informative band that would have been excluded if only SK had been considered. On the other hand the peak of the SK is still present.

5 Conclusion

In this paper a new procedure for the enhancement of ball bearing condition monitoring in non-stationary conditions is presented. The main consequence in the vibration monitoring is the presence of a strong contribution from non-stationary, non-Gaussian, impulsive, cyclic signal source which is strictly related with the variable load of the motor a part from the presence of damage in the bearing. This machine contribution makes hard the condition monitoring with techniques based on kurtosis indicator or simply the envelope analysis due to its strong influence on the residual signal. The suggested procedure starts from the computation of the STFT analysis of vibration data and allows to select an optimal informative frequency band from the spectrogram. The methodology is based on the calculus of both the spectral kurtosis and the energy distribution. In the first stage these quantities are normalized with respect to the mean values computed along the spectrum, and then the ratio between normalized kurtosis and energy is performed to obtain a distribution that selects bands in which there are simultaneously high kurtosis and low energy content.

Acknowledgements. The authors wish to thank the Inter Departmental Research Center INTERMECH MoRE of the University of Modena and Reggio Emilia for the financial support (M. Cocconcelli, R. Rubini).

This paper was also financially supported by State Committee for Scientific Research 2010–2013 as research project (W. Bartelmus, R. Zimroz).

References

El-Shafei, N., Rieger, N.: Automated Diagnostics of Rotating Machinery. In: Proceedings of 2003 ASME Turbo Expo., Atlanta, GA, USA, vol. 4, pp. 491–498 (2003)

Dalpiaz, G., Rivola, A., Rubini, R.: Effectiveness and Sensitivity of Vibration Processing Techniques for Local Fault Detection in Gears. Mechanical Systems and Signal Processing 14, 387–412 (2000)

Jardine, A.K.S., Lin, D., Banjevic, D.: A Review on Machinery Diagnostics and Prognostics Implementing Condition-Based Maintenance. Mechanical Systems and Signal Processing 20, 1483–1510 (2006)

Randall, R.B., Antoni, J.: Rolling Element Bearing Diagnostics—A Tutorial. Mechanical Systems and Signal Processing 25, 485–520 (2011)

Potter, R.: A new order tracking method for rotating machinery. Sound Vib. 24, 30–34 (1990)

Fyfe, K., Munck, E.: Analysis of computed order tracking. Mechanical Systems and Signal Processing 11(2), 187–205 (1997)

Baydar, N., Ball, A.: Detection of gear deterioration under varying load conditions by using the instantaneous power spectrum. Mechanical Systems and Signal Processing 14, 907–921 (2000)

Stander, C., Heyns, P., Schoombie, W.: Using vibration monitoring for local fault detection on gears operating under fluctuating load conditions. Mechanical Systems and Signal Processing 16(6), 1005–1024 (2002)

Zhan, Y., Makis, Y., Jardine, A.: Adaptive state detection of gearboxes under varying load conditions based on parametric modelling. Mechanical Systems and Signal Processing 20(1), 188–221 (2004)

Cocconcelli, M., Secchi, C., Rubini, R., Fantuzzi, C., Bassi, L.: Comparison Between Time-Frequency Techniques to Predict Ball Bearing Fault in Drives Executing Arbitrary Motion Profiles. In: Proceedings of the ASME International Mechanical Engineering Congress and Exposition, Boston, Massachusetts, USA, pp. 249–255 (2008)

Combet, F., Zimroz, R.: A new method for the estimation of the instantaneous speed relative fluctuation in a vibration signal based on the short time scale transform. Mechanical Systems and Signal Processing 23, 1382–1397 (2009)

Bassi, L., Cocconcelli, M., Secchi, C., Rubini, R., Fantuzzi, C.: An algorithm to diagnose ball bearings faults in servomotors running arbitrary motion profiles. In: Proceedings of the International Conference on Noise and Vibration Engineering (ISMA 2010), Leuven, Belgium (2010)

Curcurù, G., Cocconcelli, M., Rubini, R.: Wavelet decomposition and energy distribution as ball-bearing diagnostics tools in direct-drive motors. In: Proceedings of 17th International Congress on Sound and Vibration, Cairo, Egypt (2010)

Bartelmus, W., Chaari, F., Zimroz, R., Haddar, M.: Modelling of gearbox dynamics under time varying non-stationary operation for distributed fault detection and diagnosis. European Journal of Mechanics - A/Solids 29, 637–646 (2010)

Makowski, R.A., Zimroz, R.: Adaptive Bearings Vibration Modelling for Diagnosis. In: Bouchachia, A. (ed.) ICAIS 2011. LNCS(LNAI), vol. 6943, pp. 248–259. Springer, Heidelberg (2011)

Cocconcelli, M., Bassi, L., Secchi, S., Fantuzzi, C., Rubini, R.: An algorithm to diagnose ball bearing faults in servomotors running arbitrary motion profiles. Mechanical Systems and Signal Processing 27, 667–682 (2012)

Chaari, F., et al.: Gearbox vibration signal amplitude and frequency modulation. Shock and Vibration (in press, 2012); doi:10.3233/SAV-2011-0656

Zimroz, R., Bartelmus, W.: Application of adaptive filtering for weak impulsive signal recovery for bearings local damage detection in complex mining mechanical systems working under condition of varying load. Solid State Phenomena 180, 250–257 (2012), http://www.scientific.net/SSP.180.250

Zimroz, R., et al.: Measurement of Instantaneous Shaft Speed By Advanced Vibration Signal Processing - Application To Wind Turbine Gearbox. Metrology and Measurement Systems XVIII(4), 701–712 (2011)

Antoni, J., Randall, R.B.: Differential diagnosis of gear and bearing faults. ASME Journal of Vibration and Acoustics 124(2), 165–171 (2002)

Antoni, J., Randall, R.B.: Unsupervised noise cancellation for vibration signals. Part I—Evaluation of Adaptive Algorithms. Mechanical Systems and Signal Processing 18(1), 89–101 (2003)

Antoni, J.: The spectral kurtosis: a useful tool for characterising non-stationary signals. Mechanical Systems and Signal Processing 20(2), 282–307 (2006)

Sawalhi, N., Randall, R.B., Endo, H.: The enhancement of fault detection and diagnosis in rolling element bearings using minimum entropy deconvolution combined with spectral kurtosis. Mechanical Systems and Signal Processing 21(6), 2616–2633 (2007)

Boustany, R., Antoni, J.: Blind extraction of a cyclostationary signal using reduced rank cyclic regression - A unifying approach. Mechanical Systems and Signal Processing 22, 520–541 (2008)

Wang, Y., Liang, M.: An adaptive SK technique and its application for fault detection of rolling element bearings. Mechanical Systems and Signal Processing 25(5), 1750–1764 (2008)

Combet, F., Gelman, L.: Optimal filtering of gear signals for early damage detection based on the spectral kurtosis. Mechanical Systems and Signal Processing 23(3), 652–668 (2009)

Immovilli, F., Cocconcelli, M., Bellini, A., Rubini, R.: Detection of Generalized-Roughness Bearing Fault by Spectral-Kurtosis Energy of Vibration or Cur-rent Signals. IEEE Transactions on Industrial Electronics 56(11), 4710–4717 (2009)

Barszcz, T., Randall, R.B.: Application of spectral kurtosis for detection of a tooth crack in the planetary gear of a wind turbine. Mechanical Systems and Signal Processing 23(2), 1352–1365 (2009)

Zimroz, R., Bartelmus, W.: Gearbox condition estimation using cyclo-stationary properties of vibration signal. Key Engineering Materials 413-414, 471–478 (2009)

Barszcz, T., Jabłoński, A.: A novel method for the optimal band selection for vibration signal demodulation and comparison with the Kurtogram. Mechanical Systems and Signal Processing 25(1), 431–451 (2011)

Wang, Y., Liang, M.: An adaptive SK technique and its application for fault detection of rolling element bearings. Mechanical Systems and Signal Processing 25(5), 1750–1764 (2011); doi:10.1016/j.ymssp.2010.12.008

Wang, Y., Liang, M.: Identification of multiple transient faults based on the adaptive spectral kurtosis method. Journal of Sound and Vibration 331(2), 470–486 (2012)

Detecting AE Signals from Natural Degradation of Slow Speed Rolling Element Bearings

Mohamed Elforjani and David Mba

School of Engineering, Cranfield University,
Cranfield, Beds, MK43 0AL, UK
elforjani@gmail.com

Abstract. Rolling element bearing diagnosis using high frequency Acoustic Emission (AE) signals has been on-going since the late 1960's. This paper attempts to demonstrate the use of AE measurements to detect natural defect initiation and propagation in a rolling element bearing. To facilitate the investigation a special purpose test-rig was built to allow for accelerated natural degradation of a bearing race. It is concluded that sub-surface initiation and crack propagation is detectable with AE technology.

Keywords: condition monitoring, acoustic emission, and rolling element bearings.

1 Introduction

Acoustic Emission (AE) is transient elastic waves generated by the rapid release of energy from localized sources within a material [1]; typical frequency content of AE is between 100kHz to 1MHz. A tremendous amount of work has been undertaken over the last 20-years in developing the application of the Acoustic Emission technology for bearing health monitoring [2]. The high sensitivity of AE in detecting the loss of mechanical integrity at early stages has become one of the significant advantages over the well-established vibration monitoring technique. Jamaludin et al. [3] presented the challenges faced with using the vibration technology to monitor the mechanical integrity of slow speed bearings (less than 60rpm) and suggested that the AE technology could overcome such difficulties. Sources of AE in rotating machinery include impacting, cyclic fatigue, friction, turbulence, etc. For instance, the interaction of surface asperities and impingement of the bearing rollers over a defect on an outer race will result in the generation of acoustic emission. These emissions propagate on the surface of the material as Rayleigh waves and are measured with an AE sensor. Other wave types associated with the propagation of AE include Lamb, Longitudinal and Shear waves.

To date most published work on the application of the AE to monitoring bearing mechanical integrity have been conducted on artificially or 'seeded' damage which are generally induced with an electrical discharge system, engraving machine or by introducing debris into the lubricant [2 and 3]. However, Price et al.

[4] showed the applicability of AE to monitor naturally generated scuffing and pitting defects in a four-ball lubricant test machine. To date the only published work of Yoshioka [5] could be considered the first that directly addressed identification of the onset of natural degradation in bearings with AE. It is worth noting that Yoshioka employed a bearing with only three rolling elements which is not representative of a typical operational bearing. Moreover, Yoshioka terminated AE tests once AE activity increased as such the propagation of identified sub-surface defects to surface defects was not monitored. This work builds further on the work of Yoshioka by monitoring not only the initiation of cracks, but also its propagation to spalls or surface defects on a conventional bearing with the complete set of rolling elements.

2 Test Rig Layout and Experimental Procedure

One of the challenges is to enhance the crack signatures at the early stage of defect development. To implement this, bearing run to failure tests were performed under natural damage conditions on this specially designed test rig. A schematic of the data acquisition process is detailed in figure 1. To accelerate crack initiation, a combination of a thrust ball bearing and a thrust roller bearing was selected. One race of ball bearing (SKF 51210) was replaced with a flat race taken from the roller bearing (SKF 81210 TN) of the same size. As a consequence the rolling ball elements on a flat track caused very high contact pressure in excess of 6,000MPa. The test bearing rotated at 72 rpm. A coupling system was carefully selected to absorb any vibration as a result of attaching the shaft to the geared motor. The procedure and theories employed to determine the test duration to the onset of surface fatigue has been previously described by Elforjani et al. [6]. The test rig rotational speed was 72 rpm and an axial load ranging from 20, 35 and 50kN was employed for these particular tests.

A commercially available piezoelectric sensor (Physical Acoustic Corporation type “PICO”) with an operating range of 200 kHz – 1MHz was used. Four acous

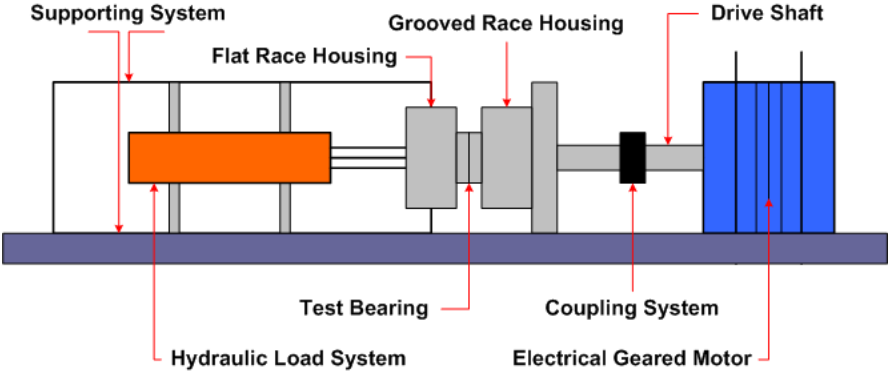

Fig. 1 Schematic of test-rig layout

tic sensors, together with two thermocouples were attached to the back of the flat raceway using superglue. One accelerometer (ENDEVCO-236-M-ISOEASE-PF44), attached to the stationary block, was used to measure the vibration. The acoustic sensors were connected a data acquisition system via a preamplifier, set at 40db gain. The system was continuously set to acquire AE waveforms at a sampling rate of 2MHz sampling rate. The software (signal processing package "AEWIN") was incorporated within the PC to monitor AE parameters such as energy (recorded at a time constant of 10ms and sampling rate of 100Hz).

3 Bearing Test

Four experimental cases are presented that reflect the general observations associated with over a dozen experimental tests. Two different approaches to ascertaining the applicability of the AE technology for monitoring cracks on slow speed bearings were undertaken. The first programme involved accelerating crack/spalls on the test bearing at three load conditions, 20, 35 and 50kN. The second involved running a test under conditions of grease starvation at two different loads of 20 and 50kN. It is worth stating that for the lubricated test cases, the test bearing was lubricated during the testing with Castrol Moly Grease (650-EL).

Observations of AE energy monitored continuously for all three load conditions are detailed in figure 2. It should be noted that each plot presents two different cases at the same applied load; for this particular paper, case I, II, III and IV are discussed. Results showed that during the first hour of the test, an increase in AE energy levels was noted; see figures 2. This was attributed to the 'run-in' phase, as after this period (approximately 1-hr) the measured AE energy remained relatively constant. It was observed that for all tests AE energy levels started to rise approximately few hours before the termination; 6.5-hrs for 50kN test, 6-hrs for 35kN test and 5-hrs for 20kN test. Also it was noted that during the final stages of bearing life AE energy levels were higher for the higher load conditions. A sample of AE waveforms at the end of the tests are shown in figures 3. Interestingly the AE waveforms associated with the damaged bearing showed higher amplitude levels for the AE bursts associated with the higher test loads; for instance see 50kN and 35kN of figure 3. Further, the defect frequency of the bearing was 9Hz. To ensure a consistent lubricant viscosity throughout the tests period, the measurement of lubricant temperature was also undertaken. These tests clearly illustrated that surface fatigue, such as flaking, could be initiated on the flat race within a few days depending on the load condition. It should be noted that the theoretical estimation of rolling contact fatigue is known to be subject to variability or scatter when compared to experimental results and this has been attributed to the probability of inclusions in the steel material located in the highest load zones of the race. It is also worth noting that the actual test period leading to visual damage on the race was much faster than the theoretical calculations. This variation was random but always earlier than predicted, see table1. This is attributed to issues such as misalignment, unbalance, etc., which are not incorporated in theoretical life estimates; however, best efforts were undertaken to minimize these issues.

Table 1 Predicted and experimental life of test bearing races (Approach I).

Case	Load (kN)	Predicted Life (hr)		Experimental Life (hr)	
		Flat Race	Grooved Race	Flat Race	Grooved Race*
I	50	24	432	16	-
II	35	72	1272	20	-
III	20	384	6864	50	-

*Tested were terminated once the crack has occurred on the flat races.

The second program (Grease Starvation Test) presents different trends to that noted in the prior cases, see figure 2. Observations of AE levels did not show any considerable rise at the start of the test. A significant rise in AE energy levels was observed at approximately 792-seconds and the AE activity gradually increased with time until the test was terminated (900-seconds). The increase in AE energy levels from the start of the test to the termination was in the order of 36,90 %. This significant rise in AE energy levels also suggested that damage had occurred on the bearing.

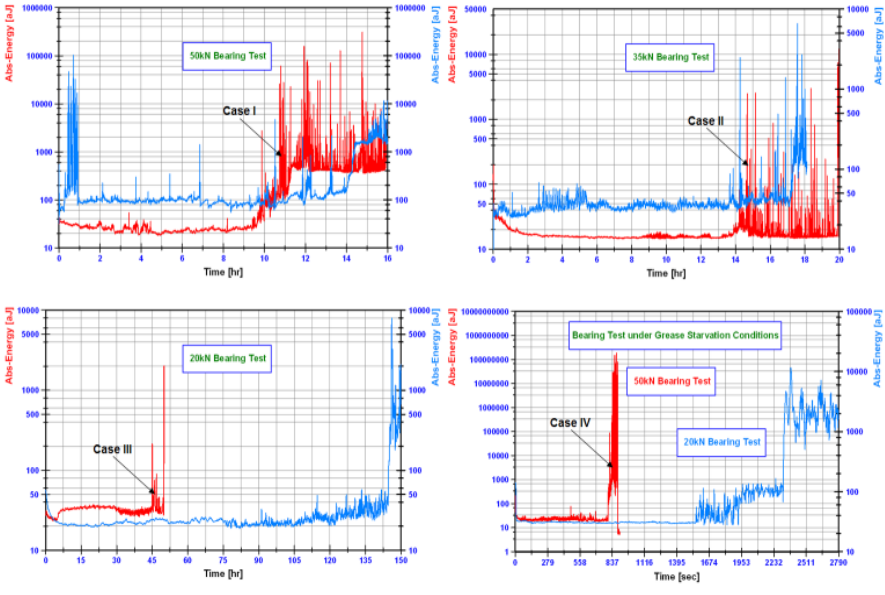

Fig. 2 General trend of AE energy throughout the bearing tests (Approach I & II)

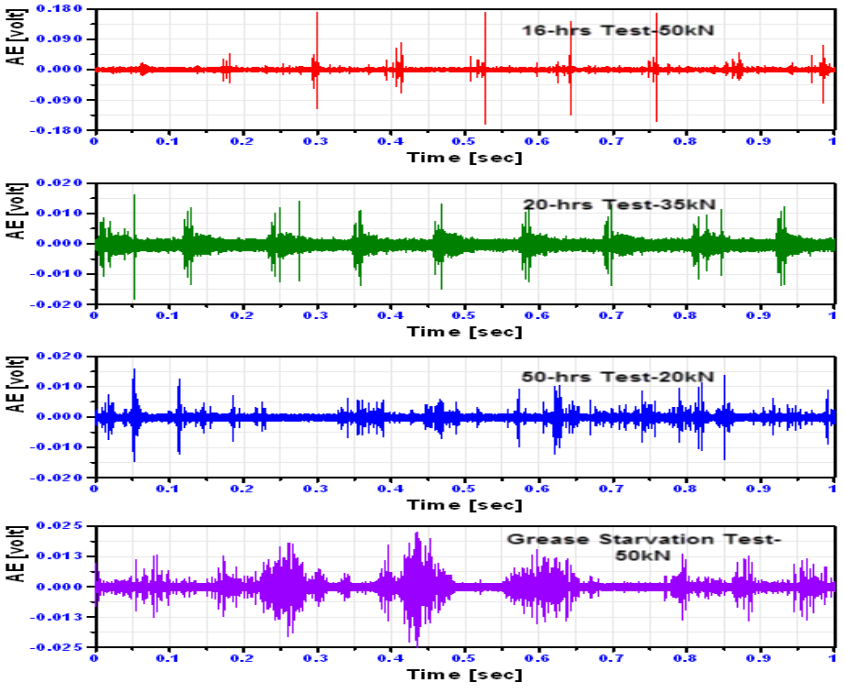

Fig. 3 AE waveforms on the termination of bearing tests

4 Fault Index Extraction Techniques

The Acoustic Emission technique was successfully employed by Elforjani et al. [7] to identify the presence and size of a natural defect on bearings that were tested throughout this investigation. Having established that AE parameters such as energy showed sensitivity to changes in AE activity it was thought prudent to correlate other processing techniques with the natural defect size on bearings. To accomplish this, a dimensionless ratio (R), which is a ratio between the defect size (L) and the rolling element diameter (D), was used. The techniques employed for this assessment included the Information Entropy, Kurtosis and Energy Index. These techniques were calculated using the following mathematical equations [8, 9, and 10]. A notation list of the mathematical symbols used in the equations is presented in the table 2.

$$\text{Information Entropy} = -\sum_{i=1}^{N} P_i \times \log(P_i) \tag{1}$$

$$\text{Kurtosis} = \frac{1}{N}\sum_{i=1}^{N}\left(\frac{X_i - \mu}{\sigma}\right)^4 \tag{2}$$

$$\text{Energy Index} = \left(\frac{\text{RMS}_{\text{Segment}}}{\text{RMS}_{\text{overall}}} \right)^2 \quad (3)$$

Table 2 Notation list of the mathematical symbols used in the analysis

Mathematical Symbol	Definition	Unit
Pi	Probability Distribution	-
N	Date Points	-
Xi	Signal Amplitude	Volt
μ	Mean of AE Waveform	Volt
σ	Standard Deviation of AE Waveform	Volt
RMS	Root Mean Square of AE Waveform	Volt

From the results presented in figure 4, it can be concluded that as the presence of the small defects on bearings is pronounced all factors become very sensitive indicators, whilst Kurtosis and Energy Index values come down when the damage size is well advanced. This can be attributed to the surface of the damage, which becomes greater than the space among two consecutive rolling elements. As consequence of this, continuous, not impulsive, signals will be produced; i.e. the first impulse does not expire before the second one is produced and eventually a Gaussian distribution in the values of Kurtosis and Energy Index may be observed.

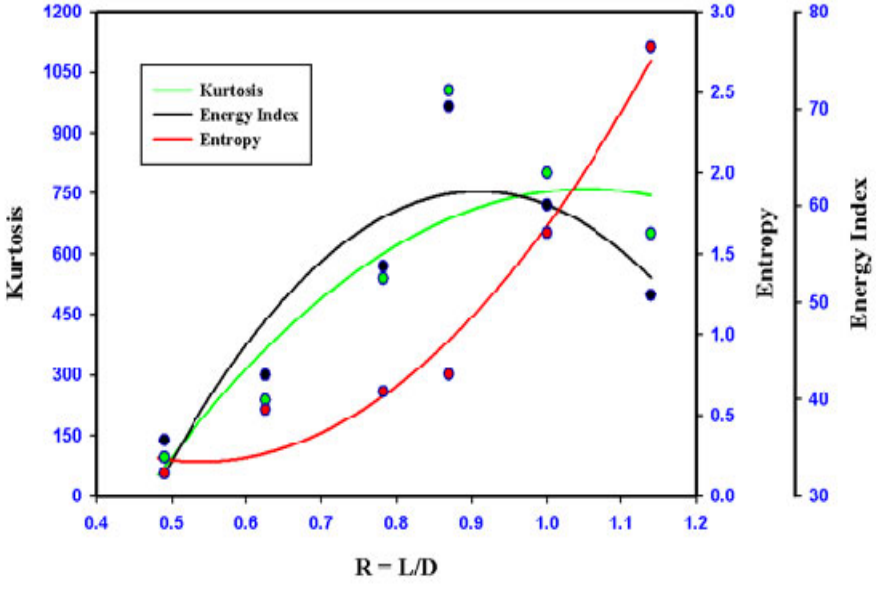

Fig. 4 General trend of fault indicators associated with the defect size

Results also revealed that Information Entropy is more sensitive and representative than Kurtosis and Energy Index with increasing defect size. Further, a steady increase in the Information Entropy levels was noted. This was expected as in statistical mechanics, the Entropy is described as the measure of the amount of disorder or chaos in a given system and it is highly depending on the probability distribution [8 and 11]. As the defect size increases, the internal randomness, or molecular chaos within the test bearing will increase. Hence the continuous monitoring of bearings employing techniques such as the Information Entropy would offer the operator a relatively more sensitive tool for observing high transient type activity.

5 Conclusion

This paper presents the early developments in the application of the AE technology to monitoring sub-surface crack initiation in rolling element bearings. The study has demonstrated that AE parameters such as energy are more reliable, robust and sensitive to the detection of incipient cracks and surface spalls in slow speed bearing. It was also shown that by employing a range of data analysis techniques such as Information Entropy, the growth of the natural defect size on bearings could successfully be identified.

References

1. ISO (International Standards Organization Documents) 22096; Condition monitoring and diagnosis of machines – Acoustic Emission (2008)
2. Mba, D., Rao, R.B.K.N.: Development of Acoustic Emission Technology for Condition Monitoring and Diagnosis of Rotating Machines: Bearings, Pumps, Gearboxes, Engines, and Rotating Structures. The Shock and Vibration Digest 38, 3–16 (2006)
3. Jamaludin, N., Mba, D., Bannister, R.H.: Condition Monitoring of Slow-Speed Rolling Element Bearings Using Stress Waves. In: Proceedings of the IMECHE Part E Journal of Process Mechanical Engineering 215(4), 245–271(27)
4. Price, E.D., Lees, A.W., Friswell, M. I.: Detection of Severe Sliding and Pitting Fatigue Wear Regimes Through the use of Broadband Acoustic Emission. IMechE Journal of Engineering Tribology 219(2), 85–98 (2005)
5. Yoshioka, T.: Detection of Rolling Contact Subsurface Fatigue Cracks Using Acoustic Emission Technique. Journal of the Society of Tribologists and Lubrication Engineers 49 (1992)
6. Elforjani, M., Mba, D.: Observations and Location of Acoustic Emissions for a Naturally Degrading Rolling Element Thrust Bearing. Journal of Failure Analysis and Prevention (May 2008); ISSN: 1547-7029 (Print) 1864-1245 (Online)
7. Elforjani, M., Mba, D.: Accelerated Natural Fault Diagnosis in Slow Speed Bearings with Acoustic Emission. Journal of Engineering Fracture Mechanics 77(1), 112–127 (2010)
8. Liangsheng, Q., Liangming, L., Jay, L.: Enhanced Diagnostic Certainty Using Information Entropy Theory. Advanced Engineering Informatics, vol. 17, pp. 141–150 (2003)

9. Lihui, W., Robert, X.G., Pham, D.T.: Condition Monitoring and Control for Intelligent Manufacturing. (Springer Series in Advanced Manufacturing). Springer-Verlag London Limited, London (2006)
10. Al-Balushi, R., Samanta, B.: Gear Fault Diagnosis Using Energy-Based Features of Acoustic Emission Signals. Proceedings of the Institution of Mechanical Engineers Part I, Journal of Systems and Control Engineering 216, 249–263 (2002)
11. Sethna, P.J.: Statistical Mechanics: Entropy, Order Parameters and Complexity. (Oxford Master Series in Physics). Clarendon Press, Oxford (2011)

Leak Detection in Viscoelastic Pipe by Transient Analysis

Lamjed Hadj Taïeb, Lazhar Ayed, and Ezzeddine Hadj Taïeb

UR Mécanique des Fluides Appliquée et Modélisation,
Ecole Nationale d'Ingénieurs de Sfax, B. P. W 3038 Sfax, Tunisia
{lamjed_hadjtaieb,hlzed}@yahoo.fr, Ezed.Hadj@enis.run.tn

Abstract. The use of fluid transients has the potential to provide insight into effect of leaks in pipeline systems and hence provide leak detection method. This paper presents a technique for detection and location of leaks in a single viscoelastic pipe by means of transient analysis. The method uses transient pressure waves initiated by the sudden closure of an upstream valve. The presence of a leak in a pipe partially reflects these pressure waves and allows for the location and magnitude of leaks. The two constitutive equations of continuity and momentum yield a set of two partial differential equations of hyperbolic type. The viscoelastic behaviour of the pipe wall material is represented by a generalized Kelvin-Voigt model. The computed results obtained by the method of characteristics describe the influence of the leak on head and discharge time-histories. The effect of the pipe wall viscoelasticity on the leak detection and sizing is also discussed.

Keywords: leak detection, viscoelastic pipe, water hammer.

1 Introduction

In current years the management of pressurised pipe systems has been of great attention not only to guarantee their security and good performance but also to more understand their physical behaviour among existing problems. The detection and location of leaks in pipeline systems are one of major problems and leakage control has become high priorities for water supply utilities and authorities (Covas 2003). This is not only because there is a greater understanding of the economic and social costs associated with water losses, but there is also an imperative to make best possible use of the natural source that is water.

Several techniques for leak detection in pipe have been presented in the literature using different methods include acoustic technology (Tafuri 2000), ground penetration radar or infrared spectroscope (Hunaidi and Giamou 1998), transmission and reflection of pressure waves (Brunone 1999) and (Misiunas 2005),

sequential statistical analysis (Buchberger and Nadimpalli 2005), and transient analysis methods (Brunone and Ferrante 2001).

Some of the current numerical methods for locating and identifying leaks are either complicated or imprecise; most of them are time consuming. These methods usually used the acquisition and the analysis of extensive real-time data. Often, these data are either not available or costly to obtain.

The ideal technology for leak detection and location should be non-intrusive, faster and cheaper and should not require cessation of pipeline operations for long period of time. Since transient test data can give more information about a pipe system than steady state measurements, leak detection methodologies based on transient analysis can achieve this goal.

The purpose of this paper is to detect leaks in a single plastic pipe system using transient event (water hammer signals) generated by the sudden closure of a downstream valve. A pressure wave travels along the system at high speed and is modified by the system during its travel. To apply the procedure of leak detection with confidence and success, special attention has to be given to the dynamic effects related to the energy dissipation, namely the friction and the mechanical behaviour of the viscoelastic pipe wall (Soares and Covas 2007).

Although the viscoelastic behaviour of polymers is well known, this behaviour tends to be forgotten in hydraulic transient analysis in plastic pipes (Covas et *al.* 2004, 2005). The viscoelastic behavior is characterized by elastic strain and gradual retarded strain. This retarded behaviour of the pipe wall causes significant transient pressure attenuation which poses difficulty in detecting leak reflection.

The focus here is mainly to study the leak affects on transient pressure and to locate leak in viscoelastic pipe.

Leaks within a viscoelastic pipe partially reflect these pressure signals and allow for the accurate location and sizing of a leak by measuring the period of time which the pressure wave takes to travel from the measurement section to the leak and vice-versa.

In this study, we proceed to develop a mathematical model through the simplified formulations for the transient flow of fluid in viscoelastic pipes.

The characteristics method is used for the numerical solution of the obtained equations. The viscoelastic behavior of the pipe wall material is simulated by a generalized Kelvin-Voigt model.

2 Water Hammer Model

2.1 Basic Equations

Viscoelastic pipes have different behaviour in comparison with metal and concrete pipes. In this case, strain can be decomposed into an instantaneous elastic strain ε_{ϕ}^{e}, and retarded strain ε_{ϕ}^{r}

Taking into account the relationship between the pipe cross-section A and the total circumferential strain, the elastic strain, the retarded strain and the state equation of a barotropic fluid, the simplified one-dimensional continuity and momentum equations that describe transient flow in viscoelastic pipe are (Hadj Taieb and Hadj Taieb 2009):

$$\frac{\partial H}{\partial t}+V\frac{\partial H}{\partial x}+\frac{C^2}{gA}\frac{\partial Q}{\partial x}+\frac{2C^2}{g}\left(\frac{\partial \varepsilon_{\phi}^{r}}{\partial t}+V\frac{\partial \varepsilon_{\phi}^{r}}{\partial x}\right)=0 \tag{1}$$

$$g\frac{\partial H}{\partial x}+\frac{1}{A}\left(\frac{\partial Q}{\partial t}+V\frac{\partial Q}{\partial x}\right)+\frac{g\lambda Q|Q|}{2DA^2}=0 \tag{2}$$

where H is the pressure head, Q is the flow rate, C is the elastic wave speed, g is the gravitational acceleration, A is the pipe cross-sectional area, D is the internal pipe diameter, λ is the coefficient of friction, x is the spacial coordinate and t is the time.

The pressure wave celerity C is defined by the following expression (Stuckenbruck et *al.* 1985):

$$C=\left(\frac{\rho}{K}+\rho\frac{cD}{Ee}\right)^{-1/2} \tag{3}$$

where K is the bulk modulus of liquid, c is the pipe constraint factor, e is the pipe-wall thickness and E is the Young's modulus of elasticity of the pipe.

The retarded circumferential strain is represented by a generalized Kelvin-Voigt model of n elements:

$$\varepsilon_{\phi}^{r}=\sum_{j=1}^{n}\varepsilon_{\phi,j}^{r}(x,t)=\sum_{j=1}^{n}\left\{\frac{cD}{2e}\int_0^t\left[p(x,t-t')-p_0(x)\right]\frac{J_j}{\tau_j}e^{-t'/\tau_j}dt\right\} \tag{4}$$

where J *is* the creep compliance function described by (Cavas et *al.* 2005):

$$J(t)=J_0+\sum_{j=1}^{n}J_j\left(1-e^{-t/\tau_j}\right) \tag{5}$$

in which J_0 represents the creep-compliance of the first spring, J_j is the creep-compliance of the spring of j-element and τ_j is the retardation time of the dash-pot of j-element (figure 1).

The retarded strain time-derivative in equations (1) is calculated by:

$$\frac{\partial \varepsilon_{\phi}^{r}}{\partial t}=\sum_{j=1}^{n}\frac{\partial \varepsilon_{\phi,j}^{r}(x,t)}{\partial t}=\sum_{j=1}^{n}\frac{cD}{2e}\frac{J_j}{\tau_j}\left[p(x,t)-p_0(x)\right]-\frac{\varepsilon_{\phi,j}^{r}(x,t)}{\tau_j} \tag{6}$$

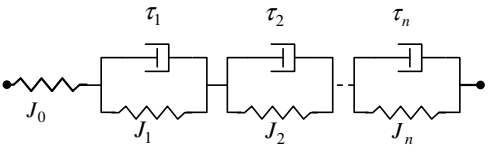

Fig. 1 Generalized Kelvin-Voigt model

2.2 Leak Modeling

A leak represents a flow loss without head loss. A leak is modelled as an orifice and the discharge, Q_ℓ , through it is assumed to be given by the following equation (Brunone and Ferrante 2001):

$$Q_\ell = C_d A_\ell \sqrt{\frac{2(p_\ell - p_0)}{\rho}} \tag{7}$$

where C_d is a discharge coefficient, A_ℓ is the orifice area and p_ℓ is the pressure on either side of the orifice assumed to be equivalent.

3 Numerical Resolution

The equations (1) and (2) are of hyperbolic type so they can be solved by the method of characteristics (MOC).

When the fluid is water, the fluid velocity is negligible compared to the elastic wave speed ($V << C$), the convective terms in equation systems (1) and (2) can be neglected. This leads to approximately straight characteristic lines $\mathrm{d}x/\mathrm{d}t = \pm C$

Equations (1) and (2) can be transformed into a system of ordinary differential equations and solved by MOC. The compatibility equations are:

$$Q_{Pi} - Q_{i-1} + \frac{gA}{C}\left(H_{Pi} - H_{i-1}\right) + \frac{\lambda}{2DA} Q_{i-1}\left|Q_{i-1}\right|\Delta t + 2CA\Delta t\left(\frac{\partial \varepsilon_\phi^r}{\partial t}\right)_{i-1} = 0 \tag{9}$$

along the positive characteristic line ($\Delta x/\Delta t = +C$), and

$$Q_{Pi} - Q_{i+1} - \frac{gA}{C}\left(H_{Pi} - H_{i+1}\right) + \frac{\lambda}{2DA} Q_{i+1}\left|Q_{i+1}\right|\Delta t - 2CA\Delta t\left(\frac{\partial \varepsilon_\phi^r}{\partial t}\right)_{i+1} = 0 \tag{10}$$

along the negative characteristic line ($\Delta x/\Delta t = -C$),

where i is the node number, Δx and Δt are the distance ant the time steps respectively (figure 2).

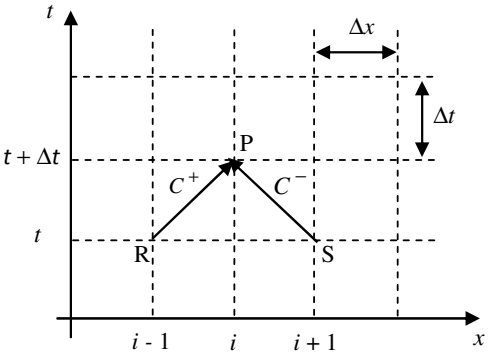

Fig. 2 Characteristic lines: Regular grid

3.1 Initial Conditions

Initial conditions must be provided at the time 0 in order to solve the problem. These conditions can be determined by computing the solution of the following system of ordinary differential equations deduced from equations (1) and (2):

$$\begin{cases} \dfrac{dQ_J}{dx} = 0 \\ \dfrac{dH_J}{dx} = -\dfrac{\lambda Q_J^2}{2gDA^2} \end{cases} \tag{11}$$

where subscript J refers to the pipe number.

The solution of this system is

$$\begin{cases} Q_J(0,x) = Q_J(0,0) \\ H_J(0,x) = H_J(0,0) - \dfrac{\lambda Q_J^2}{2gDA^2}\, x \end{cases} \tag{12}$$

At the leak

$$Q_J(0, L - X) = Q_{J+1}(0,0) + Q_{\ell 0} \tag{13}$$

3.2 Boundary Conditions

Transient flow is created by the fast closure of the valve at the downstream end ($x = L$). At this section $Q(t,L) = 0$. At the upstream end, $x = 0$ and $t > 0$, the condition is given by the reservoir at fixed level $H(t,0) = H_0$.

At a leak, equation (7) is implemented in the MOC as an internal boundary condition. The tow relationships that relate the upstream head and flow to the downstream head and flow are (figure 3):

$$H_{1P,\,N_1+1} = H_{2P,1} = H_P \tag{14}$$

$$Q_{1P,\,N_1+1} = Q_{2P,1} + Q_\ell = Q_{2P,1} + C_d A_\ell \sqrt{2gH_P} \tag{15}$$

The compatibility equations either side of the leak are given by equations (16) and (17):

$$\begin{aligned} Q_{1P,\,N_1+1} - Q_{1,\,N_1} + \frac{gA}{C}\left(H_{1P,\,N_1+1} - H_{1,\,N_1}\right) + \frac{\lambda}{2DA} Q_{1,\,N_1}\left|Q_{1,\,N_1}\right|\Delta t + \\ + 2CA\Delta t\left(\frac{\partial \varepsilon_\phi^r}{\partial t}\right)_{1,N1} = 0 \end{aligned} \tag{16}$$

$$\begin{aligned} Q_{2P,1} - Q_{2,\,2} - \frac{gA}{C}\left(H_{2P,1} - H_{2,\,2}\right) + \frac{\lambda}{2DA} Q_{2,\,2}\left|Q_{2,\,2}\right|\Delta t - \\ - 2CA\Delta t\left(\frac{\partial \varepsilon_\phi^r}{\partial t}\right)_{2,2} = 0 \end{aligned} \tag{17}$$

Equations (15) to (17) form a set of quadratic equation in $\sqrt{H_P}$ that is solved using the quadratic formula:

$$H_P = \left[\left(-C_d A_\ell \sqrt{2g} + \sqrt{\Delta}\right) \Big/ \left(4\frac{gA}{C}\right)\right]^2 \tag{18}$$

where

$$\begin{aligned} \Delta = \left(C_d A_\ell \sqrt{2g}\right)^2 - 8\frac{gA}{C}\Big[\left(Q_{2,\,2} - Q_{1,\,N_1}\right) \\ - \frac{\lambda\Delta t}{2DA}\left(Q_{2,\,2}\left|Q_{2,\,2}\right| - Q_{1,\,N_1}\left|Q_{1,\,N_1}\right|\right) \\ - \frac{gA}{C}\left(H_{2,\,2} + H_{1,\,N_1}\right) + 2CA\Delta t\left(\left(\frac{\partial \varepsilon_\phi^r}{\partial t}\right)_{1,N1} + \left(\frac{\partial \varepsilon_\phi^r}{\partial t}\right)_{2,2}\right)\Big] \end{aligned} \tag{19}$$

Once H_P is determined the upstream and downstream flows are calculated using the positive and negative compatibility equations (9) and (10) respectively.

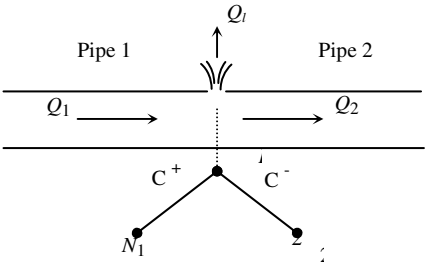

Fig. 3 Leak implementation in the MOC

4 Application and Results

As an example, considering the polyetelene pipe rig at Imperial college (Covas et *al.* 2004). The pipeline is made of high-density polyetelene SDR11 PE100 with 50.6 mm inner diameter; 6.2 mm wall thickness and the total length of pipeline is 277 m (length between the reservoir and the global valve). Numerical results are calculated for the initial flow of $1.008\, ls^{-1}$ and for a leak located at intermediate section. The transient event is caused by the valve closure, the pipeline rheological behaviour linear viscoelastic is described by the creep compliance function represented by three-element Kelvin-Voigt model. Parameters J_k and τ_k are:

$$J_0 = 0.7E-9\, Pa^{-1}s, J_1 = 0.0805E-9\, Pa^{-1}s, J_2 = 0.1083E-9 Pa^{-1}s,$$
$$J_3 = 0.57635 Pa^{-1}s, \tau_1 = 0.05s, \tau_2 = 0.5s, \tau_3 = 10s.$$

Figure 4 shows the head history at the valve obtained by the numerical simulation for leaks located at various positions along the pipe $(X = L/2, 3L/5, 2L/3, 3L/4, 4L/5, 5L/6)$, where X is the location of the far from the valve. Friction effects are ignored $(\lambda = 0)$ to highlight the impact of the leak on the head of pressure evolution. To more observe the leak effect on pressure head, Figure 5 is plotted to calculate the instance at which wave is reflected by the leak (t_{f1}).

Figure 6 shows the head pressure history at leaks located at the previous positions but the friction effects are considered $(\lambda = 0.08)$. One can observe the significant difference. In fact, the transient event is damped much more rapidly than in the system where the leak does not exist. It can be interpreted by the effect of the leak on the features of the pressure wave propagating along the pipe. Indeed, the leak causes partial reflections of wave fronts that became small pressure discontinuities in the original pressure trace and increase the damping of the overall

pressure signal. Hence, through correctly interpreting the head-time history at the valve it is possible to extract information on leak location and leak discharge.

Figure 5 and figure 7 are an enlargement of the results of figure 4 and figure 6, respectively. The location of leak is given by:

$$X = \frac{t_{f1}}{t_0} L \tag{20}$$

where t_{f1} is the time difference between the initial transient wave and the reflected wave at the leak section (time corresponding to the sudden change of head from ΔH_1 to ΔH_2) and $t_0 = 2L/C$ is the pipe characteristic time. Table 1 and Table 2 summarize values of t_{f1} for the considered leak locations for $\lambda = 0$ and $\lambda = 0.08$ respectively.

By analysing the head-time transient in figure 5, the leak discharge may be obtained by:

$$Q_{\ell_0} = \frac{gA}{C}\left(\Delta H_0 - \Delta H_1\right) \tag{21}$$

ΔH_0 and ΔH_1 are head rises provoked by the sudden closure of the valve when there is or there is no leak respectively.

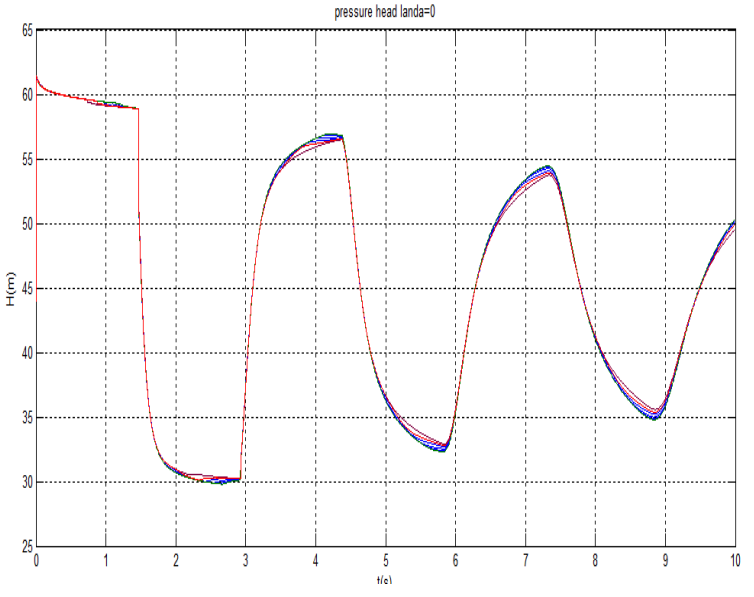

Fig. 4 Piezometric head at different leak locations $(\lambda = 0)$

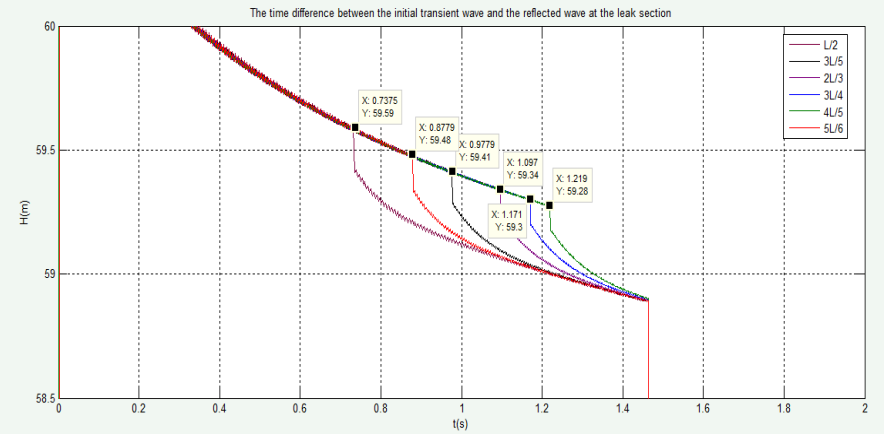

Fig. 5 Different times leak reflection for different leak locations shown in fig.4

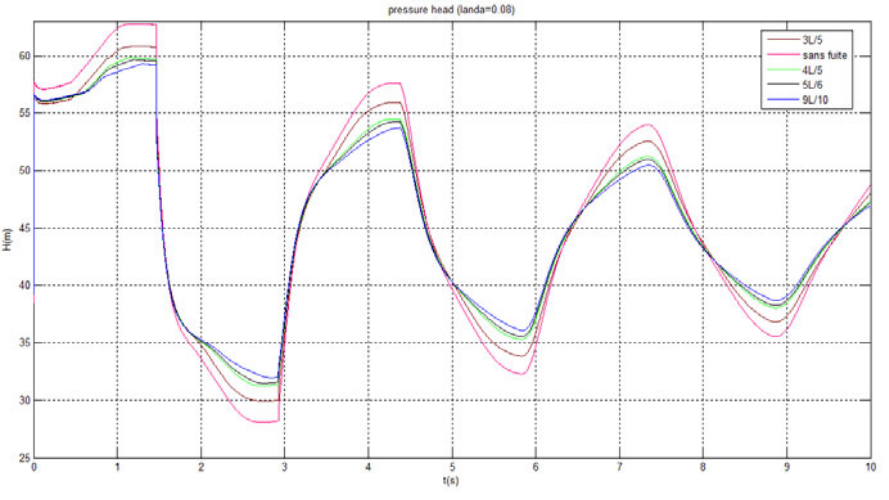

Fig. 6 Piezometric head at different leak locations $(\lambda = 0.08)$

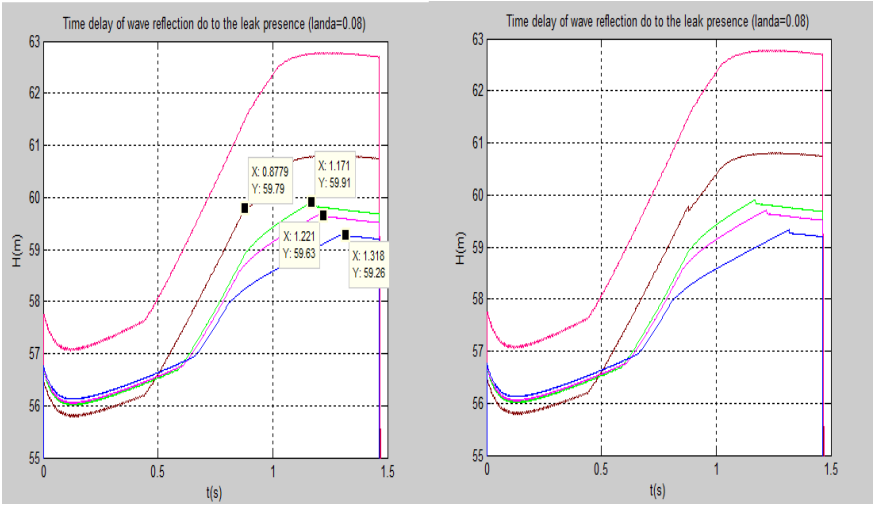

Fig. 7 Different times leak reflection for different leak locations shown in fig.6

Table 1 Leak location $(\lambda = 0, t_0 = 1.463\ s)$

Leak location	$L/2$	$3L/5$	$2L/3$	$3L/4$	$4L/5$	$5L/6$
$X/L = t_f/t_0$	0.502	0.60	0.66	0.749	0.76	0.833

Table 2 Leak location $(\lambda = 0.08, t_0 = 1.463\ s)$

Leak location	9L/10	5L/6	4L/5	3L/5
$X/L = t_f/t_0$	0.90	0.8345	0.80	0.60

5 Conclusion

The current paper presented the leak detection in plastic pipes taking into account the viscoelastic behavior of pipe-wall. The method of characteristics, which requires less computer cost, is directly used to determine the magnitude of leaks by developing relations between the location and amplitude of the reflected wave at the leak section.

Furthermore, it is necessary to register the pressure time-history in just one section of the pipe (for example the downstream end) and then the proposed technique can strongly reduce leak detection survey costs in safe conditions.

Transient head obtained for a viscoelastic pipeline with leak showed a fast attenuation and the retardation of the overall pressure wave in time, these significant results make difficult leak location and sizing.

References

Brunone, B.: Transient Test-Based Techniques for Leak Detection in Outfall Pipes. Journal of Water Resources Planning and Management 125, 302–306 (1999)

Brunone, B., Ferrante, M.: Detecting leaks in pressurized pipes by means of transients. Journal of Hydraulic Research 39, 539–547 (2001)

Buchberger, S., Nadimpalli, G.: Leak Estimation in Water Distribution Sys-tems by Statistical Analysis of Flow Readings. Journal of Water Resources Planning and Management 130, 321–329 (2004)

Covas, D., Stoianov, I., Graham, N., Maksimovic, C., Ramos, H., Bulder, D.: Water hammer in pressurized polyethylene pipes: conceptual model and experi-mental analysis. Urban Water Journal 1(2), 177–197 (2004)

Covas, D., Stoianov, I., Mano, J., Helena, R., Graham, N., Maksimovic, C.: The dynamic effect of pipe-wall viscoelasticity in hydraulic transient. Part II- model development, calibration and verification. J. of Hydraulic Reseach 43, 56–70 (2005)

Covas, D., Stoianov, I., Ramos, H., Graham, N., Maksimovic, C.: The dissipation of pressure surges in water pipeline systems. In: First Joint Conf. IAHR-IWA on Pump. Electromechanical Devices and Systems (PEDS 2003), Valencia, Spain (2003)

Hadj Taïeb, E.: Leak detection by using water hammer and impedance methods. In: Ulanicki, et al. (eds.) Water Mangement Challenges in Global Change, Taylor & Francis Group, London (2007)

Hadj Taieb, L., Hadj Taieb, E.: Numerical simulation of transient flow in viscoelastic pipes with vapour cavitation. International Journal of Modelling and Simulation 29(2), 206–213 (2009)

Hunaidi, O., Giamou, P.: Ground-Penetrating Radar for Detection of Leaks in Bur-ied Plastic Water Distribution Pipes. In: Seventh International Conference on Ground-Penetrating Radar, Lawrence, Kansas (1998)

Misiunas, D., Vitkovsky, J., Olsson, G., Simpson, A., Lambert, M.: Pipeline Break Detection Using Pressure Transient Monitoring. Journal of Water Resources Planning and Management 131, 316–325 (2005)

Soares, A.K., Covas, D., Reis, L.F.R.: Inverse transient analysis for leak detection in PVC pipe network. In: Ulanicki, et al. (eds.) Water Mangement Challenges in Global Change, pp. 337–344. Taylor & Francis Group, London (2007)

Stuckenbruck, S., Wiggert, D.C., Otwell, R.S.: The influence of pipe motion on acoustic wave propagation. Transactions of the ASME 107, 518–522 (1985)

Tafuri, A.: Locating Leaks with acoustic technology. American Water Works Association Journal 92, 57–66 (2000)

Taghvaei, M., Beck, S., Taszewski, S.: Leak detection in pipelines using cep-strum analysis. In: Measurement Science and Technologie, vol. 17, pp. 367–372. IOP Publishing Ltd., UK (2006)

Gear Fault Detection under Fluctuating Operating Conditions by Means of Discrepancy Analysis

Theo Heyns[1] and Stephan Heyns[2]

[1] Department of Electronic and Computer Engineering,
University of Pretoria, Private Bag X20 Hatfield 0028 South Africa
theoheyns@gmail.com
[2] Dynamic Systems Group, Department of Mechanical and Aeronautical
Engineering, University of Pretoria, Private Bag X20 Hatfield 0028 South Africa
stephan.heyns@up.ac.za

Abstract. A study is presented where an autoencoder is used to learn non-linear principal components (PCs) which are representative of windowed samples from a vibration signal which are generated by a gearbox in a healthy condition. The PCs are optimized to represent hidden characteristics of the healthy data as experienced over different operating conditions. The auto-encoder may thus be used to detect signal distortions (discrepancies) in a novel signal, where the discrepancies are the result of machine faults. By analyzing the vibration signal piece-wise by means of block windows it is possible to generate a discrepancy signal. The discrepancy signal indicates the time instances and associated severity of individual signal discrepancies. The periodicity of the discrepancy signal, as analyzed by means of its spectrum and cepstrum, allows for insight into which gear components are damaged. The case study assumes that neither any additional transducers, nor any historical fault data are available.

Keywords: condition monitoring, fluctuating operating conditions, discrepancy analysis, change detection, auto-encoder, spectrum, cepstrum

1 Introduction

The performance of many conventional machine condition monitoring strategies (e.g. spectral analysis) tends to be impeded if the machine is subject to fluctuating operating conditions (Jardine et al. 2006). Change detection offers a practical way to conduct condition monitoring, since it does not depend on extensive historical fault representative data. Advanced change detection strategies may be implemented, which are capable of operating under fluctuating operating conditions. Essentially a data driven model is used to represent a baseline signal which is generated by the machine while in good condition. The data driven model may be augmented by additional sensors (such as a tachometer) which conveys information

regarding the instantaneous operating conditions. Non-operating condition related deviations from the baseline vibration response is assumed to be due to the onset of damage.

Timusk et al. (2008) investigate a number of advanced modeling methodologies for detecting anomalies which might indicate the onset of damage. A number of extracted signal features are monitored for changes, some which include time and order domain statistical features such as RMS, Kurtosis and Skewness, as well as auto-regressive model coefficients. A number of different data driven models are investigated, including an Autoencoder, K-means clustering, Principal component analysis, Nearest neighbor, Support Vector Machine, Gaussian probability densities, and a combination classifier. The models are augmented with information regarding the motor current, drive voltage, and shaft speed. The methodology proved effective at identifying defective components even in the presence of fluctuating operating conditions.

This paper investigates a change detection methodology based on the application of an autoencoder. A experimental study is presented where the vibration signal from a healthy gearbox which is subject to a fluctuating torque is monitored. Novel to our approach is that the vibration signal is evaluated in a piece-wise manner. This renders it possible to generate a signal transform, which is referred to as a discrepancy signal. The proposed methodology is implemented based on the assumption that only a vibration signal is available, with no additional transducers (e.g. tachometer) or fault histories. The discrepancy signal indicates the positions in time, and severity to which a vibration signal deviates from a reference signal. The discrepancy signal can subsequently be analyzed based on its spectrum and cepstrum to identify the periodicity of the signal discrepancies. The periodicity information offers insight into the nature of the fault condition. The spectra and cepstra of the discrepancy signal proved significantly more sensitive to initial gear tooth damage compared to those of the raw signal.

2 Methodology

The implemented methodology comprises two key steps, namely computing a discrepancy signal, and then analyzing its spectrum and cepstrum.

2.1 Piecewise Signal Evaluation

The signal is evaluated in a piecewise manner. This renders it possible to obtain a discrepancy signal, which indicates the severity and periodicity of fault related signal outliers. Short signal segments are analyzed individually. This is done by means of a sliding block window which extracts m successive datum points from the vibration waveform. One such window represents a single sample $\boldsymbol{s_i}$, where i indicates the sample number. Let $\mathbf{x}$ represent the vibration signal of length n, so that $\boldsymbol{s_1}$ denotes the first sample of m datum points, $\boldsymbol{s_1} = [x_1, x_2, \ldots, x_m]$. The block window is subsequently advanced by a single datum point to generate the

following sample $\boldsymbol{s_2} = [x_2, x_3, \ldots, x_{m+1}]$. This process is repeated until $n - m$ samples have been created.

These samples are typically selected to be of very short duration, for instance approximately as long as the duration that a single tooth is in mesh. In this paper the sample length is selected to consist of 10 datum points, $m = 10$. It will later be indicated that 10 datum approximately corresponds to the time period during which a single tooth is in mesh.

2.2 Autoencoder

An autoencoder is a form of auto-associative neural network which may be used to detect non-linear principal components for a data set (Kramer 1991). The autoencoder is used to model the reference samples from the healthy machine. During training a signal sample $\boldsymbol{s}$ is both used as input and as the target output. The neural network consist of five layers (with sigmoid activation functions), to ensure sufficient non-linear characteristics (Bishop 2006). The middle layers contain fewer neurons than the input/output layers. This bottleneck is used to extract the non-linear principal components (Bishop 2006). The principal components represent hidden features of the data in a lower dimension than that of the original data.

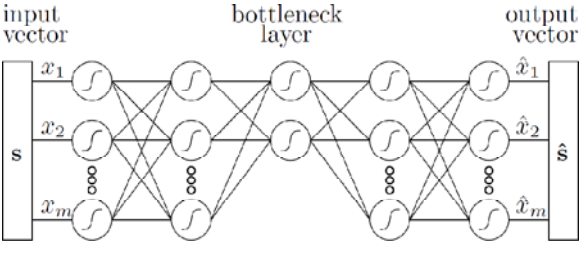

Fig. 1 An autoencoder is used to extract hidden non-linear principal components from data samples which represent the machine in good condition

The neural network is optimized so as to select principal components which best represent the hidden characteristics of the set of healthy data as generated over the range of typical conditions under which the machine is operated. As such the principal components tend to be specific to the healthy data. The optimized autoencoder will not be able to produce accurate outputs for samples which deviates from the reference samples. The difference between the predictions of the autoencoder, and the input can thus be used to obtain a measure of discrepancy d_i. The discrepancy is calculated as the root mean square of the errors,

$$d_i = \sqrt{\frac{1}{m}(e_i^2 + e_{i+1}^2 + \cdots + e_{i+m-1}^2)} \quad (2)$$

where the errors $\boldsymbol{e_i} = [e_i \ldots e_{i+m-1}]$ are computed as the differences between the sample values $\boldsymbol{s}_i = [s_i \ldots s_{i+m-1}]$ and the estimated output from the autoencoder $\hat{\boldsymbol{s}}_i = [\hat{s}_i \ldots \hat{s}_{i+m-1}]$, so that $\boldsymbol{e_i} = \boldsymbol{s_i} - \hat{\boldsymbol{s}}_i$.

A discrepancy value is computed for every sample, so that a total of $n - m$ discrepancy values $\boldsymbol{d} = [d_1, d_2, \ldots, d_{n-m}]$ are obtained. A discrepancy signal is thus obtained which exhibits periodic impulsive behavior which corresponds to the presence of fault related signal distortions in the measured signal.

3 Experimental Setup

The proposed methodology is investigated on experimental data which were recorded in the Sasol Laboratory for Structural Mechanics at the University of Pretoria (Stander and Heyns 2005). Dr. C.J. Stander generously made available the data for this study.

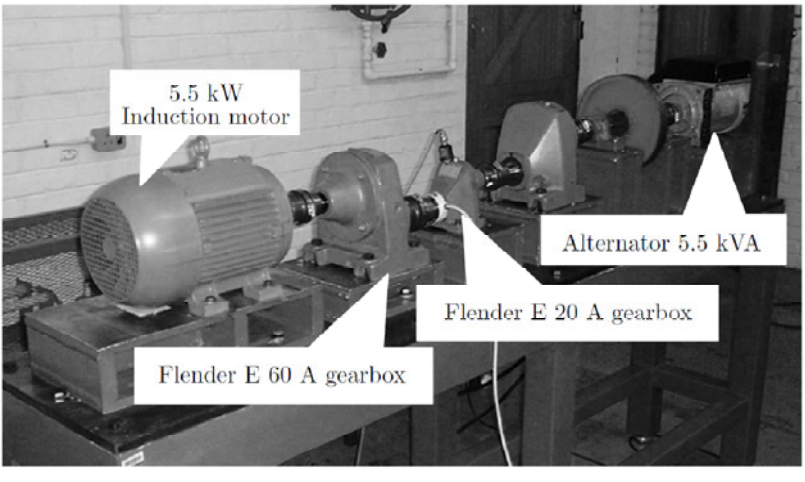

Fig. 2 Experimental setup

Gear damage was investigated on a single stage Flender E20A gearbox which had a rated load of 20 Nm, was fitted with helical gears. The monitored gearbox was mounted between two Flender E60A gearboxes, the first of which served to step the torque up and the second to step the torque down. The step down gearbox was driven by a 5.5 kW three phase four pole WEG squirrel cage electric motor. The step up gearbox was connected to a flywheel which in turn was coupled with a 5.5 kVA Mecc Alte Spa three phase alternator to apply the load. The gearbox was subjected to a fluctuating load. The load consisted of a 0.5 Hz sinusoidal

component with an amplitude of 3.35 *Nm* which was superimposed on a mean torque of 11.05 *Nm*. The gear casing acceleration response was measured in the vertical direction by means of a 10 V/g PCB integrated circuit piezoelectric industrial accelerometer. The vibration was sampled at 50 kHz, but was later low pass filtered with an eighth-order Butterworth filter which had a cut-off frequency at 1000 Hz. The signal was down sampled to 2500 samples per second.

The monitored gear had 43 teeth and rotated at approximately 5.19 Hz. The corresponding pinion had 22 teeth and rotated at approximately 10.12 Hz. The gear mesh frequency was close to 223 Hz. This means that each tooth is in mesh approximately for the duration of 10 datum points (0.004 s).

Three levels of damage (referred to as damage states 1, 2 and 3) were induced, by respectively removing 100, 200 and 300 μm material from the tooth face. Damage state 0 refers to the healthy data.

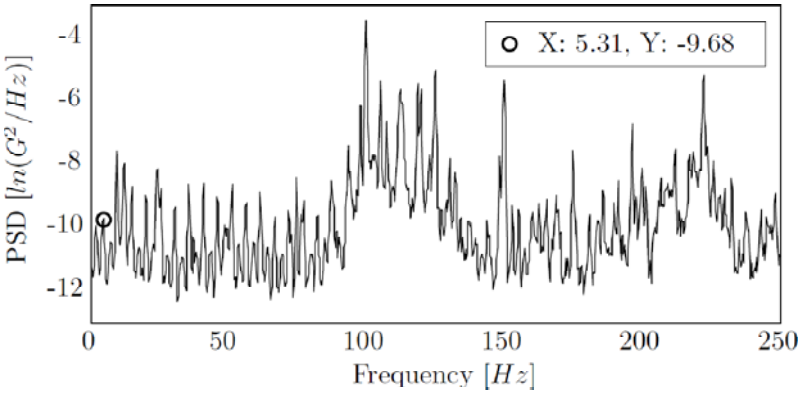

Fig. 3 Limited performance of vibration PSD even for advanced damage (state 3)

The natural logarithm of the power spectral density (PSD) for the vibration signal as measured for the 300 μm damage condition is presented in figure 3. Significant energy is observed at the gear mesh frequency of approximately 223 Hz. Using the logarithmic scale, some energy is also observed at the gear rotational frequency of approximately 5.19 Hz (fluctuates somewhat according to shaft rotational speed and PSD resolution). However, as indicated in table 1 the response at these frequencies do not consistently increase for greater damage. Figure 3 indicates the most advanced state of damage. As expected do the PSDs of the lesser two states of damage offer even less evidence of gear damage.

Table 1 ln PSD values at frequencies of interest for the raw vibration signals

Damage state	0	1	2	3
5.31 Hz	-10.49	-8.03	-9.68	-6.91
230 Hz	-6.175	-7	-5.198	-4.68

4 Implementation

An autoencoder is used to model the healthy data. A window block length of 10 datum points were used to construct individual samples. The block length is so chosen as to reflect the approximate duration that a single tooth is in mesh. The autoencoder is optimized by means of back propagation. The first, second, fourth and fifth layers in the neural network all contains 10 nodes. The nodes are fully connected to all the nodes of the adjacent layers. The middle (bottleneck layer) contains three nodes. Trial and error was used to find the number of nodes in the middle layer which offered a good compromise between performance on the training set, and compression.

The vibration data from each of the four damage states are subsequently transformed to discrepancy signals. The discrepancy signal performance is found to be fairly robust given different numbers of principal components. Good results were also obtained by using 2-7 nodes. For interest was conventional (linear) PCA also investigated. Linear PCA (based on the Eigen-values of the sample covariance matrix) significantly reduced the cost of learning the reference model, but it was less successful of modeling the data under the transient operating conditions.

5 Experimental Results

Figure 4 illustrates the PSD spectrum for the discrepancy signal from damage state 1 (100 μm face removal). Unlike the PSD from the raw signal where the gear damage could not be detected, does the discrepancy signal PSD contain a clear dominant term at 5.31 Hz which corresponds to the gear rotational frequency.

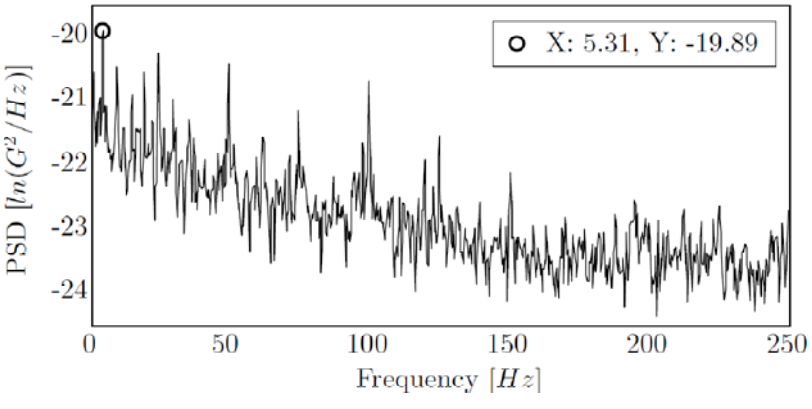

Fig. 4 The discrepancy PSD for damage state 1 clearly indicates the damage.

Table 2 indicates how the gear rotational frequency component increases with the onset of damage. Not only is the increasing trend much more evident, but the

gear rotational frequency dominates for the PSD of the first damage state. The cepstrum of the second and third states clearly indicate that the discrepancies correspond to the gear.

Table 2 ln PSD at the gear rotational frequencies of the discrepancy signal

Damage state	0	1	2	3
5.31 Hz	-19.8	-19.16	-14.71	-12.02

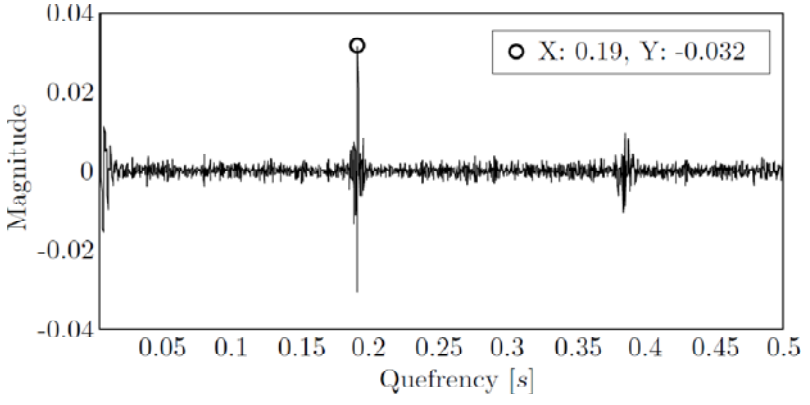

Fig. 5 The discrepancy Cepstrum for damage state 2 clearly indicates the damage.

The discrepancy signal for the second state of damage is very impulsive (due to the greater degree of damage). This impulsive nature results in a PSD which is subject to significant harmonics. The discrepancy now becomes more suitable to cepstrum analysis which is capable of collecting families of uniformly spaced sidebands and harmonics (Randall 2011). The real cepstrum is computed as the inverse Fourier transform of the real logarithm of the magnitude of the Fourier transform of the discrepancy signal. The real cepstrum of the discrepancy signal for the second damage state is presented in figure 5. A clear energy component is evident at a quefrency of 0.19 s, which corresponds to the gear rotational frequency. The cepstrum did however fail to detect the gear fault for the discrepancy signal from the 1st state of damage. The cepstrum should be used as auxiliary tool to the spectrum.

6 Conclusion

A methodology was presented were an autoencoder is used to compute a discrepancy signal. The discrepancy signal tends to be more sensitive to fault related signal distortions compared to the raw vibration signal. The cepstrum of the

vibration is well suited to the impulsive nature of the discrepancy signal. It is believed that the methodology is simple to implement, as it requires little understanding of the system, does not depend on historical fault data, and may be implemented without the need for additional sensors or signal resampling if the speed fluctuations are limited.

References

Jardine, A.K.S., Daming, L., Banjevic, D.: A review on machinery diagnostics and prognostics implementing condition-based maintenance. Mechanical Systems and Signal Processing 20(7), 1483–1510 (2006)

Timusk, M., Lipsett, M., Mechefske, C.K.: Fault detection using transient machine signals. Mechanical Systems and Signal Processing 22(7), 1724–1749 (2008)

Stander, C.J., Heyns, P.S.: Instantaneous angular speed monitoring of gearboxes under non-cyclic stationary load conditions. Mechanical Systems and Signal Processing 30(4), 817–835 (2005)

Kramer, M.: Nonlinear principal component analysis using auto-associative neural networks. AIChE Journal 37(2), 233–243 (1991)

Bishop, C.M.: Pattern recognition and machine learning. Springer Science + Business Media, LLC (2006)

Randall, R.B.: Vibration-based condition monitoring. John Wiley & Sons, Ltd. (2011)

Bearing Fault Diagnosis Using Neural Network and Genetic Algorithms with the Trace Criterion

Ridha Ziani[1], Rabah Zegadi[2], Ahmed Felkaoui[2], and Mohammed Djouada[2]

[1] Ecole nationale supérieure de technologie ENST- ex CT siège DG .SNVI,
Route Nationale N°5 Z.I.Rouiba, Alger , Algeria
ziani_lmpa@yahoo.fr
[2] Laboratoire de mécanique de précision appliquée Université de Sétif 19000, Algeria
rzegadi@yahoo.fr, a_felkaoui@yahoo.fr,
djouada_lmpa@yahoo.fr
Phone / Fax: (+213) 36 92 51 34

Abstract. Condition monitoring of rolling element bearings through the use of vibration analysis is an established technique for detecting early stages of component degradation. This study is presented to compare the performance of bearing fault detection using artificial neural networks (ANNs) and genetic algorithms (GA). The time domain vibration signals of a rotating machine with normal and defective bearings are processed for feature extraction. The extracted features from preprocessed signals are used as inputs to ANN classifier for five-class recognition (one normal and four with different levels of fault). The system of features selection is based on genetic algorithms as optimization method and the trace criterion from the linear discriminant analysis (LDA) as evaluation function. . The ANNs are trained with a subset of the experimental data for known machine conditions, and tested using the remaining set of data. The procedure is illustrated with and without features selection. The results show the efficiency of the proposed methodology.

Keywords: condition monitoring, genetic algorithms, trace, vibration, neural network, rotating machines.

1 Introduction

The monitoring of machines is gaining much importance in the industry because of the need to increase machine reliability and reduce the loss of potential production due to failures caused by different defects. The use of vibration signals is quite common in the field of condition monitoring of rotating machines. Many currently available techniques require a lot of expertise to implement them successfully; it requires new techniques that allow relatively unskilled operators to make reliable decisions without knowing the mechanism of the system and

analyze the data. New techniques are required to monitor a mechanical system. Therefore, reliability should be the most important criterion of the operation.

Artificial neural networks (ANNs), is a powerful technique for pattern recognition and have been applied to the classification of real systems faults (Jack and Nandi 2000a), (Jack and Nandi 2000b), (Benahmed 2002).

Genetic algorithms (GA) have been presented in several references (Jack and Nandi 2002), (Samanta et al. 2001). In the short period of their development, the AG showed their superior capabilities and has been successfully applied in many fields.

2 Artificial Neural Network

An Artificial Neural Network (ANN) is an information processing paradigm inspired by biological nervous systems. The human learning process may be partially automated with ANN's, which can be configured for a specific application, such as pattern recognition or data classification, through a learning process.

An artificial neuron is composed for some connections, which receive and transfer information, also there is a net function designed for collect all information (weights x inputs + bias) and send it to the transfer function, which process it and produces an output.

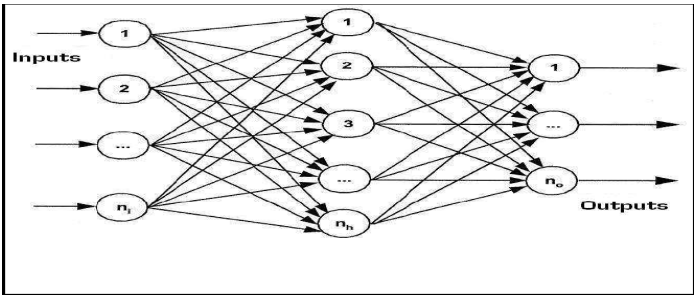

Fig. 1 Typical MLP structure

The most popular network used for classification purposes is the multilayer perceptron (MLP). An MLP is a network of simple neurons called perceptrons. The basic concept of a single perceptron was introduced by Rosenblatt in 1958 (Chinil et al. 2008). The perceptron computes a single output from multiple real-valued inputs by forming a linear combination according to its input weights and then possibly putting the output through some nonlinear activation function. An example MLP work is shown in Fig 1.

3 Genetic Algorithms (GA)

The GA used in this experiment is a simple GA. The GA uses a population size of size Np, and starts with a random generation of chromosomes. Each chromosome

is of size Nb equal to the number of features used. Elitist model of the population is used, ie the best individual in the population is kept prior to the new population, which prevents the decrease in the performance of the AG with the growth in the number of generations.

3.1 Coding of Chromosomes

To solve our problem of feature selection, we chose to use binary encoding, where the number of bits in each chromosome (individual) is the number of possible features that can be included in the original set. Thus, a binary string is composed by M bits. If the jth (i = 1, ..., M) bit is a unit value, then the indicator should be selected and participated in the classification else if the jth bit has value 0, then the feature should be excluded

3.2 Generating the Initial Population

The initial population consists of a set of individuals (chromosomes) randomly generated. The number of individuals in a population or population size is an important parameter for the AG that it will be determined. The representation of the population *P* is:

$$P = \left[P_1 \;\; P_2, \cdots \;\; P_i \cdots \;\; P_{Np} \right]^T \tag{1}$$

where P_i represents the *ith* chromosome in the population and *Np* is the number of chromosomes in the population. All chromosomes in our case were randomly generated.

3.3 The Fitness Function

In the present work we will use a genetic approach that optimizes the choice of parameters by minimizing a cost function. The latter is chosen according to the Trace criterion of the linear discriminant analysis (LDA).

In discriminant analysis (Jieping and Ravi 2004), three scatter matrices, called within-class, between-class, and total class matrices, are defined to quantify the quality of the class. In the present work, we have chosen to minimize the trace criterion of the within-class given by:

$$\text{J= trace } (S_w) \tag{2}$$

$$\text{With} \quad S_{\text{w}} = N_1 S_{w1} + N_2 S_{w2} + \cdots + N_c S_{N_C} = \sum_{i=1}^{N_C} N_i S_{wi} \tag{3}$$

Sw is the matrix of within-class of the class w_i. It is calculated using the following equation:

$$S_{w_i} = \frac{1}{N_i} \sum_{j=1}^{N_i} (x_{ij} - m_i)(x_{ij} - m_i)^T \tag{4}$$

With:

N_c: Number of classes
N_i : Number of vectors in each class
x_{ij}: jth vector of the class,
m_i: centroid of the ith class.
The global centroid m is defined by:

$$m = \left[m_1 \, m_2 \ldots m_j \ldots m_M \right]^T \tag{5}$$

Obtained from all samples

$$m_j = \frac{1}{N} \sum_{i=1}^{N} x_{ij} \tag{6}$$

3.4 Stopping Criterion

Stopping the algorithm is fixed according to a stopping criterion. In the present work, the algorithm stops when it reaches a number of 500 generations. This number is initially given.

3.5 Selecting Individual for Reproduction

To generate new offspring (children) in our case, parents are selected based on their evaluation function, and then mechanisms of crossover and mutation are applied. To select the best chromosomes in a population, we chose to use the truncation selection. A mortality rate of 20% is considered, that is to say that 80% of the strongest individuals are selected for reproduction, while 20% of the weak disappear without being able to reproduce. The crossing is in place so that new chromosomes retain the best part of old chromosomes. However, it is still important part of the population survive to the next generation because it is likely that the best chromosomes are not replicated in the next generation. That is why the model elitist was also adopted

4 Vibration Data

The vibration data used in this paper were taken from "Bearing Data Center,"[1] As shown in Fig. 2. The test bed consists mainly of a motor (left), a coupling (center), a dynamometer (right) and control circuits (not shown).

[1]: `www.eecs.cwru.edu\laboratory\bearing\welcome_overview.htm`

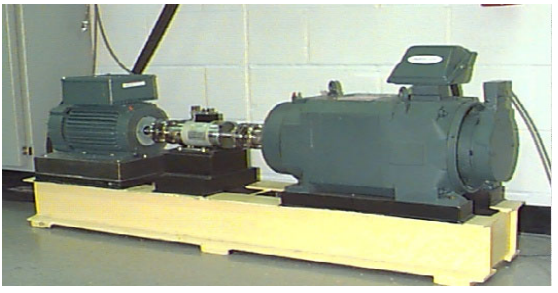

Fig. 2 Bearing test stand[2]

Motor bearings were seeded with faults using electro-discharge machining (EDM). Faults ranging from 0.007 inches in diameter to 0.040 inches in diameter were introduced separately at the inner raceway, rolling element (i.e. ball) and outer raceway. Faulted bearings were reinstalled into the test motor and vibration data was recorded for motor loads of 0 to 3 horsepower (motor speeds of 1797 to 1720 RPM).

In this work we limit ourselves to the study of defects created on the inner raceway. Table 1 show fault specification:

Table 1 Fault specification

Bearing	Fault Location	Diameter	Depth	Bearing Manufacturer
Drive end	Inner Raceway	0,007	0,011	SKF
Drive end	Inner Raceway	0,014	0,011	SKF
Drive end	Inner Raceway	0,021	0,011	SKF
Drive end	Inner Raceway	0,028	0,050	NTN

Vibration data was collected using accelerometers, which were attached to the housing with magnetic bases. Fig 3 shows time domain signals for normal and faulty bearing

Accelerometers were placed at the 12 o'clock position at both the drive end and fan end of the motor housing. During some experiments, an accelerometer was attached to the motor supporting base plate as well. Vibration signals were collected using a 16 channel DAT recorder, and were post processed in a Matlab environment. Digital data was collected at 12.000 samples per second, for drive end bearing faults. Speed and horsepower data were collected using the torque transducer/encoder and were recorded by hand.

[2] http://csegroups.case.edu/bearingdatacenter/pages/apparatus-procedures

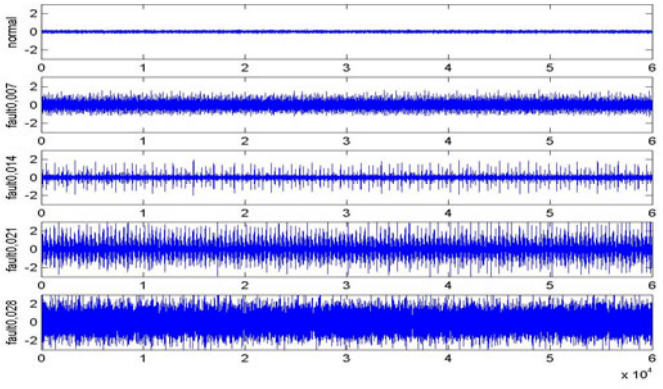

Fig. 3 Time domain signals for normal and faulty bearing

5 Features Extraction

For each condition (normal and faulty inner raceway) we have 4 signals recorded for four different speeds. So we have, 20 signals sampled at 12 kHz. Samples were divided into two segments of 61068 samples each.; one used for the training of ANN and the other for the test In the present work we chose to calculate two sets of features:

5.1 Statistical Features

After a preliminary analysis, samples were processed in four adjacent bands [1-1500] Hz, [1500-3000] Hz, [3000-4500] Hz and [4500-6000] Hz to extract six features (1–6): root mean square, variance, skewness, kurtosis and normalized five and six central moments. The procedure of feature extraction was repeated for five bearing conditions (normal and faulty) giving a total set of 40×24 features

5.2 Spectral Features

Spectral features were generated by calculating the power spectral density PSD around the frequencies in the four bands mentioned above, giving a total set of 40×4 features.

Each of the features was normalised dividing each row by its absolute maximum value keeping the inputs within ±1 for better speed and success of the network training.

The global data set of 40×28 was divided into two sets of 20×28; the first is used to train the neural network, while the second is used for the test.

6 Results and Discussion

The data set were split in training and test sets of size 20×28 using Matlab. The number of output node of MLPs was five with three hidden layers . Results are presented to see the Performance of ANNs without and with feature selection based on GA. The training success for each case was 100%.

6.1 Performance Classification of ANNs without Features Selection

Table 2 shows the classification performance for statistical and spectral features sets and the combined set without selection by AG

Table 2 Performance classification of ANNs without features selection

Data set	Training succès (%)	Test succès (%)	misclassified (in test)	Number of iteration
Statistical	100	90	5 ,8	7
spectral	100	100	-	100
combined	100	85	5 ,8, 9	11

The results show that the network is trained with a 100% performance for different sets of features. We got a performance test of 90% using statistical set and better performance of 100%, with the spectral sets, while we have a performance of 85% with the combined sets (statistical and spectral features). This can be explained by the redundancy of some features.

6.2 Performance Classification of ANNs with Features Selection by GA

In this step the network is trained and tested using the optimal features obtained by the genetic algorithm we proposed. Several tests were performed to test the convergence of our algorithm.

Table 3 shows the performance of classification after selecting the most relevant indicators. The results show an improvement in performance test of ANN, using the optimal features .for the various tests. This performance is 100%. (All comments are correctly assigned to classes) with a reduced number of features. The separation of the five classes is, therefore, carried out with an error rate of zero.

We can see that for the various tests, the optimal vector form is not the same. This is quite normal since the initial population is generated in a random manner. However, some indicators are repeated, (7 13 19 and 24 which correspond to the rms value calculated in the bands [1500-3000] [3000-4500] [4500-6000] and at the six central moment calculated in the band [4500-6000]. We also find that the classification is performed with a 100% performance using only two features 7 and 13.

Table 3 Performance classification of ANNs without features selection

Tests	Selected features	Training success (%)	Test success (%)	Number of iterations
Test 1	7 13 18 19	100	100	100
Test2	7 13 19 24	100	100	100
Test3	7 13 19 24	100	100	100
Test 4	7 13	100	100	87

7 Conclusion

This work has presented a novel approach to diagnose. The roles of different vibration signals and signal processing techniques have been investigated. The results show the potential application of GAs with trace criterion in the selection of features, allowing early fault detection at incipient levels in machine condition detection.

References

Jack, L.B., Nandi, A. K.: Comparison of neural networks and support vector machines in condition monitoring applications. In: Proceedings of 13th Conference on Condition monitoring and Diagnostic Engineering Management (COMADEM), Houston, TX, USA, pp. 721–730 (2000a)

Jack, L.B., Nandi, A.K.: Support vector machines for detection and characterisation of rolling element bearing faults. Proceedings of Institution of Mechanical Engineers. Part C: Journal of Mechanical Engineering Science 215, 1065–1074 (2000b)

Samanta, B., Al-Balushi, K.R., Al-Araimi, S.A.: Use of genetic algorithm and artificial neural network for gear condition diagnostics. In: Proceedings of COMADEM 2001, pp. 449–456. University of Manchester, UK (2001)

Benahmed, N.: Optimisation de réseaux de neurones pour la reconnaissance de chiffres manuscrits isolés: sélection et pondération des primitives par algorithmes génétiques, Thèse of doctorat, University of Québec (2002)

Casimir, R.: Diagnostic des défauts des machines asynchrones par reconnaissance des formes, Thèse de doctorat, Ecole Centrale de Lyon (2003)

Jack, L.B., Nandi, A.K.: Fault detection using support vector machines and artificial neural networks, augmented by genetic algorithms. Mechanical Systems and Signal Processing 16(2002), 373–390 (2002)

Chinil, R., Shamekhi, A., Behroozi, M., Samadani, E.: A Neural Network Fault Diagnosis Method Applied for Faults in Intake System of a Spark Ignition Engine Using Normalized Process Variables. In: International Conference on Control, Automation and Systems (2008)

Ye, J., Janardan, R.: An Optimization Criterion for Generalized Discriminant Analysis on undersampled problems. IEEE Transactions on Pattern Analysis and Machine Intelligence 26(8) (2004)

Chapter 2
Modelling of Dynamics and Fault in Systems

The vibration based faults detection in machinery such as misalignment, unbalance, local damages, … is widely developed and extensively used in practice. However, the quantification and the location of defects is still a research subject for many years ago. In the last decades, an increase of interest was observed for model based approaches to provide mathematical explanation of the dynamics of machinery especially in presence of faults and in non-stationary operations.

Through simulations it is possible to classify vibration signatures and distinguish changes in dynamic response induced by different kinds of defects and existing in the same time at different locations of the studied machines. Also, with simulations it is possible to verify the experimental knowledge and understand complex phenomena acting on machines such as time varying loading conditions. Recent advances in this field will be discussed in this chapter. The main research development in modeling that is presented through this chapter covers a certain number of mechanical systems such as gears, rotors, wind turbines. The dynamic behavior in presence of defects, as well as in time varying operations is discussed in this chapter.

Using Parametric Dynamical Models to Determine Observability Requirements for Condition Monitoring Systems

Michael G. Lipsett

Department of Mechanical Engineering, University of Alberta,
Edmonton, Alberta, Canada T6G 2G8
mlipsett@ualberta.ca

Abstract. An effective condition monitoring system depends on good observability of the effects of a fault. For many damage mechanisms that affect the reliability of components in systems, parametric models have been developed that describe the rate at which damage accumulates, based either on empirical or theoretical models of the physics of the damage process. These models can inform the reliability analyst about observability of the damage process, and the effect of time-varying system behavior on the observable damage effects. Simulations of system processes with integral damage models can then be used to determine how overall system processes affect damage accumulation in components, particularly in time-varying processes, how damage accumulation compromises performance of the overall system, and the sensitivity of features extracted from signals with respect to fault detection and identification. A simple framework is described for incorporating damage accumulation into lumped-parameter system models. Examples are given for a material handling pipeline process and for a haul truck tire, which highlights some specific challenges of relating overall process state variables to state variables of a damage process, for choosing sensors for a condition monitoring system.

Keywords: parametric modeling, damage models, observability.

1 Introduction

In considering the condition of a technological system comprising a set of connected subsystems (such as machines) made up of components, the condition can be characterized on three levels: the overall system level, the machine level, and the component level.

At the system level, probabilistic models of condition are generally used, because there are too many variables and too little observability to describe the condition at the component level mechanistically. Probabilistic methods are effective for systems that have stationary random processes for inputs and disturbances [1];

but a time-varying system requires conditional probabilities, because the state of nature can affect the sensitivity of classification methods.

At the component level, physics-based deterministic models of damage accumulation can be developed to represent a priori knowledge of how the condition of a component changes with time. The damage process may be based on a theoretical understanding of how the component changes with time. Such models are usually empirically based, relating a set of variables to a damage output measure through an analytical relationship that is not necessarily physics-based, for example, the well-known kinematic models for rolling-element vibrations that are functions of shaft speed [2]. More commonly, relationships between measurable condition indicators and damage severity are empirically based, employing features extracted statistically from signals under known conditions. Any unmodeled dynamics are considered stochastic disturbances to the feature extraction and classification process. Insights in the physics allow phenomena to be included in the model, rather than being lumped into the unknown disturbances. Inputs to a model of damage accumulation may be different from the system variables that characterize how the component contributes to system dynamics.

Between these levels of abstraction is the machine level, in which a machine is an assembly of interacting components, with some environmental inputs and disturbances. Models of machine condition may be based on hybrid models that combine deterministic and stochastic processes. The machine-level system allows for subsystems related to damage accumulation to link to process-system level dynamics of time-varying processes. These non-stationary processes occur in many applications, including process plants with variable feedstock, earthmoving machinery, vehicles, and power generation and distribution systems.

Lumped-parameter system modeling is an appropriate formulation of the dynamics of most machine systems. The level of abstraction can be defined in constitutive relationships for each element in the system. Graphically, the system is represented by a network of elements connected at nodes. Node variables must sum at a node, and the changes in loop variables around a closed network path must sum to zero. The constitutive relationship for each element consists of a through variable (such as electrical current, volumetric flow rate, heat flux, etc.) and a change in an across variable (such as voltage difference, pressure drop, temperature change, etc.). These complementary variables are also sometimes referred to as effort and flow variables. Dynamic relationships entail time derivatives of one or both variables.

The governing equations of a system can be formulated in a number of ways. The most general approach is based on state vector $\mathbf{x}$ and constitutive relationships, which describe the dynamics of a system (comprised of a set of connected elements within the system) and the vector of outputs $\mathbf{y}$. In a fully observable system, $\mathbf{y} = f(\mathbf{x})$ includes all elements of $\mathbf{x}$. In dynamical systems, the lumped-parameter physics of efforts across (or flows through) each element contribute to a set of differential equations, which describe how energy is distributed within the elements of the system, how elements are storing and releasing energy, how energy is transformed to other forms, and how energy is dissipated within the system. The eigenvalues of a dynamical system determine its natural frequencies, which

informs the condition monitoring analyst on the required bandwidth for data acquisition [3].

Dissipative elements represent losses in a system. Dissipation elements cause energy to leave system, increasing entropy. For example, in a mechanical system, a damper dissipates energy as heat. In a mixed dynamical system model, actuator elements transform energy from one type to another, for example, a motor in an electromechanical system. If there is a dissipative load in the mechanical subsystem, such as a brake, then the electrical energy is first converted to mechanical energy, and then some of that energy is eventually lost as heat.

Ideally a dissipative element remains intact forever; but in reality the element will eventually become damaged or degrade over time. Other elements of the system may also develop some damage, through some dissipative process that inflicts damage on a part of the system. System models generally neglect degradation, which typically accumulates over a long time interval compared to the time frame of interest for modeling (and simulating) the dynamics of overall system processes. Energy lost by the system over time may be due to non-damaging dissipative processes, but energy loss may also be due to processes that contribute to damage. In this way, a dynamic model of a system can also incorporate models of damage mechanisms (or at least to determine whether there is a change in the system that may be due to damage accumulation). This approach is fairly simple if the damage mechanism is a function of a system variable, and it is known what fraction of energy lost results in damage.

A model is formulated based on the phenomena of interest and the observability of the system necessary to present features that are relevant for fault detection and identification. A system fault model thus provides a logical approach for selection of condition indicators, sensors, and signal processing methods appropriate for observing (and identifying) a fault of interest.

2 Damage Modeling in a Lumped-Parameter System

A damage process depends on a dissipation of energy; and the energy either comes from the process system or comes from the environment outside the system boundary. There may be a transformation of energy to a form that results in damage accumulation D, which is a function of the "local" damage variables, which in turn relate to the process variables that provide the energy through some function of time. The damage accumulation from time T_o to time T_{int} can be written as

$$D_{T_{\text{int}}} - D_{T_0} = \int_{T_0}^{T_{\text{int}}} \dot{D} dt \tag{1}$$

where $\dot{D}$ is the damage accumulation rate. A damage process can then be included in the system model by adding a new element representing the constitutive relationship of the damage. Figure 1a shows a second element added to a system graph network with no change in the through variable q. There is a change in the system due to the presence of a new across variable ΔP_d due to the damage

process. Figure 1b shows a second element added when there is no change in the across variable ΔP, with new complementary damage variable q_d.

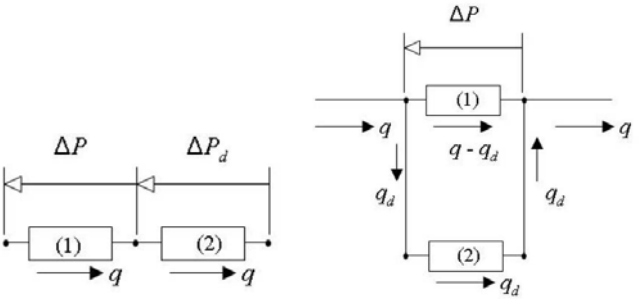

Fig. 1 Damage Element (2) with no change in a) through variable q b) across variable ΔP

Damage variables ΔP_d (with complementary variable q) and q_d (with complementary variable ΔP) yield damage energy rate $\dot{D}$.

If there is a change in the physical process between the system of interest and the damage mechanism, then a mixed-model formulation can be used. Two-port transducer elements allow mixed energy subsystems to be represented in a single model, related by coupling coefficient α which may be nonideal (allowing losses). A damage mechanism can be incorporated into a process as illustrated by Figure 2. The driver subsystem is the main process, providing the energy consumed by the damage process, with a transducer element connecting the two systems. There may be a transformation of energy to a form that results in damage accumulation. This accumulation D is a function of the "local" damage variables, which in turn relate to process variables through some function. Transducer elements can be used to represent this transformation; and, in this way, the system process can be modeled with the damage process in a single model [4].

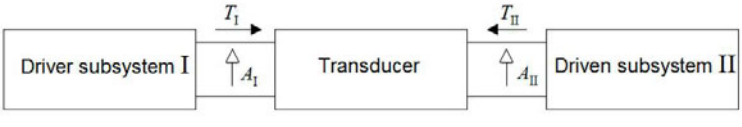

Fig. 2 Driving main process and driven damage process

Figure 3 illustrates the inclusion of a damage element in a system model where there is a change in variable type. Element (1) is part of the main system. The damage process in element (3) is described by through variable y and across variable Δd. A transducer element (2) represents how energy comes from the main system (based on a constitutive relationship between through variable q and across variable ΔP_d), into the subsystem in which that energy produces damage. This has the effect of increasing the number of variables of state, and so the observability

of the process relies on having some condition monitoring of at least one of the following: 1) the damage variable; 2) its complementary variable; or 3) indirect monitoring of some other variable that is closely related to the damage variable.

Multiple energy transformations may occur, in which case a set of transducers can be employed to relate the main system to the damage process.

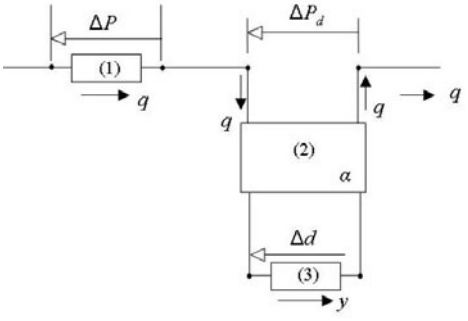

Fig. 3 Damage elements with change in variable type

3 Example 1: Pneumatic Tire Damage

Consider a tire on a vehicle driving on a surface at a linear velocity $v(t)$. Each tire requires torque τ to offset the road friction caused by the tire absorbing some mechanical energy, which is then dissipated as heat, at an elevated tire temperature above the ambient temperature [5]. The coupling relationship describing how the tire torque τ is transformed into heat flux h is described by

$$h = C\tau, \tag{2}$$

where C is an experimentally determined that depends on the tire material, the pressure inside the tire, and the road conditions. Damage accumulation rate is

$$\dot{D} = Be^{a\Delta T} \tag{3}$$

where a and B are constants, and ΔT is the temperature of the tire above ambient temperature. The system can be represented by process variables expressed in terms of the tire (torque and angular velocity), a transducer that transforms mechanical energy to thermal energy, a transducer that transforms heat flux & temperature to damage & temperature, and a damage element as shown in Figure 4.

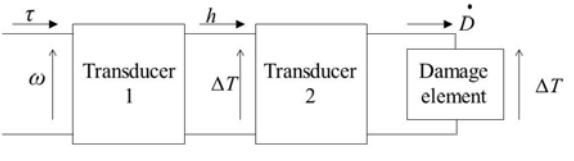

Fig. 4 Multiple variable transformations in damage modeling for a tire

In the mechanical subsystem, the complementary variables are torque τ and angular velocity $\omega = v/r$ for a tire with radius r. The mechanical/thermal transducer relationship yields

$$\Delta T = \frac{v}{rC} \tag{4}$$

The thermal/damage transducer relationship is $\dot{D} = \alpha \dot{h}$; and the transducer relationship between across variables is $\Delta T = \alpha \Delta T$; and so $\alpha = 1$. An expression that describes the damage rate in terms of the vehicle velocity $v(t)$ is found by taking the expression for temperature change ΔT and substituting it in the damage equation to yield an expression for the damage rate as a function of $v(t)$

$$\dot{D} = Be^{\left(\frac{a}{rC}\right)v(t)} \tag{5}$$

and the damage accumulation in the time interval t_0 to t_f

$$D = \int_{t_0}^{t_f} Be^{\left(\frac{a}{rC}\right)v(t)}\, dt + D_0 \tag{6}$$

where D_0 is the initial amount of tire damage at time t_0. This very simple model neglects any variability in the process due to changing road conditions, which may mean that a, B, and C may actually be variables with respect to time, in that the vehicle may drive over different roads with different amounts of rolling resistance and under different circumstances heat generation may aggravate the damage rate. Instead of measuring these variables as a function of time directly, it would be more appropriate to monitor more readily observable features that contribute to a particular variable. For example, rolling resistance $C(t)$ may depend on external features, such as road conditions (height variability related to ruts and sharp stones, etc.), as well as tire pressure. Then, by monitoring when the vehicle is on particular road conditions, $C(t)$ can be observed.

This example illustrates how fault classification accuracy improves with increased knowledge of the state of nature and appropriate condition monitoring.

2 Example 2: Wear Damage in a Slurry Pipe

In hydraulic systems, a simple dissipation element is flow resistance in a section of pipe. The constitutive relationship for energy dissipation rate within the process in terms of the pressure drop is

$$\dot{E} = \frac{[\Delta P(t)]^2}{S} \tag{7}$$

where S is assumed to be a constant and $\Delta P(t)$ is a function of time. The loss of energy over time is

$$E = \int_0^{T_{\text{int}}} \dot{E} dt = \int_0^{T_{\text{int}}} \frac{[\Delta P(t)]^2}{S} dt \tag{8}$$

This energy dissipation does not cause damage; it is merely a consequence of the process of transporting a fluid. A slurry pipeline, however, carries solid particles in a carrier fluid. Abrasive wear can occur as particles moving in the flow contact the wall. Not all slurry flows are homogeneous. When solids concentration, particle size, and particle density increase, then the flow rate may not be high enough to keep all of the particles fully suspended in the dense slurry. In that case, there is a concentration gradient. Flow in a dense bed slurry pipeline can be modeled as a two-layer system [6]. The upper layer flows at an average velocity v_u and has a low concentration of solids in the fluid C_u. The lower bed is a dense multiphase fluid with a high concentration of solids C_l at a low average velocity v_l. The two-layer model for slurry flow is illustrated in Figure 5, showing the idealized relationship between solids concentration C and velocity profile v. The energy dissipation in the bed layer (on the bottom) due to friction is usually modeled as a Coulomb friction process, which is not dependent on velocity.

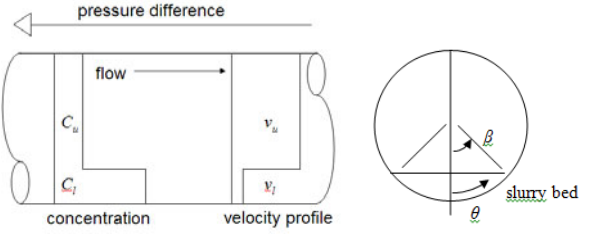

Fig. 5 Two-layer slurry transport model

For a moving bed, the friction of the bed against the wall of the pipe F_l (per unit length of pipe) is described by the following expression:

$$F_l = \frac{1}{2} g D^2 \eta_s (\rho_s - \rho_f)(C_l - C_u)(\sin\beta - \beta\cos\beta) \tag{9}$$

where η_s is the coefficient of sliding friction (usually assumed to be 0.5), ρ_s is the density of solids, ρ_f is the density of the fluid, C_l is the concentration of the bed, and C_u is the concentration of the bulk, D is the pipe diameter, g is acceleration due to gravity, and β is the subtended angle (in radians) that defines the (modeled) interface between the bed layer and the bulk fluid layer. Most of the energy dissipated due to friction is lost as heat without pipe damage; however, in some conditions, a fraction of this energy dissipation may result in damage, which accumulates over time. The wear rate $\dot{d}$ is described by

$$\dot{d} = \alpha^* \left[V^* (\tau - \tau_o) \right] \tag{10}$$

where τ is the shear stress due to the contact of unsuspended particles scraping along the wall of the pipe that results in wear (in units of force/area), τ_0 is a parameter that represents the threshold stress for wall damage to occur, α^* is an experimentally determined proportionality constant, and V^* is the velocity corresponding to the wear component (the particles in the bed) in units of length/time [7]. For this case $V^* = v_l$. When the shear stress on the pipe is lower than the threshold stress for damage τ_o, then no damage accumulation occurs. The friction F_t is related to the average shear stress on the wall in contact with the slurry by

$$F_t = \tau_{avg} R(2\beta) \tag{11}$$

where friction is a shear force acting along only the part of the pipe wall that the slurry bed contacts. The average damage accumulation rate in terms of the process parameters and variables can be expressed as

$$\dot{d} = \alpha^* \left[v_l \left(\frac{F_t}{\beta D} - \tau_0 \right) \right] \tag{12}$$

where $F_t/\beta D$ is the average shear stress on the pipe wall. In the case of a heterogeneous flow, it is more important to know the rate at which wall thinning occurs at specific locations around the pipe circumference, in order to predict when the pipe has reached a minimum allowable thickness. In a pipe with a two-layer concentration of slurry, friction F_t is a function of the angle θ, because of the pressure due to the relative mass of particles in the slurry bed pressing on the wall, similar to hydrostatic pressure with an effective density ρ_{eff}, expressed as

$$\rho_{eff} = (C_l - C_u)(\rho_s - \rho_f) \tag{13}$$

The depth of the bed x with respect to angle α is

$$x = R[\cos(\theta) - \cos(\beta)] \tag{14}$$

The pressure on the wall due to the bed at angle θ is $P_\theta = \rho_{eff} g x$; and the pressure multiplied by the coefficient of static friction yields the shear stress on the wall at angle θ:

$$\tau(\theta) = \eta_s P_\theta \tag{15}$$

which, over a length $Rd\theta$, gives differential friction per unit length of the pipe

$$\tau(\theta) R d\theta = \eta_s P_\theta R d\theta \tag{16}$$

From this expression, we can write

$$dF_t = \eta_s \rho_{eff} g R^2 [\cos(\theta) - \cos(\beta)] d\theta \tag{17}$$

Integrating this expression from $-\beta$ to β yields the friction of the bed on the wall due to particle contact only. The damage rate as a function of θ is thus found to be

$$\dot{d}(\theta) = \alpha^* v_l \left\{ \eta_s \left(\rho_s - \rho_f \right) \left(C_l - C_u \right) gR[\cos(\theta) - \cos(\beta)] - \tau_0 \right\} \tag{18}$$

The pipe wall will thus wear the fastest at θ=0, that is, at the bottom of the pipe. This has been observed in some operating slurry pipelines. In an actual process, the time-varying variables include not only the velocity v_l, but also the concentrations C_l & C_u, the height of the bed (and thus β), and possibly the density of the solid phase ρ_s. For a time-varying slurry process, these variables make the wall loss observable without having to have ongoing thickness measurement of the pipe around its circumference and along its length. This is important in pipelines that are not easy to inspect, such as buried pipes and pipes in remote locations.

3 Conclusions

Structured parametric dynamic modeling can reveal the variables necessary for direct measurement of equipment condition. The key challenge in any system is to have appropriate constitutive relationships for the energy lost in damage to system components, and methods to validate them in service. These relationships may be related to the derivatives of variables of state rather than the variable itself, and will often involve variable transformations. The two examples presented illustrate how simple process dynamic relationships and damage models can yield insights into what condition indicators will be observable from the system. Future work will consider how to combine stochastic diagnostic models with parametric dynamic models, as well as symbolic representations of system behaviour.

References

1. Jardine, A.K., Lin, D., Banjevic, D.: A review on machinery diagnostics and prognostics implementing condition-based maintenance. Mech. Sys. & Sig. Proc. 20(7), 1483–1510 (2006)
2. Randall, R.B.: Vibration-Based Condition Monitoring. Wiley, Chichester (2011)
3. Crandall, S.H.: Engineering Analysis. Krieger, Malabar (1956)
4. Lipsett, M.G.: Incorporating Damage Models in Deterministic System Models to Model Reliability in Time-Varying Systems. In: Proc. BINDT Condition Monitoring Conf. Dublin (2009)
5. Benedict, R., Shepler, P., Fischer, M., Wagner, D.: Talking Tires – A Basis for Tire Diagnostics. SAE International, 01–1279 (2003)
6. Gillies, R.G., Shook, C.A.: Modeling high concentration settling slurry flows. Canadian Journal of Chemical Engineering 78, 709–716 (2000)
7. Roco, M.C., Addie, G.R.: Erosion wear in slurry pumps and pipes. Powder Technology 50(1), 35–46 (1987)

Impedance Method for Modeling and Locating Leak with Cylindrical Geometry

Lazhar Ayed, Lamjed Hadj Taïeb, and Ezzeddine Hadj Taïeb

R.U. Applied Fluid Mechanics and Modeling. ENIS, BW 1173 - 3038 Sfax, Tunisia
{Hlzed,lamjed_hadjtaieb}@yahoo.fr, Ezed.Hadj@enis.run.tn

Abstract. This paper uses transient frequency methods to locate a leak in a pipeline system when a leak is modeled as a *small cylindrical pipe element open to atmospheric pressure on one end*. The impedance of the leak as a small cylindrical pipe is included in the transfer function equation at the closed valve in a reservoir-pipe-valve system. The impedance diagram of this system with cylindrical leak is plotted and analyzed; the influence of the *pipe thickness* on leak locations is studied. The numerical study relying on impedance method shows that the cylindrical leak geometry approach allows *secondary peaks to be detected only for thick pipes*. By imposing a periodic pattern on the resonant responses, the leak with cylindrical geometry can be located and its location is based on an *empirical relation*. The computed results show satisfactory agreement with previous works when leak is modeled by a circular orifice.

Keywords: Cylindrical leak, impedance diagram, Transient flow, leak depth, wave reflection.

1 Introduction

Energy producing mechanisms are generally formed by piping systems used for transporting fluids between their different components. Leaks in piping systems pose a major problem such as energy dissipation and physical process disruption causing a decrease of the energetic system efficiency. In previous works such as (Mpesha et al. 2001), (Chaudry et al. 2002), (Ferrante and Brunone 2003-a, 2003-b), (Al-Khomairi 2005), (Covas et al. 2005), (Hadj-Taieb 2007), (Lee et al 2006, 2007) and (Gao et al 2009) different methods are developed for leak detection and location in pipeline system, such as Frequency Response Diagram, Extended Kalman Filter, Characteristic Numerical Method, Standing Wave Difference Method, Impedance Method, Impulse response method and cross correlation method etc.

Numerous works have investigated the behavior of different leak geometries such as (Brunone, and Ferrante 2001). Overall previous works use to treat the leak discharge as an orifice relation and lump all losses in the discharge coefficient.

In this paper the leak is considered as a small pipe element open to the atmospheric pressure on one end. The basic cylindrical surface of the leak is located on the pipe circumferential and with small diameter.

The leak locations are based on the harmonic analysis of the presence of additional peaks due to the leak depth.

Two location cases are studied either leak near the reservoir or near the valve.

The impedance method is also used to study the influence of the leak depth on frequency response of leaking pipeline system.

The numerical results are compared with (Covas et al. 2005).

2 Mathematical Flow Modeling

2.1 Motion Equations

The simplified one dimensional continuity and momentum equations that describe transient flow in horizontal cylindrical pipe, of linear elastic behavior according to Hooke law, are adapted from the analytical model developed by Wylie et al. (1993):

$$\frac{\partial Q}{\partial x}+\frac{gA}{C^2}\frac{\partial H}{\partial t}=0 \tag{1}$$

$$\frac{\partial H}{\partial x}+\frac{1}{gA}\frac{\partial Q}{\partial t}+\frac{\lambda Q|Q|}{2gDA}=0 \tag{2}$$

where Q is the fluid discharge, A is the pipe cross section area, C is the wave celerity, λ is the friction coefficient, D is the diameter of the main pipe, H is the pressure head, t is the time and x is the distance along the pipe.

2.2 The Impedance Method

Equations (1) and (2) can be solved in frequency domain by the impedance method, which allows explaining the harmonic analysis of the pressure wave through the pipe.

The pressure head H and the discharge Q are composed of two parts, the average values $\overline{H}$ and $\overline{Q}$ and the fluctuated oscillatory complex terms h and q.

Substituting H and Q in Eqs. (1) and (2), and considering the average terms time independent, the linearized equations are:

$$\frac{\partial q}{\partial x}+\frac{gA}{C^2}\frac{\partial h}{\partial t}=0 \tag{3}$$

$$\frac{1}{gA}\frac{\partial q}{\partial t}+\frac{\partial h}{\partial x}+Rq=0 \tag{4}$$

The solution of this set of equations can be obtained by the technique of separation of variables (Wylie and Streeter 1993).

Accordingly, the complex head and discharge are given by transfer equations

$$h(x)=h_U\cosh(\gamma x)-Z_C q_U\sinh(\gamma x) \tag{5}$$

$$q(x)=-\frac{h_U}{Z_C}\sinh(\gamma x)+q_U\cosh(\gamma x) \tag{6}$$

Where h_U, q_U =head and discharge at the upstream end; γ = propagation constant, $\gamma=\alpha+i\beta$ where:

$$\alpha=\left(\frac{Ag\omega}{C^2}\right)^{1/2}\left[\left(\frac{\omega}{gA}\right)^2+R^2\right]^{1/4}\sin\left(\frac{1}{2}\tan^{-1}\left(\frac{RgA}{\omega}\right)\right) \tag{7}$$

$$\beta=\left(\frac{Ag\omega}{C^2}\right)^{1/2}\left[\left(\frac{\omega}{gA}\right)^2+R^2\right]^{1/4}\cos\left(\frac{1}{2}\tan^{-1}\left(\frac{RgA}{\omega}\right)\right) \tag{8}$$

The hydraulic impedance at the distance x along the pipe is the ratio of the head fluctuation h to the discharge fluctuation q Thus,

$$Z(x)=\frac{h}{q}=\frac{Z_U-Z_C\tanh(\gamma x)}{1-\frac{Z_U}{Z_C}\tanh(\gamma x)} \tag{9}$$

where:

Z_C is the characteristic impedance defined by the following equation

$$Z_C=\frac{\gamma C^2}{i\omega gA}=\frac{C^2}{\omega gA}(\beta-i\alpha) \tag{10}$$

and

Z_U is the upstream impedance at $x=0$ and Z_D is the downstream impedance at $x=L$ (fig. 1)

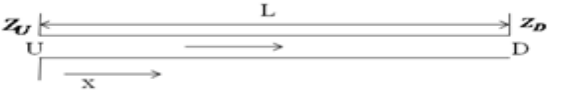

Fig. 1 Simple pipeline

2.3 Boundary Conditions

In order to apply the impedance solution to the hydraulic installation considered in this work and composed by constant head reservoir in the upstream pipe section and a valve in the downstream pipe section (fig. 2), one must represent the boundary conditions as terminal impedances.

At the upstream end, constant head reservoir

$$H_U = 0 \; then \; Z_U = \frac{H_U}{Q_U} = 0 \tag{11}$$

At the downstream end $x = 0$, the hydraulic impedance is deduced by substituting the eq.11 in the eq.9, then:

$$Z_D = Z_{out} = \frac{H_D}{Q_D} = -Z_C \tanh(\gamma L) \tag{12}$$

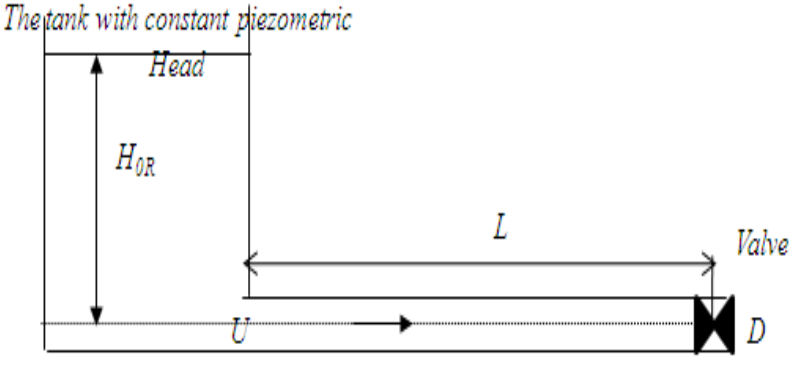

Fig. 2 Reservoir-pipe-valve systems without leak

2.4 Hydraulic Impedance for a Simple Pipeline System Having a Leak with Cylindrical Geometry

The development of the flow does not depend only on the distance but depend also on the Reynolds number, the diameter and discharge of the leak, the triggering of fully developed flow that figures in (Drust, F et al works 2005) allows to consider that for a leak depth less than 2 cm and a low leak discharge, the *flow can be approximate to be one dimensional*. The one dimensional motion equations are used to study the flow throw the leak.

The main diagnostic tool in this paper is to consider that the leak has a cylindrical geometry. That yields to consider that the leak is a small cylindrical pipe which diameter is the difference between the length of the pipe without a leak and the sum of the pipe lengths upstream and downstream the leak (fig.3).

$$D_\ell = L - (L_1 + L_2) \tag{13}$$

The length of the leak pipe is the thickness e of the main pipe. Using the impedance method one can insert the impedance of the cylindrical leak in the impedance at the end section of the leaking system Z_{D2} to obtain the head pressure variation between the upstream and the downstream of the leak.

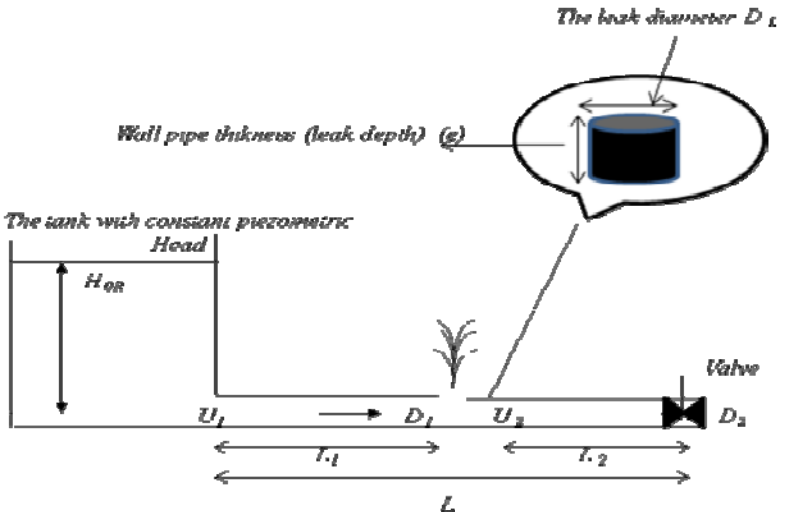

Fig. 3 Reservoir-pipe-valve systems with cylindrical leak

The leak as considered is an *opened pipe to the free atmosphere*, its impedance is written as follows:

$$Z_\ell = -Z_{C\ell} \tanh(\gamma_\ell e) \tag{14}$$

Where

$Z_{C\ell}$ is the characteristic impedance of the pipe leak and γ_ℓ is the propagation wave coefficient in the *cylindrical leak*.

To obtain the *characteristic impedance of the leak modeled by a cylindrical pipe*, one can substitute the expressions of α and β in eq.10 by α_ℓ and β_ℓ, also the pipe section A must be substituted by the leak section A_ℓ. The wave celerity is considered constant through the total pipeline system. In this case the characteristic impedance of the leak is represented by the eq.15.

$$Z_{C\ell} = \frac{C^2}{\omega g A_\ell}(\beta_\ell - i\alpha_\ell) \tag{15}$$

The impedance at the upstream and the downstream of the second pipe are respectively written:

$$Z_{U2} = \frac{Z_{D1} Z_{\ell}}{Z_{\ell} - Z_{D1}} \tag{16}$$

$$Z_{D2} = \frac{Z_{U2} - Z_{C2} \tanh(\gamma_2 L_2)}{1 - \frac{Z_{U2}}{Z_{C2}} \tanh(\gamma_2 L_2)} \tag{17}$$

By substituting the eq.16 in the eq.17, the impedance at the valve is:

$$Z_{D2} = \frac{\frac{Z_{D1} Z_{\ell}}{Z_{\ell} - Z_{D1}} - Z_{C2} \tanh(\gamma_2 L_2)}{1 - \frac{\frac{Z_{D1} Z_{\ell}}{Z_{\ell} - Z_{D1}}}{Z_{C2}} \tanh(\gamma_2 L_2)} \tag{18}$$

Substituting eq.14 in eq.18 and considering that the pipes downstream and upstream the leak have the same characteristic impedances and the same wave propagation constants, respectively $Z_{C1} = Z_{C2} = Z_C \; and \; \gamma_1 = \gamma_2 = \gamma_{\ell}$.

The impedance at downstream of the pipe with leak begins (Ayed. L et al 2011)

$$Z_{D2} = \frac{Z_C Z_{C\ell} \tanh(\gamma_{\ell} e) \tanh(\gamma L_1) + Z_{C2} Z_{C\ell} \tanh(\gamma_{\ell} e) \tanh(\gamma_2 L_2) - Z_C^2 \tanh(\gamma L_1) \tanh(\gamma L_2)}{-Z_{C\ell} \tanh(\gamma_{\ell} e) + Z_C \tanh(\gamma L_1) - Z_{C\ell} \tanh(\gamma_{\ell} e) \tanh(\gamma L_1) \tanh(\gamma L_2)} \tag{19}$$

3 Cylindrical Leak Detection Using Impedance Frequency Spectrum Analysis

The hydraulic system installation in fig. 3 is characterized by the wave celerity $C = 1200 ms^{-1}$, the friction coefficient $\lambda = 0.04$, the pipe thickness $e = 0.02m$, the pipe diameter's $D = 1m$, the resolution of the frequency is equal to $\Delta\omega = 10^{-4}$ and the pipe length is $L = 1600m$.

In this part of the paper, attention is focused on the transients occurring in a single pipe system with a known transfer function at the upstream end.

The problem is to determine the impedance at the downstream end of the system without leak, or with leak modeled by a small cylindrical pipe. The leak discharge is $Q_{\ell 0} = 10\% Q_0$, where the flow discharge at the upstream of the main pipe is $Q_0 = 0.1 m^3 s^{-1}$.

3.1 The Leak Is Near the Tank

Figures 4(a) and 4(b) represent a comparison of the impedance at the downstream end of the pipe without leak to the impedances at the downstream end of the pipe with leak located respectively at $L/6 and\ 2L/5$, from the reservoir .

In this case the leak is near the tank $(L_1 \le L/2)$.

The impedance curves at the downstream end of the identical pipe with and without leak show an interesting result, which is giving rise to new (secondary) peaks, due to the leak depth consideration.

Only one new peak type is born due to the leak presence in different leak location with the same leak size represented by the leak area $A_\ell = 28.26\,mm^2$.

For different leak locations, the impedance diagram analysis shows that two peaks occurring successively at the normalized frequencies $\omega_{r\ell k-1}$ and $\omega_{r\ell k}$ are separated by the same band of frequency for each leak location.

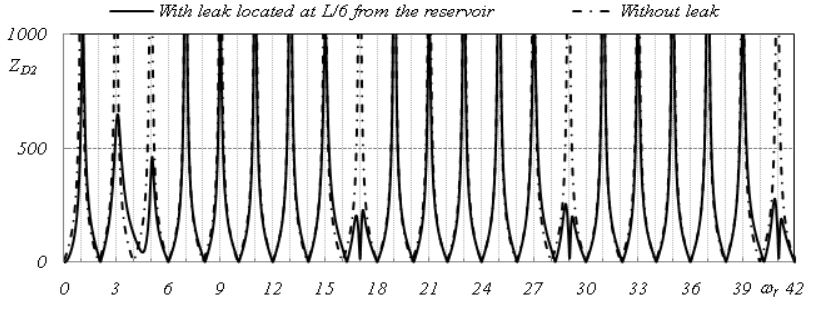

(a)

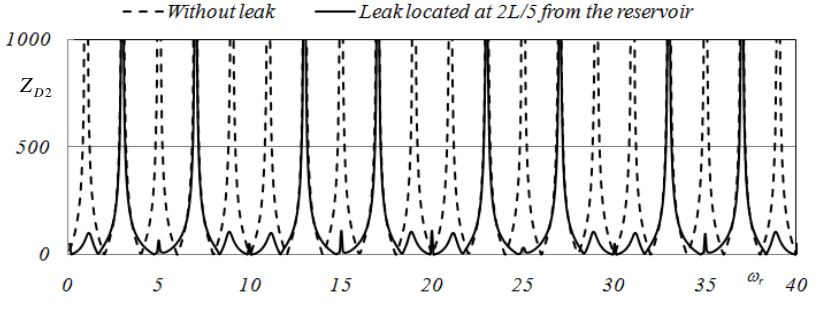

(b)

Fig. 4 Frequency response functions for different leak location from the reservoir

If we note the band frequency width between two successive peaks due to the leak (frequency period of the leaking pipe impedance) $\Delta\omega_{r\ell(k-1,k)} = \omega_{r\ell k} - \omega_{r\ell k-1}$ and the frequency period of the impedance at the downstream of the pipe without leak by $\Delta\omega_{r,\text{int act pipe}}$, the leak locations from the reservoir, can be calculated by multiplying the total length of intact pipe by the ratio of the frequency period of the downstream impedance of intact pipe to the frequency period of the downstream impedance of leaking pipe. So one gets *the next empirical leak location equation:*

$$L_1 = \frac{\Delta\omega_{r,\text{int act pipe}}}{\omega_{r\ell k} - \omega_{r\ell k-1}} L \tag{20}$$

where ω_r is the normalized frequency and $\omega_{r\ell k-1}$ is the normalized frequency at which occurs the $k-1^{th}$ peak due to the leak presence (*leak depth*).

$\omega_{r\ell k}$ is the normalized frequency at which occurs the k^{th} peak due to the leak presence (leak depth).

By applying the eq.20, one can calculate the location of the leak for each figure case.

In fig.4 (a) for frequency width plotting of 40, one can detects three new peaks occurring successively at the frequency

$\omega_{r1} = 17; \omega_{r2} = 29; \omega_{r3} = 41$

In addition the normalized frequency period of the response function at the downstream end of the pipe without leak is equal to $\Delta\omega_{r,\text{int}actpipe} = 2$. So, and the values of corresponding series are:

$$L_1 = \frac{\Delta\omega_{r,\text{int act pipe}}}{\omega_{r\ell,(k,k-1)}} L = \frac{\Delta\omega_{r,\text{int act pipe}}}{\omega_{r\ell 2} - \omega_{r\ell 1}} L = \frac{\Delta\omega_{r,\text{int act pipe}}}{\omega_{r\ell 3} - \omega_{r\ell 2}} L = \frac{L}{6}$$

By the same procedure one can get the leak locations after calculating the normalized frequencies at which occurs the secondary peaks of responses when leak is either located at $2L/5$ from the reservoir.

3.2 The Leak Is Near the Valve

In this case, the leak is near the valve $(L_2 < L/2)$. As an example for the leak located at $L/n(n>2)$ from the valve there are $n-1$ types of peaks. This result is clarified by the fig. 5 in which the leak is located at $L/6$ from the valve and we can observe five peak types differentiated by the monotony; the form and the amplitude. Compared to the case when the leak is near the reservoir there is a difference explained by the effect of the mother wave sent by the valve. This wave is sending back $(n-1)$ times by the leak, before being absorbed by the reflected

negative wave coming from the reservoir. In the case presented and when leak is located at $L/n(n \geq 2)$, two successive peaks for the same peak type are separated by the same band of frequency which is the period of the response function at the downstream of pipeline system. This band of frequency is equal to $n\Delta\omega_{r,\ell}$. To deduce the location of the leak having cylindrical geometry one must calculate the frequencies at which occurs this peaks and differentiate their different types.

After the leak location is deduced by the same process like the case when leak is near the reservoir, but L_1 must be substituted by L_2 and $\Delta\omega_{r\ell,(k,k-1)}$ must be substituted by $\Delta\omega_{r\ell,(jk,jk-1)}$, so the leak location from the valve is deduced by the eq.21

$$L_2 = \frac{\Delta\omega_{r,\text{int}\,actpipe}}{\omega_{r\ell,(jk,jk-1)}} L \tag{21}$$

$\Delta\omega_{r\ell,(jk,jk-1)}$ is the *band frequency width between two successive peaks*, with the same type (j^{th} type), due to the leak depth (pipe thickness).This band frequency is also the frequency response function period.

In fig.5, the leak is located at $\frac{L}{6}$ from the valve. For the frequency width-plotting of 40, one can detect fifteen new peaks distributed on five types. As an example we consider one peak type that we note it as the first peak type. The secondary peaks of the first type are occurring successively at these frequencies:

$$\omega_{r\ell 11} = 3.36; \omega_{r\ell 12} = 15.371; \omega_{r\ell 13} = 27.36; \omega_{r\ell 14} = 39.359$$

In addition the normalized frequency period of response function at the downstream end of the pipe without leak is equal to $\Delta\omega_{r,\text{int}\,act\ pipe} = 2$, so the values of the corresponding series are:

$$L_2 = \frac{\Delta\omega_{r,\text{int}\,actpipe}}{\omega_{r\ell,(jk,jk-1)}} L \xrightarrow{for\ j=1\&k\in\{1;2;3;4\}} L_2 = \frac{\Delta\omega_{r,\text{int}\,actpipe}}{\omega_{r\ell,(12,11)}} = \frac{\Delta\omega_{r,\text{int}\,actpipe}}{\omega_{r\ell,(13,12)}} = \frac{\Delta\omega_{r,\text{int}\,actpipe}}{\omega_{r\ell,(14,13)}} = \frac{L}{6}$$

Also, the fig.5 shows respectively the second, the third, the fourth and the fifth types of peaks appearing for a leak located at $\frac{L}{6}$ from the valve.

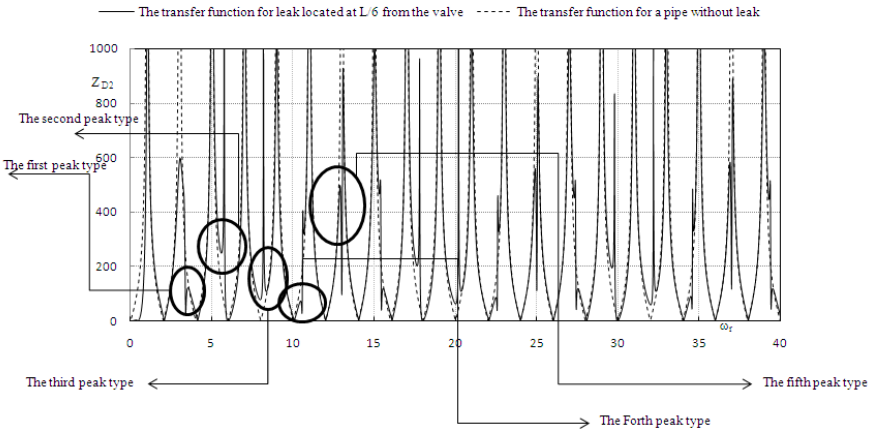

Fig. 5 Different peak types of the frequency response functions of pipe with leak located at $L/6$ from the valve

For a width frequency plotting of 40, three peaks are observed for each peak type. These peaks are occurring successively at these frequencies:

$$\omega_{r\ell 21} = 5.72; \omega_{r\ell 22} = 17.72; \omega_{r\ell 23} = 29.7658; \omega_{r\ell 31} = 8.152; \omega_{r\ell 32} = 20.155; \omega_{r\ell 33} = 32.174$$
$$\omega_{r\ell 41} = 10.527; \omega_{r\ell 42} = 22.564; \omega_{r\ell 43} = 34.5669; \omega_{r\ell 51} = 12.971; \omega_{r\ell 52} = 24.981; \omega_{r\ell 53} = 36.99$$

These frequencies are substituted in the eq. 21 to get the location of the leak.

4 Leak Depth Influence on Downstream Impedance of Leaking Pipe

The proposed method: based on the leak reflections as a tool for the leak detection, relying on cylindrical leak geometry inquiries the pipe thickness effects to demonstrate the importance of this consideration. For this reason fig. 6 is plotted to explain physical signification of the pipe thickness which is assumed in this work to be the length of the leak as a cylindrical pipe. In previous works the leak impedance *is defined as, the ratio of the double pressure head at the orifice by the leak discharge, described by linearizing the discharge law* (Wylie and Streeter). In this paper the hydraulic *leak impedance is that of a cylindrical pipe with free discharge in the atmosphere*, as figure 6 shows the downstream impedance of leaking pipes having the same conditions of the monitoring flow, but different pipe thickness. This illustrates an important result and information contained in pipe thickness influence on the leak reflections, so the necessity of considering the cylindrical leak geometry to facilitate the leak location. This figure shows for the same friction value and different thickness, the *leak reflections* are detected only in the case where $e > 0$ but not detected when $e = 0$.

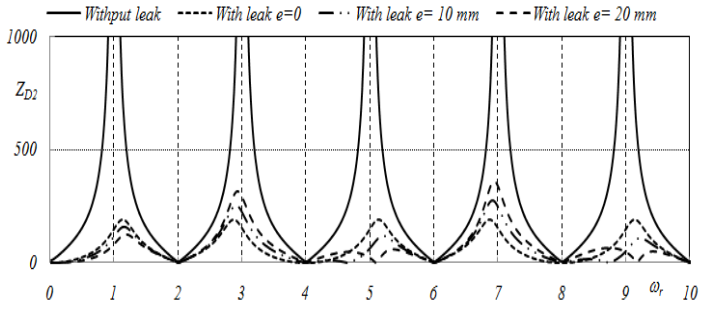

Fig. 6 frequency response functions of pipes with different pipe thickness $L_1/L = 1/2 and\ \lambda = 0.04$

5 Validation of the Cylindrical Geometry Approach

The technique presented in this paper identifies periodicity in the frequency response at the downstream of pipeline system with cylindrical leak. The underlying mechanism is identical to that presented in numerous previous works such as (Lee, P et al 2005_2006) and (Covas et al 2005).

To validate the mathematical approach used in this paper and to focus on the importance of the cylindrical geometry of the leak figure 7 is picketed with similar conditions as shown by (Covas et al. 2005). One can observe in this figure plotted with logarithmic scale, the presence of resonant peaks occurring at the same normal frequencies calculated by Covas and related directly with the leak location $L_2 = 200m$ and the total pipe length $L = 1000\,m$. The leak with the cylindrical geometry provokes, in addition to secondary peaks due to the thickness of the main pipe as a depth of the leak modeled by a small pipe, some resonant peaks occurring at the following frequencies:

$$\omega_{r\ell 1} = 5;\ \omega_{r\ell 2} = 15;\ \omega_{r\ell 3} = 25$$

These normalized frequencies are needed to locate leak by applying the standing wave difference method for leak detection given in Covas work.

Comparing figures 7 and 8 we can conclude that for a small thickness such as $e = 0.00001\,m$, the results show a great concordance with that given by Covas in figure 8.

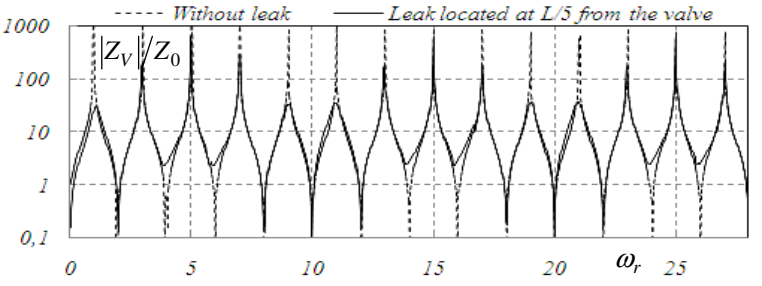

Fig. 7 Frequency responses at valve site. Undamaged pipe and leaking pipe with one leak $L_2/L = 1/5 \quad e = 0.00001\,m$

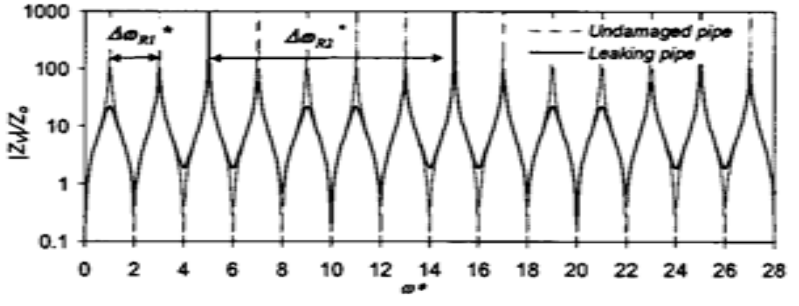

Fig. 8 Frequency responses at valve site. Undamaged pipe and leaking pipe with one leak $L_2/L = 1/5$ [Covas et al. (2005)].

6 Conclusion

This paper has presented the importance of *cylindrical leak geometry* consideration to locate the leak. The impedance method indicates that it is possible to include the leak geometry in the downstream impedance by including its impedance, as a cylindrical pipe opened in the free atmosphere in the impedance equation at the downstream end of the leaking pipe (valve). This equation is needed to facilitate the analysis of the wave reflections due to the leak depth and to demonstrate that the thickness of the principal pipe influences the leak reflections. Cylindrical leak in the pipeline system provokes secondary peaks caused by the leak depth. The results of simulation show that geometrical consideration can provide better physical information about the leak presence. This paper shows that *the simplicity of the leak location decreases with the leak depth dimension* because of the clarity of the wave reflected by the leak in the impedance spectrum at the end of the leaking pipe.

The results of numerical simulation were validated by (COVAS work 2005), they have shown a great concordance for *small pipe thicknesses.*

A difference appears only when the thickness increases. This difference is noted on the appearance of the secondary peaks related directly to the leak depth and allows leak location.

An empirical formulae was derived for leak locations in thick pipes, for other case and when there's a lack of secondary peaks a numerous analytical formulae were given and demonstrated in literatures.

Notations

The following symbols are used in this paper:

Q = Discharge

H = Head

C = Wave celerity

h = Head fluctuation

q = Discharge fluctuation

A = Pipe cross sectional area

A_ℓ = Area of cylindrical leak

f = Darcy-Weisbach friction factor

g = Acceleration due to gravity

x = Distance

L = Pipeline length

L_1 = Leak position from the tank

L_2 = Leak location from the valve

Z_U = Upstream impedance

Z_D = Downstream impedance

$\overline{H}$ Average of pressure head

$\overline{Q}$ Average of flow

Z_C = Characteristic impedance of main pipe

$Z_{C\ell}$ = Leak characteristic impedance.

D = Pipe diameter

D_ℓ = Leak diameter

e = Pipe thickness

t = Time

Z_{D1} = Impedance upstream the leak

Z_{U1} = The upstream impedance of leaking pipe.

Z_{U2} = Impedance downstream the leak

Z_{D2} = Impedance downstream the leaking pipe.

$n; j; k$ Integer

Greek symbols

ω = Frequency

ω_r = Normalized frequency

$\omega_{r\ell}$ = Normalized frequency at which appears new peaks

$\omega_{r,\text{int}\,act\,pipe}$ = Frequency impedance period of no leaked pipe

$\Delta\omega_{Lr,(jK;Jk-1)}$ = Frequency period of the impedance at the downstream end (Leak near the valve).

$\Delta\omega_{\ell r,(K;k-1)}$ = Frequency period of the impedance at the downstream end (leak near the reservoir)

$\lambda = 4f$

References

Alkhomairy, M.: Use of the steady state orifice equation in the computation of transient flow through pipe leaks. The Arabian Journal for Science and Engineering IB 30, 33–45 (2005)

Ayed, L., Hadj Taieb, L., Hadj Taieb, E.: Response function phase diagram analysis for location of leak with cylindrical geometry in pipes. In: 4th Intrnational Congress: Design and Modeling of Mechanical Systems, ID 276 (2011)

Brunone, B., Ferrante, M.: Detecting leaks in pressurized pipes by means of transients. J. Hydraulic Res. 39(4), 1–9 (2001)

Covas, D., Ramos, H., Betamio de Almeida, A.: Standing wave difference for leak detection in pipeline systems. J. Hydraulic Eng., 1106–1116 (2005)

Drust, F., Ray, S., Unsal, B.O.A.: Development lengths of laminar pipe and channel flow. J. Fluids Eng. 127, 1154–1160 (2005)

Ferrante, M., Brunone, B.: Pipe system diagnosis and leak detection by unsteady-state tests 1: Harmonic analysis. Advances in Water Resources 26, 95–105 (2003a)

Ferrante, M., Brunone, B.: Pipe system diagnosis and leak detection by unsteady-state tests 2: Wavelet analysis. Advances in Water Resources 26, 107–116 (2003b)

Gao, Y., Brennan, M.J., Joseph, P.F.: On the affects of reflections on time delay estimation for leak detection in buried plastic water pipes. Journal of Sound and Vibration 325, 646–663 (2009)

Hadj-Taieb, E.: Leak detection by using water hammer and impedance method. In: Water Management Challenges in Global Change, pp. 445–452. Taylor and Francis Group, London (2007)

Lee, P.J., Lambert, M.F., Simpson, A.R., Vitkovsky, J.P.: Experimental verification of the frequency response method leak detection. J. Hydraul. Res. 44(5), 693–707 (2006)

Lee, P.J., Vitkovsky, J.P., Lambert, M.F., Simpson, A.R., Ligget, J.A.: Experimental validation of frequency response coding for the location of leaks in single pipeline systems. The practical application of surge analysis for design and operation. In: 9th International Conference on Pressure Surges, March 24-26, pp. 239–253. BHR Group, UK (2004)

Lee, P.J., Vitkovsky, J.P., Lambert, M.F., Simpson, A.R., Ligget, J.A.: Leak locations in pipelines using the impulse response function. J. Hydraul. Res. 44(5), 643–652 (2006)

Lee, P.J., Vitkovsky, J.P., Simpson, A.R., Lambert, M.F., Ligget, J.A.: Discussion to leak detection in pipes by frequency response method using a step excitation. J. Hydraul. Res. 41(2), 221–223 (2003b)

Mpesha, W., Chaudry, M.H., Gassman, S.L.: Leak detection in pipes by frequency response method using a step excitation. J. Hydraul. Res. 40(1), 55–62 (2000)

Mpesha, W., Gassman, S.L., Chaudry, M.H.: Leak detection in pipes by frequency response method. J. Hydraulic. Eng. 127(2), 134–147 (2001)

Wylie, E.B., Streeter, V.L., Suo, L.: Fluid transients in systems. Prentice-Hall, Englewood Cliffs (1993)

Influence of the Acyclism on the Dynamics of a Spur Gear System

Noussa Bouchaala, Mohamed Taoufik Khabou, Fakher Chaari,
Tahar Fakhfakh, and Mohamed Haddar

Dynamics of Mechanical Systems Research Unit,
National School of Engineers of Sfax, BP 1173 – 3038, Sfax, Tunisia
noussa.bouchaala@hotmail.fr, mtkhabou@hotmail.com,
fakher.chaari@gmail.com, tahar.fakhfakh@enis.rnu.tn,
Mohamed.haddar@enis.rnu.fr

Abstract. The aim of paper is to study the dynamic behavior of a single stage spur gear reducer in transient regime. The gear excitation is the result of the motor torque variation in addition to the fluctuation of meshing stiffness due to the variation of input rotational speed. Then, the dynamic response is solved using implicit type numerical integration technique Newmark-β. A parameter study is made on spur gear powered by four strokes four cylinders diesel engine. Dynamic responses come to confirm a significant influence of the transient regime on the dynamic behavior of a gear set.

Keywords: Spur gear reducer, transient regime, diesel engine.

1 Introduction

It is well-known that gear transmissions are frequently used to provide speed and torque conversions from a rotating power source to connected mechanical devices. In operation, these systems deform, vibrate and generate noise. There are internal and external sources of excitations for the gear set. The motor is one of the most important excitations which cause the noise radiated by a gear. The training system can be achieved either by an electric motor or combustion engine (Bouchaala N et al, 2011, Khabou M T et al, 2011).

The internal combustion engine by design and operation, it remains an important source of vibrations. During operation, the pistons undergo cycles of internal combustion 2 or 4 stroke. The different phases between the pressure forces created in the cylinders combined with the effects of moments of inertia systems rods generates a torque variation and speed transmitted to the flywheel, creating the acyclism. We can say therefore that the acyclism depends on the number of cylinders, but also the firing order for them and the engine speed (low speed, slow motion, high speed) (Ligier J L, Baron E, 2002).

Another parameter that should be taken into account is the transient behaviour of a gear transmission caused by the fluctuation of the rotational speed. Bouchaala

N et al (2011), Khabou M T et al (2011) showed that the transient regime influences significantly the dynamic behaviour of the transmission.

Therefore the aim of this paper is to use the numerical simulation based on the Newmark integration method, to study the dynamic behavior of spur gear system in the transient regime powered by four strokes four cylinders inline diesel engine.

2 Acyclism Notion

The combustion engine (figure 1) is subject to two types of solicitation, those from the combustion gases and those related to the phenomena of inertia.

In a cylinder gases produce a variable pressure in the cycle, which at the moment of combustion, generates an effort called "effort gases" on the piston. This effort is the cause of the piston displacement and traction engine. Similarly, the moving parts (piston, rod, ...) undergo efforts called " inertia effort ".

Generalized efforts, which represent the resultant forces and moments when applied to the engine, assess the movements of the latter on his pads and the rotation of the crankshaft. As the rotation of the crankshaft is not regular, it is called "irregularities of rotation" or more commonly "acyclism" (Ligier J L, Baron E, 2002).

Fig. 1 Combustion engine

3 Combustion Engine Modeling

The acyclism combustion engine is characterized by variations of the displacement, velocity or angular acceleration of the crankshaft, but it can be related to engine torque.

Combustion engine creates torque to spin the crankshaft. This engine torque C_m is the sum of combustion moment C_{vg} and engine moment of inertia C_{vi} (Ligier JL, Baron E).

$$C_m = C_{vg} + C_{vi} \tag{1}$$

The engine torque expression C_m is given by the following formula:

$$C_m \simeq C_{vg} = \overline{C_m} + \frac{P_{\max}}{192} V_{cyl} \left(0.46 \sin 2\alpha_c + 0.24 \sin 4\alpha_c + 0.03 \sin 6\alpha_c\right) \tag{2}$$

where $\overline{C_m}$ is the average friction torque of the engine, $P_{\max}$ is the maximum gas pressure inside cylinders, V_{cyl} is the engine cubic capacity and α_c is the crankshaft angular position.

4 Numerical Simulation

We are interested in this work to study the dynamic behavior of spur gear system powered by a four strokes four cylinders inline diesel engine.

A single stage spur gear transmission model with eight degrees of freedom is proposed (Figure 2). It is divided into two main blocks.

- Block1 includes the driving motor and the pinion connected by a shaft. This block is supported by a bearing. The Pinion has Z_1 teeth and moment of inertia J_{11}.
- Block 2 includes the wheel and the load connected by a shaft; it is supported by a second bearing. The wheel has Z_2 teeth and moment of inertia J_{22}.

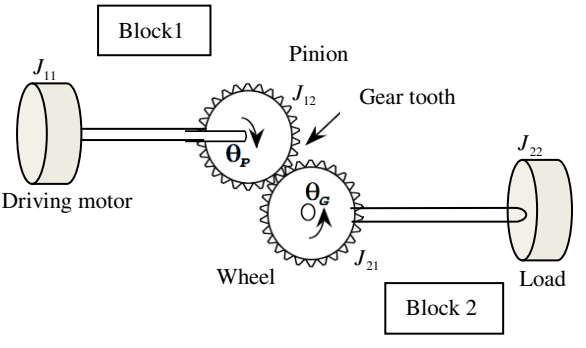

Fig. 2 Model of a single stage spur gear transmission with eight degrees of freedom

x_i and y_i are the translations of block i ($i = 1,2$). θ_{ij} is the angular displacement of the component j in block i ($i, j = 1,2$).

Numerical simulation based on Newmark integration method is used to study the dynamic behavior of the studied gear set in the transient regime. Taking into

account the Lagrange formalism, the differential equation of motion of the adopted system can be expressed by:

$$[M]\{\ddot{q}\}+[C]\{\dot{q}\}+[K(t)]\{q\}=\{F_{ext}(t)\} \tag{3}$$

$q=\{x_1, y_1, \theta_{11}, \theta_{12}, x_2, y_2, \theta_{22}, \theta_{21}\}^T$ is the vector of the degrees of freedom
M represents the mass matrix given by:

$$M=\begin{bmatrix} m_1 & & & & & & & \\ & m_1 & & & & & & \\ & & J_{11} & & & & & \\ & & & J_{12} & & & & \\ & & & & m_2 & & & \\ & & & & & m_2 & & \\ & & & & & & J_{22} & \\ & & & & & & & J_{21} \end{bmatrix} \tag{4}$$

where m_i are the masses of block i ($i=1,2$).
$K(t)$ includes the bearings stiffness k_{xi}, k_{yi} ($i, j=1,2$) the shafts torsional stiffness $k_{\theta i}$ and the time varying gearmesh stiffness $k_e(t)$.

$$K(t)=\begin{bmatrix} s_3k_e(t)+k_{x1} & s_5k_e(t) & 0 & s_7k_e(t) & -s_3k_e(t) & -s_3k_e(t) & 0 & s_9k_e(t) \\ s_5k_e(t) & s_4k_e(t)+k_{y1} & 0 & s_6k_e(t) & -s_5k_e(t) & -s_4k_e(t) & 0 & s_8k_e(t) \\ 0 & 0 & k_{\theta 1} & -k_{\theta 1} & 0 & 0 & 0 & 0 \\ s_7k_e(t) & s_6k_e(t) & -k_{\theta 1} & k_{\theta 1}+s_7k_e(t) & -s_7k_e(t) & -s_6k_e(t) & 0 & s_{12}k_e(t) \\ -s_3k_e(t) & -s_5k_e(t) & 0 & -s_7k_e(t) & s_3k_e(t)+k_{x2} & s_5k_e(t) & 0 & -s_9k_e(t) \\ s_5k_e(t) & -s_4k_e(t) & 0 & -s_6k_e(t) & s_5k_e(t) & s_4k_e(t)+k_{y2} & 0 & -s_8k_e(t) \\ 0 & 0 & 0 & 0 & 0 & 0 & k_{\theta 2} & -k_{\theta 2} \\ s_9k_e(t) & s_8k_e(t) & 0 & s_{12}k_e(t) & -s_9k_e(t) & -s_8k_e(t) & -k_{\theta 2} & k_{\theta 2}+s_{11}k_e(t) \end{bmatrix} \tag{5}$$

$K(t)$ can be divide into a mean stiffness matrix $\left[\overline{K}\right]$ and a time varying matrix $[k(t)]$.

$$K(t)=\overline{K}+k(t) \tag{6}$$

$[C]$ is the proportional damping matrix expressed by:

$$C=0.05M+10^{-5}\overline{K} \tag{7}$$

$\{F_{ext}(t)\}$ is the external applied torques vector. It can be written as

$$F_{ext}(t) = \{0, 0, C_m(t), 0, 0, 0, -C_r(t), 0\}^T \tag{8}$$

Where

$$C_r(t) = \frac{Z_2}{Z_1} C_m(t) \tag{9}$$

Let us suppose a spur gear system with characteristics given in Table 1 powered by four strokes four cylinders inline diesel engine with the specifications given in Table 2.

Table 1 Parameters of the spur gear

	Pinion	Wheel
Teeth numbers	20	40
Mass (Kg)	0.6	2.5
Inertia moment (Kg m²)	$2.6\ 10^{-4}$	0.0045
Base circle (m)	0.05	0.11
Module (m)		0.003
Bearing stiffness(N/m)		$k_{x1} = k_{y1} = k_{x2} = k_{y2} = 10^8$
Torsional stiffness (N rd/m)		$k_{\theta 1} = k_{\theta 2} = 10^5$
Pressure angle		$\alpha = 20^\circ$
Teeth width (m)		0.023
Contact ratio		$c_{12} = 1.6$

Table 2 Four strokes four cylinders inline diesel engine specifications

Motor type	Diesel engine
Inertia of the connecting rod at its center of gravity I_{Gx} (kgm^2)	0.004
Mass of the connecting rod m_b (kg)	0.9
Mass of the piston with rings and pin included m_p (kg)	1.1
Distance between the axis of the big end of the rod bearing and the center of gravity L (m)	0.04
Distance between the axis of the small end of the rod bearing and the center of gravity (m)	0.084
Maximum gas pressure inside cylinders P_{max} (bar)	49
The average friction torque of the engine $\overline{C_{m4}}$ (Nm)	17.5
Engine cubic capacity $V_{cyl}(cm^3)$	2000 5400
Engine regime at maximum torque $N_{c\max}(rpm)$	850
Engine regime N(rpm):idle engine regime	

Acyclism can be related to engine torque and during this loading state the rotational speed of engine is not constant but it has an average value. For the studied

gear set the pinion speed for rigid-body conditions can be expressed as Fourier series by (Sika G and Velex P, 2008):

$$\Omega_{10}(t) = \Omega_{10}\left(1 + \sum\nolimits_n \rho_n(\Omega_{10})\sin(n\Omega_{10}t + \varphi_n)\right) \tag{10}$$

where Ω_{10} is the nominal average angular velocity, n is the harmonic of the rotational speed, ρ_n is the corresponding dimensionless amplitude and φ_n is the initial phase.

For the harmonic n equal to 2 and a percentage of acyclism is equal to 2.5%. The evolution of the rotational speed transmitted to the spur gear system with respect to time computed according to Eq. (10) is shown in Figure 3.

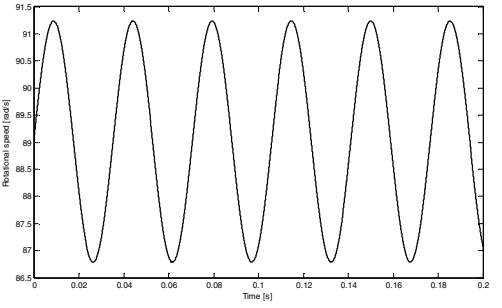

Fig. 3 Input rotational speed evolution of the gear set

When coupled to the studied gearbox, the periodic variation of the rotational velocity generates a periodic fluctuation of the meshing stiffness period as shown in Figure 4. Thus we can assume that transient regime is modeled by periodic fluctuation of the meshing stiffness with a rotational period average called acyclism period given by (Sika G, 2008)

$$T_{acy} = T_{10} = \frac{2\pi}{\Omega_{10}} \tag{11}$$

Pinion bearing time acceleration signal and the corresponding spectrum are respectively shown in Fig. 5a and b. The acceleration is periodic with T_{acy} as aperiod. An important variation of the vibration level over one cycle is observed. The spectrum of acceleration shown in Fig. 5b is characterized by an average mesh frequency f_{gm} $\left(f_{gm} = Z_1 f_{acy}\right)$ and its harmonics with sidebands surrounding f_{gm}. Sidebands are the consequence of input speed fluctuations of the gear set.

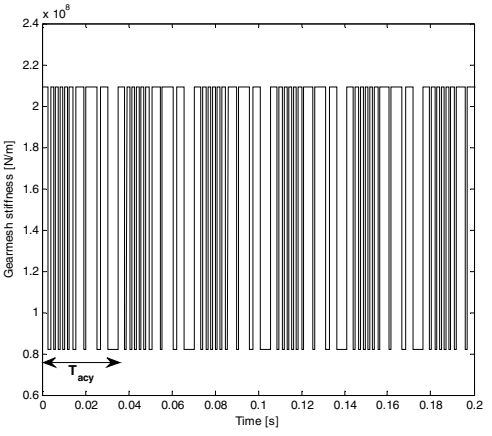

Fig. 4 Periodic fluctuation of the gearmesh stiffness

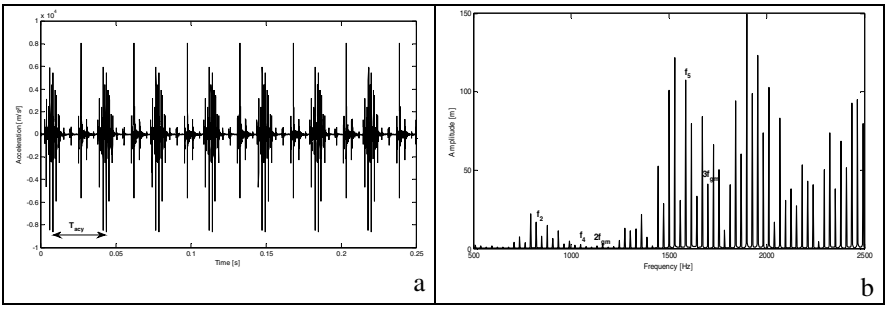

Fig. 5 Pinion bearing acceleration (a)and the corresponding spectrum (b).

5 Conclusion

In this paper, we studied the dynamic behavior of single stage spur gear reducer in transient regime powered by a combustion engine. The variations of input rotational speed and the phenomenon of acyclism generated by combustion engine are studied as well. The equation of motion is recovered and solved using the Newmark scheme. The numerical simulation results are analysed in time and frequencies fields. These results confirm the influence of the acyclism on the dynamic behaviour of the system.

References

Bouchaala, N., Chaari, F., Khabou, M.T., Fakhfakh, T., Haddar, M.: Influence of the non-linear Hertzian stiffness on the dynamics of a spur gear system under transient regime and tooth defects. Int. J. Vehicle Noise and Vibration 7(2) (2011)

Bartelmus, W., Chaari, F., Zimroz, R., Haddar, M.: Modelling of gearbox dynamics under time varying non-stationary operation for distributed fault detection and diagnosis. European Journal of Mechanics - A/Solids 29(4), 637–646 (2010)

Khabou, M.T., Bouchaala, N., Chaari, F., Fakhfakh, T., Haddar, M.: Study of a spur gear dynamic behavior in transient regime. Mechanical Systems and Signal Processing (2011)

Ligier, J.L., Baron, E.: Acyclisme et vibrations: Applications Aux Moteurs Thermiques et Aux Transmissions, vol. 1. Technip, Paris (2002)

Sika, G.: Dynamique Des Transmissions en régime Transitoire, Ph.D, INSA Lyon, France (2008)

Sika, G., Velex, P.: Analytical and numerical analysis of gears in the presence of engine acyclism. ASME J. Mech. Des. 130 (2008)

Velex, P.: Contribution à L'analyse du Comportement Dynamique de Réducteurs à Engrenages à Axes Paralléles, Ph.D, INSA Lyon, France (1988)

Walha, L., Louati, J., Fakhfakh, T., Haddar, M.: Dynamic response of two stages gear system damaged by teeth defects. Mach. Dyn. Prob. 29, 107–124 (2005)

Chaari, F., Baccar, W., Haddar, M.: Effect of spalling or tooth breakage on gearmesh stiffness and dynamic response of a one-stage spur gear transmission. Eur. J. Mech. A/Sol. 27(4), 691–705 (2008)

Chaari, F., Fakhfakh, T., Haddar, M.: Analytical modelling of spur gear tooth crack and influence on gearmesh stiffness. Eur. J. Mech. A/Sol. 28, 461–468 (2009)

Rakopoulos, C.D., Giakoumis, E.G.: Diesel Engine Transient Operation. Springer, London (2009)

Harris, S.L.: Dynamic loads on the teeth of spur gears. Proc. Inst. Mech. Eng. 172, 87–112 (1958)

Model Based Investigation on a Two Stages Gearbox Dynamics under Non-stationary Operations

Fakher Chaari[1], Radoslaw Zimroz[2], Walter Bartelmus[2],
Tahar Fakhfakh[1], and Mohamed Haddar[1]

[1] Dynamics of Mechanical Systems Research Unit,
National School of Engineers of Sfax, BP 1173, 3038, Sfax, Tunsia
Fakher.chaari@gmail.com,
{taher.fakhfakh,Mohamed.haddar}@enis.rnu.tn
[2] Wroclaw University of Technology
{radoslaw.zimroz,walter.bartelmus}@pwr.wroc.pl

Abstract. Machinery in industry using gearboxes covers many applications. The efficiency of such transmission cannot be achieved without a special attention to their dynamic behavior. Meshing as internal excitation, variable loads as external excitation and the presence of errors are the main factors that affect the dynamic behavior. This paper will discuss through a model based approach the influence of all of the three factors with an application on a two stages spur gears transmission. The transmission is modeled with a time varying loading conditions, the corresponding evolution of meshing stiffness function is derived and a local damage is introduced. The dynamic response is simulated. The responses show correlation between amplitude/energy of signal and applied value of load. It means that traditional energy based diagnostic approach should be revised for non-stationary operations

Keywords: two stages gearbox, time varying loading conditions, dynamic response, local damage, meshing stiffness, modification under varying speed.

1 Introduction

Gears are the most important mechanical systems for transmitting power or rotation. They are widely used in several sorts of machineries. Requirements for good running operations from these transmissions are low vibration and noise in addition to high efficiency. However, these requirements cannot be satisfied completely. In fact, the presence of defects will alter the normal operating conditions leading to higher vibration levels and a decrease in the efficiency of the transmission. On the other hand, the presence of variable loading conditions will accentuate the problem. In fact, load change induce variation in speed of the transmission and this will lead to other kind of modulation called frequency modulation which will complicate more and more the right diagnosis of the transmission health.

Several authors discussed the transient phenomena induced by the time variability of parameters in gear transmissions and its effect on dynamic response in presence of defects. Bartelmus and Zimroz [1, 2] showed that the identification of the varying external load is important when diagnosing a planetary gearbox. Randall [3] studied the vibration of gearbox casing vibration and observed a modulation between meshing frequency and fluctuation of torque load. Model based explanation of this phenomenon was not largely treated in literature. Bartelmus et al. [4] demonstrated by a model based and experimental approaches the sensivity of a gear transmission in terms of vibration levels to the increase of loading condition. They showed that a defected transmission is more sensitive to load increase by generation of higher vibration. Chaari et al [5] proposed a model of mesh stiffness variation based on the mechanical characteristic of driving motor and the loading conditions. Results of simulations on a one stage spur gear transmission lead to the presence frequency modulations of the mesh stiffness and its harmonics with a perfect agreement when compared to experimental results.

This paper is an extension of the last mentioned paper to a model of a two stages spur gearbox submitted to time varying loading condition and in presence of a local damage.

Increment of gearbox complexity is important issue here. It was highlighted by Bartelmus [6] that for multistage gearboxes one may find interaction between stages, which make dynamic response much more complicated and nonlinear. It was investigated for stationary load. Additional modulation (mesh frequency by mesh frequency) causes increased complexity of frequency structure which makes interpretation of signal much more difficult. We expect that these findings combined with non-stationary load condition are an important problem both from scientific and practical point of view. It is worth to notice that such combination (complexity of gearbox and varying load) can be often met in reality (wind turbines, mining machines, helicopters, etc.) [1,2,7]

The model formulation will be first presented incorporating a time varying mesh stiffness with relation to variable load. Numerical simulations and experimental validations will be finally presented and discussed.

2 Modeling of the Transmission

In this section, a two stage gearbox model is presented (fig. 1). This model will include both local damage and variable load/speed conditions. The model is composed of two pinions and two wheels supported by three bearings, one for the input shaft, the second for the intermediate shaft and the third for the output shaft. The transmission is driven by a motor which transmits torque to the input shaft by a coupling. A load is applied at the end of output shaft.

The system has 12 degrees of freedom (DOF) which can be detailed as follows:

- Translations of input block (having the mass m_1) composed of motor, input, coupling, and pinion1 along x (horizontal) and y (vertical) directions. The corresponding DOF are x_1 and y_1.

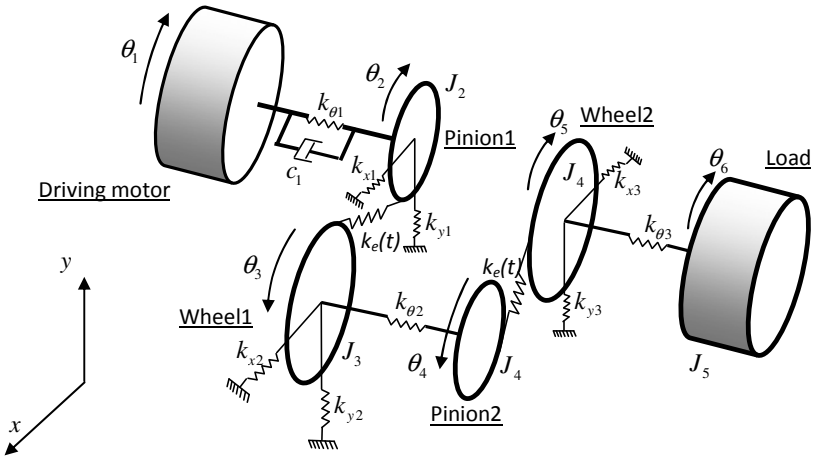

Fig. 1 Model of the transmission

- Translations of intermediate block (having the mass m_2) composed of wheel1, intermediate shaft and pinion2 along x and y directions. The corresponding DOF are x_2 and y_2.
- Translations of output block (having the mass m_3) composed of wheel2, output shaft and load, and pinion1 along x and y directions. The corresponding DOF are x_3 and y_3.
- Rotations of motor θ_1, pinion1 θ_2, wheel1 θ_3, pinion2 θ_4, wheel 2 θ_5.

The following inertias are considered: J_1 for the motor, J_2, for the pinion1, J_3 for wheel1, J_4 for pinion2, J_5 for wheel2 and J_6 for load.

Input, output and intermediate shafts elasticity is modeled by torsional stiffness respectively $k_{\theta 1}$, $k_{\theta 2}$ and $k_{\theta 3}$. Bearings supporting input shaft are modeled by linear springs k_{x1} and k_{y1} acting along x and y axis. Bearings supporting intermediate shaft are modeled by linear springs k_{x2} and k_{y2}. Bearings supporting output shaft are modeled by linear spring k_{x3} and k_{y3}.

An input torque C_m is applied to the motor and a resisting torque C_r is opposed by the load. A coupling is inserted between the motor and pinion 1 and modeled by a damping c_1 in parallel to the torsional stiffness $k_{\theta 1}$. Damping is introduced in parallel of each stiffness.

The time varying mesh stiffness is chosen to be a step function. Two mesh stiffness functions $k_{e1}(t)$ and $k_{e2}(t)$ are introduced between pinion1 and wheel1 and between pinion2 and wheel2.

Applying the Lagrange formulation will lead to the equation of motion given by [8,9]:

$$[M]\{\ddot{q}\}+[C]\{\dot{q}\}+\left[K(t)\right]\{q\}=\{F(t)\} \tag{1}$$

Where $[M]$ is the mass matrix, $[C]$ is damping matrix and $[K(t)]$ is the time varying stiffness matrix and $\{F(t)\}$ is the applied forces vector given by:

$$\{F\} = \langle 0 \quad 0 \quad C_m \quad 0 \quad 0 \quad 0 \quad 0 \quad C_r \rangle^T \tag{2}$$

$\{q\}$ is the vector of the degrees of freedom expressed by :

$$\{q\} = \{x_1 \quad y_1 \quad \theta_1 \quad \theta_2 \quad x_2 \quad y_2 \quad \theta_1 \quad \theta_2 \quad x_3 \quad y_3 \quad \theta_3 \quad \theta_4\}^T \tag{3}$$

The transmission is driven by an asynchronous motor. The load torque is variable, according to [5], this will induce a variability in the speed of the system. As consequence the two mesh stiffness functions will no longer be periodic.

3 Numerical Simulations

The dynamic response of the two stages gearbox transmission is simulated in presence of a time varying loading conditions. The parameters of the transmission are given in table1. The load profile is given in fig2. The mean value of this load is 45 Nm. Which leads to a mean mesh frequency for stage 1 : f_{m1} = 660 Hz and for stage 2 : f_{m2} = 440 Hz. The characteristics of the driving motor are taken from [5].

The evolution of mesh stiffness for the healthy case and defected case are presented in fig. 3. A breakage defect is modelled by a 60% loss of mesh stiffness.

As it was mentioned before, real machines are usually subjected to non stationary operating conditions. Selection of the model (shape) of load profile is important issue and should be related to analyzed machine. In previous work the authors tested different types of load variation profiles commonly used in literature

Table 1 Parameters of the model.

	Motor	Pinion1	Wheel1	Pinion2	Wheel2	Load
Teeth numbers		30	45	30	45	
Mass moment of inertia (kgm^2)	0.0005	0.002	0.008	0.002	0.008	0.0005
Mass (Kg)		1.2		2.9		2.1
Rotation speed (rpm)		1325		883		588
Modulus (mm)				4		
Base circle diameter (mm)		112.8	169.1	112.8	169.1	
Mean gearmesh stiffness (N/m)				$\overline{K_g} = 2\times10^8$		
Pressure angle				$\alpha = 20°$		
Contact ratio				c = 1.6		
Bearing stiffness (N/m)				$k_{x1} = k_{v1} = k_{x2} = k_{v2} = k_{x3} = k_{v3} = 10^8$		
Torsional stiffness (N rd/m)				$k_{.1} = k_{.2} = k_{.3} = 10^5$		

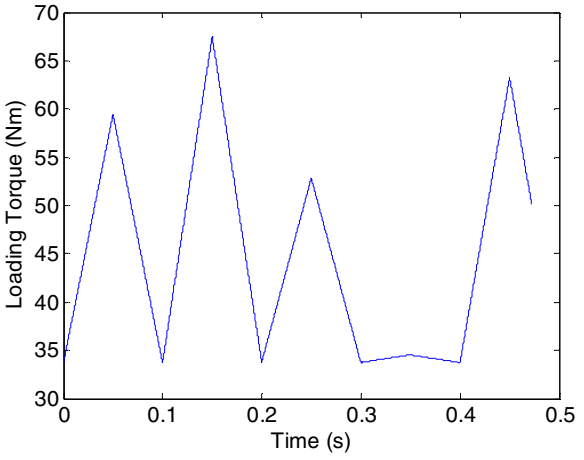

Fig. 2 Variation of load for the simulation

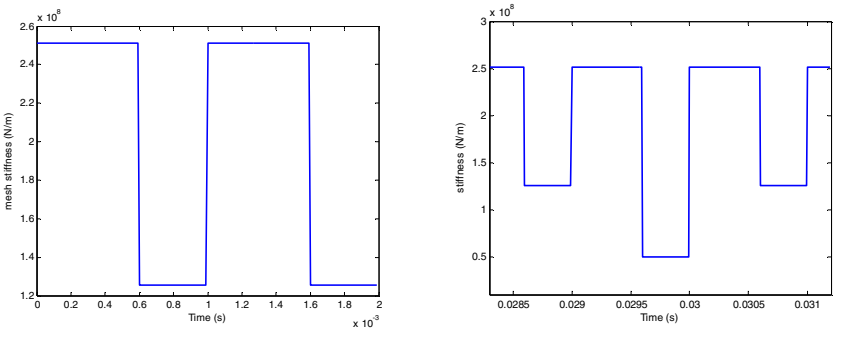

Fig. 3 Evolution of mesh stiffness function for healthy and local damage cases

(sine wave, step..., etc) but model presented in Fig 2 is the most suitable from validation point of view. It includes: linear increment/ decrement of load, its cyclicity and randomness of maximum load for each cycle. Evolution of mesh stiffness, and its modification for damaged tooth is commonly used for spur gears.

3.1 Healthy Case with Time Varying Loading Conditions

In the first simulation, of the healthy case is considered. The transmission is subjected to the variable load presented in fig.2. Fig. 4 shows the accelerations registered on the first bearing (input shaft) and Fig. 5 shows its STFT.

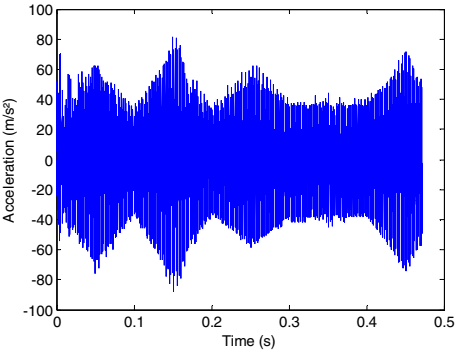

Fig. 4 Acceleration on the three bearing for the healthy case

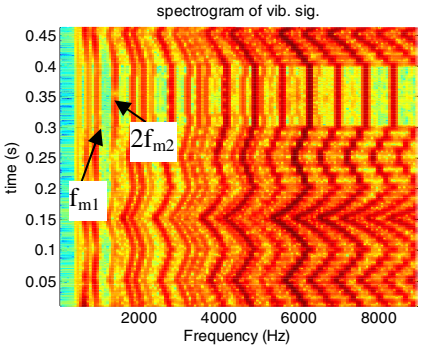

Fig. 5 STSFT of the Acceleration on the first bearing for the healthy case

It is well noticed from Fig.4 an increase of the vibration level as the load increases. This result is in conformity with previous works done by Bartelmus [1,4]. STFT map (Fig 5) shows clearly the frequency modulation induced by the period variability of the two mesh functions. It is also shown the increase of the range of frequency variation as the harmonic number increases. As it was mentioned before, spectral structure of the signal is time varying and much more complicated than for single stage. Analysis of whole spectrum, i.e. investigation on variability of characteristic components and their correlation with load variation is difficult. It is better to analyze single mesh component (other behave in the same way). Figure 6 shows the instantaneous mesh frequency (4^{th} harmonic of f_{m1}) along the time observation of the response.

It is well known, that if tachometer signal is not available, the Instantaneous Frequency (IF) may be estimated in different ways: for example in time-frequency domain [10], by FM demodulation (Hilbert Transform [11]) , Time_scale [12], parametric methods [13] and other see [14,15,16] for review. In this paper we used Hilbert transform for demodulation of band-pass filtered signal. Cut off frequencies of the band pass filter were establish by inspection of spectrogram. Fourth

harmonic of mesh frequency was selected due to good separation ability. It should be noted that used approach has limited application and can be used depending on frequency structure (multi stage gearbox makes this limitation more strict) and variability of load (it influences depth of frequency modulation). These remarks confirm that investigation on multistage gearbox and varying load is really important. Obviously, the estimation of IF a method used just for confirmation of existing phenomena, it is not the clue of the paper.

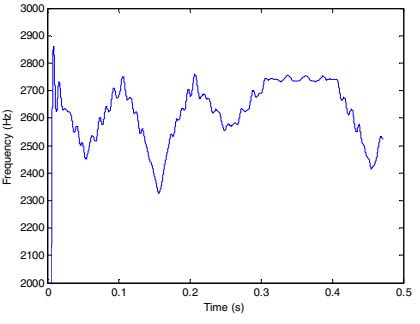

Fig. 6 Evolution of the 4th instantaneous mesh frequency f_{m1}

Fig. 7 shows for the same time axis the evolution of both load torque and the input stage speed. It is clear dependency – if load is increasing, the speed is decreasing that is obvious when consider motor characteristics.

It is clearly possible to correlate the evolution of the load profile with the fluctuation of speed at the input stage (pinion1). As the load increases, the speed

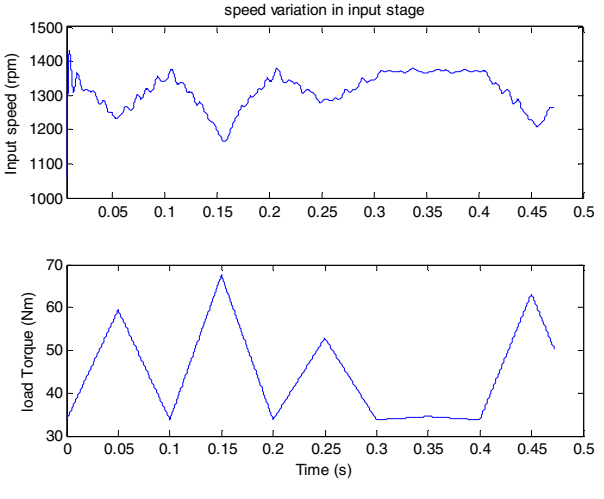

Fig. 7 input sped- load profile comparison

decrease and vice-versa. We notice a small phasing between the load variation and speed. If we look for example at load peak on 0.15s, the speed of the motor will reach its minimum value after few milliseconds.

3.2 Defected case with Time Varying Loading Conditions

A breakage is now introduced on one tooth of the pinion1. Simulations of the accelerations on the same bearing on the first stage are performed. Fig. 8 shows the acceleration on this bearing and Fig. 9 shows the corresponding STFT.

It is well observed from Fig. 7 the presence of characteristic peaks corresponding to local damage. These peaks have variable amplitudes according if the damaged tooth is in mesh at high or low loading phase. The impulses do not occur at the same period. This fact is also explained by the speed variability.

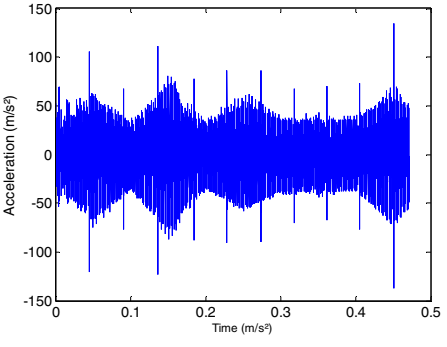

Fig. 8 Acceleration on the three bearing for the defected case

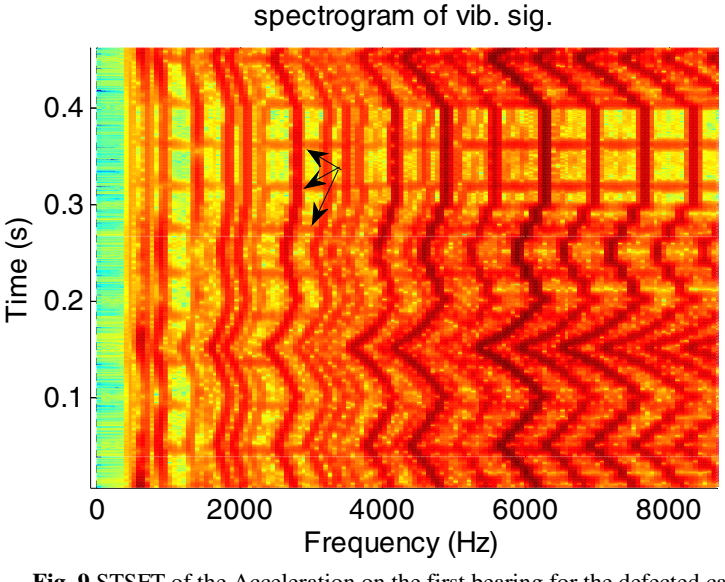

Fig. 9 STSFT of the Acceleration on the first bearing for the defected case

4 Conclusion

In this paper in order to study dynamic behavior of gearbox we proposed a model of two stage transmission, combined varying load conditions and introduced local damage of gear-pair. It has been shown that due to complexity of gearbox and variability of external load, the frequency structure of dynamic response is very complicated and time varying. In diagnostics in such a context one may use two approaches: to cancel or exploit load influence to dynamic response. Undoubtedly, the first step in both approaches is to identify dependency between load and gearbox dynamics. The easiest way it to use model based approach. The conclusions of the paper are:

- Load variability affects dynamic response of gearbox
- External Load, Instantaneous Amplitude of mesh components and Instantaneous Frequency are correlated, however load-frequency relation is negatively correlated.
- Due to load variability, dynamic response of gear with local damage is also much more complicated. Amplitudes of impulses are load dependent, too and moreover cycles between them due to speed fluctuation are not equal. It suggests that detection techniques developed for stationary case that exploits periodicity or spikiness of signal may not be effective here as proved for stationary case.

Acknowledgements. This paper was financially supported by Polish State Committee for Scientific research 2010-2013 as research project no. N504 147838.

References

1. Bartelmus, W., Zimroz, R.: Vibration condition monitoring of planetary gearbox under varying external load. Mechanical Systems and Signal Proc. 23(1), 246–257 (2009)
2. Bartelmus, W., Zimroz, R.: A new feature for monitoring the condition of gearboxes in non-stationary operation conditions. Mechanical Systems and Signal Processing 23(5), 1528–1534 (2009)
3. Randall, R.B.: A new method of modelling gear faults. Journal of Mechanical Design 104, 259–267 (1982)
4. Bartelmus, W., Chaari, F., Zimroz, R., Haddar, M.: Modelling of gearbox dynamics under time varying non-stationary operation for distributed fault detection and diagnosis. European Journal of Mechanics - A/Solids 29(4), 637–646 (2010)
5. Chaari, F., Bartelmus, W., Zimroz, R., Fakhfakh, T., Haddar, M.: Gearbox vibration signal amplitude and frequency modulation Shock and Vibration (in Press, 2012); doi:10.3233/SAV-2011-0656
6. Bartelmus, W.: Mathematical modelling and computer simulations as an aid to gearbox diagnostics. Mechanical Systems and Signal Processing 15(5), 855–871 (2001)
7. Barszcz, T., Randall, R.B.: Application of spectral kurtosis for detection of a tooth crack in the planetary gear of a wind turbine. Mech. Syst. and Signal Proc. 23, 1352–1365 (2009)

8. Chaari, F., Baccar, W., Haddar, M.: Effect of spalling or tooth breakage on gearmesh stiffness and dynamic response of a one-stage spur gear transmission. European Journal of Mechanics A/Solids 27(4), 691–705 (2008)
9. Walha, L., Fakhfakh, T., Haddar, M.: Nonlinear dynamics of a two-stage gear system with mesh stiffness fluctuation, bearing flexibility and backlash. Mechanism and Machine Theory 44(5), 1058–1069 (2009)
10. Zimroz, R., et al.: Measurement of Instantaneous Shaft Speed By Advanced Vibration Signal Processing - Application To Wind Turbine Gearbox. Metrology and Measurement Systems 18(4), 701–712 (2011)
11. Bonnardot, F., El Badaoui, M., Randall, R.B., Danière, J., Guillet, F.: Use of the acceleration signal of a gearbox in order to perform angular resampling (with limited speed fluctuation). Mechanical Systems and Signal Processing 19, 766–785 (2005)
12. Combet, F., Zimroz, R.: A new method for the estimation of the instantaneous speed relative fluctuation in a vibration signal based on the short time scale transform. Mechanical Systems and Signal Processing 23, 1382–1392 (2009)
13. Christos, Y., Gryllias, K., Antoniadis, I.: Instantaneous frequency in rotating machinery using a harmonic signal decomposition (HARD) parametric method. In: Proceedings of the ASME International Design Engineering Conference and Computers and Information in Engineering Conference IDECT/CIE, San Diego, USA (2009)
14. Urbanek, J., et al.: Comparison of amplitude based and phase based methods for speed tracking in application to wind turbines. Metrology and Measurement Systems 18(2), 295–304 (2011)
15. Boashash, B.: Estimating and Interpreting The Instantaneous Frequency of a Signal-Part 1: Fundamentals. Proceedings of the IEEE 80(4), 520–538 (1992)
16. Boashash, B.: Estimating and Interpreting the Instantaneous Frequency of a Signal-Part 2: Algorithms and Applications. Proceedings of the IEEE 80(4), 540–568 (1992)

Rotor Speed Identification Using Two Nonlinear Observers for Induction Motor Drive

Moulay Rachid Douiri[1], Mohamed Cherkaoui[2],
Ahmed Essadki[3], and Sidi Mohamed Douiri[4]

[1,2] Dept. of Electrical Engineering, Mohammadia Engineering School, Rabat-Morocco
douirirachid@hotmail.com
[3] Dept. of Electrical Engineering, Superior School of technical Education, Rabat-Morocco
ahmed_essadki@yahoo.ca
[4] Dept. of Mathematics, Faculty of Sciences, Rabat-Morocco
douirisidimohamed@hotmail.fr

Abstract. This paper proposes two approaches to achieve robust speed estimation in induction motor sensorless control, namely: Model Reference Adaptive System (MRAS), its structure consists of a reference model that doesn't involve the variable being estimated and an adjustable model that does. The error between these two models is proportional to the error in the estimation of the unknown variable. This value is used to improve the estimation of the adaptive model so that its output is equal to the output of the reference model. An alternative approach to the MRAS observer is to use an Extended Kalman Filter, EKF. This is a well established technique for controlling complicated processes involving noisy measured signals that are further disturbed by random noise. It does this by working on the assumption that noise in the measured signal is uncorrelated to the disturbance noise. The Kalman Filter's ability to provide an optimum observation in complex non linear environments means that it could potentially be used for sensorless induction motor control. The validity of the proposed methods is confirmed by the simulative results.

Keywords: extended kalman filter, model reference adaptive system, speed estimation, induction motor.

1 Introduction

The sensorless induction motor drives have been widely used due to their attractive features such as reliability, flexibility, robustness and poor cost, especially in the field of general inverter where they are used successfully. However, when a very high accuracy is desired, the performance of speed estimation is not good particularly at low speeds. The main reason of the speed estimation error is imprecise of

flux observer and the offset of the stator current sensor. Besides, it is very sensitive to the variation of motor parameters (Blaschke 1972, Hasse 1969).

The scheme based on model reference adaptive system (MRAS) is one of the major approaches for rotor speed estimation. The general idea behind Model Reference Adaptive Control (MRAC, also know as an MRAS or Model Reference Adaptive System) is to create a closed loop controller with parameters that can be updated to change the response of the system (Yang and Finch 2008). The output of the system is compared to a desired response from a reference model. The control parameters are update based on this error. The goal is for the parameters to converge to ideal values that cause the plant response to match the response of the reference model (Orlowska-Kowalska and Dybkowski 2007). An alternative approach to the MRAS observer is to use an Extended Kalman Filter, is a recursive mean squared estimator. It is capable of producing optimal estimates of system states that are not measured. The elements of the covariance matrices Q and R serve as design parameters for convergence of the system. The Kalman Filter approach assumes that the deterministic model of the motor is disturbed by centered white noise viz. the state noise and measurement noise (Ouhrouche 2002, Kim et al 1994).

2 Mathematical Model of an Induction Motor with Indirect Field Oriented Control

The dynamic behavior of an induction motor in the synchronously rotating frame can be described by the following state equations:

$$\begin{bmatrix} \dot{i}_{ds} \\ \dot{i}_{qs} \\ \dot{\Psi}_{dr} \\ \dot{\Psi}_{qr} \end{bmatrix} = \begin{bmatrix} -\frac{R_s}{\sigma L_s} - \frac{R_r(1-\sigma)}{\sigma L_r} & \omega_e & \frac{L_m R_s}{\sigma L_s L_r^2} & \frac{p\omega_r L_m}{2\sigma L_s L_r} \\ -\omega_e & -\frac{R_s}{\sigma L_s} - \frac{R_r(1-\sigma)}{\sigma L_r} & \frac{p\omega_r L_m}{2\sigma L_s L_r} & \frac{L_m R_s}{\sigma L_s L_r^2} \\ \frac{L_m R_r}{\sigma L_r} & 0 & -\frac{R_r}{L_r} & \omega_e - \frac{p}{2}\omega_r \\ 0 & \frac{L_m R_r}{\sigma L_s L_r^2} & -(\omega_e - \frac{p}{2}\omega_r) & -\frac{R_r}{L_r} \end{bmatrix} \begin{bmatrix} i_{ds} \\ i_{qs} \\ \Psi_{dr} \\ \Psi_{qr} \end{bmatrix} + \frac{1}{\sigma L_s} \begin{bmatrix} v_{ds} \\ v_{qs} \\ 0 \\ 0 \end{bmatrix} \tag{1}$$

$$\Gamma_{em} = \frac{3p}{4} . \frac{L_m}{L_r} (i_{qs} \Psi_{dr} - i_{ds} \Psi_{qr}) \tag{2}$$

In the field-oriented control for an induction motor, the ideal decoupling between the *d* and axes can be achieved by letting the rotor flux linkage in the *d*-axis, i.e.

$$\Psi_{qr} = 0, \qquad \Psi_{dr} = \hat{\Psi}_r, \qquad \frac{d\Psi_{dr}}{dt} = 0 \tag{3}$$

The desired rotor flux linkage Ψ_{dr}, in terms i_{ds} of the third row of (1) as:

$$\Psi_{dr} = \frac{(i_{ds} L_m)}{(1 + \frac{L_r L_s}{R_r})} \tag{4}$$

For the highest utility of the machine core, i_{ds} can be set constant for the desired rated rotor flux. In this situation if the dynamic characteristic of rotor flux in (4) is neglected, the torque equation (2) then becomes:

$$\Gamma_{em} = \frac{3p}{4}.\frac{L_m^2}{L_r}.i_{ds}.i_{qs} \tag{5}$$

where:

σ	: Leakage coefficient
R_s , R_r	: Stator and rotor resistance [Ω]
Γ_{em}	: Electromagnetic torque [$N.m$]
Ψ_{dr}, Ψ_{qr}	: dq-axis rotor flux [Wb]
v_{ds}, v_{qs}	: dq-axis stator voltage [V]
i_{ds}, i_{qs}	: dq-axis stator current [A]
L_m, L_s, L_r	: Magnetizing, rotor and stator inductance [H]
ω_r , ω_e	: Rotor and electrical angular speed [rd/s]
J	: Inertia moment [$Kg.m^2$]

3 Rotor Speed Estimation Using Model Reference Adaptive System (MRAS)

The open-loop speed estimation is based on the residual between the speed of rotor flux and the slip speed. The scheme described below uses the monitored stator voltages and currents to reconstruct the rotor flux, torque (Douiri et al. 2010)

$$\omega_r = \frac{\Psi_{rd}\frac{d}{dt}\Psi_{rq} - \Psi_{rq}\frac{d}{dt}\Psi_{rd}}{\Psi_{rd}^2 - \Psi_{rq}^2} - \frac{2}{3}.\frac{R_r}{p}.\frac{\Gamma_{em}}{\left\|\Psi_r\right\|^2} \tag{6}$$

This scheme requires several machine parameters, some of which vary with temperature, skin effect and saturation. Thus, the speed can only be obtained accurately if these parameters are accurately known. The rotor speed is reconstructed using the model reference adaptive system (MRAS). The MRAS principle is based on the comparison of the outputs of two estimators. The first is independent of the observed variable named as model reference. The second is the adjustable one. The error between the two models feed an adaptive mechanism to turn out the observed variable (Orlowska-Kowalska and Dybkowski 2007). In this work, the actual system is considered as the model reference and the observer is used as the adjustable one.

The reference rotor flux components obtained from the reference model are given by:

$$\frac{d}{dt}\begin{pmatrix}\Psi_{rd}\\ \Psi_{rq}\end{pmatrix} = \frac{L_r}{L_m}\left(\begin{pmatrix}v_{sd}\\ v_{sq}\end{pmatrix} - R_s\begin{pmatrix}i_{sd}\\ i_{sq}\end{pmatrix} - \sigma L_s\frac{d}{dt}\begin{pmatrix}i_{sd}\\ i_{sq}\end{pmatrix}\right) \tag{7}$$

The rotor flux components obtained from the adjustable model are given by:

$$\frac{d}{dt}\begin{pmatrix}\hat{\Psi}_{rd}\\ \hat{\Psi}_{rq}\end{pmatrix}=\begin{pmatrix}-\frac{R_r}{L_r} & -\hat{\omega}_r\\ \hat{\omega}_r & -\frac{R_r}{L_r}\end{pmatrix}\begin{pmatrix}\hat{\Psi}_{rd}\\ \hat{\Psi}_{rq}\end{pmatrix}+\frac{L_m R_r}{L_r}\begin{pmatrix}i_{sd}\\ i_{sq}\end{pmatrix} \tag{8}$$

Finally the adaptation scheme generates the value of the estimated speed to be used in such a way as to minimize the error between the reference and estimated fluxes. In the classical rotor flux MRAS scheme, this is performed by defining a speed tuning signal ε_ω to be minimized by a PI controller which generates the estimated speed which is fed back to the adaptive model. The expressions for the speed tuning signal and the estimated speed can be given as:

$$\varepsilon_\omega = \mathrm{Im}(\overline{\Psi}_r, \hat{\overline{\Psi}}^*_r) = (\Psi_{rq}\hat{\Psi}_{rd} - \Psi_{rd}\hat{\Psi}_{rq}) \tag{9}$$

$$\hat{\omega}_r = k_p\varepsilon_\omega + k_i\int \varepsilon_\omega dt \tag{10}$$

4 Rotor Speed Estimation Using Extended Kalman Filter Algorithm (EKF)

The essential idea of the Extended Kalman Filter (EKF) was proposed by S. F. Schmidt, and since then it has been called "Kalman-Schmidt" filter (Kim et al 1994). The goal is to minimize the estimation or tracking error for the states of a nonlinear system along a trajectory by applying linearization techniques, i.e., to evaluate the Taylor series expansion about the estimated trajectory on-the-fly. Then, if the problem is sufficiently observable (as evidenced by the covariance of estimation uncertainty, P), then the deviations between the estimated trajectory (along which the expansion is made) and the actual trajectory will remain sufficiently small that the linearization assumption is valid (Ouhrouche 2002).

The models and implementation equations of the discrete EKF, which have been used throughout this paper, are summarized below:

$$x_{k+1} = f(x_k, u_k) + w_k \tag{12}$$

$$z_k = h(x_k) + v_k \tag{13}$$

where x is the system state vector; f is the nonlinear state function at the current step $t + 1$ related to the previous time step t; u is the robot driven input; w and v are the process and measurement noise, respectively, which are assumed to be zero mean white noise with covariance matrix; z is a measurement vector; and h is the nonlinear measurement function of the system.

These noises are characterized by:

$$\operatorname{cov}\left[w_k, w_j\right] = E\left[w_k, w_j^T\right] = \begin{cases} Q_k & j = k \\ 0 & j \neq k \end{cases} \tag{14}$$

$$\operatorname{cov}\left[v_k, v_j\right] = E\left[v_k, v_j^T\right] = \begin{cases} R_k & j = k \\ 0 & j \neq k \end{cases} \tag{15}$$

The process covariance matrix Q_k and measurement covariance matrix R_k are symmetric and semi-definite. The EKF algorithm is as follows:

Prediction:

$$\hat{x}_{k|k-1} = F(\hat{x}_{k-1|k-1}, u_k, 0) \tag{16}$$

$$P_{k|k-1} = F_k P_{k-1|k-1} F_k^T + Q_k \tag{17}$$

$$F_k = \left.\frac{\partial f}{\partial x}\right|_{\hat{x}_{k-1|k-1}, u_k} \tag{18}$$

Updating

$$\hat{x}_{k|k} = \hat{x}_{k|k-1} + K_k\left[y_k - h(\hat{x}_{k|k-1})\right] \tag{19}$$

$$K_k = P_{k|k-1} H_k^T \left[H_k P_{k|k-1} H_k^T + R_k\right]^{-1} \tag{20}$$

$$P_{k|k} = \left[I - K_k H_k\right] P_{k|k-1} \tag{21}$$

$$H_k = \left.\frac{\partial h}{\partial x}\right|_{\hat{x}_{k|k-1}} \tag{22}$$

The state and output equations of the reduced order model of the induction motor established in stationary stator reference frame *d-q* given by (1) can be written as given below:

$$f(x_k, u_k) = A_k x_k + B_k u_k \tag{23}$$

$$h(x_k) = C_k x_k \tag{24}$$

$$A_k = \begin{bmatrix} 1 - \frac{A_R}{A_L} t_s & 0 & \frac{L_m R_r}{L_r^2 A_L} t_s & \frac{p L_m \omega_r}{2 L_r A_L} t_s & 0 \\ 0 & 1 - \frac{A_R}{A_L} t_s & -\frac{p L_m \omega_r}{2 L_r A_L} t_s & \frac{L_m R_r}{L_r^2 A_L} t_s & 0 \\ \frac{L_m}{\tau_r} t_s & 0 & 1 - \frac{1}{\tau_r} t_s & -\frac{p}{2} \omega_r t_s & 0 \\ 0 & \frac{L_m}{\tau_r} t_s & \frac{p}{2} \omega_r t_s & 1 - \frac{1}{\tau_r} t_s & 0 \\ 0 & 0 & 0 & 0 & 1 \end{bmatrix}_k$$

$$x_k = \begin{bmatrix} i_{ds} \\ i_{qs} \\ \Psi_{dr} \\ \Psi_{qr} \\ \omega_r \end{bmatrix}_k, B_k = \begin{bmatrix} \frac{t_s}{A_L} & 0 \\ 0 & \frac{t_s}{A_L} \\ 0 & 0 \\ 0 & 0 \\ 0 & 0 \end{bmatrix}_k, u_k = \begin{bmatrix} v_{ds} \\ v_{qs} \end{bmatrix}_k, \; C_k x_k = \begin{bmatrix} i_{ds} \\ i_{qs} \end{bmatrix}_k$$

where $\tau_r = \frac{L_r}{R_r}$, $A_R = R_r \frac{L_r}{R_r} + \frac{L_m^2 R_r}{L_r^2}$, $A_L = \left(1 - \frac{L_m^2}{L_r L_s}\right) L_s$

The matrices f, h, $\partial f/\partial x = F$, $\partial h/\partial x = H$ are obtained as follows:

$$f_k = \begin{bmatrix} (1 - \frac{A_R}{A_L} t_s) i_{ds} + \frac{L_m R_r}{L_r^2 A_L} t_s \Psi_{dr} + \frac{p L_m \omega_r}{2 L_r A_L} t_s \Psi_{qr} + \frac{t_s}{A_L} v_{ds} \\ (1 - \frac{A_R}{A_L} t_s) i_{qs} - \frac{p L_m \omega_r}{2 L_r A_L} t_s \Psi_{dr} + \frac{L_m R_r}{L_r^2 A_L} t_s \Psi_{qr} + \frac{t_s}{A_L} v_{qs} \\ \frac{L_m}{\tau_r} t_s i_{ds} + (1 - \frac{1}{\tau_r} t_s) \Psi_{dr} - \frac{p}{2} \omega_r t_s \Psi_{qr} \\ \frac{L_m}{\tau_r} t_s i_{qs} + \frac{p}{2} \omega_r t_s \Psi_{dr} + (1 - \frac{1}{\tau_r} t_s) \Psi_{qr} \\ \omega_r \end{bmatrix}_k$$

$$F_k = \begin{bmatrix} 1 - \frac{A_R}{A_L} t_s & 0 & \frac{L_m R_r}{L_r^2 A_L} t_s & \frac{p L_m \omega_r}{2 L_r A_L} t_s & \frac{L_m}{L_r A_L} t_s \Psi_{qr} \\ 0 & 1 - \frac{A_R}{A_L} t_s & -\frac{p L_m \omega_r}{2 L_r A_L} t_s & \frac{L_m R_r}{L_r^2 A_L} t_s & -\frac{p L_m}{2 L_r A_L} t_s \Psi_{dr} \\ \frac{L_m}{\tau_r} t_s & 0 & 1 - \frac{1}{\tau_r} t_s & -\frac{p}{2} \omega_r t_s & -t_s \Psi_{qr} \\ 0 & \frac{L_m}{\tau_r} t_s & \frac{p}{2} \omega_r t_s & 1 - \frac{1}{\tau_r} t_s & t_s \Psi_{dr} \\ 0 & 0 & 0 & 0 & 1 \end{bmatrix}_k \quad H_k = \begin{bmatrix} 1 & 0 & 0 & 0 & 0 \\ 0 & 1 & 0 & 0 & 0 \end{bmatrix}_k$$

5 Simulation Results

Induction motor parameters:

P_n=3Kw, V_n=230v, R_s=5.27Ω, R_r=5.07Ω, L_s=0.416H, L_r=0.423H, L_m=0.458H, J=0.2Kg.m², P=2.

The EKF algorithm and MRAS have been compared Acceleration of the drive is carried out in order to observe the performance of the estimator during the operation. The drive is run at various speeds by increasing it in steps to 100 *rd/s*, and 300 *rd/s* at 0.5 *s*, and 1 *s*, respectively. The speed of the motor (ω_r), estimated speed ($\hat{\omega}_r$), reference speed (ω_r^*) and speed estimation error ($\omega_r - \hat{\omega}_r$), are shown in Fig. 1.

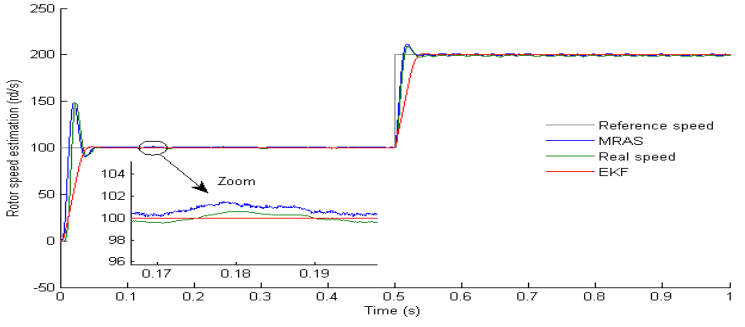

Fig. 1 Acceleration rotor speed estimation: EKF compared to MRAS

Acceleration and speed reversal is performed. A speed command of 100 *rd/s* at 0.7 *s* is given to the drive system which was initially at rest, and then the speed is reversed at 1.5 *s* (Fig. 2).

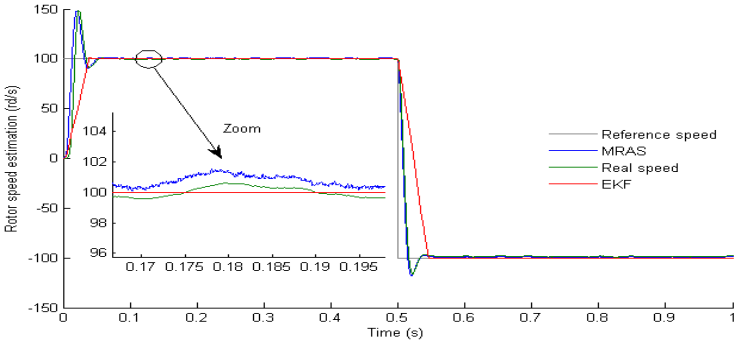

Fig. 2 Reversal rotor speed estimation: EKF compared to MRAS

6 Conclusions

In this paper, the speed sensorless indirect vector control of an induction motor is detailed and modified to improve its performance, and a comparison between two

nonlinear observers, the EKF and the MRAS is presented. The two observers are studied and compared in the same operating conditions, in order to extract their advantages and drawbacks. Simulation results show that both observers have the property of noise rejection and they are robust against parameters and load variations. The state observation performance of the EKF is quite satisfactory and slightly better. But, this type of observer requires an accurate knowledge of the load torque and needs more computational time due to heavy matrices manipulations. By contrast, the MRAS strategy doesn't need the load torque to be known and it is much easier to implement.

References

Blaschke, F.: The principle of field orientation as applied to the new transvector closed-loop control system for rotating field machines. Siemens Review XXXIX(5), 217–219 (1972)

Hasse, K.: On the dynamics of speed control of a static ac drive with a squirrel-cage induction machine. Dissertation, Tech. Hochsch. Darmstadt (1969)

Bodson, M., Chiasson, J., Novotnak, R.T.: Nonlinear speed observer for high performance induction motor control. IEEE Trans. Ind. Elec. 42(4) (1995)

Ouhrouche, M.: Estimation of speed, rotor flux and rotor resistance in cage induction motor sensorless drive using the EKF algorithm. International Journal of Power and Energy Systems 22(2), 103–109 (2002)

Menacer, A., Benakcha, A., Messaoudi, B.: The use of the direct control of stator flux and kalman filter for the direct torque Control of Induction Machine. Journal of Electrical Systems Special (1), 42–47 (2009)

Barut, M., Bogosyan, S., Gokasan, M.: EKF based sensorless direct torque control of IMs in the low speed range. IEEE Trans. on Industry Electronics, 969–974 (2005)

Kim, Y.R., Sul, S.K., Park, M.H.: Speed sensorless vector control of an induction motor using an extended kalman filter. IEEE Transactions on Industry Applications 30(5), 594–599 (1994)

Ozsoy, E.E., Gokasan, M., Bogosyan, S.: Simultaneous rotor and stator resistance estimation of squirrel cage induction machine with a single extended kalman filter. Turk. J. Elec. Eng. & Comp. Sci. 18(5) (2010); doi:10.3906/elk-0906-50.

Yang, C., Finch, J.W.: A Comparison of induction motor speed estimation using conventional MRAS and AI bsed MRAS with a dynamic reference model. In: Proceedings of the World Congress on Engineering, vol. 1 (2008)

Douiri My, R., Cherkaoui, M., Essadki, A., Nasser, T.: Direct torque control of induction motor based on artificial neural networks with estimate and regulation speed using MRAS and neural PI. Journal of Theorecal and Applied Information Technology 20(1), 15–21 (2010)

Haseeb, M.D., Amarnath, J., Khan: SVPWM - MRAS speed observer for sensorless control of induction motor drive. International J. of Engg. Research & Indu. Appls (IJERIA) 3(1), 211–223 (2010); ISSN 0974-1518

Orlowska-Kowalska, T., Dybkowski, M.: Improved MRAS-type speed estimator for the sensorless induction motor drive. COMPEL: The International Journal for Computation and Mathematics in Electrical and Electronic Engineering 26(4), 1161–1174 (2007)

Gear Transmission Dynamics Supported by Bearings Including Tooth Profile Deviations

Alfonso Fernandez del Rincon, Fernando Viadero, Miguel Iglesias, Ana de-Juan, and Pablo García

Department of Structural and Mechanical Engineering, University of Cantabria
fernandra@unican.es, viaderof@unican.es, miguel.iglesias@unican.es, ana.dejuan@unican.es, garciafp@unican.es

Abstract. In this work a non linear dynamic model of spur gear transmissions previously developed by the authors is extended to include both desired (relief) and undesired (manufacture errors) deviations in the tooth profile. The model uses a hybrid method for the calculation of meshing forces, which combines FE analysis and analytical formulation, so that it enables a very straightforward implementation of the tooth profile deviations. The model approach handles well non-linearity due to the variable meshing stiffness and the clearances involved in gear dynamics, also including the same phenomena linked to bearings. In order to assess the ability of the model to simulate the impact of the deviations on the transmission dynamics, an example is presented including profile deviations under different values of transmitted torque. Several results of this example implementation are presented, showing the model's effectiveness.

Keywords: Gear Dynamics, Bearings, Tip Relief, Profile Errors, Meshing Stiffness

1 Introduction

Today, gear transmissions are under great pressure to improve their performance, in terms of levels of power, speed, efficiency and compactness. A significant increase in operating speeds is expected in the medium and long term, and consequently dynamic phenomena will become more important in the future, justifying further interest in the development of more accurate dynamic models.

In gear dynamics there is a particular feature that governs the vibratory behavior, namely the presence of a parametric excitation as a consequence of the changes in the number of teeth couples contacting simultaneously. This aspect makes the development of dynamic models cumbersome, because a balance must be achieved between accuracy and computational time [1]. Moreover, the non-linearity inherent to contact problems, as well as to clearances and deflections of teeth and supports, changes the shape of this parametric excitation along the

meshing path depending on the magnitude of the torque to be transmitted. This fact is more pronounced in spur gears and so it must be considered if better dynamic models are desired.

Bearings have a similar behavior in the sense that they also undergo a parametric excitation, in this case due not only to the changes in the number of rolling elements supporting the transmitted load, but also because of the non-linearity related to clearances and surface contacts.

Therefore, gear transmissions should be considered as a whole, including the dynamic effects of gear and bearings, particularly if a better understanding of the transmission behavior is required for condition monitoring purposes. With this objective, in previous works the authors presented a numerical model which combines gears and bearings, which can represent all the features described above. In [2] the authors describe the model for calculation of meshing and bearing forces, carrying out several quasi-static analyses to show the differences in gear centre orbits, transmission error and meshing stiffness values for several transmitted torques. Subsequently, in [3] the procedure used for gear force calculation, based on a hybrid approach combining numerical and analytical tools, was extended including dissipative forces due friction and squeeze damping and assessed in dynamic simulations speeding up the computation time by using a pre-calculated value for meshing stiffness. Later, in [4] the dynamic model was linearized for several torque levels obtaining the natural frequencies and mode shapes which are essential to understand the vibratory behaviour of the transmission. Moreover, gear defects such as pitting, cracks and profile errors were also included, carrying out quasi-static analysis to assess the consequences [5].

In this work, profile deviations such as undesired profile errors and tip reliefs are added to the dynamic model with the aim of analysing the consequences on the dynamic behaviour under several torque loads.

2 Description of the Model

In this section the proposed model is briefly explained, paying greater attention to the formulation used to include profile deviations. More detail about the model can be found in references [2-5].

Gear forces are obtained following the proposal of Vedmar and Andersson [6] in which the deformation at each gear contact point is formulated as a combination of a global (or structural) term obtained by means of a *FE* model, and a local term described by an analytical approach which derives from Hertzian contact theory.

The tooth profile geometry necessary to build the *FE* model were generated using a rack-type tool following Litvin's vector approach [7]. The *FE* model assumes the nodes in the inner circle to be fixed, that is, where the gears are fitted to the shaft. The above *FE* model is solved considering multiple load cases each of which is defined by a unit load perpendicular to the tooth profile located at different radial positions from the root to the tip. Then the *FE* model built for each gear is solved once before the integration of dynamic equations obtaining the displacement (flexibility) of the node j due to a unitary load applied in the node i of

the loaded active flank. These flexibilities are used to solve the contact problem imposing the compatibility of geometrical separations (δ_j) and elastic deflections (u_{Tj}) submitted to the complementary condition in order to avoid non realistic negative loads arriving at the following non-linear system of equations for n contacting points

$$\delta_j(\{\vec{r}_p,\theta_p\},\{\vec{r}_w,\theta_w\}) = u_{Tj}(\{\vec{r}_p,\theta_p\}\{\vec{r}_w,\theta_w\}\{F\}) + e_{jp}(\{\vec{r}_p,\theta_p\}) + e_{jw}(\{\vec{r}_w,\theta_w\}) \qquad (1)$$
$$\textit{submitted to} \quad F_j \geq 0; \quad j = 1,...,n$$

Where $\{F\}$ is the unknowns vector, which contains the contact forces for each active contacting point. Profile deviations of pinion e_{jp} and wheel e_{iw} for the jth point of contact are added to the compatibility equation. Furthermore, meshing forces were extended including Coulomb friction and dissipative effects due to squeeze film damping (see [3]).

The elastic deflections (u_{Tj}) in (1) are obtained by addition of structural and local terms for both gears. At the same time, geometrical separations ($\boldsymbol{\delta_j}$) are obtained taking advantage of the analytical properties of involute profiles and rounding arcs introduced at the tooth tip to handle corner contacts.

As with gears, the changing number of bearing rolling elements supporting the load implies a parametric excitation as a function of the shaft rotational angle. This time, bearing clearance interacts with the magnitude of the load to be transmitted, defining the angular positions in which it changes the number of rolling elements supporting the load. To consider these facts, forces in bearings have been formulated following the model proposed by Fukata et al [8].

Gear and bearing formulations are implemented in a dynamic model of a single-stage transmission shown in Fig. 1 as a block diagram. Shaft torsional and flexural deflections are represented by spring-damper elements while non-linear forces of gears and bearings are represented by two-way arrows. A reference framework is defined with *z-axis* along the shaft centre line and the *y-axis* defined by the line between gear centres. Using the subscripts *R* and *b* to designate the gears and bearings, X_{iRj} means the displacement along the *x-axis* of gear *j* of shaft *i*. The degrees of freedom (*dof*) associated with bearings and gears are grouped in vectors $\boldsymbol{q_{ibj}} = \{x_{ibj},\ y_{ibj},\ \theta_{ibj}\}^T$ and $\boldsymbol{q_{iRj}} = \{x_{iRj},\ y_{iRj},\ \theta_{iRj}\}^T$. Furthermore, an additional rotational-only inertia and coupling are included at the output and a constant value of rotational speed is assumed at the input. Then, the individual element matrices (mass, damping and stiffness) are assembled into the dynamic matrix equation arriving at a system with 19 *dof*. This equation was subsequently arranged for numerical integration in *Matlab/Simulink*® arriving at

$$\ddot{\mathbf{q}} = \mathbf{M}^{-1}\left(\mathbf{f}_{Ext}(t) - \mathbf{C}\dot{\mathbf{q}} - \mathbf{K}\mathbf{q} - \mathbf{f}_b(\mathbf{q}) - \mathbf{f}_R(\mathbf{q},\dot{\mathbf{q}})\right) \qquad (2)$$
$$\mathbf{q} = \left\{\mathbf{q}_{1b1},\mathbf{q}_{1R1},\mathbf{q}_{1b2},\mathbf{q}_{2b1},\mathbf{q}_{2R1},\mathbf{q}_{2b2},\theta_{Out}\right\}^T$$

Where $\mathbf{M}$, $\mathbf{C}$ and $\mathbf{K}$ are constant coefficient matrices, while vectors $\mathbf{f_b}$ and $\mathbf{f_R}$ represent non-linear bearing and meshing forces.

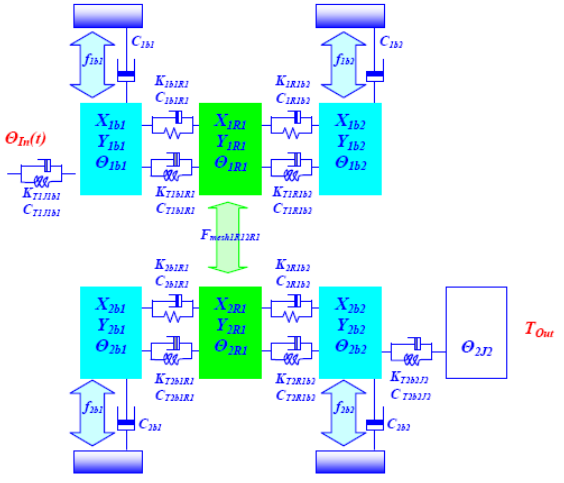

Fig. 1 Block Diagram

3 Profile Deviations

Deviations from the theoretical profile due to the manufacturing process or wear, as well as tip or bottom reliefs, are assumed not to affect the overall flexibility of the tooth or the normal direction of contact, altering only the magnitude of the actual geometrical separations (δ_j). Both errors are added and included in equation (1) as a function of the position of each wheel. Profile Errors (*PE*) usually have a similar pattern in the same flank of successive teeth. Thus in this work, PEs are considered identical for all teeth. The formulation of such errors has been carried out using the AGMA parameters [9] $f_{f\alpha}$ (Profile Form Deviation) and $f_{H\alpha}$ (Profile Slope Deviation) adopting a sinusoidal shape with amplitude $f_{f\alpha}$ and f_r cycles according to the expression (see Fig. 2).

$$e_{PE}(s)=f_{H\alpha}\frac{(s-s_0)}{(s_f-s_0)}+\frac{ff_\alpha}{2}\text{sen}\left(2\pi f_r\frac{(s-s_0)}{(s_f-s_0)}\right) \tag{3}$$

Where s is the roll path length (see Fig. 2), (s_f) and (s_0) the higher and lower involute curvature radii. Here, positive errors mean increments of the curvature radii with respect to the nominal one, while negative values indicate reductions.

Contrary to the undesired PEs, there are other cases in which profile modifications are included deliberately, as is the case of tip and bottom reliefs. Nevertheless, particularly in spur gears, the form and magnitude of these deviations must be carefully chosen depending on the level of torque to be transmitted. These profile modifications will be implemented in the model in a similar way to the profile errors. In this case, positive values of the deviation mean removal of material with respect to the nominal shape (smaller curvature radii), and negative values indicate

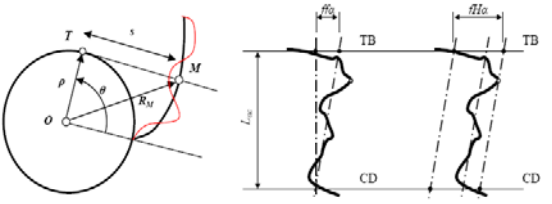

Fig. 2 Parameters defining the profile error

the opposite. The formulation of this modification is defined (see Fig. 3) by the maximum magnitude of the relief (C_{RT} for the tip and C_{RB} for the bottom) the length of the correction (ΔL_B or ΔL_T) and the shape, which is generally linear or parabolic and expressed by

$$\begin{cases} e_{TR}(s)=C_{TR}\left(\dfrac{(s-s_{T0})}{\Delta L_T}\right)^n & s\in[s_{T0},s_f] \\ e_{BR}(s)=C_{BR}\left(\dfrac{(s_{Bf}-s)}{\Delta L_B}\right)^n & s\in[s_0,s_{Bf}] \end{cases} \quad n=1,2; \tag{4}$$

Where the subscript T indicates tip relief, B corresponds to bottom relief and n takes the value 1 if the shape of the deviation is linear and 2 if it is parabolic.

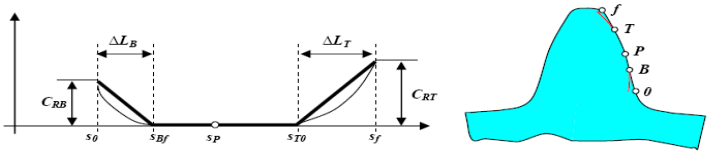

Fig. 3 Description of the tip and bottom reliefs

4 Application Example

A numerical example will be presented here whose basic parameters are listed in Table 1. Gears shafts are supported by a couple of ***209*** single-row radial deep-groove ball bearings [10]. More details can be found in [2]-[4].

Moreover, *PEs* have been included according to the values contained in Table 2 while only linear tip relief (n = 1) was considered in both gears with C_{RT} = 0.015 mm and ΔL_T = 4 mm.

In the following, some of the most noteworthy results obtained from dynamic simulations of the transmission example for a rotational speed of 1000 r.p.m. with several torque levels will be presented, in order to demonstrate the model's capability. In Fig. 4 preliminary quasi-static analyses are presented. Particularly in

Table 1 Transmission data

Parameter	*Value*	*Parameter*	*Value*
Number of teeth (gear 1&2)	28	Rack tip rounding	0.25 **m**
Module (**m**)	3.175 [mm]	Gear tip rounding	0.05 **m**
Elasticity Modulus	210 [GPa]	Gear face width	6.35 [mm]
Poisson's ratio	0.3	Gear shaft radius	20 [mm]
Pressure angle	20 [degree]	Mass (m_{iR1})	0.7999 [Kg]
Rack addendum	1.25 **m**	Gear inertia (J_{iR1})	4.0 10^{-4} [Kgm^2]
Rack dedendum	1 **m**	Oil viscosity	0.004 [Pas]
Output inertia [Kg m^2]	J_{2J2}= 3.56 10^{-4}	Shaft flex. Stiff. [N/m]	K_{ib1R1}= K_{iR1b2} = 6.24 10^8
Shaft Tor. Stiff. [Nm/rad]	K_{Tib1R1}=K_{TiR1b2}=4 10^5	Coupling Stiff. [Nm/rad]	K_{T1J1b1}= K_{T2b2J2}=4.0 10^5
Shaft Tor. Damp. [Nms/rad]	C_{Tib1R1}= C_{TiR1b2} = 0	Coupling Damp. [Nms/rad]	C_{T1J1b1}= C_{T2b2J2}=3.5761
Shaft Flex. Damp. [Ns/m]	C_{ib1R1}= C_{iR1b2} = 31.6		

Table 2 Parameters for *PE*

	f_H [mm]	f_f [mm]	f_r[mm]	s_f[mm]	s_0 [mm]
Pinion	0.002	0.003	1.8	22.8793	5.1260
Wheel	0.001	0.003	1.3	22.8793	5.1260

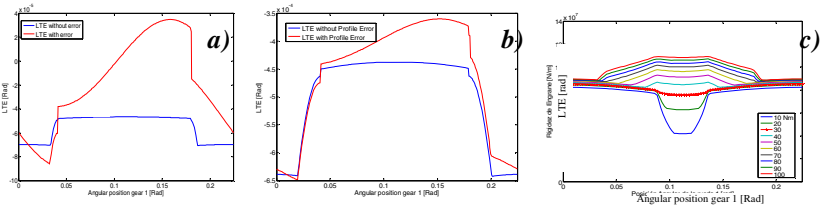

Fig. 4 a) LTE with PE (10 Nm); b) LTE with PE (100 Nm) c) Meshing Stiffness with Tip Relief.

Fig. 4 a) and b) the Loaded Transmission Error (*LTE*) for torques of 10 and 100 Nm with and without *PE* is presented. It can be appreciated that the effect of the profile error is more noticeable when the torque level is low, while the load increments reduce the differences. Fig. 4 c) shows the plot of the resultant meshing stiffness obtained from a quasi-static analysis when the tip relief is considered. The design load is close to 30 Nm and the meshing stiffness changes notably as a function of the transmitted torque. Fig. 5 a) and b) show the gear orbits and *LTE* of dynamic simulations when the ideal profile is considered. Fig. 5 c) and d) show the results obtained when *PEs* are included, while Fig. 5 e) and f) correspond to the tip relief modifications. *PE* as expected provides higher *LTE* amplitudes while tip relief shows a smoother behavior near 40 Nm of torque.

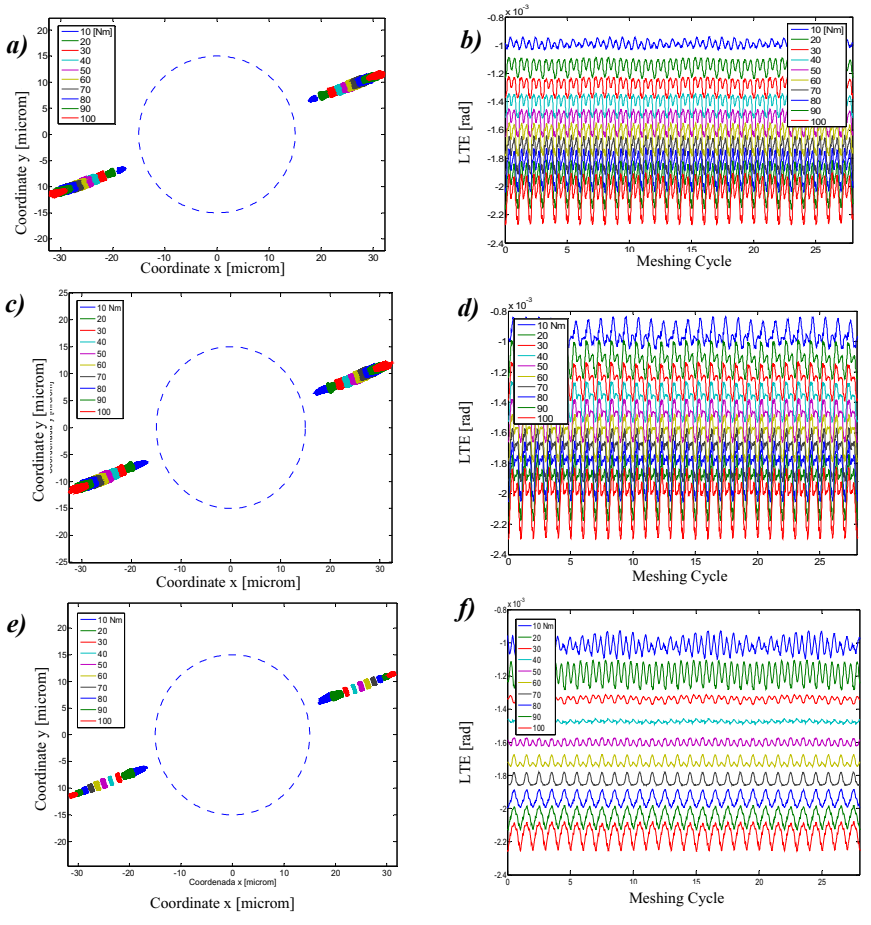

Fig. 5 Orbits (left column) and LTE (right column) for 1000 r.p.m. and several torques

5 Conclusions

A non-linear model for the dynamic analysis of a gear transmission supported by ball bearings and including tooth profile deviations was presented. The model approach used for the calculation of meshing forces, combining FE analysis and analytical formulation, enables a very straightforward implementation of the tooth profile deviations. The model's effectiveness is shown by means of an application example which assesses the consequences when deviations are considered, with particular attention to the role played by the torque level. The tip relief cases show a generalized enhancement in the amplitudes of LTE and gear centre orbits, with much less improvement for low values of torque. Regarding PE, the model is also capable of predicting the increase of the LTE amplitude and orbits along the line of action, showing a much greater effect for low torques. In addition, the model is

also able to show the bearing clearance and variable stiffness effect on the LTE results widening the orbits outside the line of action.

Acknowledgements. This paper has been developed in the framework of Project DPI2006-14348 funded by the Spanish Ministry of Science and Technology.

References

[1] Velex, P., Mataar, M.: A mathematical model for analyzing the influence of shape deviations and mounting errors on gear dynamic behavior. JSV 191, 629–660 (1996)
[2] Viadero, F., Fernandez del Rincon, A., Sancibrian, R., Garcia, P., de- Juan, A.: A model of spur gears supported by ball bearings. WIT Trans. Modelling and Simulation 46, 711–722 (2007)
[3] Fernandez del Rincon, A., Viadero, F., Sancibrian, R., Garcia, P., de-Juan, A.: A dynamic model for the study of spur gears transmissions. WIT Trans. Modelling and Simulation 48, 711–722 (2009)
[4] Fernandez del Rincon, A., Viadero, F., Iglesias, M., Garcia Fernandez, P., de-Juan, A., Sancibrian, R.: Load effects on the dynamics of spur gear transmissions. In: ESDA (2010)
[5] Fernandez del Rincon, A., Iglesias, M., de-Juan, A., Viadero, F.: Defect simulation in a spur gear transmission model. New Trends in Mechanism Science: Analysis and Design. Mechanisms and Machine Science 5, 191–198 (2010); doi:10.1007/978-90-481-9689-0_22
[6] Vedmar, L., Andersson, A.: A method to determine dynamic loads on spur gear teeth and on bearings. JSV 267, 1065–1084 (2003)
[7] Litvin, F.L., Fuentes, A.: Gear Geometry and Applied Theory. Cambridge University Press (2004)
[8] Fukata, S., Gad, E.H., Kondou, T., Ayabe, T., Tamura, H.: On the radial vibrations of ball bearings (computer simulation). Bulletin of the JSME 28, 899–904 (1985)
[9] American National Standard, Accuracy Classification System – Tangential Measurements for Cylindrical Gears. ANSI AGMA 2015-1-A01 (2002)
[10] Harris, T, A.: Rolling Bearings Analysis. John Wiley & Sons Inc. (2001)

Effects of Gyroscopic Coupling on the Dynamics of a Wind Turbine Blade with Horizontal Axis

Hédi Hamdi[1], Charfeddine Mrad[2], and Rachid Nasri[2]

[1] Department of Mechanical Engineering,
Higher Institute of Technological Studies of Mednine
Hedi.Hamdi@isetr.rnu.tn
[2] Department of Mechanical Engineering, National School of Engineers of Tunis
Charfeddine.Mrad@enit.rnu.tn, Rachid.Nasri@enit.rnu.tn

Abstract. It is about a wind turbine blade of five meters of length in composite material, Glass Fiber Reinforced Plastics (GRP), calculated using the finite elements method (FEM) to determine the influence of the gyroscopic coupling on its dynamic behavior. First, using the blade element momentum method (BEM) we wrote the aerodynamic forces applied on the blade, depending on the wind speed. Then we incorporated these expressions into the laws of structures behavior to reach a matrix formulation of the equations of motion of the blade taking into account the nonlinear deformation. The obtaining of the mechanical stiffness, geometric stiffness, mass and gyroscopic coupling matrices of the blade allows to simulate its dynamic response in transient and permanent phases under the action of its weight, and under a sudden variation of the wind speed.

Keywords: wind turbine blade, aerodynamic loads, static and dynamic behavior, gyroscopic effect.

1 Introduction

The wind turbine blades in normal operation are subject to aerodynamic, centrifugal and gravity forces. These external forces are classified into three categories: temporary, constant or cyclical. Indeed, the variation of wind speed, the change of orientation of the turbine axis due to a change in the wind direction, or the action of gravity under gyroscopic effect. These efforts, often cyclical, are the cause of the vibration of the blade and therefore disrupt the air flow around its profile, which justifies the loss of a part of the aerodynamic useful energy to decrease its performance. A wind turbine blade must resist during an emergency stop, in case of a gust of wind, in violent hurricanes, and have the power coefficient close to the theoretically maximum, the limit of Betz: 59.26% [1]. This coefficient is function of the rotor angular speed, and also depends on the airfoil, the shape and the layout of the blades. In this work we are interested in determining the action of the gyroscopic forces on a blade of five meters of length,

built of composite material, Glass Fiber Reinforced Plastics (GRP), taking into account nonlinear deformation [2].

2 Design of the Blade

The aerodynamic energy is recovered by placing against the wind flow a three bladed propeller of a wind turbine, Fig. 1. The rotor of the wind turbine is mounted in the nacelle swiveling around the axis of the mast established vertically on the ground. The optimal design of a blade is to find the best compromise between the aerodynamic and structural efficiency; these two factors affect the cost of producing electrical energy.

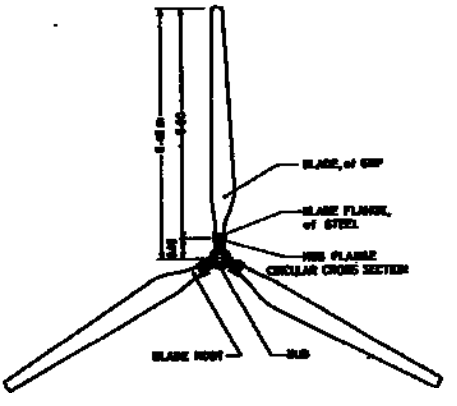

Fig. 1 Propeller of the wind turbine

Since a long time the builders of blades, for horizontal axis wind turbine, used the airfoil NACA series 23nnn or 44nn. Although the profiles NACA-44nn have acceptable aerodynamic performance, the profiles NACA-63nnn provide a higher lift coefficient C_L helping to reach the peak of power. However, these profiles are preferable for the working inner region of the blade. The profiles LS-1 provide a higher output at the region of its root, moreover, it is thick which allowing it to resist bending. The used blade profile is LS1-0421, Fig. 2a, for the root, and NACA63-621, Fig. 2b, for its interior, and FX-S66-196, Fig. 2c, for its end, because the profiles FX-S provide more stable lift coefficient C_L when the angle of attack increases [1].

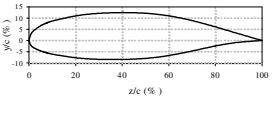

Fig. 2a Airfoil LS1-0421

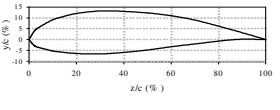

Fig. 2b Airfoil NACA-63-621

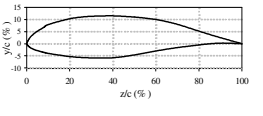

Fig. 2c Airfoil FX-S66-196

The similarity between these three profiles allows a soft transition following the span of the blade. The clamping edge of the blade on the rotor is cylindrical, external diameter of 21 cm and internal diameter of 19 cm, an adhesive joint between the blade and the rotor is used to support the efforts of installation and make the structure more flexible. The design of the blade by SolidWorks needs the exact profiles distribution; it is presented in the following, Table 1.

Table 1 Geometry of the blade.

Station (m)	Chord (mm)	Thickness (mm)	Twist (deg)	Section S (mm^2)	Profiles: NACA-63-621=N21, FXS-66-196 = F196
0.0	210	210	0.0	9966	Round
0.4	504	183	25	8465	1.00 (LS-0421)
0.8	600	178	16	15030	1.41 (N21)
1.2	562	163	12.8	15307	1.38 (N21)
1.6	524	149	10.1	14203	1.35 (N21)
2.0	486	134	7.8	13105	1.31 (N21)
2.4	448	120	5.8	12016	1.28 (N21)
2.8	410	105	4.2	10936	1.22 (N21)
3.2	371	91	2.8	9865	0.85 (N21) + 0.34(F196)
3.6	333	76	1.8	8803	0.25 (N21) + 0.90(F196)
4.0	295	61	0.9	7754	1.06 (F196)
4.4	257	47	0.4	6942	0.93 (F196)
4.8	219	32	0.2	6185	0.74 (F196)
5.0	200	25	0.0	5194	0.64 (N21)

The materials usually used in the manufacture of long blades are composite materials with thermosetting matrices reinforced by glass fibers or carbon fibers. The most common matrices in this design are the unsaturated polyester resin (UP) and epoxy resin (EP). The choice of GRP, Table 2, with polyester resin is bonded to three attributes: its lightness, its ability to resist fatigue and its availability at an acceptable price. The blade external surface is covered with the GelCoat to decrease friction, and improve its resistance to erosion.

Table 2 Mechanical properties of the GRP.

Density	ρ= 1400 kg/m^3
Tensile yield strength	Re= 63 MPa
Ultimate tensile strength	R= 129 MPa
Elasticity modulus	E= 6 GPa
Compressive strength	Rc= 170 MPa
Shear modulus	G= 2,5424 GPa
Poisson ratio	v= 0,18
Glass content	c= 50 %

3 Applied Loads

The objective is to determine the aerodynamic forces acting on the blade and their optimal parameters. The modeling of the wind action on the blade is a complex spot due to the rotation of the propeller that creates a three dimensional flow around its profile. In this work two theories are combined, the first is the axial momentum theory and the second is the blade element momentum theory (BEM). We consider an element of the blade, Fig. 3, subjected to aerodynamic forces, centrifugal inertia, and gravity load.

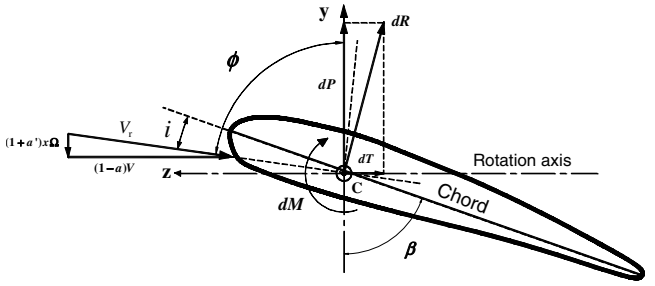

Fig. 3 Aerodynamic loads and speeds

The theory of the blade element allows us to express, according to the wind relative speed V_r, the aerodynamic loads at the aerodynamic center on an element C of the blade at width dx and in chord c located at a distance x from the rotation axis [3]:

$$\text{Thrust: } dP = \frac{1}{2}\rho_a C_y c V_{\mathbf{r}}^2 dx \tag{1}$$

$$\text{Trail: } dT = \frac{1}{2}\rho_a C_z c V_{\mathbf{r}}^2 dx \tag{2}$$

$$\text{Torque: } dM = \frac{1}{2}\rho_a C_m c^2 V_{\mathbf{r}}^2 dx \tag{3}$$

The force coefficients C_y, C_z, and the moment coefficient C_m characterize the capability of the profile to transform the energy of the wind in thrust, trail and torque forces. These coefficients depend mainly on the angle of attack ϕ of the blade as follows:

$$C_y = C_L \sin(\phi) - C_D \cos(\phi) \tag{4}$$

$$C_z = C_L \cos(\phi) + C_D \sin(\phi) \tag{5}$$

C_L and C_D are respectively the lift and drag coefficients. The experimental researches are carried out in order to know the evolution of these coefficients depending on the wind speed V, and the rotation of the blade Ω, as shown in [4], [5]. The coefficients of axial interference a and radial interference a' are within 0 and 1, characterize respectively the propeller aerodynamic efficiency and the airflow wake effect. These factors are expressed by, according to [2]:

$$a = \frac{1}{(4\sin^2\phi F)/(\sigma C_z)+1} \tag{6}$$

$$a' = \frac{1}{(4\sin\phi\cos\phi F)/(\sigma C_y)-1} \tag{7}$$

The equations (4), (5), (6) and (7) lead to find the expressions of lift and drag coefficients:

$$C_L = \frac{4F(a+a')\sin^2\phi\cos\phi}{\sigma(1-a)(1+a')} \tag{8}$$

$$C_D = \frac{4F(a\sin^2\phi - a'\cos^2\phi + aa')\sin\phi}{\sigma(1-a)(1+a')} \tag{9}$$

The local solidity ratio σ is defined as:

$$\sigma = \frac{cn}{2\pi x} \tag{10}$$

The coefficient of Prandtl F is defined as:

$$F = \frac{2}{\pi a x \cos(e^{-f})} \tag{11}$$

Where:

$$f = \frac{n(R-x)}{2x\sin\phi} \tag{12}$$

And R is the propeller radius, while ϕ is the angle of attack, calculated at a position of the blade, by:

$$\tan(\phi) = \frac{(1-a)V}{(1+a')x\Omega} \tag{13}$$

The centrifugal force dF_c applied to the blade element in rotation, is calculated by:

$$dF_c = \rho S x \Omega^2 dx \tag{14}$$

The load vector due to the weight of the blade element is expressed in the referential (O,x,y,z), related to the blade, by:

$$\boldsymbol{dP} = \rho g S(\sin(\Omega t)\boldsymbol{x} + cos(\Omega t)\boldsymbol{y})dx \tag{15}$$

4 Formulation of the Problem

It is proposed to determine the effect of weight on a wind turbine blade of 5 meters of length, using the finite elements method [6]. The blade-beam is divided into 12 elements of length *l* of different sections *S*, as shown in figure 4:

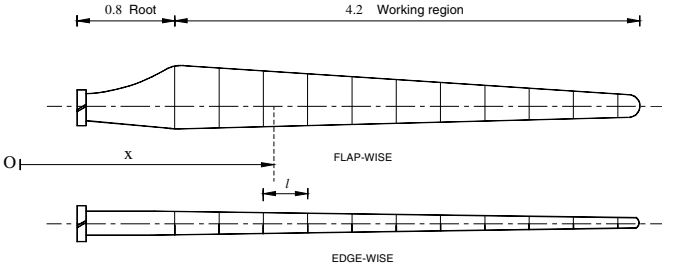

Fig. 4 Dividing of the blade in 12 beam elements

4.1 Mechanical Stiffness Matrix

The displacement vector $\boldsymbol{u}$ of any point *P* of the blade with coordinates (x,y,z) is expressed as a function of the displacement vector $\boldsymbol{U}$ relatively to the reference frame associated with the blade, as follows:

$$\boldsymbol{u} = \begin{bmatrix} 1 & 0 & 0 & 0 & z & -y \\ 0 & 1 & 0 & -z & 0 & 0 \\ 0 & 0 & 1 & y & 0 & 0 \end{bmatrix} \boldsymbol{U} \tag{16}$$

By linear interpolation, we compute the displacement vector $\boldsymbol{U}$ of a point *M* on the gravity line of the blade:

$$\boldsymbol{U} = \boldsymbol{N}\boldsymbol{q_e} \tag{17}$$

The vector elemental nodal displacements $\boldsymbol{q_e}$ containing all degrees of freedom at consecutive nodes i and j, is:

$$\boldsymbol{q_e} = (u_i,\ v_i,\ w_i,\ \alpha_i,\ \beta_i,\ \gamma_i,\ u_j,\ v_j,\ w_j,\ \alpha_j,\ \beta_j,\ \gamma_j)^T \tag{18}$$

The matrix of interpolation $\boldsymbol{N}$ is composed by the functions of interpolation $N1$ and $N2$, they are linearly centered:

$$N1 = (1-s)/2 \text{ and } N2 = (1+s)/2 \tag{19}$$

Where, s is a variable ranging between -1 and 1. The vector of linear deformations of the beam $\boldsymbol{\varepsilon_l}$ is expressed by:

$$\boldsymbol{\varepsilon_l} = \boldsymbol{B^e q_e} \tag{20}$$

The matrix of elementary deformation $\boldsymbol{B^e}$ considering the transverse shear is:

$$\boldsymbol{B^e} = \begin{bmatrix} -1 & 0 & 0 & 0 & 0 & 0 & 1 & 0 & 0 & 0 & 0 & 0 \\ 0 & -1 & 0 & 0 & 0 & -lN1 & 0 & 1 & 0 & 0 & 0 & lN2 \\ 0 & 0 & -1 & 0 & lN1 & 0 & 0 & 0 & 1 & 0 & lN2 & 0 \\ 0 & 0 & 0 & -1 & 0 & 0 & 0 & 0 & 0 & 1 & 0 & 0 \\ 0 & 0 & 0 & 0 & -1 & 0 & 0 & 0 & 0 & 0 & 1 & 0 \\ 0 & 0 & 0 & 0 & 0 & -1 & 0 & 0 & 0 & 0 & 0 & 1 \end{bmatrix} \tag{21}$$

We can determine the elemental stiffness matrix $\boldsymbol{K_e}$ by the following relation:

$$\boldsymbol{K_e} = \frac{l}{2}\int_{-1}^{1} {}^T\boldsymbol{B^e R B^e}\, ds \tag{22}$$

With $\boldsymbol{R}$ is the stiffness matrix of the material of the blade.

4.2 Geometrical Stiffness Matrix

The geometric stiffness matrix of the blade depends on the nodal displacements. It aims to express the assumption that the length of the beam remains constant after deformation, the matrix of nonlinear deformation $\boldsymbol{\varepsilon_{nl}}$ is:

$$\boldsymbol{\varepsilon_{nl}} = \frac{1}{2}\ {}^T\boldsymbol{grad(u)grad(u)} \tag{23}$$

After replacing the vector $\boldsymbol{u}$ by its expression according to equations (16), (17) et (18), we obtain three expressions of the nonlinear deformations $\varepsilon_{xx}(nl)$, $\gamma_{xy}(nl)$ and $\gamma_{xz}(nl)$ according the direction x as follows:

$$\varepsilon_{xx}(nl) = \frac{1}{2}\ {}^T\boldsymbol{q_e X q_e} \tag{24}$$

With:

$$\boldsymbol{X} = \frac{1}{l}\begin{bmatrix} 1 & 0 & 0 & 0 & 2z & -2y & 0 & 0 & 0 & 0 & -2z & 2y \\ 0 & 1 & 0 & 0 & 0 & 0 & 0 & -2 & 0 & 0 & 0 & 0 \\ 0 & 0 & 1 & 2y & 0 & 0 & 0 & 0 & -2 & 0 & 0 & 0 \\ 0 & -2z & 0 & (y^2+z^2) & 0 & 0 & 0 & 0 & -2y & -2(y^2+z^2) & 0 & 0 \\ 0 & 0 & 0 & 0 & z & 0 & 0 & 0 & 0 & 0 & -2z & 0 \\ 0 & 0 & 0 & 0 & -2yz & y & 0 & 0 & 0 & 0 & 0 & -2y \\ -2 & 0 & 0 & 0 & -2z & 2y & 1 & 0 & 0 & 0 & 2z & -2y \\ 0 & 0 & 0 & 2z & 0 & 0 & 0 & 1 & 0 & 0 & 0 & 0 \\ 0 & 0 & 0 & 0 & 0 & 0 & 0 & 0 & 1 & 2y & 0 & 0 \\ 0 & 2z & -2y & 0 & 0 & 0 & 0 & -2z & 0 & (y^2+z^2) & 0 & 0 \\ 0 & 0 & 0 & 0 & 0 & yz & 0 & 0 & 0 & 0 & z & -2yz \\ 0 & 0 & 0 & 0 & yz & 0 & 0 & 0 & 0 & 0 & 0 & y \end{bmatrix} \tag{25}$$

$$\gamma_{xy}(nl) = \frac{1}{2}\,{}^{T}\boldsymbol{q_e}\boldsymbol{Y}\boldsymbol{q_e} \tag{26}$$

With:

$$\boldsymbol{Y} = \frac{1}{l}\begin{bmatrix} 0 & 0 & 0 & 0 & 0 & N1 & 0 & 0 & 0 & 0 & 0 & N2 \\ 0 & 0 & 0 & 0 & 0 & 0 & 0 & 0 & 0 & 0 & 0 & 0 \\ 0 & 0 & 0 & 0 & 0 & 0 & 0 & 0 & 0 & 0 & 0 & 0 \\ 0 & 0 & -N1 & -yN1 & 0 & 0 & 0 & 0 & N1 & yN1 & 0 & 0 \\ 0 & 0 & 0 & 0 & 0 & zN1 & 0 & 0 & 0 & 0 & 0 & zN2 \\ 0 & 0 & 0 & 0 & 0 & -yN1 & 0 & 0 & 0 & 0 & 0 & -yN2 \\ -2 & 0 & 0 & 0 & 0 & -N1 & 0 & 0 & 0 & 0 & 0 & -N2 \\ 0 & 0 & 0 & 0 & 0 & 0 & 0 & 0 & 0 & 0 & 0 & 0 \\ 0 & 0 & 0 & 0 & 0 & 0 & 0 & 0 & 0 & 0 & 0 & 0 \\ 0 & 0 & -N2 & -yN2 & 0 & 0 & 0 & 0 & N2 & yN2 & 0 & 0 \\ 0 & 0 & 0 & 0 & 0 & -zN1 & 0 & 0 & 0 & 0 & 0 & -zN2 \\ 0 & 0 & 0 & 0 & 0 & yN1 & 0 & 0 & 0 & 0 & 0 & yN2 \end{bmatrix} \tag{27}$$

$$\gamma_{xz}(nl) = \frac{1}{2}\,{}^{T}\boldsymbol{q_e}\boldsymbol{Z}\boldsymbol{q_e} \tag{28}$$

With:

$$\boldsymbol{Z} = \frac{1}{l}\begin{bmatrix} 0 & 0 & 0 & 0 & -N2 & 0 & 0 & 0 & 0 & 0 & -N1 & 0 \\ 0 & 0 & 0 & 0 & 0 & 0 & 0 & 0 & 0 & 0 & 0 & 0 \\ 0 & 0 & 0 & 0 & 0 & 0 & 0 & 0 & 0 & 0 & 0 & 0 \\ 0 & N1 & 0 & -zN1 & 0 & 0 & 0 & -N1 & 0 & zN1 & 0 & 0 \\ 0 & 0 & 0 & 0 & -zN2 & 0 & 0 & 0 & 0 & 0 & -zN1 & 0 \\ 0 & 0 & 0 & 0 & yN2 & 0 & 0 & 0 & 0 & 0 & yN1 & 0 \\ -2 & 0 & 0 & 0 & N2 & 0 & 0 & 0 & 0 & 0 & N1 & 0 \\ 0 & 0 & 0 & 0 & 0 & 0 & 0 & 0 & 0 & 0 & 0 & 0 \\ 0 & 0 & 0 & 0 & 0 & 0 & 0 & 0 & 0 & 0 & 0 & 0 \\ 0 & N2 & 0 & -zN2 & 0 & 0 & 0 & -N2 & 0 & zN2 & 0 & 0 \\ 0 & 0 & 0 & 0 & zN2 & 0 & 0 & 0 & 0 & 0 & zN1 & 0 \\ 0 & 0 & 0 & 0 & -yN2 & 0 & 0 & 0 & 0 & 0 & -yN1 & 0 \end{bmatrix} \tag{29}$$

The linear density of the energy of the nonlinear deformation $W_{\mathrm{d}}(nl)$ is calculated by:

$$W_{\mathrm{d}}(nl) = \frac{1}{2}\int_S (\varepsilon_{xx}(nl)\sigma_{xx} + \gamma_{xy}(nl)\tau_{xy} + \gamma_{xz}(nl)\tau_{xz})dS \tag{30}$$

Assuming that the constraint due to the linear deformation is dominant [7], the equations (24), (26) and (26) give:

$$W_{\mathrm{d}}(nl) = \frac{1}{2}\,{}^{T}\boldsymbol{q_e}\left(\int_S (E\boldsymbol{X}\varepsilon_{xx} + G\boldsymbol{Y}\gamma_{xy} + G\boldsymbol{Z}\gamma_{xz})dS\right)\boldsymbol{q_e} \tag{31}$$

Then the geometric stiffness matrix $\boldsymbol{Kg_e}$ is deduced using equation (31):

$$W_d(nl) = \frac{1}{2}\,{}^{T}\boldsymbol{q_e}\boldsymbol{Kg_e}\boldsymbol{q_e} \tag{32}$$

Where:

$$\boldsymbol{Kg_e} = \boldsymbol{K1} + \boldsymbol{K2} + \boldsymbol{K3} \tag{33}$$

With:

$$\boldsymbol{K1} = E\int_S ((u_j - u_i) + z(\beta_j - \beta_i) + y(\gamma_j - \gamma_i))\boldsymbol{X}dS \tag{34}$$

$$\boldsymbol{K2} = G\int_S ((v_j - v_i) - z(\alpha_j - \alpha_i))\boldsymbol{Y}dS \tag{35}$$

$$\boldsymbol{K3} = G\int_S ((w_j - w_i) + y(\alpha_j - \alpha_i))\boldsymbol{Z}dS \tag{36}$$

This matrix ***K1***, ***K2*** and ***K3*** are function of the degrees of freedom of the blade-beam.

5 Equations of Motion

The study of the movement of an element of the blade relatively to the Galilean referential, to determine the linear expression of the kinetic energy of a finite element, gives:

$$T_e = \frac{1}{2}\rho\int_{xi}^{xj}(S(\dot{u}^2+\dot{v}^2+\dot{w}^2)+(\dot{\alpha}^2 Ix+\dot{\beta}^2 Iy+\dot{\gamma}^2 Iz-2Iyz\dot{\beta}\dot{\gamma})+(2\Omega(\dot{\beta}\alpha(Iy-Iz)-\dot{\alpha}\beta Ix)-2Iyz\Omega(2\alpha\dot{\gamma}+\alpha\Omega)))dx \tag{37}$$

The third term of the integral corresponds to the work of the Coriolis acceleration and identifies the elementary matrix of gyroscopic coupling C_e as follows:

$$\boldsymbol{C}_e = \rho l\Omega \begin{bmatrix} 0&0&0&0&0&0&0&0&0&0&0&0\\ 0&0&0&0&0&0&0&0&0&0&0&0\\ 0&0&0&0&0&0&0&0&0&0&0&0\\ 0&0&0&0&-I/3&2Iyz/3&0&0&0&0&-I/6&Iyz/3\\ 0&0&0&I/3&0&0&0&0&0&I/6&0&0\\ 0&0&0&-2Iyz/3&0&0&0&0&0&-Iyz/3&0&0\\ 0&0&0&0&0&0&0&0&0&0&0&0\\ 0&0&0&0&0&0&0&0&0&0&0&0\\ 0&0&0&0&0&0&0&0&0&0&0&0\\ 0&0&0&0&-I/6&Iyz/3&0&0&0&0&-I/3&2Iyz/3\\ 0&0&0&I/6&0&0&0&0&0&I/3&0&0\\ 0&0&0&-Iyz/3&0&0&0&0&0&-2Iyz/3&0&0 \end{bmatrix} \tag{38}$$

Where *Ix*, *Iy*, *Iz*, and *Iyz* are the quadratic moments of section of the blade in the referencial (x,y,z), and:

$$I = Ix + Iy - Iz \tag{39}$$

The potential energy of the total deformation U_e of a finite element is calculated by:

$$U_e = \frac{1}{2}{}^T\boldsymbol{q}_e(\boldsymbol{K}_e + \boldsymbol{Kg}_e)\boldsymbol{q}_e \tag{40}$$

By applying the principle of Hamilton between two date t_1 and t_2 for the system:

$$\int_{t_1}^{t_2}(\delta T_e - \delta U_e + \delta W_e)dt = 0 \tag{41}$$

With W_e is the work of the external loads. The elementary equations of motion are then:

$$\boldsymbol{M}_e\ddot{\boldsymbol{q}}_e + \boldsymbol{C}_e\dot{\boldsymbol{q}}_e + (\boldsymbol{K}_e + \boldsymbol{Kg}_e)\boldsymbol{q}_e = \boldsymbol{F}_e \tag{42}$$

In the following we realize the assembly of the stiffness matrices $\boldsymbol{K}$, the mass matrix $\boldsymbol{M}$ and the gyroscopic coupling matrix $\boldsymbol{C}$. For the numerical solution, the geometric stiffness matrix $\boldsymbol{Kg}$ must be built at each iteration, and the boundary conditions for the clamped root of the blade must be introduced. The global equations of motion are then:

$$\boldsymbol{M}\,\ddot{\boldsymbol{q}} + \boldsymbol{C}\,\dot{\boldsymbol{q}} + (\boldsymbol{K} + \boldsymbol{Kg})\boldsymbol{q} = \boldsymbol{F} \tag{43}$$

6 Numerical Application

6.1 Problem Data

It aims to simulate the dynamic response of the blade under the action of its own weight. The practical maximum power coefficient C_P of the propeller, Fig. 1, is 41.2% achieved at a wind speed V_0= 10 m/s [1]. The coefficient of axial interference a is equal 0.14 corresponding to the power coefficient mentioned previously. The value of the angular speed ω of wake of the air in the plane of rotation is the average of those located in front and behind it, so the coefficient of radial interference a' is 0.5. At the conditions of ambient temperature and pressure, the density of air is 1,25 kg/m3 and the cinematic viscosity ν is 22 cSt. The aerodynamic coefficients C_L and C_D are calculated using equations (8) and (9), the moment coefficient C_m is almost constant throughout the range of angle of attack. When starting, the blade rotation speed increases gradually to a uniform speed of 6 rad/s. The total weight of the blade is 115.73 daN, which is decomposable by projection, relatively to Ox and Oy axes, into two alternating components, with quadratic phase shift, Fig. 5. These excitations are phased of 2π/3 for two consecutive blades.

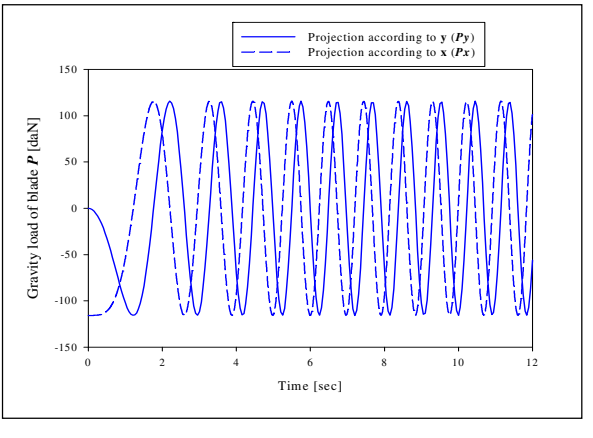

Fig. 5 Variation of the gravity load of the blade

6.2 Static Study

With the help of MATLAB, we used the Newton method [8] to solve the nonlinear equation of equilibrium. Figs. 6 and 7 illustrate the deformed configuration under the action of centrifugal and aerodynamic forces, without considering the action of gravity. The maximum deflection of the blade along the axis of rotation is of 2 cm, which verifies the non collision of the blades with the vertical mast of the wind turbine.

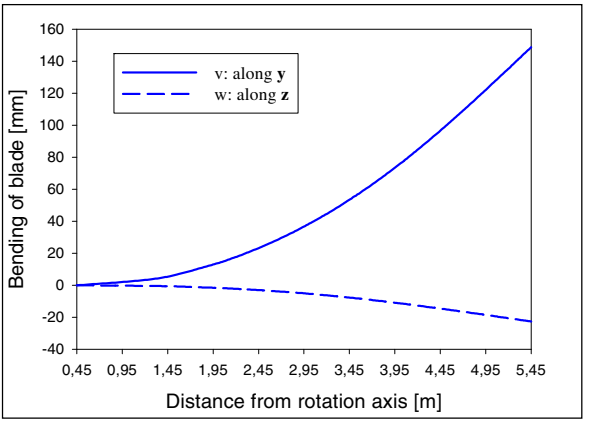

Fig. 6 Aerodynamic effect

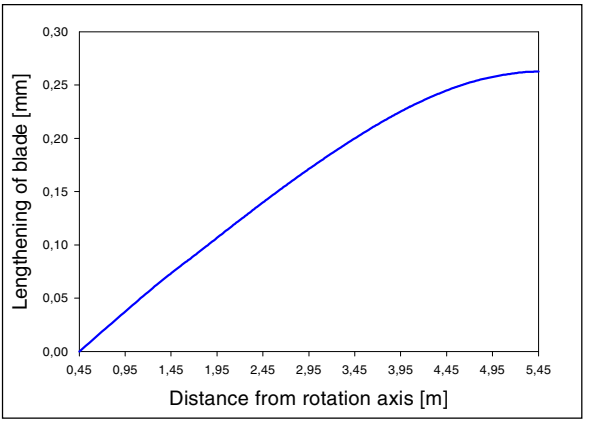

Fig. 7 Centrifugal effect

6.3 Dynamic Study

Using the explicit Newmark method we were able to demonstrate the effect of the gyroscopic coupling under the weight excitation. The structural damping factor is taken 2%. The result is a torsion beating induced by gyroscopic effect, it is transitory, Fig. 8a, then permanent, Fig. 8b. The amplitude of the torsion beating is weak but it persists. The continual action of the weight of the blade causes an angular vibration around the virtual static equilibrium position. This poses the problem of fatigue, in particular at its root where the equivalent constraint due to tension, bending and torsion, is maximal.

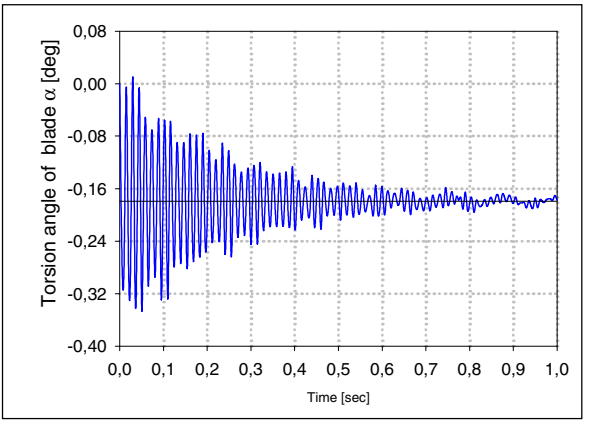

Fig. 8a Forced regime-Transient phase

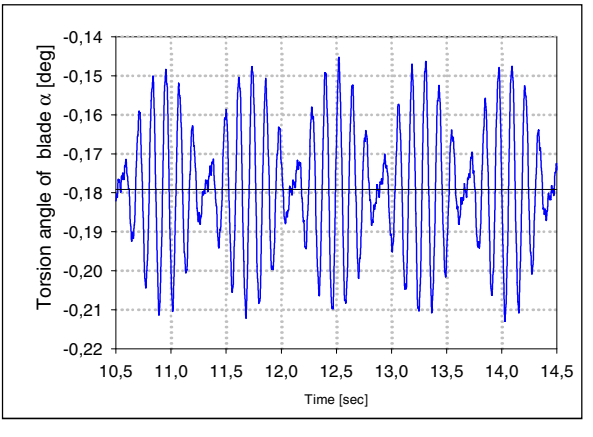

Fig. 8b Forced regime-Permanent phase

The dynamic study of the blade in the case of an abrupt cessation of the wind, the speed remains unchanged (6 rad/s), corresponds to the free regime. We simulated the dynamic response of the blade for this case, by considering the initial conditions in displacement, those of the deformed configuration shown in Figs. 6 and 7. The result was a torsion beating which disappears with time, Fig. 9a and 9b. The spectrum obtained for the free regime, Fig. 10, using the Fast Fourier Transform (FFT), shows the beating is mainly the result of the interference of two waves with close frequencies. The spectrum of the forced regime-transitory phase was also obtained and superposed on the free regime spectrum, to conclude that for both cases the blade has the same behavior. The beating first frequencies are f1=9 Hz, f2=10 Hz and f3= 68 Hz, which depend on the blade speed [9].

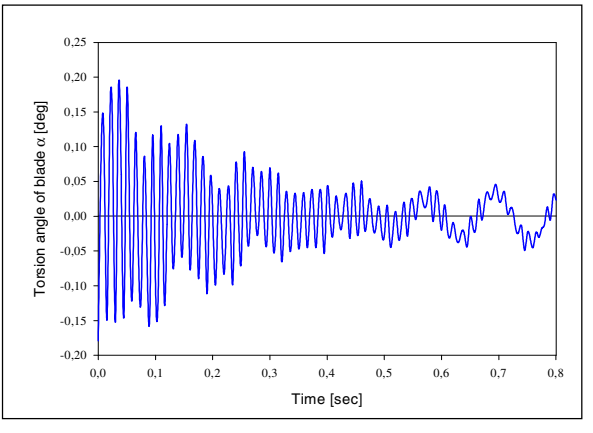

Fig. 9a Free regime-Transitory phase

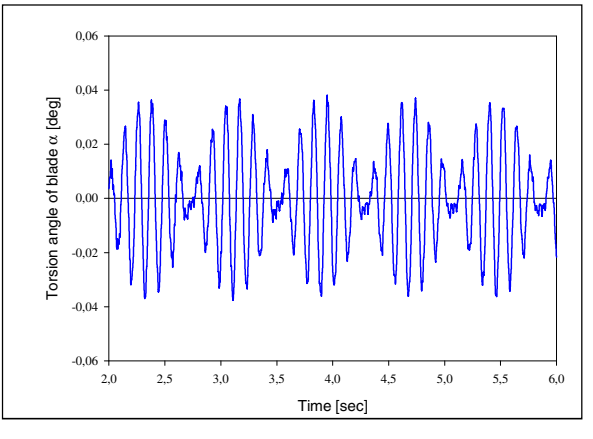

Fig. 9b Free regime-Permanent phase

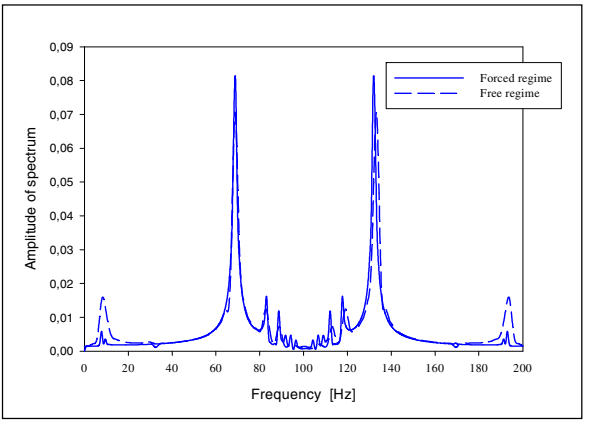

Fig. 10 FFT of torsion beating in transitory phase

7 Conclusion

The gyroscopic effect on the blade weight induces an alternating force applied on the blade to generate a flapping torsion angle of low amplitude but permanent, despite the absence of cyclic aerodynamic torques. We conclude that a wind turbine blade in rotation is subjected to a continuous vibration, which disrupts the airflow around the blade profile and consequently causes a loss in the aerodynamic useful energy transformed to acoustic energy, to induce sound pollution. From this point of view the structural properties of the blade do not only have an impact on its mechanical strength but also on the nature of the airflow through the propeller. In order to study precisely this phenomenon, which is specific to long blades, we took into account the nonlinear deformation. Even if the amplitude of the beating is low, its continuous nature leads to the need to consider closely the problem of fatigue of the blade.

References

[1] Habali, S.M., Saleh, I.A.: Local design testing and manufacturing of small mixed airfoil wind turbine blades of glass fiber reinforced plastics, Part I: Design of the blade and root. Energy Conversion & Management 41, 249–280 (2000)

[2] Traugott, J.P., Patil, M.J., Holzapfel, F.: Non-linear modeling of integrally actuated beams. Aerospace Science and Technology 10, 509–518 (2006)

[3] Younsi, R., El Batanony, I., Tritsch, J.B., Naji, H., Landjerit, B.: Dynamic study of a wind turbine blade with horizontal axis. Eur. J. Mech. A/Solids 20, 241–252 (2001)

[4] Mej, J.M., Chejne, F., Smith, R., Rodriguez, L.F., Fernandez, O., Dyner, I.: Simulation of wind energy output at Guajira, Colombia. Renewable Energy 31, 383–399 (2006)

[5] Hoogedoorna, E., Jacobs, G.B., Beyene, A.: Aero-elastic behavior of a flexible blade for wind turbine application: A 2D computational study. Energy 35, 778–785 (2010)
[6] Craveur, J.C.: Modelling of Structures by Finite Elements. Dunod (1997)
[7] Samper, S.: Dynamic behavior of composite beams preloaded: Modelling by finite elements, PhD Thesis, University Paul Sabatier of Toulouse (1994)
[8] Ladevèze, P.: Non-linear mechanics of structures, pp. 62–66. Hermes (1996)
[9] Park, J.H., Park, H.Y., Jeong, S.Y., Lee, S., Shin, Y.H., Park, J.P.: Linear vibration analysis of rotating wind turbine blade. Current Applied Physics 10, 332–334 (2010)

Eccentricity Incidence on the Nonlinear Behavior of a Helical Gear

Hentati Taissir, Abbes Mohamed Slim, Fakher Chaari,
Tahar Fakhfakh, and Mohamed Haddar

Dynamics of Mechanical Systems Research Unit,
National School of Engineering of Sfax, BP1173, 3038, Sfax - Tunisia
taissirhentati@yahoo.fr, Slim.Abbes@enis.rnu.tn

Abstract. Ball bearing is considered as source of acoustic level increasing in rotating systems. In this paper, we propose a numerical model to simulate the dynamic behavior of a one stage helical gear system in presence of different sources of non linearity such ball bearing clearance, Hertzian contact force and action of balls on bearing races. The implicit Newmark algorithm coupled with Newton Raphson iterative method is used to solve the non linear differential equation iteratively, in order to analyze the influence of a pinion eccentricity defect on the dynamic behavior of one stage helical gear transmission system under transient and stationary regimes.

Keywords: Ball bearings, nonlinear dynamic behavior, eccentricity defect, helical gear.

1 Introduction

There is no doubt about the efficiency of the gear systems to ensure transmission of high torques with minimum of power loss. But on the other hand gear transmissions remain certainly the main source of noise and vibration of several industrial applications due to the conditions of contact between gear pair teeth as well as the variation of the mesh stiffness caused by the variation of teeth number in contact. Abbes et al. 2008 simulated the vibration and the noise radiation of a single-stage gearbox associated with the changing stiffness of the meshing teeth and the effect of the fluid inside the gearbox housing is considered. Numerical simulations have been carried out to investigate the effects of the gear mesh stiffness fluctuation on the dynamic response of the coupled system. They showed that the vibration responses are significantly modified by considering the cavity fluid effect.

Walha et al. (2009) analyzed the vibrations of a two-stage gear system with mesh stiffness fluctuation, bearing flexibility and backlash. The study shows that the dynamic behavior of such structure is characterized by its complexity which comes mainly from the coupling between the periodic meshes stiffness fluctuations with the presence of backlashes between teeth.

The gear transmission failure modeling was investigated by many researches such as Choy et al. (1996), Chaari et al. (2009) and Walha et al. (2005) that focused on the tooth stiffness reduction due to damage. The loading conditions have much influence on gear transmission systems. In fact they affect more defected transmissions than healthy ones as shown by Bartelmus et al. (2010). The transient regime affects significantly the dynamic behavior of gear transmission systems and it cannot be neglected as mentioned by Sika and Velex (2008), Sika (2008) and Khabou et al. (2011).

Ball bearings are mainly used to reduce rotational friction and support axial and radial loads but at the same time they deeply affect the acoustic level of gear transmission system by their presence. Few studies were interested in the dynamic behavior of the helical gear taking account ball bearing influence. The gear and bearing interactions in the presence of faults is always neglected and the vibratory responses are usually computed by considering only the effect gear transmission error. In this context, Walha et al. (2011) have formulated a model taking into account the nonlinear dynamic behavior of an automotive clutch coupled with a helical two stage gear system. He simulated three types of nonlinearity: dry friction path, double stage stiffness and spline clearance. The effect of those defects on the nonlinear dynamic behavior of the system is investigated. In this study, bearings are considered rigid.

Abbes et al. (2011) have performed a theoretical investigation for studying the dynamic behavior of helical gears supported by defect element bearings in steady state condition monitoring. A global model predicting the dynamical behavior of a reducer supported by angular ball bearings, based on the finite element approach is developed. The developed model was derived to observe the effect of the internal excitation sources such as the gear mesh stiffness fluctuation and the ball bearing waviness on the vibration characteristics of the machine elements.

Khabou et al. (2012) have proposed a theoretical model to simulate the dynamic behavior of a spur gear taking into account both the time varying gearmesh stiffness considering nonlinear contact model and the nonlinear forces exerted by defected ball bearings supporting the transmission under transient regime working conditions. The aim of this study was to show the impact of the worn bearings on the dynamic response of the transmission.

The main idea of this work is to develop a one stage helical gear model taking into account the presence of ball bearing, eccentricity on the helical gear nonlinear Hertz contact between teeth. . The equation of motion is written and solved using the Newmark method coupled with Newthon Raphson iterative method. The dynamic response will be analyzed in order to show the impact of eccentricity on the dynamic behaviour of the transmission.

2 Single Stage Helical Gear Transmission Modeling

The study consists on analyzing structural vibrations generated by single stage helical gear transmission supported by two identical ball bearings. Bearings outer races are fixed in the rigid support (logging) while the inner races are rigidly assembled to the rotating shafts (Fig. 1).

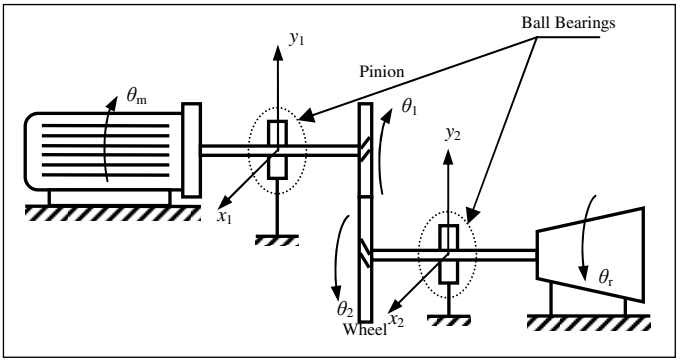

Fig. 1 Schematic of the studied single stage gear transmission (Khabou et al. 2012)

The equation of motion describing the dynamics of the system, which includes all system components, can be expressed in a general form as follows:

$$M\ddot{q} + C\dot{q} + \left[K_p + Kg(t)\right] q + Fnlb = Fext(t) + F_{ecc}(t) \tag{1}$$

where $q = \{x_1, y_1, z_1, \varphi_1, \psi_1, \theta_m, \theta_1, x_2, y_2, z_2, \varphi_2, \psi_2, \theta_2, \theta_r\}^T$ is the vector of the degrees of freedom of the system, M represents the mass matrix.

$$M = diag\left(m_1 \quad m_1 \quad m_1 \quad J_{1x} \quad J_{1y} \quad J_m \quad J_1 \quad m_2 \quad m_2 \quad m_2 \quad J_{2x} \quad J_{2y} \quad J_2 \quad J_r\right) \tag{2}$$

C is the proportional damping matrix given by Khabou et al. (2011):

$$C = a\,M + b\,K_p \qquad a = 0.05 \qquad b = 10^{-5} \tag{3}$$

K_p is the shafts torsional stiffness matrix given by the following matrix

$$K_p = \begin{bmatrix} 0 & & & & & & & & & & & & \\ & \ddots & & & & & & & & & & & \\ & & k_{\theta 1} & -k_{\theta 1} & & & & & & & & & \\ & & -k_{\theta 1} & k_{\theta 1} & & & & & & & & & \\ & & & & 0 & & & & & & & & \\ & & & & & \ddots & & & & & & & \\ & & & & & & 0 & & & & & & \\ & & & & & & & k_{\theta 2} & -k_{\theta 2} & & & & \\ & & & & & & & -k_{\theta 2} & k_{\theta 2} & & & & \end{bmatrix} \tag{4}$$

where $k_{\theta i}$ are the shafts torsional stiffness.

$Fext(t)$ is the external applied torques vector. It can be written as:

$$Fext(t) = \left\{0\ 0\ 0\ 0\ 0\ C_m(t)\ 0\ 0\ 0\ 0\ 0\ 0\ 0\ -C_r(t)\right\}^T \tag{5}$$

where $C_r(t)$ is the loading torque and $C_m(t)$ is the driving torque (time varying during start-up of the transmission).

$Kg(t)$, $Fnlb$ and F_{ecc} represent respectively the gear stiffness matrix, the nonlinear force exerted by rolling bearings and finally the force exerted by the eccentricity defect on the transmission. The expressions of $Kg(t)$, $Fnlb$ and F_{ecc} will be formulated in the following sections.

2.1 Determination of the Gear Mesh Stiffness Matrix

The gear meshing process is modelled with a time-varying stiffness matrix (Abbes et al. (2008, 2005)):

$$Kg(t) = k(t) \cdot G \tag{6}$$

where $k(t)$ is the periodic mesh stiffness obtained through measurement or calculation. For helical gears, trapezoidal waves are often used to approximate the mesh stiffness alternating between n and $n+1$ pairs of teeth in contact. The geometric characteristics matrix G is derived from of the gear pair characteristics:

$$G = \langle X \rangle^t \cdot \langle X \rangle \tag{7}$$

where:

$$\langle X \rangle = \cos\beta [\sin\alpha \quad \cos\alpha \quad \tan\beta \quad 0 \quad 0 \quad r_{b1} \quad 0 \quad -\sin\alpha \quad -\cos\alpha \quad -\tan\beta \quad 0 \quad 0 \quad 0 \quad r_{b2}] \tag{8}$$

r_{b2} and r_{b1} denotes the base circle radii of gear and pinion, α is the pressure angle and β is the helix angle.

2.2 Determination of the Non-linear Bearing Load

The forces exerted by all the rolling elements on the inner races are given by:

$$Fnlb = \sum_{j=1}^{N_b} -K \left\{ \Delta_{1_j}^{1,5} \cos\psi_{1_j} \cos\alpha_{1_j} \quad \Delta_{1_j}^{1,5} \sin\psi_{1_j} \cos\alpha_{1_j} \quad \Delta_{1_j}^{1,5} \sin\alpha_{1_j} \quad 0 \quad 0 \quad 0 \quad 0 \right. \tag{9}$$
$$\left. \Delta_{2_j}^{1,5} \cos\psi_{2_j} \cos\alpha_{2_j} \quad \Delta_{2_j}^{1,5} \sin\psi_{2_j} \cos\alpha_{2_j} \quad \Delta_{2_j}^{1,5} \sin\alpha_{2_j} \quad 0 \quad 0 \quad 0 \quad 0 \right\}^t$$

where K is the Hertz contact constant, N_b is the ball number of both bearings, ψ_{BBNB_j} is the ball angular position of the $BBNB$ ball bearing ($BBNB$ = 1: ball bearing supporting input shaft or $BBNB$ =2: ball bearing supporting output shaft), and Δ_{BBNB_j} represents the elastic deflection of the j^{th} rolling element:

$$\Delta_{BBNB_j} = \sqrt{\Delta_{BBNB_{rj}}^2 + \Delta_{BBNB_{zj}}^2} - d_{BBNB_0} - \gamma_{BBNB} \tag{10}$$

A negative elastic deformation means that no contact occurs between ball and the two races, in this case the elastic deformation is considered as null. d_{BBNB_0} is the unloaded relative distance between the inner and the outer raceway groove

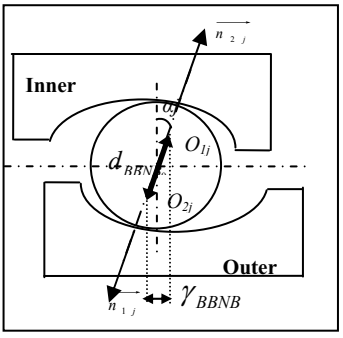

Fig. 2 Charged ball in the bearing

curvature centers O_{1j} and O_{2j}. The internal clearance γ_{BBNB} defined the gap between inner or outer race with the ball. $\Delta_{BBNB_{rj}}$ and $\Delta_{BBNB_{zj}}$ are the radial and axial elastic deformations corresponding the *BBNB* ball bearing:

$$\Delta_{BBNB_{zj}} = x_{1,2}\cos\psi_j + y_{1,2}\sin\psi_j + d_{1,2_0}\cos\alpha_0 \ , \qquad \Delta_{BBNB_{rj}} = z_{1,2} + d_{1,2_0}\sin\alpha_0 \tag{11}$$

2.3 Determination of the Eccentricity Load

In presence of the eccentricity defect, an additional load is exerted on the structure. The eccentricity load is given by (Walha et al. 2011):

$$F_{ecc}(t) = F_{ecc1}(t) + F_{ecc2}(t) \tag{12}$$

where $F_{ecc1}(t)$ and $F_{ecc2}(t)$are forces due respectively to the additional kinetic energy and the additional strain energy:

$$\begin{cases} F_{ecc\,1}(t) = -m_1 \cdot e \cdot \Omega^2 [0 \quad 0 \quad 0 \quad \cos(\Omega t - \lambda) \quad \sin(\Omega t - \lambda) \quad 0 \quad .... \quad 0]^T \\ F_{ecc\,2}(t) = e \cdot k(t) \cos\beta [\sin\alpha \quad \cos\alpha \quad \tan\beta \quad 0 \quad 0 \quad r_{b1} \quad 0 \\ \qquad\qquad\qquad \sin\alpha \quad -\cos\alpha \quad -\tan\beta \quad 0 \quad 0 \quad 0 \quad r_{b2}]^T \end{cases} \tag{13}$$

where e, Ω and λ are respectively the eccentricity defect amplitude, the angular speed of the gear and the initial phase of the eccentricity defect.

3 Numerical Results

The equation of motion is solved to obtain the dynamic response of the gear-bearing system. The Newmark method coupled with the iterative Newton Raphson

method, which resolve the system equilibrium at each step, are used to compute the system time responses. The main characteristics of the gear transmission and ball bearings are given in table 1.

Table 1 Helical gear and bearing parameters (Khabou et al (2012))

Gear parameters	
Teeth number (pinion, wheel)	$Z_1 = 20, Z_2 = 30$
Helix angle, Pressure angle (deg)	$\beta = \alpha = 20°$
Mass (pinion, wheel) (Kg), Inertia moment (pinion, wheel, Motor, receiver) (Kgm^2)	$m_1 = 0.46, m_2 = 0.588$ $J_1 = J_m = 10^{-4}, J_2 = J_r = 3\ 10^{-4}$
Base circle (pinion, wheel) (mm)	$r_{b1} = 18.8, r_{b2} = 28.8$
Ball bearing parameters	
Ball number , Hertz constant, Contact angle (deg)	$Nb = 8, K = 6.27\ 10^{12}, \quad \alpha_0 = 0$
Inner race, Ball diameter (mm)	$D_i = 18.738, d = 4.762$

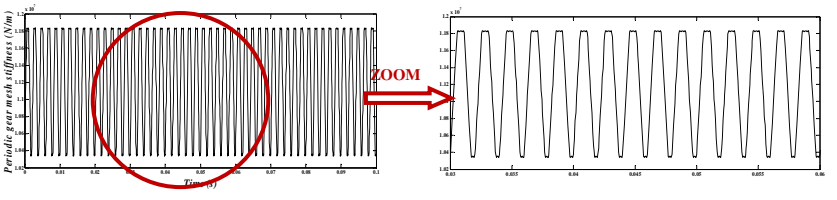

Fig. 3 Periodic gear mesh stiffness evolution with time

The displacements at x direction of the input and output shafts and their spectra are shown in Fig 4. We notice the presence of the meshing frequency F_{eng} = 460 Hz and its harmonics, this fact is induced by the time varying mesh stiffness escitation at this frequency (Fig. 3). We note also the presence of rolling parts passage frequencies F_{pb1} or F_{pb2} with their harmonics which occur at 67.5 Hz for the input shaft and 45 Hz for the output shaft. A modulation between meshing frequency and ball passage frequency is noted.

Figure 5 present the spectra of the transmission error for a defected (eccentricity $e = 10^{-3}$ m) and healthy pinion. We note, in addition of the meshing frequency and ball passage frequencies, the presence of eccentricity defect frequency, that occurs at rotational frequency of the input shaft F_{r1} = 25 Hz. We note also a modulation between meshing frequency and eccentricity defect frequency.

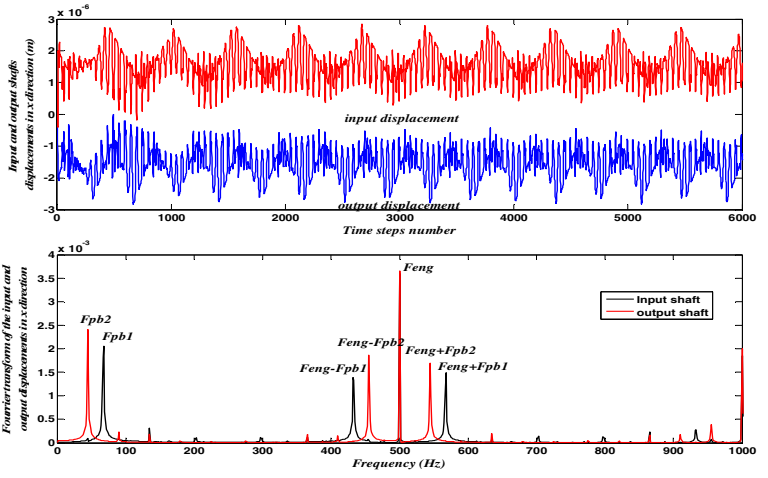

Fig. 4 Input and output x displacements and their spectra

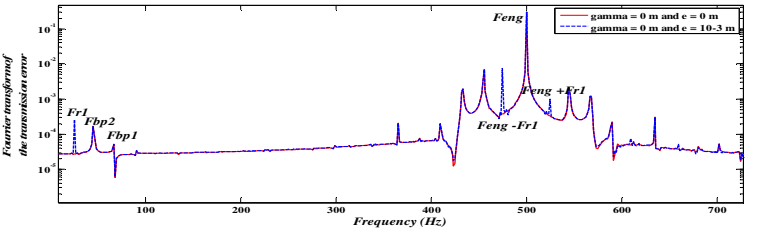

Fig. 5 Fourier transform of the transmission error

4 Conclusion

In this paper a helical gear transmission is modeled including bearing and eccentricity defect. For healthy pinion, dynamic responses are dominated by mesh frequency and harmonics; we note also the presence of ball passage frequency and harmonics and a modulation between mesh frequency and ball passage frequency. When we introduce eccentricity defect on the pinion we note the presence of the rotational input shaft frequency. A modulation between meshing frequency and input rotational frequency is also observed.

References

Abbes, M.S., Hentati, T., Maatar, M., Fakhfakh, T., Haddar, M.: Dynamic analysis of helical gears supported by rolling elements bearings. Journal of Theoretical and Applied Mechanics 41, 33–50 (2011)

Bartelmus, W., Chaari, F., Zimroz, R., Haddar, M.: Modelling of gearbox dynamics under time-varying nonstationary load for distributed fault detection and diagnosis. Eur. J. Mech. A/Sol. 29, 637–646 (2010)

Bouchaala, N., Chaari, F., Khabou, M.T., Fakhfakh, T., Haddar, M.: Influence of the non-linear Hertzian stiffness on the dynamics of a spur gear system under transient regime and tooth defects. Int. J. Vehicle Noise and Vibration 7, 149–177 (2011)

Chaari, F., Baccar, W., Haddar, M.: Effect of spalling or tooth breakage on gearmesh stiffness and dynamic response of a one-stage spur gear transmission. Eur. J. Mech. A/Sol. 27, 691–705 (2008)

Chaari, F., Fakhfakh, T., Haddar, M.: Analytical modelling of spur gear tooth crack and influence on gearmesh stiffness. Eur. J. Mech. A/Sol. 28, 461–468 (2009)

Choy, F.K., Polyshuk, V., Zakarajsek, J.J., Handscuh, R.F., Townsend, D.P.: Analysis of the effects of surface pitting and wear on the vibration of gear transmission system. Trib. Int. 29, 77–83 (1996)

Faik, S., Witteman, H.: Modelling of impact dynamics: a literature survey. In: International ADAMS User Conference, Canada (2000)

Hentati, T., Maatar, M., Dammak, F., Fakhfakh, T., Haddar, M.: Quasi static analysis of a ball bearing having geometrical imperfection (waviness). International Journal of Engineering Simulation 9, 22–29 (2008)

Jang, G., Jeang, S.W.: Nonlinear Excitation Model of Ball Bearing Waviness in a Rigid Rotor Supported by Two or More Ball Bearings Considering Five Degrees of Freedom. Trans. of ASME, Journal of Tribology 124, 82–90 (2002)

Jang, G., Jeang, S.W.: Vibration Analysis of a Rotating System due to the Effect of Ball bearing Waviness. Journal of Sound and Vibration 269, 709–726 (2004)

Kahraman, A., Singh, R.: Non-linear dynamics of a spur gear. J. Sou. Vib. 142, 49–75 (1990)

Khabou, M.T., Bouchaala, N., Chaari, F., Fakhfakh, T., Haddar, M.: Study of a spur gear dynamic behavior in transient regime. Mechanical Systems and Signal Processing 25, 3089–3101 (2011)

Khabou, M.T., Hentati, T., Abbes, M.S., Chaari, F., Haddar, M.: Nonlinear modeling and simulation of a spur gear with defected bearings (in press, 2012)

Lim, T.C., Singh, R.: Vibration Transmission through Rolling Element Bearings. Part I: Bearing Stiffness Formulation. Journal of Sound and Vibration 139, 179–199 (1990)

Sika, G., Velex, P.: Instability analysis in oscillators with velocity-modulated time-varying stiffness applications to gears submitted to engine speed fluctuations. J. Sou. Vib. 318, 166–175 (2008)

Sika, G.: Dynamique des transmissions en régime transitoire. PhD, INSA Lyon. France (2008)

Velex, P.: Contribution à l'analyse du comportement dynamique de réducteurs à engrenages à axes parallèles. PhD, INSA Lyon. France (1988)

Walha, L., Louati, J., Fakhfakh, T., Haddar, M.: Dynamic response of two stages gear system damaged by teeth defects. Mach. Dyn. Prob. 29, 107–124 (2005)

Walha, L., Driss, Y., Khabou, M.T., Fakhfakh, T., Haddar, M.: Effect of eccentricity on the nonlinear dynamic behavior of the mechanism clutch-helical two stage gear. Mechanism and Theory Machine 46, 986–997 (2011)

A Maintenance Alarm for Alternators Based on Eigensolutions

Antoine Kuczkowiak[1,2], Scott Cogan[1], Morvan Ouisse[1], Emmanuel Foltête[1], and Mathieu Corus[2]

[1] FEMTO-ST Institute - Applied Mechanics Department - 24, rue de l'Épitaphe, 25000 Besançon, France
[2] Électricité de France R&D - Department of Mechanic and Acoustic Analysis - 1, avenue du Général de Gaulle, 92141 Clamart, France
antoine.kuczkowiak@femto-st.fr

Abstract. The complex structural dynamic behaviour of turbo-alternators and their sub-assemblies must be well understood in order to insure their reliable and safe operation. In practice, important variations in response behaviours are observed in a population of otherwise nominally identical installations due to numerous and significant sources of variability: construction differences, manufacturing and assembly tolerances, variable thermal and nonlinear effects, and so on. These physical variations can sometimes lead to unexpectedly high response levels in the stator and a decision indicator is sought to signal the need for special maintenance procedures. Ideally, measurements in operation would be performed to obtain the necessary information but, for technical reasons, this is not currently possible. Meanwhile, the machines are generally disassembled for standard maintenance every five years. In this article, a maintenance alarm is formulated based on modal tests performed on the stator with the rotor removed. The objective is to usefully bound the stator response in operation based on the identified eigensolutions obtained on the stator alone. However, it is known that thermal and nonlinear mechanical effects of the functioning alternator modify the associated eigenparameters. Since these effects are not well known, an info-gap robustness analysis is performed to investigate the impact of this lack of knowledge on the response levels of interest. A stator assembly must be able to tolerate reasonable levels of uncertainty without exceeding a critical response level or it will require maintenance and repair. The proposed methodology is illustrated on a simplified numerical model of a stator.

1 Introduction

The complex structural dynamic behaviour of turbo-alternators and their sub-assemblies (Figure 1) must be well understood in order to insure their reliable and safe operation. In practice, important variations in response behaviours are observed in a population of otherwise nominally identical installations due to numerous and significant sources of variability: construction differences, manufacturing and assembly tolerances, variable thermal and nonlinear effects, and so on. Indeed,

the stator itself is a complex assembly of non-homogeneous prestressed parts composing the magnetic circuit with residual electrical loads and non negligible thermo-mechanical effects (see Figure 2). As a result, it proves to be extremely difficult to construct a reliable physics-based model of a stator. Meanwhile, these physical variations sometimes lead to unexpectedly high response levels in the stator which can cause premature aging. For this reason, a decision indicator is sought to signal the need for special maintenance procedures. Given the low credibility of numerical simulations, an indicator primarily based on experimental data is required. While measurements in operation would be ideal, limited space and high electromagnetic loads currently render this approach impracticable. Alternators are generally disassembled for routine maintenance every five years and modal testing using impact hammers is often performed at this time. The maintenance alarm proposed in this article will be formulated on the basis of these identified eigensolutions.

Although developments in the field of structural health monitoring address certain aspects of this class of problem (see for example the literature reviews Farrar *et al* [2], Sohn *et al* [5], and Worden *et al* [6]), relatively little attention has been given to the difficulties of extrapolating diagnostics from one structural configuration to another. While this is indeed an ambitious goal in generaI, in the present case the relevant dynamic behaviours of the stator are assumed to be relatively stable.

The proposed maintenance alarm is based on a predicted useful bound for the dynamic stator response in operation. This response will synthesized from the eigensolutions identified on the stator of a dismantled alternator under a rotating electromagnetic load. The question is how to account for the thermal and nonlinear mechanical effects induced by the functioning alternator? Since these effects are not well known, an info-gap robustness analysis is performed to investigate the impact of this lack of knowledge on the response levels of interest. Indeed, it is assumed that a stator assembly must be able to tolerate reasonable levels of uncertainty without exceeding a critical response level or it will require maintenance and repair. In the present work, the impact of lack of knowledge in the identified eigenfrequencies, eigenvector norms, and modal damping will be investigated. The proposed methodology is illustrated on a simplified numerical model of a stator which is used to simulate the experimental measurements.

Fig. 1 Alternator in power plant

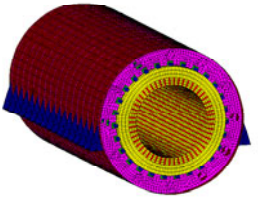

Fig. 2 Finite Element Model of a Simplified Stator

2 Formulation of a Maintenance Alarm

The approach adopted here is to synthesize the response of the stator assembly based on the eigensolutions (eigenfrequencies, eigenvectors, and modal damping factors) identified with the rotor dismantled. A rotating dynamic load is introduced to simulate the interactions with the rotor in operation. The impact of lack of knowledge in the eigenparameters is then investigated using an info-gap robustness analysis.

The info-gap methodology is useful for the analysis, planning, and design under severe uncertainty [1] and it has been applied in very diverse domains including engineering, economics, medicine, and business management. An info-gap model quantifies the difference - the gap - between the information that is known, for example the nominal value of a parameter, and the information that has to be known in order to insure a critical level of performance. An application of info-gap analysis to structural health monitoring can be found in [3]. The essential components of this non-probabilistic approach to uncertainty quantification are briefly described below.

The info-gap robustness analysis requires the definition of three components:

1. **System model**
   The system model establishes the functional relationship between the uncertain model parameters and the response features of interest. In the present case, the response features of interest is the displacement at the operation frequency and the uncertain model parameter is the identified modal basis. That's why, we use the modal frequency response function (4) to establish the relationship between the uncertain model parameters and the response features of interest. In practice, it is assumed that an experimental modal analysis has been performed in order to obtain the eigenparameters required to calculate the system response in the frequency band of interest Ω. Let $(\omega_v^e, \phi_v^e, \xi_v^e) \in \mathbb{R}^m \times \mathbb{R}^{c,m} \times \mathbb{R}^m$ be the identified modal basis with ω_v^e the eigenfrequencies, ϕ_v^e the eigenvectors, ξ_v^e the diagonal modal damping factors, m the number of extract eigenmodes and c the number of degree of freedom known by the sensors. Given the distributed nature of the excitation, the modal matrix must be interpolated to a large number of degrees of freedom (DOFs). Toward this end, the SEREP (System Equivalent Reduction Expansion Process) expansion method [4] is used to expand experimental modal basis to the required DOFs. A discretized model using finite element (FE) method is used to take into account the complexity of the structure. The equation of motion is given by:

$$M\ddot{y}(t) + C\dot{y}(t) + Ky(t) = f(\theta, t) \in \mathbb{C}^N \tag{1}$$

   with M,C and K respectively the mass, the damping and the stiffness matrices of the structure, $f(\theta, t)$ the excitation given in (5) and N the number of DOFs ($N >> c$) of the model. A numerical modal analysis is performed to have available the numerical modal basis $(\omega_v^n, \phi_v^n, \xi_v^n)$. Let $\Phi^e = (\phi_1^e, \cdots, \phi_m^e) \in \mathbb{R}^{c,m}$ and $\Phi^n = (\phi_1^n, \cdots, \phi_m^n) \in \mathbb{R}^{N,m}$ be respectively the experimental and the numerical modal matrix. The expand modal matrix Φ is given by:

$$\begin{aligned} \Phi &= \Phi^n X_0 \\ X_0 &= \underset{X}{\operatorname{argmin}}(||C\Phi^n X - \Phi^e||^2) \end{aligned} \tag{2}$$

with $C \in \mathbb{R}^{c,N}$ the observation matrix which establish the link between the DOFs of the sensor and the DOFs of the FE model. The quality of this expansion will strongly depend on the credibility of the underlying physics-based model. Ultimately, the uncertainty associated with this process will need to be introduced as well.

We finally obtain $m-$eigenparameters (ω_v,ϕ_v,ξ_v). The dynamic flexibility matrix $\Gamma(\omega)$ can be expressed as a function of the diagonal eigenvalue matrix $\Lambda_m = \text{diag}(\omega_1^2 \cdots \omega_m^2)$, of the diagonal modal damping matrix $B_m = \text{diag}(2\omega_1\xi_1 \cdots 2\omega_m\xi_m)$ and of the expand modal matrix Φ:

$$\Gamma(\omega) = \Phi(\Lambda_m + i\omega B_m - \omega^2 I_m)^{-1}\Phi^T \in \mathbb{C}^{N,m} \tag{3}$$

Finally, the relationship between the uncertain model parameters (in $\Gamma(\omega)$) and the response features of interest ($y(\omega)$) is given by:

$$y(\omega) = \Gamma(\omega)\mathscr{F}(\omega) \in \mathbb{C}^N \tag{4}$$

where the force $\mathscr{F}$ is the discrete Fourier transform of the following stationary excitation at the frequency ω_0. The excitation derives from the electromagnetic field in the stationary state where θ is the angle of rotation as shown in Figure 4:

$$f(\theta,t) = A.sin(\omega_0.t + 4\theta) \tag{5}$$

2. **Performance requirement**
The performance requirement represents the quantity of interest upon which a decision or set of decisions will be based. In the present case, the maximum response level of the stator at an operating frequency ω_0 should be less than or equal to some critical value y^C:

$$||y(\omega_0)|| \leq y^C \tag{6}$$

3. **Uncertainty model**
The info-gap uncertainty model defines an ensemble of nested sets of realizable designs as a function of the horizon of uncertainty α. Here, lack of knowledge in the eigenparameters will be represented by a fractional error model:

$$\mathscr{U}(\alpha, c^{(0)}) = \left\{ c : \left| \frac{c_i - c_i^{(0)}}{c_i^{(0)}} \right| \leq w_i\alpha, \forall i \in \{1, \cdots, 3m\} \right\} \tag{7}$$

with:

$$\begin{cases} c \in \mathbb{R}^{3m} \\ \alpha \geq 0 \quad \text{the horizon of uncertainty} \\ w \geq 0 \qquad \text{a vector of weighting coefficients} \end{cases}$$

The column vector c is defined by:

$$c = (\frac{\omega_1}{2\pi} \cdots \frac{\omega_m}{2\pi}, ||\phi_1|| \cdots ||\phi_m||, \xi_1 \cdots \xi_m)^T \tag{8}$$

and $c^{(0)}$ defines the nominal eigenparameters extracted from modal tests:

$$c^{(0)} = (\frac{\omega_1^{(0)}}{2\pi} \cdots \frac{\omega_m^{(0)}}{2\pi}, ||\phi_1^{(0)}|| \cdots ||\phi_m^{(0)}||, \xi_1^{(0)} \cdots \xi_m^{(0)})^T \tag{9}$$

Finally, the robustness to uncertainty is defined as the greatest horizon of uncertainty α that can be tolerated without exceeding the critical performance requirement y^C. It is obtained by solving the following optimization problem:

$$\hat{\alpha}(c^{(0)}, y^C) = \max \left\{ \alpha : \max_{c \in \mathscr{U}(\alpha, c^{(0)})} ||y(\omega_0)|| \leq y^C \right\} \tag{10}$$

However, for a given performance requirement, we have to solve the costly non linear optimization (equation 10) in order to get a value of robustness. Practically speaking, this optimization problem is resolved by a set of the following optimization problem:

$$y^C(\alpha_i) = \max_{c \in \mathscr{U}(\alpha_i, c^{(0)})} \{||y(\omega_0)||\} \tag{11}$$

where the horizon of uncertainty was discretized by a series of increasing values: $\hat{\alpha} = \{0, \alpha_1, \alpha_2, \cdots, \alpha_p\}$. We finally obtain the robustness curve $\hat{\alpha} = f(y^C)$.

3 Numerical Application

3.1 Case Study

The simplified stator model depicted in Figure 3 is used to simulate the results of the experimental modal identification. Orthotropic solid elements are used to represent the magnetic circuit (in yellow) while the support structure is modeled with shell elements (in red) and six axial springs (in blue). Concerning the boundary conditions, the free ends of the springs are grounded. The model contains a total of $N = 5580$ DOFs.

A numerical modal analysis is performed to obtain the eigenproperties defining $c^{(0)}$. The frequency of interest is 95 Hz and the three neighboring eigensolutions shown in Figure 5 are retained to perform the robustness analysis.

The nominal response of the stator is calculated for an excitation amplitude of $A = 1$ N and an excitation frequency $\frac{\omega_0}{2\pi} = 95$ Hz. The excitation force is applied to all 220 nodes on the inner surface of the stator. The frequency response amplitude at the node s (see Figure 3) is plotted in Figure 6.

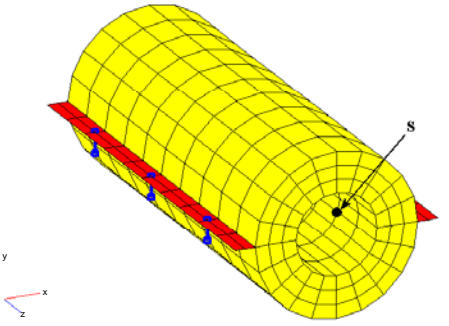

Fig. 3 Simplified stator FE model

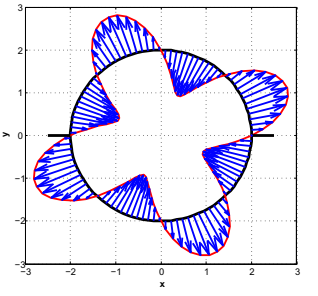

Fig. 4 Spatial distribution of the dynamic loading

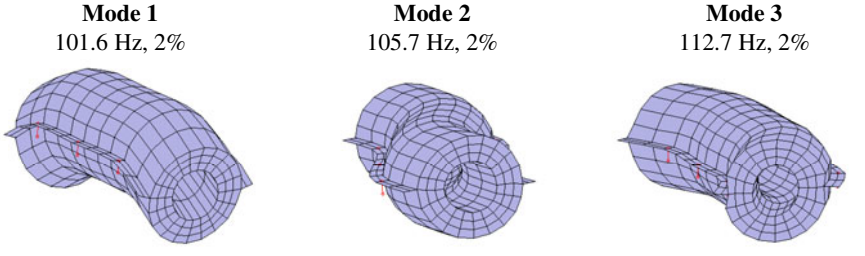

Fig. 5 Eigensolutions retained for the robustness analysis (eigenfrequency, damping coefficient)

3.2 Info-Gap Robustness Analysis

The weighting vector (which define among others the uncertainty model) w expresses the relative confidence between the different eigenparameters and is defined on the basis of engineering judgement. For illustration purposes, w will be defined as follows:

$$w = (1,1,1,\frac{1}{2},\frac{1}{2},\frac{1}{2},\frac{3}{2},\frac{3}{2},\frac{3}{2}) \tag{12}$$

Globally speaking, the smaller w is, the more confidence in the uncertain parameter we have. In this example, we have relative good confidence in the eigenvector norms ($w_i = \frac{1}{2}$ for $i \in \{4,5,6\}$) contrary to the diagonal damping factor ($w_i = \frac{3}{2}$ for $i \in \{7,8,9\}$). We have to be careful with the definition of w because the robustness to uncertainty function depends on the weighting vector (see Figure 8 and 9).

Moreover, additional constraints on the eigenfrequencies will be applied in order to insure that the physical relationship between the different bending modes is maintained.

The robustness function is finally shown in Figure 7 for $0 \leq \alpha \leq 0.3$.

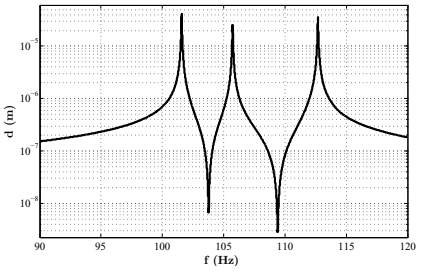

Fig. 6 Frequency response amplitude at node *s*

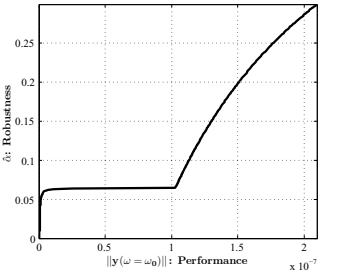

Fig. 7 Info-gap robustness function

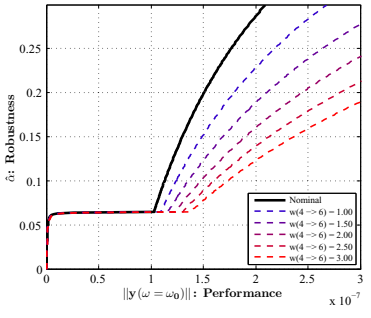

Fig. 8 Influence of different eigenvector weights

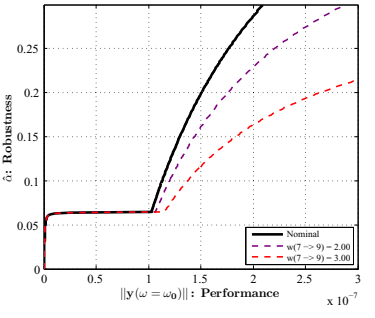

Fig. 9 Influence of different damping factor weights

In this example, the robustness curve is composed of 3 zones:

- $\hat{\alpha} < 0.06$: The horizon of uncertainty is not yet large enough for the first eigenfrequency to shift to the excitation frequency. The performance in this zone is seen to be very robust to uncertainty.
- $\hat{\alpha} \sim 0.06$: The horizon of uncertainty is large enough for the first stator eigenfrequency to align with the excitation frequency. The performance in this zone is clearly very vulnerable to increasing uncertainty.
- $\hat{\alpha} > 0.06$: The performance in this zone is now relatively robust with increasing response amplitudes due exclusively to the effects of eigenvector norm and damping errors.

Figures 10 show the evolutions of the relative variations in the eigenparameters (13) as a function of the horizon of uncertainty.

$$d_i(\alpha) = \frac{c_i(\alpha)}{c_i^0} \quad ,\forall i \in \{1, \cdots, 9\} \tag{13}$$

For example, the red line in Figure 10(a) indicates that the frequency of the first eigenfrequency shifts downward until it reaches the excitation frequency at which the maximum frequency response is obtained. It then remains at this frequency even for increasing horizons of uncertainty.

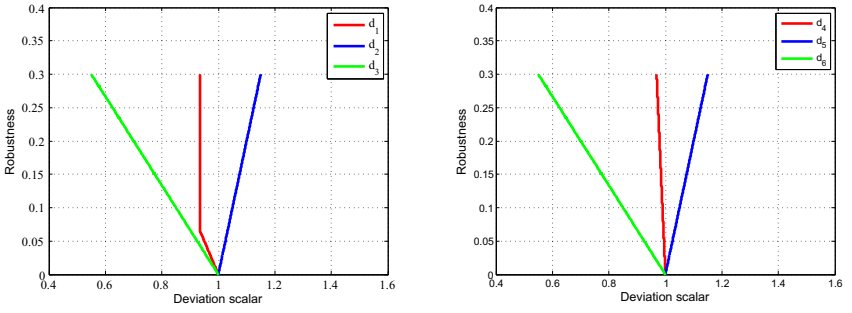

Fig. 10 Robustness vs relative variations for mode 1 (a) and 2 (b)

3.3 Discussion

There are at least 2 applications of the robustness:

- First, we want to know if the thermal effects lead to a critical system performance. On one hand, for illustration purpose, we suppose the relation between the eigenfrequencies and the temperature as linear, as indicated in Figure 11. Thus, the thermal effects lead to a maximum variation of 0.10% for each mode. On the other hand, the system is considered as faulty when the relative displacement in operation is 21 μm at node s. For that performance requirement, the robustness curve shows that the thermal effects do not lead to a fault in the system performance.
- Then, that curve can be used as a decision making tool for maintenance. As indicated previously, the robustness curve is composed of 3 zones and each zone define a different state of robustness. Following the experimental modal analysis, the decision maker have to take a decision: he wants to know the risk of failure if he decides to restart the machine. For a given performance requirement - maximum acceptable displacement in operation - he is able to known if the alternator is robust to uncertainties or not. In the case of non robust state, he should prefer additional maintenance procedure in order to preserve eigenmode in a robust state.

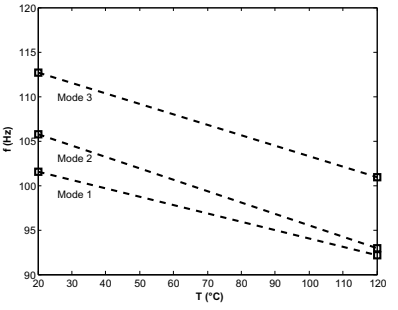

Fig. 11 Possible eigenfrequencies evolution in operation

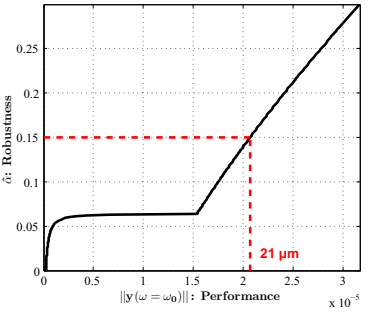

Fig. 12 Robustness function

4 Conclusion

The objective of this work is to bound the dynamic response levels of the stator component of a turbo-alternator based on the experimentally identified eigensolutions obtained during routine maintenance operations. In order to account for variations in the eigenparameters in operation, a maintenance alarm is formulated via an info-gap robustness analysis in order to investigate the impact of this lack of knowledge on the calculated response behaviour. Low robustness to uncertainty indicates that the stator requires specific maintenance operations. The present study was limited to epistemic uncertainties in the eigenfrequencies, eigenvector norms, and the diagonal modal damping factors. The proposed methodology is illustrated on a numerical test case using a simplified stator model.

Future work will extend the approach to include the impact of uncertainty in the mode shapes resulting from either the expansion process or thermo-mechanical effects. Indeed, this can significantly alter the degree of coupling with the rotating load. Moreover, partial information obtained from tests in operation will be used to refine the info-gap uncertainty models. Finally, the maintenance alarm will be applied to data available from stators tested in the past in order to evaluate the relevance of the proposed maintenance alarm.

Acknowledgement. The authors would like to acknowledge EDF R&D for their generous support.

References

1. Ben-Haim, Y.: Information-Gap Theory: Decisions Under Severe Uncertainty. Academic Press, London (2001)
2. Farrar, C.R., Doebling, S.W., Nix, D.A.: Vibration-Based Structural Damage Identification. Philosophical Transactions of the Royal Society: Mathematical. Physical & Engineering Sciences (2001)
3. Keren, C., Ben-Haim, Y.: Info gap Bayesian Classification, Master Thesis, Haifa (2009)

4. O' Callahan, J.C., Avitabile, P., Riemer, R.: System equivalent reduction expansion process (SEREP). In: IMAC VII, pp. 29–37 (1989)
5. Sohn, H., Farrar, C.R., Hemez, F.M., Shunk, D.D., Stinemates, D.W., Nadler, B.R., Czarnecki, J.J.: A Review of Structural Health Monitoring Literature, Los Alamos (2004)
6. Worden, K., Farrar, C., Manson, G., Park, G.: The Fundamental Axioms of Structural Health Monitoring. Philosophical Transactions of the Royal Society: Mathematical, Physical and Engineering Sciences 463(2082), 1639–1664 (2007)

Multi-objective Discrete Rotor Design Optimization

Ibrahim M'laouhi[1], Najeh Ben Guedria[2], and Hichem Smaoui[3]

[1] Higher Institute of Technologic Studies of Sousse, Tunisia
Brahim.Mlaouhi@isetso.rnu.tn
[2] Higher Institute of Transport and Logistics of Sousse, Tunisia
najehbenguedria@gmail.com
[3] National Engineering School of Tunisia, Tunisia
hichem.smaoui@enit.rnu.tn

Abstract. The present work focuses on multi-objective optimization of rotors design described by discrete variables. The aim is to modify the design of a rotor in order to avoid some resonance frequencies. The multi-objective optimization problem consists: on the one hand, in minimizing the total mass of the rotor, and on the other hand, in shifting the critical speeds to avoid the operating frequency of the rotor. The design variables are the diameters of the shaft sections that are assumed to be available only in a set of pre-specified values. To solve the discrete rotor design problem, a Multi-Objective Genetic Algorithm (MOGA) is used. A 88 degrees of freedom model of a rotor is considered as a numerical example. In order to select optimal values of MOGA control parameters, a set of numerical experiments are carry out where crossover and mutation rates are varied. The results of optimal designs of the rotor are reasonable solutions each of which satisfies the objectives at an acceptable level without being dominated by any other solution.

Keywords: optimization, discrete variable, MOGA, rotor, critical speed.

1 Introduction

In the design of rotors, the multiple requirements of effectiveness, reliability, maintainability, etc… can lead in certain cases to critical speeds close to the operational speed, dangerous response due to unbalance, significant shaft deformation, high loads transmitted to the bearings. Several papers devoted to rotor design optimization problems discussed the various means to improve the dynamic behavior of rotating machines, such as by increasing the rigidity of the shaft [1], decreasing the rotor mass [2], shifting critical speeds [3,4,5] or reducing the forces transmitted to the bearings and foundation [6]. In addition, the stability of the rotating machines could be improved by the anisotropy of the bearing and the optimization of their geometric parameters [7]. Two types of design variables were largely used in the preceding studies. The first type describes the geometry

of the rotors, such as the diameters of the shaft, the dimensions and locations of discs and bearings [8,9]. The second types are the support system parameters, such as the stiffness, the damping of the bearings and foundation [4].

In all previous work on rotor design optimization, the problem is considered as a single objective optimization problem where an optimization method would return a single solution for only one objective. However, some studies devoted to multi-objective optimization of the rotors, by combining the individual objective functions into a single composite function or move all but one objective to the constraint set, but in many cases the objectives (or goals) are in conflict with another, where an improvement in one objective leads to a worse solution for at least one of the other objectives. Moreover, design variables were treated as continuous variables. In practical situations the rotor components are available only in standard dimensions, therefore continuous solutions are practically non realizable.

In this paper, the rotor design multi-objective optimization problem is considered with discrete design variables, selected in a predefined set of values in order to obtain a practically realizable solution. Section 2 is devoted to the formulation of the rotor design multi-objective optimization problem. Next, Section 3 gives a brief presentation of the optimization algorithm MOGA, used in this work. Finally, a rotor dynamics model is considered in Section 4 as a numerical example to illustrate the effectiveness of this algorithm.

2 Multi-objective Rotor Design Optimization Problem

Consider an n dimensional decision variable vector $\mathbf{x} = \{x_1, x_2, ...x_n\}$, in the solution space, find a vector $\mathbf{x}^*$ that minimizes a given set of k objective functions, If all objective functions are for minimization, a feasible solution x is said to dominate another feasible solution y $(x > y)$ if $f_i(x) < f_i(y)$ for $i = 1.....k$.

A solution is said to be Pareto optimal if it is not dominated by any other solution in the solution space. The set of all feasible *non-dominated* solutions in the solution space is referred to as the Pareto optimal set, and for a given Pareto optimal set, the corresponding objective function values in the objective space are called the *Pareto front*.

The multi-objective rotor design optimization problem can be written as follows:

$$\begin{aligned} &\text{Objective 1:} && \min_{\mathbf{x}\in\mathbf{D}} f_1(\mathbf{x}) = \min_{\mathbf{x}\in\mathbf{D}} \; Mass(\mathbf{x}) \\ &\text{Objective 2:} && \min_{\mathbf{x}\in\mathbf{D}} f_2(\mathbf{x}) = \min_{\mathbf{x}\in\mathbf{D}} \left[\sum_{i=1}^{N} \left| \omega_i(\mathbf{x}) - \omega_i^*(\mathbf{x}) \right| \right] \\ &\text{Subject to} && \mathbf{x} \in \mathbf{D} \end{aligned} \tag{1}$$

Where f_1 is the first objective function which present a total mass of the rotor, f_2 is a second objective function, ω_i and ω_i^* are the critical speed of the i^{th} mode and

the corresponding desired one, N is the number of degree of freedom of the rotor, $\mathbf{x}$ is a vector of discrete design variables, each belonging to a predefined set $\mathbf{D}$. The design variables considered in this work are the diameters of the shaft sections.

Given the discrete nature of the multi-objective optimization problem in Eq. (1), a Multi-Objective Genetic Algorithm (MOGA), known for their global optimization capability, is chosen to find an optimum design.

This algorithm has been applied in diverse fields of engineering for solving optimization problems such as structural design [10], rotary regenerator [11], compressor blade design [12], etc. In most applications, only continuous problems have been considered. In this paper, the rotor design problem is formulated in terms discrete variables and MOGA algorithm is chosen to solve the resulting discrete multi-objective optimization problem.

3 Optimization Algorithm

This section is devoted to a brief description of the Multi-Objective Genetic Algorithm (MOGA), used to solve the rotor design multi-objective optimization problem. Genetic algorithms are inspired by the mechanisms of natural selection which favors the survival of the individuals with the best performance [13]. The ability of MOGA to simultaneously search different regions of a solution space makes it possible to find a diverse set of solutions for difficult problems with non-convex, discontinuous, and multi-modal solutions spaces. Therefore, MOGA has been the most popular heuristic approach to multi-objective design and optimization problems [14].

To apply MOGA to the rotor design multi-objective optimization problem, a predefined set of 32 discrete diameters, noted **D**, is considered. The index of each diameter is coded into 5 binary digits as shown in **Table1**. Hence the design variable vector or chromosome is represented by string binary digits of length (5 x numbers of design variables)

Table 1 Example of coding a design variables vector

Discrete diameters	x_1	x_2	x_3	.....	x_i	.....	x_n
Index of x_i in **D**	Ind(x_1)	Ind(x_2)	Ind(x_3)	.....	Ind(x_i)	.....	Ind(x_n)
Chromosome	**01001**	**11010**	**01010**	.....	**01001**	.....	**00111**

4 Numerical Example

In order to verify the efficiency of the MOGA algorithm for solving the discrete rotor design multi-objective optimization problem, a finite element model of a rotor, shown in **Figure 1**, is considered. The modeled rotor system consists of a flexible shaft supported by two bearings and three rigid disks rigidly fixed to the shaft.

The shaft has a diameter $d = 76.2mm$ (3 inches), a length $L = 812.8mm$ (32 inches), a Young's module $E = 2.1\times10^{11} N/m^2$, a mass density $\rho = 7810\ kg/m^3$ and a Poisson's ratio $\nu = 0.3$. The disks (1), (2) and (3) are fixed respectively at $l_1 = 431.8$ mm, $l_2 = 381$ mm and $l_3 = 25.4$mm, from the left side of the shaft. All three disks parameters are shown in Table 2. The inside diameter of each disk is assumed to be the outside diameter of the associated shaft element. The two bearings are modeled using springs and dashpots as shown in Figure 1. All springs and dashpots have, respectively the same stiffness and damping coefficients:

$$K_{xx1} = K_{xx2} = K_{yy1} = K_{yy2} = 5.643\times10^6 N/m \text{ and } C_{xx1} = C_{xx2} = C_{yy1} = C_{yy2} = 10^3\ Ns/m.$$

The rotor shaft is modeled with 21 shaft finite elements using Euler-Bernoulli beam model in which the gyroscopic and the inertia of rotation effects are included. Thus, the system has 22 nodes. Each node has four degrees of freedom; therefore, the model has 88 degrees of freedom. Length of shaft finite elements is 25.4 or 50.8mm as shown in figure 1. The two bearings are located, respectively, at nodes 2 and 15, the three disks are respectively fixed at the 10^{th}, 12^{th} and 21^{th} node. The gyroscopic effect of the disks has also been included in the model. The rotor is therefore a damped asymmetric system due to the gyroscopic effects and the damping of the bearing dashpots.

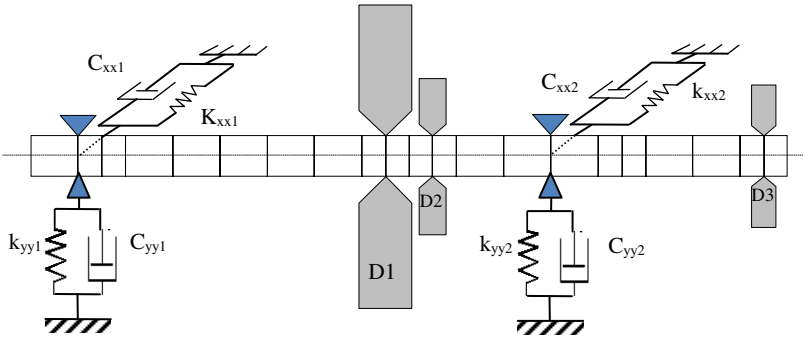

Fig. 1 A 88 DOF finite element rotor model

Table 2 Disks parameters

	Disk 1 at node 10	**Disk 2 at node 12**	**Disk 3 at node 21**
External diameter [mm]	558,8	279,4	254
Thickness [mm]	50,8	50,8	50,8
Diametral Inertia [kgm²]	1,9188	0,12287	0,08434
Polar Inertia [kgm²]	3,7966	0,23605	0,16081

Figure 2 shows the Campbell diagram which represents the change in the damped natural frequency with respect to rotor speed. Note that the first two critical speeds are respectively located at 2152 and 5080 rpm. The rotor operating speed is chosen to be 2300 rpm.

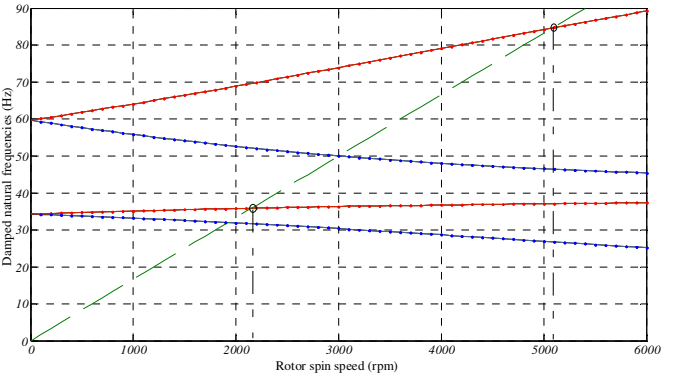

Fig. 2 The Campbell diagram of the initial rotor

The mass of the initial design of the rotor is 165,25 kg. Table 3 shows respectively the first two critical speeds of the initial rotor and the corresponding two desired critical speeds.

Table 3 The first two critical speeds associated with the initial rotor.

DOF	Initial critical speeds	Desired critical speeds
1	2152.8 rpm	1937.52 rpm
2	5080.8 rpm	4572.72 rpm

The desired critical speeds are chosen by decreasing their initial values by a factor of 10%. The decision variable vector is given by $\mathbf{x} = \left[d_1\ d_2\ d_3 \ldots\ldots d_j \right]$, where $d_j \left(j = 1 \ldots\ldots 21 \right)$ are the shaft element diameters.

In order to adjust the control parameters of the MOGA, for the discrete rotor design optimization problem, the crossover and the mutation rates are chosen to take respectively the values Pc= 0.1, 0.4, 0.8 and 1.0 and Pm= 0.001, 0.05, 0.1 and 0.8. for each couple of crossover and mutation rate values, the algorithm is executed with a population size equal to 100, a uniform selection technique, a Pareto fraction equal to 0.2 and a stopping criteria defined by a maximum of 100 iterations. Figures (3.a), (3.b), (3.c) and (3.d) show the Pareto fronts correspondent respectively to Pc = 0.1, 0.4, 0.8 and 1.0. For each value of Pc, the mutation rate is

varied in the set $\{0.001, 0.05, 0.1, 0.8\}$. The four best rotor designs in terms of objectives satisfaction are shown in Figures (3.a), (3.b), (3.c) and (3.d), which are obtained respectively for the couple of crossover and mutation rates (0.1,0.05), (0.8,0.8), (0.4,0.1) and (1.0,0.8). The best of them correspond to that illustrated in Figure 3.b, which minimize simultaneously the total mass of the rotor and the sum of the difference between the first and second critical speeds and the corresponding desired ones.

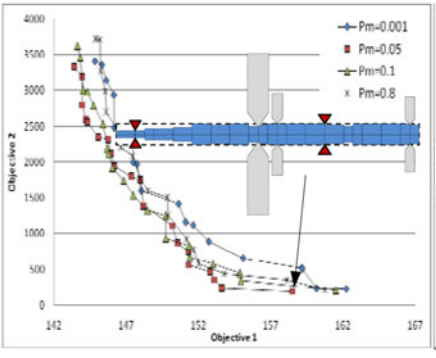

Fig. (3.a) Pareto optimal set and best rotor design obtained with Pc = 0.1 and Pm = 0.05

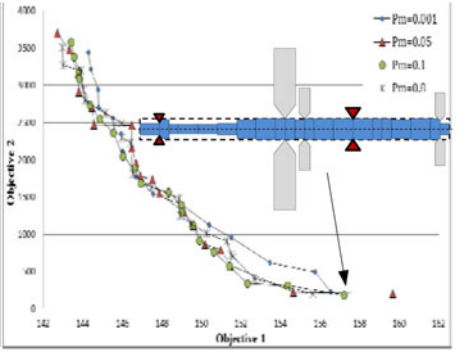

Fig. (3.c) Pareto optimal set and best rotor design obtained with Pc = 0.4 and Pm = 0.1

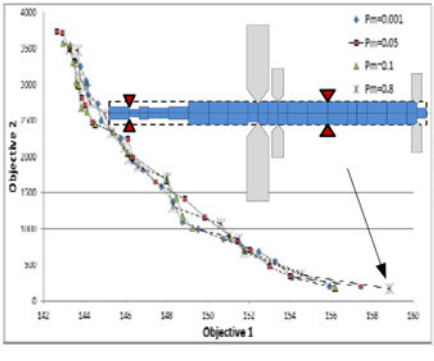

Fig. (3.b) Pareto optimal set and best rotor design obtained with Pc = 0.8 and Pm = 0.8

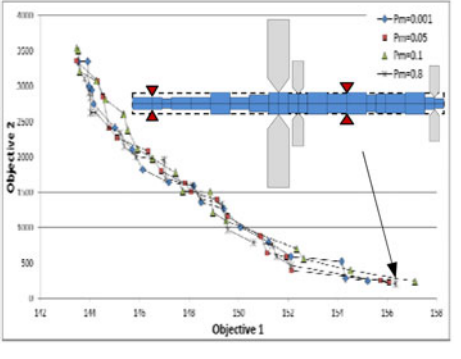

Fig. (3.d) Pareto optimal set and best rotor design obtained with Pc = 1 and Pm = 0.8

In typical GA implementations, the mutation rate (probability of changing the properties of a gene) is very small and depends on the length of the chromosome. Therefore, the new chromosome produced by mutation will not be very different from the original one. Mutation plays a critical role in MOGA. Crossover leads the population to converge by making the chromosomes in the population alike. Mutation reintroduces genetic diversity back into the population and assists the search escape from local optima. However, crossover holds up a well exploration of search space.

The ultimate goal of a multi-objective optimization algorithm is to identify the best solutions in the Pareto optimal set. However, in the multi-objective optimization of the rotor design problem, the two objectives are in conflict between them, where an improvement in one objective leads to a worse solution for the other objective; Figure 4 illustrate three different rotor designs in the Pareto optimal set, though the first best solution shown a model of rotor with a minimum mass, which leads to an worst solution in terms of satisfaction of critical speeds limits, However, the third optimal design which give best solution in terms of the second objective.

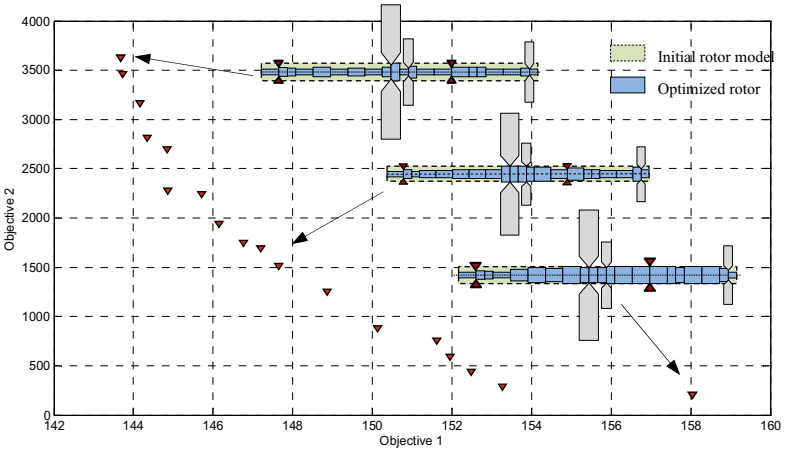

Fig. 4 Illustration of the rotor designs in the Pareto optimal set obtained by MOGA.

5 Conclusion

In order to improve the dynamic behavior of flexible rotors, a design modification problem is formulated as a multi-objective optimization problem where the mass and the shift of critical speeds of a rotor were two objective functions. The shaft elements diameters are considered as discrete design variables to obtain practically realizable solutions. To solve the discrete rotor design multi-objective optimization problem, the Multi-Objective Genetic Algorithms (MOGA), is used. In order

to verify the efficiency and the capability of the MOGA in solving this type of rotor optimization problem, a finite element model of a rotor, with 88 degrees of freedom is considered as a numerical example. The designs obtained by MOGA algorithm are practically realizable solutions represented by a Pareto optimal set. However, the results revealed the level of confliction between the two objectives, where an accomplishment in one objective leads to a worse solution for the other objective. Hence, to be able to make a decision, it is necessary to seek a compromise with respect to the objectives.

References

[1] Choi, B.G., Yang, B.S., Kim, W.C.: Optimum shape design of shaft using genetic algorithm. In: Proceedings of the Fifth Asian International Conference on Fluid Machinery, Seoul, Korea, pp. 85–92 (1997)
[2] Chen, T.Y., Wang, B.P.: Optimum design of rotor-bearing systems with eigenvalue constraints. ASME J. Eng. Gas Turbines Power 115, 256–260 (1993)
[3] Choi, B.G., Yang, B.S.: Optimum shape design of shaft using genetic algorithm. J. Vib. Control 6(1), 207–222 (2000)
[4] Choi, B.G., Yang, B.S.: Multi-objective optimization of rotor bearing system with dynamic constraints using IGA algorithm. ASME J. Eng. Gas Turbines Power 123(1), 78–81 (2001a)
[5] Choi, B.G., Yang, B.S.: Optimal design of rotor-bearing systems using immune-genetic algorithm. ASME J. Vib. Acoust. 123(3), 398–401 (2001b)
[6] Nataraj, C., Ashrafiuon, H.: Optimal design of centred squeeze film dampers. ASME J. Vib. Acoust. 115, 210–215 (1993)
[7] Wang, J.H., Shih, F.M.: Improve the stability of rotor subjected to fluid leakage by optimum diameters design. ASME J. Vib. Acoust. Stress Reliab. Des. 112, 59–64 (1990)
[8] Strauβ, F.: Design optimization of rotating bodies. PhD thesis, Ru-precht-Karls-universitat Heidelberg (2005)
[9] Strauβ, F., Inagaki, M., Starke, J.: Reduction of vibration level in rotordynamics by design optimization. Industrial Applications Journal 34, 139–149 (2007)
[10] Bahai, H., Farahani, K., Djoudi, M.S.: Eigenvalue inverse formulation for optimizing vibratory behaviour of truss and continuous structures. Computers and Structures 80, 2397–2403 (2002)
[11] Sanaye, S., Hajabdollahi, H.: Multi-objective optimization of rotary regenerator using genetic algorithm. International Journal of Thermal Sciences 48, 1967–1977 (2009)
[12] Liou, M.-S., Lian, Y.: Multi-Objective Optimization of Transonic Compressor Blade Using Evolutionary Algorithm. Journal of Propulsion and Power 21(6) (2005)
[13] Konak, A., Coit, D.W., Smith, A.E.: Multi-objective optimization using genetic algorithms. Reliability Engineering and System Safety 91, 992–1007 (2006)
[14] Jones, D.F., Mirrazavi, S.K., Tamiz, M.: Multi-objective meta-heuristics: an overview of the current state-of-the-art. Eur. J. Oper. Res. 137(1), 1–9 (2002)

A Critical Speed Optimization of Rail Vehicle System Based on Safety Criterion

Mohamed Nejlaoui[1], Ajmi Houidi[2], Zouheir Affi[1], and Lotfi Romdhane[3]

Laboratoire de Génie Mécanique, Tunisia,
[1] Ecole Nationale d'Ingénieurs de Monastir, Tunisia
zouhaier.affi@enim.rnu.tn
[2] Institut Supérieur des Sciences Appliquées et de Technologie de Sousse, Tunisie
ajmi.houidi@issatso.rnu.tn
[3] Ecole Nationale d'Ingénieurs de Sousse, Tunisie
lotfi.romdhane@enim.rnu.tn

Abstract. This paper deals with the critical speed optimization of a rail vehicle system moving in curved track with relatively high speed. Indeed the roll motion of the car body will be included in the dynamic model in order to study its effects. Based on the structural characteristics of the rail vehicle and its curved motion, a critical speed optimization as a function of the radius of curvature and the rail vehicle design parameters is performed using the genetic algorithms. The safety criterion is evaluated using the derailment angle. The outcomes of this work could help the designer in his choice of the adequate design parameters yielding the best compromise between critical speed and radius of curvature.

Keywords: Modeling, optimization, rail vehicle, curved tracks.

Nomenclature

i,j,k	Index of wheel set,wheel and bogie respectively	y_{ki}	Transversal displacement of the wheelset i of bogie k
$m+\hat{m}$	Wheelset and bearing body mass	γ_{nc}	Lateral acceleration of the vehicle
$M,\bar{M}$	Mass of bogie and car body respectively.	α_{ki}	Yaw angle of the wheelset i of the bogie k
γ_e	Equivalent conicity	$\alpha_k,\bar{\alpha}$	Yaw angle of the bogie k and Car body respectively
R_c	Radius of curve	$\theta_k,\bar{\theta}$	Roll angle of the bogie k and Car body respectively
h_0	Vertical distance between the primary suspension and the bogie centre of mass	$\bar{d}$	Transversal distance between the secondary suspension and the Car body centre of mass
δ	The rail inclination	θ_{ki}	Roll angle of the wheelsets ki

d	Transversal distance between the primary suspension and the bogie centre of mass	$y_k, \overline{y}$	Transversal displacement of the bogie k and car body respectively
$\overline{K}_u$	Spring stiffness of the secondary suspension in the direction u	K_u	Spring stiffness of the primary suspension in the direction u

1 Introduction

By traveling on short radius curves, the rail vehicle (RV) should achieve acceptable performance in particular with respect to safety. Elkins and Wu (1999) considered the ratio of the lateral force to the vertical force applied by each wheel on the rail, as a derailment criterion. Suda (1990) used the angle of attack and the lateral displacement of a wheelset, as two independent parameters, to predict the curving performance of the RV. In his study, the system is considered to have no flange rail contact.

Other works treated the effect of the designs of a RV system on its behavior. He and McPhee (2005) used a multibody dynamics modeling software to determine the equations of motion of the RV models. Based on this model, mono-objective optimization design was conducted using Genetic Algorithms method. The objective function was a weighted combination of the angle of attack and the ratio of the lateral force to the vertical force applied by each wheel on the rail. Rejeb et al. (2007) optimized the critical speed as a function of the design variables of the rail vehicles system in rectilinear motion using the Genetic Algorithm method.

Based on the improved model, presented in a previous work (Nejlaoui et al.2010), the goal of this work is to develop a critical speed optimization of a RV moving with a relatively high speed using safety criteria. In section 2, the improved dynamic model of the RV system developed in (Nejlaoui et al.2010) will be presented. This model considers the roll motions due to the fact that the RV circulates with relatively height speed and the presence of the different suspension systems. In section 3, the optimization of the critical speed as a function of the radius of curvature will be developed. Various solutions will be presented and discussed. Some concluding remarks will be given in section 4.

2 Model of the RV System

2.1 The Rail Vehicle Model

The RV model is made of a car body, two bogies and four wheelsets. The car body C is connected to the bogies C_k by 4 secondary suspensions. Each bogie is connected to 2 wheelsets S_{ki} using 4 primary suspensions. The RV system has 21

degrees of freedom, supposed independent, which are identified by the lateral displacements, the roll and the yaw motions of the car body, two bogies and four wheelsets (Rejeb et al. 2007).

Based on the RV symmetry and due to the fact that we focus on the transversal dynamics, it is proved that the study of the dynamic modeling of the system can be reduced to the modeling of its quarter as presented by (Figure 1) (Nejlaoui et al.2009). Therefore the rail vehicle motion is represented by the generalized coordinate's vector q defined by: $\mathbf{q} = \left[\bar{y}, \bar{\alpha}, \bar{\theta}, y_1, \alpha_1, \theta_1, y_{11}, \alpha_{11}, y_{12}, \alpha_{12} \right]^T$ (1)

Vector **q** gives the different motions at the equilibrium after the lateral displacement y_0 produced by the inertia of the rail vehicle system in curved tracks.

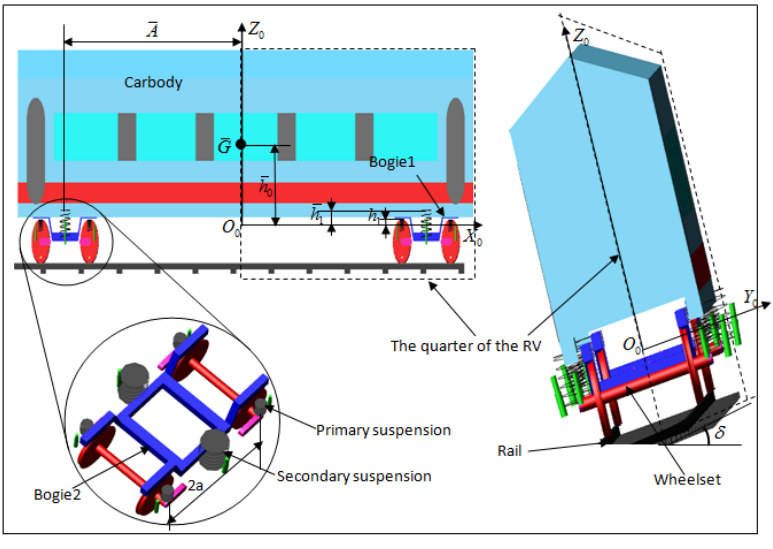

Fig. 1 The rail vehicle model

The analytical model of the rail vehicle system is obtained based on the Lagrange formalism and can be expressed as follows:

$$\mathbf{A}(\mathbf{q})\mathbf{q} = \mathbf{b} \tag{2}$$

The matrix **A** and the vector **b** are given in the appendix. For more details see (Nejlaoui et al.2010).

In this study, we assume that the rail curve radius and the rail inclination δ are constant. Moreover, due to the fact that the RV speed V is constant, we will neglect the damping forces, which were proved to be not significant, compared to the elastic ones (Majka and Hartnett 2008).

2.2 Safety Modeling

In curved tracks with a low radius, we have a flange rail contact. This contact leads to a lateral force F_{1i} (Fig. 2b) that if it exceeds a certain limit, it can cause the derailment of the RV system. In what follows, we will give, in a closed form, the forces responsible of the derailment.

When there is a flange – rail contact, the generalized coordinate y_{1i} of vector q is constant and it presents a known value. By using the constraint equation $\dot{y}_{1i} = 0$, in the dynamic model (Eq.2), the lateral forces F_{1i} can deduced from the Lagrange multiplier:

$$F_{1i} = \sum_{i=1}^{i=2} K_y \left(y_{1} - y_{11} - (-1)^i a\alpha_1 - y_{12} - y_0 + h_1\theta_1 \right) - (-1)^i \bar{K}_x \frac{\bar{d}^2}{2a} \left(\bar{\alpha} + \frac{y_1}{\bar{A}} - \frac{y_{11} - y_{12}}{2a} - \alpha_1 + \frac{\bar{A}}{R_c} \right) \quad (3)$$
$$+ \sum_{i=1}^{i=2} (-1)^i \frac{K_x d^2}{2a} \left(\alpha_1 - \alpha_{1i} + \frac{y_{11} - y_{12}}{2a} - (-1)^i \frac{a}{R_c} \right) + 2\chi C_{22} \alpha_{1i} \Sigma_i + (m + \hat{m}) \gamma_{nc} + W\zeta \left(y_0 + y_{1i} \right)$$

Where: C_{22} is the Kalker's coefficient (Datoussaid 1998). Σ_i, χ, W and ζ are defined in the appendix.

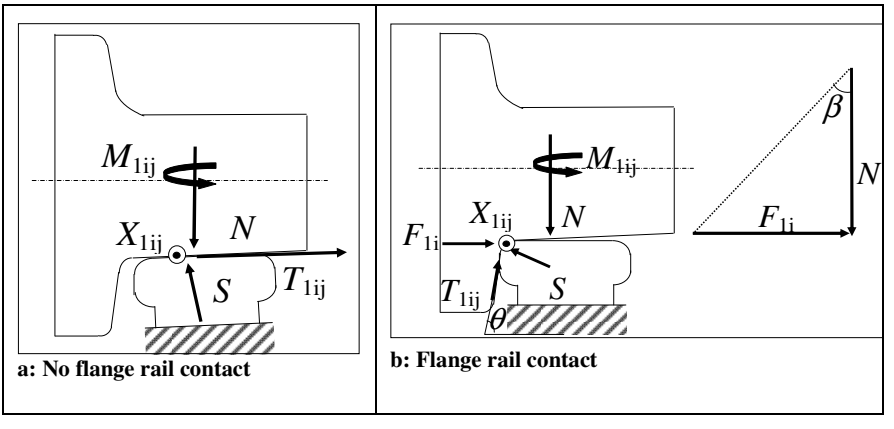

Fig. 2 The Wheel – Rail contact forces.

The analysis of the equilibrium of forces in vertical and lateral directions gives:

$$\frac{F_{1i}}{\mathrm{N}} = \frac{\tan\theta - \frac{T_{1ij}}{S}}{1 + \frac{T_{1ij}\tan\theta}{S}} \quad (4)$$

The maximum of safety is obtained when this term is $\left(\frac{F_{1i}}{\mathrm{N}}\right)$ minimal (Elkins and Wu 1999). The maximum of $\left(T_{1ij}/S\right)$ corresponds to the friction coefficient μ. Therefore, at a given $\theta_{\max}$, to avoid the derailment, we should have:

$$\frac{F}{N} < \frac{\tan\theta_{\max} - \mu}{1 + \mu \tan\theta_{\max}} \quad (F = \max(F_{1i})) \tag{5}$$

$$\text{This gives } \tan\beta < \frac{\tan\theta_{\max} - \mu}{1 + \mu \tan\theta_{\max}} \quad (\tan\beta = \frac{F}{N}) \tag{6}$$

β is the derailment angle.

To determine the force *F*, we should have the expressions of the generalized coordinates of the system. To achieve this goal, we developed an algorithm based on the Broyden's method (Nocedal and wright 1999). This algorithm solves the model for **q**. The values of *F (F = max (F_{1i}))* is calculated using equation (3).

3 Optimization of the Critical Speed

It is worth mentioning that the best optimization should be accomplished for various lateral accelerations $\gamma_{nc} = \frac{V^2}{R_c} - g\delta$ which coupled *V* to R_c (Fig 3); However, the RV model (eq.3) shows that R_c intervened on γ_{nc} and on the lateral force *F*. For this reason, the optimization is accomplished for different RV traveling speed *V* with a given radius of curves R_c.

3.1 Formulation of the Optimization Problem

From the eq. 03, for each Radius of curvature R_{ci}, the critical speed V_{ci} can be given by:

$$V_{ci} = \left[\frac{R_{ci}}{(m+\hat{m})} \left[\begin{array}{l} F_{\max} - \sum_{i=1}^{i=2} K_y \left(y_1 - y_{11} - (-1)^i a\alpha_1 - y_{12} - y_0 + h_1\theta_1 \right) - 2\chi C_{22}\alpha_{11}\Sigma_1 \\ -\bar{K}_x \frac{\bar{d}^2}{2a} \left(\bar{\alpha} + \frac{y_1}{\bar{A}} - \frac{y_{11} - y_{12}}{2a} - \alpha_1 + \frac{\bar{A}}{R_{ci}} \right) - W\zeta \left(y_0 + y_{11} \right) \\ -\sum_{i=1}^{i=2} (-1)^i \frac{K_x d^2}{2a} \left(\alpha_1 - \alpha_{1i} + \frac{y_{11} - y_{12}}{2a} - (-1)^i \frac{a}{R_{ci}} \right) + (m+\hat{m}) g\delta \end{array} \right] \right]^{\frac{1}{2}} \tag{8}$$

Where: $F_{\max} = \frac{\tan\theta_{\max} - \mu}{1 + \mu \tan\theta_{\max}} N$.

In what follows, we will optimize the design variables x_i that have a significant effect on the dynamic behavior of the RV system. The search domain $D(x_i)$ of each design variables xi are listed in Table 1.

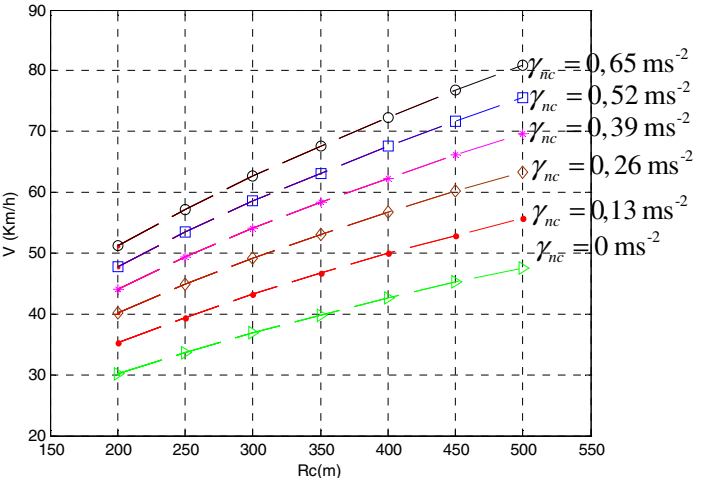

Fig. 3 Case of study

Table 1 Design variables and their search domains

Variables x_i	D (x_i)	Variables x_i	D (x_i)
$K_x(N/m)$	[10^6, 10^8]	$\bar{K}_z(N/m)$	[10^4, 10^6]
$K_y(N/m)$	[10^6, 10^8]	γ_e	[0.05, 0.2]
$K_z(N/m)$	[10^6, 10^8]	$a(m)$	[1,2]
$\bar{K}_x(N/m)$	[10^4, 10^6]	$\bar{M}(Kg)$	[30000,45000]
$\bar{K}_y(N/m)$	[10^4, 10^6]	$M(Kg)$	[3000,3500]

Thus, the problem can be presented as follows:

$$\begin{cases} \text{Maximize} \quad V_{ci}(x_i) \\ \text{under the constraints :} \\ \qquad \beta \le \beta_{\max} \\ \qquad x_i \in D(x_i) \end{cases}$$

For $\theta_{\max} = 75$ degrees (Elkins and Wu 1999) and $\mu = 0,31$ Joly 1985), we obtained $\beta_{\max} = 58$ degrees (see Eq.06)

3.2 The Optimization Method

The optimization is based on the classical genetic algorithms. The advantage of the type of GA is its simplicity, its robust response to changing circumstances, and its flexibility (Bouazizi et al.2009). We start with a randomly selected first generation. Every individual in this generation is evaluated and a fitness value is assigned. Next, a new generation is produced by applying the reproduction operator. Pairs of individual of the new generation are selected and a crossover is performed. With a certain probability, genes are mutated before all solutions and evaluated again. This procedure is repeated until a maximum number of generations is reached. While doing this, the best solution is stored and returned at the end of the algorithm (Bouazizi et al.2009).

3.3 Results and Discussion

The application of the optimization program, for different *R*c, gives the results in fig4. One can note that when the radius of curvature *R*c increases the critical speed *V*c increases too. In fact, the increases of *R*c decreases the centrifugal forces received by the vehicle.

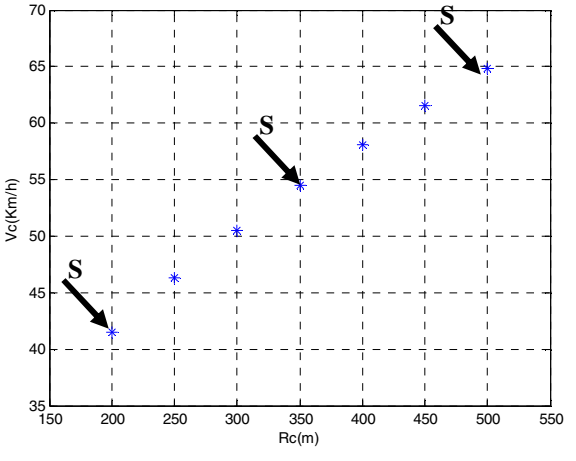

Fig. 4 Optimization results

Moreover, we can note that we have a constant γ_{nc} for all the optimal solutions. This result is not related to the Vc and γ_{nc} dependency but also to the RV design parameters which are optimized for every combination of *V*c and *R*c. Thus we can define a critical lateral acceleration γ_{ncc}. By varying, in the optimization program, $\beta_{\max}$ the γ_{ncc} changed (see fig.5).

One can note, also, that when $\beta_{\max}$ increases γ_{nc} increases too (fig.5); this can be explained by the fact that the increase of the maximal derailment angle $\beta_{\max}$ allows the increase of the critical speed V_c; and consequently the increase of the critical lateral acceleration γ_{ncc} .

In what follows, we will analyse the particularity of the solutions presented in fig.4. Therefore, for each design vectors corresponding to solutions S_1, S4 and S_7 we determine in fig 6 the evolution of *V*c as a function of Rc

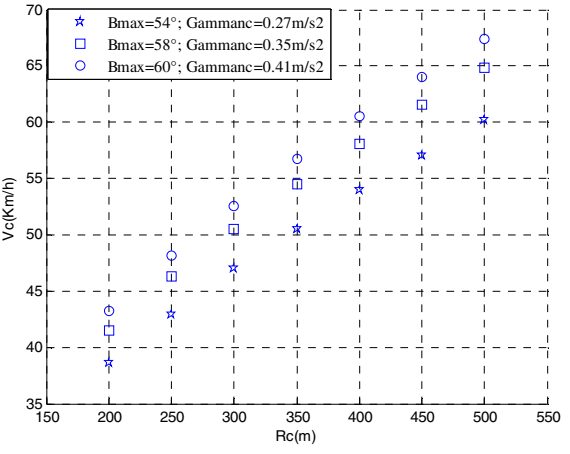

Fig. 5 Optimization results at different $\beta_{\max}$

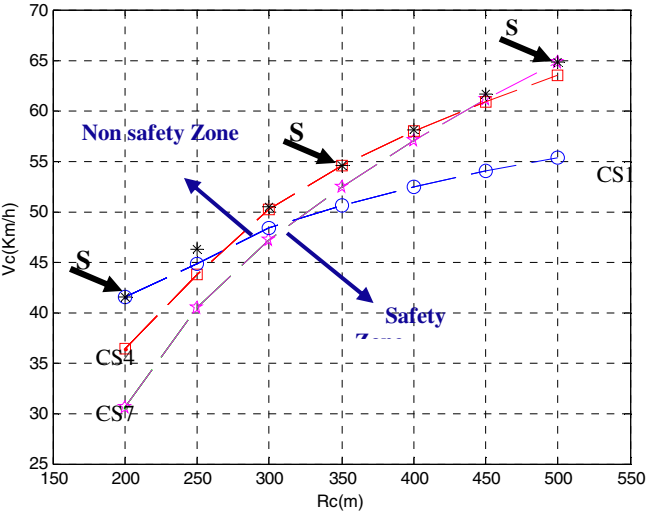

Fig. 6 Evolution of *V*c as a function of R_c

We define the corresponding curves CS1, CS4 and CS7 to S_1, S_4 and S_7 respectively. One can note that each curve represent the limit between two areas; the safety and the non safety zones.

One can note that if we use the design vector of S1, at *R*c= 200m, we can increase the speed of 10.5 m/s2 (see table 3). For the same design vector, at *R*c= 500m, we lose 9.5 m/s2 in speed.

In the other hand, if we use the design vector of S7, at *R*c= 500m we can increase the speed of 9.5 m/s2. But, at *R*c= 200m, we lose 10.5 m/s2 in speed. This behavior is due to the optimized design vector and *V*c as function of *R*c. Thus, to find a best compromise between the critical speeds at 200m and 500m, the designer can select a middle solution from the different *R*c defining a given trajectory of the RV.

4 Conclusion

This work deals with the critical speed optimization of the rail vehicle moving in curved tracks with relatively high speeds. Based on the improved analytical quasi static model that considers the roll motion generated by the centrifugal forces, an optimization was performed using the genetic algorithm in which the critical speed is maximized. The obtained solutions are analyzed for several design parameters. The presented analysis could help the designer in the choice of the most adequate design parameters of a set of rail vehicles systems yielding the maximum of safety.

References

Bouazizi, M.L., Ghanmi, S., Nasri, R., Bouhaddi, N.: Robust optimization of the non linear behavior of a vibrating system. European Journal of Mechanics A/Solids 28, 141–154 (2009)

Datoussaid, S.: Optimisation du comportement dynamique et cinématiques des systèmes multicorps à structure cinématique complexe, Ph.D these, Service de mécanique rationnelle, dynamique et vibration, Faculté polytechniquede Mons (1998)

Elkins, J., Wu, H.: Angle of attack and distance based criteria for flange climb derailment. Vehicle System Dynamics Supplement 33, 293–305 (1999)

He, Y., McPhee, J.: Optimization of curving performance of rail vehicles. Vehicle System Dynamics 43, 895–923 (2005)

Joly, R.: Circulation d'un véhicule ferroviaire en courbe de faible rayon. Inscription des essieux. Efforts d'interaction, Journal de mécanique théorique et appliqué 4, 813–832 (1985)

Majka, M., Hartnett, M.: Effects of speed, load and damping on the dynamic response of railway bridges and vehicles. Computers and Structures 86, 556–572 (2008)

Nejlaoui, M., Affi, Z., Houidi, A., Romdhane, L.: Analytical modeling of rail vehicle safety and comfort in short radius curved tracks. C. R. Mecanique 337, 303–311 (2009)

Nejlaoui, M., Houidi, A., Affi, Z., Romdhane, L.: An improved Analytical model of rail vehicle system moving in curved tracks. In: The First International Congress Passive and Active Mechanical Innovation, IMPACT (2010)

Nocedal, J., Wright, S.J.: Numerical Optimization. Springer, New York (1999)

Rejeb, H., Affi, Z., Bettaieb, H.: Optimization of the design variables of rail vehicles system in rectilinear motion. In: The Second International Congress Design and Modeling of Mechanical Systems, CMSM (2007)

Suda, Y.: Improvement of high speed stability and curving performance by parameter control of trucks for rail vehicles considering independly rotating wheelsets and unsymmetric structure. JSME International Journal, Series III 33, 176–182 (1990)

Zboifiski, K.: Dynamical investigation of railway vehicles on a curved track. Eur. J. Mech. A/Solids 17, 1001–1020 (1998)

Appendix A

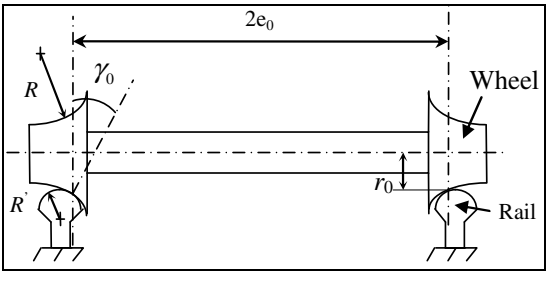

Fig. A1 The contact parameters of wheel-rail.

$$\gamma_{nc} = \frac{V^2}{R_c} - g\delta \,,\ \sigma_i = 1 - \frac{C_{11}}{3\mu N}\frac{\gamma_e}{r_0} y_{1i} + \frac{{C_{11}}^2}{27\mu^2 N^2}\left(\frac{\gamma_e}{r_0} y_{1i}\right)^2 \,,\ \Sigma_i = 1 - \frac{C_{22}}{3\mu N}\alpha_{1i} + \frac{{C_{22}}^2}{27\mu^2 N^2}{\alpha_{1i}}^2 \quad \text{(A1)}$$

$$\zeta = \frac{1}{(R - R')}\left(\frac{e_0 + R\gamma_0}{e_0 - r_0\gamma_0}\right)^2 \,,\ \chi = \frac{e_0}{(e_0 - r_0\gamma_0)} \,,\ \Gamma = \frac{\gamma_0}{(e_0 - r_0\gamma_0)} \,,\ \varepsilon_0 = (R + 2r_0)\gamma_0 - e_0 \quad \text{(A2)}$$

And $W = (\frac{\bar{M}}{4} + \frac{M}{2} + m + \hat{m})g$, e_0, r_0, γ_0, R_w and R_r are given in figure A1

$$\mathbf{A}=\begin{bmatrix}
\bar{K}_y & \bar{K}_y\bar{A} & \bar{K}_y\bar{h}_1 & -\bar{K}_y & 0 & -\bar{K}_y\bar{h}_1 & 0 & 0 & 0 & 0\\
\bar{K}_y\bar{A} & \bar{K}_y\bar{d}^2+\bar{K}_y\bar{A}^2 & \bar{K}_y\bar{A}\bar{h}_1 & \dfrac{\bar{K}_y\bar{d}^2}{\bar{A}}-\bar{K}_y\bar{A} & -\bar{K}_y\bar{d}^2 & -\bar{K}_y\bar{A}\bar{h}_1 & \dfrac{\bar{K}_y\bar{d}^2}{2a} & 0 & \dfrac{\bar{K}_y\bar{d}^2}{2a} & 0\\
\bar{K}_y\bar{h}_1 & \bar{K}_y\bar{A}\bar{h}_1 & \bar{K}_y\bar{h}_1^2+\bar{K}_y\bar{A}^2 & -\bar{K}_y\bar{h}_1 & 0 & -\bar{K}_y\bar{h}_1^2-\bar{K}_y\bar{A}^2 & 0 & 0 & 0 & 0\\
-\bar{K}_y & \left(\dfrac{\bar{K}_y\bar{d}^2}{\bar{A}}-\bar{K}_y\bar{A}\right) & -\bar{K}_y\bar{h}_1 & \left(\dfrac{\bar{K}_y\bar{d}^2}{\bar{A}^2}+\bar{K}_y+2K_y\right) & \dfrac{\bar{K}_y\bar{d}^2}{\bar{A}} & \left(\bar{K}_y\bar{h}_1+2K_yh_1\right) & \left(\dfrac{\bar{K}_y\bar{d}^2}{2a\bar{A}}-2K_y\right) & 0 & \left(\dfrac{\bar{K}_y\bar{d}^2}{2a\bar{A}}-2K_y\right) & 0\\
0 & -\bar{K}_y\bar{d}^2 & 0 & -\dfrac{\bar{K}_y\bar{d}^2}{\bar{A}} & \left(\bar{K}_y\bar{d}^2+2K_yd^2\right)+2K_ya^2 & 0 & \left(\bar{K}_y\dfrac{\bar{d}^2}{2a}+K_y\dfrac{d^2}{a}\right) & -K_yd^2 & \left(-\bar{K}_y\dfrac{\bar{d}^2}{2a}-K_y\dfrac{d^2}{a}\right) & -K_yd^2\\
-\bar{K}_y\bar{h}_1 & -\bar{K}_y\bar{A}\bar{h}_1 & -\bar{K}_y\bar{h}_1^2-\bar{K}_y\bar{A}^2 & \bar{K}_y\bar{h}_1 & 0 & K_yh_1^2+\bar{K}_y\bar{A}^2+2K_ya^2 & -2K_yh_1 & 0 & -2K_yh_1 & 0\\
0 & -\dfrac{\bar{K}_y\bar{d}^2}{2a} & 0 & \left(-\dfrac{\bar{K}_y\bar{d}^2}{2a}-2K_y\right) & \left(\bar{K}_y\dfrac{\bar{d}^2}{2a}+K_y\dfrac{d^2}{a}\right) & -2K_yh_1 & \left(\dfrac{\bar{K}_y\dfrac{\bar{d}^2}{4a^2}+K_y\dfrac{d^2}{2a^2}}{+2K_y+W\zeta}\right) & \left(-K_y\dfrac{d^2}{2a}-2\chi C_{22}\Sigma_1\right) & \left(\dfrac{-\bar{K}_y\dfrac{\bar{d}^2}{4a^2}-K_y\dfrac{d^2}{2a^2}}{+2K_y}\right) & -K_y\dfrac{d^2}{2a}\\
0 & 0 & 0 & 0 & -K_yd^2 & 0 & -K_y\dfrac{d^2}{2a}+2e_0C_{11}\dfrac{\gamma_c}{r_0}\sigma_1 & \left(\dfrac{K_yd^2-W\gamma_cf_0}{+2C_{23}}\right) & \dfrac{K_yd^2}{2a} & 0\\
0 & \dfrac{\bar{K}_y\bar{d}^2}{2a} & 0 & \left(\dfrac{\bar{K}_y\bar{d}^2}{2a}-2K_y\right) & \left(-\bar{K}_y\dfrac{\bar{d}^2}{2a}-K_y\dfrac{d^2}{a}\right) & -2K_yh_1 & \left(\dfrac{-\bar{K}_y\dfrac{\bar{d}^2}{4a^2}-K_y\dfrac{d^2}{2a^2}}{+2K_y}\right) & K_y\dfrac{d^2}{2a} & \left(\dfrac{\bar{K}_y\dfrac{\bar{d}^2}{4a^2}+K_y\dfrac{d^2}{2a^2}}{+2K_y+W\zeta}\right) & K_y\dfrac{d^2}{2a}-2\chi C_{22}\Sigma_2\\
0 & 0 & 0 & 0 & -K_yd^2 & 0 & \dfrac{-K_yd^2}{2a} & 0 & K_y\dfrac{d^2}{2a}+2e_0C_{11}\dfrac{\gamma_c}{r_0}\sigma_2 & \left(\dfrac{K_yd^2-W\gamma_cf_0}{+2C_{23}}\right)
\end{bmatrix} \tag{A3}$$

$$\mathbf{b}=\left[\frac{\bar{M}}{4}\gamma_{nc}\quad -\bar{K}_x\bar{d}^2\frac{\bar{A}}{R_c}\quad \frac{\bar{M}}{4}\bar{h}_0\gamma_{nc}\quad \begin{pmatrix}\frac{M}{2}\gamma_{nc}-\bar{K}_x\dfrac{\bar{d}^2}{R_c}\\+2K_yy_0\end{pmatrix}\quad \bar{K}_x\bar{d}^2\frac{\bar{A}}{R_c}\quad \left(\frac{M}{2}h_0\gamma_{nc}+2K_yy_0\right)\quad \begin{pmatrix}(m+\hat{m})\gamma_{nc}+\dfrac{\bar{K}_x\bar{d}^2}{2a}\dfrac{\bar{A}}{R_c}\\-(W\zeta+2K_y)y_0\end{pmatrix}\quad K_xd^2\frac{a}{R_c}\quad \begin{pmatrix}(m+\hat{m})\gamma_{nc}-\dfrac{\bar{K}_x\bar{d}^2}{2a}\dfrac{\bar{A}}{R_c}\\-(W\zeta+2K_y)y_0\end{pmatrix}\quad -K_xd^2\frac{a}{R_c}\right]^T \tag{A40029}$$

Dynamic Behavior of an Aerodynamics Turbine Coupled to a Multiplier Helical Three-Stage Gear

Yassine Driss*, Kamel Abboudi, Moez Bayaoui, Lassaad Walha, Mohamed Maatar, and Mohamed Haddar

Laboratory of Mechanics, Modeling and Production (LA2MP)
Mechanical Engineering Department, National School of Engineers of Sfax,
BP 1173-3038 Sfax, Tunisia
drissyassine@yahoo.fr

Abstract. This paper presents an overall wind turbine model including a helical three stage gear system having twenty eight degree of freedom. First, the excitation of the model is induced by the periodic variation of the mesh stiffnesses and the aerodynamic forces are supposed constant. Then, the calculation of the dynamic response is performed by a step-by-step time integration method (Newmark method). Finally, the variation of the aerodynamic forces is introduced in the model. An analysis of the effects of these forces on the gear system dynamic behavior is then treated.

Keywords: Helical three-stage gear, wind turbine, meshes stiffnesses.

1 Introduction

Generally, a modern wind turbine consists of three main parts: a rotor on a horizontal axis, a nacelle and a tower. The vibrations occurred, in one of these parts, are transmitted to the other by the relative motions between the mechanical components such as shafts, gears, bearings… [1].

In response to internal and external forces, the motion of each component, functions to convert wind energy into electrical energy, is dependent on the nature of those forces and their dynamic characteristics, which are not easy to predict.

Most of the work [2] [3] [4] considers the wind turbine can be modeled by two masses connected to a single rotating shaft on a general-purpose configuration without considering the internal effects like the vibrations caused by the moving work piece and especially the static transmission error, which is the dominant excitation caused by the periodic meshes stiffness fluctuations. Moreover there are other sources of excitation like the aerodynamic torque fluctuations and the electromagnetic torque fluctuations. These force fluctuations in turn cause the frequency variability, because the induction machine will vary with the turning force applied to it.

* Corresponding author.

The aim of the present paper is to investigate the dynamic behavior of a three stage gear system in a typical wind turbine. The numeric results concerning the dynamic response are obtained by using numerical integration algorithm.

2 Aerodynamics Model

In this section, the aerodynamic torque can be determined from the coefficient of power noted Cp. This parameter is the ratio of power actually captured by the rotor blades versus the total kinetic power in the wind passing through the swept area S. The maximum limit for Cp is 0.59 according to Betz's Law, but CP-value is less than 0.59. This difference is due to the assumptions and simplifications that were made by Betz.

Turbine manufacturers usually provide some general background information like Cp vs λ curve. Without giving a specific features to help researchers in the field to calculate the turbine efficiency and its specific design. For this reason, researchers have proposed numerous strategies to find analytical expressions of this curve.

To estimate the aerodynamic power coefficient, [5] [6] are developed an analytical expressions of the power coefficient based on a linear regression model. Another way to calculate Cp that is developed in the work of [7], which takes into account the number of blades and their primary geometric or aerodynamic characteristics (length, sections, etc.).

The power coefficient can be expressed by taking into account the various losses in a wind turbine. There are many different types of loss including profile losses (η_{profil}), end losses (η_{end}), eddy losses ($C_{Pschmitz}$) and blade number losses [7].

The power coefficient can be written as:

$$C_P = C_{PSchmitz}(\lambda)\,\eta_{profil}(\lambda, g)\,\eta_{end}(\lambda, B) \tag{1}$$

Schmitz' theory of losses due to the angular momentum, can be written as:

$$C_{PSchmitz} = \int_0^1 4\lambda\tau^2 \frac{\sin^3\left(\dfrac{2\,\operatorname{atan}\left(\dfrac{1}{\tau\lambda}\right)}{3}\right)}{\sin^2\left(\operatorname{atan}\left(\dfrac{1}{\tau\lambda}\right)\right)}\,d\tau \tag{2}$$

Here τ is the non-dimensional radial position of a wind turbine blade.

$$\tau = \frac{r}{R} \tag{3}$$

The blade tip-speed-ratio' λ ' and the number of slip (slide) 'g' are defined as follows [8]:

$$\lambda = \frac{\Omega R}{V}, \qquad \eta_{profil}(\lambda, g) = 1 - \frac{\lambda}{g} \tag{4}$$

g is the number of slip (slide), with C_L is the lift coefficient and C_D is the coefficient dragged.

$$g = \frac{C_L}{C_D} \tag{5}$$

The differential pressure between the upper and lower surfaces of the blade creates a rotating flow that increase towards the tip. This phenomenon is taken into consideration by this expression:

$$\eta_{end}(\lambda, B) = 1 - \frac{1.84}{B\lambda} \tag{6}$$

B is the number of blades.

Le couple aérodynamique C_{aero} qui s'exerce sur l'arbre lent du capteur éolien :

$$C_{aero} = 0.5\rho_{air} S R C_Q V^2 \tag{7}$$

The torque coefficient C_Q Can Be derived from the power coefficient C_P by:

$$C_Q = \frac{C_P}{\lambda} \tag{8}$$

The thrust coefficient of the wind turbine rotor C_T is modeled is modeled by [9] that is supposed to fit for most of the modern

$$C_T = \frac{7\ c}{V_{hub}} \tag{9}$$

Here c is a constant equal to 1 m/s.

In this study we ignore the wind shear, for this reason V_{hub}=V

The thrust can be written as:

$$F_{axial} = 0.5\rho_{air} C_T S V^2 = 3.5\rho_{air} S V \tag{10}$$

Figure 1 shows the Time signal and the frequency spectrum of the torque input calculated from the above methodology.

3 Model of the Three–Stage Gear System

Three-stage gear system is composed of three trains of gearings. Every train links two blocks. So, the gear system has in totality three blocks (j=1 to 3). Every block (j) is supported by flexible bearing the stiffness of which kxj, kyj, kzj, $k_{\phi j}$ and $k_{\psi j}$ are the traction-compression and the bending stiffness.

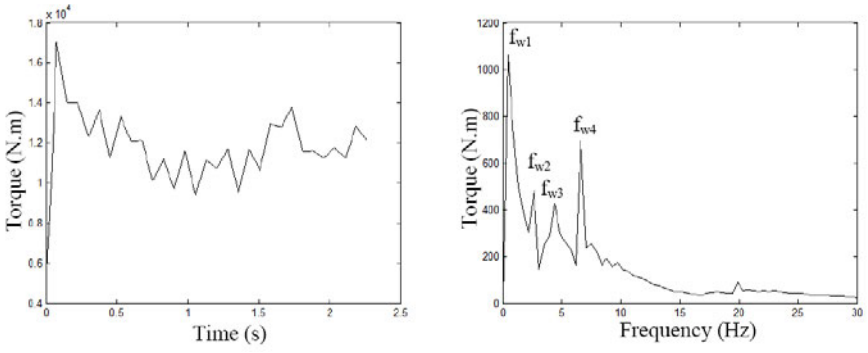

Fig. 1 Time signal and frequency spectrum of the torque

Moreover, the shafts (j) are only submitted to the torsional motion and admit some torsional stiffness kθj. The wheels (11) and (42) characterize respectively the motor side and the receiving machine side which inertias are Im and Ir. The other helical gears constitute the gearbox. The gear meshes are modeled by linear spring along the lines of action (figure 2). xj, yj and zj are supposed the linear displacements of the bearing. The shaft lengths are considered of the same order of the teeth width. Moreover, it is supposed that the shafts mass less.

The mesh stiffness variation ki(t) (figure 2) is modeled by trapezoidal waves that depend on the features of the gearings. It is proportional of the length of contact line [10].

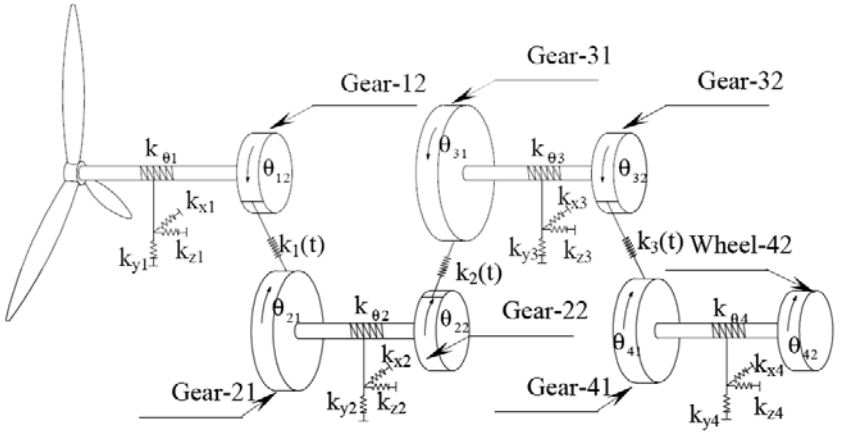

Fig. 2 Dynamic model of the aerodynamics turbine coupled to a helical three stage Multiplier

4 Expression of the Teeth Deflections

The First teeth deflection $\delta_1(t)$ is written as follows:

$$\delta_1(t) = u_1(x_2 - x_1) + u_2(y_1 - y_2) + u_3(z_1 - z_2) + u_4\phi_1 + u_5\psi_1 + u_6\theta_{12} + u_7\phi_2 + u_8\psi_2 + u_9\theta_{21} \quad (11)$$

The second teeth deflection $\delta_2(t)$ is written as follows:

$$\delta_2(t) = v_1(x_2 - x_3) + v_2(y_3 - y_2) + v_3(z_2 - z_3) + v_4\phi_2 + v_5\psi_2 + v_6\theta_{22} + v_7\phi_3 + v_8\psi_3 + v_9\theta_{31} \quad (12)$$

The third teeth deflection $\delta_3(t)$ is written as follows:

$$\delta_3(t) = w_1(x_4 - x_3) + w_2(y_3 - y_4) + w_3(z_3 - z_4) + w_4\phi_3 + w_5\psi_3 + w_6\theta_{32} + w_7\phi_4 + w_8\psi_4 + w_9\theta_{41} \quad (13)$$

The distances p_1 and p_2 are defined as follows:

$$p_1 = Rb_{12}tg\alpha_1 \quad ; \quad p_2 = Rb_{21}tg\alpha_1 \quad (14)$$

The distances p_2' and p_3 are defined as follows:

$$p_2' = Rb_{22}tg\alpha_2 \; ; \quad p_3 = Rb_{31}tg\alpha_2 \quad (15)$$

The distances p_3' and p_4 are defined as follows:

$$p_3' = Rb_{32}tg\alpha_3 \quad ; \quad p_4 = Rb_{41}tg\alpha_3 \quad (16)$$

Rb_{ij} is the basic radius of the wheel j related to block i
The constants u_i, v_i and w_i are calculate by Walha L. and al [11].

5 Equations of Motion

Lagrange formalism leads to the set of differential equations governing for the model. They are expressed in the system of equations (17).

The calculation of the dynamic response is performed by a step-by-step time integration method (Newmark method).

$$
\begin{cases}
m_1\ddot{x}_1 + k_{x1}x_1 - k_1(t)u_1\delta_1(t) = 0 \\
m_1\ddot{y}_1 + k_{y1}y_1 + k_1(t)u_2\delta_1(t) = 0 \\
m_1\ddot{z}_1 + k_{z1}z_1 + k_1(t)u_3\delta_1(t) = 0 \\
m_2\ddot{x}_2 + k_{x2}x_2 + u_1k_1(t)\delta_1(t) + v_1k_2(t)\delta_2(t) = 0 \\
m_2\ddot{y}_2 + k_{y2}y_2 - u_2k_1(t)\delta_1(t) - v_2k_2(t)\delta_2(t) = 0 \\
m_2\ddot{z}_2 + k_{z2}z_2 - u_3k_1(t)\delta_1(t) + v_3k_2(t)\delta_2(t) = 0 \\
m_3\ddot{x}_3 + k_{x3}x_3 - v_1k_2(t)\delta_2(t) - w_1k_3(t)\delta_3(t) = 0 \\
m_3\ddot{y}_3 + k_{y3}y_3 + v_2k_2(t)\delta_2(t) + w_2k_3(t)\delta_3(t) = 0 \\
m_3\ddot{z}_3 + k_{z3}z_3 - v_3k_2(t)\delta_2(t) + w_3k_3(t)\delta_3(t) = 0 \\
m_4\ddot{x}_4 + k_{x4}x_4 + w_1k_3(t)\delta_3(t) = 0 \\
m_4\ddot{y}_4 + k_{y4}y_4 - w_2k_3(t)\delta_3(t) = 0 \\
m_4\ddot{z}_4 + k_{z4}z_4 - w_3k_3(t)\delta_3(t) = 0 \\
(I_{11x}+I_{12x})\ddot{\phi}_1 + k_{\phi1}\phi_1 + k_1(t)u_4\delta_1(t) = 0 \\
(I_{11y}+I_{12y})\ddot{\psi}_1 + k_{\psi1}\psi_1 + k_1(t)u_5\delta_1(t) = 0 \\
(I_{21x}+I_{22x})\ddot{\phi}_2 + k_{\phi2}\phi_2 + u_7k_1(t)\delta_1(t) + v_4k_2(t)\delta_2(t) = 0 \\
(I_{21y}+I_{22y})\ddot{\psi}_2 + k_{\psi2}\psi_2 + u_8k_1(t)\delta_1(t) + v_5k_2(t)\delta_2(t) = 0 \\
(I_{31x}+I_{32x})\ddot{\phi}_3 + k_{\phi3}\phi_3 + v_7k_2(t)\delta_2(t) + w_4k_3(t)\delta_3(t) = 0 \\
(I_{31y}+I_{32y})\ddot{\psi}_3 + k_{\psi3}\psi_3 + v_8k_2(t)\delta_2(t) + w_5k_3(t)\delta_3(t) = 0 \\
(I_{41x}+I_{42x})\ddot{\phi}_4 + k_{\phi4}\phi_4 + w_7k_3(t)\delta_3(t) = 0 \\
(I_{41y}+I_{42y})\ddot{\psi}_4 + k_{\psi4}\psi_4 + w_8k_3(t)\delta_3(t) = 0 \\
I_{11}\ddot{\theta}_{11} + k_{\theta1}(\theta_{11} - \theta_{12}) = C_m \\
I_{12}\ddot{\theta}_{12} - k_{\theta1}(\theta_{11} - \theta_{12}) + u_6k_1(t)\delta_1(t) = 0 \\
I_{21}\ddot{\theta}_{21} + k_{\theta2}(\theta_{21} - \theta_{22}) + u_9k_1(t)\delta_1(t) = 0 \\
I_{22}\ddot{\theta}_{22} - k_{\theta2}(\theta_{21} - \theta_{22}) + v_6k_2(t)\delta_2(t) = 0 \\
I_{31}\ddot{\theta}_{31} + k_{\theta3}(\theta_{31} - \theta_{32}) + v_9k_2(t)\delta_2(t) = 0 \\
I_{32}\ddot{\theta}_{32} - k_{\theta3}(\theta_{31} - \theta_{32}) + w_6k_3(t)\delta_3(t) = 0 \\
I_{41}\ddot{\theta}_{41} + k_{\theta4}(\theta_{41} - \theta_{42}) + w_9k_3(t)\delta_3(t) = 0 \\
I_{42}\ddot{\theta}_{42} - k_{\theta4}(\theta_{41} - \theta_{42}) = -C_r
\end{cases}
\tag{17}
$$

6 Results and Discussion

First, the aerodynamic forces are supposed constant. Consequently, the excitation of the model is induced only by the periodic variation of the mesh stiffnesses.

Figure 3 represents the frequency response of linear displacements resulting on the third bearing. It is clearly noticed the presence of several peaks in every signal. These peaks correspond to the three mesh frequencies fe1= 67 Hz , fe2= 182 Hz and fe3 = 481 Hz with their harmonics.

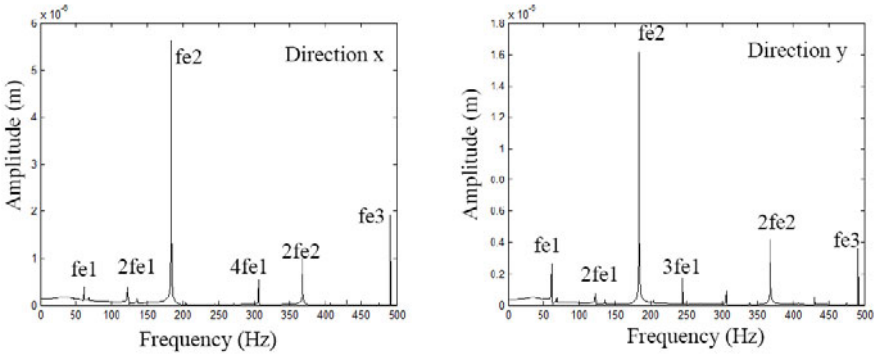

Fig. 3 Frequency dynamic response of the third bearing

Then, the aerodynamic forces variations are introduced in the model. Figure 4 represents the dynamic frequency responses of the third bearing. The existing peaks correspond to the three mesh frequencies fe1, fe2 and fe3 with their harmonics, and the frequencies of the wind f_{wi}. So, we can conclude that the effects of wind are transmitted to the bearings through the intermediary of the gears.

Note that vibration signal plotted as amplitude vs. frequency for each bearing along the direction x, y and z shown below display the same information, but the emphasis is changed.

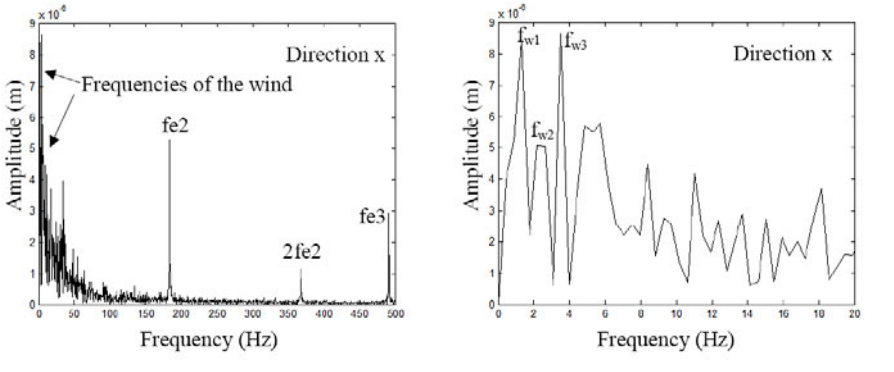

Fig. 4 Frequency dynamic response of the third bearing

7 Conclusion

In this paper, the helical three-stage gear system was modeled by twenty eight degrees of freedom system. In the first time, the dynamic behavior of the three stage gear system was made. A step-by-step time integration method (Newmark algorithm) was used to obtain this dynamic behavior. In the second time, the helical three-stage gear system behavior is affected by the aerodynamic forces variations. The effects of wind are transmitted to the bearings through the intermediary of the gears.

References

[1] Abboudi, K., Walha, L., Driss, Y., Maatar, M., Fakhfakh, T., Haddar, M.: Dynamic behavior of a two-stage gear train used in a fixed-speed wind turbine. Mechanism and Machine Theory 46, 1888–1900 (2011)
[2] Veritas, D.N., Risø: Guidelines for design of wind turbine, 1st edn., p. 65. National Laboratory (2001)
[3] Hartwanger, D., Horvat, A.: 3D medelling of a wind turbine using CFD. In: NAFEMS Conference, United Kingdom (2008)
[4] Gabriele, M., Hansen, A.D., Hartkopf, T.: Variable speed wind turbines – Modeling, Control and Impact on Power Systems. In: European Wind Energy Conference and Exhibition, Brussels (BE) (2008)
[5] Jafari, H.K., Radan, A.: Wind Turbine Model and Maximum Power Tracking Strategy. Wind Turbine-Intech., 593–622 (2011)
[6] Mota, W.S., Barros, L.S.: Dynamic simulations of wind generators connected to distribution systems. In: 18th International Conference on Electricity Distribution (CIRED),
Turin (2005)
[7] Yurdusev, M.A., Ata, R., Çetin, N.S.: Assessment of optimum tip speed ratio in wind turbines using artificial neural networks. Energy 31, 2153–2161 (2006)
[8] Çetin, N.S., Yurdusev, M.A., Ata, R., Özdemir, A.: Assessment of optimum tip speed ratio of wind turbines. Mathematical and Computational Applications 10(1), 147–154 (2005)
[9] Frandsen, S.T.: Turbulence and turbulence-generated structural loading in wind turbine clusters, Risø National Laboratory Report Nr. Risø-R-1188(EN) (2007)
[10] Yakhou, K.: Validation expérimentale d'un modèle dynamique globale de boîte de vitesses automobile, Thèse de l'Institut National des sciences appliquées de Lyon (2002)
[11] Walha, L., Driss, Y., Khabou, M.T., Fakhfakh, T., Haddar, M.: Effects of eccentricity defect on the nonlinear dynamic behavior of the mechanism clutch-helical two stage gear. Mechanism and Machine Theory (46), 986–997 (2011)

Chapter 3
Signal Processing and Pattern Recognition

Modern condition monitoring extensively employs signal processing and pattern recognition techniques. Signal processing is using for both signal enhancement (de-noising, separation, reconstruction, filtering… etc) and feature extraction (parametric models, two dimensional plane representation)

In some cases, damage detection can be performed using simple rules i.e. “if feature_value bigger than threshold than damage else undamaged” however when consider complex mechanical systems, especially in time varying conditions, problem of classification of features becomes much complicated. In such a case, feature selection procedures are proposed and advanced data classifiers are used. In this chapter mentioned issues are addressed.

Gearbox Fault Diagnosis Using Time-Wavelet Energy Spectral Analysis

Jin Zhang[1], Zhipeng Feng[2], Zhaoye Qin[1], and Fulei Chu[1]

[1] Department of Precision Instruments and Mechanology, Tsinghua University, Beijing 100084, China
Zhangjin08@tsinghua.org.cn, {qinzy,chufl}@mail.tsinghua.edu.cn
[2] School of Mechanical Engineering, University of Science and Technology Beijing, Beijing 100083, China
zhipeng.feng@yahoo.com.cn

Abstract. The impulses in vibration signals and their spectral features are the key indicators for diagnosing localized gear damage. A new method, called time-wavelet energy spectrum, is proposed to extract the characteristic frequency of faulty gears. The analysis of gearbox experimental signals show that the time-wavelet energy spectrum can highlight impulses, and is effective in extracting the repeating frequency of periodic impulses. It cannot only extract the relatively significant fault feature of gear tooth missing, but also can extract the weaker fault features of gear tooth wear.

Keywords: gearbox, fault diagnosis, wavelet transform, time-wavelet energy spectrum.

1 Introduction

Gearbox fault diagnosis is a main topic in the field of machinery fault diagnosis. So far, many techniques have been proposed for gear fault diagnosis, such as cepstrum, envelope spectrum, and time domain synchronous average, etc [1-4]. However, in engineering applications, it is not easy to extract the fault features from gearbox vibration signals, due to the complicated signal components and the background noise interferences [5, 6].

A large percentage of gear faults are induced by localized gear damage, like pits, chips, and cracks on gear tooth surface which eventually result in tooth breakage. Such damage usually generate periodic impulses in the vibration signals during the running of damaged gears, with the period of impulse train depending on the number of damaged teeth and their distribution over the gear. In a word, periodic impulses characterize the vibration of damaged gears, and provide an intuitively understandable indicator of localized damage. Hence, how to extract impulses from vibration signals is a key issue for gear damage detection and location.

In time-frequency domain, the energy of an impulse concentrates in a narrow rectangular area (which tends to be a line) vertical to the time axis whereas parallel to the frequency axis. This characteristic is useful to identify the periodic impulse train induced by gear damage, and thereby to detect and locate the damage [5]. In most cases, the feature of an impulse train is weak even in time-frequency domain due to background noise interferences. Thus, how to extract the periodicity of impulse train in time-frequency domain is a key issue. This paper addresses this issue by exploiting the merit of wavelet transform in detecting transient phenomena and that of Fourier transform in revealing the periodicity of signals.

2 Time-Wavelet Energy Spectrum

2.1 Principle

Our idea of time-wavelet energy spectral analysis is inspired by the energy distribution property of impulses on time-frequency plane. The energy of an impulse spans over a wide frequency band and localizes at the time instant when it occurs, thus concentrating in a very narrow rectangular area vertical to the time axis whereas parallel to the frequency axis. If we integrate the time-frequency energy distribution of an impulse train along the frequency axis, the derived time-evolving energy is expected to show peaks at the instants when an impulse occurs.

In an ideal case without any interference, we can identify the repeating period of impulse train according to the time interval between adjacent peaks in the time-evolving energy waveform. However, in most cases, it is difficult to do so, because background noise often coexists with and thus weaken the feature of impulses induced by gear damage. In such cases, to reveal the repeating frequency of an impulse train, we apply Fourier transform to the derived time-evolving energy, by exploiting its function in extracting the periodicity of signals.

Wavelet transform is effective in detecting transient components in signals, so we use it to do time-frequency analysis, and we name the finally derived Fourier spectrum of time-evolving energy as time-wavelet energy spectrum.

2.2 Wavelet Transform

For a signal of limited energy $x(t)$, its wavelet transform is defined as

$$W(a,t) = \frac{1}{\sqrt{a}} \int_{-\infty}^{\infty} x(\tau)\psi(\frac{\tau - t}{a})\mathrm{d}\tau \tag{1}$$

where $\psi(t)$ is the wavelet basis, τ the time shift, and a the scale.

The energy conservation property of wavelet transform states that

$$\int_{-\infty}^{\infty} |x(t)|^2 \, \mathrm{d}t = \int_{-\infty}^{\infty} E(t)\mathrm{d}t = \frac{1}{C}\int_{-\infty}^{\infty}\int_{-\infty}^{\infty} \frac{1}{a^2} |W(a,t)|^2 \, \mathrm{d}a\mathrm{d}t \tag{2}$$

where

$$C = \int_{-\infty}^{\infty} \frac{1}{|\omega|} |\hat{\psi}(\omega)|^2 \, \mathrm{d}\omega < \infty \tag{3}$$

and $\hat{\psi}(\omega)$ is the Fourier transform of the wavelet basis $\psi(t)$.

From Eq. (2), the instantaneous energy of the signal at any instant t can be derived as

$$E(t) = \int_{-\infty}^{\infty} \frac{1}{a^2} |W(a,t)|^2 \, \mathrm{d}a \tag{4}$$

It equals the integral of squared modulus of wavelet transform over scale, namely the integral of wavelet scalogram along the frequency axis, so it is called time-wavelet energy in this paper.

Among various types of wavelet basis, Morlet is commonly used in many applications. It is defined as

$$\psi(t) = \frac{1}{\sqrt[4]{\pi}}[\exp(-j\omega_0 t) - \exp(-\frac{1}{2}\omega_0^2)]\exp(-\frac{1}{2}t^2) \tag{5}$$

When $\omega_0 \geq 5$, the second exponential term in the square bracket tends to be zero, then Morlet can be simplified as

$$\psi(t) = \frac{1}{\sqrt[4]{\pi}}\exp(-j\omega_0 t)\exp(-\frac{1}{2}t^2) \tag{6}$$

Eq. (6) shows that Morlet is a squared exponentially decaying function [7, 8]. Its waveform well matches the characteristics of a damped impulse vibration. So it is used to extract transient phenomena and especially the impulse characteristic of gear damage in this paper.

3 Gearbox Vibration Signal Analyses

3.1 Specification of Gearbox Experiment

The gearbox experiments are conducted on a SpectraQuest test rig as shown in Fig. 1. The motor drives the gearbox through a power train which is composed of shaft 1, a convey belt (transmission ratio 2.5), and shaft 2. No load is applied to the gearbox. The parameters of the drive gear 1 and driven gear 2 are listed in Table 1.

An accelerometer is mounted on top of the gearbox casing. During the experiment, the motor runs at a stable speed of 1000 rpm. The vibration signals are collected at a sampling frequency of 6400 Hz.

Three statuses of the gearbox are simulated. In the normal case, both gear 1 and gear 2 are perfect. In faulty case 1, one tooth of gear 1 is missing (see Fig. 2 (a)), whereas gear 2 is perfect. In faulty case 2, one tooth of gear 1 is worn (see Fig. 2 (b)), whereas gear 2 is perfect.

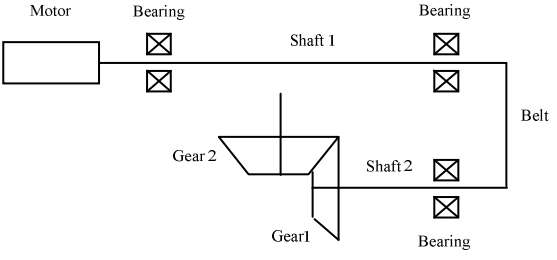

Fig. 1 Schematic diagram of gearbox test rig

Table 1 Gearbox parameters

Values list	Gear 1	Gear 2
Number of gear teeth	18	27
Rotating frequency (Hz)	6.667	4.444
Meshing frequency (Hz)	120	

(a) (b)

Fig. 2 Tooth damage of gear 1: (a) tooth missing, and (b) tooth worn

3.2 Signal Analysis

For comparison study, we firstly analyze the normal gearbox vibration signal. Fig. 3 shows its waveform, Fourier spectrum and time-wavelet energy spectrum. The maximum peak in the Fourier spectrum appear at 100 Hz equal to twice the electrical power frequency, and it also exists in the following faulty cases, thus we do not consider it in our analysis. In the time-wavelet energy spectrum, the first two biggest peaks at 116 Hz and 233 Hz correspond approximately to the meshing frequency and its second harmonic.

Next, we analyze the vibration signal of tooth missing case to illustrate the effectiveness of time-wavelet energy spectrum in diagnosing gearbox fault. Fig. 4 shows the analysis result. There are significant impulses in the vibration signal waveform, repeating at a frequency of 6.4 Hz corresponding approximately to the rotating frequency of gear 1. This indicates that gear 1 is faulty. However, the Fourier spectrum has a similar structure to that of the normal gearbox. Therefore, we cannot detect the tooth missing fault based on traditional Fourier spectral analysis, even though the gear fault is severe. In the time-wavelet energy spectrum, many significant peaks appear, and they correspond to the rotating frequency of gear 1 and its higher order harmonics. In particular, sidebands appear around 119 Hz equal approximately to the meshing frequency of with a spacing of 6.4 Hz close to the rotating frequency of gear 1. These findings indicate that gear 1 is faulty, and the time-wavelet energy spectrum is more effective in extracting gear fault symptom than the conventional Fourier spectrum.

Finally, we analyze the signal of tooth wear case to show the performance of time-wavelet energy spectrum in extracting the symptom of weak gear faults. Fig. 5 shows the analysis result. Compared with gear tooth missing, tooth wear is a slight fault, so the vibration signal does not show significant difference from that of normal case, either in time domain or frequency domain. Therefore, we cannot detect the gear tooth wear by traditional waveform or Fourier spectral analysis. However, more harmonics of meshing frequency appear in the time-wavelet energy spectrum than that of the normal case. This characteristic indicates that the gearbox is faulty. To locate the gear fault, we zoom in the time-wavelet energy spectrum around the meshing frequency. Sidebands appear around the meshing frequency, and their spacing of 6.4 Hz equals approximately the rotating frequency of gear 1, indicating that gear 1 is faulty. These findings show that the proposed time-wavelet energy spectrum is able to detect and locate weak gear fault.

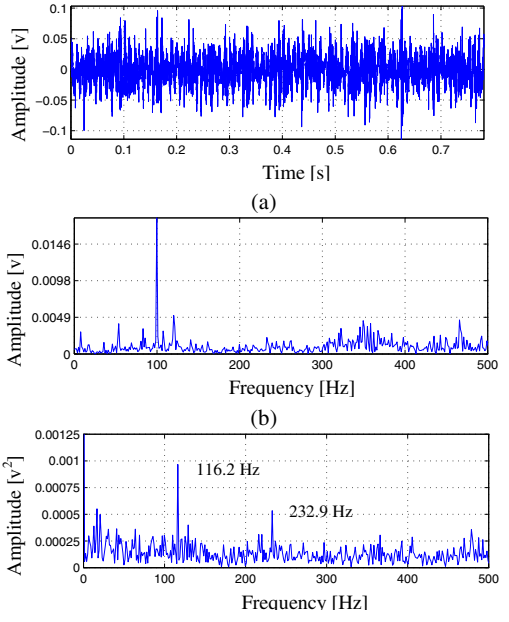

Fig. 3 Normal: (a) waveform, (b) Fourier spectrum, and (c) time-wavelet energy spectrum

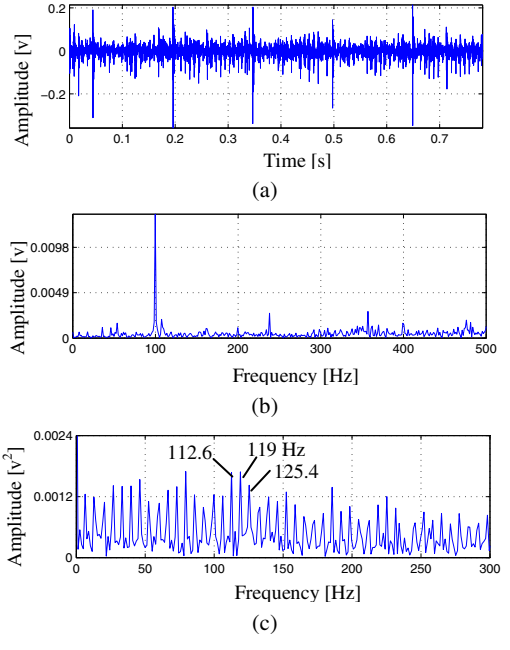

Fig. 4 Tooth missing: (a) waveform, (b) Fourier spectrum, and (c) time-wavelet energy spectrum

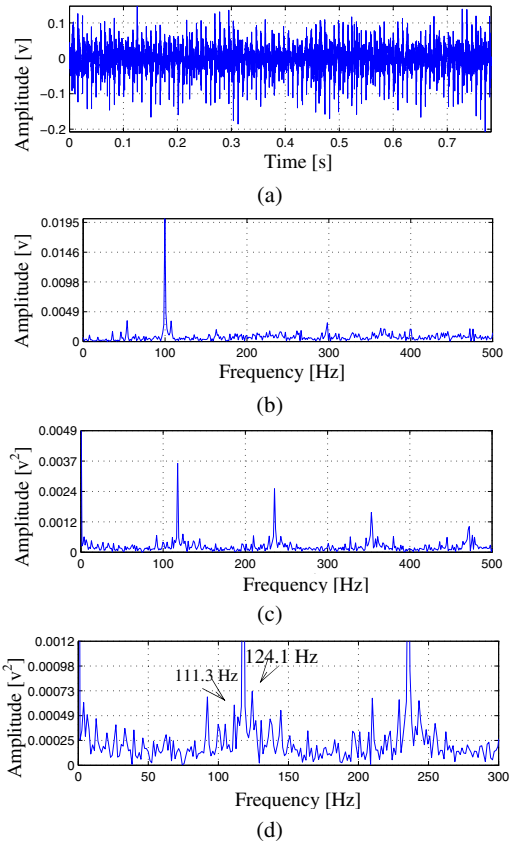

Fig. 5 Tooth worn: (a) waveform, (b) Fourier spectrum, (c) time-wavelet energy spectrum, and (d) zoomed-in time-wavelet energy spectrum

The above analysis results are all consistent with the experimental settings. It shows the effectiveness of the time-wavelet energy spectrum in detecting and locating gear faults, especially the good potential in extracting the symptom of weak gear faults.

4 Conclusions

In order to extract the periodicity of impulse train induced by gear damage, we propose a new method called time-wavelet energy spectrum. It can highlight the impulses induced by gear damage, and thereby we can detect and locate gear fault by matching the spectral peaks with the gear fault characteristic frequency. We

validate the proposed method using gearbox experimental vibration signals. The analysis results show that the method is effective not only in diagnosing severe gear fault, but also in extracting the symptom of weak gear fault. In the future, we will validate this method using industrial gearbox vibration signals.

Acknowledgements. This work is supported by National Natural Science Foundation of China (51075224, 51075028) and Tsinghua University Research Project.

References

[1] Randall, R.B.: A new method of modeling gear faults. J. Mech. Design 104, 259–267 (1982)
[2] Randall, R.B.: Cepstrum analysis and gearbox fault diagnosis. Maint. Manage. Int. 3, 183–208 (1982)
[3] McFadden, P.D.: Detecting fatigue cracks in gears by amplitude and phase demodulation of the meshing vibration. ASME J. Vib. Acoust. 108, 165–170 (1986)
[4] McFadden, P.D.: Interpolation techniques for time domain averaging of gear vibration. Mech. Syst. Signal Pr. 3, 87–97 (1989)
[5] Feng, Z.P., Chu, F.L.: Application of atomic decomposition to gear damage detection. J. Sound Vib. 302, 138–151 (2007)
[6] Feng, Z.P., Zuo, M.J., Hao, R.J., Chu, F.L.: Gear damage assessment based on cyclic spectral analysis. IEEE T. Reliab. 60, 21–32 (2011)
[7] Mallat, S.: A Wavelet Tour of Signal Processing: The Sparse Way. Academic Press, San Diego (2009)
[8] Daubechies, I.: Ten Lectures on Wavelets. SIAM, Philadelphia (1992)

Numerical Investigations on the Magnitude of Disturbance That Could Be Detected through IAS* Monitoring

Bourdon Adeline[1], André Hugo[2], and Rémond Didier[1]

[1] LaMCoS, Campus Lyon Tech la Doua, Insa de Lyon, Bâtiment Jean d'Alembert – 18-20 rue des Sciences-69621 Villeurbanne cedex, France
{adeline.bourdon,didier.remond}@insa-lyon.fr
[2] Maia Eolis, Tour de Lille, Boulevard de Turin, Lille, 59000, France
handre@maiaeolis.fr

Abstract. The aim of this paper is to use a numerical model to estimate the minimum amplitude of a localized and angularly periodic perturbation which should be detected through the analysis of Power Spectral Density (PSD) of Instantaneous Angular Speed (IAS). To that purpose, a numerical torsional model of a test bench is developped. Particular attention is paid to precise introduction of this perturbation in the numerical device. It is modelled in the angular domain as a half sinus without any loss of generalization. The main results is that perturbation with a magnitude 300 times lower than the friction bearing torque should be detected through the analysis of the PSD of IAS for a representative inertia.

Keywords: Instantaneous Angular Speed, Angular Approach, Non Stationary, Numerical angular model.

1 Introduction

Experimental measurements performed on rotating systems have shown that the presence of certain mechanical defects, such as bearing faults, is detectable on measurements of Instantaneous Angular Speed (IAS). It seems reasonable to attribute this variation of angular velocity to a variation of external torque ΔTp further reffered to the disturbance. As the purely experimental approach gives some surprising sensitivity results but does not allow to investigate the potential of this disturbing torque, a numerical approach is proposed in this paper. Consequently, a numerical model of a test bench is proposed and used to determine the minimum amplitude of the disturbance T_p so that its effects are detectable on the Power Spectral Density (PSD) of IAS measurements.

* IAS: Instantaneous Angular Speed.

2 Models and Simulations

The mechanical system considered is the shaft of a test bench under construction (Fig. 1). This bench is designed to allow finer investigations on the relationship between bearing faults and the consequences on the IAS measurement. It consists of a shaft supported by two tapered roller bearings that may present defects. This shaft is driven in rotation by an electrical motor providing torque T_M. An optical encoder measuring the rotational speed is located at the other end of the shaft. A disc of inertia Io, not presented in Figure 1, can be introduced. A radial loading device is made using a knuckle and springs. An axial preload can be introduced through a Belleville washer.

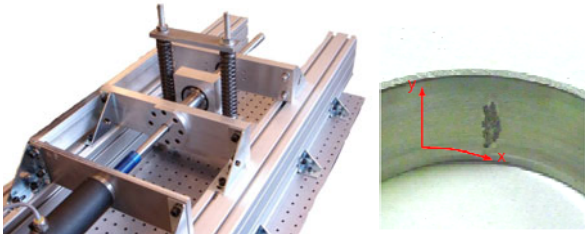

Fig. 1 Test bench modeled and example of bearing outer ring with fault.

A simplified dynamic model of this device is made using 10 torsional beam elements. An equivalent viscous dampers C_{ei} representative of external damping (bearings, knuckle, ...) are also introduced. Disturbing torque T_p can be introduced at one bearing node (dof #4). A schematic representation of this model is given in the following figure.

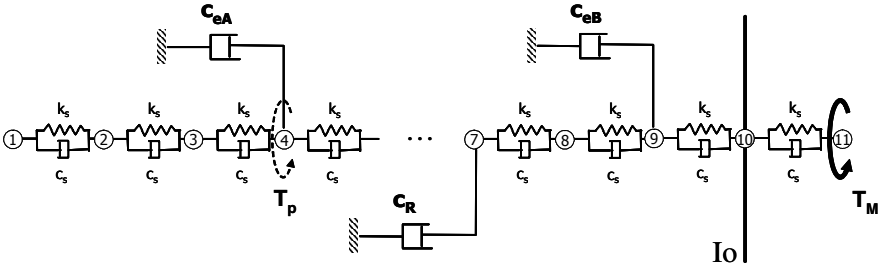

Fig. 2 Torsional model definition.

Elementary torsional stiffness is $k_s = 6.3 \times 10^4$ Nm/rad, the elementary inertia $I_s = 5.08 \times 10^{-6}$ Kg.m^2. The structural damping c_s was set at 0.0036 Nms/rad, which corresponds to 0.66% of critical damping. The damping coefficients of bearings and knuckle are estimated from the moments of friction provided by SKF [2] for

these types of bearings. Let $C_{eA} = C_{eB} = 1.1x10^{-2}$ Nms / rad for taper rolling bearings and $CR = 7.9x10^{-3}$ N.ms / rad for the knuckle. The 3 first eigenmodes of this system are defined in next table:

Table 1 First Eigenmodes of device

Eigenvalue (rad/s)	$1.102x10^4$	$3.33x10^4$	$5.66x10^4$
Modal damping	0.0073	0.0034	0.0041

The disturbance considered in this document is intended to be representative of the presence of a localized fault on a rotating system. It is characterized by its angular period θ_o and its angle length L_θ assumed to be small. The choice was made to model it as a half sine of amplitude Q, but obviously other shapes can be imagined. However, Dirac pulses do not seem relevant because they are not representative of physical reality and lead to numerical instabilities. Fig. 3 shows the different parameters used for disturbance modeling.

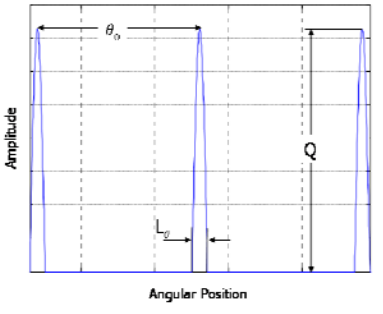

Fig. 3 Parameter definition of the disturbance modeling.

The numerical solution is achieved using an angular approach extension of the methodology proposed previously to multi-DOF models. At the end of the numerical calculation the following quantities are obtained:

-a vector $\{\theta_c\}$ of angular positions of the "sensor" dof (dof#1),
-a time vector $\{T_c\}$ corresponding to the instants of calculation.

The following post-processing is applied to obtain a vector $\{\omega_m\}$of Instantaneous Angular Speed (IAS) comparable to those measured. Let R be the resolution of the encoder and let F_c the clock's frequency.

Step 1: Definition of angular positions corresponding to sampling angles:

$$\{\theta_e\} = \{0 \quad \Delta\theta \quad 2.\Delta\theta \quad \cdots\} \quad \text{with} \quad \Delta\theta = \frac{2\pi}{R} \tag{1}$$

Step 2: Estimation of elapsed time $\{T_e\}$ when the angular positions $\{\theta_e\}$ are reached. This step is done by linear interpolation of time at the angular sampling positions $\{\theta_e\}$ from the values of $\{T_c\}$ computed at positions $\{\theta_c\}$.

Step 3: Calculation of time "measured" by the counting method1:

$$T_{mi} = \langle T_{ei}.F_c \rangle . \frac{1}{F_c} \tag{2}.$$

Step 4: Calculation of time differences τ between two sampling angular positions:

$$\tau_m(i\Delta\theta) = \tau_m(\theta_{ei}) = \tau_{mi} = T_m(\theta_{ei}) - T_m(\theta_{ei-1}) \tag{3}$$

Step 5: Calculation of average angular speed on each angular interval $[\theta_{i-1}\ \theta_i]$:

$$\omega_{mi} = \frac{2\pi}{R.\tau_{mi}} \tag{4}$$

The sets of values $\{\tau_m\}$ and $\{\omega_m\}$ are then comparable to values obtained from experimental measurements. These signals are then analyzed using dedicated processing tools comparable to those used on the experimental signals: Hanning windowing, angular FFT.

3 Investigations on the Magnitude of the Disturbance

The aim of this part is to estimate the minimum amplitude of the disturbance that leads the variations in rotating speed to be detected by the Power Spectral Density (PSD) of Instantaneous Angular Velocity. Three operating conditions are simulated:

- **A**: Constant input torque : T_{M1}= 2.04 N/m, leading to constant rotating speed $\omega 1$ = 68 rad/s,
- **B**: Constant input torque : T_{M2}= 7.1 N/m, leading to constant rotating speed ω_2 =237.5 rad/s,
- **C**: Input torque varying linearly : T_{M3} = To + 0.5t, leading to varying speed between ω_{3_1} = 68 rad/s and ω_{3_2} =239.5 rad/s.

For all simulations, the angular period θ_o and angular width L_θ of the disturbance are set to θ_o= 0.86 rad and L_θ=0.127 rad. That leads to a cyclic frequency of 7.3 even/rev (event per revolution). Simulations are made of 250 shaft revolutions and therefore lead to cyclic frequency resolution of 0.004 even/rev, thus ensuring that the harmonics of the disturbance are located on exact channels in the PSD calculation.

[1] Where <x> is the function that rounds x to the higher integer.

3.1 Simulations with No Fault (Q=0)

To get a reference to determine the smallest amplitude of the perturbation that can be detected through IAS measures, a first serie of simulations is performed for a device without defects (Q = 0). Resulting PSD are ploted in fig 4.

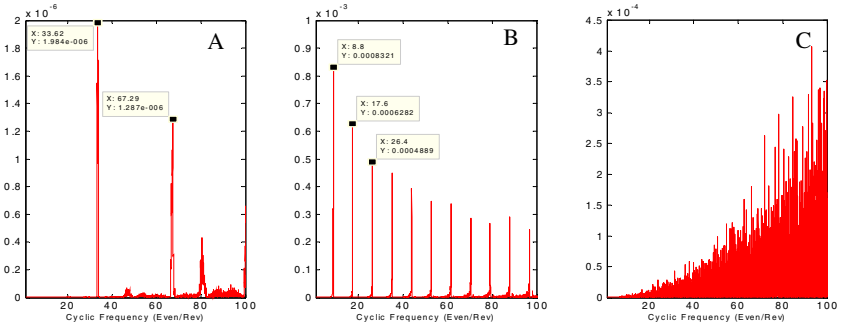

Fig. 4 PSD of IAS with no fault

The previous figure shows the existence of noise even in numerical simulations. This noise is the superposition of the noise associated with numerical resolution methods and the measurement noise associated with the counting method used to estimate IAS. In the case of a steady speed, the measurement noise results in the appearance of harmonics in the PSD without mechanical meaning. Those amplitudes can be very large. These harmonics are named artifacts. The position and amplitude of these artifacts are very sensitive to the value of speed as shown on fig. 5.

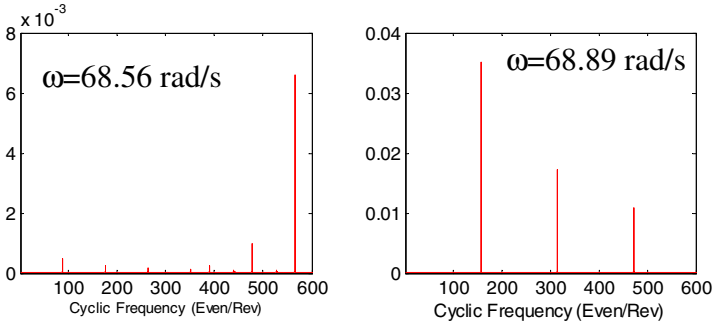

Fig. 5 Influence of rotating speed value on artifacts due to measurement method

3.2 Simulations with Fault

Figures 6, 7, 8 present the PSD of IAS computed with disturbance of magnitude respectively $1.0x10^{-6}$ N.m, $1.0x10^{-5}$ N.m, $1.0x10^{-3}$ N.m.

In the first case, consequence of the disturbance on the PSD can not be detected accurately as noise and artifacts are still important. For simulation B, only the 6th harmonic of the disturbance, located at 43.8 even/rev, emerges clearly. In this analysis, it is interesting to notice that the first eigenmode (1.102×10^4 rad/s) for a steady rotating speed of 237.45 rad/s, stands at 46.4 even/rev. Conversly, peaks at 94.54 even/rev (case A) and 58.83 even/rev (case B) have no obvious mechanical meaning.

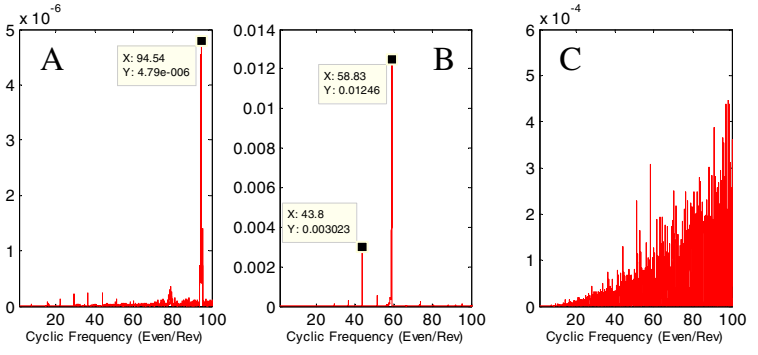

Fig. 6 PSD of IAS in case of fault with magnitude $Q=1.0 \times 10^{-6}$ N.m

The effects of a perturbation with an amplitude of 1.0×10^{-5} N.m, 10 times higher than in the previous case, can be detected on the PSD of instantaneous velocities as shown in fig.7. However this result must be analysed with the operating conditions. Indeed, for a stationary low-speed, 68 rad/s (case A), amplitudes of the harmonics of the disturbance are low and measurement artifacts are mixed with them. In the other hand, PSD obtained for the highest stationary speed (case B) shows harmonics with the higher levels and here again amplitude of the 6th harmonic of the perturbance is the highest due to the vicinity of the first eigenmode.

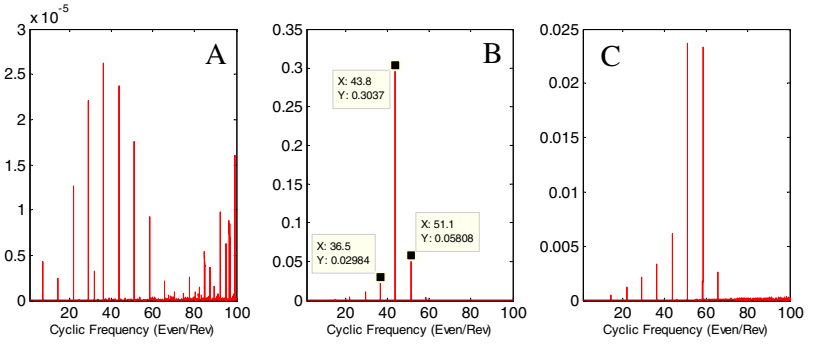

Fig. 7 PSD of IAS in case of fault with magnitude $Q=1.0 \times 10^{-5}$ N.m.

For larger magnitude of disturbance, $1.0x10^{-3}$ N.m, effects appears clearly on both simulations (Fig. 8.) but number and amplitude of harmonics depend largely on operating conditions.

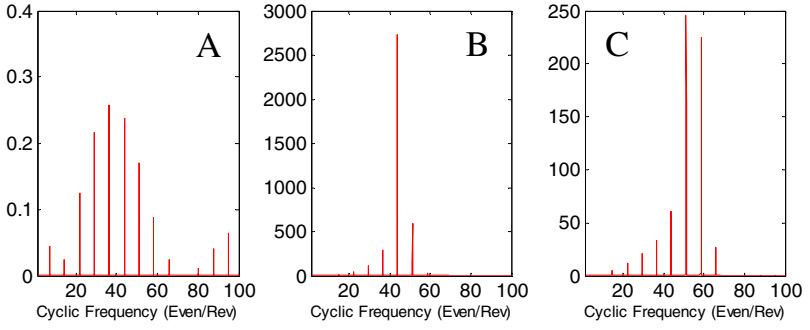

Fig. 8 PSD of IAS in case of fault with magnitude $Q=1.0x10^{-3}$ N.m.

3.3 Analysis

Early studies show that the presence of a fault leading to a disturbing torque with amplitude greater than $1.0x10^{-5}$ Nm are detectable through the IAS measuremets. The amplitude of this torque is low compared with other torques present in the mechanism: driving torque between 2 and 10 Nm and friction bearing torque close to $3.0x10^{-3}$ Nm. This finding is consistent with the hypothesis, made a priori, that the disturbances induced by mechanical faults such as bearing spalls have low amplitudes. This work enlightens the needs to perform studies aiming a better understanding of the relationship between the existing defect and its influence over the IAS measurements.

Moreover, these simulations confirm that the only study of the amplitude peaks in the PSD cannot be an indicator of the evolution of a fault. Indeed, the simulations clearly show the influence of operating condition and of the first torsional mode on the amplitudes of the harmonics of the disturbance on the PSD of the IAS signal.

4 Conclusion

The numerical approach presented in this paper completes the experimental ones that have demonstrated the usefulness of the IAS measurements and of the use of angular approaches to monitor rotating mechanical systems. Although the torsional model proposed is simplistic, it brings the theoretical confirmation to argued experimental findings such as the ability of IAS analysis to detect low or very low speed variations. Futhermore, this model can establish the link between the amplitude of a disturbance related to the presence of a mechanical defect and its

signature on the PSD of the IAS. It appears that the consequence of fault on the IAS is detectable even with very low magnitude of the disturbance regarding other mechanical characteristics like inertia. Of course, the increase in the magnitude of the disturbing torque results in an increase in the amplitude of the peaks of the PSD. Harmonic peaks emerge clearly of the measurement noise if the magnitude of the disturbing torque is important. But the reverse is not true as a change in amplitude of a harmonic of the cyclic frequency may also reflect a change in the modal contributions related to ranges of rotating speed variations.

It also appears that in case of very small perturbation noise is important in the PSD of IAS. Large part of this noise is due to the method used for measuring rotating speed. In case of constant speed, this method creates, in the PSD, artifacts that may have large amplitudes, but without any mechanical meaning. Such artifacts might not appear in experimental measurements as an actal constant speed does not exist, but will surely appear in numerical simulations and must be kept in mind for accurate analysis.

All these results and finalization of the previously mentioned test bench opens the door to numerous works for, hopefully, a better understanding of the nature of the disturbances resulting from the presence of a mechanical defect in rotating machines. In this aim , it will be necessary to refine the proposed model, in particular concerning damping characteristics.

References

Journal Article

Renaudin, L., Bonnardot, F., Musy, O., Doray, J., Rémond, D.: Natural rollerbearing fault detection by angular measurement of true instantaneous angular speed. Mechanical Systems and Signal Processing 24(7), 1998–2011 (2010)

Bourdon, A., André, H., Rémond, D.: A new way of writing motion equations in rotating machines by translation into the angular domain. In: Proceedings of the 8th IFToMM International Conference on Rotordynamics, KIST, Seoul, Korea, September 12-15 (2010)

André, H., Bourdon, A., Rémond, D.: On the use of the Instantaneous Angular Speed measurement in non stationary mechanism monitoring. In: Proceedings of the ASME 2011 International Design Engineering Technical Conferences & 23rd Biennal Conference on Mechanical Vibration and Noise IDETC/CIE2011, Washington, DC, USA (2011)

Online Document

`http://www.skf.com/skf/productcatalogue/calculationsFilter?lang=fr&newlink=&prodid=&action=Calc5`

Time-Frequency Analysis Techniques Review and Their Application on Roller Bearings Prognostics

Mohamed Boufenar[1], Said Rechak[2], and Mohamed Rezig[1]

[1] Nuclear Research Center of Draria, Algiers, Algeria
boufmed@hotmail.com, mohrezig@yahoo.fr
[2] National Polytechnic School, Department of Mechanical Engineering, Algiers, Algeria
saidrechak@gmail.com

Abstract. The purpose of this review work is to present a summary about the application of the time-frequency analysis techniques for roller bearings condition monitoring. For roller bearings, periodic impulses indicate the occurrence of faults in the components. However, it is difficult to detect the impulses because they are noisy and rather weak. Unfortunately, the FFT-based methods are not suitable in this case because they are not able to reveal the inherent information of non-stationary signals. In order to suppress any undesired information and highlight the features of interest and because of the disadvantages of the FFT analysis, it is necessary to find supplementary methods for non-stationary signal analysis. Time-frequency analysis is the most popular method for the analysis of transient signals. The objective of the present work is to study, compare and modify the time-frequency representation techniques such as: Short Time Fourier Transform (STFT), Wigner–Ville Distribution (WVD) and Wavelets which can be used to analyses non-stationary phenornena.

Keywords: Time-frequency, Wavelet, de-noising, roller bearings, Morlet wavelet.

1 Introduction

The initial appearance of a defect in a machine can produce transient phenomena in the vibration signal. Passage of a ball over a localized defect in a bearing, contact of a damaged tooth with other teeth in the gearbox, and piston slap in the engine are examples of well-known industrial problems generating transient events. Frequency domain vibration analysis methods, such as the power spectrum, average the transient events so that they do not appear clearly in the spectral lines. Time domain methods which are also used to analyse transitory signals, can loose the frequency information of different machine components. Thus, it appears, therefore, that it is necessary to employ a new technique which would combine frequency information with amplitude changes in time. Therefore, rather than

separate observation of the time from observation of the frequency characteristics of a signal, it is necessary to use a joint time-frequency (TF) techniques. The earliest time-frequency method is known as the Spectrogram or Short Time Fourier Transform (STFT). In recent years, various TF techniques, such as the Wigner-Ville Distribution and Wavelet transforms, have been developed in the signal processing field. In this paper, the theory of the time-frequency methods is briefly explained and some practical examples of simulated signal and defective bearing are analyzed. In conclusion, the effectiveness and advantages of each method are demonstrated. Furthermore, as an application of wavelets, a de-noising technique has been developed to remove noise from signals. Because, the performance of traditional wavelet decomposition based de-noising methods is greatly impacted by relative energy levels of signal coefficients and white noise coefficients. The wavelet threshold de-noising techniques introduced earlier are all based on orthogonal wavelet transforms and assume that the property of the noise is known, that is, the noise is Gaussian. These techniques do not utilize any information regarding the signal to be identified. When dealing with smooth signals, satisfactory results can generally be achieved by manipulating the threshold (Neumann and Sachs 1995). The underlying reason is because with smooth signals, a small number of large coefficients can characterize the original signal and the transient components that vary rapidly are treated as noise. These de-noising techniques are not suitable for vibration signal analysis from roller bearings because the impulses to be isolated are not smooth. Therefore, it is much more challenging to de-noise impulse series signals where wavelet coefficients are not so concentrated.

2 Simulation and Experimental Procedure

The impulses generated by mechanical damaged of a roller bearing often exhibit the shapes shown in Fig. 1. The signal shown in Fig. 2 which is artificially corrupted by Gaussian noise is used to test the effectiveness of the proposed method. We wish to extract weak periodical impulses from the vibration signals with heavy background noise. Furthermore, to investigate the effectiveness of time-frequency methods a series of vibration signals collected from a test rig were analyzed for detecting faults. Vibration signals are collected from accelerometer mounted on the bearing housing. Starting from the undamaged condition, artificial defects (pits of approximately 1 mm and 2 mm wide) were introduced to the bearings. Time and spectral amplitude representing the effect of the crossing of the balls over artificial spalls are presented in Fig. 3, and Fig. 4. On the grounds of these observations, it appears clear that the effectiveness of the spectral analysis for the bearing diagnostics proves inadequate to operate correct monitoring.

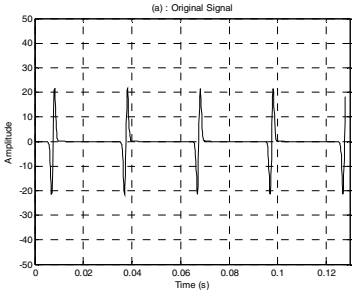

Fig. 1 Simulated impulses

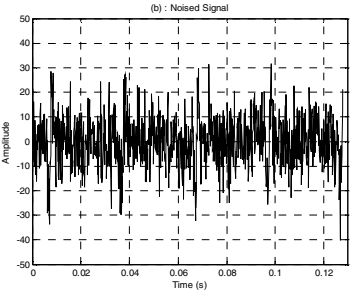

Fig. 2 Simulated impulses with heavy Gaussian noise l

The bearing faults cannot be diagnosed with certainty since spectra provide peaks, located at the fault characteristic frequencies, whose amplitudes are comparable to the corresponding ones related to the bearing in sound condition. Noise prevails over the effect of periodic impulses.

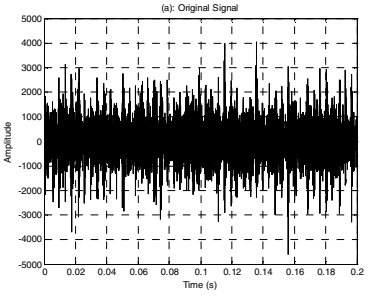

Fig. 3 Vibration signal with small defect on outer raceway

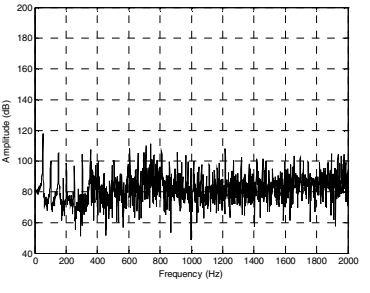

Fig. 4 Power spectrum of the signal

3 Short-Time Fourier Transform (STFT)

The Short-Time Fourier Transform (STFT) is the fastest and the easiest method in terms of its implementation and the visual representation of the results. The STFT may be considered a method that breaks down the non-stationary signal into many small segments which can be assumed to be locally stationary, and applies the conventional FFT to these segments. The STFT of a signal $x(t)$ is achieved by multiplying the signal by a window function, $h(t)$, centered at 't', to produce a modified signal.

$$F(f,b) = \int_{-\infty}^{\infty} x(t)h(t-b)e^{-i(2\pi f)t}dt \quad (1)$$

Fig. 5 and Fig. 6 shows, respectively, STFT with different width of window $h(t)$,of the signal composed of a train of impulses and the same signal artificially corrupted by Gaussian noise. Both spectrograms were calculated using rectangular window. The spectrograms give a relatively good description of the signal behaviour in both cases. However, a great difference of time-frequency localization in the STFT representation of the signal is apparent if the width of the window is changed. The bandwidth limitation imposed by the window function mean that if we want to get better resolution in time we must sacrifice resolution in frequency and vice versa.

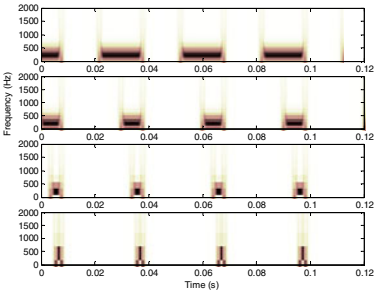

Fig. 5 STFT of simulated impulses

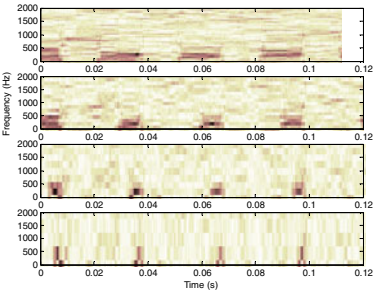

Fig. 6 STFT of corrupted impulses

However, in the case of multi-component signal, because of the poor time-frequency resolution, the components of the collected signal from the test rig are poorly represented. To give a good representation of all components in this signal requires good resolution in both time and frequency, which cannot be achieved using the spectrogram.

4 Wigner-Ville Distribution

The Wigner-Ville distribution of signal $x(t)$ is defined as (Hyun et al. 2001):

$$W_x(t,f) = \int_{-\infty}^{\infty} x\left(t+\frac{\tau}{2}\right) x^*\left(t-\frac{\tau}{2}\right) e^{-i2\pi f\tau}\, d\tau \tag{2}$$

Where $x(t)$ is a continuous complex signal. The Wigner Distribution possesses very high resolution in both time and frequency. Despite the desirable properties of the Wigner Distribution, it has two major draw-backs: 1. It often gives negative values, which makes the interpretation of the distribution difficult. 2. This distribution is a bilinear function producing interferences or cross terms for multi-component signals. The WVD of the sum of two signals $x(t)+y(t)$ is:

$$W_{x+y}(t,f) = W_x(t,f) + W_y(t,f) + 2\Re\{W_{x,y}(t,f)\} \tag{3}$$

Figures below show the effect of 'cross-terms' in the WVD. Fig. 7 shows the WVD of of the signal composed of a train of impulses and Fig. 8 the same signal artificially corrupted by Gaussian noise. Others impulses has been added to the signal in both cases. Although there is a good representation of the behaviour of both signals. The one obvious advantage that the WVD has over the STFT is its improved time-frequency resolution. Concentration of energy at the instantaneous frequency and other theoretically desirable properties also make the WVD preferable to the STFT in many signal processing applications.

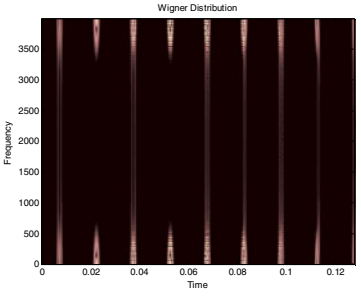

Fig. 7 WVD of simulated impulses

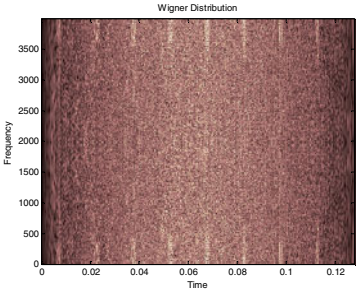

Fig. 8 WVD of corrupted impulses

5 Wavelet Transform

Wavelet analysis relies upon a family of basis functions, called wavelets, for signal processing in the time-frequency domain. Wavelets are defined with respect to several mathematical properties such as square integrability and admissibility; however, they can be essentially considered as finite-duration waveforms for the limited purposes of this paper. The continuous wavelet transform (CWT) of a finite energy signal $x(t)$, with the analyzing wavelet $\psi(t) \epsilon L^2(R)$ is the convolution of $x(t)$ with a scaled and conjugated wavelet as follows (Jiang et al. 2010):

$$W_\psi(a,b) = \langle x(t), \psi_{a,b}(t) \rangle = \frac{1}{\sqrt{a}} \int_{-\infty}^{\infty} x(t) \psi^*{}_{a,b}(t) dt \qquad (4)$$

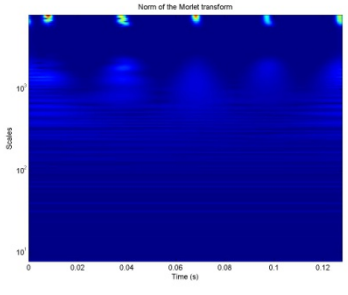

Fig. 9 CWT of impulses corrupted by GN

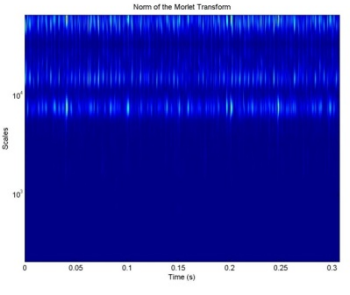

Fig. 10 CWT of the signal with small defect

From Fig. 9, it is possible to notice that, in the case of Morlet wavelet, the time-frequency signal features become more explicit in the CWT map. The wavelet analysis highlights the exact time location of the transient spike however it does not accurately measure the frequency of the spike. Besides, from Fig. 10 one can note that it is hard to find any periodic impulses in the original test rig signal with small defect. Obvious periodic impacts are hardly seen unless the damage of the defective component is very serious and near fatal breakdown. Therefore, the discrete wavelets transform (DWT), whose main idea is the process of multi-resolution analysis (MRA) proposed by Mallat is one of the most appropriate techniques to make a joint time-frequency analysis of discrete-time signals. Fig. 11 and Fig. 12 shows respectively, the waveforms of the simulated and the tested bearing, with small defect, signals in which 'db4' wavelet is employed as the basic wavelet. The waveforms have clear impulses. Obvious periodic impulses in Fig. 12 appear in the subplot of scale 4 and in the subplot of scale 3, while no impulses exist in other subplots. As a result, one can notice that distinct evenly spaced impulse clusters can be observed from the reconstructed signal, whose duration is equal to the BPFO of the tested bearing, providing an effective representation of the fault development.

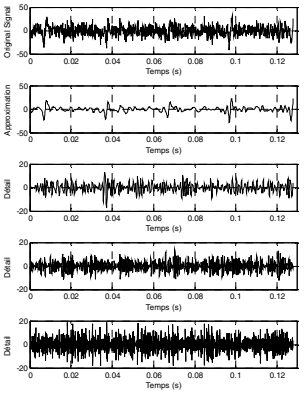

Fig. 11 DWT of impulses corrupted by GN

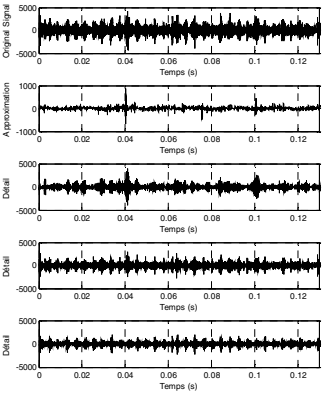

Fig. 12 CWT of the signal with small defect

6 Sparse Code Shrinkage De-noising Using Optimal Morlet

The impulse detection results generated by wavelet decomposition and de-noising are still not easy to be identified especially when the signal to noise ratio (SNR) of the detected signal is low. In view of this, Hyvärinen has proposed a so-called sparse code shrinkage method 'SCS' to estimate non-Gaussian data under noisy conditions.

It is based on the maximum likelihood estimation (MLE) principle and is successfully used for image de-noising. It demands that the non-Gaussian variable follow a sparse distribution. To represent a sparse distribution, Hyvärinen proposes the following function form for a very sparse probability density function pdf (Hyvärinen 1999):

$$p(s) = \frac{1}{2d}\frac{(\alpha+2)[\alpha(\alpha+1)/2]^{(\alpha/2+1)}}{\left[\sqrt{\alpha(\alpha+1)/2} + |s/d|\right]^{(\alpha+3)}} \tag{5}$$

Where: $d = \sqrt{E\{s^2\}}$ is the standard deviation of the impulses to be isolated and $\alpha = \frac{2-k+\sqrt{k(k+4)}}{2k-1}$ is the parameter controlling the sparseness of the pdf with $k = d^2 p_s(0)^2$. For an impulse whose pdf can be represented by Eq. 5, Hyvärinen proposes the following thresholding rule:

$$\mathrm{g}(u) = \mathrm{sign}(u)\max\left(0, \frac{|u| - ad}{2} + \frac{1}{2}\sqrt{(|u| + ad)^2 - 4\sigma^2(\alpha+3)}\right) \tag{6}$$

Where: $a = \sqrt{\alpha(\alpha+1)/2}$, σ is the standard deviation of the noise. The reconstruction results from shrunken wavelet coefficients using the thresholding rule given in Eq. 6 represent an approximation of the impulses. The modified Morlet wavelet function used in this paper is:

$$\psi(t) = exp^{-\beta^2 t^2/2}\left(exp^{j\omega_0 t} - exp^{-(\omega_0)^2/2}\right) \tag{7}$$

Where ω_0 is an arbitrary centre frequency and β is the shape parameter. $\beta = 0.7$ is used as a result of optimization using minimal Shannon entropy. The results of applying this proposed approach are presented on Fig. 13 and Fig. 14.

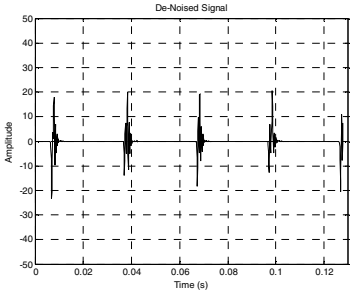

Fig. 13 SCS de-noised impulses

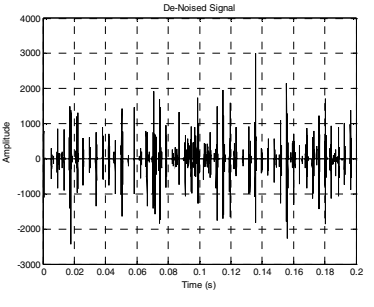

Fig. 14 SCS de-noised signal with small defect

From Fig. 14 distinct evenly spaced impulse clusters can be observed from the reconstructed signal and no fake impulses exist. These quasi-periodic intervals are equivalent to the inverse of the ball-passing frequency outer-race (BPFO) which is 0.0041 sec. The obtained results have shown that the proposed approach is very effective in the extraction of weak periodical impulses under heavy noise, and its performance is much better than the traditional methods.

7 Conclusion

By comparing the results obtained from time-frequency analysis of different vibration signals, we can conclude that: Time-frequency analysis has definite advantages over time-based vibration analysis or frequency-based vibration analysis and these advantages make it a powerful tool in machine monitoring. Therefore, the STFT can give a satisfactory representation of a signal in the time-frequency plane provided that an appropriate length of window for cutting the signal is chosen. However, the Wigner-Ville is not able to produce a satisfactory representation of multi-component signals due to the presence of cross terms. In practical applications, the Wigner-Ville Distribution requires some smoothing in order to suppress the cross terms. Wavelet Analysis was also introduced as an alternative to be compared throughout the offline data analysis. Finally, we have investigated the capabilities of SCS de-noising method based on an adaptive Morlet wavelet. The approach is based on maximum likelihood estimation of non-Gaussian random variables corrupted with additive, uncorrelated Gaussian noise. The SCS method proposed in this paper is effective at extracting the impulsive features buried in the noisy signals even when the SNR is very low.

References

Mallat, S., Hwang, W.L.: Singularity detection and processing with wavelet. IEEE Transactions on Information Theory 38(2) (1992)

Neumann, M.H., Sachs, R.V.: Wavelet Thresholding: Beyond the Gaussian i.i.d. Situation. In: Wavelets and Statistics. Lecture Notes in Statistics, vol. 103, pp. 281–300. Springer, Heidelberg (1995)

Hyvärinen, A.: Sparse Code Shrinkage: De-noising of Non-Gaussian Data by Maximum Likelihood Estimation. Neural Computation, 1739–1768 (1999)

Lin, J., Qu, L.: Feature extraction based on Morlet wavelet and its application for mechanical fault diagnosis. Journal of Sound and Vibration 234(1), 135–148 (2000)

Hyun, J.L., Kim, J., Kim, H.-J.: Development of Enhanced Wigner–Ville Distribution Function. Mechanical Systems and Signal Processing 15(2), 367–398 (2001)

Lin, J., Zuo, M.J.: Gearbox fault diagnosis using adaptive wavelet filter. Mechanical Systems and Signal Processing, 1259–1269 (2002)

Lin, J., Zuo, M.J., Fyfe, K.R.: Mechanical Fault Detection Based on the Wavelet De-Noising Technique. Journal of Vibration and Acoustics 126 (2003)

Qiu, H., Lee, J., Lin, J., Yu, G.: Wavelet filter-based weak signature detection method and its application on rolling element bearing prognostics. Journal of Sound and Vibration 289, 1066–1090 (2006)

Jafarizadeh, M.A., Hassannejad, R., Ettefagh, M.M., Chitsaz, S.: Asynchronous input gear damage diagnosis using time averaging and wavelet filtering. Journal of Mechanical Systems and Signal Processing (22), 172–201 (2008)

Jiang, Z., He, W., Qin, Q.: A joint adaptive wavelet filter and morphological signal processing method for weak mechanical impulse extraction. Journal of Mechanical Science and Technology 24(8), 1709–1716 (2010)

Reconstruction of Sound Sources of Gear Transmission Mechanism by Planar Near Field Acoustical Holography

Abbassia Derouiche[1], Nacer Hamzaoui[2], and Taoufik Boukharouba[1]

[1] Laboratoire de Mécanique Avancée, Faculté de Génie Mécanique et Génie des procédés, USTHB, BP 32 El Alia 16111 Bab Ezzouar, Alger, Algérie
derouichea@gmail.com
[2] Laboratoire Vibrations Acoustique, INSA Lyon, Bt Antoine de Saint Exupéry, 25 bis, avenue Jean Capelle 69621 Villeurbanne Cedex, France
nacer.hamzaoui@insa-lyon.fr

Abstract. This study is to reconstruct the sound sources of the transmission mechanism for spur gear. The inverse technique used is based on the planar near field acoustical holography. The measurements were performed in acoustics and vibration laboratory (LVA) of the INSA of Lyon, in a semi-anechoic room, where the floor is concrete and the walls are covered with glass wool. Accelerometers are positioned on the casing, they serve as reference. The complex acoustic pressures are measured by a rectangular antenna composed of regularly spaced microphones, which is placed above the noisy gear mechanism on a parallel plane. The source reconstruction is an inverse problem, it is classified as a so-called ill-posed problems, hence the necessity of applying regularization. Veronesi filter and Tikhonov method coupled with the L-curve function can reconstructed the image of noise sources on a plane parallel and tangent to the gear mechanism considered open and sometimes closed.

Keywords: acoustic holography, inverse problem, sound source, regularization, Veronesi, Tikhonov, L curve.

1 Introduction

In most work on the gear noise radiation, the researchers consider the vibration analysis rather than the acoustic analysis. This study considers the acoustic side with the aim of making the acoustic isolation and maintenance of defects.

And among the techniques for the localization, characterization and ranking, with satisfaction of the vibratory and/or acoustic sources radiating in free space of the acoustic field mention the imaging techniques spatial-temporal. Today, they have proved their worth and are considered as powerful tools in some areas (automotive, aerospace, aeronautics). They can provide access to maps of various quantities (sound pressure, normal speed, sound intensity, power, impedance etc.)

providing information on relative or absolute amplitudes of the potential sources. Among these theoretical and experimental techniques that were developed to identify vibroacoustic sources, the near-field acoustic holography plane (PNAH) is a method of high performance acoustic imaging, it is implemented in different institutions and companies. The use of evanescent waves makes it a high-resolution method. It can also provide information in wave number by measuring just the sound pressure in the near field of a surface source. However, this reconstruction is an ill-posed inverse problem which results in numerical instabilities resulting in poor quality of the solution, the regularization methods are required.

In this work, we use the imaging technique based on the acoustic PNAH, Veronesi filter and Tikhonov method coupled with the L-curve allows the regularizations of the solution in order to reconstruct the sound field radiated at the source by the gear transmission mechanism operating considered open and sometimes closed.

2 Process of PNAH and Regularization

2.1 Overview of PNAH

Theory and the basic foundations of the planar near-field acoustic holography (PNAH) are widely reported in the literature, and the first mentioned are those of Maynard (Maynard and Williams 1985), Williams et al 2003 and followed by Veronesi and Maynard in the years 1980. The PNAH is based on the fact that the sound pressure in a plane can be expressed by the two-dimensional convolution of a propagator and the pressure on another plane. This technique allows the reconstruction of three-dimensional sound field from the measured complex pressure on a surface called a hologram, located in the near field of the sources.

PNAH theory is based on the Helmholtz integral equation and the 2D spatial transform. The representation of the wave equation in the frequency domain, and introducing the wave number k is written as:

$$\nabla^2 p(x, y, z, \omega) + k^2 p(x, y, z, \omega) = 0 \quad with \quad k = \omega / c \tag{1}$$

The basic idea is to take advantage of the complexity and the richness of information in the near field of sources in order to ensure the presence of evanescent waves carrying valuable information in the measured data, as shown by Williams (Williams 1999). This is done by performing a series of acoustic measurements in a plane parallel and covering the sound sources responsible for the acoustic radiation in the surrounding field (Fig.1).

The theoretical steps that arise in the treatment of PNAH are presented briefly; in the first place, the complex sound field measured by microphones placed on a regular grid (or hologram) is decomposed into a set of plane waves with two dimensions based on the analysis of the spatial Fourier transform.

The space wave number is composed of the wave number k, $k \perp (k_x, k_y) = k_z$, orthogonal components spectra of plane waves. The spectra of pressure in this space, called k-space are obtained by the following expression:

$$P(k_x, k_y, z_H, \omega) = \int_{-\infty}^{\infty}\int_{-\infty}^{\infty} p(x, y, z_H, \omega)\, e^{-j(xk_x + yk_y)} dxdy = TF(p(x, y, z_H, \omega)) \tag{2}$$

Second, the spectra of plane waves obtained in this plan are propagated back from the measurement plane (or hologram) to the source plane. This requires knowledge of the propagation Green function, in general, the Green function is used in free field.

Without any filtering operation, the acoustic pressure field is reconstructed on the source plane using the inverse Fourier transform. The spatial distribution of pressure on the source plane at the angular frequency ω is written as:

$$p(x, y, z_S, \omega) = TF^{-1}\left(P(k_x, k_y, z_H, \omega) \times G^{-1}(k_z, z_S - z_H)\right) = p(x, y, z_H, \omega) \otimes TF^{-1}\left(G^{-1}(k_z, z_S - z_H)\right) \tag{3}$$

The diagram below summarizes the operation of PNAH without regularization (Paillasseur 2009).

$$p(x, y, z_H, \omega) \xrightarrow{TF2D} P(k_x, k_y, z_H, \omega) \xrightarrow[\times G^{-1}(k_z, z_S - z_H)]{Back-propagation} P(k_x, k_y, z_S, \omega) = \xrightarrow{TF2D^{-1}} p(x, y, z_S, \omega)$$

With $k_z^2 = k^2 - k_x^2 - k_y^2$, the propagator G is defined as:

$$G(k_z, z_S - z_H) = e^{-jk_z(z_S - z_H)} \tag{4}$$

Two cases are used to specify the form of $G^{-1}(k_z, z_S - z_H)$, the inverse propagator:

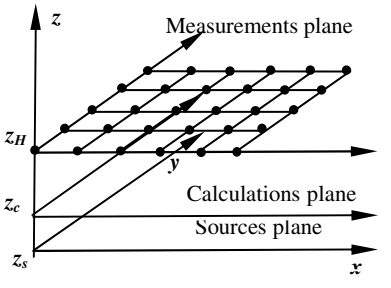

Fig. 1 Pressure field reconstructed from the back-propagation of the pressure field measured in z_H

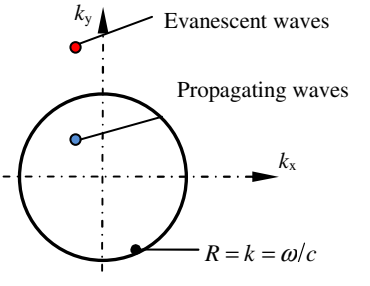

Fig. 2 Evanescent and propagating waves in k-space

$$P(k_x,k_y,z_S \prec z_H,\omega) = P(k_x,k_y,z_H,\omega)\, e^{-jk_z(z_S-z_H)} \quad if\ k^2 \geq k_x^2 + k_y^2 \tag{5}$$

$$P(k_x,k_y,z_S \prec z_H,\omega) = P(k_x,k_y,z_H,\omega)\, e^{+jk_z(z_S-z_H)} \quad if\ k^2 \prec k_x^2 + k_y^2 \tag{6}$$

At the back-propagation, the amplitudes of propagating waves are not changed; against those in of the evanescent waves will grow exponentially.

Figure 2 shows in the space of wave numbers and outside the circle of radius $R = k = \omega/c$ we find the amplitude of the evanescent wave, the wave number transform decomposes the sound field in propagating and evanescent waves.

2.2 Regularization for PNAH

Regularization techniques are needed (Williams 1999) to this type of inverse problem. Two distinct stages occur in the regularization process for plane near-field acoustic holography (PNAH), first, a function of low pass filter is defined and then a stopping rule is applied to determine the optimal parameters of the filter for acoustic imaging. Two regularization methods are used, the Veronesi and Tikhonov. The method of Tikhonov regularization with the choice of the parameter optimization based on the L-curve is used in our case. The application of low pass filter to pressure field p or propagator G which has optimized the shape, slope and the cutoff frequency can mitigate the influence of evanescent waves responsible for distortions in the back-propagation.

If we want to reconstruct the acoustic pressure signal in the plane source from measurements of the hologram and the propagator G, the compromise between filtering too low and too high is obtained by the optimal position of β giving the trough of the curve that corresponds to the maximum curvature (Paillasseur 2009, Scholte 2008), if we set:

$$\rho = \log_{10}\left(\left\|Gp_{s\beta} - p_H\right\|\right), \quad \eta = \log_{10}\left(\left\|p_{s\beta}\right\|\right) \tag{7}$$

Curvature $C(\beta)$ is given by:

$$C(\beta) = \frac{\rho'\eta'' - \rho''\eta'}{\sqrt{\left((\rho')^2 + (\eta')^2\right)^3}} \tag{8}$$

Where the symbols ' and " represent the first and second derivatives with respect to the regularization parameter β, thus it is possible to determine the optimal value of regularization parameter by finding the maximum curvature $C(\beta)$ (Paillasseur 2009, Scholte 2008).

2.3 PNAH Resolution

To optimize the spatial resolution, the evanescent waves must be included in the measured data (Williams 1999). Theoretically, the resolving power of holography is infinite (Hald 2001) but in practice, due to the inadequacy of the measurement chain, there is a limiting resolution which depends on the frequency of the acoustic signal, the dynamics of the chain acquisition and the distance between the hologram and the sources plane (Paillasseur 2009, Scholte 2008) The resolution is defined as follows:

$$Res = \pi \Big/ \sqrt{\left(\frac{2\pi f}{c}\right)^2 + \left(\frac{D \ln 10}{20(z_H - z_S)}\right)^2} \tag{9}$$

Where D is the dynamic range of the acquisition chain; z_H is the position of the plane of measurement or hologram and z_S, the position of the plane sources.

3 Experimental Measurements

3.1 Description of the Gear Transmission Mechanism

Transmission gears simplified, consists of a spur gear including a couple of teeth 45/65. The main characteristics of this gear are given in Table 1. The solid steel wheels are mounted on shafts with a diameter of 0.020 m. The input shaft is connected to the engine through a flexible coupling. The shafts are guided in rotation by the bearings. The simple casing is of dimensions (0.40m x 0.35m x 0.16m) and 0.025m thickness except for the wall 5, it is 0.005m. The casing is made of two materials, steel and Plexiglas, the Young's modulus is $2{,}1.10^{11}$ N/m^2 and $3{,}3.10^9$ N/m^2, the density is 7800kg/m^3 and 1190kg/m^3 and Poisson's ratio is 0.3 and 0.37 respectively for steel and Plexiglas. The walls 3 and 5 (cover) are of Plexiglas, and the rest of steel.

Table 1 Main characteristics of the gear.

	Pinion	Gear
Number of teeth	45	65
Module (m)	0.002	0.002
Tooth width (m)	0.02	0.02
Base radius (m)	0.045	0.065
Pressure angle (dg)	20	20

Fig. 3 Experimental Setup in a semi-anechoic room (left) Gear transmission mechanism open (right)

Figure 3 shows the semi-anechoic room, in which were carried out measurements of the complex acoustic pressures, the antenna carrying the microphones is directed by a robot and OROS with 32 channels has been used for the acquisition of temporal data measured and transferred in format .mat to be treated under Matlab environment.

3.2 Experimental Exploitation

We will be interested to calculate the acoustic radiation corresponding to the most energetic frequencies giving the highest sound levels depending on the case of closed and open mechanism. These two frequencies of study shown in Figure 4 are 133Hz and 1856Hz for closed and open mechanism respectively. The speed rotation is equal to 41.2 Hz. These spectra give the level sound pressure (LSP) in dB (ref 2e-5) and it clear that it insufficient to interpret these results, while imaging is necessary to find the sound sources of the mechanism for any frequency.

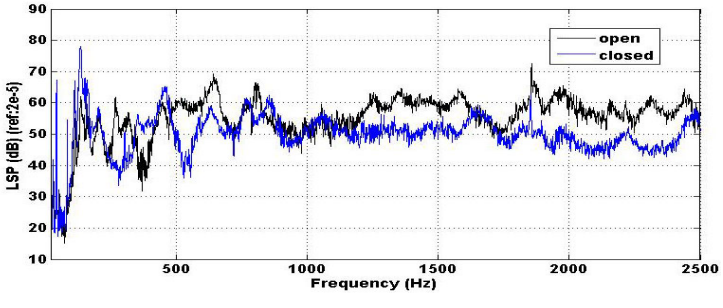

Fig. 4 Sound pressure levels in dB and frequency in Hz Mechanism closed (black), Mechanism open (blue)

For frequencies of 133Hz and 1856Hz with a dynamic range of 60dB and a distance of 0.18m between the hologram plane and the plane source, a resolution of the order of less than 0.01m is achieved. The performances of holography in terms of resolution are very interesting.

In Figure 5 are reported the plots of the L curves and the choice of regularization parameters located at 0.09705 to optimize the imagery of the mechanism closed radiating at frequency of 133Hz, and 0.01812 for the one that optimizes the image of the mechanism open at a frequency of 1856Hz with back propagation distance d=0.15m, the package of P.C. Hansen has been used for these calculations (Hansen 1994).

On the images of figure 6, giving the back propagation of the source field of the mechanism considered closed at a frequency of 133Hz, we note that they correspond to the mode (1.1) of the cover which is excited, the results obtained by both methods of regularization are quite comparable in terms of the positions of hot spots in relation to components of the mechanism. This natural mode (1.1) of the cover was calculated by modal analysis software under LMS Pimento.

The images in Figure 7 reconstruct the source field of the mechanism considered open at a frequency of 1856 Hz. This frequency equals the frequency of meshing of the mechanism (fe=45x41.2), we note that the results obtained at this frequency by the two methods of regularization are similar in terms of location of hot spots in relation to components of the mechanism with a concentration of sources on the gear itself.

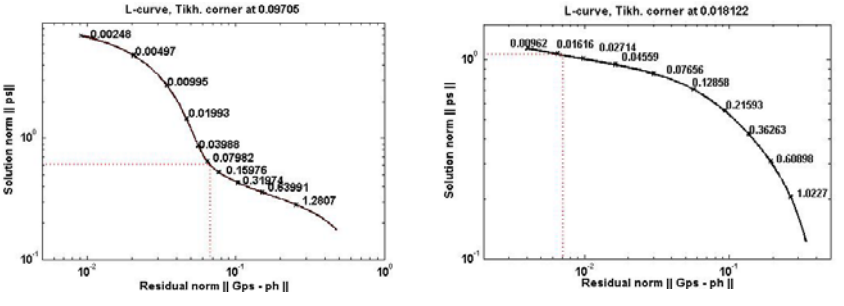

Fig. 5 The L-curves and optimal parameters

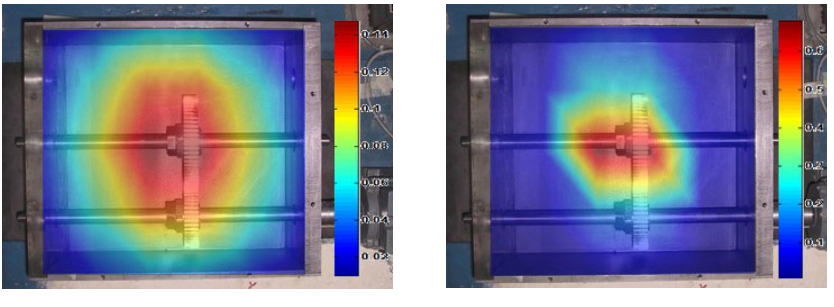

Fig. 6 Back-propagation of level sound pressure (Pa)Veronesi (left) and Tikhonov (right)

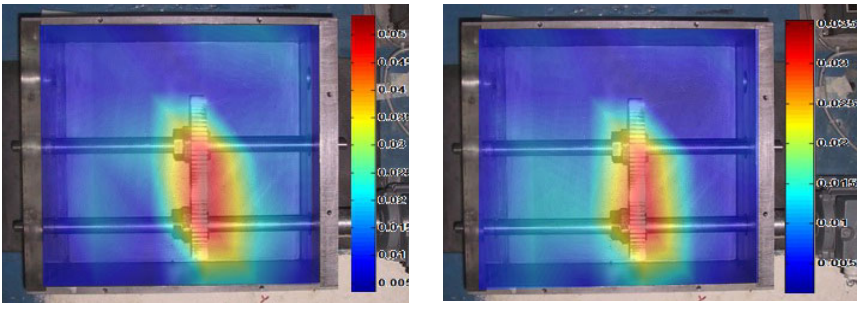

Fig. 7 Back-propagation of level sound pressure (Pa) Veronesi (left) and Tikhonov (right)

5 Conclusion

The technique of the method provided us an evaluation of the pressure distribution in a plane very close to the sources. This is an acoustic imaging method based on the inverse solution of the wave equation, where the acoustic information plane at a distance from the source, known as hologram, was used as input in the process. In the field of wave number, one of the most influential on the final result is the low pass filter in two dimensions. For high resolutions of PNAH, determining the cutoff filter is crucial, this wave number serves as the regularization of the parameter in the reverse process is ill-posed. Tikhonov regularization based on the L-curve allowed us to optimize our results.

The PNAH allowed us by a back-propagation of the waves picked up a few centimeters from the source, to access through a mapping of existing noise nearly at the surface of the equipment or the transmission mechanism. In terms of resolution of the method PNAH, the performances of holography are therefore very interesting. Totally ignoring the sources, the method of PNAH merely objectively reconstructed the acoustic field, making the tangent plane of reconstruction on the mechanism of in which is obtained easily interpretable images of sources. These images or visualizations of spatial acoustic fields facilitate the understanding of the complex phenomena of radiation.

In this study, we have considered the acoustic analysis instead of vibration and that with the aim of making the acoustic isolation and maintenance of defects. Our results have been compared with the beamforming technique, the latter gives results qualitative rather than quantitative. The comparison of these results will be introduced in a future work.

References

[1] Maynard, J.D., Williams, E.G., Lee, Y.: Near-field acoustic holography: I. Theory of generalized holography and the development of NAH. J. Acoust. Soc. Am. 78(4), 1395–1413 (1985)

[2] Williams, E.G., Houston, B.H., Herdic, P.C.: Fast Fourier transform and singular value decomposition formulations for patch near field acoustical holography. J. Acoust. Soc. Am. 114(3), 1322–1333 (2003)
[3] Veronesi, W.A., Maynard, J.D.: Digital holographic reconstruction of sources with arbitrarily shaped surfaces. J. Acoust. Soc. Am. 85, 588–598 (1989)
[4] Williams, E.G.: Fourier Acoustics: Sound radiation and Near-field Acoustical Holography. Elsevier Academic Press (1999)
[5] Paillasseur, S.: Développement de la technique d'holographie acoustique de champ proche temps réel pour l'analyse de sources de bruit fluctuantes. PhD thesis, Université du Maine (2009)
[6] Lopez, S.R.: Experimental application of high precision k-space filters and stopping rules for fully automated near field acoustical holography. International Journal of Acoustics and Vibration 13(4), 157–164 (2008)
[7] Hald, J.: Time domain acoustical holography and its application. Sound and Vibration Magazine 2, 16–25 (2001)
[8] Hansen, P.: Regularization Tools: A Matlab Package for Analysis and Solutions of Discrete Ill-Posed Problems. Numericals Algorithms 6, 1–35 (1994)

Application of Empirical Mode Decomposition for Impulsive Signal Extraction to Detect Bearing Damage – Industrial Case Study

Jacek Dybała[1] and Radoslaw Zimroz[2]

[1] Warsaw University of Technology, Institute of Vehicles, ul. Narbutta 84, 02-524 Warsaw, Poland
jdybala@simr.pw.edu.pl
[2] Diagnostic and Vibro-Acoustic Science Laboratory, Wroclaw University of Technology 50-370 Wroclaw, Poland
radoslaw.zimroz@pwr.wroc.pl

Abstract. Bearings damage detection is one of the most important topic in condition monitoring. Main problem in industrial application of bearing vibration diagnostics is the masking of informative signal by interfering signals. It requires the usage of techniques based on advanced signal enhancement in order to extract useful diagnostic components from the measured vibration signals. The paper shows application of Empirical Mode Decomposition (*EMD*) in extraction of weak impulsive signal from raw vibration signals generated by complex mechanical systems employed in the industry (driving units of belt conveyors). Impulsive character of the vibration signals is very often associated with a mechanical fault. The purpose of this processing is decomposition of the signal in order to detect impacts related to the damages in rolling element bearings (*REB*).

Keywords: Rolling element bearings, Damage detection, Empirical Mode Decomposition (EMD), Intrinsic Mode Function (IMF), Signal extraction.

1 Introduction

Non-invasive diagnostics uses the signals generated during the facility operation as a media informing about its condition. The signals being recorder usually contain many individual ones generated by the facility, and the form of their "composition" may be of various form. In this case, signal recorded on the bearings casing is notably disturbed by the signal generated by the gearbox, in spite of the distance between them.. It is difficult to analyse the recorded signal effectively when the signal related to the bearings damage is significantly weaker than the interfering signal (generated by gearbox) [10, 11]. It is required to separate both signals [14] or in other words to extract informative part from vibration signal being

analysed [16]. Recent publications on *EMD* [6, 7, 9] show its advantages for non-stationary signals processing and confirm its effective application in many diagnostics tasks . In this paper *EMD*-based approach for separation of deterministic (generated by the gearbox mesh) and random, non-deterministic (generated by the damaged bearing) parts [15] was applied. It works even if machine is under non-stationary operations.

2 Empirical Mode Decomposition (*EMD*) – Brief Description

Based on the *EMD* algorithm, an original signal $x(t)$ can be strictly reconstructed by a linear superposition:

$$x(t) = \sum_{i=1}^{n} c_i(t) + r(t) \tag{1}$$

where $c_i(t)$ is i-th empirical mode and $r(t)$ is the final residue which can be interpreted as the mean trend of $x(t)$.

Each empirical mode $c_i(t)$, called Intrinsic Mode Function (*IMF*), fulfills the following two conditions [4]: 1) in the whole empirical mode, the number of mode local extremes and the number of mode zero-crossings are equal or differ at most by one and 2) at any point, the local average of upper and lower envelope is zero. The algorithm for the extraction of *IMF*s from original signal $x(t)$ is called sifting process and it consists of the following steps:

Step 1: Define the residue as $r(t) = x(t)$.
Step 2: Identify all the local extremes (maxima and minima) of $x(t)$.
Step 3: Connect all the local maxima (respectively minima) with a line known as the upper envelope $E_{max}(t)$ (respectively the lower envelope $E_{min}(t)$).
Step 4: Construct the mean of upper and lower envelope $m(t) = 0.5 \cdot (E_{min}(t) + E_{max}(t))$.
Step 5: Define the detail (proto-*IMF*) as $d(t) = x(t) - m(t)$ and replace $x(t)$ by $d(t)$.
Step 6: Repeat steps 2÷5 until $d(t)$ meets the *IMF* conditions and the stoppage criterion of the sifting process is fulfilled, then derive an *IMF* from $d(t)$ and replace $x(t)$ by $r(t) = r(t) - d(t)$.
Step 7: If the stoppage criterion of the signal's decomposition is fulfilled then finish the decomposition process; otherwise, go to step 2.

The second *IMF* condition is too rigid to use, so it is necessary to change it to implement the *EMD*. The local average of upper and lower envelope must be close to zero according to some criterion. The evaluation of how small is the amplitude of the local mean has to be done in comparison with the amplitude of the corresponding mode. In [8] authors introduce a new criterion based on the mode amplitude

$a(t) = 0.5 \cdot (E_{max}(t) - E_{min}(t))$ and the evaluation function $\sigma(t) = |m(t)/a(t)|$. In this paper, $d(t)$ meets the second *IMF* conditions, when $max(\sigma(t)) < \theta$ (the coefficient θ was in the range [0.025, 0.275]).

A critical part of the *EMD* procedure is the stoppage criteria of the sifting process and decomposition process. Many different sets of *IMF*s can be obtained by changing the stoppage criteria. The stoppage criterion of the sifting process determines the point when sifting is complete and a new *IMF* has been found (it determines the number of sifting steps to produce an *IMF*). The stoppage criterion of the decomposition process determines how many components will be extracted from the signal.

Three different stoppage criteria of the sifting process were considered. The first stoppage criterion is determined by using a Cauchy type of convergence test [4]. If the two details (proto-*IMF*s) from successive iterations are close enough to each other, it is assumed that the extracted detail is an *IMF*. The normalized squared difference SD_k between two successive details $d_{k-1}(t)$ and $d_k(t)$ during k-th iteration is defined as:

$$SD_k = \frac{\sum_t [d_{k-1}(t) - d_k(t)]^2}{\sum_t d_{k-1}^2(t)} < T_D \tag{2}$$

If this squared difference SD_k is smaller than a predetermined T_D value, the sifting process will be stopped. In this paper, the following values of T_D were used: T_{D1} = 1e-6 for the first half of the total number of siftings and T_{D2} = 1e-5 for the second half of the total number of siftings. The second stoppage criterion of the sifting process is based on the agreement of the number of zero-crossings and extremes. The sifting process is stopped when the numbers of zero-crossings and extremes are the same for S successive siftings [5]. In this paper, the following values of S were used: $S_1 = 10$ for the first half of the total number of siftings and $S_2 = 3$ for the second half of the total number of siftings. The third stoppage criterion of the sifting process determines the maximum number of siftings. The sifting process stops when the replications of sifting procedure exceed the predefined maximum number. Selecting a maximum number of siftings prevents the sifting procedure from locking in a never-ending loop. This number should be set large enough to guarantee that *IMF* is extracted. In this case, the maximum number of siftings was 500.

The sifting process also stops when $x(t)$ has less than two extremes (the signal must have at least two extremes, one maximum and one minimum, to successfully decompose the signal into *IMF*s).

The decomposition process can be stopped finally by any of the following predetermined criteria: 1) the absolute values of the last *IMF* or the residue $r(t)$ are smaller than tolerance level; 2) no more *IMF*s can be extracted from signal $x(t)$;

3) the replication of decomposition procedure exceeds the predefined maximum number. Here the criterion of the signal's value level is described by the following relationship:

$$\max\left(\left|y(t)\right|\right) < \gamma \cdot \left(\max(x_O(t)) - \min(x_O(t))\right) \tag{3}$$

where $y(t)$ is the last *IMF* or the residue $r(t)$, $x_O(t)$ is the original signal (the subject of decomposition) and g is a tolerance coefficient (here: $\gamma = 0.01$).

In order to clarify the decomposition process, Fig. 1 shows the flow chart of the applied *EMD* algorithm.

3 Denoising and Detrending Using Empirical Mode Decomposition

Empirical Mode Decomposition is the iterative process of extracting empirical modes, called *IMF*s, from the signal. The successive *IMF*s include signal components from different frequency bands ranging from high to low frequency. Therefore, *EMD* corresponds to an adaptive (data-driven) filtering [2]. The filter associated to the first *IMF* is essentially high-pass, the *IMF*s of higher indices are characterized by a set of overlapping band-pass filters [3]. The proposed *EMD*-based denoising and detrending approach is based on the assumption that the *IMF*s derived by *EMD* will be divided generally into three classes of *IMF*s: noise-only *IMF*s, signal-only *IMF*s and trend-only *IMF*s. A noise-only part of signal and a signal-only part of signal are generated from the sum of the noise-only and from the sum of the signal-only *IMF*s, respectively. A trend-only part of signal is generated from the sum of the trend-only *IMF*s and the final residue.

The problem is to identify correctly the noise-only and trend-only *IMF*s. Typically, the noise is expected to be captured by *IMF*s of low indices and the trend is expected to be captured by *IMF*s of high indices. The specificity of various signals makes it impossible to distinguish all three classes of *IMF*s in each signal. If it is not possible to isolate the trend-only *IMF*s, the final residue is added to the signal-only part of signal.

Some methods of identification of noise-only and trend-only *IMF*s are presented in the literature [1, 2]. They are based on the empirically observed energy and mean of signal components. The proposed method of noise-only and trend-only *IMF*s identification is based on Pearson correlation coefficient of *IMF* and original signal. The *IMF*s of low indices with low value of Pearson correlation coefficient are identified as the noise-only *IMF*s. The *IMF*s of high indices with low value of Pearson correlation coefficient are identified as the trend-only *IMF*s.

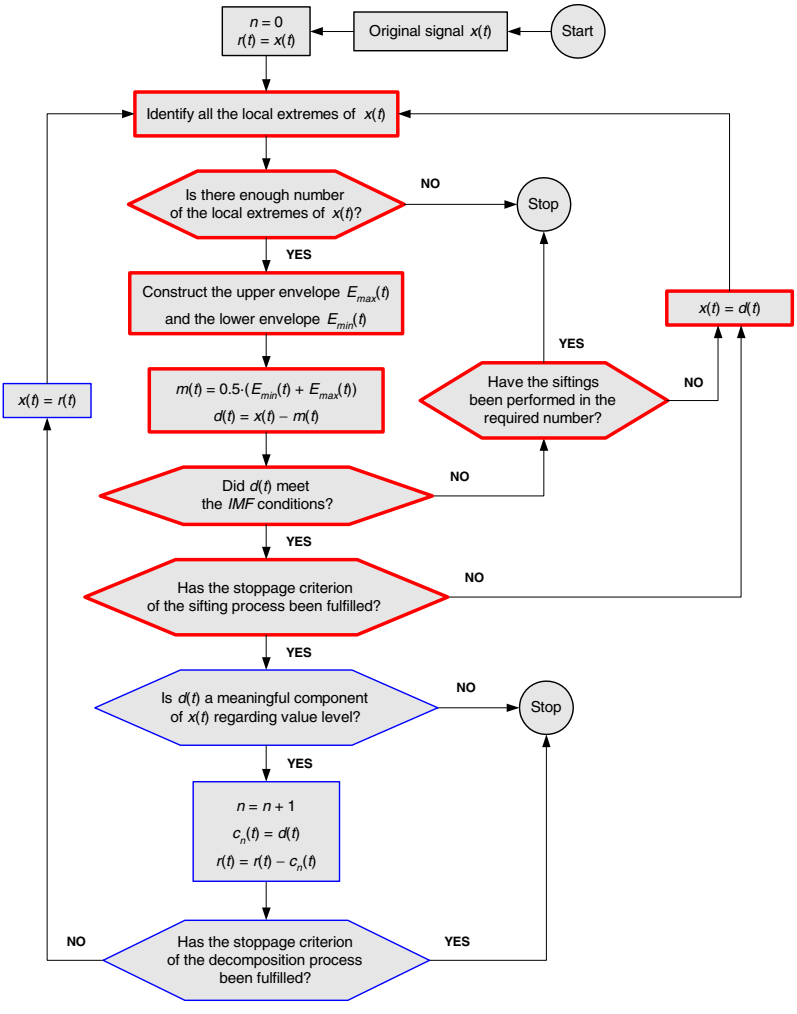

Fig. 1 *EMD* algorithm flow chart

4 Application of Proposed *EMD*-Based Denoising and Detrending Approach in Vibration Signal Analysis

4.1 Machine and Experiment Description

A scheme and photographs of the machine working in the mining company during experiments are presented in Fig. 2. A several acquisition sessions have been performed. Location of accelerometer is shown in Fig. 2d: sensor has been mounted using screw, in horizontal direction. Characteristic damage frequencies (calculated

based on shaft rotational speed and geometry of the bearings) are: 8.9 Hz, 12.35 Hz and 16.1 Hz (rolling element, outer race, inner race fault respectively). For each measurement signal was acquired with following parameters: sampling frequency f_s = 19200 Hz, duration T = 2.5 s.

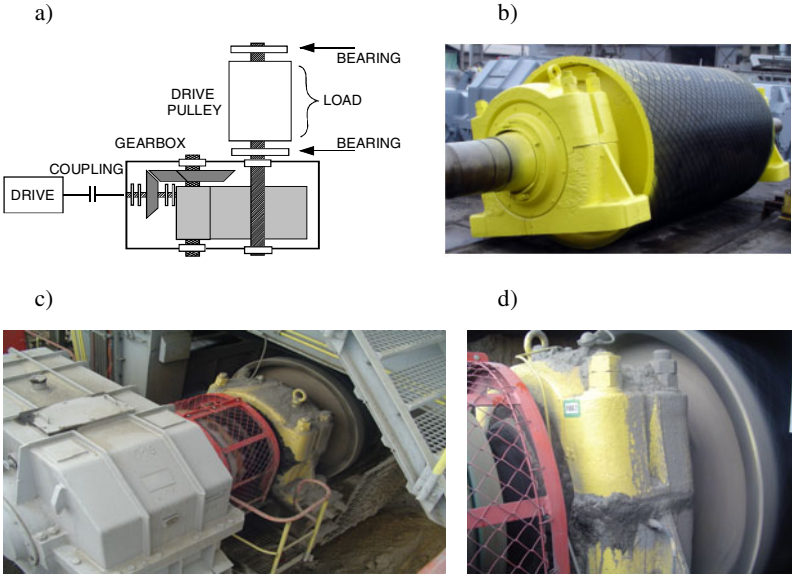

Fig. 2 Diagnosed object: a) Scheme, b) Pulley with bearing housing mounted on shaft, c) View on joint of output shaft in gearbox with pulley, d) View on sensor location on pulley

The task defined here (from diagnostics point of view) is to detect local disturbance signal with one of cycles corresponding to the fault frequency. Unfortunately, signal of interest (impulsive, cyclic contribution related to the damaged bearings) is completely masked by high-energy source i.e. the gearbox located nearby (see Fig. 2a,c).

In the paper the task is limited to extraction of the signal of interest by *EMD*. Further identification of fault type should be a classical one i.e. the detection using statistical indicators (e.g. kurtosis) or envelope analysis [14]. More information can be found in other papers concerning diagnostics of these machines (for example [12, 13]).

4.2 Analysis of Decomposition Results

The decomposition results of rolling element bearing signal are presented in Fig. 3. The results of signal's part identification are presented in Fig. 4.

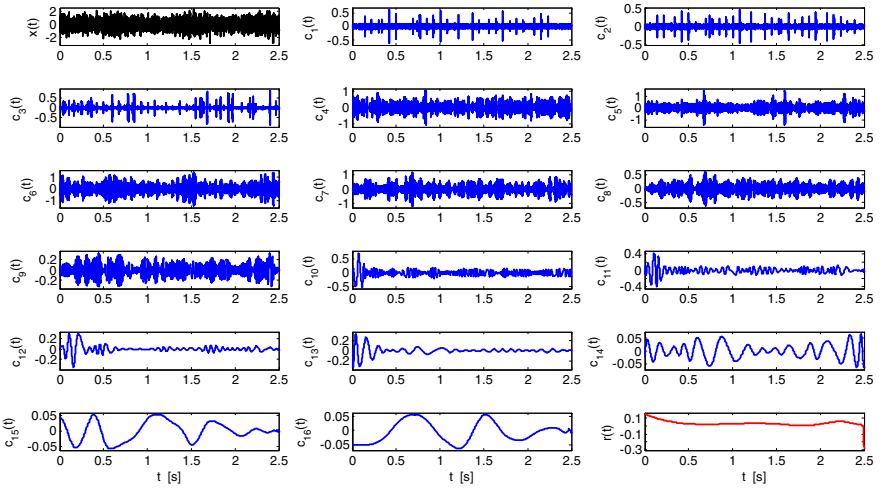

Fig. 3 Decomposition of original signal $x(t)$ [m/s2] /16 empirical modes (*IMF*s) $c_i(t)$ [m/s2] and final residue $r(t)$ [m/s2]/

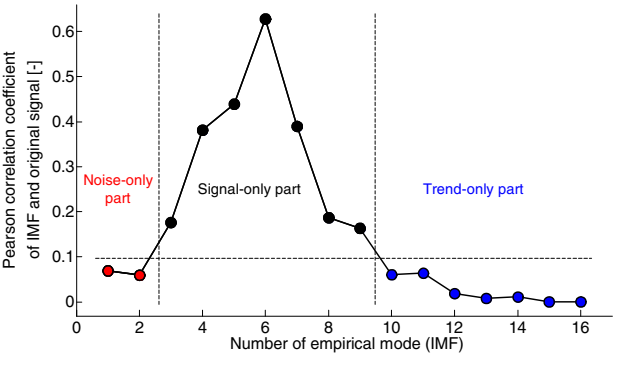

Fig. 4 Identification of signal parts

Fig. 5 presents the waveforms of the noise-only, signal-only and trend-only signal's part. Amplitude spectra of this signal's parts are presented in Fig. 6. The noise-only signal's part is very clear to interpret. The observed impulses come from mechanical impacts (impulses arise when bearing elements roll over damaged locations). Classical envelope analysis is given in Fig. 7. Identified frequency (12.72 Hz) corresponds to outer race fault frequency.

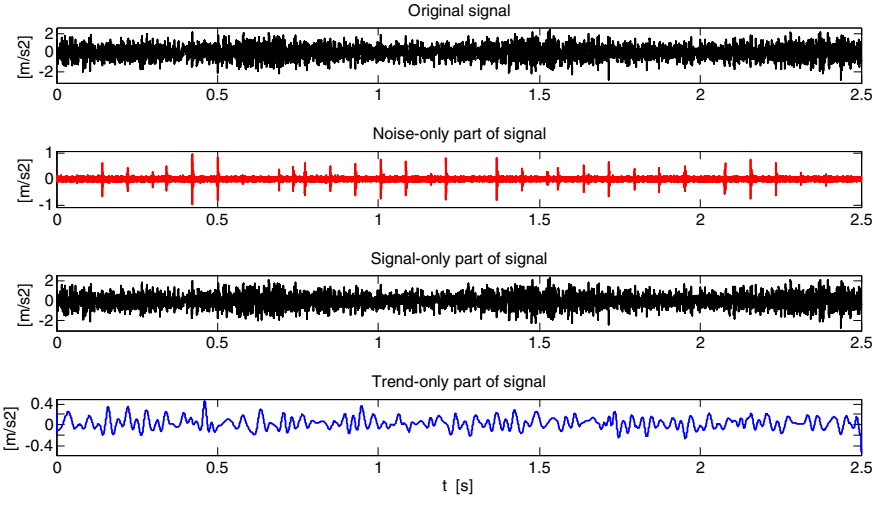

Fig. 5 Parts of original signal

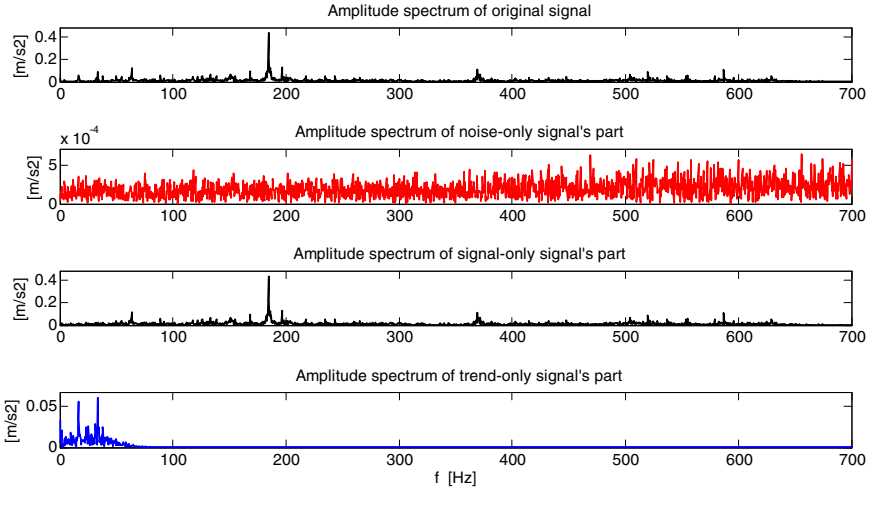

Fig. 6 Amplitude spectra of signal's parts

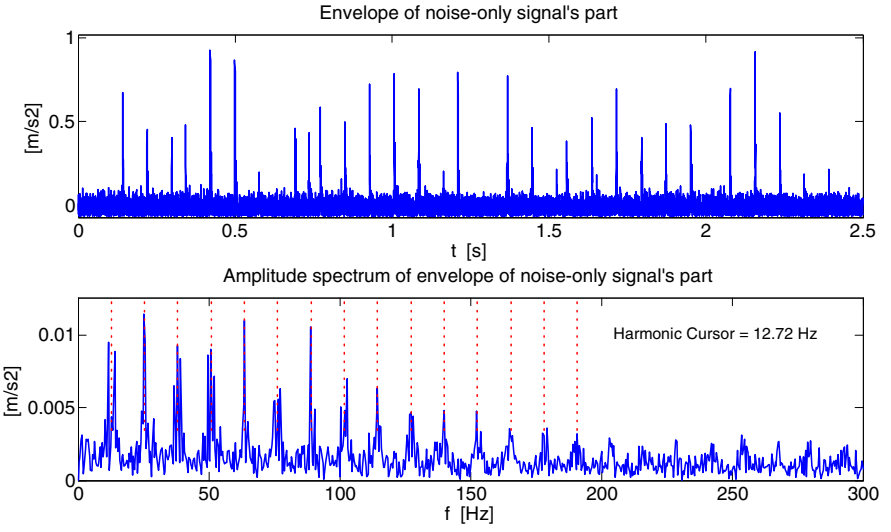

Fig. 7 Analysis of noise-only signal's part: envelope (top)and amplitude spectrum of envelope (bottom)

5 Conclusion

In this paper, *EMD*-based denoising and detrending approach to vibration signals from complex mechanical systems was presented. The main goal was to extract weak impulsive signal from raw vibration signals, that are usually associated with bearing faults. It was shown that in case of signals from pulley bearings, it is possible to extract the impulsive signal, after which diagnosis of the fault becomes easy.

References

1. Boudraa, A.O., Cexus, J.C.: EMD-based signal filtering. IEEE Transactions on Instrumentation and Measurement 56(6), 2196–2202 (2007)
2. Flandrin, P., Gonçalvès, P., Rilling, G.: Detrending and denoising with empirical mode decomposition. In: Proceedings of the 12th European Signal Processing Conference (EUSIPCO 2004), Vienna, Austria, September 6-10, pp. 1581–1584 (2004)
3. Flandrin, P., Rilling, G., Gonçalvès, P.: Empirical Mode Decomposition as a Filter Bank. IEEE Signal Processing Letters 11(2), 112–114 (2004)
4. Huang, N.E., Shen, Z., Long, S.R., Wu, M.L.C., Shih, H.H., Zheng, Q.N., Yen, N.C., Tung, C.C., Liu, H.H.: The empirical mode decomposition and the Hilbert spectrum for nonlinear and non–stationary time series analysis. Proc. of the Royal Society of London, Series A – Mathematical Physical and Engineering Sciences 454, 903–995 (1998)
5. Huang, N.E., Shen, Z., Long, S.R.: A new view of nonlinear water waves: The Hilbert Spectrum. Annual Review of Fluid Mechanics 31, 417–457 (1999)

6. Liu, B., Riemenschneider, S., Xu, Y.: Gearbox fault diagnosis using empirical mode decomposition and Hilbert spectrum. Mechanical Systems and Signal Processing 20(3), 718–734 (2006)
7. Loutridis, S.J.: Damage detection in gear systems using empirical mode decomposition. Engineering Structures 26(12), 1833–1841 (2004)
8. Rilling, G., Flandrin, P., Gonçalvès, P.: On Empirical Mode Decomposition and its algorithms. In: Proceedings of the 6th IEEE-EURASIP Workshop on Nonlinear Signal and Image Processing (NSIP 2003), Grado, Italy, June 8-11 (2003), http://perso.ens-lyon.fr/patrick.flandrin/NSIP03.pdf
9. Yu, D., Cheng, J., Yang, Y.: Application of EMD method and Hilbert spectrum to the fault diagnosis of roller bearings. Mechanical Systems and Signal Processing 19(2), 259–270 (2005)
10. McFadden, P.D., Smith, J.D.: Vibration monitoring of rolling element bearings by the high frequency resonance technique: a review. Tribology Intern. 17, 3–10 (1984)
11. Ho, D., Rand, R.B.: Optimization of bearing diagnostic techniques using simulated and actual bearing fault signal. Mechanical Systems and Signal Processing 14(5), 763–788 (2000)
12. Makowski, R.A., Zimroz, R.: Adaptive bearings vibration modelling for diagnosis. In: Bouchachia, A. (ed.) ICAIS 2011. LNCS(LNAI), vol. 6943, pp. 248–259. Springer, Heidelberg (2011)
13. Zimroz, R., Bartelmus, W.: Application of adaptive filtering for weak impulsive signal recovery for bearings local damage detection in complex mining mechanical systems working under condition of varying load. Solid State Phenomena 180, 250–257 (2012)
14. Randall, R.B., Antoni, J.: Rolling element bearing diagnostics—A tutorial. Mechanical Systems and Signal Processing 25(2), 485–520 (2011)
15. Barszcz, T.: Decomposition of Vibration Signals Into Deterministic and Nondeterministic Components and Its Capabilities of Fault Detection and Identification. Int. J. Appl. Math. Comput. Sci. 19(2), 327–335 (2009)
16. Barszcz, T., Jabłoński, A.: A Novel Method of Optimal Band Selection for Vibration Signal Demodulation. Mechanical Systems and Signal Processing 25(1), 431–451 (2011)

On the Use of Fourier-Bessel Series Expansion for Gear Diagnostics

Gianluca D'Elia, Simone Delvecchio, and Giorgio Dalpiaz

University of Ferrara Engineering Department,
Via Saragat 1, I - 44100 Ferrara, Italy
{gianluca.delia,simone.delvecchio,giorgio.dalpiaz}@unife.it

Abstract. This work seeks to study the potential effectiveness of Fourier-Bessel (FB) series expansion for gear fault diagnostics. FB series expansion is a method for cross-terms suppression in Wigner-Ville distribution (WVD). In particular, FB series expansion is used as a signal decomposition technique in order to subdivide the signal into its components before WVD evaluation. The pros and cons of this method are highlighted by the analysis of experimental results. In particular two case studies are taken into account: a fatigue crack at the tooth root and spalls of different sizes. The presented results highlight the conditions in which FB decomposition technique is effective in WVD cross-term suppression, the limitations, as well as the advantages in terms of fault identification.

Keywords: Fourier-Bessel series expansion, Wigner-Ville distribution, diagnostics.

1 Introduction

Localised faults in rotating machines (e.g. localised defects in gears), generally introduce non-stationary signal components [1, 2], which cannot be properly described by ordinary spectral methods. Thus, joint time-frequency distribution is needed in order to focus the time-local properties of the signal. Wigner-Ville distribution (WVD) is a time-frequency technique which found many successful applications in the area of rotating machine diagnostics, due to its *infinite* resolution both in time and frequency domain. However, the WVD of multi-component signals exhibits severe cross-terms between components in different time-frequency regions due to its non-linear behaviour. These cross-terms are spread both in the time and frequency domain adding noise to the distribution and leading to further misinterpretation and confusion. Cross-terms can be reduced by time smoothing procedures [3], but this method leads to poor time resolution. Therefore, efforts have been made in order to efficiently suppress cross-terms without loss of time-frequncy resolution. In particular, the two main methods developed for cross-term suppression deal with the adaption of the distribution kernel [4] or signal decomposition [5]. However, such methods are either computationally expensive or have a very limited adaptation range.

In the last few years, Pachori and Sircar [6] proposed a new technique based on Fourier-Bessel (FB) series expansion. This method combines FB expansion and WVD in order to obtain a time-frequency representation without introducing cross-terms. In particular, FB expansion is used as a signal decomposition technique. Therefore, before the evaluation of the WVD, the multi-component signal is subdivided into its constituents by the use of FB series expansion. The advantage of this method is twofold: (i) its numerical implementation is simple and (ii) it does not need any prior information about the signal frequency band.

FB series expansion is the subject of this work, in particular effectiveness for fault detection is assessed by the analysis of experimental results concerning local faults in gears. More in depth, a brief theoretical background is provided in Section 2, highlighting cross-term drawbacks and the signal decomposition method using FB series expansion. Finally, Sections 3 and 4 seek to point out the effectiveness of FB series expansion for fault detection in gears on the basis of experimental results. Different types of gear tooth faults are taken into account: fatigue cracks and tooth spalls of different sizes.

2 Theoretical Background

The genuine formulation of the Wigner distribution (WD) was introduced by Wigner in 1932 in the quantum mechanics field [7]. Let $x(t)$ be a continuous signal, the WD of the signal $x(t)$ is defined as the Fourier transform of the instantaneous autocorrelation function with respect to the time lag variable τ:

$$W_x(t,\omega) = \int_{-\infty}^{+\infty} x\left(t+\frac{\tau}{2}\right)x^*\left(t-\frac{\tau}{2}\right)e^{-j\omega\tau}d\tau \tag{1}$$

where x^* denotes the complex conjugate of x. In 1948, Ville suggested the use of the analytic signal in the WD assessment [8]. The Wigner distribution of the analytic signal is termed Wigner-Ville distribution (WVD).

WVD is a powerful tool for the time-frequency analysis of vibration signals. Unfortunately, one of the pivotal problems concerning WVD is its nonlinear behaviour, arising from the product of the time-shifted analytical signal with its complex conjugate. De facto, cross-terms arise in the WVD of a multi-component signal for every pair of auto-components. These cross-terms mean that the distribution shows energy which does not actually exist at these particular time-frequency co-ordinates. This is a pivotal drawback of WVD, as vibration signals produced by mechanical systems generally contain several components.

The theory of series representation is a well known subject in the realm of speech and image processing. Let $x(t)$ be a continuous time signal considered over an arbitrary time interval $(0,a)$, Fourer-Bessel series expansion is given by [9]:

$$x(t) = \sum_{l=1}^{L} C_l J_0\left(\frac{\lambda_l}{a}t\right) \tag{2}$$

where $J_0(\cdot)$ is the zero-order Bessel function of the first kind, which arises from the solution of Bessel's differential equation and λ_l are the ascending positive roots of equation $J_0(t) = 0$. The FB coefficients C_l are computed via the following equation:

$$C_l = \frac{2\int_0^a tx(t)J_0(\frac{\lambda_l}{a}t)dt}{a^2[J_1(\lambda_l)]^2} \tag{3}$$

where $J_1(\cdot)$ is the first-order Bessel function of the first kind and the integral in the numerator of the right-end side of equation (3) is the well-known finite Hankel transform. One can notice that, as in contrast to the sinusoidal basis functions in the Fourier series, the Bessel functions decay within the signal range a.

The bandwidth of the reconstructed signal can be obtained from the Fourier transform of the Bessel function. As explained by Arfken in [9], the approximate bandwidth of the l^{th} term in the right-end side of equation (2) is $\omega_{Bl} \cong \lambda_l/a$. Thus, if L terms are taken into account in the reconstruction of the signal $x(t)$, a maximum bandwidth of $\omega_{max} \cong \lambda_L/a$ can be obtained. Therefore, in order to plot FB coefficients vs frequency, the generic l^{th} FB coefficient is associated to frequency f_l given by:

$$f_l = \frac{\lambda_l}{2\pi a} \tag{4}$$

When the signal is in angle domain, $x(\theta)$, instead of time domain, in equations (2) - (4) time and frequency are respectively replaced by angle (expressed in umber of revolutions of a reference rotor) and order of rotation frequency. Thus, parameter a becomes the angle range of analysis, expressed in revolutions, and equation (4) gives the order associated to the l^{th} FB coefficient.

For a multi-component signal, i.e. a signal $x(t)$ that is the sum of M components $x_i(t)$, each component can be expanded in FB series via equation (2), so the FB series coefficients of a multi-component signal can be obtained as:

$$C_l = \sum_{i=1}^{M} C_{li} \tag{5}$$

If the components of the composite signal are well separated in the frequency domain, then the signal components will be associated with various distinct clusters of non-overlapping FB coefficients. Therefore, each component of the signal can be separately reconstructed by identifying and separating the corresponding FB coefficients. However, some requisite conditions are needed, which are listed in [6]. In particular the dc signal component has to be removed prior to the decomposition, because of FB expansion can approximate only the oscillatory signal part.

As previously said, FB series expansion can be suitable in order to perform the WVD of multi-component signals. The procedure consists of three stages [6]:

1. The FB series coefficients of the multi-component signal are evaluated using equation (3). Assuming that every component is associated to non-overlapping FB coefficients, it is possible to choice separate clusters of FB coefficients; each

cluster is used in order to reconstruct the corresponding mono-component signal by equation (2).
2. The WVD for each mono-component signal is evaluated.
3. The mono-component WVDs are summated in order to obtain the WVD of the composite signal.

3 Diagnostics of Gear Tooth Cracks

Hereafter a localised gear fault is taken into account, i.e. a fatigue crack at the root of one tooth. The experimental raw data are obtained from a previous work by Dalpiaz et al. [2]. In that work, tests were performed on a power circulating gear testing machine composed of two identical single-stage gear units which were mounted back to back, with locked-in torque. Each gear unit contains a carburised spur gear pair of module 3 mm composed of a 28 tooth pinion and a 55 tooth wheel. Further data about gears and experimental apparatus can be found in [2]. A real fatigue crack is present in one of the wheel teeth mounted in one gear unit. The experimental data considered in this work deal with a crack length corresponding to about 20% of whole fracture surface after breakage, and are relative to nominal pinion torque of 385 Nm and nominal pinion speed of 1000 rpm; thus the meshing frequency is 466.67 Hz. The vibration signal was measured by means of a piezoelectric accelerometer placed close to the wheel bearings in a radial direction. The signal was integrated by the preamplifier to obtain velocity signal.

Firstly, the vibration velocity signal is synchronously averaged over 28 wheel revolutions. After that, WVD is performed and plotted in Figure 1(a). Several horizontal dashed lines are present in the time-frequency distribution, some of them are related to the fundamental and harmonics of the meshing frequency, i.e. 55^{th} wheel order and its multiples, the others are cross-terms that are due to the non-linear behaviour of the transformation. Moreover, this energy distribution does not clearly reveal the presence of the defect. Therefore, TSA vibration velocity is firstly decomposed into its fundamental components and then the WVD of each mono-component is evaluated and the total WVD is obtained by the summation of the partial WVDs. Figure 1(b) depicts the FB series coefficients of this decomposition, where a is equal to one wheel revolution and L is equal to 1000. Using this plot, one can see that the meshing frequency and its harmonics produce eight non-overlapping clusters of FB coefficients. Each of these clusters is rather wide, containing several coefficients of high amplitude surrounding the coefficients corresponding to each harmonic. The high wideness of these clusters is probably due to modulation effects affecting the meshing harmonics.

Figure 1(c) plots the WVD obtained by the FB decomposition technique, where the chosen C_l coefficients for the reconstruction of the TSA velocity signal are summarised in Table 1. As one can see, this energy distribution is unaffected by cross-terms. Moreover, the meshing frequency harmonics are clearly depicted, and a localised increment of the WVD amplitude is visible at the 275^{th} wheel order (fifth meshing harmonic), at about 150 degrees. However, this transient event is not enough for a complete fault detection. So, in order to look for local alterations,

one can observe the signal component obtained from the FB decomposition, corresponding to the 5^{th} harmonic. This choice is confirmed by Figure 1(b), where the 5^{th} meshing harmonic seems to be the most sensitive to the local defect. In fact, a significant family composed by several neighbouring components arises around the 275^{th} wheel order. The reconstructed component is plotted in Figure 1(d). De facto, an abrupt fall is clearly visible at about 150 degrees, which corresponds to the cracked tooth engagement.

Table 1 C_l wheel order bands used for the reconstruction of the TSA velocity signal (gear tooth crack)

Components (meshing harmonics)	1^{st}	2^{nd}	3^{rd}	4^{th}	5^{th}	6^{th}
C_l wheel order bands	49 – 62	105 – 117	157 – 172	209 – 230	250 – 300	305 – 351

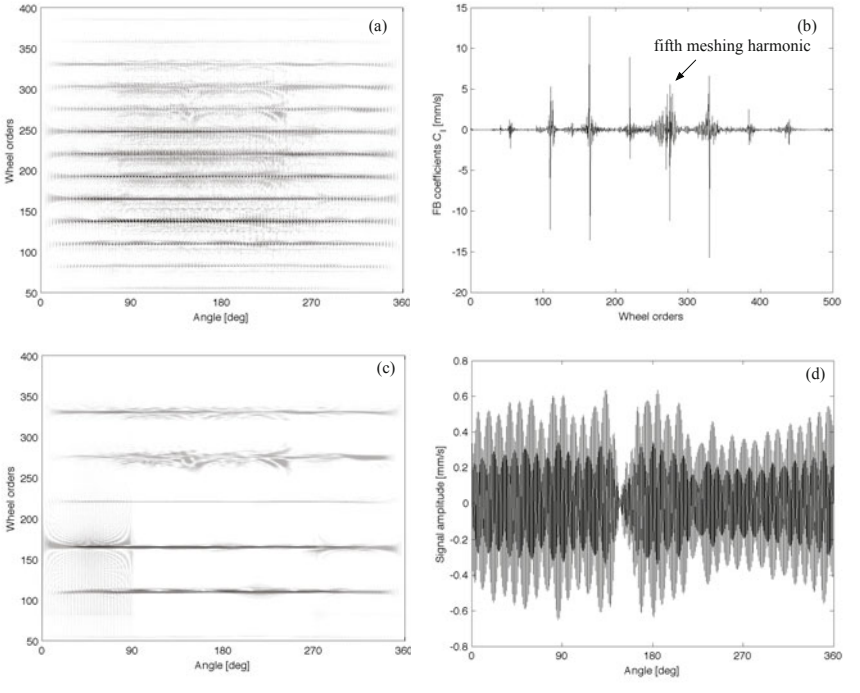

Fig. 1 Gear tooth crack: (a) Wigner-Ville distribution and (b) Fourier-Bessel coefficients of TSA velocity signal (c) Wigner-Ville distribution reconstructed through FB decomposition technique and (d) reconstructed component concerning the 5^{th} meshing harmonic.

4 Diagnostics of Gear Spalls

This section concerns the study of tooth spalls in helical gears. Artificial tooth spalls are mechanically introduced via a milling process in helical gears of module 1.04 mm, helix angle 26° and 71 teeth. In order to compare the sensitivity of the presented method, spalls of different sizes were introduced along the gear tooth face. In more detail, two different spall lengths are taken into account in this work, which are located at the mean point of the gear tooth face. The spall dimensions are given with respect to the tooth face width and are listed in Table 2. Moreover, sound wheels are tested for comparison. After the milling process, the faulty gears are mounted in the first stage of a two-stage gear unit. The experimental apparatus consists of a base, two induction motors controlled by inverters and a gear unit. The gear unit contains two helical gear pairs, one having 18 and 71 teeth, the other one 12 and 55 teeth, for a global speed reduction ratio of 18.1; further details can be found in [10, 11].

The vibration signal has been acquired by means of a piezoelectric accelerometer mounted in radial direction near the bearing support of the first stage pinion. The signal is acquired with a sample frequency of 104.2 kHz to an extent of 50 s. The results presented in this work are relative to a nominal driving motor speed of 3600 rpm (60 Hz) and nominal output shaft torque of 48.8 Nm.

First of all, the acceleration signal is synchronously resampled, with 1024 points per wheel revolution, and TSA is computed over 200 wheel revolutions. After that, the WVD of the TSA signal is performed.

Figures 2(a) and (b) plot the WVD evaluated in the 50-400 wheel order band, which includes the main meshing harmonics. One can see the meshing frequency at the 71^{th} order and no other harmonics. However, for each pair of spectrum components a cross-term arises and a high level of background noise is present. These troubles strongly affect the WVD concerning the case of Sp25% (Figure 2(a)), hiding local distribution changes as well as modulation effects due to the engagement of the faulted tooth. Thus it is difficult to obtain diagnostic information. Only in the case of Sp100% the fault can be detected in Figure 2(b), where the location of the faulted tooth is highlighted by the changes in the WVD around 340 degrees in the 50-100 wheel order band. Therefore, the Fourier-Bessel decomposition of the synchronous averages is needed in order to obtain a WVD which is suitable for fault detection.

Figures 2(c) and (d) show the results of this operation, where a is equal to one wheel revolution and L is equal to 1000. Table 3 summarizes the chosen FB coefficient bands for the reconstruction of the TSA vibration signals. The reconstructed distribution can be more clearly interpreted: the gear meshing frequency remains the highest (horizontal dark line at 71^{st} order), but it is now possible to distinguish several modulation sidebands around this component in the two faulted cases (Figures 2(c)and (d)). In particular, the presence and location of fault Sp25% might be detectable by analysing Figure 2(c), where the meshing frequency and one of its sidebands exhibit an amplitude change around 150 degrees. Unfortunately, this is not enough for sure fault detection.

However, even if amplitude modulation effects can be visible for the smallest spall size (Figures 2(c)), the engagement of the faulted tooth is practically undetectable by this technique and further investigations are needed [10].

Table 2 Dimensions of gear tooth spalls

ID	Fault description
Sp25%	2 *mm* along the tooth profile, 0.6 *mm* depth, 4 *mm* across the tooth face (25% of the tooth face width)
Sp100%	2 *mm* along the tooth profile, 0.6 *mm* depth, 15.5 *mm* across the tooth face (100% of the tooth face width)

Table 3 C_l wheel order bands used for the reconstruction of the TSA acceleration signals (gear spalls)

Components	A	B	C
C_l wheel order bands for the Sp25%	$45-75$	$138-146$	$211-216$
C_l wheel order bands for the Sp100%	$32-114$	$208-217$	$350-363$

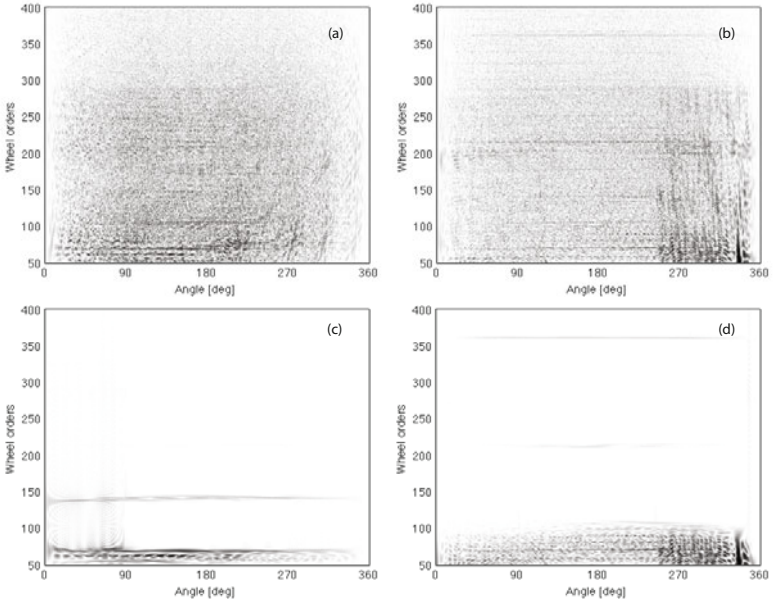

Fig. 2 WVD of acceleration TSA: (a) Sp25%, (b) Sp100%; WVD of acceleration TSA reconstructed through FB decomposition technique: (c) Sp25%, (d) Sp100%.

5 Concluding Remarks

In the realm of WVD cross-term suppression methods, this work focuses attention on Fourier-Bessel (FB) series expansion [6]. This technique has several advantages over the usual methods presented in the literature [4, 5], as it is of simple numerical implementation and it does not need any prior information about the signal frequency content.

In the two experimental cases of localised gear faults, FB decomposition technique is effective in the suppression of WVD cross-terms due to the frequency interference between the meshing harmonics. This allows the identification of the localised amplitude changes of one of the meshing harmonics and its sidebands, as symptoms of faults producing signal modulation. It is worth noting that in the original WVD these amplitude changes were hidden because of cross-terms and noise.

As a further result, the signal decomposition through FB series expansion makes it possible to separate and reconstruct the waveform of the most important signal components, reducing the effects of noise and minor inessential components. This can be very useful for diagnostic purposes even in that cases where WVD cross-terms cannot be suppressed, as shown by the experimental results. In the signal concerning a gear fatigue crack, the reconstructed component relative to one of the meshing harmonics exhibits an abrupt fall corresponding to the cracked tooth engagement. This allows the detection and localisation of the fault.

As a general conclusion, FB decomposition technique produces good results for cross-term suppression in the case of frequency interference in WVD; on the other hand, reconstructed waveforms in proper FB coefficient bands can give useful information for diagnostic purposes.

Acknowledgement. This work has been developed within the Advanced Mechanics Laboratory (MechLav) of Ferrara Technopole, realized through the contribution of Regione Emilia-Romagna Assessorato Attivitá Produttive, Sviluppo Economico, Piano telematico - POR-FESR 2007-2013, Attivitá I.1.1.

References

1. Randall, R.B.: A new method of modeling gear faults. J. Mech. Design 104, 259–267 (1982)
2. Dalpiaz, G., Rivola, A., Rubini, R.: Effectiveness and sensitivity of vibration processing techniques for local fault detection in gears. Mech. Syst. Signal Pr. 14, 387–412 (2000)
3. McFadden, P.D., Wang, W.: Time-frequency domain analysis of vibration signals for machinery diagnostics (II) the weighted Wigner-Ville Distribution. University of Oxford, Department of Engineering Science, OUEL 1891/1891 (1991)
4. Choi, H.I., Williams, W.J.: Improved time frequency representation of multicomponent of signals using exponential kernels. IEEE Transaction on Signal Processing 37, 862–871 (1989)
5. Sattar, F., Salomonsson, G.: The use of a filter bank and the Wigner–Ville distribution for time-frequency representation. IEEE Transaction on Signal Processing 47, 1776–1783 (1999)

6. Pachori, R.B., Sircar, P.: A new technique to reduce cross terms in the Wigner distribution. Digital Signal Processing 17, 466–474 (2007)
7. Wigner, E.P.: On the quantum correction for the thermodynamic equilibrium. Physics Reviews 40, 749–759 (1932)
8. Ville, J.: Théorie et applications de la notion de signal analytique. Cables et Transmission 2A, 61–74 (1948)
9. Arfken, G.: Mathematical methods for physicists. Accademic Press, New York (1966)
10. D'Elia, G.: Fault detection in rotating machines by vibration signal processing techniques. PhD Thesis, University of Bologna (2008)
11. Dalpiaz, G., D'Elia, G., Delvecchio, S.: Design of a test bench for the vibro-acoustical analysis and diagnostics of rotating machines. In: Proceeding of Second World Congress on Engineering Asset Management and the Fourth International Conference on Condition Monitoring, Harrogate, UK, June 11-14 (2007)

Genetic Optimization of Decision Tree Choice for Fault Diagnosis in an Industrial Ventilator

Nour El Islem Karabadji[1], Ilyes Khelf[2],
Hassina Seridi[1], and Lakhdar Laouar[2]

[1] Electronic Document Management Laboratory (LabGED),
Badji Mokhtar-Annaba University, Algeria
{Karabadji,Seridi}@labged.net
[2] Laboratoire de Mécanique Industrielle,
Badji Mokhtar-Annaba University, Algeria
ilyeskhelf@gmail.com

Abstract. Fault diagnosis and condition monitoring of industrial machines have known significant progress in recent years, particularly with the introduction of pattern recognition and data-mining techniques for their development. The decision trees are among the most suitable techniques for the diagnosis and have several algorithms for their construction. Each building algorithm has its advantages and drawbacks which make the optimal choice of adapted method to the desired application difficult. In this paper we propose the diagnosis accomplishment of an industrial ventilator based on the combination vibration analysis-decision trees. For the choice of the adapted decision tree building algorithm a method based on genetic algorithms was used. Its results were commented and discussed

Keywords: rotating machines, faults diagnosis, decision tree, genetic algorithm.

1 Introduction

In modern industry, equipment maintenance is an important factor to ensure a constant production. Establishing systems for fault diagnosis and condition monitoring of machines is an important part of maintenance policies (Jardine et al. 2006). For the monitoring of industrial machines several techniques have been used as oil analysis, pressure and acoustic emission (Tan et al. 2007). One of the most common methods remains the vibration analysis with the use of transducers like Accelerometers and signal processing techniques (wavelets and Fast Fourier Transforms). Vibration analysis can provide reliable indicators for the diagnosis of industrial machinery (Khelf and Laouar 2011).

To improve the efficiency of conventional diagnostic methods and automate their use, Pattern recognition and data-mining techniques are shown as a solution. Among the most used techniques in industrial field there are the decision trees (Sugumaran et al. 2007) (Yang et al. 2009) thanks to the ease for users to understand the behavior of the built models against other data-mining techniques.

Decision trees technique is based on the idea of making a classification of an object by a test suite on its indicators. To construct a decision tree, we have to choose the indicator that undergoes the first test. This indicator should be that which separates the different classes more significantly. This choice is regarding the type of selected tree (Chaud, Cart, Id3..). Each one has its specificities which makes the choice difficult to justify. One solution is to generate all trees and choose the best one by measuring performance on a separate and selected validation set data and conducting statistical tests. This solution is the most widely used although, it tests the performance on fixed and predefined training and validation sets, while an optimal decision tree for an application must be the most efficient regardless of the couple (Training, Validation sets) choice. To measure the performance of decision trees without falling into combinatorial problems many algorithms have been developed as well as Tabu search, Particle Swarm Optimization or more commonly genetic algorithms could be a solution (Worden et al. 2008).

In this work, a procedure for faults diagnosis of an industrial machine (Industrial Ventilator) was performed on several stages. First, the vibration signatures have been recorded on the machine in various operating conditions, where several indicators have been extracted from their frequency spectra. Second, a genetic method was used to get the best tree for this application regardless of the couple (Training, Validation sets) choice. Finally, the best trees were proposed to construct algorithms for robust fault diagnosis.

2 Materials and Methods

2.1 Experimentations

Industrial ventilators are among the most machines used in industry. The studied plant is shown in Figure 1 and then diagrammed in Figure 2.

The ventilator is NAKASHIMA model connected to an electric motor (HELMKE) through a flexible coupling spring. The equipment runs on a constant speed of 1490 rpm. An accelerometer is installed on the bearing housing for recording vibration signals.

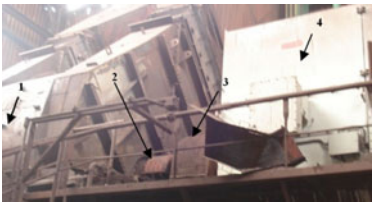

Fig. 1 Dedusting plant 1-Ventilator 2- Bearing housing 3- Coupling 4-Motor

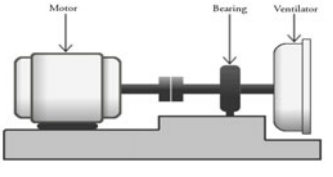

Fig. 2 Schematization of the plant

The frequency domain analysis is a reliable technique for the fault diagnosis in rotating machinery. In this work four of the most common faults were monitored those affecting inner and outer races of rolling bearings, the mass unbalance and fixation fault. A frequency band of 400 Hz was used to obtain frequency spectra. Figure 3 shows spectra of vibration signatures recorded in the different monitored operating conditions.

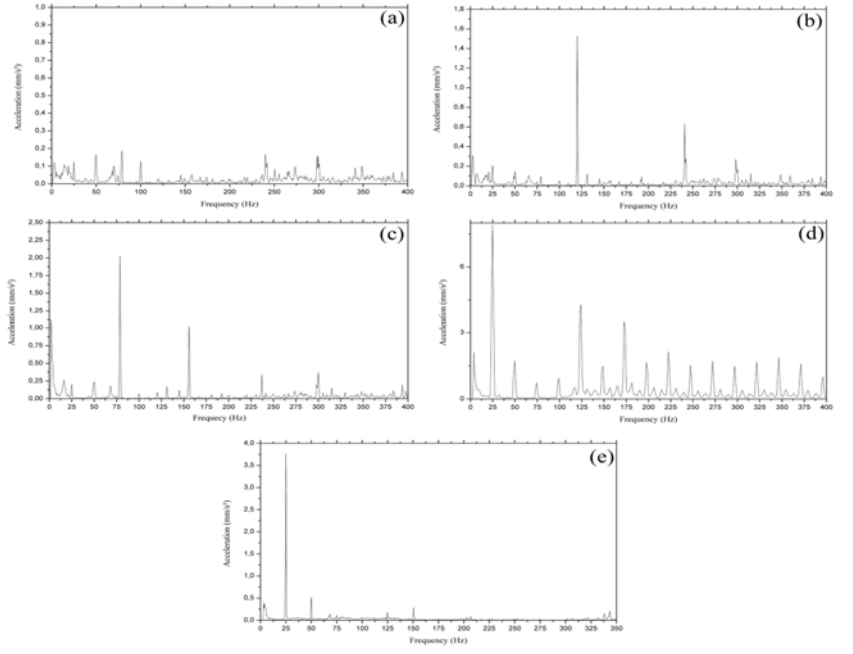

Fig. 3 Frequency spectra of recorded signals (a) Healthy condition (b) The inner race of roller bearing fault (c) The outer race of roller bearings faults (d) failure of fixation (e) mass unbalance fault

2.2 Indicators Extraction and Data-Set Post-treatment

Five indicators were extracted for each spectrum in three frequency bands: [0-200Hz], [200-400Hz] and [0-400Hz], for a total of 15 indicators by spectrum.

The five indicators are: the root mean square level, the amplitude of the biggest peak, the frequency of the biggest peak, the distance between the frequencies of the two biggest peaks and the average amplitudes the 5 biggest peaks.

In the next step the database composed of 150 indicator vectors was divided in two sets; the first, for training and the second, for validation. There are several sampling methods (simple, stratified, ...) And each method has its specific features. Stratified sampling was chosen in order to take same rate of different classes in order to reflect the variability of the phenomena during generalization and validation of the trees and prevent their specializations.

2.3 Decision Tree

Decision trees are among the most used classifier in industrial application due to the compressibility and ease of interpretation of their results in contrast to the black box classifier "neural networks". Decision trees are built recursively, following a top-down approach; they are composed of a root and several nodes, branches and leaves, where a branch represents the paths from the root to the leaf (class) going through nodes (indicators).

The indicators used as nodes are selected using the criterion depending on construction algorithm. In our study, the decision trees implemented on the open source platform Weka have been explored (Hall et al. 2009). Twelve trees were extracted {BFTree, DecisionStump, FT, J48, J48graft, LADTree, LMT, NBTree, RandomForest, RandomTree, REPTree, SimpleCart}. Trees were indexed from 0 ... 11, ordered as above.

2.4 Genetic Algorithm

To choose the optimal decision tree independently of the couple (training validation) choice without falling into combinatorial problems, several optimization algorithms exist, Among them Genetic Algorithms *GA* are ones of most reliable and popular. They are based on the natural evolution and selection, and survival of the fittest ideas. The genetic algorithm represents a solution to the problem as a genome (or chromosome). It then creates a population of possible solutions and applies genetic operators such as mutation and crossover to evolve the fittest solution.

In this works a genetic algorithm was implemented in Java-code where the individuals (chromosome) were coded by setting in the first gene the index of decision tree (extracted from Weka classes) and in the second gene the index of validation sample. Figure.4 shows the flow chart of the programmed algorithm.

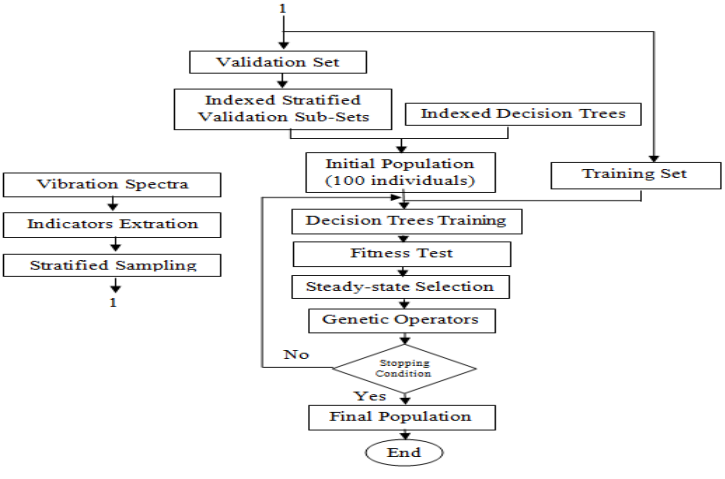

Fig. 4 Adopted Genetic Algorithm flow chart

The development of the *GA* pursues the following steps:

2.4.1 Trees Training

In this step is proposed a generation of a set of decision trees using different training samples. For each individual in the population, a stratified subset (composed of 60 vectors) is pulled out randomly, in order to generate the indexed tree of the first gene of this individual.

2.4.2 The Evaluation

This step is the heart of data mining. The performance of a model can be calculated from its classification accuracy *CA* on the validation set. This performance can be converted it into a confusion matrix from which we can derive various statistics on the performance of the model.

The proposed evaluation phase was defined by the following fitness function:

$$F(x) = \text{Mean}\ (CA)$$

It represents the average classification accuracy of the tree with different training sets on the validation set found on the same chromosome. This procedure is to prevent the risk of falling into the cases of random performance on certain validation sets distorting the evaluation of the trees. This fitness guarantee robustness and reliability of selected trees tested with various training sets.

2.4.3 The Selection

The steady-state selection is used. The genetic algorithm then runs as follows. In every generation few chromosomes are selected (among the fittest ones) to create children. Subsequently, the worst chromosomes are removed and replaced randomly with new other ones.

2.4.4 Evaluation Operators

Crossover: it applies on two different individuals. As a result it gives a chromosome formed from genes of both parents; two children are "products" for the next generation. A percentage of crossovers is set and a cross at a point applied. This procedure allows the change of the two genes on chromosome.

Mutation: it applies to an individual by modifying one or more genes, chosen randomly from the parent and one new child comes. The percentage of mutation in our case is set to 1%. This ratio defines the probability to change an index by another randomly without interaction with other chromosomes.

2.4.5 Stopping Criterion

The algorithm stops at one of the following criteria

- Maximum number of iterations = 100.
- 50 % of the population of chromosomes is similar as the first gene.

The results will be one or more trees in a given configuration. The trees can be used to classify new examples.

3 Results and Discussion

Table 1 presents the used classification trees, ranked according to their Classification accuracy obtained by classic validation.

Table 1 Classic validation classification accuracy.

Tree	*CA*
NBTree	96,07
RandomForest	94,11
LADTree	92,15
RandomTree	90,19
REPTree	84,31
SimpleCart	84,31
LMT	84,31
BFTree	84,31
FT	82,35
J48	78,43
J48graft	78,43
DecisionStump	33,33

Table 2 shows the occurrence frequency of each tree in the population during the last generation of *GA*

Table 2 Appearance frequency of trees in the GA.

Tree	*Appearances*
RandomForest	11
LMT	10
LADTree	9
FT	8
NBTree	7
RandomTree	5
REPTree	0
SimpleCart	0
BFTree	0
J48	0
J48graft	0
DecisionStump	0

Among the trees providing the best classification accuracy with the classic validation, some of them do not appear or rarely in the final population of *GA* as REPTree or SimpleCart, which proves their lack of robustness against the variability of examples in the data set. The use of such trees can be risky because their success ratio can significantly change facing of new examples to classify.

In the other hand, trees like Nbtree and Random forest show good classification accuracy but also high appearance frequency in the final population of *GA*. These trees are a priori the most adapted for the classifiers construction in fault diagnosis of machines. They provide good results independently of the used couple (Training, Validation).

4 Conclusion

Data mining techniques have been introduced to implement an automatic fault diagnosis of an industrial ventilator and several decision trees have been explored.

For the choice of the optimal decision tree method based on genetic algorithms was used, where the performance of decision trees were tested on different couples (training, validation sets) to meet the most robust of them.

Decision trees *Nbtree* and *Random forest* have been proposed for the establishment of automated fault diagnosis tools in the machine, Due to their robustness and good performances.

Future work will focus on establishing more effective fitness function for selecting the best classifiers.

References

Jardine, A., Lin, D., Banjevic, D.: A review on machinery diagnostics and prognostics implementing condition-based maintenance. Mechanical Systems and Signal Processing 20, 1483–1510 (2006), doi:10.1016/j.ymssp.2005.09.012

Tan, C., Irving, P., Mba, D.: A comparative experimental study on the diagnostic and prognostic capabilities of acoustics emission, vibration and spectrometric oil analysis for spur gears. Mechanical Systems and Signal Processing 21, 208–233 (2007); doi:10.1016/j.ymssp.2005.09.015

Khelf, I., Laouar, L.: Influence du choix des indicateurs lors du diagnostic des machines tournantes. In: Proceeding of the 4th International Congress Design and Modeling of Mechanical Systems (CMSM 2011), Sousse, Tunisia (2011)

Sugumaran, V., Muralidharan, V., Ramachandran, K.: Feature selection using Decision Tree and classification through Proximal Support Vector Machine for fault diagnostics of roller bearing. Mechanical Systems and Signal Processing 21, 930–942 (2007); doi:10.1016/j.ymssp.2006.05.004

Yang, B.-S., Di, X., Han, T.: Random forests classifier for machine fault diagnosis. Journal of Mechanical Science and Technology 22, 1716–1725 (2009), doi:10.1007/s12206-008-0603-6

Worden, K., Manson, G., Hilson, G., Pierce, S.: Genetic optimisation of a neural damage locator. Journal of Sound and Vibration 309, 529–544 (2008); doi:10.1016/j.jsv.2007.07.035

Hall, M., Frank, E., Holmes, G., Pfahringer, B., Reutemann, P., Witten, I.: The WEKA Data Mining Software: An Update. SIGKDD Explorations 11(1) (2009)

Combining RBF-PCA-ReliefF Filter for a Better Diagnosis Performance in Rotating Machines

Ilyes Khelf[1], Lakhdar Laouar[1], Hocine Bendjama[2], and Abdelaziz Mahmoud Bouchelaghem[1]

[1] Laboratoire de Mécanique Industrielle,
Badji Mokhtar-Annaba University,
Algeria
ilyeskhelf@gmail.com,
lakla_55@yahoo.fr,
bouchazizdz@yahoo.fr
[2] Unité de Recherche Appliquée en Sidérurgie et Métallurgie URASM/CSC,
Annaba, Algérie
hocine_bendjama@yahoo.fr

Abstract. Condition monitoring and faults diagnosis in rotating machinery is a current research field. In this direction the use of pattern recognition combined with non-destructive testing techniques such as' vibration analysis and signal processing can be very helpful. In this paper is proposed, a diagnosis method of rotating machinery using vibration signatures using a Radial Basis Function classifier. Recorded signals were preprocessed with a Wavelet Decomposition and indicators were extracted both in temporal and frequency domains. To improve diagnosis performance, two techniques for dimension reduction of indicators space were combined; Principal Component Analysis and the ReliefF filter. The method was tested on real signatures from a vibration test rig, operating under several conditions, the results showed the interest to look closely at the choice of indicators in order to obtain best diagnosis performances.

Keywords: diagnosis, rotating machinery, principal component analysis, RBF.

1 Introduction

Considered as a vital part in any industry, rotating machines must have the utmost care and increased monitoring of their operating states. Early detection of faults in these machines can avoid economic losses to industry. In this way the research on non-destructive testing receive a particular interest, and have been greatly developed. Tools such as acoustic emission, oil analysis (Tan et al. 2007) and instantaneous angular speed (Renaudin et al. 2010) among others were used. But the most explored technique remains vibration analysis, thanks to the ease of its implementation. The vibration signal can be exploited in different ways to extract useful and

needed information to make a diagnosis (Jardine et al. 2006). There are several techniques in the literature of its exploitation; with the use of temporal signals or their transformation in the frequency space, and more recently with the wavelet technique in its various forms (Bendjama et al. 2010) (Al-Badour et al. 2011). Choosing the right technique is a sensitive problem before a diagnosis procedure.

For the separation and recognition of the operating states of rotating machines, progress in the field of artificial intelligence and data mining can be a solution. Among theirs tools we found Bayesian networks, support vector machines or more intensely artificial neural networks as classifiers (Khelf and Laouar 2011). The vibration signatures can provide, according to their exploitation technique, reliable indicators for the classification of operating conditions.

The indicators choice is an important factor before any classification procedure, in order to avoid falling on phenomena such as the correlation between indicators, the over-learning problems and the unnecessary and disruptive indicators. Such phenomena could degrade the performance of classification and diagnosis. To resolve this problem we find in the literature two approaches: the first aims to reduce the number of indicators on selecting the best such as filter and wrapper techniques (Khelf and Laouar 2011), the second aims to transform the indicators from one space to another of lower dimension such as Principal Component Analysis *PCA* (Bendjama et al. 2010).

In this work, experiments were conducted on a test rig representing a rotating machine, where vibration signatures were extracted under different conditions, with various types of faults and running on different rotation speeds. On each signature multi-resolution wavelet decomposition was performed and a transformation in the frequency space was applied to the temporal signatures and their different approximations and details, to extract the maximum of information. In order to reduce the indicators space a hybrid technique based on *PCA* and the filter ReliefF was used. The classification of operation states was performed via an artificial neural network: the Radial Basis Function classifier, its performances before and after reduction were compared.

2 Material and Methods

2.1 Experimentation

The experiments conducted on a test rig available in the laboratory URASM - Annaba, are photographed in Figure 1 and shown schematically in Figure 2. The test rig consists mainly of three shafts, with for the movement transmission, two gears (one with 60 teeth and the other with 48 teeth), four bearings housings, a coupling and a belt. The system is driven with an induction motor of power 0.18 kW with a rotational speed ranging from 0 to 1500 rpm controlled by a variable speed drive.

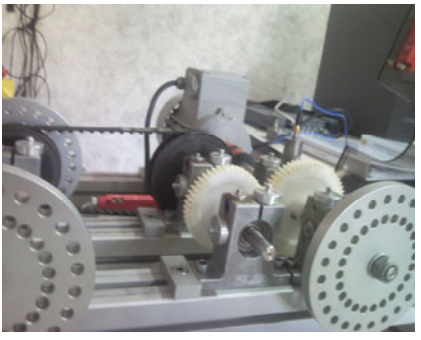

Fig. 1 Test rig

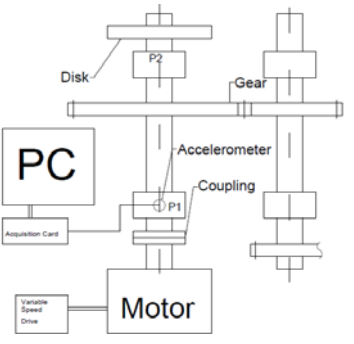

Fig. 2 Schematization of the test rig

An accelerometer was fixed in position P1 shown in figure 2, connected to a data acquisition system equipped with OROS software to record vibration signals per windows of 400 milliseconds with a sampling rate of 5120 sample/second.

The vibration signatures have been recorded in several operating conditions: without the presence of faults, with the presence of a gear fault and with the presence of mass unbalance. This was done in three different rotational speeds: 1500 rpm, 900 rpm and 300 rpm.

2.2 Signal Processing

The use of wavelet transform has seen a significant growth and a particular interest in vibration analysis in recent years, and in particular its discrete variant requiring less computing time than the continuous, the both transformations are represented as follows:

$$CWT(a,b) = \frac{1}{\sqrt{|a|}} \int_{-\infty}^{+\infty} s(t)\psi^*\left(\frac{t-b}{a}\right)dt \tag{1}$$

$$DWT(j,k) = \frac{1}{\sqrt{2^j}} \int_{-\infty}^{+\infty} s(t)\psi^*\left(\frac{t-2^j k}{2^j}\right)dt \tag{2}$$

Effective use of the *DWT* was developed (Mallat 1989), by applying a succession of low-pass and high-pass filter to the signals and this on several levels, the resulting signals are called approximations and details. Figure 3 shows the principle of DWT decomposition.

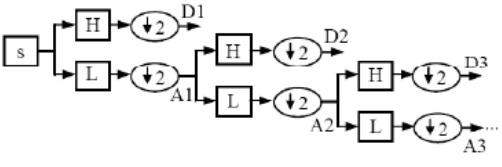

Fig. 3 DWT Decomposition

In the present study Daubechies wavelet Db2 with three levels of decomposition was used to extract approximations and details of original signals.

A transformation in the frequency space using Fast Fourier Transform *FFT* was performed on each original signal as well as on each of its approximation and details as shown in figure 4 for the example of gear fault under a rotational speed of 900 rpm.

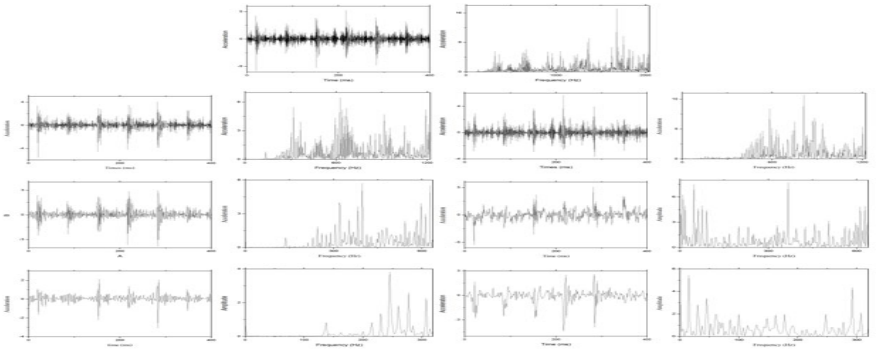

Fig. 4 Example of gear fault signature and its transformations

2.3 Indicators Extraction

38 original signals were recorded in 3 different operating conditions and 3 different rotational speeds, for a number of 342 original signals.

The DWT Decomposition has allowed us to represent each original signal in 7 signals, based on approximations and details. From each of them, four indicators were extracted and three others from their frequency spectra, for a total of 49 indicators by original signal.

From temporal forms of signals were extracted the crest factor, shape factor, root mean square and the kurtosis.

From frequency spectra of signals were extracted the maximum amplitude value, the frequency of the maximum amplitude value and the root mean square of the spectra.

2.4 Indicators Space Dimension Reduction

For the dimension reduction of the indicators space two methods were combined; Principal Component Analysis (correlation between indicators reduction) and ReliefF filter (indicators abilities for classification estimation).

2.4.1 Principal Component Analysis

The principal component analysis transforms the original indicators from one space to another of smaller size. The new indicators are called principal components.

The indicators as well created have a small correlation level, this solve, in theory, one of the main problems of artificial learning.

From each vector of originals indicators, ten new uncorrelated indicators were created with the *PCA*.

2.4.2 ReliefF Filter

Based on the work of (Kira and Rendell 1992), ReliefF assigns a score for each indicator and sorts them according to this score.

The algorithm estimates the quality of indicators depending on the distance between nearest neighbors. For this purpose, given a randomly selected example *A* from a data set *S* with *k* indicators, ReliefF search the data set to its nearest neighbors: one from the same class, called nearest hit *H*, and others from different classes, called nearest miss *M*. It updates the quality estimation *W [INI] INi* for all indicators based on the values of difference function *diff ()* to *X*, *H* and *M*. *m* times, where *m* is a parameter defined by the user. For example, *I1*, *I2*, the function *diff (A, I_1, I_2)* calculates the difference between the values *(I1i, I2i)* for the indicator IN_i

$$Diff\,(A, I_1, I_2) = \frac{\left|value(A, I_1) - value(A, I_2)\right|}{\max(A) - \min(A)} \tag{3}$$

Quality *W [INI]* is updated as follows

$$W\left[INI\right] := W\left[INI\right] - \sum_{j=1}^{k} Diff\,(A, R_i, H_j)/(m.k) + \sum_{C \neq cl(R_i)} \left[\frac{P(C)}{1 - P(class\,(R_i))} \sum_{j=1}^{k} Diff\,(A, R_i, M_j(C))\right]/(m.k) \tag{4}$$

P(c) I is the prior probability of the class and *1-P (class (r))* represents the sum of probabilities for the misses' classes.

2.5 *Operating Condition Classification with the Radial Basis Function Classifier*

A Radial Basis Function Network (Khelf and Laouar 2011) is a feed forward neural network type with one input layer, one hidden layer "a layer RBF" and one output layer. Widely used for classification tasks due to its efficiency and speed of his training. Each layer is fully connected to the next. Each neuron in the hidden layer contains a Gaussian $g_j(x)$ centered on a point of the input space. For a given input *x*, the output of the neuron in the hidden layer is the amplitude of the Gaussian at that point

$$g_j(x) = \exp\left(-\frac{\left\|x - \gamma_j\right\|^2}{2\beta_j^2}\right) \tag{5}$$

The output of the network is a linear combination of the outputs of neurons in the hidden layer weighted by the weight of their respective connections. The answer depends on the function of the distance between the input vector *x*, the vector

prototype (center) γ_j and the size of the influence field β_j that can be estimated from the training set by minimizing a quadratic criterion regularized.

$$f_j(x) = \sum_{j=1}^{N} w_j g_j(x) + w_0 \tag{6}$$

The classifier was trained to separate three classes of operating condition: a class for operating with no faults, a class for operating with a gear fault and a third for operating with a mass unbalance.

Each class includes vectors, obtained from the signals collected in the operating states with three different rotational speeds.

A data set of 114×3 vector was used for training, where a cross-validation algorithm was used during learning and performance-test of the classifier.

2.6 *Diagnosis Automation Algorithm*

After the extraction of the 49 original indicators from each signal, the indicators were transformed into *N* principal components $\{C_1, C_2, ..., C_N\}$, the value of components was then evaluated and ranked using the ReliefF filter.

A *RBF* classifier was then trained using, at first the complete set of components as input and at each iteration, reduced the number of inputs, starting with the lowest ranked of them with the filter ReliefF.

The set of *N* components, providing the highest classification accuracy is selected. The flow chart of the proposed algorithm is described in figure 5.

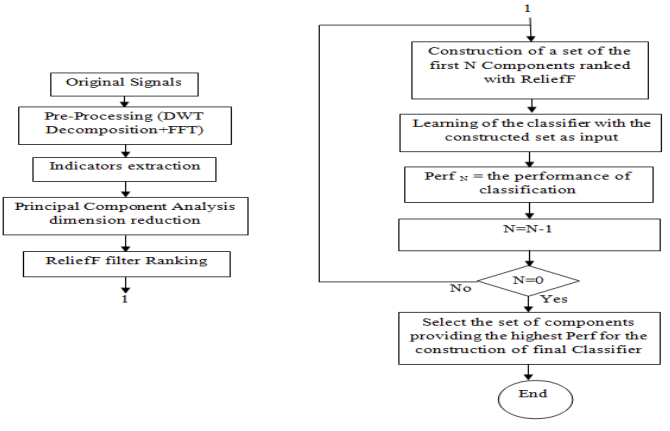

Fig. 5 Flow chart of the proposed algorithm

3 Results and Discussion

The figure 6 shows the evolution of performance according to the number of components used at the input of RBF.

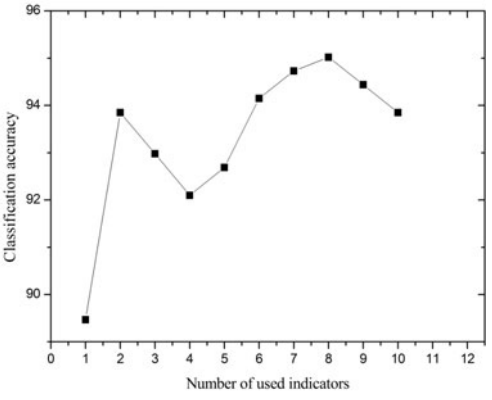

Fig. 6 Evolution of performances

The accuracy of classification has changed according to the number of used components as input and reached its best performance with the use of the 8 best components, with the diminution of the number of used components the performance drop except for the case of 2 and 3 components, and even fall below 90% with the use of a single component.

The table 1 shows the diagnosis performances *Perf* and the number of used indicators *Nbr* as input of the classifier: the original 49 indicators *ORG*, the complete set of components *CSC* and the selected set of components *SSC* with the proposed algorithm.

Table 1 Diagnosis performances.

	ORG	CSC	SSC
Nbr	49	10	8
Perf	90,64	93,85	95,02

Using directly the 49 original indicators as input of the *RBF*, a performance of 90.64% of correct diagnosis was obtained. The performance has been improved to 93.85% of correct classification with the use of the components created by the *PCA*, the selection of components has enabled us then to achieve a better performance with 95.02% of correct diagnosis.

Reducing the space dimension of indicators using *PCA* enabled us to achieve better diagnosis performances, but interfere with the evaluation and understanding of the physical behavior of the original indicators.

4 Conclusion

The selection of indicators at the base of the diagnosis is very important to achieve the best performances. In this work an algorithm for the diagnosis of

rotating machines faults was built based on vibration recorded in operation, under various conditions and with different rotational speeds.

The recorded vibrations were treated using signal processing techniques (DWT Decomposition, FFT) in order to have all the necessary information to make a diagnosis and a large number of indicators were extracted from the signals. The dimension of the indicators space was then reduced by combining two techniques *PCA* and *ReliefF* filter, which enabled us to improve the diagnosis performance.

Some points remain to be improved especially on the understanding and the justification of the original indicators performance.

References

Tan, C., Irving, P., Mba, D.: A comparative experimental study on the diagnostic and prognostic capabilities of acoustics emission, vibration and spectrometric oil analysis for spur gears. Mechanical Systems and Signal Processing 21, 208–233 (2007); doi:10.1016/j.ymssp.2005.09.015

Renaudin, L., Bonnardot, F., Musy, O., et al.: Natural roller bearing fault detection by angular measurement of true instantaneous angular speed. Mechanical Systems and Signal Processing 24, 1998–2011 (2010); doi:10.1016/j.ymssp.2010.05.005

Jardine, A., Lin, D., Banjevic, D.: A review on machinery diagnostics and prognostics implementing condition-based maintenance. Mechanical Systems and Signal Processing 20, 1483–1510 (2006); doi:10.1016/j.ymssp.2005.09.012

Bendjama, H., Bouhouche, S., Boucherit, M.S., Mansour, M.: Vibration signal analysis using Wavelet-PCA-NN technique for fault diagnosis in rotating machinery. Mediterranean Journal of Measurement and Control 6, 145–154 (2010)

Al-Badour, F., Sunar, M., Cheded, L.: Vibration analysis of rotating machinery using time–frequency analysis and wavelet techniques. Mechanical Systems and Signal Processing 25, 2083–2101 (2011); doi:10.1016/j.ymssp.2011.01.017

Khelf, I., Laouar, L.: Influence du choix des indicateurs lors du diagnostic des machines tournantes. In: Proceeding of the 4th International Congress Design and Modeling of Mechanical Systems (CMSM 2011), Sousse, Tunisia (2011) (in french)

Mallat, S.G.: A Theory for Multiresolution Signal Decomposition: The Wavelet Representation. IEEE Transactions on PAMI 11(7), 674–693 (1989)

Kira, K., Rendell, L.A.: A practical approach to feature selection. In: Proceedings of the Ninth International Workshop on Machine Learning, pp. 249–256. Morgan Kaufmann Publishers Inc. (1992)

Khelf, I., Laouar, L.: Amélioration du diagnostic d'une machine tournante par la sélection du vecteur d'entrée. In: Proceding of Congrès Français de Mécanique 2011, Besançon, France (2011) (in french)

Acoustical Holography for Non-Stationary Sources Using Orthogonal-Like Fractional Octave Band Filters

Fedia Maalej[1], Jérôme Antoni[2],
Mohamed Haddar [1], and Tahar Fakhfakh[1]

[1] Ecole Nationale d'Ingénieurs de Sfax,
Unité Dynamique des Systèmes Mécaniques,
Sfax, Tunisie,
maalej_fedia@yahoo.fr
[2] Vibrations and Acoustic Laboratory, INSA of Lyon,
Bâtiment St. Exupéry, 25 bis avenue Jean Capelle,
F-69621 Villeurbanne Cedex, France
Jerome.antoni@insa-lyon.fr

Abstract. The Fourier transform is suitable for analysis of stationary acoustic sources only. In contrast wavelet analysis provides information localized both in frequency and in time, which makes it highly appropriate for the study of non-stationary signals. Near field acoustic holography (NAH) is an experimental technique that makes it possible to reconstruct an image of the spatial acoustic field at one frequency, or in a frequency band, from pressure measurements returned by a microphone array. Several variants of NAH have been proposed to characterize non-stationary sources in time rather than in the domain. The idea of this paper is to develop a new NAH method based on orthogonal-like wavelets that can achieve a fractional octave band analysis without relying on the Fourier transform. An inverse problem is posed with relates the wavelet coefficients of the source field to those of the measured pressure. This is then solved with Monte-Carlo simulations. Numerical and experimental results finally illustrate the efficiency of the proposed approach.

Keywords: acoustical holography / wavelets / orthogonal-like fractional octave band filters / inverse problem / Monte-Carlo simulation.

1 Introduction

NAH is based on Fourier transform and some processing in the frequency-wave number domain (Paillaseur et al. 2011). This procedure generates extremely length computational time and introduces aliasing problems for non stationary signal. As the application of this method lies particularly in transportation field, in which most sources are non-stationary, several methods have been developed for this purpose, such as the time domain holography (TDH) which requires several

iterations of standard NAH (Hald 2001, Hald 1995). Another method developed to non-stationary signal analysis named RT-NAH which keeps the time dependence throughout the signal processing (Paillaseur 2009) and permits to continuously reconstruct the pressure field on the source plane (Paillaseur et al. 2011). As the wavelet analysis provides a multiresolution analysis of non-stationary signals, the aim of this study is to develop a procedure of near field acoustical holography method based on wavelet basis instead of Fourier transform analysis. We propose in this paper to use the orthogonal-like fractional octave band filters as a wavelet basis. As well-known that the inverse problem of acoustical holography is an ill-posed problem, we have chosen to solve this inverse problem by Monte-Carlo simulations. A numerical validation of this proposed approach is shown then an experimental one based on pressure field radiated by a Renault diesel engine has also validated this approach.

2 Orthogonal-Like Fractional Octave Band Filters

Fractional-octave-band filters are of wide-spread use in acoustics and vibrations (Antoni 2010). Using orthogonal-like fractional-octave-band filters approach , the bandedge frequencies can be made arbitrarily. As an example of this approach is a bank of 1/n-th octave filters which made of a cascade of constant percentage bandwidth (CPB) bandpass filters and divide octaves into n subintervals (Antoni 2008). The signal to be analyzed by this method is then divided into contiguous bands. The basis functions used to decompose the signal respect the orthogonality condition.

The signal decomposition from the basis functions forms the signal coefficients. These coefficients are the inner product of the signal by these basis functions which may be expressed as (Antoni 2010):

$$X_{ij} = \left\langle x, \psi_{ij}(n) \right\rangle \tag{1}$$

where x is the signal to be analysed.

The next step is to compute the filtered output in the i-th band. These signals outputs are reconstructed from the wavelet coefficients as the sum of the continuous product of these coefficients with the basis functions:

$$x_i(n) = \sum_j X_{ij} \psi_{ij}(n) \tag{2}$$

During this decomposition we must respect two requirements. The first requirement is to compute the partial energies through each band of the filter bank as the overall signal energy. The second condition which is the perfect reconstruction requires that the sum of all outputs to the filter-bank is equal to the original signal such as:

$$x(n) = \sum_{i=1}^{I} x_i(n) \tag{3}$$

3 Inverse Problem Resolution

As well-known the direct problem is explained by the fact that the pressure field emitted by a set of sound sources is measured by an array of microphones. In this study the direct problem is expressed in frequency domain (time dependence $e^{-i\omega t}$) as :

$$p_m(\bar{\omega}) = \int_{S_0} G(r_m, \mathrm{r}, \bar{\omega}) S(\mathrm{r}, \bar{\omega}) dS_0(r) + \upsilon_m(\bar{\omega}), \quad m = 1, ..., M \tag{4}$$

where S_0 the source surface, $p_m(\omega)$ the acoustic pressure measured by the m-th microphone $G(r_m, r, \omega)$ is the Green function characterised by Neumann condition and $\upsilon_m(\omega)$ is the measurement noise.

We assume in this study that the source distribution admits a space-time decomposition on a selected basis functions:

$$S(r, t, \bar{\omega}) = \sum_k \sum_{ij} c_k^{ij}(\bar{\omega}) \psi_{ij}(t) \phi_k^i(r) \tag{5}$$

where c_k are the coefficients of this wavelet basis, r is the space variable, t is the time variable, $\phi_k(r,t)$ the spatial basis functions and K their number, ψ_{ij} the basis function of the fractional-octave-band filters, i is the band index and j is the time index.

After propagation on a selected microphone array, each measured pressure has the wavelet decomposition $p_m(\omega) = \sum_{ij} P_m^{ij} \Psi_{ij}(\omega)$.

Taking into account the decomposition of the source distribution in both fractional-octave-band filters basis and selected basis functions, then the decomposition of each measured pressure by the array of microphone, the purpose of this study is to estimate the source distribution coefficients back-propagation functions of the measured pressures coefficients. As the inverse problem of acoustical holography is an ill-posed problem (which lead to multiple solutions with a low perturbations of the input data), on another hand as known that the statistical approach allows the resolution of this inverse problem, we have chosen to solve this estimation by Monte-Carlo simulations. This inverse problems should be tackled by applying deterministic optimization methods to a regularized least squares formulation of the problem. As the L-Curve and the generalized cross validation methods of regularisation give often a solution to a linear problem, we have applied the Bayesian approach which is an effective tool with two dimensions

problems. This formulation of this inverse problem of acoustical holography contains three part. The first one is the learning phase which aims to source distribution reconstruction from a prior distribution using the Monte-Carlo simulations.

The associated transfer function of this problem is given then by:

$$\underline{\underline{\hat{C}}}_i^a = \left[\sum_{\bar{\omega}} S_{ij}(\bar{\omega}) P^{H\,a}_{\;\;i}(\bar{\omega})\right]\left[\sum_{\bar{\omega}} P_i^a(\bar{\omega}) P_i^a(\bar{\omega})^H\right]^{-1} \tag{6}$$

The second part is the regularization operator and the inverse operator calculation. The reformulation of the second term of this transfer matrix into an eigenvalue problem, then the estimation of the optimal solution using the appropriate regularisation method are expressed as :

$$\left[\sum_{\bar{\omega}} P_i^a(\bar{\omega}) P_i^a(\bar{\omega})^H\right]^{-1} = U_k\, diag(1/(s_k + \lambda)) U_k^H \tag{7}$$

where s_k are non-negative scalars and U_k M*1 eigen-vectors, index H means the conjugate transpose of the eigen-vectors.

The third part is the source reconstruction considering the measured pressure as explained:

$$S_{ij} = \sum_k c_k^{ij}(\bar{\omega}) \phi_k^i(r) = \Phi^{it} C_{ij} \tag{8}$$

4 Results and Discussions

In this first part we will look at digital signals of the proposed approach in acoustical holography. We begin by examining the results of a linear frequency modulated signal which amplitude is modulated by a Gaussian, the choice of the signal was made for its highly non-stationary temper, the minimum frequency is f_{min}=20Hz, the maximum frequency is f_{max}=1400Hz. The signal length is L=2^12, it's decomposed by 1/3-th octave filters. The sampling frequency is 8192 Hz. The array of microphones used to measure the pressure is rectangular, planar, with a radius of 1m, it contents 81 microphones. It is placed parallel to the source surface at a distance z = 0.2m. Reconstructed source distributions from the inverse problem are compared with the imposed source distribution.

A perfect agreement is found in figure 1 between the reconstructed signal using the fractional-octave-band filters decomposition and Monte Carlo simulations in this inverse problem and the original signal, the error is calculated as the average of the absolute value of ($S_{initial}$-$S_{reconstructed}$) divided by the average of the absolute value of $S_{initial}$. The higher minimum and maximum frequency of non-stationary signal is framed by lower cut-off frequency and the half of the sampling frequency the lower the error difference sources are.

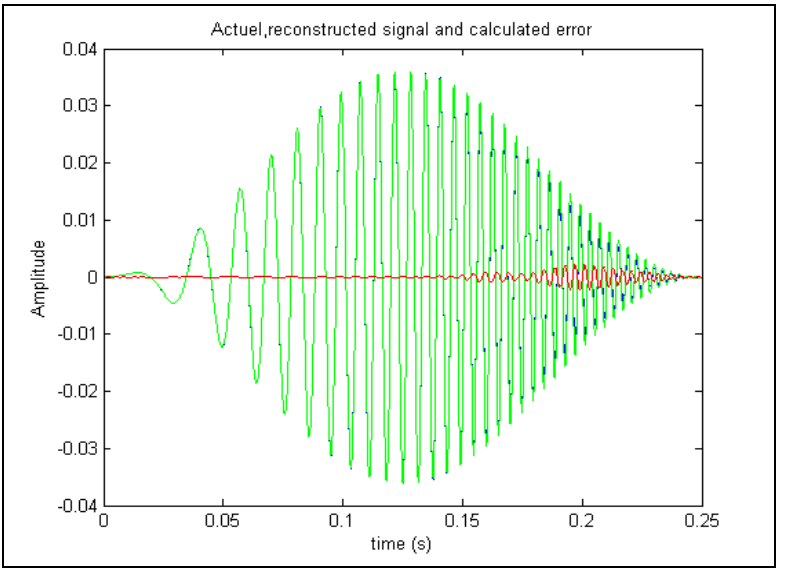

Fig. 1 Reconstructed time signals (green line), the actual signal (blue line), the calculated error (red line)

In a second step we present the results of Monte-Carlo simulation for reconstructing a random signal, the source distribution is composed of three random source which coordinates are respectively (0.4,0.7), (0.7,0.4) and (0.45,0.45) . The signal length is L=2^12, It's decomposed by 1/3-th octave filters. The sampling frequency is 16384 Hz. The array of microphones used to measure the pressure is rectangular, planar, with a radius of 1m, it contents 81 microphones. It is placed parallel to the source surface at a distance z = 0.2m. Reconstructed source distributions from the inverse problem are compared with the imposed source distribution.

We show in figure 2 the random signal decomposition in orthogonal 1/3 octave filters bank superposed with the actual signal decomposition in each band. We show also in this figure the calculated error in all band of the decomposition. It is noticed here that the calculated errors in all band doesn't exceed 10%, so we validate this proposed approach based on stochastic algorithm and fractional-octave-band filters decomposition in inverse problem of acoustical holography.

Figure 3 shows the modulus of the actual source distribution (in the left) and the reconstructed distribution (in the right) in 6392 Hz 1/3 –octave band. A perfect agreement is seen between the actual source distributions and the reconstructed ones by scanning all frequency bands. An important remark is found in the simulation of the proposed approach using the pressure measured by a microphone array

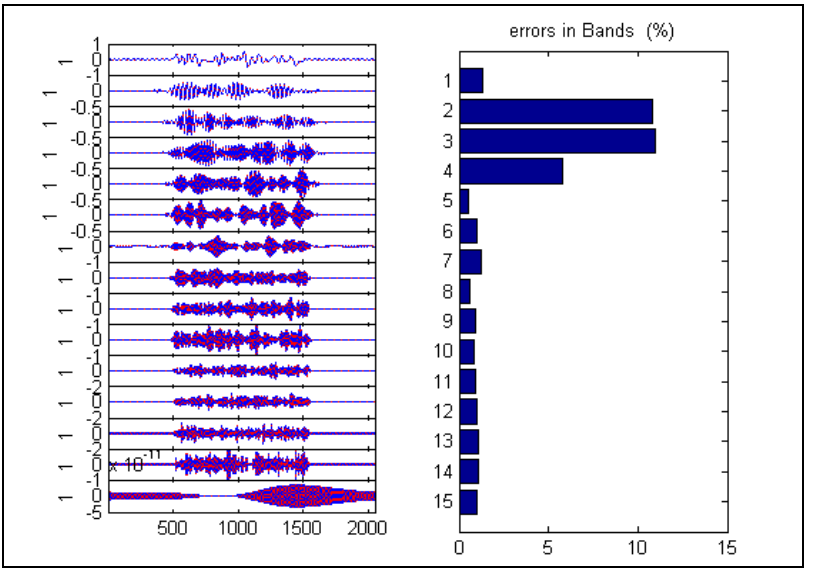

Fig. 2 Decomposition of the random source in 1/3-th octave filters and calculated error in each band

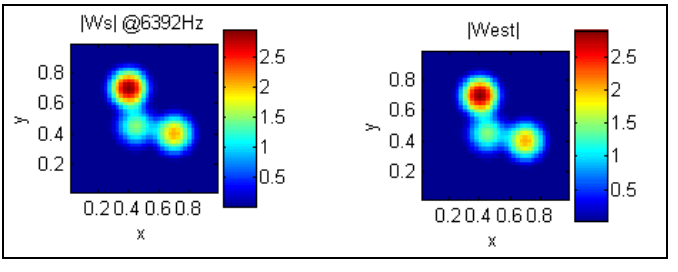

Fig. 3 Modulus of the actual and reconstructed source distribution

placed at z=0.18m from a diesel motor which demonstrates its advantage over the conventional method, with this proposed approach we obtain simultaneously the maps in all thirds octave band while we get the map for one band when we use the Time Domain Holography (TDH) method (Lafon,2009). In addition when we concentrate on the noise source localization (figure 4) a light difference is noted on a linear scale between the proposed approach and TDH method, this difference is important especially in terms of spatial location which is more better with the proposed approach (in the left) than the other (in the right) which shows ghost source due to its simple principle.

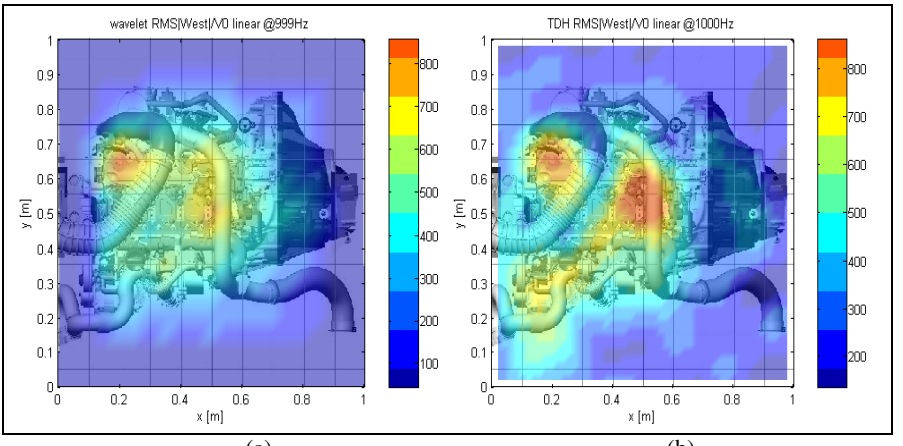

Fig. 4 Roots mean square velocity from wavelet coefficents (a) and TDH method (b) in the 1000 Hz 1/3 –octave band

5 Conclusion

In this paper the problem of characterizing non-stationary sources using the method based on the decomposition on the fractional-octave band filters and using Monte-Carlo simulations has been validated numerically as well as experimentally prooved. The comparison of the obtained maps with the method based on plane waves leads to understand that the proposed approach allows substantial reduction in computation time.

Acknowledgements. The authors would like to thank the Laboratory Roberval of University of Technology of Compiegne and the Dynamics Unit of the Mechanical Systems for their support.

References

Hald, J.: Time domain acoustical holography and its applications. Sound Vib. 35, 16–25 (2001)

Antoni, J.: Orthogonal-like fractional-octave-band filters. Journal of the Acoustical Society of America 127, 884–895 (2010)

Paillaseur, S., Thomas, J.-H., Pascal, J.-C.: Regularization for improving the deconvolution in real-time near-field acoustic holography. J. Acoust. Soc. Am. 129, 3777–3787 (2011), doi:10.1121/1.3586790

Hald, J.: Time domain acoustical holography. In: Proceedings of Internoise, pp. 1349–1354. Newport Beach (1995)

Antoni, J.: Orthogonal 1/n-th octave-band filters: derivation and application to the measurement of instantaneous sound intensity. In: ISMA Conference on Advanced Acoustics and Vibration Engineering, Leuven, Belgium, pp. 15–17 (2008)

Paillaseur, S.: Development of the real-time near-field acoustic holography technique for analysis of fluctuating noise sources. PhD Thesis (in French), University of MAINE, France (2009)

Lafon, B.: Noise Source Separation Coupled to Acoustical Imaging Techniques, Application to Sound Radiation of Diesel Engines. PhD Thesis (in French), University of Technology of Compiegne, France (2009)

Application of Schur Filtering for Local Damage Detection in Gearboxes

Ryszard Makowski[1] and Radoslaw Zimroz[2]

[1] Signal Theory Section
Wroclaw University of Technology,
Wybrzeze Wyspianskiego 27
ryszard.makowski@pwr.wroc.pl
[2] Diagnostic and Vibro-Acoustics Science Laboratory
Wroclaw University of Technology,
Wybrzeze Wyspianskiego 27
radoslaw.zimroz@pwr.wroc.pl

Abstract. Local damage (crack, pitting, spall, breakage, etc.) in gearboxes produces short in time (impulsive) and wideband in frequency, disturbance in vibration response. Detection of such cyclic changes is often very difficult due to presence of high level of noise, i.e. narrowband signal related to normal operation of gear-pair. Most of approaches available in literature propose two-stage methodology: firstly - signal enhancement related mostly to signal pre-filtering in order to extract so called signal of interest (SOI), and finally damage detection/recognition in time domain (spikes detection) or frequency domain (envelope analysis). In this paper we will follow this philosophy. In order to enhance local changes of signal statistics, an adaptive algorithm for vibration signal modelling is proposed in the paper. The discussed approach is based on the normalized exact least-square time-variant lattice filter (adaptive Schur filter). It is characterized by an extremely fast start-up performance, an excellent convergence behaviour, and a fast parameter tracking capability what makes this approach interesting. The method is well-adapted for analysis of the non-stationary time-series, so it seems to be very promising for diagnostics of gearbox working in time varying load/speed conditions.

Keywords: adaptive stochastic modelling, adaptive Schur filter, damage detection, gearbox, vibration time series.

1 Introduction

Localized damage detection in gearboxes is an important problem in condition monitoring. In many cases damage detection is rather difficult because energy of the signal remains similar for healthy and damage condition. From the literature it is known that vibration signal associated with localized damage should be cyclic/periodic and impulsive [22,25]. In the case of complex machine and high energy produced by the other part of machine, localized damage signature is completely masked by other sources. So there is a need to enhance signal (extract Signal of

Interest called SOI or in other words improve SOI-to-Noise Ratio) by advanced signal processing techniques. Variety of filtering techniques are described in the literature, most advanced solution uses wavelets or Empirical Mode Decomposition, Wiener Filter, adaptive filters, cyclostationary modelling and blind source separation, etc [1-25]. Very successful recent application of the Schur filter in respect of bearings vibration signals [14] motivated us to use the similar approach for gearbox vibration. It appeared that our gearbox data are more difficult than bearings signal so further development of damage detection procedure using Schur modelling is presented in this paper.

2 Schur Filter for Time Series Modelling

2.1 Schur Filter Description

Parametric signal processing based on AR models is commonly used [33], however it was designed for stationary time series. In case of localized damage detection, vibration signals are in general non-stationary. In fact such signal is a mixture of stationary and non-stationary ones, i.e. cyclic/periodic impulsive (related to damage) parts. In such case to track changes in the signal it is not possible to use the predictive filter with constant coefficients. However, it is possible to use adaptive Schur filter (ASF) that calculates for every time instant t, optimal (in mean-square sense), so called reflection coefficients, which are strictly related to innovative filter coefficients. It means that such filter is able to follow changes of second order statistics of time series (auto-covariance in this case). The ladder-form realization of the adaptive Schur filter is show on Fig.1 [31].

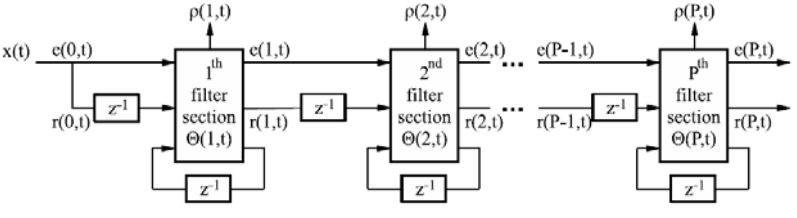

Fig. 1 The ladder-form realization of the adaptive Schur filter

Schur Filter consists of P sections, where P means filter order. Each section is fully described by time dependent reflection coefficient (RC). Inputs for each section are: forward prediction error, backward prediction error and reflection coefficient for every time instants.

Inputs of the first section are normalized samples of signal. For each time instant t, the value of reflection coefficient is updated. The results of updating procedure are based on current sample of time series or prediction error from previous sections. Updating is basically optimization procedure that minimizes error in

mean square sense. In fact whole algorithm (after initialization) is described by 3 recursive equations [30, 31, 33, 14]:

$$\begin{aligned}
\rho(n+1,t) &= \rho(n+1,t-1)(1-e^2(n,t))^{\frac{1}{2}}(1-r^2(n,t-1))^{\frac{1}{2}} - e(n,t)r(n,t-1)) \\
e(n+1,t) &= (1-\rho^2(n+1,t))^{\frac{1}{2}}(1-r^2(n,t-1))^{\frac{1}{2}} - [e(n,t)+\rho(n+1,t)r(n,t-1))] \\
r(n+1,t) &= (1-\rho^2(n+1,t))^{\frac{1}{2}}(1-e^2(n,t))^{\frac{1}{2}}[\rho(n+1,t)e(n,t)+r(n,t-1))]
\end{aligned} \tag{1}$$

It should be noted that before using the rules mentioned above, Schur filter required to be initialized. Due to lack of space, the initialization procedure is omitted here, however it can be found for example in [14, 31].

2.1 Novel Diagnostic Feature for Damage Detection

In previous application of adaptive filter (LMS, AR) for machine condition monitoring the prediction error was used as the output signal with diagnostic potential [11,13,15]. In case of the Schur filter, both prediction error and reflection coefficients for each section can be used. When for given time instant t, a significant change of signal will be present (i.e. impulse will appear), its short-term second order statistics will change, so reflection coefficients will change too and predication error will increase. It is proposed here to use RCs based features, because they seem to be more clear to interpret than variation of prediction errors.

In fact, for damage detection purposes it is necessary to search for changes of RCs instead of their values, thus derivatives of RCs should be used.

$$d(p,t) = \rho(p,t) - \rho(p,t-D); \qquad D = \{1,2,...\};\ t > D \tag{2}$$

Moreover, it was noticed that for our data, the RCs (both single section and sum) manifest some inertia in changes of statistics of signals, so formula for derivatives calculation should take into account the additional parameter D. In this paper results for D=3,4 will presented. Finally, sum of derivatives of RCs for D=3,4 was used as a feature.

It is not convenient to analyze the results from each section separately, it would be better to use single time series that based on P sub-signals obtained from P sections. Initially, simple sum of reflection coefficients is used.

$$d(t) = \sum_{n=1}^{P} d(n,t) \tag{3}$$

Other important parameters used for signal processing were: adaptation (forgetting) constant (required for signal normalization) assumed here to be λ=0.999 and number of sections P = 10.

3 Case Study: Damage Detection in Two Stage High-Power Gearbox

In this section an application of Schur filter to industrial data will be presented. First, the diagnosed object will be briefly presented, next current technique used for damage detection will be discussed and example of such analysis will be provided. Finally the results of novel, proposed here filtering procedure will be shown and compared to previous results.

2.1 Object and Experiment Description

This section provides a brief description of the diagnosed objects. Deep understanding [26,28] of machine design and condition of operation are of fundamental importance in condition monitoring (selection of parameters for data acquisition system, choice of signal processing methods, reasoning rules etc). Mining machines seem to be a special class of machines – high-power, complex design, time-varying load, unique scenario of degradation (due to environmental impact), etc [26-29].

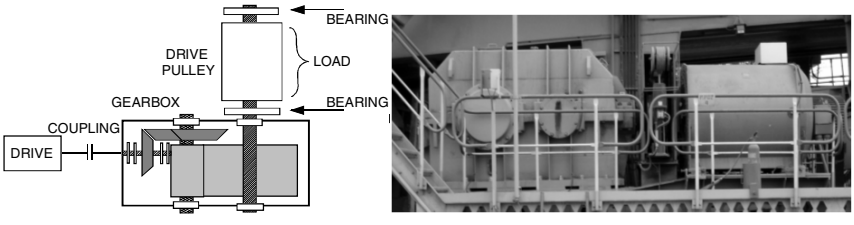

Fig. 2 Scheme and photo of diagnosed object

On Fig 2 the scheme of the driving unit for a belt conveyor is shown. It consists of two sets: motor, coupling and two stage gearbox connected with a pulley. The connection between gearbox output shaft and a pulley is through the coupling. The diagnostic task is to detect a local damage/fault in the gearbox.

2.2 Data Analysis

The classic procedure used for localized damage detection in gearboxes includes visual inspection of time series, calculation of kurtosis in time domain as simple indicator of damage (search for spikiness of the signal) and envelope analysis for signal, both time series and envelope spectrum, see Fig 3.

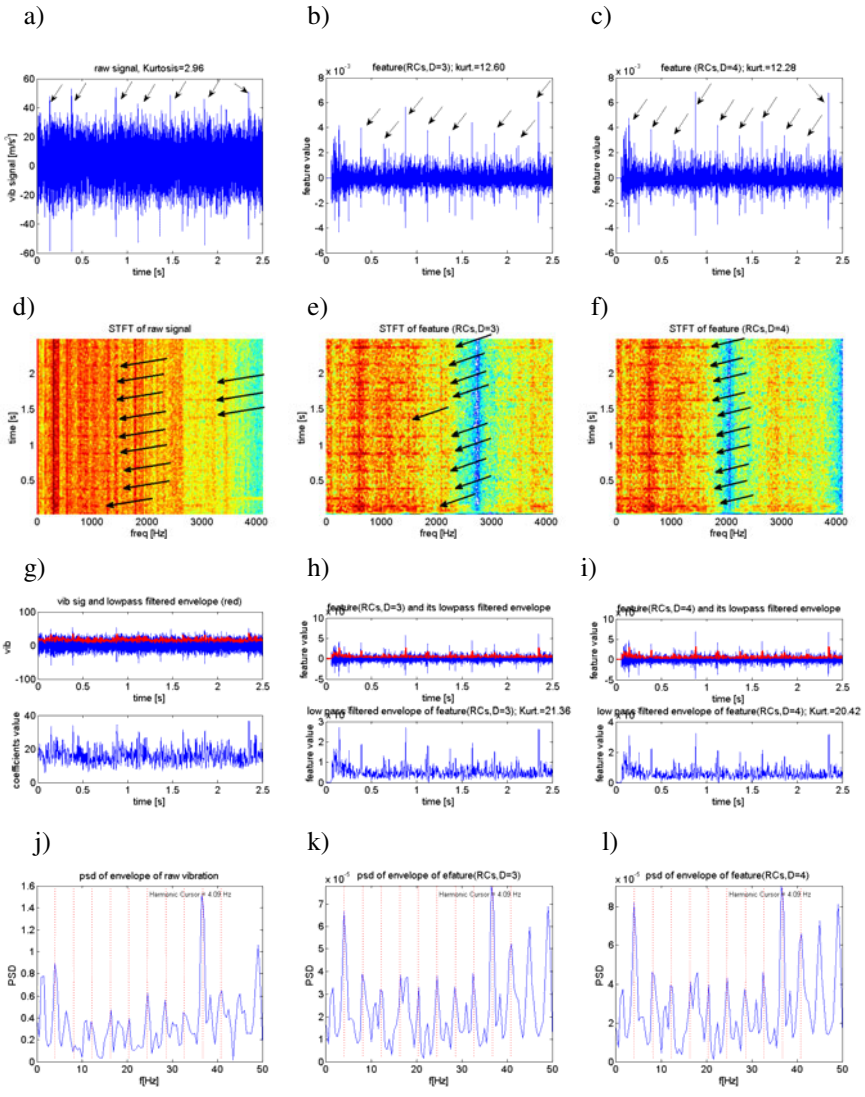

Fig. 3 Results of raw data and enhanced data a) raw vibration signal, b,c) sum of derivates of reflection coefficients for D=3 and D=4 d) spectrogram of raw signal, e,f) STFT of coefficients for D=3 and D=4 g,h,i) signal and its envelope (low passed envelope, fcut=100Hz) for raw signal and coefficients time series for D=3 and D=4 j,k,l) envelope spectrum with identified harmonics related to damage for raw signal and coefficients time series for D=3 and D=4

As it can be seen, kurtosis value for raw time series is quite small and reflects rather Gaussian nature of the signal (Fig3a). Some spikes (marked by arrows) are visible but they seem to be irregular. Also STFT map (Fig 3d) confirms some in-

teresting properties of signal (see some excitation in 800-1200 frequency range). AM demodulation (for wideband) is not successful, neither (Fig 3 g,j). For raw vibration, ability of fault related frequency identification is rather poor.
Below, the results of the same procedure, but after proposed filtering, is discussed. Two examples will be considered, for D=3 and D=4. Signal after filtering for both cases (D=[3,4]) is much more spiky than raw vibration so kurtosis value is higher (see Fig 4). Time-frequency representations of filtered signals have much clear structure (wideband excitation are better visible than for raw signal). Also envelopes of enhanced data are easier to interpret and they are also impulsive (kurtosis values higher than 20) and finally spectra of envelope reveal harmonic structure of the envelope signals, main contribution is related to 4.1Hz, that is middle shaft rotational frequency (again first ten harmonics are marked by harmonic cursor). Finally it may be concluded that application of proposed Schur filter allow to enhance the impulsive contribution and makes damage detection possible.

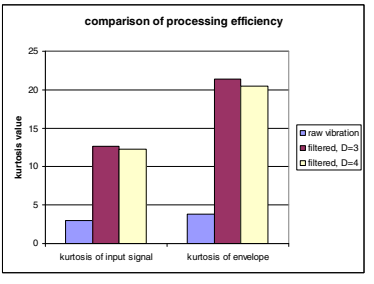

Fig. 4 Comparison of detection efficiency in time domain expressed by kurtosis value for input signal and envelope for both raw and processed data

5 Conclusions

A novel technique of vibration signals analysis based on the adaptive Schur filter is presented in the paper. It was investigated in the context of gear local damage detection. It is suggested to use Schur Filter as a pre-processor i.e. adaptive filter for stochastic modelling of non-stationary signal. Instead of using prediction errors some new features for diagnosis basing on reflection coefficients variation have been tested. The new parameters are: the reflection coefficients, derivative of RCs and sum of derivative of RCs. Based on visual inspection it was decided that the best results are related to sum of derivative of RCs and these are discussed in the paper. Further efforts will be focused on aggregation of information from P sections. First results show that adding some weights for each section before sum may improve final results. It needs to be noticed that, without signal preprocessing, detection of impulses (that indicate local damage) is not possible at all. Results presented in this paper were obtained basing on real signals captured from machines working in mining industry.

Acknowledgements. This paper was financially supported by Polish State Committee for Scientific research 2009-2012 as research project (R. Zimroz).

References

1. Antoni, J.: Fast computation of the Kurtogram for the detection of transient faults. Mechanical Systems and Signal Processing 21(1), 108–124 (2007)
2. Antoni, J.: The spectral kurtosis: a useful tool for characterizing non-stationary signals. Mechanical Systems and Signal Processing 20(2), 282–307 (2006)
3. Barszcz, T., Randall, R.B.: Application of spectral kurtosis for detection of a tooth crack in the planetary gear of a wind turbine. Mechanical Systems and Signal Processing 23, 1352–1365 (2009)
4. Combet, F., Gelman, L.: Optimal filtering of gear signals for early damage detection based on the spectral kurtosis. Mechanical Systems and Sig. Proc. 23(3), 652–668 (2009)
5. Barszcz, T., Jabłoński, A.: A Novel Method of Optimal Band Selection for Vibration Signal Demodulation. Mechanical Systems and Signal Processing 25(1), 431–451 (2011)
6. Lin, J., Zuo, M.: Gearbox fault diagnosis using adaptive wavelet filter. Mechanical Systems and Signal Processing 17(6), 1259–1269 (2003)
7. Peng, Z.K., Chu, F.L.: Application of the wavelet transform in machine condition monitoring and fault diagnostics: a review with bibliography. Mechanical Systems and Signal Processing 18(2), 199–221 (2004)
8. Ricci, R., Pennacchi, P.: Diagnostics of gear faults based on EMD and automatic selection of intrinsic mode functions. Mechanical Systems and Signal Processing 25, 821–838 (2011)
9. Chaturvedi, G.K., Thomas, D.W.: Adaptive noise cancelling and condition monitoring. Journal of Sound and Vibration 76(3), 391–405 (1981)
10. Lee, S.K., White, P.R.: The enhancement of impulsive noise and vibration signals for fault detection in rotating and reciprocating machinery. Journal of Sound and Vibration 217(3), 485–505 (1998)
11. Antoni, J., Randall, R.B.: Unsupervised noise cancellation for vibration signals. Part I—evaluation of adaptive algorithms. Mech. Syst. and Sign. Proc. 18(1), 89–101 (2003)
12. Khemili, I., Chuchane, M.: Detection of rolling element bearing defects by adaptive filtering. European Journal of Mechanics A/Solids 24, 293–303 (2005)
13. Barszcz, T.: Decomposition of Vibration Signals Into Deterministic And Nondeterministic Components and Its Capabilities of Fault Detection and Identification. Int. J. Appl. Math. Comput. Sci. 19(2), 327–335 (2009)
14. Makowski, R.A., Zimroz, R.: Adaptive Bearings Vibration Modelling for Diagnosis. In: Bouchachia, A. (ed.) ICAIS 2011. LNCS(LNAI), vol. 6943, pp. 248–259. Springer, Heidelberg (2011)
15. Zimroz, R., Bartelmus, W.: Application of adaptive filtering for weak impulsive signal recovery for bearings local damage detection in complex mining mechanical systems working under condition of varying load. Solid State Phenomena 180, 250–257 (2012)
16. Antoni, J., Bonnardot, F., Raad, A., Badaoui, M.: Cyclostationary Modelling of Rotating Machine Vibration Signals Mechanical Systems and Sig. Proc. 18, 1285–1314 (2004)

17. Antoni, J.: Cyclostationarity by examples. Mechanical Systems and Signal Processing 23(4), 987–1036 (2009)
18. Zimroz, R., Bartelmus, W.: Gearbox condition estimation using cyclo-stationary properties of vibration signal. Key Engineering Mater. 413-414, 471–478 (2009)
19. Baydar, N., Chen, Q., Ball, A., Kruger, U.: Detection of incipient tooth defect in helical gears using multivariate statistics. Mechanical Systems and Signal Processing 15(2), 303–321 (2001)
20. Antoni, J.: Blind separation of vibration components: Principles and demonstrations. Mechanical Systems and Signal Processing 19, 1166–1180 (2005)
21. Boustany, R., Antoni, J.: Blind extraction of a cyclostationary signal using reduced rank cyclic regression - A unifying approach. Mechanical Systems and Signal Processing 22, 520–541 (2008)
22. Stewart, R.M.: Some useful data analysis techniques for gearbox diagnostics, Applications of time Series Analysis. ISVR, University of Southampton (1977)
23. Brie, D., Tomczak, M., Oehlmann, H., Richard, A.: Gear Crack Detection By Adaptive Amplitude And Phase Demodulation. Mechanical Systems and Signal Processing 11(1), 149–167 (1997)
24. Gelman, L., Zimroz, R., et al.: Adaptive vibration condition monitoring technology for local tooth damage in gearboxes. Insight: Non-Destructive Testing and Condition Monitoring 47(8), 461–464 (2005)
25. Samuel, P.D., Pines, D.J.: A review of vibration-based techniques for helicopter transmission diagnostics. Journal of Sound and Vibrat. 282(1-2), 475–508 (2005)
26. Bartelmus, W., Zimroz, R.: Vibration condition monitoring of planetary gearbox under varying external load. Mech. Syst. and Signal Proc. 23(1), 246–257 (2009)
27. Bartelmus, W., Zimroz, R.: A new feature for monitoring the condition of gearboxes in non-stationary operation conditions. Mech. Syst. and Signal Proc. 23(5), 1528–1534 (2009)
28. Bartelmus, W., Chaari, F., Zimroz, R., Haddar, M.: Modelling of gearbox dynamics under time varying non-stationary operation for distributed fault detection and diagnosis. European Journal of Mechanics - A/Solids 29(4), 637–646 (2010)
29. Combet, F., Zimroz, R.: A new method for the estimation of the instantaneous speed relative fluctuation in a vibration signal based on the short time scale transform. Mechanical Systems and Signal Processing 23, 1382–1392 (2009)
30. Zarzycki, J.: Multidimentional Nonlinear Schur Parametrization of Non-Gausian Stochastic Signals, Part One: Statement of the problem. Multidimensional Systems and Signal Processing 15(3), 217–241 (2004)
31. Lopatka, M., Adam, O., Laplanche, C., Zarzycki, J., Motsch, J.-F.: Effective Analysis of Non-Stationary Short-Time Signals Based on The Adaptive Schur Filter. In: IEEE/SP 13th Workshop on Statistical Signal Proc., pp. 251–256 (2005)
32. Lee, D.T.L., Morf, M., Friedlander, B.: Recursive least squares ladder estimation algorithms. IEEE Trans. Circuit and Systems 28(6), 627–641 (1981)
33. Haykin, S.: Adaptive Filter Theory, 4th edn. Prentice-Hall (2005)

Feature Selection for Diesel Engine Fault Classification

Ezzeddine Ftoutou[1], Mnaouar Chouchane[1], and Noureddine Besbès[2]

[1] Ecole Nationale d'Ingénieurs de Monastir,
Avenue Ibn Eljazzar, 5019 Monastir, Tunisia
ezzeddine.ftoutou@edunet.tn, mnaouar.chouchane@enim.rnu.tn
[2] Ecole Supérieure d'Ingénieurs des Equipements Rurales de Medjez El Bab,
Route de Kef - km5 - 9070 Medjez El Bab, Tunisia
Besbes_Noureddine@yahoo.fr

Abstract. This paper investigates the supervised classification of an injection fault of an internal combustion Diesel engine using vibration measurement. The S-transform is used to produce a time-frequency representation of the vibration signal. The matrix representation of the time frequency image is then reduced to a lower size matrix using a two-dimensional non-negative matrix factorization. Four algorithms are tested for feature selection from this reduced size matrix and the features are sorted according to their ability in fault classification. A Neural Network classifier is then trained and applied to classify test data. The performances of the four considered selection methods are then evaluated by comparing their percentage of correct classification and the computer execution time. It has been found that the performance of the classifier is enhanced when the number of retained feature is increased for the four investigated selection methods.

Keywords: feature selection, time-frequency vibration analysis, two-dimensional non negative matrix factorization, fault classification, Diesel engine injection fault.

1 Introduction

Feature selection [1] is an active research area in several fields such as pattern recognition, statistics, data mining, supervised and unsupervised fault diagnosis and in applications using large datasets. The major objective of a feature selection algorithm is to find a feature subset that produces higher correct classification rate and eliminate redundant and irrelevant features.

Automatic fault detection and diagnostic techniques commonly use classification algorithms which rely on the features extracted from the measured signals. Features from vibration signals may be extracted in the time domain [2] the frequency domain [3] and the time-frequency domain [4]. The time frequency transformation is in general considered to be the most adequate signal processing tool for the unstationary engine vibration signal.

The S-transform (ST), introduced by Stockwell et al. [5], is used in this paper to find a time frequency representation of the vibration signal. The S-transform has the combined strengths of both the Short Fourier transform and the wavelet transform so that a better energy concentration is achieved over the time-frequency domain. The ST has been recently applied to process non-stationary signals generated by internal combustion Diesel engines [6].

The large dimension of the matrix representation of the time frequency image prohibits the direct use of the matrix elements as a feature set. Significant reduction of the size of this matrix is therefore required. The 2D non negative matrix factorization (*2DNMF*) proposed by Zhang et al. [6] is a promising reduction technique which can be used to transform the matrix representation of the time frequency image into a reduced size matrix with only non negative elements. The elements of the reduced matrix can then be used to construct a feature set. Few researchers have used the 2DNMF for mechanical signal applications [6]. A subset of features is then selected using a feature selection algorithm. The selected features are generally sorted according to their classification ability.

In this paper, the classification of an injection pressure fault of an IC diesel engine is investigated. The classification is based on the selected features extracted from vibration signals measured at the middle of the engine block for three levels of the injection pressure fault at both the idle speed of 700 rpm and at a higher speed of 1400 rpm. Using the S-transform, all vibration signals are transformed to time-frequency grey images. Feature reduction is then applied using a two dimensional non-negative matrix factorization of the time-frequency matrix representation. To sort the available features according to their relevance and to further reduce the feature set, four feature selection algorithms are tested. Subsequently, a neural network with backpropagation algorithm (BP-NN) is used to classify the test data into three fault classes and to compare the performances of the four feature selection algorithms.

This paper is organized as follows. Section 2 describes feature extraction in time-frequency domain from engine vibration signals using S-transform as a time-frequency representation and feature reduction by the 2DNMF. Four feature selection algorithms are briefly described in section 3. The measurement set up and the signal acquisition and processing system as well as the simulated fault are described in section 4. The methods presented in section 2 and 3 are then used with an ANN classifier in section 5 to evaluate the performances of the selection algorithms. The paper is concluded in section 6.

2 Feature Set Extraction and Reduction

Vibration signals measured on the engine block are non-stationary due to the variable angular speed of the crankshaft. Time-frequency analysis is often considered as the adequate signal processing tool in this case. In this paper, the recently developed S-transform, proposed by Stockwell et al. [5], is used as a joint time frequency representation of the vibration signal. The S-transform combines the strengths of both the Short Fourier Transform (SFT) and the Wavelet Transform (WT). The time frequency representation is usually used to construct a high

dimensional matrix representation of the signal similar to the representation of the grey level of an image. The pixel values of each image can not be used directly as features in classification due to the high size of the image matrix. Instead, two steps are carried out before classification. First, the image matrix is reduced using 2DNMF by reducing the size of both lines and columns of the high dimensional image matrix to a matrix of a more reasonable size. Further details are given next about both the feature extraction and feature reduction steps.

2.1 S-Transform

The continuous S-transform $S(\tau,t)$ of a function $x(t)$ is defined as,

$$S(\tau,f)=\int_{-\infty}^{+\infty}x(t)\frac{|f|}{\sqrt{2\pi}}e^{-f^2(t-\tau)^2/2}e^{-i2\pi f\,t}dt \tag{1}$$

where τ is the instant of time which controls the position of the Gaussian window on the time axis and f is the instantaneous frequency.

It should be noted that the standard deviation of the Gaussian window decreases with the frequency f.

A key feature of the S-transform is that it uniquely combines a frequency dependent resolution of the time-frequency space with absolutely referenced local phase information [5].

2.2 Feature Set Reduction by Two-Dimensional Non-negative Matrix Factorization (2DNMF)

In a two-dimensional non-negative matrix factorization (*2DNMF*) method [6], the 2D image matrix is transformed into a low dimensional matrix following two steps. At first step, we align the m time-frequency images into a $p\times qm$ matrix $\boldsymbol{X}=\left[\boldsymbol{A}_1,\boldsymbol{A}_2,...,\boldsymbol{A}_m\right]$, where each $\boldsymbol{A}_k$ denotes the time-frequency image of the k-th sample measured signal. 2DNMF finds $p\times d$ non-negative matrix $\boldsymbol{L}$ and $d\times qm$ non-negative matrix $\boldsymbol{H}$ such that

$$\boldsymbol{X}\approx\boldsymbol{L}\boldsymbol{H} \tag{2}$$

Here $\boldsymbol{L}$ and $\mathbf{H}$ are the bases functions and combining coefficients respectively. For convenience, we divide $\boldsymbol{H}$ into m $d\times q$ sub-matrices as $\boldsymbol{H}=[\mathbf{H}_1,\ \mathbf{H}_2,\ \ldots,\ \mathbf{H}_m]$, where $\boldsymbol{H}_k$ denotes the combining coefficients of the image $\boldsymbol{A}_k$. Since each column of $\boldsymbol{X}$ corresponds to a column of the original time-frequency representation, we also call $\boldsymbol{L}$ as column bases. Thus, the k-th time-frequency representation $\boldsymbol{A}_k$ can be written as a weighted sum of the column bases $\boldsymbol{L}$ as follows:

$$\boldsymbol{A}_k\approx\boldsymbol{L}\boldsymbol{H}_k,\ k=1,2,...,m \tag{3}$$

At the second step of *2DNMF*, we compute the row bases. For this raison, at first we construct a new *qxpm* matrix $\boldsymbol{X}'=\left[\boldsymbol{A}_1',\boldsymbol{A}_2',...,\boldsymbol{A}_m'\right]$, with $\boldsymbol{A}_k'$ is the transpose

of $\boldsymbol{A}_{\mathrm{k}}$. Secondly, using 2DNMF, we seek a *qxg* non-negative matrix $\boldsymbol{R}$ and *gxdm* non-negative matrix $\boldsymbol{C}$ such that

$$X^{'} \approx \boldsymbol{RC} \tag{4}$$

Here $\boldsymbol{R}$ and $\boldsymbol{C}$ are the row bases and combining coefficients respectively. We divide $\boldsymbol{C}$ into m $g \times d$ sub-matrices as $\boldsymbol{C} = [\boldsymbol{C}_1, \boldsymbol{C}_2, \ldots, \boldsymbol{C}_m]$, where $\boldsymbol{C}_k$ denotes the coefficients of the matrix $\boldsymbol{A}_{\mathrm{k}}$. Thus, the k-th time-frequency representation $\boldsymbol{A}_k^{'}$ can be written as:

$$\boldsymbol{A}_k^{'} \approx \boldsymbol{RC}_k,\ k = 1, 2, \ldots, m \tag{5}$$

By now, we have obtained the $p \times d$ dimensional column bases $\boldsymbol{L}$ and the $q \times g$ dimensional row bases R.

A matrix $\boldsymbol{D}_{\mathrm{k}}$ of a reduced size giving a new representation of the matrix $\boldsymbol{A}_{\mathrm{k}}$ can be obtained by projection of matrix $\boldsymbol{A}_{\mathrm{k}}$ on the column bases $\boldsymbol{L}$ and the row bases $\boldsymbol{R}$. Thus,

$$\boldsymbol{D}_k = \boldsymbol{L}^T \boldsymbol{A}_k \boldsymbol{R},\ k = 1, 2, \ldots, m \tag{6}$$

$\boldsymbol{D}_{\mathrm{k}}$ is a *dxg* matrix called the encoding matrix of $\boldsymbol{A}_{\mathrm{k}}$ and contains the most important information contained in the matrix $\boldsymbol{A}_{\mathrm{k}}$.

3 Feature Selection

Following feature reduction, a subset of features are selected from the reduced size matrix and sorted in increasing order of relevance. Four algorithms are considered in this paper for this step. Further details are given next about each selection algorithm. Features are selected according to their ability to separate several fault conditions referred to as fault classes. In addition, several features may be used together in order to improve class separation when a number of observations are available.

3.1 Feature Selection Using Analysis of Variance (FSAV)

Stepwise variable selection method is based on univariate and multivariate one-way Analysis of Variance methods [2]. FSAV is used to sort the variables according to their diagnostic ability and to construct by a step-by-step procedure, known as stepwise selection, a set of features to be used in the classification analysis. Each additional feature included in the set is expected to enhance further fault class separation. This procedure is stopped when the addition of more variables does not make any significant enhancement to classification.

3.2 Genetic Algorithms and Information Theory (GAIT)

This algorithm was developed by Ludwig Oswaldo [7] and performs the combinatorial optimization by using Genetic Algorithms (GA). The selection of features is

based on the principle of minimum-redundancy/maximum-relevance (mRMR). The application of the principle of mRMR corresponds to searching the set of features indexes that satisfies the maximization of an objective function.

3.3 Sequential Forward Floating Feature Selection (SFFS)

The sequential floating forward selection algorithm (SFFS) [8, 9], finds an optimum subset of features by insertions (i.e. by appending a new feature to the subset of previously selected features) and deletes ones (i.e. by discarding a feature from the subset of ready selected features). The criterion employed in Sequential floating feature selection is the correct classification rate of the Bayes classifier assuming that the features obey the multivariate Gaussian distribution.

3.4 Fuzzy Entropy Measures with Similarity Classifier (SMFEL)

Luukka [10] introduced a new feature selection method based on fuzzy entropy measures with similarity classifier. The fuzzy entropy measure is suggested by Luca and Termini [11]. Similarities are first calculated and then sorted in a matrix format from which the fuzzy entropy values are calculated for each feature. The feature with the largest fuzzy entropy is removed from the data set. The procedure can then be repeated.

4 Measurement Set-Up and Fault Simulation

Vibration is measured using a piezoelectric accelerometer on a four stroke, internal combustion (IC) diesel engine mounted on a testing bench. The vibration is measured, approximately, at the middle point of the engine in the horizontal direction. An inductive sensor has been used for the acquisition of the top dead centre (TDC) signal of cylinder 1 as shown in Figure 1.

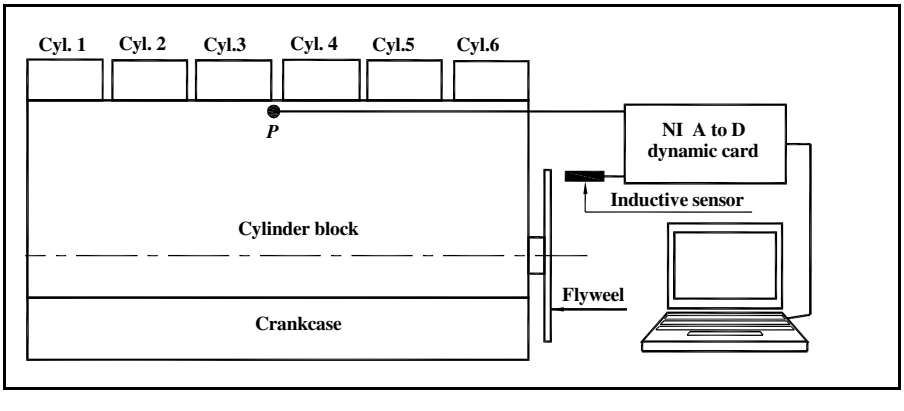

Fig. 1 Measurement set-up for vibration data acquisition on a diesel engine

The simulated injection fault is a reduction of the injection pressure in cylinder 1. A partial loss of the injection pressure is a common injection fault, which may be caused by a leak in the fuel line, or a fault in the injector itself. Using the tarring screw, the injection pressure in cylinder 1 has been gradually reduced from its nominal value 260 bars (*P0*) to 245 bars (*P1*) and 230 bars (*P2*). The injection pressure of other cylinders has not been modified. Thus, three fault classes are simulated.

Vibration signal is measured for the engine speed of 700 rpm and 1400 rpm and without external load. Each signal has a length of 300 engine cycles.

Each cycle contains 4096 data points (respectively 2048 data points) corresponding to a sampling frequency close to 24 kHz. For the engine speed of 700 rpm, the signal of 4096 points was resampled to 2048 points.

For each measured vibration signal, a 1024 x 2048 time-frequency matrix is computed based on the S-transform described in section 2. The high number of the pixels in each image, 1024x2048, prohibits the direct exploitation of the pixel values as features. Thus, a method of reduction of the image matrix representation to a reasonable number of features should be used. The construction of the feature set is based on two steps. First, the matrix of the image pixel values is reduced using the two dimensional non-negative matrix factorization (*2DNMF*) to a matrix of a more reasonable size. Then, four methods have been tested for feature set selection.

The *2DNMF*, described in section 2, is used to extract low-dimensional feature subset from the time–frequency matrix. One hundred time–frequency matrices for each fault class are used to calculate the column basis matrix $\boldsymbol{L}$, row basis matrix $\boldsymbol{R}$ and therefore the encoding matrix $\boldsymbol{D}_k$. After some preliminary experiments, the parameters of reduction d, g and the maximum number of iterations r of the *2DNMF* were set to 10, 5 and 100, respectively. For each engine rotating speed, the size of the reduced matrix is therefore dxg so that 50 (10x5) features are extracted for each time-frequency image. Feature samples are divided into two sets. One-half of the samples are used for training and the other half is used for testing. The 100 features obtained by the *2DNMF* method are reduced further using one of the four selection methods described in section 3.

The ANN classifier is constructed with three layers, the input layer containing a number of neurons equal to the number of features, one hidden layer containing five neurons, and the output layer containing three neurons for the three fault classes. The ANN classifier is trained by the back-propagation learning rule until the mean squared errors are less than 1.10-5. The sigmoid function is used as the activation function in the ANN classifier.

5 Results and Discussion

Using the FSAV and SFFS feature selected algorithms, the number of features is reduced from the 100 available features obtained by the 2DNMF, respectively, to 33 and 38. For GAIL and SMFEL algorithms, the number of selected feature is fixed to be 33. The features are sorted by each algorithm according to their relevance. The time required by each algorithm to complete the selection step is given

in table 1. The algorithms present large discrepancies in selection time from less than one second for the SMFEL algorithm to more than two hundred seconds for the SFFS algorithm.

Table 1 Average CPU time in seconds for feature selection

Method	FSAV	GAIL	SFFS	SMFEL
nf	33	33	38	33
ACPU	32.43	79.33	227.52	0.62

The ANN classifier has been subsequently applied using an increasing number of features selected by each of the four selection algorithms. The average percent of correct classification (*PCC*) for a number of features varying between one and 30 is presented in table 2 and figure 2 for the four algorithms. As expected, the percentage of correct classification generally increases with the number of

Table 2 Average percentage of correct classification (PCC) for an increasing set of features

nf	1	2	3	4	5	6	7	8	9	10	20	30
FSAV	59.33	82.67	79.33	86.67	87.33	84.00	87.33	93.33	88.67	92.67	89.33	94.33
GAIT	69.33	75.33	74.67	77.33	79.33	76.67	74.67	79.33	76.67	77.33	92.00	91.53
SFFS	80.00	80.00	76.00	80.00	82.00	79.33	82.67	83.33	83.33	80.67	88.67	93.66
SMFEL	74.00	73.33	80.00	82.00	82.00	78.00	73.33	74.67	78.67	76.00	80.67	82.66

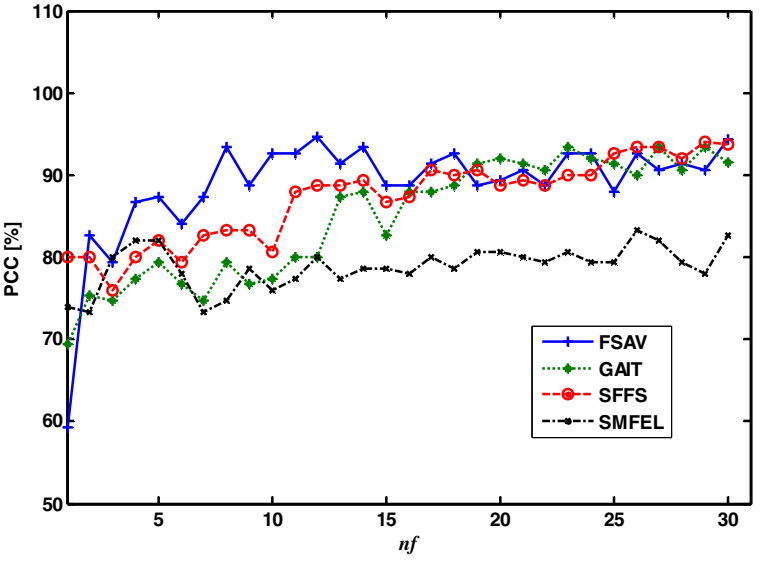

Fig. 2 Average percentage of correct classification (PCC) for an increasing set of features

retained features. The *PCC* significantly increases when passing from one to two features. The SFFS algorithm has the best *PCC* for a single feature. The threshold of 90% is reached first by the FSAV algorithm for eight features. The FSAV algorithm also reaches the highest *PCC*, 94.33 %, for the maximum retained 30 features. The *PCC* of the FSAV algorithm exceeds the *PCC* of the other three algorithms when the number of features used in classification is more than two and less than 20.

The classification results for the first two selected features by each of the four considered selection algorithms are shown in figure 3. The test data containing 50 data points for each fault class are classified by the ANN algorithm into three fault classes. The boundaries between the classes are shown in the figure. The subfigure 3.a and 3.b show that fault classes may spread over more than one area in the feature space. In addition to the percentage of correct classification, the selection algorithms may be evaluated according to the CPU time required for training the classifier and for classifying the test data. Table 3 shows the average CPU time required for training the ANN classifier for a number of retained features varying between one and 30. The CPU time does not necessarily increase monotonically with the number of features used by the classifier. Table 3 shows that for more than five features, the SMFEL algorithm requires the highest training time and the FSAV requires the lowest training time. For less than five features, the SFFS algorithm needs the least training time followed by the FSAV algorithm.

Table 3 Average training CPU time[s] for the ANN classifier

nf	1	2	3	4	5	6	7	8	9	10	20	30
FSAV	11.1	13.8	22.0	12.2	41.0	37.6	29.9	16.0	17.1	21.1	10.8	17.1
GAIT	7.2	35.5	65.1	170.0	124.0	135.7	93.8	175.0	100.9	68.4	34.5	14.1
SFFS	5.7	5.1	5.0	7.6	16.7	105.5	119.7	102.7	171.3	41.5	15.5	12.8
SMFEL	9.6	16.9	17.9	15.6	77.9	149.7	514.4	231.5	276.8	217.4	147.7	133.1

For classification of the test data, the average CPU time is given in table 4 in milliseconds for an increasing number of retained features. It can be noted that the classification time is significantly lower than the training time. Furthermore, the classification time is of the same order for features selected by any of the four considered selection algorithms. The classification time generally slightly increases with the number of retained features. The increase is not monotonous.

Considering now the overall performances of the selection algorithms including classification and CPU time for training and testing. The four algorithms perform a better classification with at least two features. The FSAV algorithm has generally a higher correct classification rate for a higher number of features and requires the least training time. The classification time is roughly the same for the four algorithms. The evaluation criteria used in this paper seem to favor the FSAV algorithm and its statistical density function modeling.

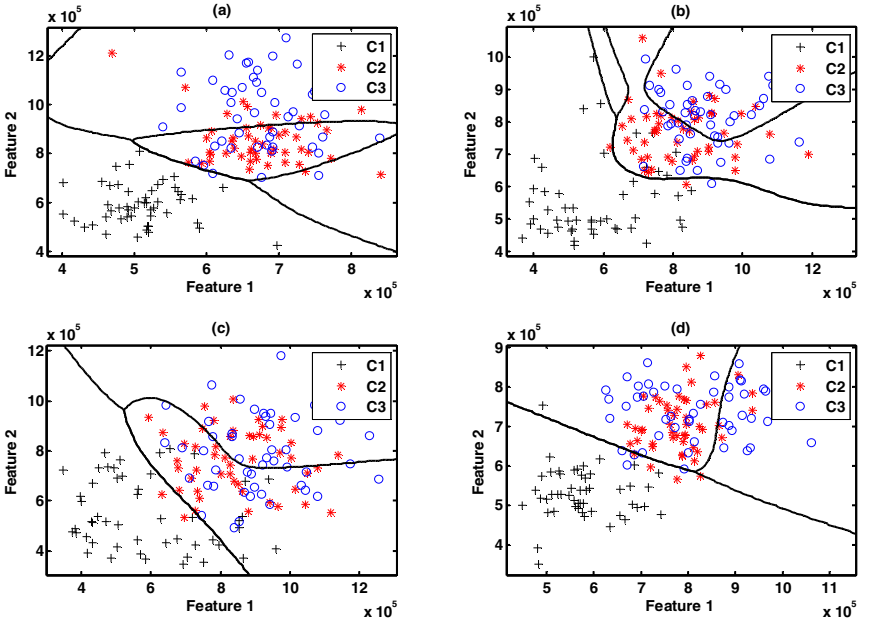

Fig. 3 Test data classification by the ANN algorithm for the first two features selected by each of the four selection algorithms: a) FSAV; b) GAIT; c) SFFS; d) SMFEL.

Table 4 Average testing CPU time [ms]

nf	1	2	3	4	5	6	7	8	9	10	20	30
FSAV	71.9	76.6	63.5	69.8	71.9	66.7	77.1	79.2	83.3	75.0	90.6	98.2
GAIT	68.8	75.5	69.3	67.2	80.2	73.4	78.6	78.6	76.0	77.1	92.2	95.3
SFFS	62.5	62.5	62.5	62.5	78.1	78.1	78.1	78.1	78.1	78.1	93.7	109.3
SMFEL	62.5	62.5	67.2	65.6	71.9	82.8	96.9	71.9	96.9	68.8	100	71.9

6 Conclusion

In this paper, the classification of a diesel engine injection fault using vibration analysis is investigated. Features are extracted from the time-frequency domain using S-transform and *2DNMF* and selected by four different algorithms. For each sample of the measured vibration signal, corresponding to a temporal signal of 2048 points (one engine cycle), a 1024 x 2048 time-frequency matrix is computed based on the S-transform. Using *2DNMF* to extract low-dimensional feature subset from the time–frequency matrix, only 50 features are extracted for each time-frequency image.

An artificial neural network (ANN) algorithm is used as a classifier. It has been shown that for any of the selection algorithms, the use of a larger number of features generally leads to a higher percent of correct classification (*PCC*). Significant increase in accuracy is obtained when using more than one feature in classification. The FSAV algorithm has the highest accuracy for feature set of size lower than 15. For a larger feature set size, the three algorithms, FSAV, GAIT and SFFS have roughly the same classification accuracy. The SMFEL algorithm has a noticeably lower performance for a number of features greater than 12.

References

[1] Liu, H., Motoda, H.: Computational methods of feature selection. Chapman & Hall/CRC, Taylor & Francis Group, New York (2008)
[2] Ftoutou, E., Chouchane, M., Besbès, N.: Internal combustion engine valve clearance fault classification using multivariate analysis of variance and discriminant analysis. Transactions of the Institute of Measurement and Control (2011); doi:10.1177/0142331211408492
[3] Wu, X., Chen, J., Wang, W., Zhou, Y.: Multi-index fusion-based fault diagnosis theories and methods. Mechanical Systems and Signal Processing 15(5), 995–1006 (2001)
[4] Wang, C., Zhong, Z., Zhang, Y.: Fault diagnosis for diesel valve trains based on time-frequency images. Mechanical Systems and Signal Processing 22, 1981–1993 (2008)
[5] Stockwell, R.G., Mansinha, L., Lowe, R.P.: Localization of the complex spectrum: the S transform. IEEE Transactions on Signal Processing 44(4), 998–1001 (1996)
[6] Li, B., Zhang, P.L., Liu, D.S., Mi, S.S., Rena, G., Tiana, H.: Feature extraction for rolling element bearing fault diagnosis utilizing generalized S transform and two-dimensional non-negative matrix factorization. Journal of Sound and Vibration 330, 2388–2399 (2011)
[7] Ludwig, O., Nunes, U.: Novel Maximum-Margin Training Algorithms for Supervised Neural Networks. IEEE Transactions on Neural Networks 21(6), 972–984 (2010)
[8] Ververidis, D., Kotropoulos, C.: Fast and accurate feature subset selection applied into speech emotion recognition. Els. Signal Process 88(12), 2956–2970 (2008)
[9] Ververidis, D., Kotropoulos, C.: Optimum feature subset selection with respect to the information loss of the Mahalanobis distance in high dimensions. PAMI (2009)
[10] Luukka, P.: feature selection using fuzzy entropy measures with similarity classifier. Expert Systems with Applications 38, 4600–4607 (2011)
[11] De, L., Termini, S.: A definition of non-probabilistic entropy in setting of fuzzy set theory. Information Control 20, 301–312 (1971)

Gears and Bearings Combined Faults Detection Using Hilbert Transform and Wavelet Multiresolution Analysis

Issam Moumene and Nouredine Ouelaa

Laboratory of Mechanics and Structures,
University of Guelma, B.P. 401- 24000, Algeria
{i_moumene,i_ouelaa}@yahoo.fr

Abstract. Rotating machinery represents a significant class of mechanical systems, in which gears and bearings are the important and frequently encountered components that find wide spread industrial applications. Currently, vibratory analysis becomes the most reliable tool for the conditional maintenance of rotating machines. The associated techniques evolved so much that one passed from a simple late detection to the diagnosis, even the prediction. Researches in this field are directed towards the possibility of anearly detection, several signal processing techniques, often adapted to a precise defect type, were established throughout these last years. From those, demodulation by wavelets multiresolution analysis combined with Hilbert transform (Envelope analysis), which allowing making filtering and the demodulation at the same time. The objective of this work is the application of this technique for the detection of the faults in the rotatory machines and more particularly the gears and bearings combined faults.

Keywords: Vibratory analysis, gears and bearings combined faults, combined faults simulation, envelope analysis, wavelets multiresolution analysis.

1 Introduction

The vibratory analysis most known and is the most employed in conditional maintenance. It makes it possible to practically detect all types of faults likely to appear in the rotatory machines, an unbalance, gears fault, bearing fault …. These faults result in a variation of the internal efforts which the machine undergoes, and thus with a modification of its vibratory behavior for example a frequency or amplitude modulation in the case of gears and bearings signals. Several work was carried out, using the vibratory analysis for the detection and the diagnosis the gears faults [1-2], but not to take into account the bearings faults, which can caused serious problems during the operation of the rotatory machines. In the early studies, Fourier analysis has been the dominating signal analysis tool for gears and bearings faults detection, but, there are some crucial restrictions of the Fourier transform. The signal to be analyzed must be strictly periodic or stationary; other-wise, the resulting Fourier spectrum will make little physical

sense. Unfortunately, the gears and bearings vibration signals are often non-stationary and represent non-linear processes, and their frequency components will change with time. Therefore, the Fourier transform often cannot fulfill the gear box fault diagnosis task pretty well. On the other hand, the time–frequency analysis methods can generate both time and frequency information of a signal simultaneously through mapping the one-dimensional signal to a two dimensional time frequency plane. Among all available time–frequency analysis methods, the wavelet transforms may be the best one and have been widely used for gears and bearings fault detection. The main issue for the detection and the diagnosis of the bearings faults for example in the gear boxes of the rotatory machines; it is that the vibratory signal of the bearings is masked by the meshing signal [3]. To resolve this type of problem we propose a technique which makes it possible to separate or extract the bearing signal from the gears signal (meshing signal), based on filtering (debruitage) and the demodulation of the signals generated by combined faults of gears and bearings which are shock type signals. The approach used for the simulation of the signals of combined faults is simple, taking the case where the two signals of gears and bearing are additive, which the case where the separation of the two signals is carried out by two passes band filtering, one covers the meshing frequency and the other covers the resonance frequency of bearing, using the Wavelet Multiresolution Analysis combined with the Hilbert transform for the calculation of the envelope of the two signals, at end to extract the characteristic frequencies of gears or bearing faults, according to the envelope spectrum of the two filtered signals. The wavelets are comparable to a band pass-filter.

2 Envelope Analysis Theory (Demodulation)

2.1 Principle of the Demodulation

The principle of method HFRT (High Frequency Resonance Technique), it based on Hilbert transform, which can be represented into four stages:

1. Identification of the resonance frequency (carrier frequency);
2. Selection of the zone to demodulate (bandwidth) at end to carry out a passes band filtering around the selected frequency;
3. Calculation of the envelope of the signal $S(t)$ corresponding by **Hilbert transform** given by the following expression [4]:

$$H[S(t)] = \frac{1}{\pi} \int_{-\infty}^{+\infty} \frac{S(t)}{t-\tau} d\tau = S(t) * \frac{1}{\pi \times t} \tag{1}$$

The envelope of the signal noted $N(t)$ is defined by: $N(t) = \sqrt{S(t)^2 + (H[S(t)])^2}$

4. Calculation of the spectrum of this envelope by the application of the transform of Fourier on the envelope of signal $N(t)$.

2.2 Wavelets Multiresolution Analysis Theory (WMRA)

The Discrete Wavelet Transform (DWT), still called Wavelet Multiresolution Analysis (WMRA), consists to introduce a signal $S(t)$ in low-pass (L) and high pass (H) filters. In this level, two vectors will be obtained, cA_1 and cD_1. The elements of the vector cA_1 are called approximation coefficients, they correspond to the low frequencies of the signal, while the elements of the vector cD_1 are called detail coefficients and they correspond to the highest of them. The procedure can be repeated with the elements of the vector cA_1 and successively with each new vector cA_j obtained. The process of decomposition can be repeated n times, with n the number of levels.For this purpose, Stephan Mallat had the idea to consider the wavelet analysis as a decomposition of the signal by a cascade of filters, associating a pair of filters with each level of resolution [5]. Figure 1represents an example of waterfall decomposition for $n = 3$. During the decomposition, the signal $S(t)$ and vectors cA_j undergo a down sampling, this is why the approximation cA_j and detail cD_j coefficients pass through two new reconstruction filters (LR) and (HR).Two vectors result; A_j called approximations and D_j called details [5].Where i and j are integers.

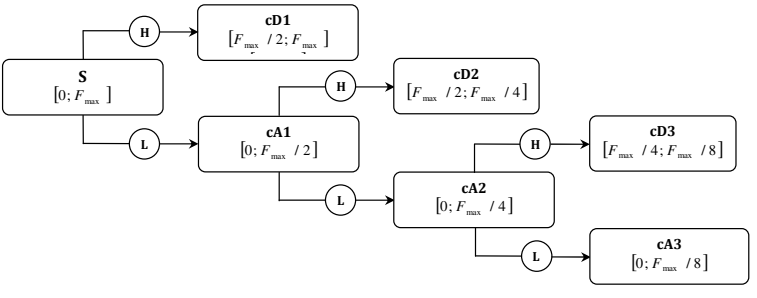

Fig. 1 Example of waterfall decomposition at 3 levels (n=3)

Indicating by $F_{\max}$ the maximum frequency of the measured signal, the frequency bandwidth of each level i returns to $\left[0; F_{\max}/2^{i-1}\right]$ for the approximations and $\left[F_{\max}/2^{i}; F_{\max}/2^{i-1}\right]$ the details. Knowing that the maximum frequency of the level approximation (i) is equal to the measured signal maximum frequency $F_{\max}$ divided by 2^i, we obtain for the last level n:

$$F_{\max}(A_n) = \frac{F_{\max}}{2^n} \tag{2}$$

And as it was shown in [6]:

$$\frac{F_{\max}}{2^n} = 3F_c \Rightarrow n = 1.44 \log\left(\frac{F_{\max}}{3F_c}\right) \tag{3}$$

With n an integer rounded with the higher value, which represents the optimal number of levels, F_c is the shock frequency.

The choice of a maximum frequency of a signal is carried out in such way that at least one or more details will be band-width of the resonance frequency, this is completely possible mathematically. Knowing that the band of each detail (i) is $\left[F_{\max}/2^i ; F_{\max}/2^{i-1}\right]$. So that the resonance frequency F_L is covered by this band, it must satisfy:

$$F_L = \frac{F_{\max}/2^i - F_{\max}/2^{i-1}}{2} \Rightarrow F_{\max} = F_L \frac{2^{i+1}}{3} \tag{4}$$

Many applications of the wavelets analysis were proposed in its continuous version [7-8], discrete (or Multiresolution) [9-10], or with packets [11-12]. In present work, the discrete wavelet family, daubechies wavelets "db5" is used for feature extraction.

3 Gears and Bearings Combined Faults Simulation

The combined faults signals digital simulation, is carried out under Matlab© environment. We propose for the combined faults simulationas the summation of the two models existing in the bibliography such as the model of C. Pachaud for the case of the bearings [13], and the model used by C. Capdessus for the case of the gears [14]. The resulting signal, noted $S_c(t)$, can be expressed mathematically by the expression (5):

$$S_c(t) = S_r(t) + S_{en}(t) \tag{5}$$

with:

$$S_r(t) = Ae^{-t/\tau} \sin 2\pi F_L t * \sum_{k=0}^{+\infty} \delta(t - kT_d) \tag{6}$$

$$\tau = \frac{Q}{\pi F_0} \text{ and } F_L = F_0\sqrt{1 - 1/4Q^2} \quad \text{avec} \quad Q \succ \frac{1}{2} \tag{7}$$

In these expressions, $S_r(t), \tau, F_L, F_0$ and Q, respectively represent the signal simulating the fault of bearing, the relaxation time, the resonance frequency, the free oscillations frequency, and amplification factor. $S_{en}(t)$, represents the gears fault model simulation given by:

$$S_{en}(t) = \left(\sum_{k=-\infty}^{+\infty} S_e(t - n \times \tau_e) \right) * \left(1 + \sum_{m=-\infty}^{+\infty} S_{r1}(t - m \times \tau_{r1}) + \sum_{p=-\infty}^{+\infty} S_{r2}(t - p \times \tau_e) \right) \quad (8)$$

With: τ_e is the meshing period, τ_{r1} and τ_{r2} those of the modulations, $S_e(t)$ the value of the meshing signal on τ_e the flow time of tooth. $S_{r1}(t)$ and $S_{r2}(t)$, are the modulations over the duration of a turn of wheel, (i.e. over durations τ_{r1} and τ_{r2}). S_e, S_{r1} and S_{r2} are sinusoidal functions [14]. Indeed, the period of meshing is by definition a multiple entirety of those of rotation, therefore $\tau_{r1} = Z_{r1} \times \tau_e$ and $\tau_{r2} = Z_{r2} \times \tau_e$. The modulation signals $S_{r1}(t)$ and $S_{r2}(t)$ are of weak energy compared to the meshing signal $S_{en}(t)$. Substituent the expressions (6) and (8) in (5), we obtain, the expression of the combined signal:

$$S_c(t) = \left(Ae^{-t/\tau} \sin 2\pi F_L \right) * \sum_{k=0}^{+\infty} \delta(t - kT_d) + \left(\sum_{k=-\infty}^{+\infty} S_e(t - n \times \tau_e) \right) * \left(1 + \sum_{m=-\infty}^{+\infty} S_{r1}(t - m \times \tau_{r1}) + \sum_{p=-\infty}^{+\infty} S_{r2}(t - p \times \tau_e) \right) \quad (9)$$

If one takes into account a random noise $B(t)$ which can be generated by the operation of the machine and the measuring instruments, the expression (5) is written in the form:

$$S_c(t) = S_r(t) + S_{en}(t) + B(t) \quad (10)$$

Figure 2 (a) represents a simulated signal including combined faults, gears faults (pinion) and bearing faults (Outer racefault + Inner race fault). Figure 2 (b), represents the spectrum of this signal.

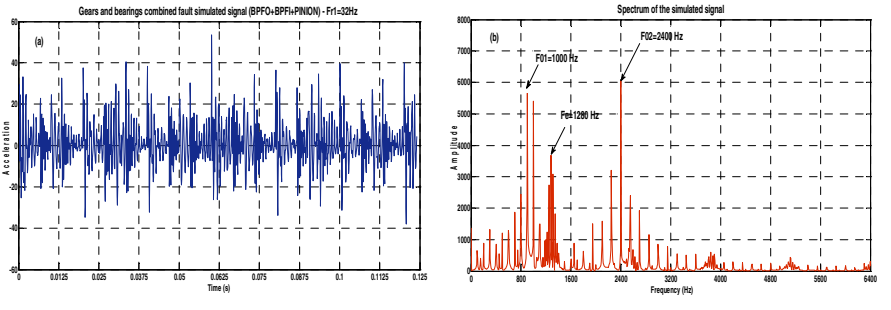

Fig. 2 (a) Combined fault simulated signal, (b) Spectrum of the simulated signal.

In summary, the resulting signal from a gearbox with a gear tooth and bearing combined fault has the following characteristics:

- Presence of modulations;
- Modulating signal frequencies represent fault features generated by gears, bearings or shafts. These frequencies are focused in the low-frequency region.
- The modulating signal may be non-stationary due to the fluctuation of gear/shaft, shocks generated by a bearing fault and lubrication variations.

The enveloping approach that a simulating/measured signal contains a low-frequency component that acts as the modulator of a high-frequency carrier signal. In gear fault detection, the low-frequency modulating signal is the gear rotation frequency and the high-frequency carrier is the meshing frequency. Therefore, in the bearing fault detection, the low-frequency modulating signal is the bearing fault characteristic frequencies and the high-frequency carrier is the resonance frequency.

4 Experiments

4.1 Measurements Points and Used Material

We present on figure 3 on the left, the experimentswere carried out on a test rig designed by laboratory of mechanics and structures (see Fig. 3 at left side). We present on the right side the two points of measurements where we fixed by pins the two transducers, on stage 2 of the driving shaft (CHA) and on stage 3 of the driven shaft (CHB).

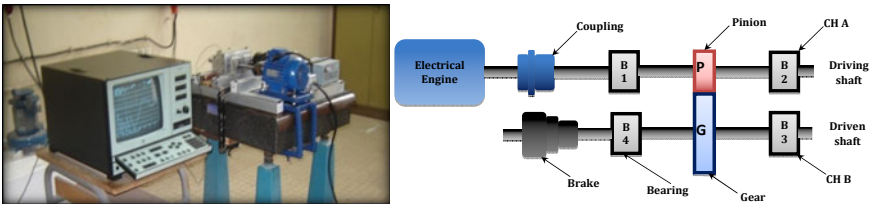

Fig. 3 Gears and bearings test rig designed by laboratory of mechanics and structures / Points of measurements (CHA and CHB).

4.2 Geometrical Characteristics of Bearing Test

On table 1, one represents the various geometrical characteristics of the bearing used in the tests, such as n the number of balls and d the diameter of the ball, D_i , D_e and D_m are respectively the internal diameter, external and means of the bearing, and β the contact angle.

Table 1 Geometrical characteristics of the used bearings

Bearing type	Geometrical proprieties					
	n [bille]	d [mm]	D_i [mm]	D_e [mm]	D_m [mm]	β [degré]
Ball bearing SKF BC 6003	10	4.76	17	35	26	0

4.3 Gears and Bearings Faults Characteristic Frequencies

For better localized the faults frequencies on the spectrum, we calculated the characteristic frequencies of gears and bearing faults (table 2).

Table 2 Gears and bearing faults frequencies

Gears type	Helicoids	
Gears proprieties	Transmission ratio U = 53/40 = 1.325	
	Rotation speeds[Hz]	
	Pinion « CH A » 32.50	Gear « CH B » 24.52
Bearings faults		
BPFO [Hz]	132.74	100.15
BPFI [Hz]	192.26	145.05
Gears faults		
z (Dent)	40	53
F_e [Hz]	1300	

One gear fault was created on the pinion of the drive shaft. Therefore, two types of faults were created on a 6203 ball bearings of P3; faults were artificially localized in aninner, outer race by a diamante tool turning with 50000 RPM. The faults size are (width × depth) = (1×0.3) for the outer race defect and (1.3×0.7) for the inner race. Table 1 and 2 shows some details concerning the experiments conditions. Measurements were taken by a ENDEVCO 2215E type accelerometer and a B&K 2035 type analyzer, the post processing is carried out on Matlab©. The driving shaft rotation frequency was 32 Hz.

5 Application of the Proposed Method on a Measured Combined Faults Signal

Figure 4 (A) represents the combined fault measured acceleration signal on the output shaft of the reducer, the faults were caused on the outer and inner race of the bearing of P3 and on a tooth of the pinion. The measurement of the signal is taken hard stage 3 of the driven shaft which turns at the frequency of 24.52 Hz with a sampling rate 16384 Hz. The spectrum of this last signal is presented on figure 4 (b), which does not make it possible to have a clear diagnosis on gears or bearings state. Some modulations are apparent on the spectrum, which it's due probably to the bearings resonance frequencies. Figure 4 (c), represents the approximations and the details of the decomposition of measured signal in 4 levels.

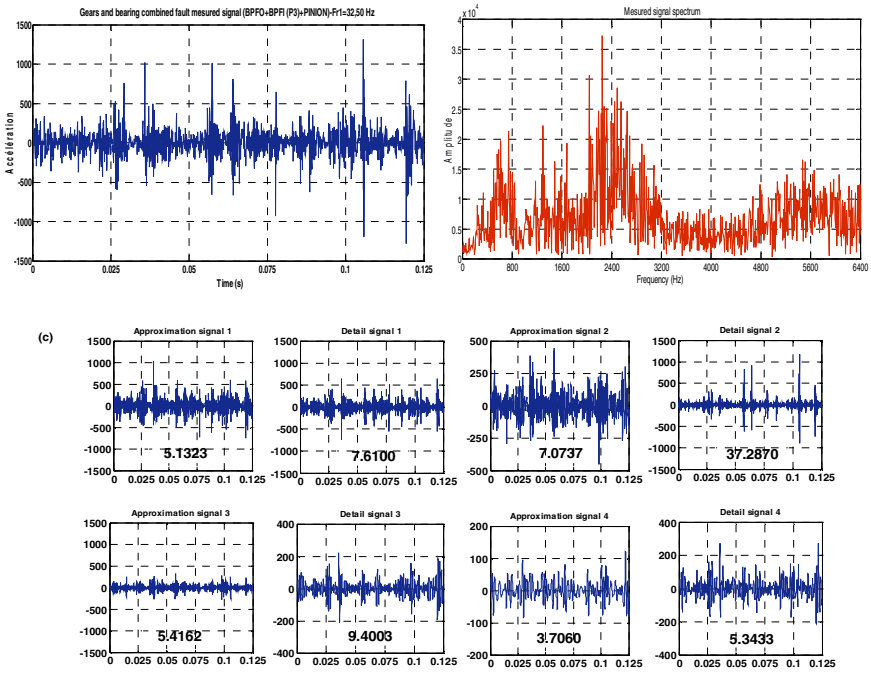

Fig. 4 (A) Combined fault measured signal, (b) its spectrum and (c) decomposition of the measured signal in 4 levels.

The reconstructed signal extracting from the 2nd detail which has a kurtosis equalizes 37.2870, its frequency bandwidth is [1600; 3200Hz], which covers the resonance frequency of the bearing equalizes approximately 2400 Hz. Figure 5 (a), famous of the very clear impacts which are due to the faults of bearing. The reconstructed signal thus appears more informative than that measured. Its spectrum of envelope (fig. 5 (b)), was calculated with Hilbert transform, appears the frequencies of the outer race faults BPFO=96 Hz and the inner race BPFI=144 Hz, and their harmonics. Figure 5 (c), presents the reconstructed signal extracting from the 3rd detail, which has a kurtosis value equalizes to 9.4003, its frequency bandwidth is from [800 Hz; 1600 Hz], which covers the meshing frequency Fe=1280 Hz, its spectrum of envelope (fig. 5 (d)) appears the rotational frequency of the driving shaft carrying the faulty pinion, and several of its harmonics, characterizing the presence of the fault on the pinion. The increase in the amplitude of the third harmonic in the spectrum of envelope of 3th detail, is justified by the coincidence of the peak of bearing fault BPFO=96 Hz, with the third harmonic of the rotational frequency of the pinion Fr1= 32 Hz.

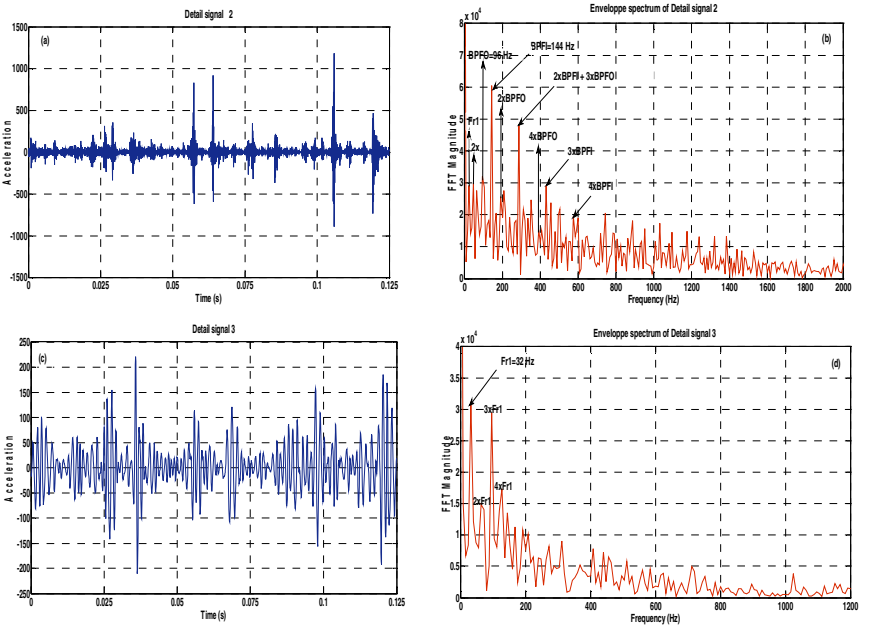

Fig. 5 (A) Reconstructed signal from the 2nd detail, (b) its spectrum of the envelope, (c) Reconstructed signal from 3rd detail and (d) its spectrum of the envelope.

The variations, from 1 to 4 Hz, between the calculated characteristic frequencies of faults such as BPFO= 100.15 Hz, BPFI=145.05 Hz and Fr1=32.5 Hz, and those measured such as BPFO= 96 Hz, BPFI=144 Hz and Fr1=32 Hz, which are mainly due to the frequency resolution step Δf=8 Hz and to the variation of the stalling torque on the output shaft of the reducer.

6 Conclusion

We presented in this work a simulation model of gears and bearing combined faults,and we separate the meshing signal (gears faults signal) from bearings faults signals in the simple case where the two signals were additive based on the proposed technique. We applied the WMRA combined with the Hilbert transform which makes it possible to make a passes band filtering and a demodulation allowing the extraction of the faults from the envelope spectrum of the two optimal vectors having the greatest value of the kurtosis and which covers one of the resonance frequencies of the bearing and the meshing frequency. Wavelet coefficients envelope spectrum allow a clear visualization of the defect characteristic frequency offering the possibility of an early detection.

References

[1] Drouiche, K., Sidahmed, M.: Détection de défauts d'engrenages par analyse vibratoire. J. Trait. Sign. 8, 331–343 (1992)
[2] Wang, W., McFadden, J., P.D.: Application of wavelets to gearbox vibration signals for fault detection. J. Soun. Vibr. 192, 927–939 (1996)
[3] Randall, R.B.: Detection and diagnosis of incipient bearing failure in helicopter gearboxes. J. Engi. Fail. Anal. 11, 177–190 (2004)
[4] Djebala, A., Ouelaa, N., Hamzaoui, N.: Detection of rolling bearing faults using discrete wavelet analysis. J. Mecc. 43, 339–348 (2008)
[5] Mallat, S.: A theory for multiresolution signal decomposition: the waveletrepresentation. IEEE Transaction on Pattern Analysis and Machines Intelligence 11(7), 674–693 (1989)
[6] Djebala, A.: Application de la transformée par ondelettes à l'étude et l'analyse vibratoire des systèmes mécaniques, Thèse de doctorat, Université de Mai 08 1945, Guelma, Algérie (2008)
[7] Baydar, N., Ball, A.: Detection of gear failures vibration and acoustic signals using wavelet transform. J. Mech. Syst. Sign. Proc. 17, 787–804 (2003)
[8] Sung, C.K., Tai, H.M., Chen, C.W.: Locating faults of a gear system by the technique of wavelet transform. J. Mech. Syst. Sign. Proc. 35, 1169–1182 (2000)
[9] Castejon, C., Lara, Garcia-Prada, J.C.: Automated diagnosis of bearings using MRA and neural networks. J. Mech. Syst. Sign. Proc. 24, 289–299 (2010)
[10] Saravanan, N., Ramachandran, K. I.: Incipient gear box fault diagnosis using discrete wavelet transform (DWT) for feature extraction and classification using artificial neural network (ANN). J. Expe. Syst. Appl. 37, 4168–4181 (2010)
[11] Nikolaou, N.G., Antoniadis, I.A.: Rolling element bearing fault diagnosis using wavelet packets. J. NDT & E Inte. 35, 197–205 (2002)
[12] Fan, X., Zuo, M.: J, Gearbox fault detection using Hilbert and wavelet packet transform. J. Mech. Syst. Sign. Proc. 20, 966–982 (2006)
[13] Pachaud, C., Salvetat, R., Fray, C.: Crest factor and kurtosis contributions to identify faults inducing periodical impulsive force. J. Mech. Syst. Sign. Proc. 11, 903–916 (1997)
[14] Capdessus, C., Sidahmed, M.: Analysise des vibrations d'un engrenage: cepstre, corrélation, spectre. J. Trait. Sign. 8, 635–672 (1992)

Artificial Immune System for Condition Monitoring Based on Euclidean Distance Minimization

Luca Montechiesi[1], Marco Cocconcelli[2], and Riccardo Rubini[2]

[1] Faculty of Mechatronics Engineering,
University of Modena and Reggio Emilia,
Reggio Emilia, 42122, Italy
71277@studenti.unimore.it
[2] Department of Science and Engineering Methods,
University of Modena and Reggio Emilia,
Reggio Emilia, 42122, Italy
{marco.cocconcelli,riccardo.rubini}@unimore.it

Abstract. In recent years new alternative diagnostics methodologies have emerged, with particular interest to machineries operating in non-stationary conditions, which have shown to be a severe limit for standard consolidated approaches. In particular this paper focuses on the condition monitoring of ball-bearings in variable-speed applications. In this context the paper aims to present a simple method inspired and derived from the mechanisms of the immune system, and its application in a real case of bearing faults recognition. The proposed algorithm is a simplification of the original process, adapted to a particular case of a much bigger class of algorithms and methods grouped under the name of Artificial Immune Systems, which have proven to be useful and promising in many different application fields. The proposed algorithm is based on the Euclidean distance minimization in the evaluation of the binding between antigens. Experimental results are also provided with an explanation of the algorithm functioning.

Keywords: Condition monitoring, Artificial Immune Systems, ball-bearing, Euclidean distance minimization.

1 Introduction

One of the main problem in the industrial production field is avoiding machines to be stopped by component faults. Statistical evidences prove that the majority of unexpected stops (about 50-60%) are due to faulted bearings. This makes bearing diagnostics a prime research field to improve industrial mechanical systems efficiency and durability. Ideal diagnostics should also provide a real time condition of the components in order to monitor them until the appearance of the first signals of malfunctioning. This could ensure a longer lifetime of the parts than e.g. that provided by a preventive maintenance, where components are substituted at

given time intervals independently of their actual conditions, with a relevant economic advantage. Up to now the problem has been solved analytically studying the bearing as a planetary gear in order to define the dependence of selected damage parameters from the working condition of the bearings. In particular the presence of a damage introduces a specific frequency in the vibration spectrum called *fault frequency*. The proportionality between this frequency and the frequency of bearings rotation is proved. Although this method revealed to be the best one for the monitoring of bearings subjected to stationary conditions, it becomes useless in case of machines that operate at different speeds or even different rotation directions. This problem is sensible in presence of the recent servomotors, which have the characteristics to be very flexible, performing complex motion laws of the shaft. These recent developments have shown the necessity of totally different kinds of approaches than the classic model-based methods. For example the so-called supervised learning systems are awakening the interest of many researchers. In particular artificial neural network (ANN) produced good results in fault detection and a great number of other application. This success increased the interest of scientist and engineers to model and mimic the main natural cognitive systems just like it has been made for ANN [Worden2011, Widodo2007]. These techniques have been applied successfully in the diagnostics of mechanical components such as bearings [Cocconcelli2011, Cocconcelli2011b] and gears [Zimroz2011, Bartkowiak2011, Bartkowiak2012]. One of the most recent field of research among cognitive systems are the *artificial immune systems* (AIS) [Greensmith2010] which can be referred to as the totality of the algorithms and computational methods derived by the study of human immune system. In the next section an introduction to AIS is provided, while in section 3 will be introduced an original AIS algorithm based on Euclidean distance minimization. Finally section 4 reports the results of an experimental activity to prove the feasibility of the algorithm.

2 Artificial Immune Systems

As previously said AIS cover a multitude of different algorithms and methods and their description is out of the scope of this paper [DeCastro1999]. Only the main concepts necessary to understand one of them – the AbNet – will be provided. Concepts will be initially explained from human body perspective to finally be converted into data and algorithm functions. First of all, it is important to distinguish between two fundamental entities which we will refer to:

- *Antigens*: external pathogen agents which are able to cause damage to human body tissue if unstopped.
- *Antibodies:* proteins produced by human body which are able to neutralize Antigens.

The elimination of an antigen is performed so that only the antibodies that couple a specific antigen will stimulate the immune response against it. This coupling process takes place only when the complementarity between the antigen and the

antibody exceeds a fixed threshold. For better explaining and evaluating this phenomenon scientists have created the idea of *shape space* i.e. a space identified by L dimensions where L is the number of different features that influence the coupling process of antibody-antigen (e.g. chemical, geometrical…features).

There are two important immune principles that must be considered: the *clonal selection principle* and the *negative selection principle.* Human systems always generate new antibodies to contrast the enormous number of antigens that strike us every day. But a singular antibody is not a cognitive entity and it is not able to distinguish between antigens (*non self*) and other antibodies (*self*), so the immune system could attack and destroy itself (the so-called autoimmune disease). Moreover antibodies generation – through a pure randomization process – could provide a weak and inefficient immune response. Therefore the human body uses the two principles previously cited to avoid these two problems: clonal selection principle ensures that only the most suited antibodies will be cloned, that is the antibody which couples with more antigens is the one more to reinforce immune response against that precise antigen. Negative selection principle, on the other hand, avoids antibodies to attack what is *self*, eliminating those which attack each other. These simple concepts have been used by De Castro to create an immune algorithm , AbNet , which has already been used with success in machinery diagnostics [Lucifredi2011]. The idea at the base of AbNet is to transform antigens and antibodies into data and to use the previously explained principles to operate in the field of pattern recognition. The algorithm of De Castro requires the data to be necessary in binary form so it has to be defined a new distance for evaluating antigen-antibody binding. This type of distance is computed between two binary arrays calculating the number of complementary bits between them and is called *Hamming distance*. So the higher the complementarity between the two array, the higher will be this distance. In this way it is possible to apply the shape-space formalism to a binary space identified by L dimensional binary strings. Again, the binding occurs when the distance (H) between them overcomes a certain threshold value (E). Working on these concepts AbNet is able to generate – once an arbitrary number of L dimensional binary arrays which represent the antigens and a threshold binding value E are defined – the minimum number of antibodies which can bind every inserted antigen. If E is set to 0 the number of antibodies generated will be exactly the same of the antigens, and every antibody will be the perfect complement of an antigen. On the other hand if E is set to a different value, e.g. 3, will be generated less antibodies than antigens because some antibodies will be able to bind more than one antigen, and the complementarity won't be perfect anymore. Applying this algorithm it is possible to create from a bearings dataset (which represent our antigens), passing through a binary conversion of the data, a set of antibodies which are able to recognize not only antigens belonging to the dataset, but also new unknown antigens. Following this method [Lucifredi2011] and [Strackeljan2008] used AbNet as an expert system obtaining very good results. Like any other supervised learning system this implementation of AbNet is

composed of two different phases: the training phase and the testing phase, as shown in Fig. 1. As previously said this kind of AbNet application was able to recognize well malfunctioning bearings, and could also determine what kind of break they were subject to. The method proved to work very well in case of multiple accelerometers used to survey vibration signals and more generally with a very large quantity of information in the training phase, while its detection efficiency decreases unacceptably using only one accelerometer. This is a sensible drawback in industrial maintenance where only a limited number of accelerometers are used.

In this paper an alternative method called Euclidean distance minimization (EDM) is proposed, based on the shape space formalism. The EDM method is derived from the AbNet concept and it allows to solve and simplify the diagnosis process.

3 Euclidean Distance Minimization

The definition of the Euclidean distance between a set of two n-dimensional vectors $\overline{P} = (p_1, p_2, ..., p_n)$ and $\overline{Q} = (q_1, q_2, ..., q_n)$ is reported in Eq. 1.

$$\text{distance}\left\{\overline{P}, \overline{Q}\right\} = \sqrt{\Sigma_{i=1}^{n} \left(p_i - q_i\right)^2} \tag{1}$$

Unlike AbNet which works on arrays of binary numbers, the proposed method works directly on arrays of real numbers and it is reduced to a least squares problem. The shape space is now a normal Euclidean space with L dimensions. Moreover the antibodies can be neglected since they are not really needed at computational level. In fact the antibodies are considered as a biological mechanism used by the human body to compare new antigens with those previously eliminated, so it should be possible classify the new ones as non self and remove them too. These simplifications lead to only two types of basic entities:

- *Training antigens*: antigens relative to bearings of which the health state is known a priori. Let's refer to these as Ag-train.
- *Testing antigens*: antigens relative to bearings of which the health state is to be determined. Let's refer to these as Ag-test.

The algorithm performs Euclidean distance between a set of Ag-train and Ag-test in order to classify the Ag-test according to the proximity to a certain group of Ag-train which represents a specific health condition of the observed bearing.

Figures 1 and 2 show the flowchart of the training and test phases for the AbNet and EDM immune systems respectively. In the next section the algorithm will be implemented to a real case of bearing diagnostics to evaluate its efficiency.

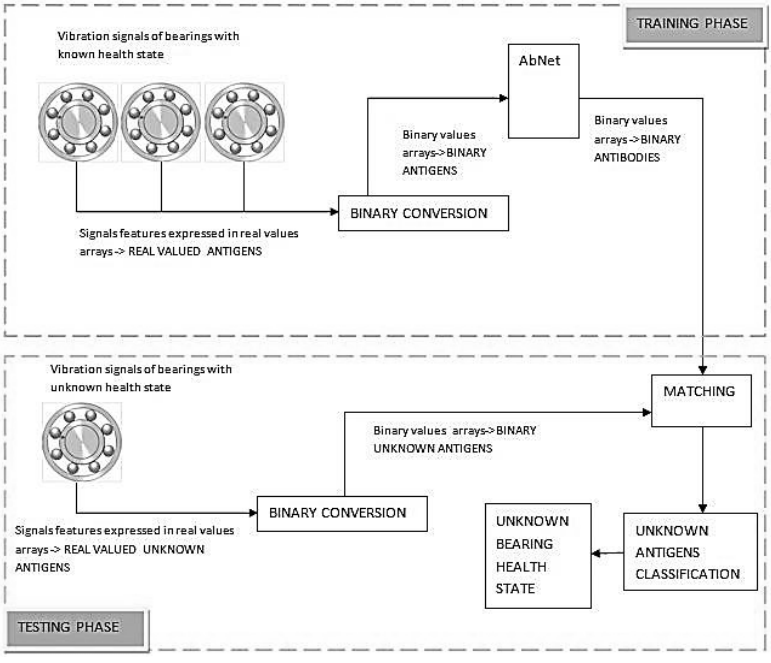

Fig. 1 Block diagram representing AbNet application in bearings diagnosis.

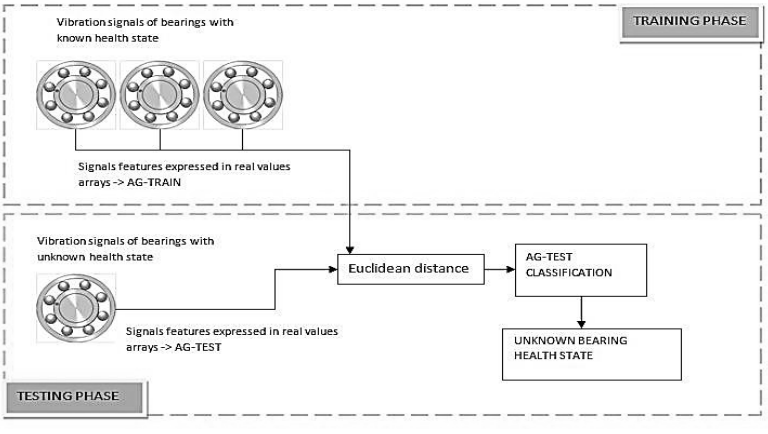

Fig. 2 EDM block diagram

4 Results

The algorithm has been tested on an industrial application. In particular the experimental activity regarded the condition monitoring of a Rockwell Automation AC

Brushless servomotor used in a packaging machine. It must be noticed that the condition monitoring of servomotors is not trivial. In fact these motors don't have a constant rotational speed, but they move following complex speed profile (e.g. polynomial), i.e. there is a continuous change in the rotational speed with also the motion inversion. The experiment took into account 13 bearings, 7 of them were healthy and 6 were damaged at different levels. The bearings were tested on dedicated test-bench which simulated the packaging machine. An accelerometer recorded the vibration signal for a period of 50 seconds at a sampling rate of 10 kHz. The bearing have been tested at different hourly capacity of the packaging machine (i.e. same motion profile but performed at different levels): 5000, 7000 and 9000 packages per hour. A total of 35 acquisitions were taken into account. Among these, 29 have been used in the training phase and 6 for the testing. Note that all the 6 test acquisitions came from different bearings, three of them was faulted and three was healthy.

From every training sample relative antigens were created with the following method:

1. the signal was divided into single cycles of the machine;
2. for every cycle of the machine three real valued features were determined: Kurtosis, Jerk-peak, RMS;
3. the hourly capacity of the machine was added as fourth feature;
4. all these features relative to the same part of the signal (namely a single cycle) were combined in a single array which now represents our antigen;
5. a final operation of normalization has been applied to the antigens to make the shape space uniform: for each feature the maximum value has been determined between all the computed antigens. The maximum values for each features has been taken as reference. Finally each antigen has been proportionally changed in order to align each maximum value to the reference;

The creation of the antigen from the acquired vibration signal is reported in Fig. 3.

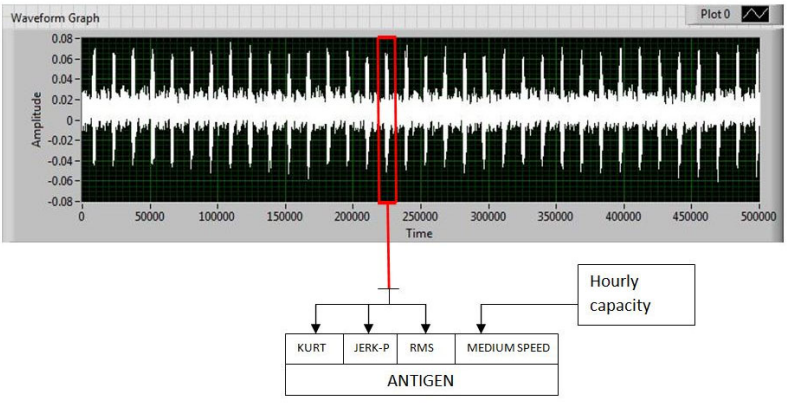

Fig. 3 Antigen extrapolation from the original bearing signal

Once the antigens are created, they can be used in the testing phase. The vibration signal acquired from "unknown" bearings is used to compute the antigens Ag-test with the same features described above. In particular also the normalization is done in order to compare Ag-train with Ag-test.

The Ag-train were divided in two categories: broken (B), working (W), but it's possible to insert more categories (e.g. inner race fault, outer race, etc…).

The classification of a Ag-test is done performing all Euclidean distances between the Ag-test and all the Ag-train, and then considering which antigen and which category (B or W) is associated with the minimum Euclidean distance.

At the end of the process all Ag-test are classified into the B category and/or the W category. The largest population of one of the two categories will provide the final classification.

The classification scheme is summarized in Fig. 4, while Fig. 5 reports the results of the proposed algorithm on the classification of tested data.

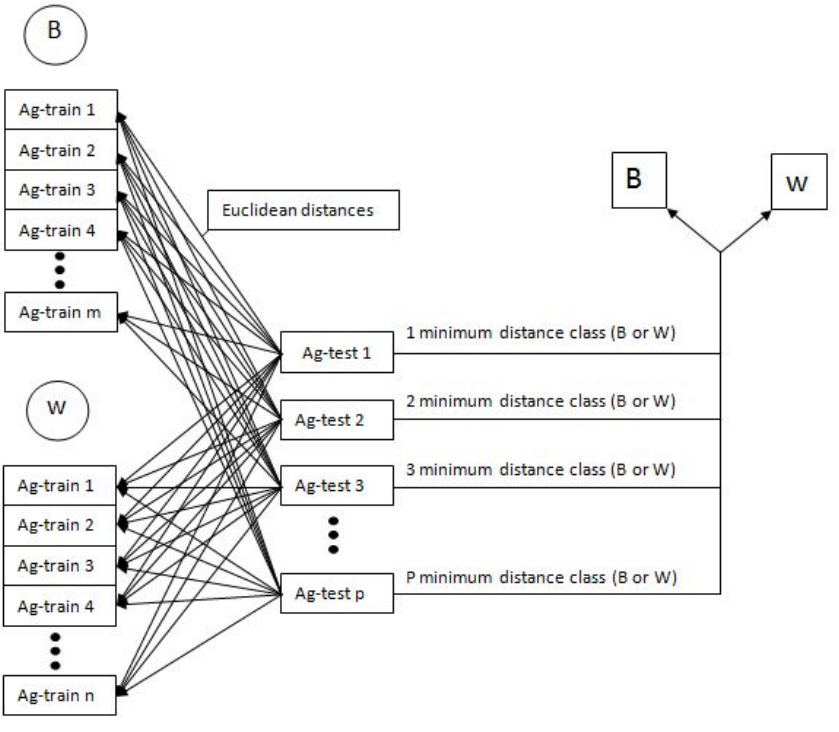

Fig. 4 Classification scheme: for every Ag-test the distances with every Ag-train are performed, then the quantity of minimum distances relative to the two classes are compared to obtain the final classification. The totality of Ag-test (1,2,3,…p) represents all the features extracted from the signal of the bearing to be classified.

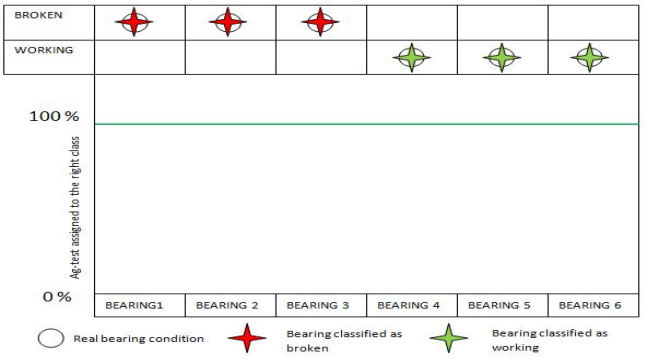

Fig. 5 Classifications of the tested bearing into broken and healthy conditions.

In the examined cases the method was able to recognize the totality of the 6 testing acquisitions and all with the 100% of testing antigens assigned to the right class. Furthermore it must be noticed that some of these (in the working conditions) presented very high values of RMS because they were never been run before, but this condition seemed to give no problem in bearings classification. It's a good signal to prove algorithm's flexibility.

5 Conclusions

The paper aims to present a simple method inspired and derived from the mechanisms of the immune system, and its application in a real case of bearing faults recognition. The proposed algorithm is a simplification of the original process, adapted to a particular case of a much bigger class of algorithms and methods grouped under the name of Artificial Immune Systems, which have proven to be useful and promising in many different application fields. The proposed algorithm is based on the Euclidean distance minimization in the evaluation of the binding between antigens.

Applied to bearing diagnostics the generic antigen used is created collecting together four features computed from the vibration signal: Kurtosis, Jerk-peak, RMS and the hourly capacity of the packaging machine the motor is mounted on. A normalization with respect to the maximum computed value of the features is required in order to compare the antigens developed in training phase with the antigens under classification.

Experimental activity proved the suggested methodology, obtaining maximum results but further test are required for a complete evaluation of its performance and its limits. Moreover the capability to differentiate the type of fault (e.g. inner or outer race) will be developed in the future steps.

Acknowledgements. The authors wish to thank the Inter Departmental Research Center INTERMECH MoRE of the University of Modena and Reggio Emilia for the financial support.

References

Widodo, A., Yang, B.-S.: Support vector machine in machine condition monitoring and fault diagnosis. Mechanical Systems and Signal Processing 21(6), 2560–2574 (2007)

Worden, K., Staszewski, W.J., Hensman, J.J.: Natural computing for mechanical systems research: A tutorial overview. Mechanical Systems and Signal Processing 25(1), 4–111 (2011)

Dasgupta, D.: Artificial Neural Networks and Artificial Immune Systems: Similarities and Differences. In: Proceedings of the IEEE International Conference of Orlando (1997)

Greensmith, J., Whitbrook, A.M., Aickelin, U.: Artificial Immune Systems. CoRR (2010)

Nunes de Castro, L., Von Zuben, F.J.: Artificial immune systems: Part1 Basic theory and and applications. Technical Report. TR-DCA 01/99 (1999)

Lucifredi, A., Silvestri, P., Arrighi., S.: Studio ed applicazione su modelli di macchine rotanti di un algoritmo di diagnostica basato sul metodo del sistema immunitario artificiale. In: Proceedings of XX Congresso AIMETA (2011) (in italian)

Strackeljan, J., Leivska, K.: Artificial Immune System approach for the Fault Detection in Rotating Machinery. In: Proceedings of the CM 2008 Conference, Edinburgh, UK (2008)

Zimroz, R., Bartkowiak, A.: Investigation on Spectral Structure of Gearbox Vibration Signals by Principal Component Analysis for Condition Monitoring Purposes. J. Phys. Conf. Ser. 305, 012075 (2011)

Bartkowiak, A., Zimroz, R.: Outliers analysis and one class classification approach for planetary gearbox diagnosis. J. Phys. Conf. Ser. 305, 012031 (2011)

Bartkowiak, A., Zimroz, R.: Data dimension reduction and visualization of multidimensional data with application to gearbox diagnostics data: comparison of several methods. Solid State Phenom. 180, 177–184 (2012); doi:10.4028/www.scientific.net/SSP.180.177

Cocconcelli, M., Rubini, R.: Support Vector Machines for condition monitoring of bearings in a varying-speed machinery. In: Proceedings of Eighth International Conference on Condition Monitoring, Cardiff, UK, June 20-22 (2011)

Cocconcelli, M., Rubini, R., Zimroz, R., Bartelmus, W.: Diagnostics of ball bearings in varying-speed motors by means of Artificial Neural Networks. In: Proceedings of Eighth International Conference on Condition Monitoring, Cardiff, UK, June 20-22 (2011b)

Conditioning of a Spectral Indicator for the Detection of Rotor Faults of an Induction Motor by Using the TSA Method

Nabil Ngote[1], Saïd Guedira[1], and Mohamed Cherkaoui[2]

[1] Laboratoire CPS2I (Commande,
Protection et Surveillance des Installations Industrielles),
ENIM (Ecole Nationale de l'Industrie Minérale),
BP 753, Agdal, Rabat, Maroc
{Ngotenabil,guedirasaïd}@gmail.com
[2] Equipe de Recherche en Machines Electriques,
EMI (Ecole Mohammadia d'Ingénieurs),
BP 765, Agdal, Rabat, Maroc
cherkaoui@emi.ac.ma

Abstract. The purpose of this paper is to present a method to detect and diagnose an induction motor rotor fault, by exploiting the cyclostationary characteristics of electrical signals. In fact, the induction motor defects are the most complex in terms of detection since they interact with the 50 Hz carrier frequency within a restricted band around 50 Hz. The test bench includes an industrial three-phase wound rotor asynchronous motor of 400V, 6.2A, 50Hz, 3kW, 1385rpm characteristics. The rotor fault has been carried out by adding an extra 40mΩ resistance on one of the rotor phases (i.e. 10% of the rotor resistance value per phase, R_r=0,4Ω). From the stator voltage and current acquisition, and by application of the Time Synchronous Averaging (TSA), the electrical signal is conditioned in order to obtain a sensitive spectral indicator allowing to diagnose the motor defects by the Motor Current Signature Analysis (MCSA) method.

Keywords: Cyclostationarity, Time Synchronous Averaging (TSA), Monitoring; Rotor fault, Spectral analysis, Motor Current Signature Analysis (MCSA).

1 Introduction

The electrical drives using asynchronous machines are very common within industrial applications due to their low costs, high performance and robustness. However, there are various electrical or mechanical-type reasons, which can sometimes affect the well-functioning of these machines [1,2]. The appearance of a fault in the drive modifies its operation and affects its performance. There are mainly two approaches for the monitoring of the electrical-drive system: the mechanic's, based on the vibration, speed and torque measures, and the electro-technician's, based on the current and voltage measures.

A previous work [14] was devoted to develop a statistical indicator from the electrical signals (motor current and voltage) and that enables the monitoring of the machine. In this paper, an approach combining the TSA (Time Synchronous Averaging) and the MCSA (Motor Current Signal Analysis) methods is presented in order to diagnose the induction motor faults.

Indeed, the current signal presents a non-stationary behavior related to the machine operating process and the electrical phase fluctuations [3]. Very little work has been done to exploit the electrical-signal cyclostationary characteristics [3], and it seems interesting to adapt these signal treatment tools to the electrical signal case. The particular case of rotor failures will be considered. Those generally lead to an increase of a one-phase rotor resistance value [1,4-6]. Therefore, a rotor defect is created by adding a 10% value extra resistance on one phase of the rotor.

A simple comparison between the stator current spectrum in the healthy and defective modes of the no-load machine does not allow to detect the failure (the lines of the spectra are quasi confused). The 50 Hz electrical frequency presence set a mask effect on the whole spectrum. Due to the restricted band around 50 Hz of defects sidebands, a simple filtering out of this frequency lead to information complete loss.

A preliminary conditioning of this spectrum will precisely make it possible to exploit the stator current cyclostationarity. By application of the TSA method [7,8], the residue related to the machine mechanics is obtained by subtraction. After conditioning, the new spectrum will allow the easy diagnosis of the defect.

2 Motor Current Signal Analysis (MCSA)

The occurrence of a fault in the drive modifies its operation and affects its performance. The purpose of searching defect kinematic signatures is to characterize the system operation and identify type and origin of each defect. There are several techniques that can be used to detect induction motor defects.

The Motor Current Signal Analysis (MCSA) is one of the most popular used methods because of the following reasons. Firstly, it is noninvasive. The stator current can be detected from the terminals without breaking off the drive operating. Secondly, it can be measured online therefore makes online detection possible. Thirdly, most of the mechanical and electrical faults (such as broken rotor bars, short circuit and bearing damage and air gap eccentricity) can be detected by this method [17].

MCSA is based on the spectral decomposition of stator current through the Fast Fourier Transform FFT. In the MCSA method, the current frequency spectrum obtained and specific frequency components are analyzed. These frequencies are related to well-known machine defects. Therefore, after the stator current treatment, it is possible to conclude about the machine's condition [15-17].

The frequencies of the signals induced by each fault are calculated as a function of some of the motor's characteristic data and operating conditions. In this work, the broken bars defect will be studied. The characteristic frequencies of this defect are given by the following relations [5]:

$$f_{b1} = (1 - 2 \cdot s) \cdot f_s \quad (1)$$

$$f_{b2} = (1 + 2 \cdot s) \cdot f_s \quad (2)$$

Where f_s is the electrical supply frequency and s is the per unit slip.

As shown, given a motor's characteristic data, its current's samples and the value of the slip, it is possible to determine the frequencies of the signals induced by the fault.

3 Signal Synchronization

The asynchronous motor operating process and the electric supply fluctuations cause the non-stationary behavior of the stator current signal. Previous research [10-12] has applied time/frequency representation techniques with an aim of identifying the signatures of the faults not in the frequency field, but in the time/frequency plan.

However, there has been very little work [3] exploiting the electrical-signal cyclostationary characteristics to identify the faults which occur in an asynchronous-motor drive. The idea is to extend the application of these signal-processing tools to the case of electrical signals.

In this work, the first-order cyclostationarity of stator current and voltage is largely exploited. However, a problem of cycle drift from one electric cycle to another, due to the electrical supply fluctuations, is noticed. Fig.1 (top figures) represents the superposition of 1000 electric cycles acquired in a temporal way, and it clearly illustrates the shift between the 1st and the 1000th current signal cycle in the healthy and defective cases. The sampling rate taken is 25.6 kHz (25.6k/50 = 512 samples per average cycle of 50Hz).

The cyclic statistic rules cannot be directly applied to these signals to extract desired information, except if a way to compensate these fluctuations is proposed.

A preliminary stage is needed: the current and voltage signals must be re-sampled according to a reference which "follows" these fluctuations: it's "the synchronization of the current and voltage signal". Therefore, a re-sampling algorithm which allows synchronizing the acquired signals (stator current and voltage) is developed. Synchronization is operated by compensation of the delay between the various electric cycles.

The purpose is to synchronize all electric cycles according to the same reference, so all cycles must be superimposed after the synchronization process.

To do this, current and voltage signals ares first cut out in slices, each one corresponding to one period (20 ms), and each period containing an integer number of samples N. In this case, the sample rate is 25.6 kHz, so N = 512 samples per period (512 = 25.6kHz x 20ms). Then, the shift between the first period, taken as a reference, and the others is estimated. Then, each period is shifted to make it coincide with the first one (reference). If the two periods are already synchronous, the shift is then null. The obtained signals are represented in Fig.1 (down figures).

Once all cycles are synchronized, the signal is rebuilt by setting these cycles end to end. All cycles will be synchronous now and the "synchronous averaging" can be carried out.

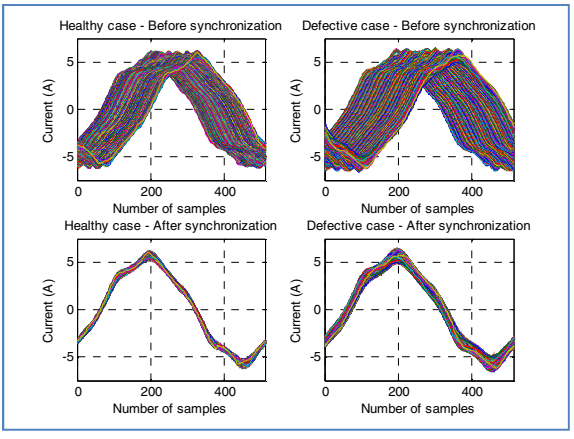

Fig. 1 Stator current shapes

4 Time Synchronous Averaging (TSA)

A rotor fault can be detected by highlighting a stator-current amplitude or phase modulation. However, the modulated-signal weak frequency band makes it too difficult to detect modulation. An alternative to overcome this difficulty is proposed by [7]: the Time Synchronous Averaging (TSA) method. It's a way to reshape the signal before its processing. The TSA method allows the separation between the excitation sources and, consequently, fault identification.

The stator current $I_s(t)$ can be decomposed as follows:

$$\boldsymbol{I_s(t) = I_{s_h}(t) + I_{s_{mec}}(t) + n(t)} \tag{3}$$

Where $I_{s_h}(t)$, $I_{s_{mec}}(t)$ and $n(t)$ are respectively the stator-current harmonic component, the mechanical-structure-related stator current and the noise.

In fact, the asynchronous motor monitoring consists of supervising the signal harmonic part. So, the harmonic frequency (50Hz) which is related to electrical phenomena and mechanical-structure-related frequency must be separated.

For this purpose, the TSA method will be applied to the stator current. In fact, the stator current is the sum of a determinist signal ($I_{s_h}(t)$) and a random signal (sum of $I_{s_{mec}}(t)$ and b(t)); whose average value is zero:

$$I_s(t) = I_{s_h}(t) + I_{s_{rand}}(t) \tag{4}$$

$I_{s_{rand}}(t)$ is the stator-current random component.

The synchronous averaging of N stator-current samples is done by:

$$I_{s_{avg}}^{N}(n \cdot T_{samp}) = \frac{1}{N}\sum_{k=1}^{k=N} I_s^k\,(n \cdot T_{samp}) \tag{5}$$

Where:

- $T_{samp} = \frac{1}{f_{samp}}$, where f_{samp} is the sampling rate (25.6kHz)
- I_s^k is the k[th] synchronized stator current cycle
- n is the sample row (n=1 to 512; 512=25.6k/50; 512 is the number of samples per 50Hz cycle)

For the large value of N:

$$\lim_{N\to\infty} I_{s_{avg}}^{N}(t) = I_{s_h}(t) \tag{6}$$

Note that only the harmonic part $I_{s_h}(t)$ corresponding to 50Hz frequency remains in the averaged signal; since the random-component average value is zero.

Thus, the synchronous averaging allows an effective separation between electrical-related and mechanical-related components. The subtraction between the stator current $I_s(t)$ and the synchronous averaged current $I_{s_{avg}}^{N}(t) \approx I_{s_h}(t)$ (for the large value of N) gives the residual current $I_{s_{res}}(t) = I_{s_{rand}}(t)$ where only mechanical-related frequencies remain.

It's a very interesting property that will allow to condition a mechanical-structure-related indicator monitoring eventual faults (such as rotor defects.)

The residual signal is obtained by subtraction of the TSA signal from the synchronized signal. This action reduces the electrical contribution, and, consequently, makes the extraction of mechanical-related information easier.

5 Stator Current FFT Analysis

The signal must be conditioned in order to develop an asynchronous motor monitoring indicator. Two tests are carried out: no-loaded motor (Test n°1) and motor with a 65% nominal load (Test n°2).

The rotor fault has been carried out by adding an extra 40mΩ resistance on one of the rotor phases. The current and voltage signals are acquired using a data acquisition system and the velocity is measured with an optical tachometer.

Table 1 below summarizes the values of the per unit slip for the two tests:

Table 1 Measurements summary.

	Healthy (Test n°1)	Defective (Test n°1)	Healthy (Test n°2)	Defective (Test n°2)
Per unit slip	2.06%	2.2%	5.53%	6.2%

As a first step, a spectral analysis to stator current is applied. The predominance of the 50Hz component in the stator current spectrum does not allow detecting easily the failure. Especially, in the no-loaded case, the healthy-case and the faulty-case spectra are quasi combined, as shown in Fig. 2. In Fig.3, the spectrum allows the rotor defect visualization. There are two sidebands at frequencies $f_1 = 43.75$Hz and $f_2 = 56.25$Hz; but their amplitude are very low compared to the 50 Hz line's amplitude (respectively 10 and 50 times lower).

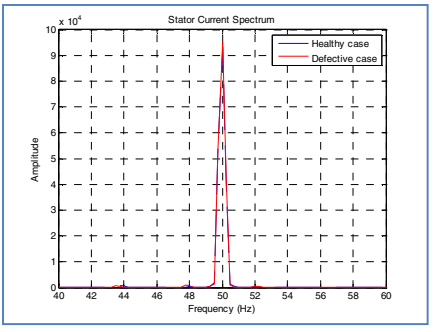

Fig. 2 No-loaded motor

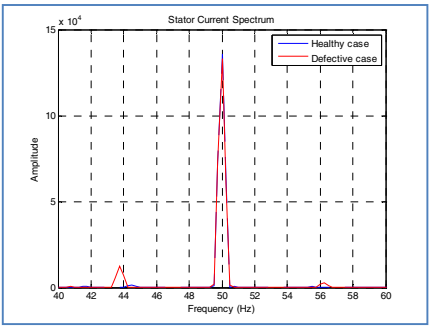

Fig. 3 Motor with a 65% nominal load

The idea is to make the residual-stator-current spectral analysis:

- In the no-loaded case, the faulty residual current spectrum presents clearly two sidebands at frequencies $f_1 = 47.75$Hz and $f_2 = 52.25$Hz (Fig. 4), while in the healthy residual current spectrum, there was no particular sideband. The measured slip value is 2.2% (Table 1) and the electrical supply frequency value is 50Hz; so the theoretical values of f_{b1} and f_{b2} determined from the relations (1) & (2) are respectively 47.8Hz and 52.2Hz. These values correspond to the values f_1 & f_2 deduced from the spectrum.
- Also in the case of motor with a 65% nominal load, the rotor fault is considerably easier to detect in the residual current spectrum (Fig. 5). Indeed, the two sidebands at frequencies $f_1 = 43.75$Hz and $f_2 = 56.25$Hz are more visible now. The measured slip value is 6.2% (Table 1) and the electrical supply frequency value is 50Hz; so the theoretical values of f_{b1} and f_{b2} are respectively 43.8Hz and 56.2Hz, which correspond exactly to the values f_1 & f_2 deduced from the spectrum.

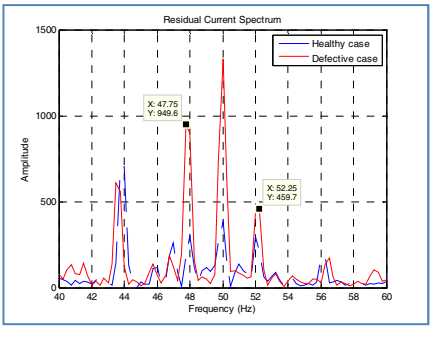

Fig. 4 No-loaded motor

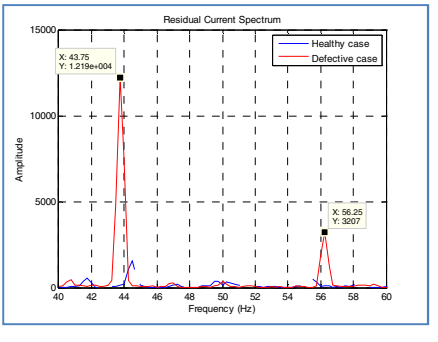

Fig. 5 Motor with a 65% nominal load

6 Conclusion

In this article, the proposed method of asynchronous-motor-failure monitoring has two major advantages:

- First, it is a method which is based on the analysis of the "current" and "voltage" signals. Therefore, it can be applied even to the inaccessible engines (such as the engines immersed in the motor-driven pump groups), unlike the methods based on the analysis of the accelerometer signal, where a direct access to the engine is necessary.
- Besides, the approach is relatively simple: the monitoring of the residual current spectrum makes it possible to clearly detect the defective case. In fact, with a no-load engine, where the fault is hardest to detect, the spectrum shows clearly the sidebands at specific frequency of the defect.

References

[1] Ondel, O.: Thèse: Diagnostic par reconnaissance des formes: Application à un ensemble Convertisseur – Machine asynchrone, Ecole Centrale de Lyon (2006)
[2] Didier, G.: Thèse: Modélisation et Diagnostic de la machine asynchrone en présence de défaillances, Université Henri Poincaré Nancy-I (2004)
[3] Ibrahim, A.: Thèse: Contribution au diagnostic de machines électromécaniques: Exploitation des signaux électriques et de la vitesse instantanée, Université Jean Monnet (2009)
[4] Fiser, R., Ferkolj, S.: Modeling of dynamic performance of induction machine with rotor faults. In: Proceedings ICEM 1996, Vigo, Spain, vol. 1, pp. 17–22 (1996)
[5] Didier, G., Razik, H.: Sur la détection d'un défaut au rotor des moteurs asynchrones. Revue 3EI., Numéro 27 (2001)
[6] Boumégoura, T., Yahoui, H., Clerc, G., Grellet, G.: Observation des paramètres du moteur asynchrone à cage d'écureuil avec un observateur non linéaire. In: Colloque EF 1999, Lille, vol. 30&31, pp. 375–379 (March 1999)
[7] McFadden, P.D., Smith, J.D.: A signal processing technique for detecting local defects in a gear from the signal average of the vibration. Proceedings of the Institution of Mechanical Engineers 199(4), 287–292 (1985)
[8] McFadden, P.D.: A revised model for the extraction of periodic waveforms by time domain averaging. Mechanical Systems and Signal Processing 1(1), 83–95 (1987)
[9] Bennett, W.R.: Statistics of regenerative digital transmission. Bell System Technical Journal 37, 1501–1542 (1958)
[10] Bonnardot, F.: Thèse: Comparaison Entre les Analyses Angulaire et Temporelle des Signaux Vibratoires de Machines Tournantes. Etude du Concept de Cyclostationnarité Floue. Institut National Polytechnique de Grenoble (2004)
[11] Benbouzid, M.E.H., Vieira, M., Theys, C.: Induction motors faults detection and localisation using stator current advanced signal processing techniques. IEEE Transactions on Power Electronics 14(1), 14–22 (1999)
[12] Benbouzid, M.E.H., Kliman, G.B.: What stator current processing-based technique to use for induction motor rotor faults diagnosis? IEEE Transactions on Energy Convers 18(2), 238–244 (2003)

[13] Salles, G.: Thèse: Surveillance et diagnostic des défauts de la charge d'un entraînement par machine asynchrone, Université Lyon 1 (1997)
[14] Ngote, N., Guedira, S., Cherkaoui, M.: Conditioning of a statistical indicator for the detection of rotor faults of an asynchronous machine. Surveillance 6 (October 2011)
[15] Thomson, W.T., Gilmore, R.J.: Motor Current Signature Analysis to Detect Faults in Induction Motor Drives- Fundamentals, Data Interpretation, and Industrial Case Histories. In: Proccedings of 32rd Turbomachinery Symposium (2003)
[16] Thomson, W.T.: A Review of On-Line Condition Monitoring Techniques for Three-Phase Squirrel-Cage Induction Motors – Past, Present and Future. The Robert Gordon University, Schoolhill (1999)
[17] Thomson, W.T., Fenger, M.: Case Histories of Current Signatura Analysis to Detect Faults in Induction Motor Drives. In: IEMDC IEEE Electrical Machines and Drives, vol. 3, pp. 1459–1465 (June 2003)

Numerical Tool for Extraction of Modal Parameters Based on Continuous Wavelet Transform

Olivier Riou[1], Guy-Marie Rakoto Razafindrazato[2],
Pierre-Olivier Logerais[1], and Jean-Félix Durastanti[1]

[1] Laboratoire CERTES,
Université Paris Est Créteil Val de Marne,
IUT Sénart Fontainebleau,
Avenue Pierre Point 77127 Lieusaint – France
olivier.riou@u-pec.fr
[2] Institut Supérieur de Technologie d'Antananarivo,
Ampasampito BP. 8122, Antananarivo 101, Madagascar
rakotogmi@gmail.com

Abstract. Any mechanical system possesses its own vibrating characteristics from which functioning can be understood and foreseen. Modal parameters such as natural frequencies and damping ratios are the main examples. This paper presents homemade numerical analyzer for characterizing them. The procedure is based on complex Morlet wavelet transform with particular use of translated version for better detection of closed modes. The code has been successfully tested through simulated signals. Experimental validation was carried out through the modal analysis of a gear motor on which repeatable and reliable results were obtained.

Keywords: natural frequency, damping ratio, complex Morlet wavelet, gear motor.

1 Introduction

Dynamic behaviour of engineering structures and machineries depends on their functioning conditions, but also largely on their mechanical characteristics. Some of them are the so-called modal parameters such as natural frequencies, damping ratios and modal shapes. Among actual identification techniques of these quantities, modal experimental method represents one of the most used, because of its effectiveness and practical convenience. It is generally based on response data, consisting in analyzing signals issued from a given known excitation or impulse one. The central problem is how to extract the impulse response from the raw signal. Numerous works have been conducted in this field, using various methods, like the natural excitation technique, the random decrement one, etc. All of these approaches give quite satisfying results on simple structures and well-separated vibrating modes. Difficulties present when it is necessary to identify closed ones

which is an usual case with complex machineries. Wavelet transform has also been used by researchers for this purpose [1-5].

In this paper, we present an effective continuous wavelet-based analyzer which is applied to characterize modal components. A brief review of wavelet theoretical background is first given. Then, in order to validate the method, numerical known signals are taken for which two different sorts of responses are treated: a single degree of freedom (sdof) signal and a multiple degree of freedom signal (mdof). Thereafter, effectiveness of the technique is proved through the identification of modal parameters of a skew-geared motor.

2 Mathematical Basis

The continuous wavelet transform (CWT) of a signal *x(t)* is a time-scale decomposition obtained by dilating and time translating of a chosen analyzing function $\psi(t)$. In this work, we use complex Morlet wavelet which offers a good compromise between time and frequency resolutions. One basic function can be defined in time domain by:

$$\psi(t) = (\pi k)^{-0.5} \exp(j 2 \pi f_w t) \exp(-t^2 / k) \tag{1}$$

where k is the bandwidth parameter and f_w the wavelet frequency. The *a*-dilated version of the Fourier transform is:

$$\Psi(a f) = \exp\left(-(k/4)(a f - f_w)^2\right) \tag{2}$$

which is maximum at the central frequency $f_c = f_w / a$. The wavelet transform can be viewed as a linear bandpass filter whose bandwidth is proportional to *1/a* or to the central frequency f_c. For a given value of *a*, the spectrum of the Morlet wavelet has a fixed bandwidth. If the analyzed frequency is high, the dilatation parameter is small and the wavelet spectrum becomes wide. This leads to a bad spectral resolution. An alternative to this problem is to set an optimal bandwidth parameter *k* in order to control the width of the filter. As *k* increases, the spectrum narrows, allowing a better resolution of closely spaced frequency components. Such translated version of basic wavelet will be called translated wavelet transform. It is put to use in this paper advantageously when one has to separate modes. Figure 1 shows results in time and frequency domains for a same centre frequency (f_c located at *2Hz*) but for two different values of bandwidth parameter (*k* equal to *1* and *4*). Furthermore, an elegant method to find the optimal value of *k* has been first carried out in reference [6] by minimizing the entropy of the wavelet transform. Currently, many papers exist in literature dealing with criteria for automatic adjustment of the wavelet parameters [7] which are not implemented here.

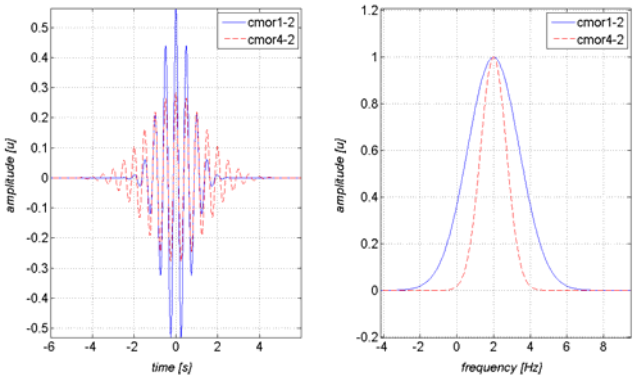

Fig. 1 Complex Morlet wavelet with different bandwidth parameters

Applied to the pulse response of a system, the continuous Morlet transform can be written as:

$$W_{a,b}(x) = \frac{\sqrt{a}}{2}(A\exp(-\xi\omega_0 b))\,\psi^*[a\,\omega_1]\exp(i(\omega_1 b + \Phi_0)) \tag{3}$$

where A is a constant depending on the intensity of impulse loading, ξ is the damping ratio, ω_0 is the undamped angular frequency, ω_1 is the damped natural frequency such as $\omega_1 = \omega_0\sqrt{1-\xi^2}$. Using Morlet or modified Morlet wavelet, the dilatation parameter is related to damped natural frequency like $a_0 = \omega_w/\omega_1$. For this parameter, the logarithm of the modulus of this complex function is:

$$\ln\left|W_{a_0,b}(x)\right| = -\xi\,\omega_0\,b + \ln\left[\frac{\sqrt{a_0}}{2}\,A\,\left|\psi^*_{a_0,\omega_1}(x)\right|\right] \tag{4}$$

Thus, the decay rate $\delta = \xi\omega_0$ can be estimated from the slope of the straight line of the logarithm of the wavelet transform modulus. The wavelet transform phase is also given by:

$$\mathrm{Arg}\left|W_{a_0,b}(x)\right| = \omega_1 b + \Phi_0 \tag{5}$$

Its derivative with respect to translation parameter b gives the damped natural frequency ω_1. This finally permits an evaluation of both damping ratio ξ and natural frequency f_0.

3 Algorithm Implementation

Processing steps are as follows:

- The complex wavelet transform of pulse response is first calculated with bandwidth parameter value $k = 1$ (classical wavelet) in large range both in time and frequency. The latter is limited by the Nyquist frequency $f_s / 2$ where f_s is the sampling one. Different frequency bands Δf_i are first identified at maxima of wavelet transform coefficients in which supposed i-vibrating mode occurs;
- For each frequency band, bandwidth parameter *k* is optimized in order to enhance resolution. Results are appreciated graphically so as to cover entirely the corresponding vibrating mode;
- Cross section drawn at maxima gives complex wavelet coefficients according to eq. 4. Then slope of modulus natural logarithm versus time is finally estimated using linear regression, leading to the value of damping ratio;
- To complete the procedure, inverse wavelet transform is applied in order to reconstruct the corresponding time signal $\tilde{x}(t)$. In most cases, once appropriate time and frequency filtering has been done, the modal nature of $\tilde{x}(t)$ appears unambiguously.

4 Applications to Theoretical Signals

In order to evaluate the effectiveness of the algorithm, two different signals are used: sdof and mdof pulse responses.

4.1 Single Modal Free Response

A theoretical shock response which represents a sdof system is simulated with given natural frequency f_0 [Hz] and damping ratio ξ. Once a wavelet maximum has been localized, cross section at this peak is calculated by the program and drawn on the domain translation coefficients (fig 2 left). Afterwards, curve expressing the logarithm of wavelet transform modulus versus time is plotted (fig. 2 right). The straight line obtained after approximation using linear regression has a slope expressed by $-\xi \omega_0 = -2 \pi \xi f_0$ where f_0 is the previously detected frequency. Lastly, the damping ratio is deduced from eq.5.

In the case of analytical noiseless signals, time-scale representation exhibits energy maxima without any ambiguity. Cross section can be dawned automatically by computing utmost times of each isovalue line. Wavelet coefficients are then extracted and analyzed according to eq. 4 and 5 in order to determine natural frequency and stiffness. One of the quality factors of any extractor is the time scale on which logarithm of modulus is linear. By comparing obtained values to

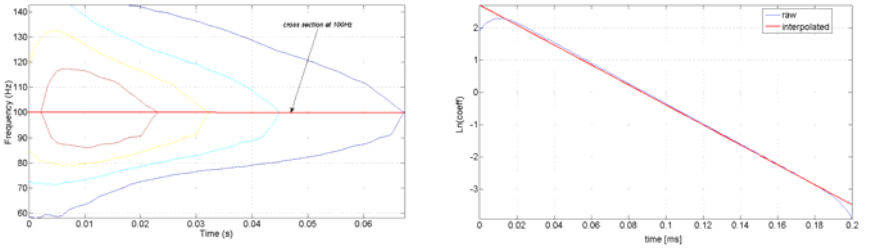

Fig. 2 Left: contour representation of the modulus of the complex Morlet wavelet for a sdof (with f_0=100Hz, ξ =0.05). Right: logarithm of the wavelet transform at peak cross section

expected ones, accuracy comes out excellent in terms of frequency (less than 0.1% of relative error) and acceptable in terms of damping (less than 2%).

In the case of real signals, difficulties arise on how to appreciate the maxima of energy. Weak position errors lead to shortening linear behaviour and make stiffness determination less accurate.

4.2 Pulse Response of a System with Several Modes

As wavelet transform is a linear representation of a signal [16], for M functions $x_i(t)$ and M complex values $\alpha_i(t)$ with $i = 1, 2, \ldots M$:

$$x(t) = \sum_{k=1}^{M} \exp\left[-2\pi\xi_k f_{0k}(t)\right] \cos\left(\sqrt{1-\xi_k{}^2}\, 2\pi f_{0k}(t)\right) \tag{6}$$

Obvious advantage of the technique emerges when modes are closed. On the example of Figure 3, a filtering operation from *75* to *145Hz* leads to foreseeing the existence of more than one mode (dense red zone) but with no further precision. Better resolution was then found by using the translated version of wavelet with a bandwidth parameter $k = 4$. Two modes loomed clearly (*98* and *122Hz*) in accordance with what we had expected.

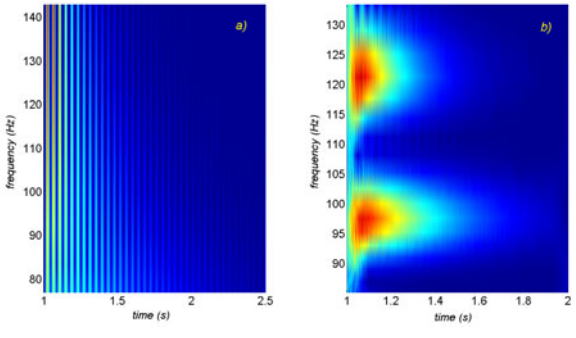

Fig. 3 Wavelet transforms in classical (a) and translated version (b) enabling to reveal two closed SDOF

In the case of closed modes, using of the translated version of the complex Morlet wavelet can clearly ameliorate significantly the resolution.

5 Application to Gear Motor

5.1 Gear Motor

Tests were conducted on an experimental bench using a helicoidal tooth and a cylindrical gear motor shown in Figure 4. It has two gear trains. Six roller bearings (*B1* to *B6*) support the whole set which possesses four pinions (*P1* to *P4*). Fed by a *380V – 50Hz* three phase electrical asynchronous motor, it turns at *1494/282 rev/min* (reduction ratio of *0.188*) with a power of *1.1kW*. The machine is located relatively to a system of orthogonal axes {*x, y, z*}. Alphanumeric characters refer to plane and measuring direction. Both kinematic and fault frequencies have been previously calculated.

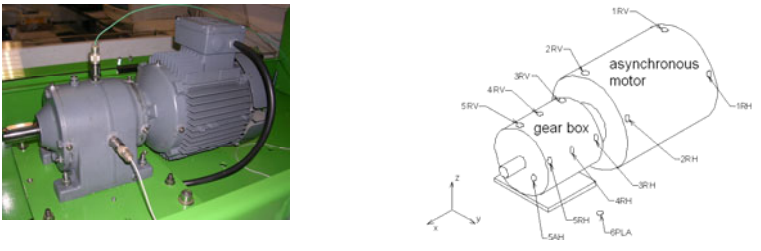

Fig. 4 Overview of the installation and localization of measuring points on the gear motor

5.2 Instrumental Setup

The measured vibrating signal is digitized using a 24 bits resolution by simultaneously employing a four-channel signal acquisition module USB 9233. The module includes built-in antialiasing device, with high stability, low noise laptop power supply filters, automatically making high-accuracy measurements from IEPE accelerometer. In the case of modal analysis, two channels are taken on to digitize impulse response and one to digitize instrumented hammer signal. For standard test, sampling rate and size are fixed up to 25 kS/s with 2^{15} samples. We operated standard IEPE accelerometer DJB A120 VTC with sensitivity of 100mV/g. Measurement bandwidth is done within [2Hz, 10 kHz] according to 0.5 dB distortion. USB 9233 is piloted using Labview and allows to adapt sample rate and size for each channel. Mathematical treatments are thus performed from data file by putting into use homemade Matlab worksheet. An important point is the possibility to digitalize simultaneously any shock impulse and related responses with very high time and sampling resolution.

5.3 Procedure

We apply an instrumented hammer to produce a shock. The impact is produced at equal distance from two measuring points. Shock impulse and related responses are then recorded simultaneously. Before any routine analysis, we check the causality of responses on the excitation by analyzing coherence function. In most cases, coherence indicator is better and goes beyond 0.9 from 100Hz. The same results are obtained if we exchange the impact position by the sensor one and vice-versa. Moreover, while disposing of two simultaneous impulse responses, we previously made use of a power spectral cross-correlation function in order to reveal and extract any common sdof modes. Associated to the classical Hilbert transform analysis, this method turns up to be very sensitive and accurate to characterize any separate modes. Our wavelet algorithm is then calibrated on previously identified single modes. Performances are finally tested on the closest modes which are generally not put into evidence by cross-correlation analysis. Operating is then applied on the horizontal, the vertical and the axial directions in order to scan 3D free response functions on which modal parameters can be determined.

5.4 Identification of Modal Parameters Using Continuous Wavelet Transforms

We handled the method based on complex Morlet continuous wavelet transform as described in section 3. With the exploration of the whole space of continuous wavelet transform, layers containing natural mode areas can be characterized. An example is given for the case of the measuring point *3RV* on which shock was applied on radial-vertical direction situated on the front bearing of the gear motor. After calculation of CWT using a translated version of wavelet with bandwidth parameter $k = 4$, filtering [0.168-0.187s] in time and [475-725Hz] in frequency has been undertaken. From reconstruction of the identified mode, existence of natural frequency is then confirmed (Figure 5). Characteristic appearance of the curve reveals the properly found mode.

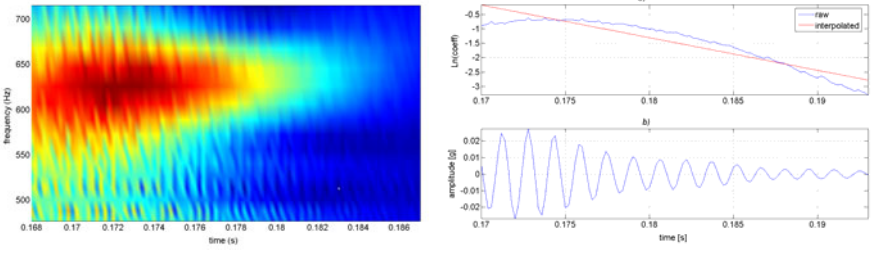

Fig. 5 Left: cmor4-1.5 continuous wavelet transform using filtering [0.168-0.187s], [475-725Hz]. Right: peak cross section and extracted mode at 625Hz

After measuring the response on all points and applying the method, numerous modes characterized as natural frequencies and damping ratios were found. Table 1 summarizes all results of modal analysis of the machine.

Table 1 Modal analysis results for the gear motor

Axial direction (x)		Radial-horizontal direction (y)		Radial-vertical direction (z)	
f_0	ξ	f_0	ξ	f_0	ξ
483.9	0.018	106.38	0.051	105.26	0.077
809.9	0.014	204.1	0.012	116.28	0.021
1 102	0.014	217.4	0.069	121.95	0.020
1 368	0.010	222.3	0.089	253.2	0.045
		410.8	0.058	277.8	0.031
		512.8	0.024	333.3	0.057
		526.3	0.024	341.2	0.032
		789.5	0.033	461.5	0.006
		1 145	0.006	625	0.024
		1 333	0.002	652.2	0.014
				1 072	0.013
				2 222	0.012
				2 334	0.011

Highest values are on the x-axis: in that direction, just a few natural frequencies can be spotted. On the contrary, that's where the lowest damping ratios are. In fact, this machine can be modelled as a laid down cylinder: the most rigid direction is the *x*-axis. As the system is placed on a horizontal plane, damping ratio in the vertical direction globally turns lower. Moreover, it clearly springs up that on zones with high frequencies, damping lies low.

6 Conclusion

In this work, procedure is based on the transversal sections of the complex Morlet wavelet transform in order to identify damping ratios. These sectioning operations are obtained for scale parameter values which depend on analyzed frequency zone. The advantage of the wavelet method stems from the capacity to decoupling a system into separated modes. We employed a specific complex Morlet analyzing function which has high frequency ability. That allowed to refine results especially in terms of mode separating. This is proved through numerical signals of different types, with efficiency and accuracy. When natural frequencies are closed, the using of the translated Morlet wavelet brings good resolution. Application on real signals measured from a complex rotating machine gave identification of modal parameters, compared to other common methods.

Acknowledgements. This work was performed with the collaboration between the High Institute of Technology of Antananarivo, Madagascar, and the Institute of Technology of Sénart-Fontainebleau, France. The authors wish to thank respectively Josoa Ramamonjisoa and Antoine Meter, the General Managers of these two institutions. They also gratefully thank Wilhelmina Logerais for having checked the English version of this paper.

References

Books

[1] Jimin, H., Fu, Z.-F.: Overview of modal analysis (2001) and Applications of modal analysis on real structures (2007)

Journal Article

[2] Dishan, H.: A wavelet-based algorithm for the Hilbert transform. Mechanical Systems and Signal Processing, 125–134 (1996)

[3] Ruzzene, M., Fasana, A., Garibaldi, L., Piombo, B.: Natural frequencies and dampings identification using wavelet transform: application to real data. Mechanical Systems and Signal Processing, 207–218 (1997)

[4] Staszewski, W.J.: Identification of damping in MDOF systems using time-scale decomposition. Journal of Sound and Vibration, 283–305 (1997)

[5] Lardies, J., Ta, M.N., Berthillier, M.: Modal parameter estimation based on the wavelet transform of output data. Archive of Applied Mechanics 73, 718–733 (2004)

[6] Yin, H.P., Duhamel, D., Argoul, P.: Natural frequencies and damping estimation using wavelet transform of a frequency response function. Journal of Sound and Vibration, 999–1014 (2004)

[7] Chiementin, X., et al.: An intelligent system for faulty-bearing detection based on vibration spectra. Journal of Vibration and Control 17, 931–942 (2011)

Integrated Modulation Intensity Distribution as a Practical Tool for Condition Monitoring – Part 1: Theoretical Investigation

Jacek Urbanek[1], Tomasz Barszcz[1], and Jerome Antoni[2]

[1] AGH University of Science and Technology
30-059 Kraków, Poland
{tbarszcz,urbanek}@agh.edu.pl
[2] Vibrations and Acoustic Laboratory, INSA of Lyon,
University of Lyon, F-69621 Villeurbanne Cedex, France
jerome.antoni@insa-lyon.fr

Abstract. Modulations present in vibration signals generated by rotating machinery might carry a lot of useful information about its technical condition. The paper describes a technique for detection of modulations in vibroacoustic signals, called modulation intensity distribution (MID), which, as proven might be considered as a generalized description of the spectral correlation density. Additionally, the paper includes the description of integrated MID (IMID) which allows to present the results of MID in a simplified form. As a conclusion, the discussion is held on the application of IMID to industrial condition monitoring systems.

Keywords: modulation intensity distribution, MID, spectral correlation, cyclostationarity, modulations.

1 Introduction

In recent years, growing demand for application of vibrodiagnostic was raised by many industries. It compels researchers to develop signal processing techniques suitable for analysis signals generated by more complex machinery, frequently exposed to significant influence of noise (Barszcz et al. 2010).

Nowadays, cyclostationarity is one of the most promising approaches for rotor machinery vibration analysis (Barszcz 2004). The variety of cyclostationarity-based methods of identification (Antoni 2009) and separation (Bonnardot et al. 2005) of signal components allows to obtain many useful information about the signal cyclic components. An important feature of the cyclostationary analysis is the ability to reveal modulations that are present in vibration signals (Antoni 2007). Modulations of various signal components may often serve as valuable indicators of fault occurrence (Makowski and Zimroz 2011). It has been proven that both gearboxes and rolling elements bearings faults manifest themselves as modulations (McFadden and Smith 1984).

As mentioned, cyclostationarity tools such as cyclic spectrum or spectral correlation density allow detection and analysis of modulations (Randall et al. 2001).

However, obtained results are frequently presented as a three dimensional plots, which makes the interpretation relatively complicated, especially for automated industrial condition monitoring systems.

In this paper, authors present the concept of modulation intensity distribution (MID) as a signal processing tool that allows to detect modulations in a vibration signal based on its cyclostationary properties (Urbanek et al. 2012). Additionally, paper introduces so- called integrated MID (IMID) which might be considered as a two-dimensional representation of MID. Theoretical investigation included in the article undertakes the problem of practical application of IMID to industrial condition monitoring systems designed to supervise the machinery of relatively complex kinematics.

The article is organized as follows. Chapter 2 introduces MID technique together with the interpretation of its results. Chapter 3 presents the IMID. Chapter 4 contains theoretical investigation of undertaken problem. First, the model of the second order policyclostationary signal is presented. Next, the results of two implementations of MID are compared. The results are discussed in the terms of practical implementation for complex machinery diagnostics.

2 Modulation Intensity Distribution

Modulation intensity distribution is a general technique for detection and identification of modulations present in a signal. The method was originally designed for gearboxes and rolling elements bearings diagnostics purposes; therefore, it is focused on detection of amplitude modulations that manifests themselves as symmetrically spaced spectral sidebands (Urbanek et al. 2012).

The core of MID is the sideband filter that allows extracting potential carrier signal together with corresponding modulation sidebands. The idea of the sideband filter is presented in the figure 1.

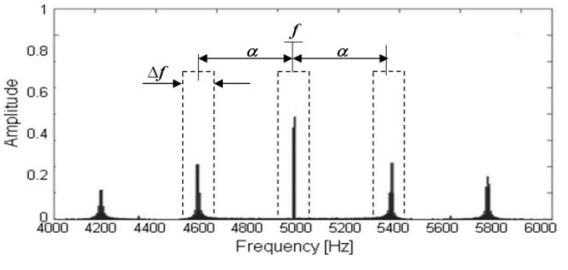

Fig. 1 The concept of the sideband filter

A time signal filtered in that way contains (in the idealized case) only the specified component with no additional signals and with highly reduced noise level. It can be then understood as a set of three elements:

$$x_i = x_{\Delta f}(t;\ f - i\alpha)\ , \text{for } i = \{-1,0,1\} \tag{1}$$

where $x_{\Delta f}(t; f)$ stands for the filtered version of x(t) in a narrow frequency-band [f-Δf/2;f+Δf/2].

The output of the presented filter may be then used for calculating so-called modulation intensity factor (MIF), which can be understood as a measure of the strength (intensity) of the modulation of selected carrier signal by the component of the frequency α.

The choice of MIF depends on the nature of analyzed signal and the desired output results. The simplest example of MIF might be a comparison between energies of symmetrically filtered signal components. However, for more demanding applications spectral correlation, spectral coherence or even kurtosis of the envelope spectrum (Barszcz and Jablonski 2011) may serve as a MIF.

Calculating the MID for each frequency f and α will results in three-dimensional modulation intensity distribution map. In general, the formula that describes MID might be presented as follows:

$$\mathrm{MID}_{\Delta f}(f;\alpha) = \mathfrak{M}[x_{\Delta f}(t;f-\alpha), x_{\Delta f}(t;f), x_{\Delta f}(t;f+\alpha)] \tag{2}$$

where $\mathfrak{M}$ is the operator for calculating the arbitrarily chosen modulation intensity factor.

In the particular case described above, the MID actually shows a closed link with the spectral correlation density defined as

$$SC_x^{\alpha}(f) = \lim_{\Delta f \to 0} \frac{1}{\Delta f} \left\langle x_{\Delta f}(t; f+\tfrac{\alpha}{2}) x_{\Delta f}^{*}(t; f-\tfrac{\alpha}{2}) e^{-j2\pi\alpha t} \right\rangle_t . \tag{3}$$

However, while the spectral correlation density returns a relationship between only two frequency components spaced by α, the proposed method operates on three separate frequency bands, which should make it more dedicated to the detection of the modulation patterns of interest. Indeed, considering the fact that the spectral correlation density is the correlation between two spectral components where one might be considered as a carrier frequency and the other one as one as its modulation sidebands $f+\alpha/2$, the MID can be described as follows:

$$MID\,(PSC)_{\Delta f}(f;\alpha) = \Delta f \left\langle SC_x^{\alpha}(f+\tfrac{\alpha}{2}) SC_x^{\alpha}(t; f-\tfrac{\alpha}{2}) \right\rangle \tag{4}$$

It is now clear that performing the product of spectral correlations calculated at frequencies $f+\alpha/2$ and $f-\alpha/2$ results in the modulation intensity distribution for a fixed bandwidth Δf. In this case, the notation MID(PSC), stands for the Product of Spectral Correlations.

In the paper, the effectiveness of this definition is illustrated on a simulated signal. Generated signal contains band-limited noise modulated by equally spaced exponentially descending impulses with additional white noise. The vibration model can be expressed as:

$$x(t) = h(t)\,g(t) + n(t) \tag{5}$$

where h(t) is the band limited noise, g(t) is the set of modulating impulses and n(t) is the additional white noise.

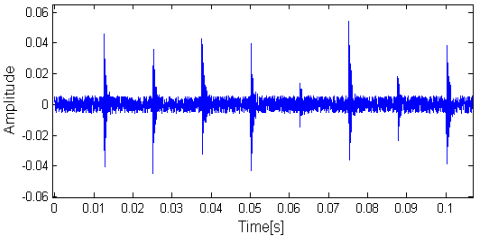

Fig. 2 Simulated exemplary signal.

The simulated signal was designed to be similar to vibration generated by a rolling element bearing with an outer race local fault. Repetition rate of excited impulses was 80 Hz and their amplitudes were randomly modulated. The carrier signal is stationary Gaussian distributed around 4 kHz. In order to achieve clear results no impulse spacing jitter was added.

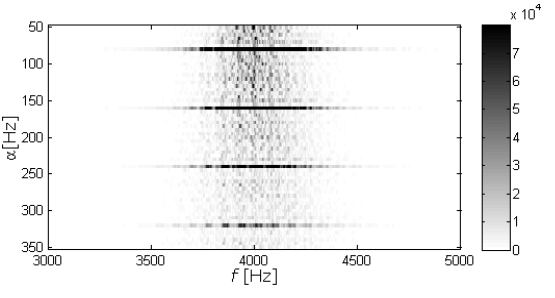

Fig. 3 Resulting MID(PSC) map of the exemplary signal from fig. 2.

Figure 3 displays the MID map for the described case. Horizontal lines spaced by 80 Hz represent the repetition rate of excitation impulses. Detected modulation components have the strongest amplitude around the 4 kHz carrier frequency.

In some practical applications of MID to vibration signals, the spectral correlation as the modulation intensity factor might not be efficient enough due to large differences of signal energy in various frequency bands. In such cases, the interpretation of MID maps might be more efficient when the measure of modulation intensity varies only between 0 and 1. For that purpose, the proposed MID(PSC) can be easily extended to the use of the spectral coherence as the modulation intensity factor:

$$MID(PSCoh)_{\Delta f}(f;\alpha) = \Delta f \left\langle \frac{SC_x^{\alpha}(f+\frac{\alpha}{2})}{\sqrt{SC_x^0(f+\frac{\alpha}{2})SC_x^0(f)}} \frac{SC_x^{\alpha}(f-\frac{\alpha}{2})}{\sqrt{SC_x^0(f-\frac{\alpha}{2})SC_x^0(f)}} \right\rangle. \quad (6)$$

3 Integrated MID

In the MID, a chosen modulation intensity factor is a function of the carrier frequency f and the modulation frequency α. However, in some particular cases, the user might not be interested in finding the specific carrier frequency range, but only in evaluating the general influence of specific modulation components on the tested signal. Moreover, three-dimensional representations might cause some significant difficulties for interpretation and automatic decision making process in industrial condition monitoring systems (D' Elia et al. 2011).

Based on this remark, it might be more convenient to represent the MID not as an image, but as a function of the modulation frequency only, after integration over a chosen frequency band. Such representation reveals information of the total modulation intensity caused by individual sources and is to be called IMD, standing for Integrated MID.

Integration over a selected carrier frequency band results in:

$$IMD_{f_1}^{f_2}(\alpha;\Delta f) = \int_{f_1}^{f_2} MID_{\Delta f}(f,\alpha)df \ , \tag{6}$$

where MID is a chosen statistical value calculated in the carrier frequency range from f_1 to f_2.

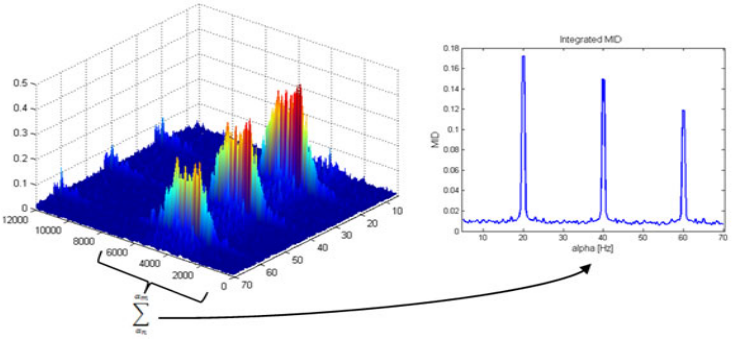

Fig. 4 The concept of integrated MID.

As explained in chapter 2, MID is related to spectral correlation (Randall et al. 2001). Therefore, integrated MID may be intuitively related to the envelope spectrum in the same manner as the spectral correlation.

4 Simulated Signal Experiment

In order to investigate the utility of IMID for identification multiple fault cases, a generated signal was used. The vibration model could be expressed as in eq.5. However, for the purpose of the experiment, generated signal contained two

unsynchronized second order cyclostationary components of different carrier frequencies ranges.

First component has the cyclic frequency equal to 50 Hz and the carrier frequency between 8 and 12 kHz. Second component with the cyclic frequency of 70 Hz is distributed from 4 to 8 kHz of the carrier frequencies range. Moreover, the energy of the second component was around five times lower than the energy of the first one. Additionally, white noise was added to the signal in order to prevent non-zero values of the spectrum.

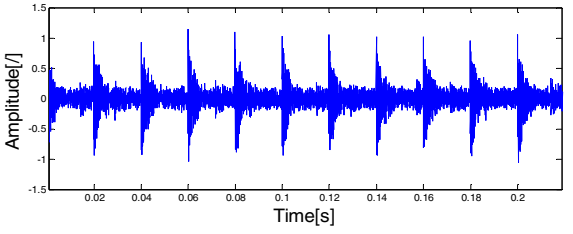

Fig. 5 Time view of the simulated signal used for the experiment.

As seen on the Fig.5, periodically spaced impulses of the first component are clearly visible, while the second component is entirely masked by the noise.

MID(PSC) obtained from the test signal reveals the presence of the first cyclic component (Fig.6). However, due to significant differences in the energies of cyclic components in the signal, second cyclic component is unrecognizable. For the same reason, recognition of the second cyclic component on the resulting IMID is impossible.

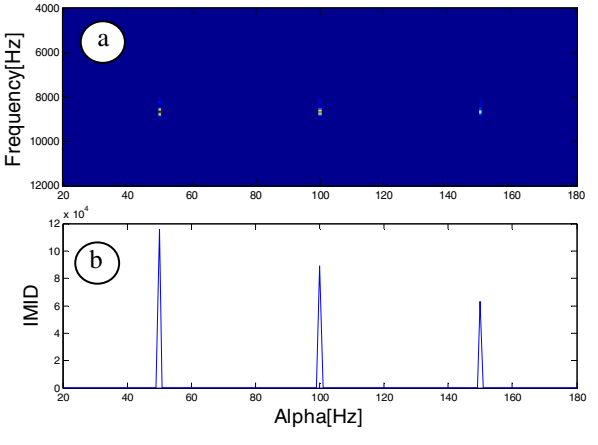

Fig. 6 MID(PSC) of the generated signal (a) with the corresponding IMID.

Based on the fact that non-cyclic signal components have coherence close to zero, MID(PSCoh) should return clearer results. Fig.7(a) presents MID(PScoh) for the generated signals together with the equivalent IMID.

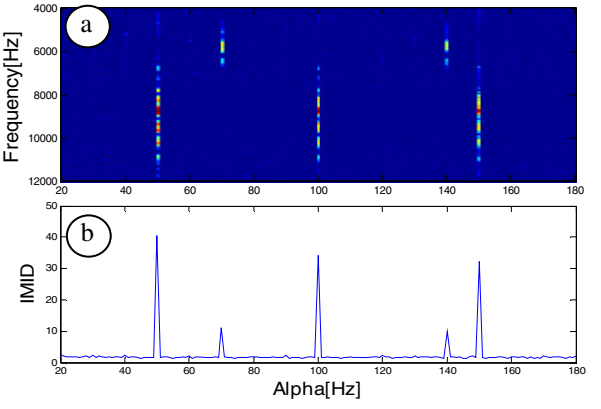

Fig. 7 MID(PSCoh) of the generated signal (a) with the corresponding IMID.

With the application of MID(PSCoh) both cyclic components are easy to recognize. Such effect is possible because the spectral coherence compensates the signal energy differences in each frequency band due to its normalization property.

5 Conclusions

MID appears to be efficient way to detect fault generated modulations in the vibration signal. By application of the product of the spectral coherences, it is possible to overcome the problem of different energy levels and different carrier frequencies of miscellaneous cyclic components in the vibration signal. Moreover, IMID contains similar information to envelope spectrum with the advantage of the immunity to the noise. It is the authors belief that with properly chosen MIF, the IMID may serve as the indicator of the fault development in the industrial condition monitoring systems.

References

1. Barszcz, T., Urbanek, J., Szumilas, L.: Selection of Efficient Monitoring Methods for Machinery Generating High Vibration Signal Disturbance. Diagnostyka 55, 55–58 (2010)
2. Zimroz, R., Bartelmus, W.: Gearbox Condition Estimation Using Cyclo- Stationary Properties of Vibration Signal. Key Engineering Materials 413-414, 471–478 (2009)
3. Antoni, J.: Cyclostationarity by examples. Mechanical Systems and Signal Processing 23, 987–1036 (2009)

4. Bonnardot, F., Randall, R.B., Guillet, F.: Extraction of Second-Order Cyclostationary Sources—Application to Vibration Analysis. Mechanical Systems and Signal Processing 19, 1230–1244 (2005)
5. Antoni, J.: Cyclic Spectral Analysis of Rolling-Element Bearing Signals: Facts and Fictions. Journal of Sound and Vibration 304, 497–529 (2007)
6. Makowski, R., Zimroz, R.: Adaptive Bearings Vibration Modelling for Diagnosis. LNCS (LNAI), vol. 943, pp. 248–259 (2011)
7. McFadden, P.D., Smith, J.D.: Vibration Monitoring of Rolling Element Bearings by The High Frequency Resonance Technique. Tribology International 17, 3–10 (1984)
8. Randall, R.B., Antoni, J., Chobsaard, S.: The Relationship Between Spectral Correlation and Envelope Analysis in the Diagnostics of Bearing Faults and Other Cyclostationary Machine Signals. Mechanical Systems and Signal Processing 15, 945–962 (2001)
9. Urbanek, J., Antoni, J., Barszcz, T.: Detection of signal component modulations using modulation intensity distribution. Mechanical Systems and Signal Processing (2012); doi:10.1016/j.ymssp.12.018
10. Barszcz, T., Jabłoński, A.: A Novel Method of Optimal Band Selection for Vibration Signal Demodulation. Mechanical Systems and Signal Processing 25, 431–451 (2011)
11. D' Elia, G., Delvecchio, S., Cocconcelli, M., Dalpiaz, G.: Combining blind separation and cyclostationary techniques for monitoring distributed wear in gearbox rolling bearings. In: Proc. of Surveillance, Compiègne, France, October 25-26, vol. 6 (2011)

Integrated Modulation Intensity Distribution as a Practical Tool for Condition Monitoring – Part 2: Case Study of the Wind Turbine

Jacek Urbanek[1], Tomasz Barszcz[1], and Jerome Antoni[2]

[1] AGH University of Science and Technology
30-059 Kraków, Poland
{tbarszcz,urbanek}@agh.edu.pl
[2] Vibrations and Acoustic Laboratory, INSA of Lyon,
University of Lyon, F-69621 Villeurbanne Cedex, France
jerome.antoni@insa-lyon.fr

Abstract. The paper investigates the utility of use of the modulation intensity distribution (MID) signal processing technique for detection of rolling elements bearing faults indicators in high noise environment. For the purpose of the test, wind turbine that suffered both advanced gearbox fault and early stage of bearing fault was chosen. Additionally, the paper undertakes the problem of practical implementation of proposed tool in the industrial condition monitoring system. In order to show the behavior of cyclic components generated by studied turbine over long periods of time, the set of MIDs integrated over the carrier frequencies was presented as a cascade plot.

Keywords: modulation intensity distribution, MID, cyclostationarity, multifault, wind turbines.

1 Introduction

Vibrodiagnostics of rotating machinery finds itself useful in many branches of the industry (Barszcz et al. 2010). Despite the rapid growth of potential fields of applications and the availability of signal processing tools dedicated to vibrodiagnostics, there are still numerous limitations and obstacles that need to be overcome in order to significantly improve the process of condition monitoring (Barszcz 2004).

One of the most challenging objects for vibration monitoring are wind turbines (Barszcz 2009). It is mostly because variable operational conditions (Urbanek et al. 2011, Zimroz et al. 2011, Zimroz and Bartelmus 2012) relatively uneasy access to the turbine, and varying weather conditions. Due to the substantial load variations caused by the altering wind, most of turbines are exposed to the risk of accelerated development of mechanical faults. Additionally, since the access to the turbine is frequently limited by the weather conditions, execution of required repairs might not be always possible.

Since the kinematics of the wind turbine is relatively complicated (Urbanek et al. 2011, Zimroz et al. 2011) and the risk of fault occurrence is significant, vibrodiagnostics tools implemented in the industrial condition monitoring systems should be selective and sensitive to the early symptoms of the fault occurrence.

In this paper, authors want to examine the utility of the method called modulation intensity distribution (MID) for detection of rolling elements bearings characteristic components of relatively low energy (Urbanek et al. 2012). MID uses cyclostationary properties of the signal (Zimroz and Bartelmus 2009, Antoni 2007) for detection of modulations generated by rotating elements (Makowski and Zimroz 2011). Because the output of the MID analysis is a three dimensional map, it might not be a clear method to present the fault development history over long period of time. Therefore, authors propose to use integrated MID (IMID) cascade plot (D' Elia et al. 2011) to show the evolution of cyclic components generated by the turbine over its monitoring history.

The paper is organized as follows. Chapter 2 introduces MID and its' two-dimensional representation, integrated MID. Chapter 3 gives a general specification of the wind turbine selected for the study. Chapter 4 includes the description of the technical condition of discussed object. Next, it presents the vibration signal generated by the turbine with significantly damaged gearbox. Subsequently, the paper presents the results of the application of the MID and discuss the utility of MID and integrated MID for analysis of vibration signals generated by wind turbines.

2 Modulation Intensity Distribution

Modulation intensity distribution is a general technique for detection and identification of amplitude modulations present in a signal (Urbanek et al. 2012). It allows to obtain relationships between spectral components of the signal in order to recognize the carrier signal of the frequency f and the modulation component of the frequency α.

Calculating the MID for each frequency f and α results in a three-dimensional modulation intensity distribution map. In general, the formula that describes MID is presented as follows:

$$\mathrm{MID}_{\Delta f}(f;\alpha) = \mathfrak{M}[x_{\Delta f}(t;f-\alpha), x_{\Delta f}(t;f), x_{\Delta f}(t;f+\alpha)] \tag{1}$$

where $\mathfrak{M}$ is the operator for calculating the arbitrarily chosen modulation intensity factor (MIF) and $x_{\Delta f}(t;f)$ is the filtered version of the signal x(t) for filter bandwidth Δf and the center frequency f.

For the purpose of described experiment, among various modulation intensity factors, the product of two symmetric spectral coherences is used as the modulation intensity factor. Applied MID can be described by following formula:

$$MID(PSCoh)_{\Delta f}(f;\alpha) = \Delta f \left\langle \frac{SC_x^{\alpha}(f+\frac{\alpha}{2})}{\sqrt{SC_x^0(f+\frac{\alpha}{2})SC_x^0(f)}} \frac{SC_x^{\alpha}(f-\frac{\alpha}{2})}{\sqrt{SC_x^0(f-\frac{\alpha}{2})SC_x^0(f)}} \right\rangle. \tag{2}$$

Where

$$SC_x^{\alpha}(f) = \lim_{\Delta f \to 0} \frac{1}{\Delta f} \left\langle x_{\Delta f}(t; f + \tfrac{\alpha}{2}) x_{\Delta f}^{*}(t; f - \tfrac{\alpha}{2}) e^{-j2\pi\alpha t} \right\rangle_t \tag{3}$$

is the spectral correlation obtained for cyclic frequency α and carrier frequency f and the annotation PSCoh stands for "product of spectral coherences".

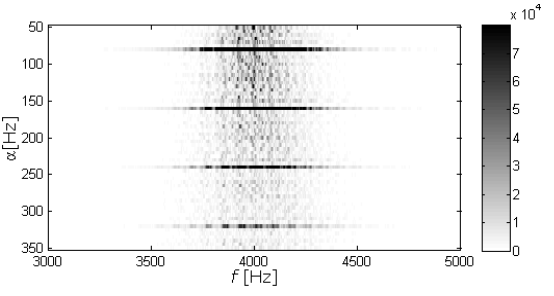

Fig. 1 Exemplary MID(PSCoh) map.

Figure 1 presents exemplary MID (PSCoh) calculated for the second order cyclostationary signal. Horizontal lines spaced by 80 Hz represent the characteristic frequency of the modulating signal. The range of frequencies of the carrier signal is distributed between 3.5 kHz and 4.5 KHz on the f axis. As shown in figure 1, proposed analysis is capable of detection of modulations in vibration signals and for identification of both, carrier and modulation components.

In order to facilitate the interpretation of obtained results, it might be more convenient to represent the MID not as an image, but as a function of the modulation frequency only, after integration over a chosen frequency band. Such representation reveals information of the total modulation intensity generated by individual sources and is to be called IMD, standing for Integrated MID.

Integration over a selected carrier frequency band results in:

$$IMD_{f_1}^{f_2}(\alpha; \Delta f) = \int_{f_1}^{f_2} MID_{\Delta f}(f, \alpha) df \ , \tag{4}$$

where $MID_{\Delta f}$ is calculated for chosen MIF in the carrier frequency range from f_1 to f_2.

Figure 2 presents the concept of IMID. It is clearly seen that information about the position of observed components on carrier frequencies axis is lost. However, obtained results are presented on two-dimensional plot, which might be more convenient and simpler for analysis. Additionally, automatic data interpretation and decision making procedures are far more complicated for three-dimensional data sets which makes their practical implementation in industrial condition monitoring systems relatively difficult and uneconomic.

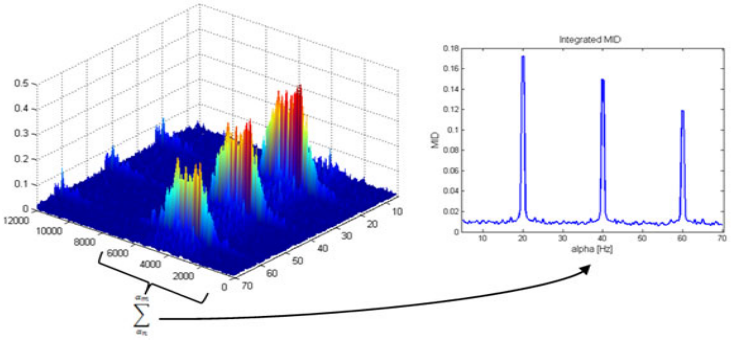

Fig. 2 The concept of integrated MID.

3 Object Description

Wind turbine chosen for the experiment was the typical commonly used turbine of 1500 kW nominal power. Such types of turbines have usually two main operational states that depend on the speed of the wind. For weaker winds, turbine operates in so called "low" stage which corresponds to 1000 kW power generation. For stronger winds, it operates with its nominal power in the "high" operational stage.

Figure 3 presents a typical layout of a wind turbine. The main rotor with three blades is supported by the main bearing and transmits the torque to the planetary gear. The planetary gear has three planets. The planets transmit the torque to the sun gear. The sun shaft is the output of the planetary gear which drives a two-stage parallel gear. The parallel gear has three shafts: the slow shaft connected to the sun shaft, the intermediate shaft and the high speed shaft, which drives the generator. The generator produces AC current of slightly varying frequency. This current is converted first into DC power and then into AC power of frequency equal to the grid frequency. Electric transformations are performed by the controller at the base of the tower. The gearbox setup changes the rotational speed from about 25 rpm on the main rotor to about 1500 rpm at the generator.

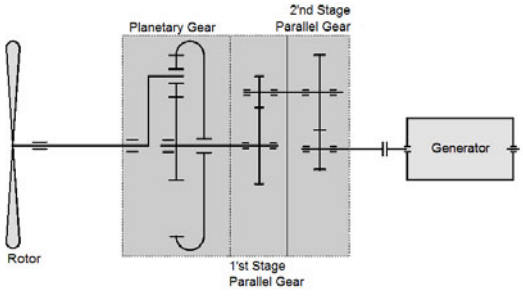

Fig. 3 Layout of a typical wind turbine

4 Case Study

Due to the report provided by the company supervising the turbine, tested object suffered from two separate faults. First fault was a chipped tooth on the high speed shaft gearwheel together with an advanced pitting. Second fault was a rolling element bearing outer race fault. The bearing was located on the intermediate shaft. Due to advanced fault size on the gearwheel, generated vibration signal component related to that fault has relatively strong energy. It was successfully masking other signal components including the one generated by the faulty bearing.

Time view of the vibration signal measured on the casing of the gearbox of the turbine is shown of figure 4.

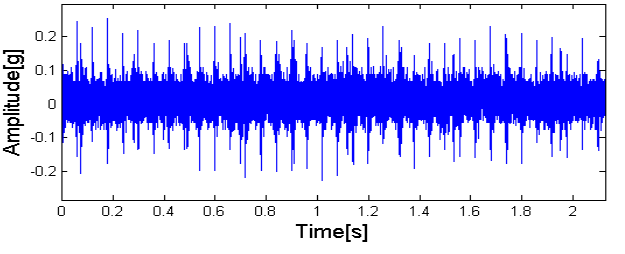

Fig. 4 Vibration signal measured on the tested wind turbine.

Impulses visible on figure 4 are generated by the faulty gearbox. Resulting envelope spectrum (fig.5) obtained from that signal contains only the components related to rotational speeds of the fast and intermediate shafts which are the ones of the faulty gearbox.

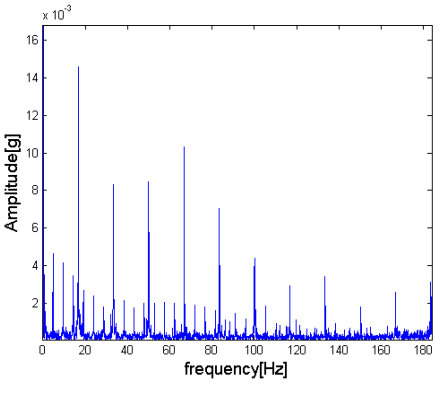

Fig. 5 Envelope spectrum of the signal from figure 2.

As seen on figure 5, envelope spectrum contains no indicators of the faulty bearing. It is because components related to the gearbox fault are masking other contents of the signal including faulty bearing characteristic component. Therefore, MID(PSCoh) analysis was applied in order to reveal more information "hidden" in the signal. Resulted MID map is shown on figure 6.

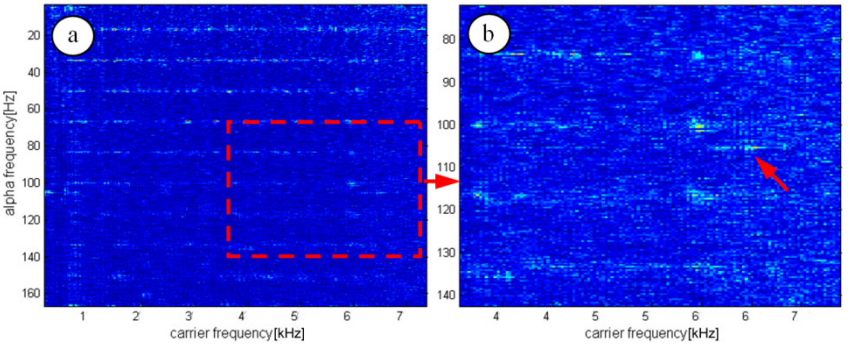

Fig. 6 MID(PSCoh) map obtained from the signal from fig.2. a – complete spectral range of the analysis, b – zoomed results.

Horizontal lines spaced apart by 18 Hz shown on figure 6a represents the gearbox fault characteristic component. However, by zooming the marked area additional component of 105 Hz cyclic frequency can be seen (fig.6b). That corresponds to the characteristic frequency of the bearing outer race fault. In order to present the results in the way more suitable for industrial condition monitoring systems, resulted MID has been integrated over the total range of the carrier frequencies (fig.7).

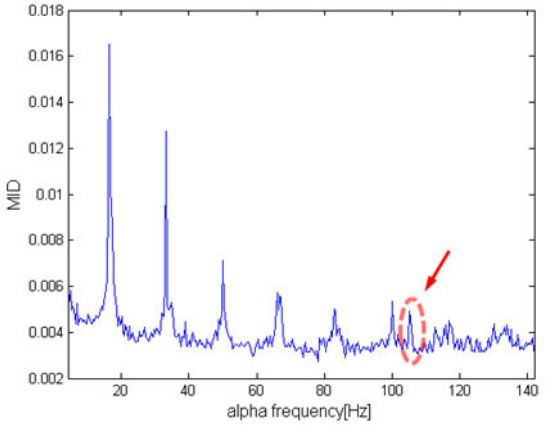

Fig. 7 IMID obtained from calculated MID(PSCoh).

Unlike the envelope spectrum, IMID results contain, except gearbox fault indicators, characteristic component of the faulty bearing. The component of interest is not masked due to normalization property of the spectral coherence.

In order to examine the utility of the IMID to the industrial condition monitoring systems, additional tests were performed. Therefore, IMID analysis was applied to the vibration data stored in the database. Historical data covered over two years of wind turbine monitoring . At this point it should be stated that because of the availability of the stored data only the signal acquired in the "low" operational state was taken into the consideration.

Figure 8a presents the cascade plot of the obtained IMIDs plotted with the respect to the observation time. As seen, the component characteristic to the gearbox fault remains constant for whole monitoring period. However, a development of the component of the 105 Hz cyclic frequency (rolling element bearing outer race) can be noticed (fig.8b).

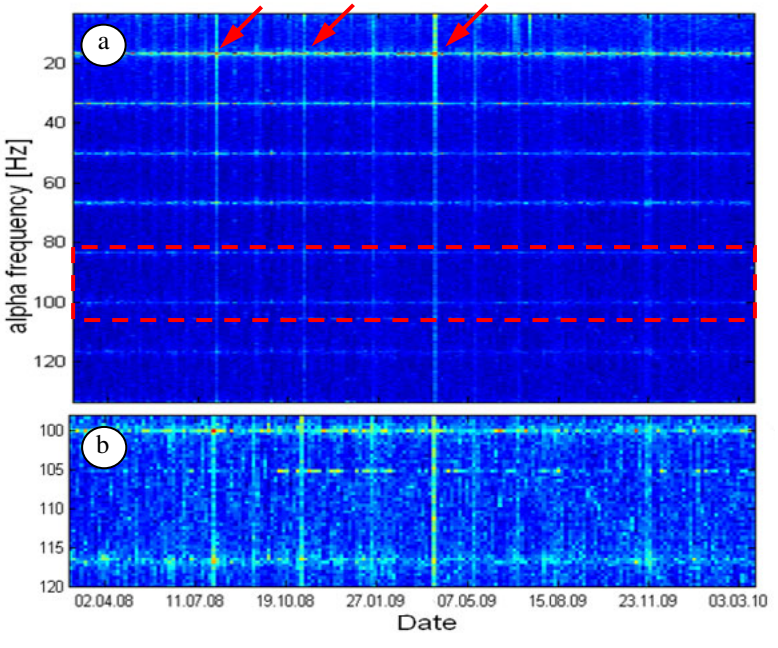

Fig. 8 Cascade plot of the IMID calculated for the wind turbine data history (a). Zoomed plot that shows the development of the component of interest (b). Color scale has been enhanced for improved visualization.

At this point the reader should note that it is rather uncommon situation for the technical object to operate with such advanced fault like described gearbox damage for such long period of time. Additionally, vertical lines on the cascade plot (marked by the red arrows on fig.8) are the results obtained from the data recorded during sudden operational conditions changes. More about this phenomena and

the method for pre-selection of the vibration data can be found in (Jablonski and Barszcz 2011).

Results shown on figure 8 can lead to the conclusion that information provided by IMID might serve as an indicator of the object's technical condition. To show the development of detected bearing fault the IMID values for 105 Hz frequency were presented as a time trend (fig.9).

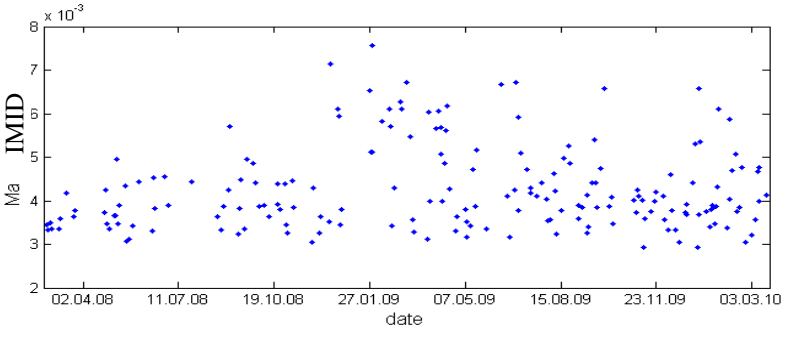

Fig. 9 Plot of the trend obtained for bearing fault cyclic frequency.

Results shown on figure 9 clearly exhibit the development of the bearing fault. Calculated modulation intensity factors reach their maximum around 27.01.09. After that the output of the analysis starts to slowly descend. That may be related to the fact that during bearing race degradation process the fault size extends from local to distributed wear.

5 Conclusions

Results presented in this paper shows that IMID may be relatively efficient tool for vibrodiagnostics. Additionally, traditional envelope spectra cascade plot can be successfully replaced with the IMID cascade plot. Obtained results clearly indicate the REB fault development even in the signal dominated with cyclic components generated by other rotating parts of the machinery. Case study shown that normalization property of MID(PSCoh) allows to obtain results that are more selective for detection and identification of cyclic components generated by complex machinery than traditional envelope spectrum. Additionally, MID approach allows to examine the signal in relatively wide frequency band which results in detection of both characteristic and carrier frequencies of the various signal components. Because of that, there is no need for selecting the optimal band for signal demodulation. Such advantage might be especially useful for industrial condition monitoring systems, especially when dealing with the machinery of relatively complex kinematics.

References

1. Barszcz, T., Urbanek, J., Szumilas, L.: Selection of Efficient Monitoring Methods for Machinery Generating High Vibration Signal Disturbance. Diagnostyka 55, 55–58 (2010)
2. Barszcz, T.: Proposal of new method of mechanical vibration measurement. Metrology and Measurement Systems 11, 409–421 (2004)
3. Barszcz, T.: Selection of diagnostic algorithms for wind turbines. Diagnostyka 50, 7–12 (2009)
4. Urbanek, J., Barszcz, T., Sawalhi, N., Randall, R.B.: Comparison of amplitude based and phase based methods for speed tracking in application to wind turbines. Metrology and Measurement Systems 18, 295–304 (2011)
5. Zimroz, R., Urbanek, J., Barszcz, T., Bartelmus, W., Millioz, F., Martin, N.: Measurement of Instantaneous Shaft Speed by Advanced Vibration Signal Processing - Application to Wind Turbine Gearbox. Metrology and Measurement Systems 18, 701–712 (2011)
6. Zimroz, R., Bartelmus, W.: Application of adaptive filtering for weak impulsive signal recovery for bearings local damage detection in complex mining me-chanical systems working under condition of varying load. Solid State Phenomena 180, 250–257 (2012)
7. Urbanek, J., Antoni, J., Barszcz, T.: Detection of signal component modulations using modulation intensity distribution. Mechanical Systems and Signal Processing (2012); doi:10.1016/j.ymssp.12.018
8. Zimroz, R., Bartelmus, W.: Gearbox Condition Estimation Using Cyclo-Stationary Properties of Vibration Signal. Key Engineering Materials 413-414, 471–478 (2009)
9. Antoni, J.: Cyclic Spectral Analysis of Rolling-Element Bearing Signals: Facts and Fictions. Journal of Sound and Vibration 304, 497–529 (2007)
10. Makowski, R., Zimroz, R.: Metaclasses and Their Application. LNCS (LNAI), vol. 943, pp. 248–259 (2011)
11. D' Elia, G., Delvecchio, S., Cocconcelli, M., Dalpiaz, G.: Combining blind separation and cyclostationary techniques for monitoring distributed wear in gearbox rolling bearings. In: Proc. of Surveillance, Compiègne, France, October 25-26, vol. 6 (2011)
12. Jabłonski, A., Barszcz, T.: Automatic validation of vibration signals in wind farm distributed monitoring systems. Measurement 44, 1954–1967 (2011)

A Non-zero Padding Method in the Angle Domain to Improve the Order Spectrum Resolution of Computed Order Tracking

KeSheng Wang[1] and Stephan Heyns[2]

[1] School of Mechatronics Engineering,
University of Electronic Science and Technology of China, 611731,
People's Republic of China
keshengwang@uestc.edu.cn
[2] Dynamic Systems Group,
Department of Mechanical and Aeronautical Engineering,
University of Pretoria, Pretoria, 0002, South Africa
Stephan.heyns@up.ac.za

Abstract. Computed order tracking is one of the effective order tracking methods to obtain an overview of rotating machine vibrations in terms of rotational speed or orders. However, this process is dependent on Fourier analysis and subject to the same assumptions. The order interval as well as the order resolution of the resultant order spectrum obtained from computed order tracking is therefore determined by the measured data through the Fourier transformation. In this paper, zero padding which has been widely used to improve frequency interval in the field of signal processing, is discussed in terms of order domain signals. A development of zero padding which comprises non-zero padding for rotating machine vibrations, is introduced. This allows improvement of both the order interval and order resolution of the resultant order spectrum for computed order tracking. The limitations of order spectrum inherent to Fourier analysis are therefore significantly reduced. The ability of the method is demonstrated through simulation studies which prove the usefulness of the method for enhancing the ability of computed order tracking in condition monitoring.

Keywords: Computed order tracking, Non-zero padding, Order tracking, Order interval, Order resolution, Rotating machine, Zero padding.

1 Introduction

Computed order tracking (COT) is widely used and researched for the analysis of rotating machines. It excludes the effects of rotational speed variation in the measured data by re-sampling time domain signals to the angle domain, so that the subsequent Fourier analysis renders clear spectrum components. Various researchers have extensively studied the theory and some applications of this

technique (Potter, 1990; Fyfe and Munck, 1997; Blough, 2003; Eggers et al., 2008). However, the assumptions and constraints inherent to the COT procedures imply several limitations. Examples include the common constant angular acceleration assumption which assumes a linear rotational speed over each revolution to re-sample the time signals to the angle domain; the use of polynomial interpolation to find re-sampled data amplitudes which violate the sinusoidal cyclic nature of rotating machine vibrations (Blough,2003); the length of the observation interval or the length of measured data that limits the order resolution in the final order spectrum; the length of sampling interval or the number of revolutions in the measure data determines the order interval in the resultant order spectrum, etc. All of these, of course, influence the accuracy of the final result and determine the diagnostic ability of COT. Therefore, methods that may avoid or improve the consequences of the above limitations of COT are beneficial to the diagnostic ability of the method.

In this paper, the zero padding method which is commonly used in discrete Fourier transformations (DFT) for a better approximation of Fourier transform is applied in the angle domain, to demonstrate the ability of the method for the improvement of order interval for the resultant order spectrum. Although this method is effective to improve the order interval of the resultant order spectrum, however it cannot increase the order resolution and therefore it cannot substantially improve the clarity of the order spectrum. Through consideration of the unique characteristics of rotating machine vibrations, a novel development of the zero padding method for rotating machine vibrations, i.e. non-zero padding method, is introduced through which improvement in both the order interval and the order resolution of the resulting order spectrum obtained from COT is possible. The non-zero padding method is then compared to traditional COT and zero padded COT methods in simulation studies in which close orders that cannot be discerned by using the traditional COT method, are resolved by both the zero and non-zero padded methods and further enhancement of the order spectrum is achieved by the non-zero padded COT method. The application of zero padding method in terms of angle domain rotating machine vibrations and the novel development of the non-zero padding method, enhances the ability of COT for rotating machine fault diagnostics.

2 Order Interval and Resolution for Computed Order Tracking

2.1 Order Interval

For computed order tracking (COT), Fourier analysis is applied to the re-sampled data where frequency variations in speed have been excluded. The Shannon equation therefore applies to the re-sampled data in terms of the angle and order instead of time and frequency. In particular, the order interval of the resultant order spectrum is determined by the number of revolutions that a machine turns through during the transformation period (Blough, 2003), that is

$$\Delta o = \frac{1}{R} = \frac{1}{N \cdot \Delta\theta}, R = N \cdot \Delta\theta \tag{1}$$

where Δo is the order interval or spacing of resulting order spectrum, R is the total number of revolutions considered, N is the total number of data points over which the transform is performed, and $\Delta\theta$ is the angular spacing of the re-sampled signal. Clearly, from Equation (1), the order interval of the resultant order spectrum (Δo) is inversely proportional to the revolutions of the measured data R , or it is determined by the length of sampling interval. The finer the order interval demands to the order spectrum, the more revolutions or longer length of sampling intervals are needed in the analyzed data.

2.2 Order Resolution

The DFT's order resolution O_{res} is however inversely proportional to the length of the total observation interval and can be expressed as,

$$O_{res} \propto \frac{1}{N \cdot R} \tag{2}$$

In fact, the order resolution of the resultant order spectrum is determined only by the length of the observation interval, however the order interval of the resultant order spectrum is determined by the length of sampling interval. When the length of observation interval is equal to the length of sampling interval, both of them will vary simultaneously, however if the length of observation interval is different from the length of sampling interval, the two of them will then vary differently.

In signal processing literature, the zero padding method is well known for its ability to improve the frequency interval of the resultant frequency spectrum through DFT. It is claimed that the method can obtain a better approximation of the Fourier transformation for a signal. However, this method is seldom transferred to order domain signals, and certainly less so in the context of order tracking diagnostic abilities. An effective diagnostic decision through COT requires any possible signal enhancement to obtain clearer order spectra. It is therefore worthwhile to discuss the method in terms of angle domain signals for computed order tracking. In the following, zero padding method in angle domain is firstly discussed.

2.3 Zero Padding Method in the Angle Domain

Usually zero padding comprises adding a string of zeros to a signal so that the frequency interval obtained for DFT of a time domain signal can be decreased, and a better approximation of the Fourier transform can be obtained (Neild et al., 2003). The zero padded signal may be thought of as an infinite signal multiplied by a

finite length rectangular window in the time domain and has the effect of introducing a convolution of the signal with a sinc function (where $\mathrm{sinc}(x) = \sin(x)/x$) in the frequency domain. The idea of the method can be transferred to the angle domain. The zero padding process for a re-sampled signal in angle domain can be generalized as,

$$\{x(n)\} = \{x(0),..., x(N-1), \underbrace{0,...0}_{(\alpha N - N)\ points}\} \tag{3}$$

where the original sequence of N samples has been increased to a sequence of αN samples in which zero values are added. If the N samples correspond to R revolutions, then αN corresponds to α times R revolutions for the angle domain data. Theoretically, a uniformly spaced angle domain signal $x(n)$ can be transformed into order components $X(k)$ through DFT, as is shown in equation (4).

$$X(k) = \sum_{n=0}^{N-1} x(n) e^{-j(2\pi k \frac{n}{N})} \tag{4}$$

$$\xrightarrow{N \to \alpha N} X_{zero}(k) = \sum_{n=0}^{\alpha N-1} x(n) e^{-j(2\pi \frac{k}{\alpha} \frac{n}{N})} \tag{5}$$

The angle domain signal therefore can be zero padded to the length of αN (i.e. the revolutions become αR). The DFT for the zero padded angle domain signals yields equation (5). Note that although the length of the signal is increased to αN, the signals that are analyzed still remain the same $x(n)$ since, outside the interval $n=0 \to N-1$, the signals are all zero valued. This means that the length of the observation interval remains the same between the original angle domain data and the zero padded angle domain data. Therefore it infers that the zero padding process does nothing with order resolution. However, this process is equivalent to multiplying a rectangular window of length of N into a signal with total length of αN. By doing so however, it is clear from equations (4) and (5) that the order interval has been decreased from k to $\frac{k}{\alpha}$ due to the addition of zero samples or the increase of the length of sampling interval. Thus, the zero padded method in angle domain clearly improves the order interval of the resultant order spectrum. Besides, it should be noticed that order domain zero padding is essentially same as time domain zero padding, the difference only being in terminology.

2.4 Non-zero Padding Method in Angle Domain

While zero padding improves the order interval of the resultant order spectrum, it does not improve the order resolution. For vibration monitoring, the clearer the order spectrum of COT, the better the diagnostic ability of COT. This suggests further exploration of the possibility to improve both order interval and order resolution of COT order spectrum.

For rotating machine vibrations, a unique and fundamental characteristic of the re-sampled angle domain data is that the order vibrations are periodic. In other words, the order vibrations will repeatedly occur in each revolution. If the observed data only contains limited revolutions, then it is reasonable to assume that the angle domain order vibration repeats itself during subsequent revolutions, so that the length of the observation interval is increased. As a result, it brings about an improvement in order resolution. Besides, with the repeated addition of the data, the length of the sampling interval is also increased which in turn leads to the improvement of the order interval for the resultant order spectrum. Thus, both order interval and order resolution can be improved through the sequential joining of angle domain vibrations, which may be viewed as a non-zero padding process. It should be noticed that this non-zero padding process is only valid in the re-sampled angle domain where order vibrations are periodic. This is not valid for the original time domain rotating machine vibrations, since the data can be non-stationary due to the variation of rotational speed, which violates the requirement of Fourier analysis. Besides, the non-zero padding process is not a further measurement of real rotating machine vibrations. The main focus of the method is to emphasize the original measured data and presents an enhanced order spectrum in terms of the improvement on both order interval and resolution. This is especially useful when only limited revolutions of the measured data are obtained for diagnostic purposes. Besides, the non-zero padding suggested here is equivalent to a wider rectangular window applied in the angle domain and therefore results in a narrower sinc function in the order domain. A true improvement of the order resolution may therefore be brought about.

Thus, the angle domain data can be non-zero padded to the length of αN with sequential jointing α times $x(n)$ which yields $x_m(n)$. The non-zero padding process therefore can be expressed as

$$\{x_m(n)\} = \{x(0),..., x(N-1), \underbrace{..., x(0),... x(N-1)}_{(\alpha N - N)\ po\ \mathrm{int}\ s}\} \tag{6}$$

The DFT on such a non-zero padded angle domain signal is shown in equation (7)

$$X_{Non-zero}(k) = \sum_{n=0}^{\alpha N-1} x_m(n) e^{-j(2\pi \frac{k}{\alpha} \cdot \frac{n}{N})} \tag{7}$$

Clearly, equation (7) illustrates that the order interval still decrease to $\frac{k}{\alpha}$ and the length of the observation interval becomes αN in which α repetitions of $x(n)$ are concatenated into one series. This result is equivalent to multiplying a rectangular window with a length of αN, which artificially increases the length of the window compared to the zero padding method discussed before, where the window length is N. As a result, both order interval and order resolution on COT order spectrum are improved through non-zero padding. This may enhance the diagnostic ability of COT. Besides, it should also be realized that due to the repeated use of $x(n)$ by α times, it therefore inevitably increases the average amplitude of resultant order spectrum, and should thus be normalized by dividing by α once the order spectrum is calculated. Further, in the traditional Fourier analysis problem, leakage of the angle domain data is also possible. Time windows, such as the Hanning window and others, may also be used to minimize the leakage effects before the non-zero padding process is applied to the data.

In summary, the angle domain signal is modified in terms of zero and non-zero padding methods. Order interval and order resolution of resultant COT order spectrum are improved through these methods. An enhancement of the COT order spectrum is therefore achieved. In order to clarify the differences between these methods, traditional computed order tracking (COT) and zero and non-zero padding COTs are compared in Table 1.

Table 1 Comparisons on COT, zero padding COT and Non-zero padding COT

	COT	Zero padding COT	Non-zero padding COT
L_o	x_n $n = 0 \rightarrow N$	x_n $n = 0 \rightarrow N$	x_m $m = 0 \rightarrow \alpha N$
L_s	N	αN	αN
Δo	k	$\frac{k}{\alpha}$	$\frac{k}{\alpha}$

L_o : length of the observation interval; L_s : length of sampling interval.

Δo : order interval of resulting order spectrum.

3 Numerical Demonstration

A 10s analytical signal consisting of a sum of three orders, that is the 3rd , 3.2th and 5th, orders, is considered. A varying rotational speed is simulated through which the rotor complete two revolutions within 10s. The details of simulated signals are listed in Table 2.

Table 2 Signal simulation

Initial conditions	Sampling rate	Angles that rotor turns through (θ)	Angular acceleration (α)	Angular speed (ω)
$t_0 = 0$; $\omega_0 = 0$ $\alpha_0 = 8\pi/100$	1024 Samples/second 500 Samples/revolutions	$\theta = \omega_0 t + \frac{1}{2}\alpha t^2$	$\alpha = 8\pi/100$ α is determined by substituting $\theta = 2 \cdot 2\pi$ $t = 10s$ into θ	$\omega = \alpha t$
Simulated analytical signals	$y_1 = \sin(3\omega t) + \sin(3.2\omega t) + \sin(5\omega t)$			
	$y_2 = \sin(3\omega t) + 0.3\sin(3.2\omega t) + \sin(5\omega t)$			

Firstly, traditional COT is applied to the simulated signal y_1, and the time waveform is firstly transformed into evenly distributed angle domain waveforms. The waveforms are plotted in Figure 1 respectively as functions of time and angle.

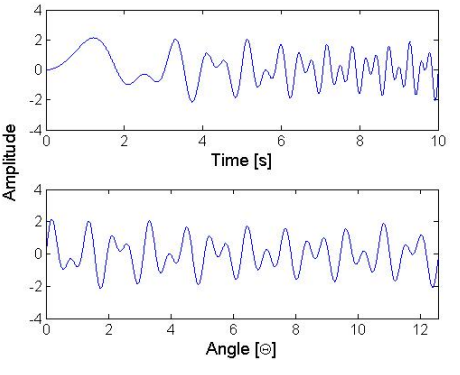

Fig. 1 Time domain and angle domain waveforms

Clearly, a non-stationary time waveform (the top figure of Figure 1) is re-sampled into the angle domain (the bottom figure of Figure 1) where frequency variation of the signal due to the variation of rotational speed has been excluded. Based upon this angle domain signal, further Fourier analyses which are followed by the traditional COT, zero padded COT and non-zero padded COT are

performed and order spectra are depicted in Figure 2(a). For zero and non-zero padding COT, 39 extra revolutions are added which leads to an order interval of $\Delta o = \frac{1}{R} = \frac{1}{40} = 0.025(order)$

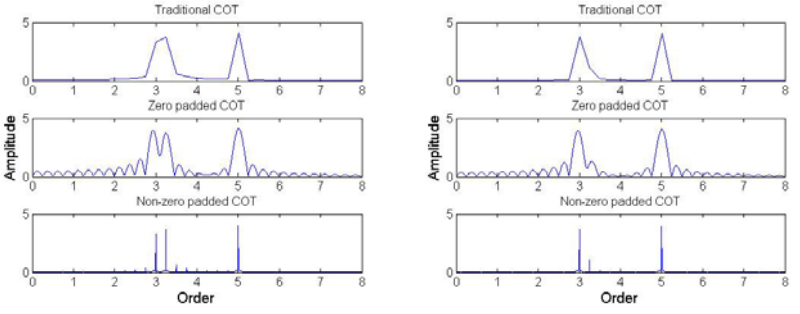

(a) Signal y_1 (b) Signal y_2

Fig. 2 COT, Zero and non-zero padded COT

As can be expected, the order interval of traditional COT is $\Delta o = \frac{1}{R} = \frac{1}{2} = 0.5(order)$. This is, of course, not good enough for the close orders, namely the 3rd and 3.2th order. It can be seen in the top figure of Figure 2(a) that 3rd and 3.2th orders are mixed together within one wide order peak. The COT cannot distinguish them. When zero padding is applied to the re-sampled angle domain signals, the new order step becomes $\Delta o = \frac{1}{R} = \frac{1}{40} = 0.025(order)$ and the order spectrum is shown in the middle figure of Figure 2(a). It is encouraging to observe that two closely spaced rounded order peaks are emerging after the zero padding. However it should also be noticed that quite a few side lobes of order peaks are evident and may possibly lead to confusion with other order peaks or sidebands. This effect is actually due to the low order resolution of the resultant order spectrum. From angle and order domain windows point of view, compared to traditional method, zero padding is similar to applying an equivalent length of the rectangular window, and does not increase with the increase of data length. Thus the corresponding sinc function in the order domain cannot be narrowed which could not improve the visibility of the resultant order spectrum map, therefore the order peak appears rounded in shape.

Non-zero padding is now applied to the re-sampled angle domain signals to overcome these drawbacks. This is shown in the bottom figure of Figure 2(a). Clearly, three distinct order peaks are rendered. There are no more side lobes and narrow order peaks are obtained. This is the result of the increase of the length of sampling interval or revolutions which improves the order interval of the resultant order spectrum and the increase of the length of observation interval which improves order resolution of the resultant order spectrum. Clearly, zero padding

cannot produce as good results as non-zero padding, although it still can pick out the close orders in this case, as is shown in the middle figure of Figure 2(a).

In order to demonstrate the advantage of non-zero padding method, a further simulation of a one-third amplitude of 3.2^{th} order compared to 3^{rd} order is considered in signal y_2. The corresponding order spectra of traditional COT, zero padded COT and non-zero padded COT are shown in Figure 2(b). It is clear that in such a case, the order peaks of traditional COT for the 3^{rd} and 3.2^{th} orders, are even less successful in separating the two close orders, compared to the previous signal y_1. Zero padding however improves the order interval, but the side lobes are equivalent to the amplitude of 3.2^{th} order, therefore no decisive conclusions can be made through this method. The spectrum is depicted in the middle figure of Figure 2(b). Again, non-zero padding features a better order spectrum which suppresses the influence from order side lobes and highlights the real 3.2^{th} order in the order spectrum, as is shown in the bottom figure of Figure 2(b). In short, zero and non-zero padded COT overcomes the limitations of traditional COT in order interval of the resultant order spectrum. The non-zero padded COT further improves the order resolution of the resultant spectrum map which enhances COT for use in rotating machine diagnostics.

4 Conclusion

In this paper, the order interval and order resolution of the resultant order spectrum through computed order tracking method are discussed. A non-zero padding method is developed to overcome both limitations of the resultant order spectrum for rotating machine vibrations. The results show that the zero and non-zero padded COT can both effectively improve the order interval of the resultant order spectrum, which is useful for distinguish close orders. The non-zero padded COT further features advantages over zero padded and traditional COT methods in improving the order resolution which is not achievable by using each of the technique alone.

References

Blough, J.R.: A survey of DSP methods for rotating machinery analysis, what is needed, what is available. Journal of Sound and Vibration 262, 707–720 (2003)

Eggers, B.L., Heyns, P.S., Stander, C.J.: Using computed order tracking to detect gear condition aboard a dragline. The Journal of Southern African Institute of Mining and Metallurgy 107, 1–8 (2007)

Fyfe, K.R., Munck, E.D.S.: Analysis of computed order tracking. Mechanical Systems and Signal Processing 11(2), 187–205 (1997)

Neild, S.A., McFadden, P.D., Williams, M.S.: A review of time-frequency methods for structural vibration analysis. Engineering Structures 25, 713–728 (2003)

Potter, R.: A new order tracking method for rotating machinery. Journal of Sound and Vibration 24, 30–34 (1990)

Fractal Based Signal Processing for Fault Detection in Ball-Bearings

Aleksandra Ziaja, Tomasz Barszcz, and Wieslaw Staszewski

AGH University of Science and Technology 30-059 Krakow, Poland
ziaja@student.agh.edu.pl, {tbarszcz,staszews}@agh.edu.pl

Abstract. A method based on a fractal theory and Wavelet Transform applied to fault detection in roller element bearings is introduced. The Orthogonal Wavelet Transform is used to decompose a vibration based signal into scale components in order to reveal self-similarities in the signal. For fault detection the wavelet coefficient variance plots both for reference and damaged data are calculated and compared. The studies are based on simulated data and real life case from a wind turbine.

Keywords: Fault detection, Orthogonal Wavelet Transform, Fractal theory

1 Introduction

Damage detection is from years an area of interest of Mechanical, Aerospace and Civil engineers. One of the most common issues, which need to be investigated, is fault detection in rotating machinery such as bearing and gearbox failures. A number of different approaches to this problem have been proposed over last decades, however still certain limitations especially in industrial applications need to be considered.

The existing signal processing methods dedicated for bearing's fault investigation include Hilbert transform, cepstrum analysis and time-frequency analysis, from which the wavelet based methods have shown especially fast development in recent ten-twenty years. A meaningful invest in the expansion of Wavelet Theory had the works of Chui (1992), Daubechies (1992) and Mayer (1993). The ability of Wavelet Transform (WT) to localize the results both in time and frequency has brought a certain potential to signal processing dedicated for damage detection. The examples of application of the WT to vibration-based signals can be found in (Samuel et al. 1998) and (Staszewski and Tomlinson 1997). Moreover, further studies have shown that WT can be also an important tool for signal processing with fractals and study of self-similarities in signals (Argoul et al. 1989; Hwang and Mallat 1993). This approach has been successfully used by Staszewski and Worden (1999) for an investigation of chaotic time series. In recent publications, approaches relying of fractal theory are limited mostly to the investigation of changes in fractal dimensions; this includes the work of Hadjileontiadisa et al. (2005), S.Yuhai et al. (2007) and M. Yuanying et al. (2010). However, it is known

that vibration signals from rotating machinery have the characteristics that exhibit phenomena, which can be analysed using signal processing with fractals.

The aim of this paper is to explore signal processing with fractals for fault detection in roller-element bearings. For this purpose the orthogonal wavelet transform and fractal theory are combined in order to detect self-similarities in a signal. The paper is organized as follows. Section 2 introduces basis of wavelet analysis. Next the theory of fractals and self-similarity is described. Section 4 formulates the procedure of the proposed method. The results from simulated and real life data are given in Section 5.

2 Wavelet Analysis

The wavelet analysis may be treated as an extension of the traditional Fourier transform with adjustable window location and size. During the transformation the time signal is decomposed into a sum of elementary functions-wavelets delivered from mother wavelet by the operations of scaling a and translation b. Two basic approaches should be distinguished: Continuous Wavelet Transform and Discrete Wavelet Transform. In order to transfer from the domain of continuous to discrete wavelets the following substitutions should be made:

$$a = a_0^m, b = na_0^n b_0, \tag{1}$$

where m, n are integers and a_0, b_0 are non-zero. Both Continuous Wavelet Transform and Discrete Transform cause redundancy in the results. The solution to this problem is Orthogonal Wavelet Transform (Staszewski 2000). The simplest orthogonal wavelets basis are given by the Haar functions, however more efficient analysis can be obtained using Daubechies' wavelets, (Daubecheies 1992).

3 Fractals and Self-similarity

There are many physical signals which show the invariance property rather to scale than translation such as geophysical or economic time series. One of the most important groups of such signals is self-similar random processes known as 1/f processes. In practice self-similarity means that signals are embedded within themselves. Such behavior may be shown on the example of the Devil's staircase, presented in Figure 1. Moreover, it can be shown that the self-similarity of a signal x(t) implies self-similarity of its Wavelet Transform in the time-scale domain (Wornell 1996). As a consequence for 1/f processes the variance of the orthogonal wavelet coefficients x_n^m of the signal x(t) is of the form:

$$var\ x_n^m = \sigma^2 2^{-\gamma m}, for\ \sigma^2 = \frac{\sigma_x^2}{2\pi}\int_{-\infty}^{+\infty}\frac{|\Psi(\omega)|^2}{|\omega|^\gamma}d\omega \tag{2}$$

where $\Psi(\omega)$ is the Fourier transform of the wavelet ψ The fractal dimension D and the self-similarity parameter H are related to γ as: 2H= γ -1 and D=2-H. Moreover, in case of rotating machinery and metallic structures the decrease of the

spectral parameter γ reflects energy redistribution from low to high frequencies. As a result this phenomenon may be used for damage detection purposes. (Staszewski 2000)

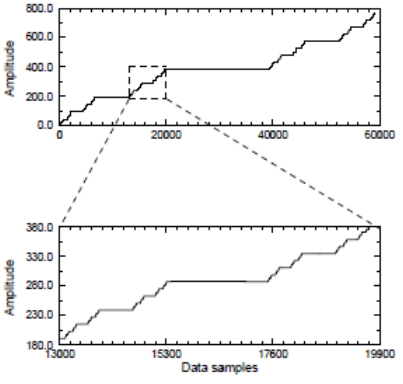

Fig. 1 Self-similar nature of Devil's staircase fractal

4 Formulation of the Method

The preliminary studies have shown the possible application of the fractal based signal processing to vibration-based signals. It was described in previous section that the variance of the orthogonal wavelet coefficient for 1/f processes show important characteristics, which can be used for damage detection purposes. The

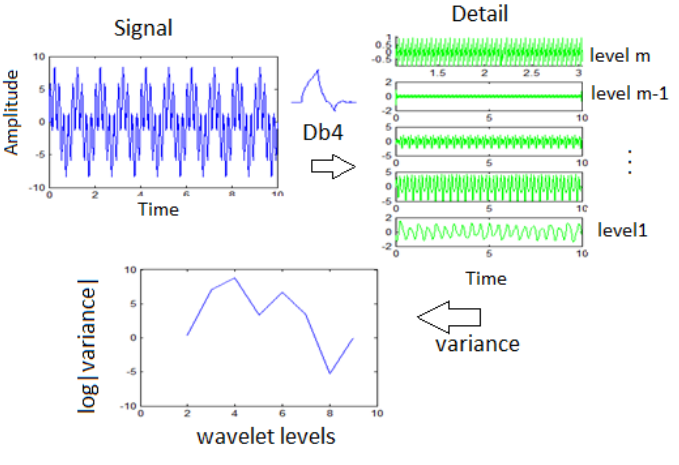

Fig. 2 Scheme of the procedure

Equation 2 implies that the logarithmic variance of x_n^m plotted against level m is a straight line with gradient –γ for signal with self-similar character. In order to apply described approach authors proposed the procedure, which is schematically presented in Figure 2. In the first step the Orthogonal Wavelet Transform is used for time series data. The 4th order Dubechies' wavelets were chosen for this purpose. As a result the decomposition of the discrete time signal x_n into m levels is obtained, where level m corresponds to the detail signal at scale 2^m. Further, the statistical variance of the coefficients x_n^m for each level is calculated. In order to obtain the wavelet coefficient variance plot, the logarithm to base 2 of the result is plotted against the wavelet level. Having both results from damaged and reference condition the assessment of the part condition should be made basing on the visible differences in the plots.

5 Case Studies

5.1 Weierstrass-Mandelbrot Cosine Function – Simulated Data

For the purpose of simulation verification of the described procedure the Weierstrass-Mandelbrot cosine function, which is an example of self-similar time series was used. The function is defined as:

$$x_i = \sum_{j=-N}^{N} \frac{(1-cosB^j \frac{j}{Np})}{B^{(2-D)j}} \tag{3}$$

where Np is a total number of samples equal 4096, N=100, B=1.5, D=1.8 and 1.5 consecutively. The results are presented in Figure 3. The approach leads to the obtained values of spectral parameter γ equal to 1.50 and 1.97 respectively, which match the expectations and confirm the correctness of the approach.

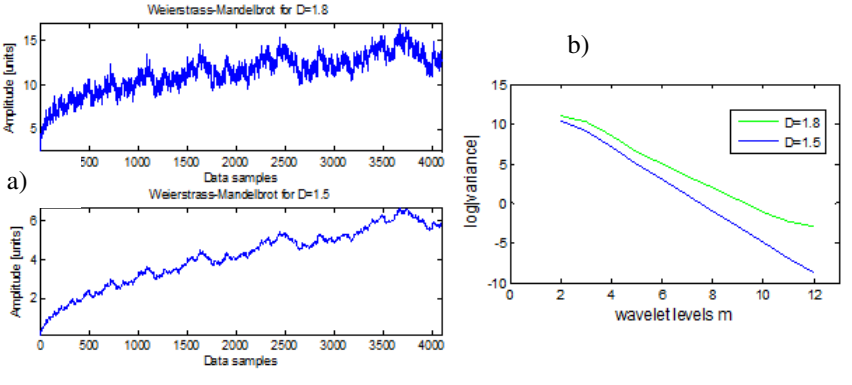

Fig. 3 (a) Signal (b) wavelet coefficient variance plot

5.2 Modulated Band-Pass Noise– Simulated Data

In order to investigate the influence of modulations on the results the band-pass noise of the frequency 3-6 kHz modulated with sin function of the frequency 10, 40 and 60 Hz respectively, as well as the same signal modulated with sawtooth function of the same assumed frequencies was used.

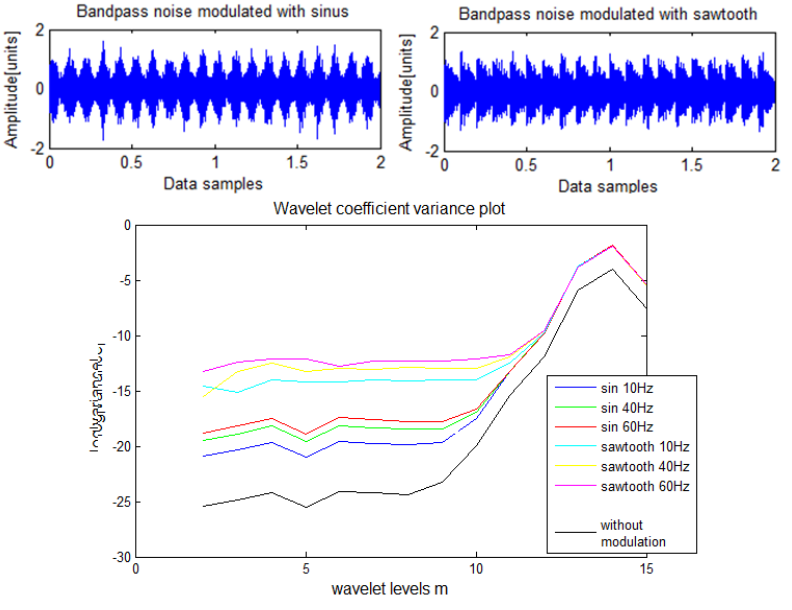

Fig. 4 Comparison of the results for different types of band-pass noise modulation

The sampling frequency was 25 kHz and the number of samples is 50 000. The results are presented in Figure 4. It was observed that depending on the type of the modulation the obtained plots differ in the range of levels 2-10 corresponding to low frequencies. What is more, in case of pure band-pass noise analysis, the plot is translated with respect to the y axis comparing to the remaining results, what is especially visible for higher levels. The reason is the fact that the modulations caused an increase of the results in range of carrier frequencies, which is in agreement with the expectations.

5.3 Wind Turbine Bearing Fault - Real Life Case

The main objective of this work was to determine whether the plots of the wavelet coefficients variance yield useful information concerning the condition of roller element bearings. For the purpose of analysis a real life data from a typical wind

turbine of a nominal power 1500 kW was used. Figure 5 provides trends of typical diagnostics estimates of vibration signal i.e. Peak to Peak (PP) and Root Mean Square (RMS) within the period of three months. The plots show a steady increase of RMS value with a maximum for data5 as well as a significant growth of PP for data described as data4 and data5. After the reparation the values of the estimates returned to the normal levels. The described phenomenon was caused by the inner-ring fault of the generator bearing, which typically manifest itself as signal's modulation with high energy impulses. Authors have decided to use time series of sampling frequency 25 kHz from different stages of fault: 1-reference to 5-severe damage for the analysis. The variance plot generated for each data set is presented in Figure 6.

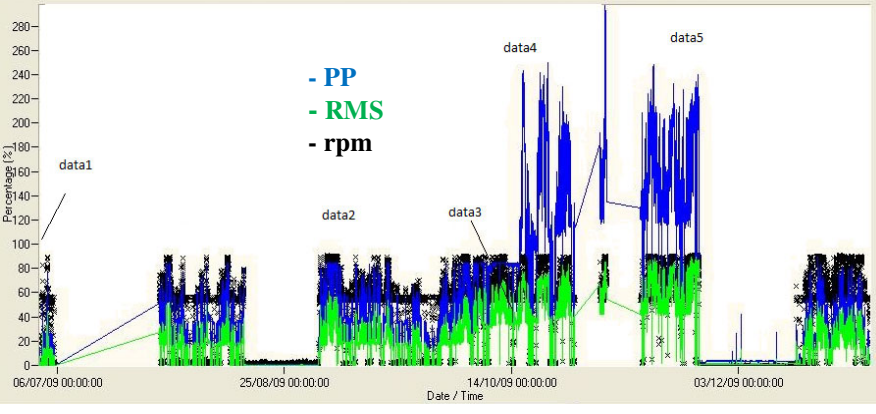

Fig. 5 Trend of Peak-Peak and RMS value

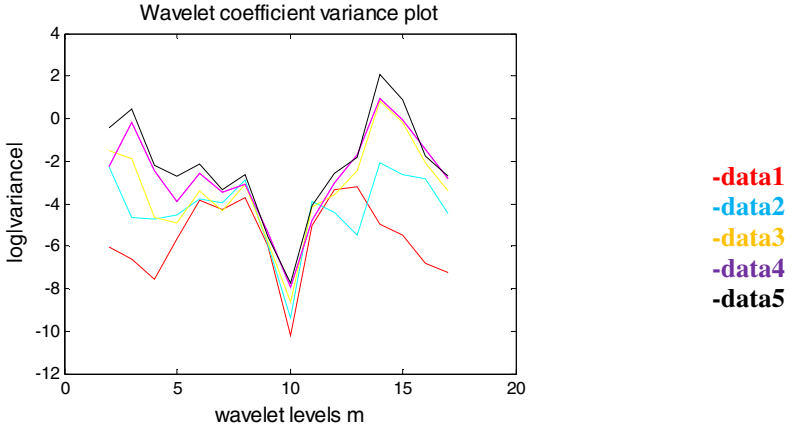

Fig. 6 Comparison of variance plots

It was observed that the reference data (red plot) can be easily differentiated. Additionally a positive correlation was found between an increase of the damage and the growth of variance values, what is significantly visible analyzing the level 14. This can be explained by the fact that the higher (structural) frequencies are strongly modulated by the Ball-pass Frequency Inner-race. Moreover, it is apparent that the severity of the damage is also reflected on the plot, as the data from the most damaged case are visually separated.

6 Conclusion

It can be generally stated that the wavelet coefficient variance plot method, which application was proposed by authors is able to successfully identify bearing's damage. Contrary to expectations, at this stage of the study, the investigation did not show fractal behavior of data from damaged structure, what could be caused by the complexity of wind turbine structure, however, the changes in plot were identified as a good indicator of fault and can be used as base for machine learning techniques. The results indicate that the method is sensitive even for small signal modulation and due to this fact it is able to react at an early stage of damage.

Acknowledgements. The work presented in this paper was supported by funding from WELCOME research project no. 2010-3/2 sponsored by the Foundation for Polish Science (Innovative Economy, National Cohesion Programme, EU).

References

Chui, C.K.: An Introduction to Wavelets. Academic Press (1992)

Daubechies, I.: Ten Lectures on Wavelets (1992)

Meyer, Y.: Wavelets: Algorithms and Applications (1993)

Samuel, P.D., Pines, D.J., Lewicki, D.G.: Fault detection in the OH-58A main transmission using the wavelet transform. In: Proc., 52nd Meeting of the Soc. for Machinery Failure Prevention Techno!': Prognosis of Residual Life of Machinery and Struct., Haymarket, Va, pp. 323–336 (1998)

Staszewski, W.J., Tomlinson, G.R.: Application of the wavelet transform to fault detection in spur gear. Mech. Sys. and Signal Processing 8(3), 289–307 (1997)

Argoul, F., Arneodo, A., Elezgaray, J., Grasseau, G., Murenzi, R.: Wavelet transform of fractal aggregates. Phys. Lett. 135(6(7)), 327 (1989)

Hwang, W.-L., Mallat, S.: Characterization of self-similar multi-fractals with wavelet maxima. Technical Report 641, Courant Institute of Mathematical Sciences, Computer Science Department (1993)

Staszewski, W., Worden, K.: Wavelet analysis of time-series: coherent structures, chaos and noise. International Journal of Bifurcation and Chaos 9(3), 455–471 (1999)

Hadjileontiadisa, L.J., Douka, E., Trochidis, A.: Fractal dimension analysis for crack identification in beam structures. Mechanical Systems and Signal Processing 19, 659–674 (2005)

Yuhai, S., Yuzhe, K., Xianagguo, C.: Fault Pattern Recognition of Turbine-Generator Set Based on Wavelet Network and Fractal Theory. In: The Eighth International Conference on Electronic Measurement and Instruments, Xian, China (2007)

Yuanying, M., Yuxiu, X., Zhiqiang, W.: Detection and Damage Diagnosis for Wind Turbine Blades based on the Theory of Length Fractal Dimension on Dynamic Properties. In: International Conference on Measuring Technology and Mechatronics Automation, Changsha, China (2010)

Staszewski, W.J.: Wavelets for Mechanical and Structural Damage Identification. In: series Studia i Materialy, Gdansk, Monograph No. 510/1469/2000, Polish Academy of Sciences Press, IMP-PAN (2000)

Flandrin, P.: Time-Frequency/Time-Scale Analysis. Academic Press (1999)

Abry, P., Gonçalves, P., Lévy Véhel, J.: Scaling, Fractals and Wavelets. ISTE Ltd. and John Wiley & Sons, Inc. (2009)

Wornell, G.W.: Signal Processing with Fractals: A Wavelet-Based Approach. Prentice-Hall (1996)

Staszewski, W.J., Ruotolo, R., Storer, D.M.: Fault Detection in Ball-Bearings Using Wavelet Variance. In: The 17th International Modal Analysis Conference (IMAC), Kissimmee, Florida, February 8-11, pp. 1335–1339. Society for Experimental Mechanics, Inc. (1999)

Chapter 4
Monitoring and Diagnostic Systems

Despite the fact that condition monitoring is well established as a scientific discipline, there is still a great need to implement results of research into the practice, as monitoring and diagnostic system. In this chapter, a good introduction is provided by Jardine describing “role of CBM for industrial equipment…”. It should be emphasized, that application of effective techniques described by scientists in well ranked journals will never be possible when only test rig will be made without reference to real machine operated in industry. The rig investigation is only the first step for success of condition monitoring method. There is still not enough experiences applied on machines. The investigation done on machines gives us what should be investigated using test rig. The test rigs investigations many times not meets industry needs. Scientists should give more attention to the industrial problems. Several good examples of problem complexity is provided in this chapter in the context of marine gas turbine, mining industry, wind turbine generator or even wind turbines farms. In such practical implementation, as multi-channel online systems, even signal quality assessment seems to be serious data-mining task.

The Role of Condition Based Maintenance for Industrial Equipment and Cancer Screening

Andrew K.S. Jardine[1], Sharareh Taghipour[1], Bart Harvey[2], Anthony Miller[2], Dragan Banjevic[1], and Neil Montgomery[1]

[1] Centre for Maintenance Optimization and Reliability Engineering (C-MORE), Department of Mechanical & Industrial Engineering, University of Toronto, Toronto ON M5S 3G8, Canada
jardine@mie.utoronto.ca, sharareh@mie.utoronto.ca, banjev@mie.utoronto.ca, neilm@mie.utoronto.ca

[2] Dalla Lana School of Public Health, Health Science Building, 155 College Street, Toronto ON M5T 3M7
bart.harvey@utoronto.ca, ab.miller@sympatico.ca

Abstract. This paper gives a brief background to the optimization of condition based maintenance (CBM) decisions, through proportional hazards modeling. It then shows how risk factors for breast cancer and its competing mortalities can be similar to condition monitoring variables and be used as predictors in a risk model.

Keywords: Condition based maintenance, Proportional hazard model, Breast cancer, Screening optimization, Competing risks.

1 Introduction[1]

Condition Monitoring (CM) has become a recognized tool for assessing the operational state of industrial equipment. Maintenance decisions can be made based on analysis of CM information, such as vibration monitoring and oil analysis data.

Control charts are one of the most commonly applied techniques for interpretation of CM data. At each inspection, levels of some measurements are compared with the corresponding predefined "warning limits" and judgment is made based on the outcome. However, control charts leave several important questions unanswered. What if there is no single variable that can provide information on true condition of the equipment? What are the optimal warning limits and should these limits change with operating age of the item?

A conventional maintenance strategy is age-based maintenance, which recommends maintenance of an item either at failure or when it reaches a certain age. This paper discusses a model which extends the age-based model with addition of analysis of CM information. Such approach to optimization of maintenance decisions is referred to as the Condition-Based Maintenance (CBM) technique.

[1] Most of this section and Section 2 are taken from Jardine et al. (2008).

The rest of this paper is organized as follows. Section 2 introduces the theory for time to failure modeling. Section 3 presents a cost-based maintenance optimization model. Section 4 describes the analogy of CBM to breast cancer screening optimization. Section 5 presents the risk factors associated to hazards of breast cancer and its competing mortalities. Concluding remarks are given in Section 6.

2 Failure Time Model

We consider a replacement model in which an item is replaced with another one "as good as new", either at failure or at planned replacement. Item histories are assumed to be independent and identically distributed random processes. A history includes the information on the item's observed lifetime, censoring information and information on diagnostic variables collected at regular discrete times during the observation period.

Diagnostic variables will be termed covariates. In practice, both the external variables (operating environment conditions) and internal (diagnostic) variables can be used as covariates for the analysis. The external covariates can affect the time to failure, and the internal variables can reflect the current state of the item. Complete details on the statistical theory presented in this section are found in (Jardine et al., 2008) and (Bangevic and Jardine, 2006).

2.1 Statistical Model

Let T be the time to failure of the item. The time-dependent condition-monitoring indicators are modeled by a non-homogeneous discrete Markov process $\{Z(t), t > 0\}$, where $Z(t) = (Z_1(t), Z_2(t), ..., Z_m(t))$ is an m-dimensional covariate process observed at regular inspections of the item. It is assumed that $Z(t)$ is a right continuous process, with left-hand limits, and each covariate $Z_i(t)$ is a discrete numerical variable with finite number of values. Let $\{0,1,2,...,n\}$ be the finite state space of $Z(t)$. The overall system can be modeled by the joint process $(I(T > t), Z(t))$ ($I(*)$ is the indicator function) with transition probabilities

$$L_{ij}(x,t) = P(T > t, Z(t) = j \mid T > x, Z(x) = i)$$

For the analysis it is convenient to represent $L_{ij}(x,t)$ in the following form

$$L_{ij}(x,t) = P(T > t \mid T > x, Z(t) = j).P(Z(t) = j \mid T > t, Z(x) = i) \tag{1}$$

Then for a short interval of time $[x, x+\Delta x]$, values of transition probabilities can be approximated as follows:

$$L_{ij}(x, x+\Delta x) = [1 - h(x,i)\Delta x].p_{ij}(x, x+\Delta x) \tag{2}$$

Where $p_{ij}(x,t) = P(Z(t) = j \mid T > t, Z(x) = i)$ is the conditional transition probability of the covariate process $Z(t)$, and $h(x,i)$ represents the hazard function. Values of $p_{ij}(x, x+\Delta x)$ can be approximated from historical data using the maximum likelihood method (details can be found in (Banjevic et al., 2001)). For longer intervals transition probabilities can be derived from (2) using the Markov property:

$$L_{ij}(x, x+m\Delta x) = \sum_k L_{ik}(x, x+(m-1)\Delta x).L_{kj}(x+(m-1)\Delta x, x+m\Delta x)$$

2.2 PHM with Time-Dependent Covariates

We use the Proportional Hazards Model (PHM) to model the influence of CM indicators on the failure time. For our analysis we consider a parametric PHM with baseline Weibull hazard function as a model for the hazard function, so

$$h(t, Z(t); \beta, \eta, \gamma) = \frac{\beta}{\eta}\left(\frac{t}{\eta}\right)^{\beta-1} e^{\sum_1^m \gamma_i Z_i(t)} \qquad \beta > 0, \eta > 0, \gamma = (\gamma_1, \gamma_2, ..., \gamma_m)$$

The method of maximum likelihood can be applied for estimation of parameters β, η, γ of the model. For more details please see (Banjevic et al., 2001).

2.3 Conditional Distribution of Time to Failure

The conditional reliability function of the item, given the current state of the covariate process can be expressed using (1) as follows:

$$R(t \mid x, i) = P(T > t \mid T > x, Z(x) = i) = \sum_j L_{ij}(x,t) \tag{3}$$

Once the conditional reliability function is calculated we can obtain the conditional density from its derivative. We can also find the conditional expectation of $T - t$, termed the remaining useful life (RUL), as

$$E(T - t \mid T > t, Z(t)) = \int_t^\infty R(x \mid t, Z(t))dx$$

In addition, the conditional probability of failure in a short period of time $[t, t+\Delta t]$ can be found as

$$P(\text{Survive during } [t, t+\Delta t] \mid t, Z(t)) = R(t \mid t, Z(t)) - R(t+\Delta t \mid t, Z(t))$$

For a maintenance engineer, predictive information based on current CM data, such as RUL and probability of failure in a certain period of time, can be a valuable tool for assessment of risks and planning appropriate maintenance actions.

3 Economic Decision Model

The objective of the economic decision model is to develop a rule for preventive replacement that minimizes the average replacement cost per unit time due to preventive and failure replacements over a long time horizon. Let $C_P = C$ be the preventive replacement cost, and $C_f = C + K$ be the failure replacement cost, per one replacement. These costs are assumed fixed for all replacements. Let $T_d = \inf\{t \geq 0 : Kh(t, Z(t)) \geq d\}$, $d > 0$ define a "control-limit" policy, i.e. if $T_d < T$, perform the preventive replacement at time T_d , and if $T_d \geq T$, perform the failure replacement at time T . Let the probability of failure replacement be denoted by $Q(d) = P(T_d \geq T)$, and the expected time until replacement be denoted by $W(d) = E(\min\{T_d, T\})$. Then the long-run expected cost of replacements per unit time $\Phi(d)$ is

$$R(t \mid x, i) = P(T > t \mid T > x, Z(x) = i) = \sum_j L_{ij}(x, t) \tag{4}$$

The value d^* that minimizes the right-hand side of expression (4) corresponds to the optimal control-limit policy $T^* = T_{d^*}$. Makis and Jardine (1991) have shown that for a non-decreasing hazard function $h(t, Z(t))$, rule T^* is the best possible replacement policy. For a non-monotone hazard function, the control-limit approach can still be viewed as providing a "near to optimal" replacement policy.

For a non-decreasing hazard function the optimal risk threshold d^* that minimizes $\Phi(d)$ can be found using the fixed point iteration algorithm. In the general case, direct numerical search can be applied.

For the PHM model with Weibull baseline distribution, the optimal replacement rule $T^* = T_{d^*} = \inf\{t \geq 0 : Kh(t, Z(t)) \geq d^*\}$ can be interpreted as

$T^* = \min\{t \geq 0 : \sum_{i=1}^{m} \gamma_i Z_i(t) \geq \delta^* - (\beta - 1)\ln t\}$, where $\delta^* = \ln(\frac{\eta^\beta d^*}{\beta K})$. The function $g(t) = \delta^* - (\beta - 1)\ln t$ can be considered as a "warning level" function for the condition of the item reflected by a weighted sum of current values of covariates. A

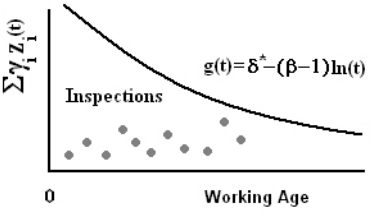

Fig. 1 Sample Economical Decision Chart (for $\beta > 1$)

plot of function $g(t)$ versus working age can be viewed as an economical decision chart which shows whether the data suggests that the item has to be replaced (Figure 1 is an example with several inspections points). Detailed case studies can be found in (Jardine et al., 2001) and (Sundin et al., 2007).

4 Breast Cancer Screening Optimization Analogous to CBM

Cancer screening is similar to the inspection of industrial machinery. Machines are inspected to detect incipient faults. People are screened to detect early stages of disease. In industry, condition monitoring identifies the factors which influence the risk of failure (hazard) of equipment and the indicators of the equipment's health status (diagnostic covariates). The extensive research has been conducted in this area. For example, the model described in the previous sections estimates the hazard depending on the age of equipment and condition monitoring data by combining the PHM and the Markov process model. There is no reason why similar models cannot be used in health care.

In April 2011, an interdisciplinary team of researchers from engineering and health sciences departments of the University of Toronto came together to conduct a collaborative research project. This project aims to model breast cancer risk prediction and mammography screening optimization. The next sections present the early results of this new research direction.

5 Risk Factors of Breast Cancer and Competing Mortalities

We use data from Canadian National Breast Screening Study (CNBSS). The CNBSS consists of two randomized controlled trials designed to evaluate the effect of mammography for women aged 40-49 and 50-59 years old. 98,948 women in these two age groups were recruited between 1980 and 1985 at 15 Canadian centers.

We consider 39 risk factors collected at the time of enrolment or at the initial physical examination of the breasts, and construct hazard models for invasive breast cancer and competing mortalities. The factors are classified in four categories as socio-demographic, lifestyle and health behaviors, history of breast disease, and reproductive factors. We consider 1989 as the cut-off year and by the end of this year, 944 women were diagnosed with invasive breast cancer, and 927 women died from other causes, of which 538 died from other types of cancer and 389 deaths were due to non-cancer causes. 87,912 women were right censored, i.e. neither were diagnosed with breast cancer nor died from other causes.

5.1 Statistical Models

- *Cause-specific hazard*

When there are K competing causes, the cause-specific hazard, which is defined as the instantaneous probability of failing from cause k is

$$h_k(t \mid Z) = \lim_{\Delta t \to 0} \frac{P(t \le T \le t + \Delta t, C = k \mid T \ge t, Z)}{\Delta t} \tag{5}$$

where Z is a vector of covariates, and the overall hazard is $h(t \mid Z) = \sum_{k=1}^{K} h_k(t \mid Z)$.

The cumulative incidence function of cause k is the probability of failing from cause k by time t and is defined as

$$I_k(t \mid Z) = P(T \le t, C = k) = \int_o^t h_k(s \mid Z) R(s \mid Z) ds \tag{6}$$

- *Hazard of subdistribution*

Fine and Gray (1999) propose a model, so-called hazard of subdistribution to perform regression directly on cumulative incidence function, defined as

$$\overline{h}_k(t \mid Z) = \lim_{\Delta t \to 0} \frac{P(t \le T \le t + \Delta t, C = k \mid T \ge t \text{ or } C \ne k, Z)}{\Delta t} \tag{7}$$

The hazard of subdistribution can be modeled using Cox proportional hazards model as $\overline{h}_k(t \mid Z) = \overline{h}_{k,0}(t) \exp(\beta_k^T Z)$, where $\overline{h}_{k,0}(t)$ is the baseline subdistribution hazard of cause k. The cumulative incidence function of cause k is then given by

$$I_k(t \mid Z) = 1 - e^{-\int_0^t \overline{h}_k(s \mid Z) ds} = 1 - \exp\left(-\exp(\beta_k^T Z) \int_0^t \overline{h}_{k,0}(s) ds \right) \tag{8}$$

5.2 Regression Models for Breast Cancer and Mortalities

The statistical methods described in Section 5.1 were used for the CNBSS data, and Table 1 shows a summary of the results. Sign "+" indicates that the factor is significant in the corresponding hazards regression model.

Table 1 Significant covariates in breast cancer and mortalities models

Significant covariates	Regression Model			
	Invasive breast cancer	All deaths	Cancer deaths	Non-cancer deaths
Age at entry	+	+	+	+
Ethnic origin (Foreign)	-	-	-	+
Interaction of age at entry and time	+	-	-	-
Ever noted lumps-right/left	+	+	-	+
Ever noted discharge-right/left	-	+	-	+

Table 1 *(continued)*

Interaction of lumps and time	+	-	-	-
Abnormality in left breast	+	-	-	-
Have/had other types of breast disease	+	-	-	-
Families with breast cancer score	+	-	-	-
Menstruation length (years)	+	+	+	-
Number of live births	+	+	+	-
Interaction of nulliparous level and time	+	-	-	-
Length of hormone used (months)	-	+	+	+
Had a hysterectomy	-	+	-	+
Had a bi-lateral oophorectomy	-	-	+	-
Breast Self examination (BSE) practice	-	+	+	-
Cigarettes smoked per day	-	+	+	+
Age at first child birth	-	+	+	-
Number of pregnancies	-	-	+	-

6 Conclusion

This paper presents a cost-based maintenance optimization model by combining the PHM and the Markov process model. The similarities of breast cancer screening optimization to CBM are described, and the risk factors associated to invasive breast cancer and its competing mortalities are presented.

Acknowledgements. We acknowledge the Natural Sciences and Engineering Research Council of Canada and the Canadian Institutes of Health Research for their financial support.

References

Banjevic, D., Jardine, A.K.S.: Calculation of reliability function and remaining useful life for a Markov failure time process. IMA. J. Manage Math. 17, 115–130 (2006)

Fine, J.P., Gray, R.J.: A proportional hazards model for the subdistribution of a competing risk. J. Am. Stat. Assoc. 94(446), 496–499 (1999)

Jardine, A.K.S., Banjevic, D., Montgomery, N., Pak, A.: Repairable system reliability: recent developments in CBM Optimization. Int. J. Perform. Eng. 4, 205–214 (2008)

Jardine, A.K.S., Banjevic, D., Wiseman, M., Buck, S., Joseph, T.: Optimizing a mine haul truck wheel motors' condition monitoring program. J. Qual. Maint. Eng. 7, 286–301 (2001)

Makis, V., Jardine, A.K.S.: Optimal replacement in the proportional hazards model. Infor. 30, 172–183 (1991)

Sundin, P.O., Montgomery, N., Jardine, A.K.S.: Pulp mill on-site implementation of CBM decision support software. In: Proceedings, International Conference of Maintenance Societies, Melbourne, Australia (2007)

Integration of Production Data in CM for Non-stationary Machinery: A Data Fusion Approach

Diego Galar and Amparo Morant

Division of Operation and Maintenance Engineering,
Luleå University of technology; Luleå, Sweden
Diego.galar@1tu.se, Amparo.morant@1tu.se

Abstract. A process control system deals with disperse information sources mostly related with operation and maintenance issues. For integration purposes, a data collection and distribution system based on the concept of cloud computing is proposed to collect data or information pertaining to the assets of a process plant from various sources or functional areas of the plant inc1uding, for example, the process control functional areas, the maintenance functional areas and the process performance monitoring functional areas. This data and information is manipulated in a coordinated manner by the cloud using XML for data exchange and is redistributed to other applications where is used to perform overall better or more optimal control, maintenance and business activities. From maintenance point of view, the benefit is that information or data may be collected by maintenance functions pertaining to the health, variability, performance or utilization of an asset. The end user, i.e. operators and maintainers are also considered. A user interface becomes necessary in order to enable users to access and manipulate the data and optimize plant operation. Furthermore, applications, such as work order generation applications may automatically generate work orders, parts or supplies orders, etc. based on events occurring within the plant due to this integration of data and creation of new knowledge as a consequence of such process

Keywords: process control, XML, cloud computing, CMMS, EAM, condition monitoring, asset.

1 Introduction

Process control systems, like those used in oil & gas industry, pulp & paper industry, or other processes, typically include one or more centralized or decentralized process controllers communicatively coupled to at least one host or operator workstation and to one or more process control and instrumentation devices, such as field devices. The process controller receives signals indicative of process measurements or process variables made by or associated with the field devices and/or

other information pertaining to the field devices, uses this information to implement a control routine and then generates control signals which are sent over one or more of the buses to the field devices to control the operation of the process. Information from the field devices and the controller is typically made available to one or more applications executed by an operator workstation to enable an operator to perform desired functions with respect to the process, such as viewing the current state of the process, modifying the operation of the process, etc. While a typical process control system has many process control and instrumentation devices, such as valves, transmitters, sensors, etc. connected to one or more process controllers which execute software that controls these devices during the operation of the process, there are many other supporting devices which are also necessary for or related to process operation. This additional equipment does not necessarily create or use process variables and, in many instances, is not controlled or even coupled to a process controller for the purpose of affecting the process operation, this equipment is nevertheless important to and ultimately necessary for proper operation of the process. In the past however, process controllers were not necessarily aware of these other devices or the process controllers simply assumed that these devices were operating properly when performing process control.

Integration of maintenance information, management and monitoring is essential to close the loop of the process that is why CMMS systems have evolved. EAM (Enterprise Asset Management) are more sophisticated software than CMMS, (Fu et al. 2002). These solutions usually enable communication with and stores data pertaining to field devices to track the operating state of the field devices. This information may be stored and used by a maintenance person to monitor and maintain these devices. Likewise, there are other types of applications which are used to monitor other types of devices, such as rotating equipment and power generation and supply devices. These other applications are sometimes available to the maintenance persons and are used to monitor and maintain the devices within a process plant. In many cases, however, outside service organizations may perform services related to monitoring process performance and equipment. In these cases, the outside service organizations acquire the data they need, run typically proprietary applications to analyze the data and merely provide results and recommendations to the process plant personnel. While helpful, the plant personnel have little or no ability to view the raw data measured or to use the analysis data in any other manner. Fig 1 shows the process of outsourced condition monitoring where the only outcome is usually the report by a third party.

Thus, in the typical plants the functions associated with the process control activities, the device and equipment maintenance and monitoring activities, and the business activities such as process performance monitoring are separated, both in the location in which these activities take place and in the personnel who typically perform these activities. Furthermore, the different people involved in these different functions generally use different tools, such as different applications run on different computers to perform the different functions. In many instances, these different tools collect or use different types of data associated with or collected from the different devices within the process and are set up differently to collect the data they need. However there should be cooperation among different

departments in an enterprise and between experts in their respective domain knowledge to succeed with the maintenance policy (Yu et al. 2004).

Typically, maintenance interfaces and maintenance personnel are a real huge of data network, (Davies and Greenough 2000); however it is located apart from process control operators, as you can see in Figure 2, although this is not always the case. In some process plants, process control operators may perform the duties of maintenance persons or vice versa, or the different people responsible for these functions may use the same interface.

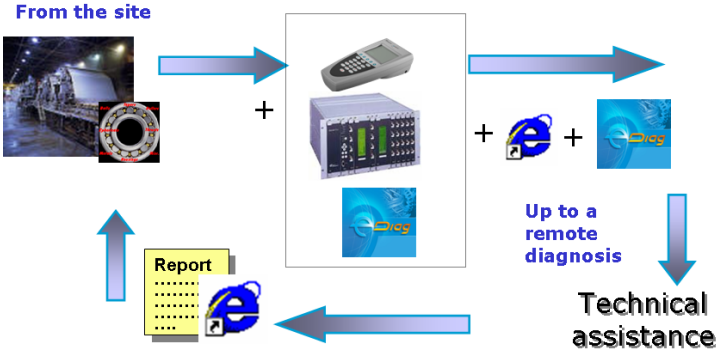

Fig. 1 Typical process of outsourcing in condition monitoring

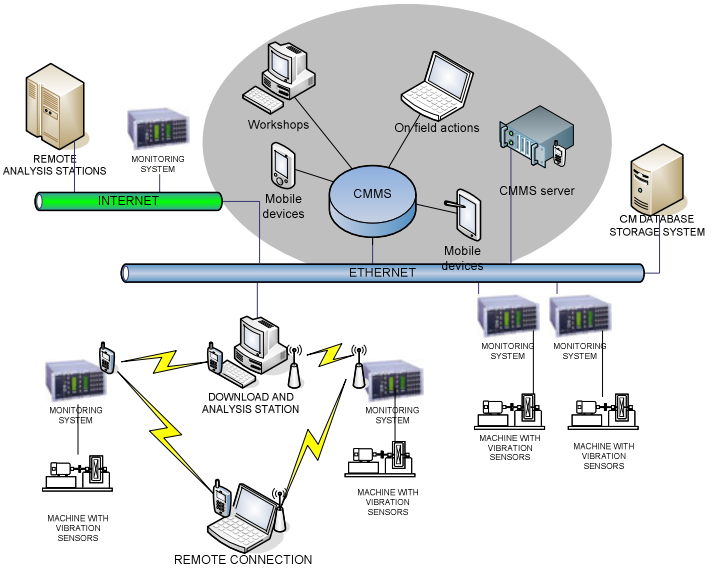

Fig. 2 Typical architecture of maintenance information system

This lack of connectivity affects seriously the performance of maintenance function. Many applications are used to perform the different functions within a plant, i.e. process control operations, maintenance operations and business operations, not integrated, thus, do not share data or information. In many cases, some of the tasks, such as monitoring equipment, testing the operation of devices, determining if the plant is running in an optimal manner, etc. are performed by outside consultants or service companies who measure the data needed, perform an analysis and then provide only the results of the analysis back to the plant personnel. In these cases, the data is typically collected and stored in a proprietary manner and is rarely made available to the plant personnel for other reasons.

2 Data Fusion: A Need in Maintenance of Processes

A process control system includes a data collection and distribution system that collects and stores data from different data sources, each of which may use it own proprietary manner of acquiring or generating the data in the first place. The data collection and distribution system then makes the stored data available to other applications associated with or provided in the process control system or to applications associated with the data sources themselves for use in any desired manner. In this manner, applications may use data from vastly different data sources to provide a better view or insight into the current operational status of a plant, to make better or more complete diagnostic or financial decisions regarding the plant, etc.

Thus, applications may be provided which combine or use data from previously disparate collection systems such as process control monitoring systems, condition monitoring systems and process performance models to determine a better overall view or state of a process control plant, to better diagnose problems and to take or recommend actions in production planning and maintenance within the plant.

This information may then be sent to and displayed to a process operator or maintenance person to inform that person of a current or future problem. This same information may be used by the process operator to correct a current problem within a loop or to change.

A process control expert may use these measurement, control and device indexes along with process variable data to optimize operation of the process. Using the disclosed data collection and distribution system, process variable data and non-process variable data may be combined,.

Likewise, the detection of a device problem, such as one which requires shutdown of the process, may cause business software to automatically order replacement parts or alert the business person that chosen strategic actions will not produce the desired results due to the actual state of the plant. The change of a control strategy performed within the process control function may cause business software to automatically order new or different raw materials. There are, of course, many other types of applications to which the fusion data related to process control, equipment monitoring and performance monitoring data can be an aid by providing different and more complete information about the status of the assets within a process control plant to all areas of the process plant, (Hall and Llinas

1997). However, because the functions are so different and the equipment and personnel used to oversee these functions are different, there has been little or no meaningful data sharing between the different functional systems within the plant.

To overcome this problem, a data collection and distribution system, hereafter the asset cloud is proposed to acquire data from the disparate sources of data, format this data to a common data format or structure and then provide this data, as needed to any of a suite of applications run at, a computer system or disbursed between workstations throughout the process control network. The applications proposed is able to fuse or integrate the use of data from previously disparate and separate systems to provide a better measurement, viewing, control and understanding of the entire plant, (Dasarathy 2001) (Dasarathy 2003).

3 XML: The Protocol for Understanding Each Other

3.1 Common Standards for Maintenance Information Exchange

The complexity of connectivity between applications is enormous since plenty of control system, maintenance management; condition monitoring and enterprise applications are involved in the management of complex, asset-intensive operations. Unfortunately, standards for information exchange have evolved independently for each of these areas. OPC (OLE for Process Control) has gained considerable acceptance as a standard for sharing information between control systems and associated manufacturing applications. MIMOSA's (Machinery Information Management Open Systems Alliance) OSA-EAI standard for sharing condition monitoring and asset health information with maintenance, operations, and enterprise systems is likewise being widely supported, (Thurston and Lebold 2001). The Instrumentation, Systems & Automation Society ISA-95 standard for integration between enterprise and production management systems in continuous, batch and discrete industries is also already being adopted by a broad range of suppliers and users in those industries. Each of these efforts addresses an important issue and has clearly made significant progress in their own right.

OpenO&M is focused on information integration between four different areas: Asset status assessment, through condition monitoring, specialized sensors and analysis tools, have been significant over the last decade. We are clearly at the point where Condition- based Maintenance (CBM) and Condition-based Operations (CBO) strategies, i.e. the performing of maintenance actions based on the information collected through condition monitoring, are becoming realizable. CBM and CBO attempts to avoid unnecessary maintenance tasks by taking maintenance actions only when there is evidence of abnormal behaviours of a physical asset, (Jardine et al. 2006). But in many organizations this information is still only being used by local technicians who maintain the equipment and not accessible for the rest of the personnel.

3.2 XML: The Protocol to Destroy the Communication Barriers

Working within the context defined by ISA-95 further ensures that this same information can be used by higher level enterprise applications like ERP or EAM. The emerging standard is specifically focused on providing value to end users by creating plug and play capabilities for faster implementation and by allowing them to pick and choose the best solutions from suppliers that comply. An extensible, open architecture based on XML and Service oriented interfaces that leverage best of breed technology and support practical interoperability and compliance is implicit in Open O&M.

Nowadays XML is maybe the most popular protocol for this communication exchange of maintenance information, (Szymanski et al. 2003). While HTML is focused on document format, XML is focused on information content and relationships. A class of software solutions is evolving which enables tighter coupling of distributed applications and hides some of the inherent complexities of distributed software systems. The general term for these software solutions is middleware. Fundamentally, middleware allows application programs to communicate with remote application programs as if the two programs were located on the same computer.

XML is accepted as communications over these industrial buses as you can see in (Wollschlaeger and Bangermann 2003), (Hausladen, Bechheim 2004) (Catterson et al. 2005). The process to transfer information between disparate sources in XML environment is as follows: Data from each of the computers involved in asset data exchange must be wrapped in an XML wrapper and sent to an XML data server. Because XML is a descriptive language, the server can process any type of data. At the server, if necessary, the data is encapsulated and mapped to a new XML wrapper, i.e., this data is mapped from one XML schema to one or more other XML schemas which are created for each of the receiving applications.

All existing data (assets, events, failures, alarms) can be modeled with XML. Among them, the most critical and difficult to represent is the layer that represents information regarding sensory inputs and outputs, whether it is a single scalar value or an array of complex data points. The standards define various data formats that may be implemented for representing sensory information. Sensory data, especially relevant in condition monitoring and process control, may be as simple as a single value or as complex as storing several synchronous sampled waveforms.

3.3 Example of Asset Data Integration Using XML

The web based technologies have been widely used and proven for eMaintenance purposes according to (Min-Hsiung et al. 2003) (Kunze 2003) (Han and Yang 2006). One architecture for collecting and integrating data from disparate data sources based on XML server based on web services is proposed in Figure 3.

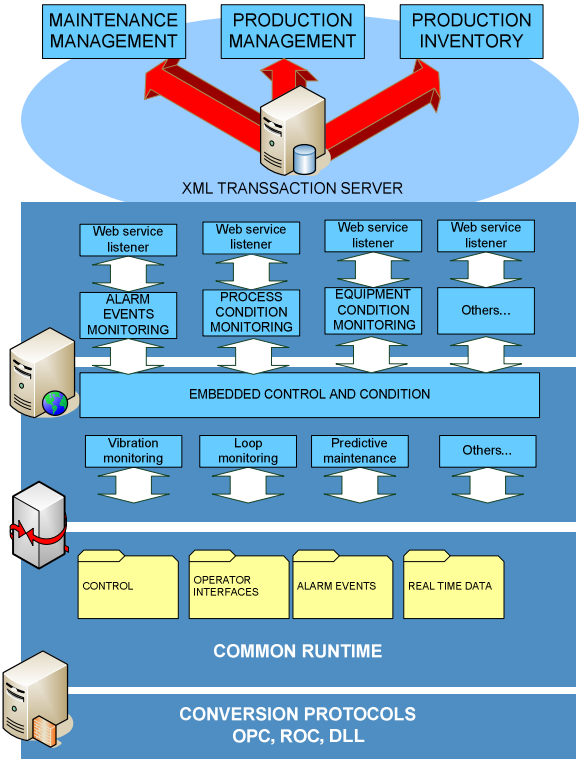

Fig. 3 Integration of disparate data sources

The figure illustrates an architectural overview of a system which implements the collection of data from disparate data sources with a process control system. Generally, the system may include a maintenance management system, a product inventory control system, a production scheduling system, as well as other systems connected by a LAN, the Internet, etc. XML is used as transaction server. The server sends XML wrapped data to the web services indicative of the data.

The web services must include a series of web service listeners which listen for or which subscribe to certain data from other data sources and provides this data to the subscribing applications. The web listening services (which may be part of the data collection and distribution system) may listen for and redistribute alarms and events data, process condition monitoring data and equipment condition monitoring data. Interfaces for this data are used to convert the data to a standard format or protocol, such as the Fieldbus or to XML as desired.

Finally, a configuration database is used to store and organize the data from the process control runtime system, including any data from the remote data sources, such as from the external web servers.

4 Cloud Computing in Asset Management: The Natural Data Repository

4.1 Introduction to Asset Cloud

Cloud computing is the next stage in evolution of the Internet. The cloud in cloud computing provides the means through which everything from computing power to computing infrastructure, applications, business processes to personal collaboration can be delivered as a service wherever and whenever you need. The cloud itself is a set of hardware, networks, storage, services, and interfaces that enable the delivery of computing as a service, (Mell and Grance 2009) (Amrhein and Quint 2009) (Rhoton 2010). Cloud services include the delivery of software, infrastructure, and storage over the Internet (either as separate components or a complete platform) based on user demand. Cloud computing, in all of its forms, is transforming the computing landscape. It will change the way technology is deployed and how we think about the economics of computing. Cloud computing is more than a service sitting in some remote data centre. It's a set of approaches that can help organizations quickly, effectively add and subtract resources in almost real time. Unlike other approaches, the cloud is as much about the business model as it is about technology. Companies clearly understand that technology is at the heart of how they operate their businesses. Business executives have long been frustrated with the complexities of getting their computing needs met quickly and cost effectively.

For asset management, the cloud seems to be the solution with such amounts of dispersed data in different repositories. The end user (maintenance or operators) don't really have to know anything about the underlying technology. The data collection and distribution applications may be dispersed throughout the network and collection of data may be accomplished at distributed locations.

The applications within the cloud may use the collected data and other information generated by the process control systems and, the maintenance systems and the business and process modelling systems as well as information generated by data analysis tools executed in each of these systems. However, the cloud may use any other desired type of expert system including, for example, any type of data mining system, already proven successful in the creation of knowledge for maintenance as one can see in (Iserman 2006) (Wylie et al. 2002) (Yang and Létourneau 2005). It may also include other applications which integrate data from various functional systems for any other purpose, such as for user information purposes, for diagnostic purposes and for taking actions within the process plant, such as process control actions, equipment replacement or repair actions, altering the type or amount of product produced based on financial factors, process performance factors, etc.

4.2 Services Provided by the Asset Cloud

Thus, the cloud, may, in one sense, operate as a data and information clearinghouse in the process plant to coordinate the distribution of data or information

from one functional area, such as the maintenance area, to other functional areas, such as the process control or the business functional areas. As a result, the cloud may use the collected data to generate new information or data which can be distributed to one or more of the computer systems associated with the different functions within the plant and may execute or oversee the execution of other applications that use the collected data to generate new types of data to be used within the process control plant.

The cloud should include or execute index generation software that collects or creates indexes associated with devices, like process control and instrumentation devices, power generation devices, rotating equipment, units, areas, etc, or that are associated with process control entities, like loops, etc. within the plant. These indexes can then be provided to the process control applications to help optimize process control and can be provided to the business software or business applications to provide the business persons more complete or understandable information associated with the operation.

The asset cloud must also provide maintenance data (such as device status information) and business data (such as data associated with scheduled orders, etc.) to a control expert associated with the process control system to help an operator perform control activities such as optimizing control. However, these control experts may additionally incorporate and use data related to the status of devices or other hardware within the process control plant or of performance data generated using process performance models in the decision making performed by these control experts. In particular, in the past, the software control experts generally only used process variable data and some limited device status data to make decisions or recommendations to the process operator.

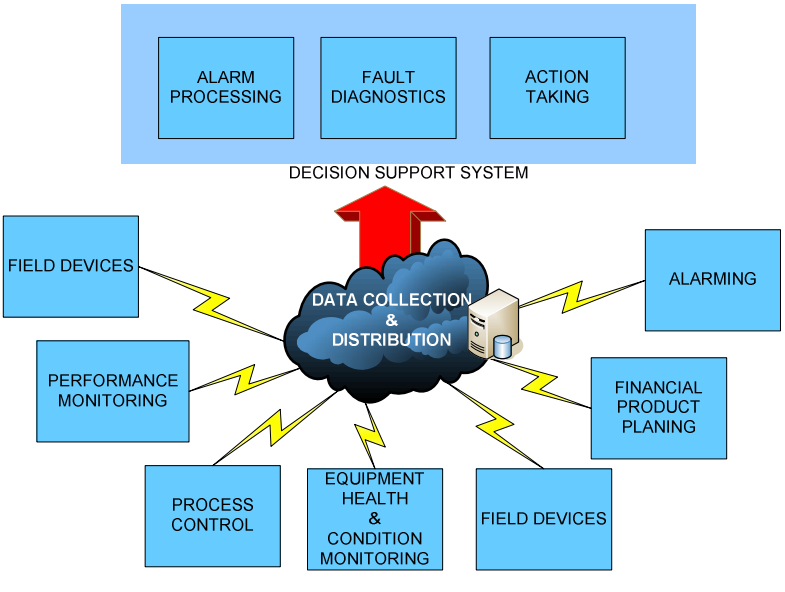

Fig. 4 Services provided by the asset cloud

Figure 4 illustrates a simplified functional block diagram of data flow and communication associated with or used by the asset cloud described herein to enable data from disparate data sources to be used by the asset cloud. In particular, the diagram includes the data collection and distribution system which receives data from numerous sources of data.

An equipment or process health data source (which may include traditional equipment monitoring applications, equipment diagnostic applications, equipment alarming applications, abnormal situation analysis applications, environmental monitoring applications, etc.) also sends data to the cloud. As a result, the source may send data acquired by or generated by any type of traditional equipment monitoring and diagnostic applications or sources.

A performance monitoring data source (which may include performance monitoring applications such optimization applications, process models used to monitor or model process operation, process or equipment health, etc.) also provides data to the system. The data source may include or provide data acquired by or generated by any type of performance monitoring equipment or applications.

5 Conclusion

In the past, the different functional areas, e.g., the process monitoring, the equipment monitoring and the performance monitoring, were performed independently and each tried to "optimize" their associated functional area without regard to the effect that given actions might have on the other functional areas. As a result, a low priority equipment problem may have been causing a large problem in achieving a desired or critical process control performance, but was not being corrected because it was not considered very important in the context of equipment maintenance. With the asset cloud providing data to the end users, however, persons can have access to a view of the plant based on two or more of equipment monitoring data, process performance data, and process control monitoring data. Similarly, diagnostics performed for the plant may take into account data associated with process operation and the equipment operation and provide a better overall diagnostic analysis.

To overcome the limitation of limited or no access to data from various external sources, the asset cloud comes up as a feasible solution that provides to collect data, convert that data if necessary into a common format or protocol that can be accessed and used by applications. The integration of the different types of functional data may provide or enable improved personnel safety, higher process and equipment uptime, avoidance of catastrophic process and/or equipment failures, greater operating availability (uptime) and plant productivity, higher product throughput stemming from higher availability and the ability to safely and securely run faster and closer to design and manufacturing warrantee limits, higher throughput stemming from the ability to operate the process at the environmental limits, and improved quality due to the elimination or minimization of equipment related process and product variations.

References

Amrhein, D., Quint, S.: Cloud computing for the enterprise: part 1: capturing the cloud, DeveloperWorks, IBM (2009)

Catterson, V.M., Davidson, E.M., McArthur, S.D.J.: Issues in integrating existing multi-agent systems for power engineering applications. In: Proceedings of the 13th International Conference on Intelligent Systems Application to Power Systems (ISAP 2005), vol. 6 (2005)

Dasarathy, B.V.: Information Fusion as a Tool in Condition Monitoring. Information Fusion 4, 71–73 (2003), http://www.data-fusion.org/article.php?sid=70

Dasarathy, B.V.: Information Fusion. What, Where, Why, When, and How? Information Fusion 2, 75–76 (2001)

Davies, C., Greenough, R.M.: The use of information systems in fault diagnosis. In: Proceedings of the 16th National Conference on Manufacturing Research, University of East London (2000)

Fu, C., Ye, L.Q., Cheng, Y.C., Liu, Y.Q., Iung, B.: MAS-based model of intelligent control maintenance- management system (ICMMS) and its application. In: Proceedings of 2002 International Conference on Machine Learning and Cybernetics, vol. 1, pp. 376–380 (2002)

Hall, D.L., Llinas, J.: An introduction to multisensor data fusion. Proceedings of the IEEE 85(1), 6–23 (1997)

Hausladen, I., Bechheim, C.: E-maintenance platform as a basis for business process integration. In: 2nd IEEE International Conference on Industrial Informatics (INDIN 2004), June 24-26, pp. 46–51 (2004)

Isermann, R.: Fault-diagnosis systems. Model-Based Condition Monitoring: Actuators, Drives, Machinery, Plants, Sensors, and Fault-tolerant Systems. Springer, New York (2006)

Jardine, A.K.S., Lin, D., Banjevic, D.: A review on machinery diagnostics and prognostics implementing condition- based maintenance. Mechanical Systems and Signal Processing 20, 1483–1510 (2006)

Kunze, U.: Condition tele monitoring and diagnosis of power plants using Web technology. Progress in Nuclear Energy 43, 129–136 (2003)

Mell, P., Grance, T.: The NIST definition of cloud computing, version 15. National Institute of Standards and Technology (NIST), Information Technology Laboratory (2009), http://www.csrc.nist.gov

Min-Hsiung, H., Kuan-Yii, C., Rui-Wen, H., Fan-Tien, C.: Development of an ediagnostics/ maintenance framework for semiconductor factories with security considerations. Advanced Engineering Informatics 17(3-4), 165–178 (2003)

Rhoton, J.: Cloud Computing Explained: Implementation Handbook for Enterprises. Recursive Press, London (2010)

Szymanski, J., Bangemann, T., Thron, M.,, Thomesse, P.J., Reboeuf, X., Lang, C., Garcia, E.: PROTEUS-a European initiative for e-maintenance platform development. In: Conference on Emerging Technologies and Factory Automation, Proceedings, vol. 2, pp. 415–420 (2003)

Han, T., Yang, B.S.: Development of an e-maintenance system integrating advanced techniques. Computers in Industry 57(6), 569–580 (2006)

Thurston, M., Lebold, M.: Open standards for condition-based maintenance and prognostic systems. In: Proceedings of MARCON (2001), http://www.osacbm.org

Wylie, R., Mottola, L., Kresta, J., Monk, R.: Lessons Learned for the I02 Project. In: COM 2002, The Conference of Metallurgists, The International Symposium on Knowledge Management in the Metals Industry, Montréal, Québec, Canada (2002)

Wollschlaeger, M., Bangermann, T.: A Web-based maintenance portal based on an XML content model. In: 2003 IEEE International Conference on Industrial Technology, vol. 1, pp. 405–410 (2003)

Yang, C., Létourneau, S.: Learning to Predict Train Wheel Failures. In Proceedings of the 11th ACM SIGKDD International Conference on Knowledge Discovery and Data Mining (KDD 2005), Chicago, Illinois, USA (2005)

Yu, R., Ye, L., Fu, C.: A multi-agent based, remote maintenance support and management system. In: Proceedings of IEEE/WIC/ACM International Conference on Intelligent Agent Technology (IAT 2004), pp. 496–499 (2004)

Instantaneous Angular Speed Monitoring of a 2MW Wind Turbine Using a Parametrization Process

Hugo André*, Adeline Bourdon, and Didier Rémond

[1] Maia Eolis, Tour de Lille, Boulevard de Turin, Lille, 59000, France
handre@maiaeolis.fr
[2] LaMCoS, Université de Lyon, 18 rue des Sciences, Villeurbanne, 69621, France
didier.remond@insa-lyon.fr

Abstract. One cannot but notice that a variable speed wind turbine utilizes the available wind resource more efficiently than a fixed speed wind turbine, especially during light wind conditions. Most wind turbines are equipped with doubly fed induction generator, thereby allowing them to keep on producing while the speed varies over a wide range. This enhancement forces the monitoring methods to deal with these large variations in speed and torque, since the conditions are seldom if ever stationary. In an original and inexpensive attempt to tackle this issue through angular sampling, this paper proposes to base the surveillance of the line shafting on the instantaneous angular speed variations experienced by the high speed shaft. The unsteady behaviour of these wind turbines is also a difficulty in term of long term diagnostic, since the comparison of successive measurements is usually performed under the same operating conditions. Parametrization of the indicators according to well chosen variables might bring a valuable tool regarding several aspects. A long term experimental study carried over a 2MW wind turbine will be presented as a first application, and will be used to dress an interesting diagnosis on another wind turbine.

1 Introduction

Several industries, including wind energy production, are demanding to observe mechanical or electrical rotating components behaviour at variable speeds. Concerning traditional frequency analysis, it appears to be difficult to develop effective algorithms for early fault detection, especially for variable speed operation [1]. Angular sampling has shown to be a dedicated tool for analysis of vibrations generated in such conditions, since the vibrations of interest are related to transmission or engine angular speed. However, this solution increases the measurement instrumentation cost and does not seem to convince the wind industry yet. An alternative way

* Corresponding author.

of bearing condition monitoring based on the Instantaneous Angular Speed (IAS) measurement has been proven able to detect localized faults in non stationary conditions, using only an encoder close from the source of the defect [2]. Many different methods have been developed for the measurement of angular speed [6], among which some does not even need a vibration sensor [7] [8].Previous work has shown the possibility to enhance IAS monitoring under non stationary conditions in such a way that the use of only one encoder might be enough to cover the whole line shafting of the 2MW wind-turbine [3].

The next step is to feed a monitoring histogram using measurements recorded under always different running conditions. At some extent, this difficulty has already been tackled in the literature. First, Bartelmus *et al* used the linear dependence between the vibration amplitude of the complex wheel excavator gearbox behaviour in regards with the strong torque variation [4]. Nevertheless, this application does not experience large speed variation and the linear approach might not be suited for wind turbines. At the same time, Mac Bain *et al* proposed an interesting monitoring methodology handling the run-up and run-down vibration measurement recorded on a simple mechanical system [5]. This method is based on the scattering of the whole signal in small periods where the signal can be assumed stationary. This solution can not be directly used in wind-turbines neither, since the complex mechanical system requires a high spectral resolution [3].

In this paper, the IAS method will be presented in a first part, along with the dedicated tools developed to enlighten mechanical phenomena under surveillance and the wind turbine set-up. Eventually, an original approach is proposed in support of these tools to dress the follow-up of the complete line shafting under the unsteady running conditions the machine experiences routinely. A two-years long experiment has been carried out on a 2MW wind turbine to qualify the ability of this monitoring system and will finally put to the test this original parametrization process. As it is quite often the case in such situations, no definite major faults developed in the period over which the machine was monitored. However, inferences can be made between the result obtained with this first turbine and those coming from another wind-turbine, presumably defective.

2 Material and Methods

2.1 Elapse Time Method

In this paper, IAS measurements are however carried out using the elapse time method on the square signal delivered by a tachometer. The elapse time method has been largely used in the measurement of torsional vibration to study gear Transmission Error measurement and shaft crack detection [9]. The data acquisition system relies on a High Frequency Counter which can be commonly found on traditional acquisition board (80Mhz). The rotating speed ω_i is estimated for each rising edge of the encoder signal by counting the pulses delivered by a high frequency clock, respecting Eqn. (1)

$$\omega_i = \frac{2\pi}{R} \cdot \frac{f_c}{t(\alpha_i) + \varepsilon} \tag{1}$$

ω_i depends on the resolution of the encoder R and on the counter frequency f_c. α_i stands for the i^{th} entire pulse cycle delivered by the tachometer which exactly correlate the IAS of the shaft carrying the sensor. Uncertainty term ε globally denote the geometrical, electrical and quantification measurement errors. It may eventually be usefull to underline that the geometric perturbations, notably induced by the encoder gratings inaccuracy, is known to be mainly concentrated on the orders of the shaft carrying the encoder [10]. Once the IAS signal is obtained, a Fourier Transform is applied on it to emphasize every cyclic periodicities and eventually be the exhaustive indicator of each elements health status. However, it must be understood that all the traditional habits linked to classical work in the spectral domain must be revised since the signal is not sampled in the time domain but in the angular one. The distinctness of this method mainly relies on the two following points:

1. The monitoring tool is only based on the shaft speed observation. (and not on the complex housing vibration)
2. The signal is sampled on an angular basis (the Fourier transform is then correlated to the cyclic frequency rather than the time frequency)

2.2 *Limitation of the Methodology*

André *et al* have recently underlined the major pitfalls to be overcome to make the IAS monitoring system operational under these peculiar measurement requirements [3]:

1. Spectral Resolution: although high transmission ratio spreads out cyclic frequencies related to each components to be monitored, some components see their characteristic frequencies close from each other and hard to differentiate using only one sensor.
2. Broad band perturbation: large speed variations induce broad band effect disturbing the measurement analysis, especially for low cyclic frequency phenomena.

For the sake of conciseness, the solution proposed in the previous paper for each issue and used in this one are just summarised. At first, the spectral resolution optimization might be circled without the use of more than one sensor by artificially reducing the resolution of the sensor installed on the high speed shaft. Secondly, the broad band effect induced by the macroscopic trend of the angular speed has been shown to be efficiently corrected once an apodization window is correctly applied to the IAS signal.

2.3 *Wind Turbine Set-Up*

Both experiments are being carried over two MM82 wind turbines. The wind turbine set-up is presented in Fig. 1 for the reader to realize the easiness of the involved

instrumentation in regards with the kinematic complexity of the turbine line shafting. The IAS signal is computed from the generator optical encoder 1 in Fig. 1. This sensor is originally used by the converter to correctly synchronize the asynchronous generator.

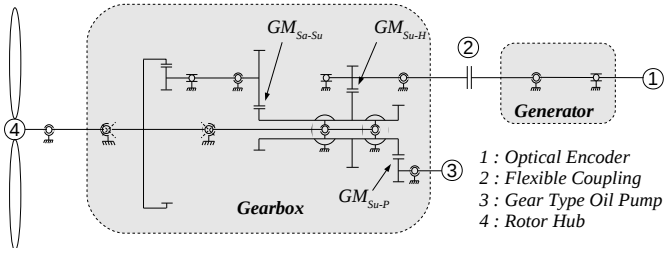

Fig. 1 Kinematic scheme of the wind turbine set-up

Although the entire line shafting presented in Fig. 1 is under surveillance, this paper focuses the observation on the three gear mesh surrounding the sun shaft, for a good reason. Another wind turbine has been briefly equipped because of a presumably deficient behaviour of its sun shaft: one of its gear is suspected to be defective, and the comparison of the results might appear valuable. The paper will therefore focus its attention upon the following gear mesh frequencies, scaled in events per high speed shaft revolutions:

- GM_{Sa-Su}: between the satellites and the sun shaft $f_{GM_{Sa-Su}} = 3.86$ ev.rev^{-1}
- GM_{Su-P}: between the sun and the mechanical pump shaft. $f_{GM_{Su-P}} = 34.5$ ev.rev^{-1}
- GM_{Su-H}: between the sun and the high speed shaft. $f_{GM_{Su-H}} = 32$ ev.rev^{-1}

3 Proposed Approach

3.1 Indicators and Operating Parameters

In general, indicators may result from any representative computation in respect with the corresponding fault appearance. Since this paper is not focused on the optimization of these indicators, they will be limited to the most classical spectral amplitude surveillance. Gears will be qualified after the amplitude of the closest discrete channel from the corresponding characteristic cyclic frequency on the amplitude spectrum of the instantaneous angular speed signal. This signal being beforehand processed through the methods presented in the previous paragraph. However, it should be noted that since the measurements are directly sampled in the angular domain, the theoretical characteristic frequencies of the gears are in coherence with the empirical ones. Figure 2 shows an expample of windowed signal and its amplitude spectrum focused around the cyclic frequency corresponding to the gear meshes coupling the three satellites to the sun gear.

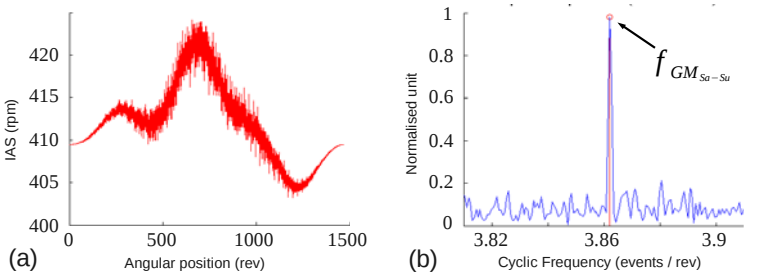

Fig. 2 Example of IAS analysis. a) windowed signal, b) Amplitude spectrum focalised around $f_{Sat-Sun}$

Every measurement has at least one indicator associated to each element under surveillance. To deal with the fact that the operating conditions are always different, these indicators are associated to at least one characteristic operating parameter. In practice, the mean running speed and the mean power generated by the turbine during the corresponding measurement are the two operating parameters that characterize any measurement from the turbines. The last gives an useful image of the torque acting on the line shaft.

3.2 Optimized Parametrization

The parametrization process is based on the following assumption: the indicator follows a multivariate normal distribution. McBain *et al* used this hypothesis with vibration indicators obtained from short stationary measurements [5] and it is here proposed to extend it to the measurement where the operating conditions are no longer stationary. In coherence with the characteristic operating parameters presented in the previous part, the statistic estimators of the Gaussian distribution are assumed to depend on the mean speed and the average torque experienced by the line shafting during the measurement.

Fig 3 (a) locate the measurements made between March and October 2010 accordingly to their operating parameters. From a first view, the relation between the average speed and the active power is not bijective. But since the measurement which average speed is below *1000rpm* are not considered because of their scarcity, it might be possible to characterize the faster measurements using only the average active power. However, the possibility to use only the encoder to achieve the surveillance urges the author to characterize the measurement which speed is between *900rpm* and *1700rpm* using only the average speed. Consequently, the measurements are sorted in this example in twelve slots, where the first eights are characterized by their mean speed, and the last fours are characterized by their average active power.

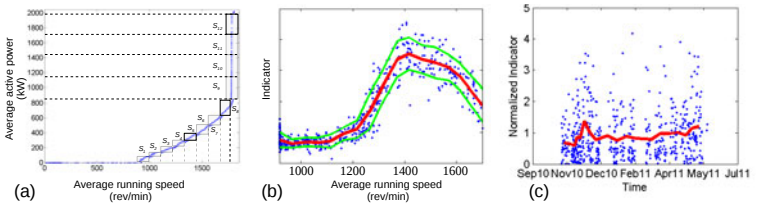

Fig. 3 Normalisation steps applied on any indicator. a) Sort all the measurements accordingly to their respective average speed and active power. b) Estimation of the Gaussian law corresponding to each parametric slot. c) normalization of the following measurements accordingly to the parametric gaussian law.

Fig 3 (b) estimates the empirical mean $\mu(\bar{\omega})$ (in red) and one standard deviation $\sigma(\bar{\omega})$ (in green) of the parametric distributions slot by slot [1]. These parametric values may be used on the following measurements to standardize the indicator accordingly to its characteristic operating parameter. Fig 3 (c) illustrates the standardized measurement obtained between November 2010 and May 2011. The red curve estimates the moving average. This example does not enlighten any evolution in the indicator since the moving average is staying close from the normalized standard deviation. But a threshold can be defined with a suitable discordance test.

4 Experimental Comparison

4.1 Results

The parametric Gaussian law estimation performed on one wind turbine can be used to give valuable information about another wind turbine, as soon as the turbines present the same machinery and are monitored using a similar protocol. Fig 4 presents the Gaussian law estimated on the first turbine for each gear mesh indicator. these estimations are made over one thousand measurements. In addition, six measurements made in a row on the second wind turbine are added on the plot as highlighted dots. As it can be seen on Fig 4 (a-b-c), the average speed of the four fastest measurements outranges the fastest slot, justifying the use of the active power as a characteristic operation parameter on Fig 4 (d-e-f).

The indicator characterizing the behaviour of gear mesh coupling the sun and the pump shaft is the only one which can be believed to follow the same Gaussian distribution. Although suitable statistical tools could be used to interpret the involved probabilities, a brief view on Fig 4 (e-f) is enough to ensure that the multivariate distributions followed by these indicators are far from equal. These differences might be interpreted as a mechanical fault on the fingered gears, but also by a difference

[1] In the exemple presented on Fig 3 (b) , 20 slots share the measurements made before October '10 and which mean speed is between 900 and 1700 *rpm*.

in the dynamic transmission separating the gears and the optical encoder, or even a difference in the acquisition systems used to perform the sampling.

In particular, the characteristic frequency of the gear mesh coupling the sun and the high speed shaft is known to be perturbed by the geometric fault on the encoder, since it is an integer multiple of the high speed shaft order [10]. The difference obtained between these results might be caused by that perturbation. The gear mesh coupling the sun and the mechanical pump shaft can unfortunately no benefit from such excuses, and is therefore expected to present an anormal behaviour.

4.2 Discussion

First, the Gaussian assumption used to perform the parametrization can be questioned. The author is aware that the indicators based on the amplitude spectrum, even in the almost stationary conditions experienced by McBain [5], can hardly follow a Gaussian distribution. Alternatively, the amplitude of the spectral coefficient could follow a chi-squared distribution since it results from a quadratic sum, would the Fourier coefficients follow a normal distribution in the first place. This last assumption might be disturbed by the fact that the measurements are long, unsteady, and the average speed does not describe the distribution with enough precision. It might therefore be useful to verify it through a classical hypothesis test, and if necessary, give more weight to the steadier measurements. Still, the number of samples used to estimate each slot distribution must be large enough for the hypothesis test to be consistent.

As Mc Bain mentioned, the amount of data needed to accurately describe the parametric distribution is increasing exponentially with the number of operation

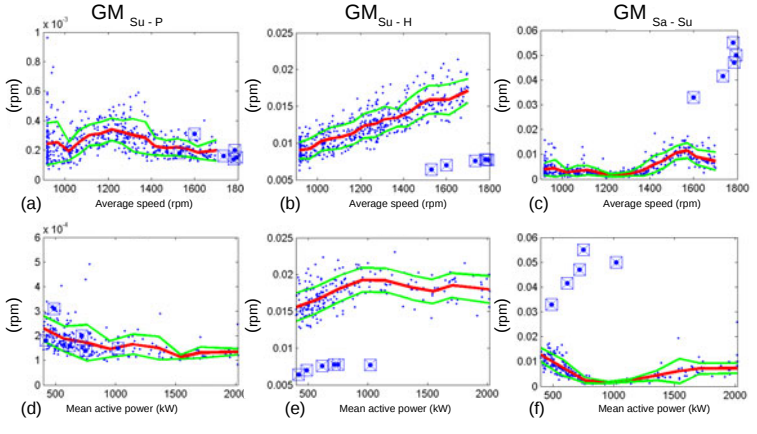

Fig. 4 Estimation of the parametric law followed by the indicator based on the fundamental frequency amplitude of the gears a-d) GM_{Su-P}, b-e) GM_{Su-O}, c-f) GM_{Sa-Su} of the healthy machine. dots correspond to the faulty machine.

parameters. However, the righteous will to distinguish speed from torque variation may not be necessary for these wind turbines, since each parameter can be used on its own to characterize most of the measurements.

If the possibility to use this parametrization to yield experience on a turbine from an other similar turbine is very attractive, it appears that the observation dressed from the parametrization should be associated to a mechanical model of the machine. This model could be used to discriminate the difference induced by unexpected variability: stiffness and damping of the dampers, the coupling or the housing, different sensor position.

Concerning the instantaneous angular speed methodology, this surveillance technique should be associated to dedicated tools differentiating the indicators representing noise from those which represent a real vibration. In other words, the need to handle the uncertainties that perturb these signals observed in the spectral domain has arisen since it may induce wrong diagnostic.

5 Conclusion

Instantaneous Angular Speed (IAS) monitoring appeared as a valuable technology to monitor a wind turbine line shafting, mainly because of its hardware simpleness. Dedicated tools have been developed to improve its adaptability to monitore a complex mechanism which is running under non stationary conditions. Nevertheless, the environnemental conditions variety imposed to the resulting indicators also interferes with the long term monitoring of such a machine. This paper proposes to adapt the parametrization process to a basic spectral indicator assuming it to follow a multivariate Gaussian distribution. Promising results have been brought from a long term study on a 2MW Wind Turbine, although the line shafting were not experiencing any major fault emergence. The possibility to use the long term parametrization in the diagnostic process of an other turbine during a one-day-test has been brought, and encourages the author to consolidate these works with a mechanical model and a video-endoscopy checkout.

References

1. Hameed, Z., Hong, Y., Cho, Y., Ahn, S., Song, C.: Condition monitoring and fault detection of wind turbines and related algorithms: A review. Renewable and Sustainable Energy Reviews 13(1), 1–39 (2009)
2. Renaudin, L., Bonnardot, F., Musy, O., Doray, J., Rémond, D.: Natural roller bearing fault detection by angular measurement of true instantaneous angular speed. Mechanical Systems and Signal Processing 24(7), 1998–2011 (2010)
3. André, H., Bourdon, A., Rémond, D.: On the use of the instantaneous angular speed measurement in non stationary mechanism monitoring. In: Proceedings of the ASME 2011 International Design Engineering Technical Conferences & 23rd Biennal Conference on Mechanical Vibration and Noise IDETC/CIE2011, Washington, DC, USA (2011)
4. Bartelmus, W., Zimroz, R.: A new feature for monitoring the condition of gearboxes in non-stationary operating conditions. Mechanical Systems and Signal Processing 23(5), 1528–1534 (2009)

5. McBain, J., Timusk, M.: Fault detection in variable speed machinery: Statistical parameterization. Journal of Sound and Vibration 327(3-5), 623–646 (2009)
6. Yuhua, L., Gu, F., Harris, G., Ball, A., Bennett, N., Travis, K.: The measurement of instantaneous angular speed. Mechanical Systems and Signal Processing 19(4), 786–805 (2005)
7. Combet, F., Zimroz, R.: A new method for the estimation of the instantaneous speed relative fluctuation in a vibration signal based on the short time scale transform. Mechanical Systems and Signal Processing 23(4), 1382–1397 (2009)
8. Zimroz, R., Barszcz, T., Urbanek, J., Bartelmus, W., Millioz, F., Martin, N.: Measurement of instantaneous shaft speed by advanced vibration signal processing- application to wind turbine gearbox. In: Proceedings of the 11th Workshop on Smart Diagnostics of Structures, p. s.p. Département Images et Signal (2010)
9. Rémond, D.: Practical performances of high-speed measurement of gear transmission error or torsional vibrations with optical encoders. Measurement Science and Technology 9(3), 347 (1998)
10. Resor, B.R., Trethewey, M.W., Maynard, K.P.: Compensation for encoder geometry and shaft speed variation in time interval torsional vibration measurement. Journal of Sound and Vibration 286(4-5), 897–920 (2005)

Application of Spectral Kurtosis to Acoustic Emission Signatures from Bearings

Babak Eftekharnejad[1], Mhmod Hamel[2], Abdulmajid Addali[2], and David Mba[2]

[1] Renewable Energy Systems Ltd, Kings Langley, Hertfordshire, England, WD4 8LR
[2] School of Engineering, Cranfield University, Bedford, England, MK43 0AL
a.addali@cranfield.ac.uk

Abstract. The application of Acoustic Emission (AE) in condition monitoring of rotating machines has been well documented. The majority of research works in this field has involved the use of conventional time domain analysis for processing the AE signals from the machines and there has been little attention given to application of more advanced signal processing methods. This research presents a study in which some advanced signal processing techniques such as Wavelet and Spectral Kurtosis (SK) has been applied to offer improved diagnosis for bearing defect detection

1 Introduction

Today's competitive market together with the revolution in consumer expectations and technology has made companies become more concerned about their productivity and performance (Rao, 1996). For industries to survive in such a complex and competitive environment it is vital to improve their product reliability whilst cutting down on production cost. Product reliability is an important factor for the manufacturer in the mining, aviation, nuclear and chemical industries where operational failure can lead to a devastating disaster. According to the report issued by Mine Safety and Health Administration (MSHA) (2009), 20% of the total fatal mining casualties in the US between 2005 and 2009 were caused by machinery failure. On the other hand, maintenance expenses can directly contribute to the final cost of product. Given the demand for product reliability, as well as the reduction in production cost, it is essential to employ condition monitoring (CM) techniques for firstly predicting the failure prior to the event and secondly preventing unexpected shutdowns of machinery. The former is particularly important in the oil and gas sector where unexpected plant shutdown can result in a major economic loss, while an unexpected failure can result in fatalities in civil aviation. There have been continuous challenges in designing robust CM systems capable of diagnosing damage in its early stages of development and predicting the remaining life of the machine.

Gearboxes are the key part in any rotating machine. In wind turbines the price of the transmission system is usually between 15-20% of the total turbine value (Whitby, 2008). McNiff et al. (McNiff et al. 1990) reported on 20% gearbox

related failure on 200 Micron 65 wind turbines over 10,000 hours of operation. There have also been some reports on gearbox related fatalities in aviation. From 1964-1974, 20% of the total helicopter accidents in the UK were due to gearbox malfunction (Tan, 2005 and Vinall, 1980). On 10th April 2009, the BBC News broadcast a report on the death of 16 people in a North Sea helicopter crash because of gearbox failure. The recent interest on condition based and predictive maintenance of industrial assets, together with product safety, has led to a growing interest in the condition monitoring of gearboxes.

There are different technologies being used for the purpose of the condition monitoring of gearboxes. Vibration and wear debris monitoring are among the most popular methods of CM in industry (Hodges and Pearce 1995, Lebold et al. 2000). The wear debris monitoring involves analyzing and measuring the wear particles and contaminates inside the used oil. This method is very time consuming and requires fairly advanced and expensive laboratory equipment (Ebersbach et al. 2006). The vibration measurement is not capable of detecting the incipient damage inside the machines because the source of vibration in machines changes in stiffness. Hence the vibration response of the machine will not show any change unless the extent of the damage is high enough to influence the mechanical integrity and therefore stiffness (Yesilyurt et al. 2003, Drosjack and Houser 1977). For the past few decades there has been an awareness for using Acoustic Emission (AE) technology in monitoring gearboxes (Mba and Rao 2006). Because of the microscopic origin of AE activity in rotating machines, AE has shown effectiveness in detecting the incipient damage in a more advanced way than wear debris and vibration monitoring.

Over the past decades, multi-resolution analysis using wavelet transform has gained ground as an effective signal-processing tool. The fundamental idea is to decompose the signal into several frequency ranges with finer resolutions, thereby achieving a better understanding of the time-frequency content of the signal (Jensen and Andres 2001). In signal processing, two types, the continuous (CWT) and discrete (DWT) wavelet transforms are employed. The function of CWT is to break up the signals into scaled and shifted versions of a transient type of signal known as the mother wavelet, ψ. The scale, a, and frequency of each wavelet are reversely correlated with each other so that the higher scale corresponds to the low frequency version of same wavelet. The coefficient, C, for each segment of the signals is determined based on the difference in energy of scaled and shifted versions of the mother wavelet and that of a particular segment, see Equation 1(Jensen and Andres 2001).

$$C(a,\tau) = \frac{1}{\sqrt{a}} \int_{-\infty}^{+\infty} x(t)\psi\left(\frac{t-\tau}{a}\right)dt \tag{1}$$

Spectral Kurtosis (SK) is gaining ground as an effective signal processing method in vibration analysis. To determine SK, the signal is firstly decomposed into the time-frequency domain after which the Kurtosis values are determined for each frequency band (Randall 2005). The concept of SK analysis was first developed

by Dwyer (1983) as a tool which was able to trace non-Gaussian features in different frequency bands using the fourth order moment of the real part of the Short Time Fourier Transform (STFT). Dwyer investigated the application of SK on stationary processes but did not account for non-stationary vibration signatures typical of rotating machines. To date the most comprehensive calculations of the SK have been developed by Antoni (2006) as the fourth order cumulant of the spectral moment *(K)*.

$$K_Y(f) = \frac{S_{4Y}(f)}{S_{2Y}^2(f)} - 2 \quad f \neq 0 \tag{2}$$

and

$$S_{nY}(f) \overset{\Delta}{=} \langle \left| Y_W(t,f) \right|^n \rangle \tag{3}$$

$Y_W(t,f)$ is estimated using the short time Fourier Transform:

$$Y_W(t,f) \overset{\Delta}{=} \sum_{-\infty}^{\infty} Y(n) \cdot W(n-t) e^{-j2\pi nf} \tag{4}$$

Where $Y(n)$ is the sampled version of the signal, $Y(t)$, and $W(n)$ is the window function having zero value outside a chosen interval.

For the above calculations to be valid, the size of window (Nw) should be smaller than the length between two repetitive impulses and longer than the length of each impulse. In other words, the analysed signal should be locally stationary. Using the definition offered by Antoni (2006), Antoni and Randall (2006) developed the concept of the Kurtogram to detect non-Gaussianity in a signal. A Kurtogram simply maps the STFT-based SK values as functions of frequency and window size. Antoni (2006) and Antoni and Randall (2006) suggested the use of the Kurtogram for designing a band-pass filter which can be applied to increase the signal-to-noise ratio, thereby preserving the impulse-like nature of the signal. Additional authors aimed to find ways to automatically determine the optimum frequency band for envelope analysis. For this research the frequency and window size (bandwidth) at which the Kurtogram is maximum was employed to build a band-pass filter that was subsequently employed for analysis of measured AE and vibration data. In a separate investigation, Antoni (2007) proposed an algorithm for fast computation of the Kurtogram. In this method instead of using STFT at different window lengths, the signal is decomposed by the means of quasi-analytic low-pass and high-pass filters to generate a pyramidal filter-bank tree with 2^k bands in each level (k). The Kurtogram is computed via calculating the kurtosis of all frequency bands, see Equation 5:

$$S^{i}{}_{nY}(f) \overset{\Delta}{=} \left\langle \left| c_k^i(n) \right|^n \right\rangle \tag{5}$$

Where $c_k^i(n)$ is the sequence of the coefficient from the *i*th filter at *kth* level.

This research presents several experimental investigations where the advanced signal processing methods were applied on recorded AE signals from a bearing that was run to failure with the purpose of improving the signal-to-noise ratio so as to enhance features of bearing damage.

2 Experimental Tests

The test rig used in this experiment is displayed in Figure 1. The bearing test rig has been designed to simulate varying operating conditions and accelerate natural degradation. The chosen bearing for this study was an SKF single thrust ball bearing, model number SKF51210. To ensure accelerated failure of the race the standard grooved race was replaced with a flat race, model number SKF 81210TN. This caused a point contact between the ball elements and the race resulting in faster degradation of the race and early initiation of sub-surface fatigue cracks. The load on the test bearing was applied by a hand operated hydraulic pump (Hi-Force No: HP110-Hand pump-Single speed-Working Pressure: 700 BAR). The flat race was fitted onto the loading shaft in a specifically designed housing. This housing was constructed to allow for placement of AE sensors directly onto the race. Modifications were made to the support of the flat bearing race so as to allow positioning of the AE sensors, see Figure 2. The motor on the rig operated at 1500rpm and the number of rolling elements in the test bearing was 14 and the ball pass frequency (BPF) was 175Hz.

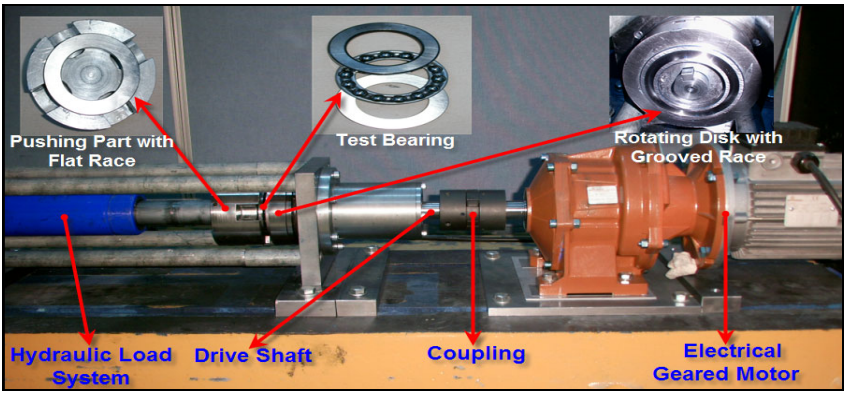

Fig. 1 Test rig assembly

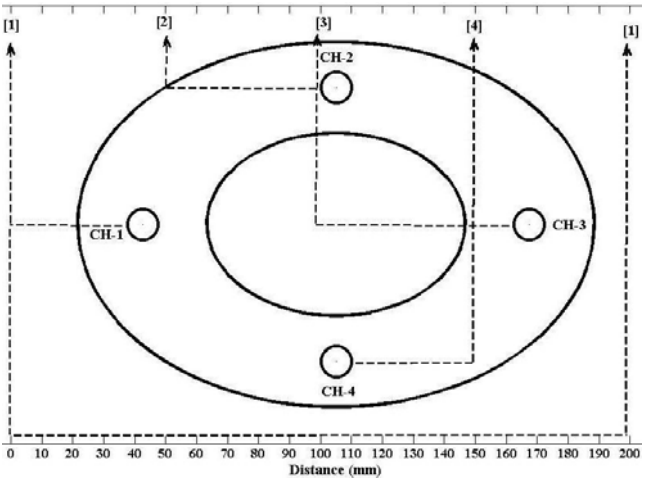

Fig. 2 Sensor arrangement on the flat race showing the circumferential distance between sensors

The AE acquisition system employed commercially available piezoelectric sensors (Physical Acoustic Corporation type 'PICO') with an operating range of 200–750 kHz at temperatures ranging from 265 to 1770C. The AE sensors were connected to a data acquisition system through a preamplifier (40dB gain). The system was set to continuously acquire AE absolute energy (atto-Joules) over a time constant of 10 ms at a sampling rate of 100 Hz. However, AE waveforms were sampled at 2MHz.

The test rig was allowed to operate until vibration levels far exceeded typical operating levels at which point the test was terminated. An axial load of approximately 50000N was applied on the bearing throughout the test and a total of three tests were performed.

Two tests are presented in this paper with quite distinct signal-to-noise ratios; Test 2 was significantly nosier for both vibration and AE measurements. This was attributed to the variation in test rig assembly, such as adjustments and sensor attachments therefore it offered a good opportunity to assess methods for diagnosis. Such challenges with AE sensor attachment and noise interference have been discussed recently (Sikorska and Mba 2008). Figure 3 presents the defect observed on termination of Test-1 clearly displaying a spall on the flat race.

The AE signals for different intervals, as set in Table 1, were chosen for further analysis, see Figure 4. Interestingly, for Test-1 at time period 'F', the AE waveform showed large transient bursts spaced at one of the bearing defect frequencies. This is a classical AE bearing defect phenomenon as noted by several investigators (Elforjani and Mba 2009, Yoshioka, 1992 and Al-Ghamd and Mba 2006). However, for the second test, the underlying noise level obscures any apparent high transient events in the waveform.

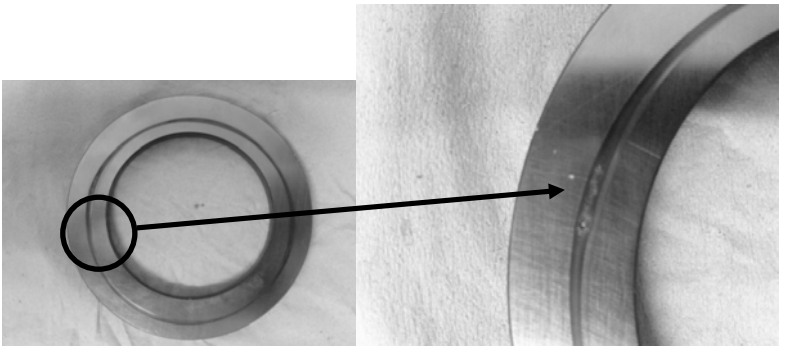

Fig. 3 Defect on the outer race of test-1, (naturally developed over hrs of praion)

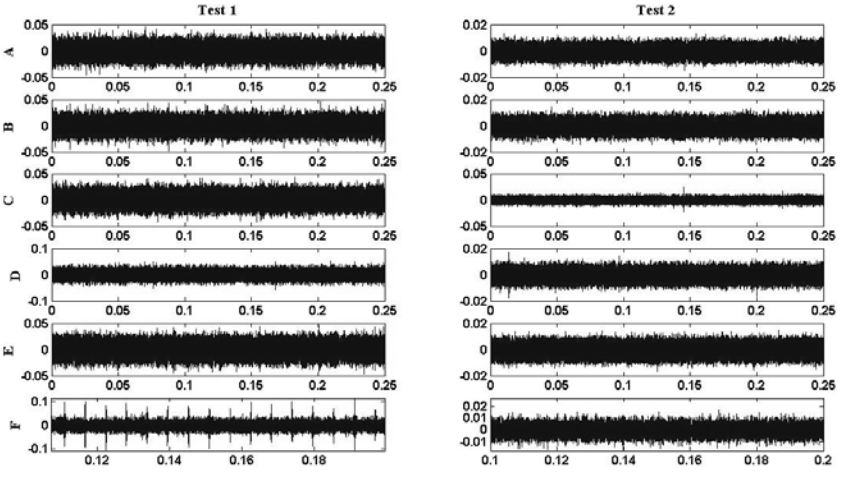

Fig. 4 The AE waveform at different time intervals [X-axis: Time (msec) / Y-axis units: Volts]

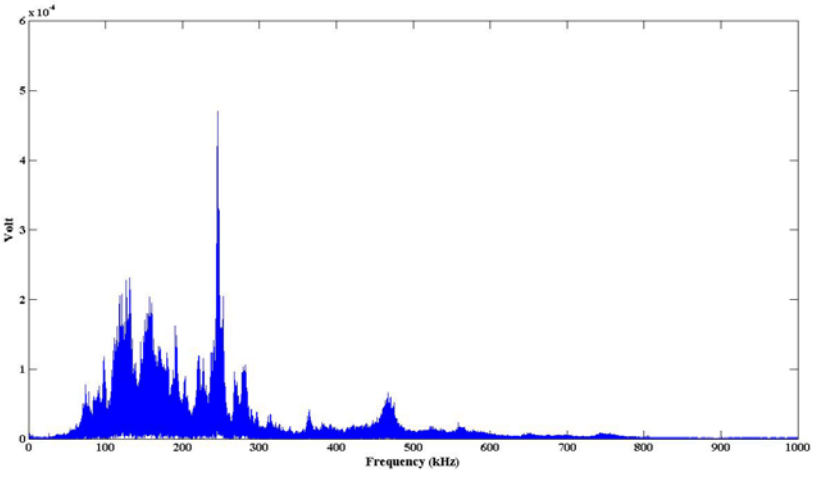

Fig. 5 Frequency spectrum of the AE signal

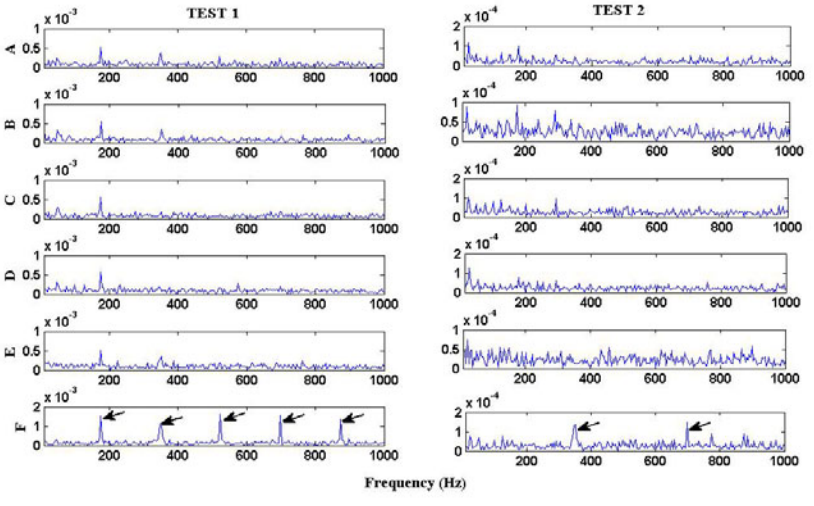

Fig. 6 The AE envelope spectrum for the first and second tests [Y-axis units: Volts]

Table 1 Operational interval at which AE and vibration data was captured

	Test 1	Test 2
A	35 min	42 min
B	70 min	87 min
C	105 min	132 min
D	140 min	174 min
E	175 min	219 min
F	210 min	267 min

The frequency spectrum of recorded AE signals show the AE activity is concentrated between 50- 450 kHz, see Figure 5. In order to identify any modulating features, the envelope spectrum of the signals were generated using the Hilbert transform. The plots of envelope spectrums for both tests are presented in Figure 6. Results from the first test show the presence of the BPF and its harmonics. Surprisingly the presence of the defect frequency 175 Hz, was noted for all the timing intervals (A-F) although the magnitude of the peak increased with time reaching a maximum at the termination of the test . For the second test, the presence of the harmonics noted in the first test were not evident though the second and fourth harmonics were noted at the end of the test, time interval 'F'. The reason for inadequate clarity in discriminating of the harmonics and fault frequency is attributed to the presence of noise and therefore a lower signal-to-noise ratio than Test-1.

As with the vibration analysis, the SK analysis was undertaken for the AE waveforms. Table 2 shows the optimum frequency bands for time intervals 'A' to 'F'. According to the table, the optimum centre frequencies associated with undamaged race (A-E) were outside the sensor measurement range. This is because for the undamaged bearing the higher frequencies within the sensor measurement range are predominantly gaussian so the maximum Kurtosis value occurs at the lower frequency range, below 30 kHz to 40 **kHz.**

Table 2 Optimum Bandwidth and Centre frequency for AE signal

	Test 1		Test 2	
	Fc (Hz)	$\log_2(N_w)$	Fc (Hz)	$\log_2(N_w)$
A	39062	7.5	31250	7
B	31250	7	31250	7.5
C	31250	7	65185	12.5
D	31250	7.5	31250	7.5
E	31250	7.5	15625	8
F	714843	8.5	61523	10.5

The filtered waveforms are presented in Figure 7 showing a significant improvement in level of SNR compared with the unfiltered signals in Figure 4. The AE spikes seen at operational interval 'F' are a direct consequence of the bearing defect. The improvement of SNR is also manifested in Figure 8 in which an average of approximately 242% and 95% increase in Crest Factor (CF) values were noted for the filtered signals on Test-1 and Test-2 respectively. The Crest Factor is a peak-to-average ratio and offers an insight into the relative amplitude of bursts under varying noise levels. Furthermore, Figure 9 illustrates the envelope spectrum of the filtered signals based on SK analysis. The BPF and its second harmonic were present across the frequency spectrum for both tests while such observations were not noted for the unfiltered envelope spectrum in Figure 6.

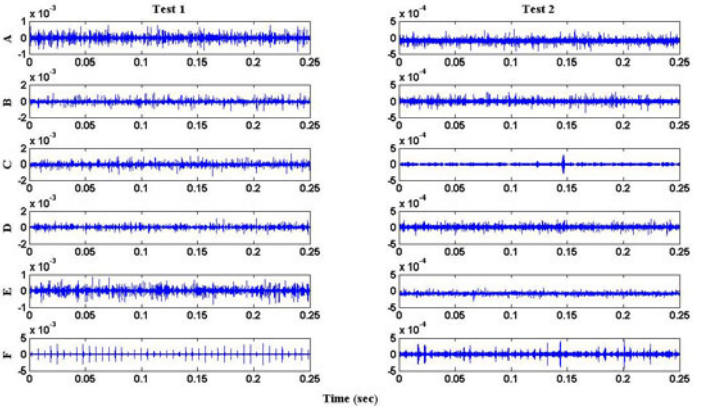

Fig. 7 AE waveforms associated with filtered signals [Y-axis units: Volts]

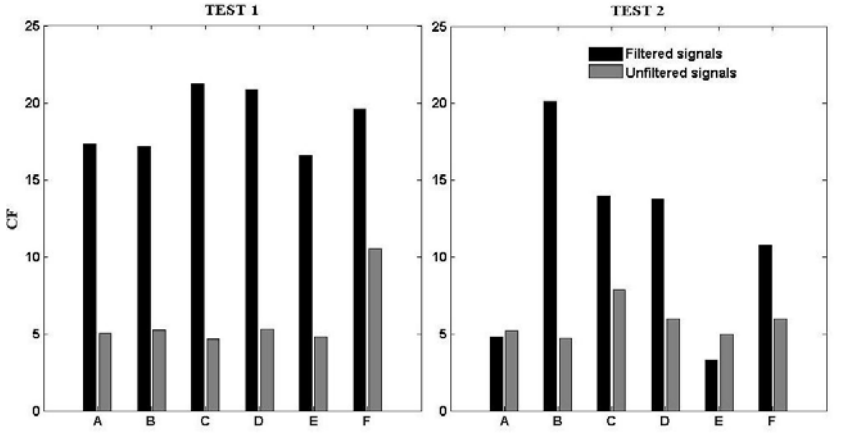

Fig. 8 Crest Factor (CF) values associated with filtered and unfiltered signals

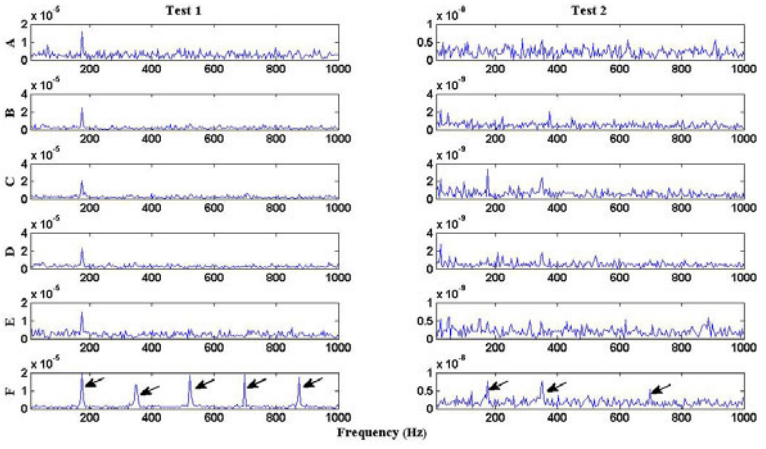

Fig. 9 Envelope spectrum of the SK-based filtered signals [Y-axis units: Volts]

Having noted the improvement in signal-to-noise ratio particularly for Test-2, the authors compared the SK to wavelet-based filter analysis. The AE signals were decomposed using Debauchies wavelet of order 8 (db8). The reason for choosing db8 as a mother wavelet is firstly because of being orthogonal and secondly the shape of it is close to the mechanical impulse. The envelope spectrum at each level of decomposition (D1-9) were carefully studied and level D1 (500 kHz - 1000 kHz) was found to be the most sensitive for identifying the presence of the defect. The envelope spectrums of the signals at D1 are presented in Figure 10 in which BPF and its harmonics are evident upon the termination of both test.

The CF values for the original filtered (SK) and decomposed (db8) signals are presented in Figure 11. In comparison to the original values of CF, the SK filtered signals showed an increase in CF of approximately 242% and 95% for Test-1 and Test-2 respectively. Crest factor values noted for decomposed signals (D1) were in the order of 18% and 70% for Test-1 and Test-2 respectively; implying the SK offered the optimum filtered characteristics for identifying impulsive effects, which are typically associated with defective bearings. The waveforms together with CF values at interval 'F' for D1, the original unfiltered waveform and the filtered waveform (SK) are also presented in Figure 12 in which the presence of impulsive AE events associated with the defective bearing are most evident for the SK filtered signals. There was only one instance where the wavelet based filter had a better CF than the SK filtered data (Test-1, interval 'F'). Although the defect frequency and its harmonics are clearly marked in the envelope spectrum presented in Figure 10, the level of signal to noise ratio for SK based filtering is relatively high. This observation reinforced the benefits of applying the SK for defect diagnosis for varying signal-to-noise ratio.

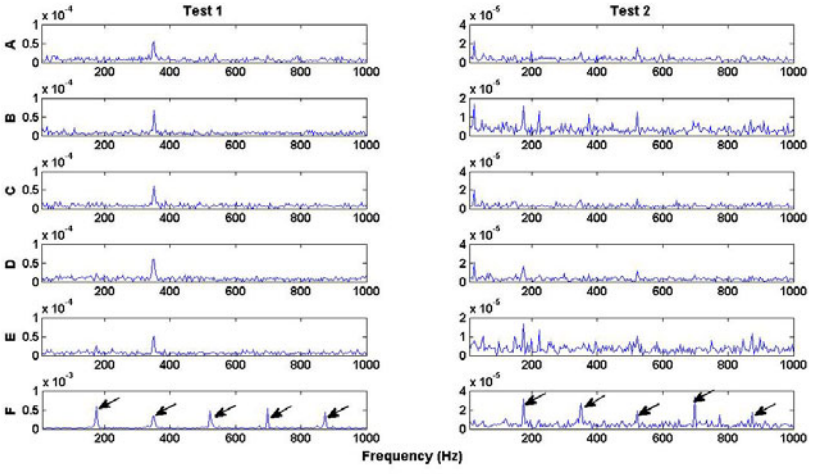

Fig. 10 Envelope spectrum of the AE signals at D1[Y-axis units: Volts]

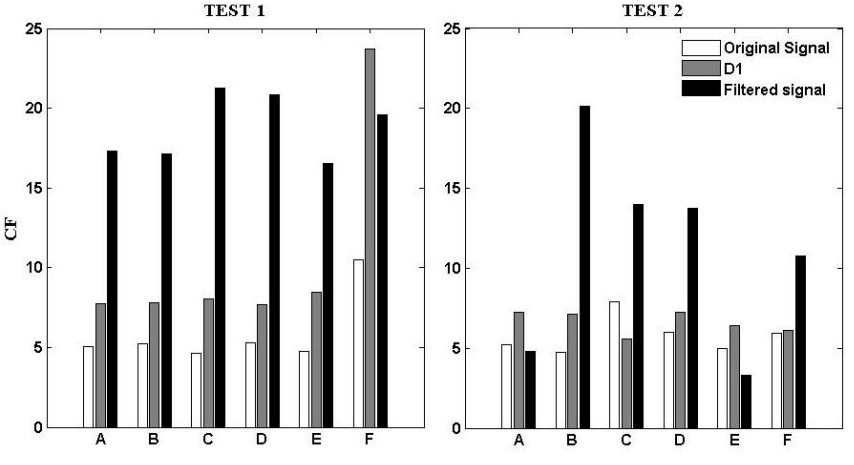

Fig. 11 CF value attributed to different diagnostic methods

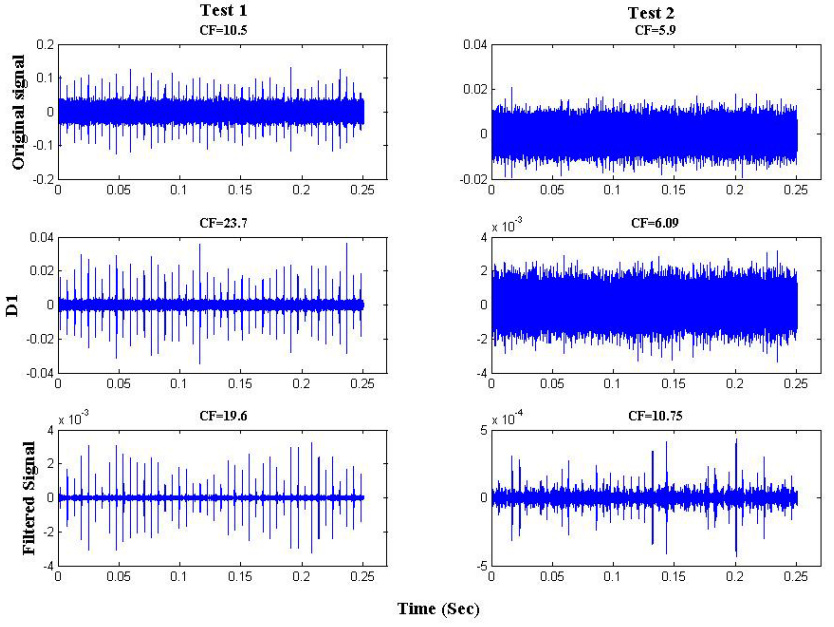

Fig. 12 Comparison between D1 and filtered signals at interval 'F'[Y-axis units: Volts]

4 Conclusion

Condition monitoring of the bearings may demand the application of the advanced signal processing methods to effectively correlate the damage accumulation with AE signals. The spectral kurtosis has demonstrated added advantages, relative to wavelet analysis, in improving the signal-to-noise ratio for AE signatures from defective bearings.

References

Al-Ghamd, A.M., Mba, D.: A Comparative Experimental Study on the use of Acoustic Emission and Vibration Analysis for Bearing Defect Identification and Estimation of Defect Size. Mechanical Systems and Signal Processing 20(7), 1537–1571 (2006)

Antoni, J.: The Spectral Kurtosis: A Useful Tool for Characterising Non-Stationary Signals. Mechanical Systems and Signal Processing 20(2), 282–307 (2006)

Antoni, J.: Fast Computation of the Kurtogram for the Detection of Transient Faults. Mechanical Systems and Signal Processing 21(1), 108–124 (2007)

Antoni, J., Randall, R.B.: The Spectral Kurtosis: Application to the Vibratory Surveillance and Diagnostics of Rotating Machines. Mechanical Systems and Signal Processing 20(2), 308–331 (2006)

Drosjack, M.J., Houser, D.R.: Experimental and Theoretical Study of the Effects of Simulated Pitch Line Pitting on the Vibration of A Geared System. American Society of Mechanical Engineers (Paper) (77-), 11 (1977)

Dwyer, R.F.: A Technique for Improving Detection and Estimation of Signals Contaminated by Under Ice Noise. Journal of the Acoustical Society of America 74(1), 124–130 (1983)

Ebersbach, S., Peng, Z., Kessissoglou, N.J.: The Investigation of the Condition and Faults of a Spur Gearbox using Vibration and Wear Debris Analysis Techniques. Wear 260(1-2), 16–24 (2006)

Elforjani, M., Mba, D.: Assessment of Natural Crack Initiation and its Propagation in Slow Speed Bearings. Nondestructive Testing and Evaluation 24(3), 261 (2009)

Hodges, D., Pearce, J.: Gearbox Condition Monitoring, Gearing and gearbox practice today. Anonymous ImechE (1995)

Jensen, A., La Cour-Harbo, A.: Ripples in mathematics: the discrete wavelet transform, p. 246. Springer, London (2001)

Lebold, M., McClintic, K., Campbell, R.: Review of vibration analysis methods for gearbox diagnostics and prognostics. In: Proceedings of the 54th Meeting of the Society for Machinery Failure Prevention Technology, 634, edn., Virginia Beach (2000)

Mba, D., Rao, R.B.K.N.: Development of Acoustic Emission Technology for Condition Monitoring and Diagnosis of Rotating Machines: Bearings, Pumps, Gearboxes, Engines, and Rotating Structures. Shock and Vibration Digest 38(1), 3–16 (2006)

McNiff, B.P., Musial, W.D., Errichello, R.: Variations in Gear Fatigue Life for Different Wind Turbine Braking Strategies, AWEA Wind Power 90. Anonymous Solar Energy Research Institute (1990)

Mine Safety and Health Administration, Metal/Nonmetal Daily Fatality Report- Year End (2009)

Randall, R.B.: Applications of Spectral Kurtosis in Machine Diagnostics and Prognostics. Key Engineering Materials 293-294, 21–30 (2005)

Rao, B.K.N.: Handbook of condition monitoring, p. 603. Elsevier Advanced Technology, Oxford (1996)

Sikorska, J.Z., Mba, D.: Challenges and Obstacles in the Application of Acoustic Emission to Process Machinery. Proceedings of the Institution of Mechanical Engineers, Part E: Journal of Process Mechanical Engineering 222(1), 1–19 (2008)

Tan, C.K.: An Investigation on the Diagnostic and Prognostic Capabilities of Acoustic Emission on Spur Gearbox. Cranfield University (2005)

Vinall, P.D.: Airworthiness of helicopter. In: Symposion on Helicopter Transmissions. Royal Aeronautical Society (1980)

Whitby, R.D.: Wind Turbine Gearbox Maintenance (2008)

Yesilyurt, I., Gu, F., Ball, A.D.: Gear Tooth Stiffness Reduction Measurement using Modal Analysis and its use in Wear Fault Severity Assessment of Spur Gears. NDT and E International 36(5), 357–372 (2003)

Yoshioka, T.: Application of Acoustic Emission Technique to Detection of Rolling Bearing Failure. J. Soc. Tribologists Lubrication Eng. 49 (1992)

Diagnosing of Rotor Systems of Marine Gas Turbine Engines in Nonstationary States

Andrzej Grządziela

Polish Naval Academy, Śmidowicza str. 69, 81-103 Gdynia, Poland
a.grzadziela@amw.gdynia.pl

Abstract. Vibration tests of marine gas turbine engines are performed as research of on-line and off-line types. On-line Systems generally monitored one or two vibration symptoms, which asses the limited and/or the critical values of parameters and they, potentially, can warn and/or shutdown engines. Off-line Systems are usually used for vibration analysis during non-steady state of work. The paper presents comparison of different methods of analysis of vibration symptoms measured under run-up and shut-down processes of marine gas turbine engines. Results of tests were recorded on gas turbine engine DR76 type of the COGAG type propulsion system. Main goal of the research was qualified on helpfulness and unambiguous result, from synchronous measurement, order tracking and auto tracking. All vibration symptoms were chosen from the methodology of the diagnosing gas turbine engines operated in the Polish Navy, called Base Diagnosing System. Second purpose of the paper was the estimation of the possibility of usage those analysis methods of gas turbine engines for on-line monitoring systems.

Keywords: dynamics, gas turbines, rotor vibration, run–up process.

1 Introduction

Exploitation of marine propulsion systems is a complex issue due to the specific characteristics of the marine environment and the need to maintain a high level of readiness for service and reliability of ships. The use of diagnostic procedures off-line or on-line allows you to use them according to their current condition. This is particularly important in the case of turbine engine, hourly plan and annual plan of technical services is the main usage criteria. This strategy of exploitation makes scheduling maintenance, logistics and security simpler and easier to implement, but also contributes to a significant increase in costs due to the need for replacement of components (often more technically efficient). Furthermore, operating such a exploitation policy makes it impossible for the early detection of other primary causes of faults that occur between appointing terminals.

Diagnostics of gas turbine engines includes a wide range of parameters, controls and maintenance procedures [1]. One of them is the control of unacceptable balance of rotors. Identification of different unbalanced states, determining its

value and the accurate placements of corrective masses is commonly known. Such procedures are carried out on Polish ships for over 20 years. Prepared and used test equipment ensures the implementation of diagnostic tests on four types of turbine engines in service. In the case of naval propulsion diagnostic procedures these are limited for several reasons. The most important of these is the need to maintain a constant readiness to start the engine, associated with the tactical requirements. In addition, due to the fact that the engines are foreign construction, there is a lack of information on the structural parameters of the engine, reducing warranty, no spare parts readily available, etc. The use of vibration diagnostics, makes the use of the engine more rational; from a technical point of view, especially towards vitality of service, which in effect will not withdraw, even a technically efficient ship, from service. Measurements and analysis of vibration parameters of marine gas turbine engines can be divided into:

- off-line (measurements performed in free-run mode, periodically);
- an on-line (real-time monitoring).

Both methods have their advantages and disadvantages. Off-line Systems are usually offered as a very simple analyzers - data collectors. Measurement path is determined in the collector interface, with preset measuring settings, so that the measurement could be performed by an average technical staff, whose main task is a precise procedure. The analysis of measurement results is carried out off the ship, sending the results to the coast laboratory. Currently, there is not many off-line data collectors, who would engage in that precise diagnostic evaluation. The main advantage of such devices is their price. It should be emphasized that the data collectors are useful mainly to assess the go-state of vibrations of turbine engines.

On-line diagnosis of vibrations provides continuous surveillance of the technical condition of gas turbine engines, including registration, analysis, forecasting and alarming. It allows you to recognize the basic signs of changes in the technical condition with the possibility of analyzing the trend of selected symptoms. On-line vibration systems usually work as part of a complex and symptomatic diagnosis of marine propulsion systems. Proper diagnosis of such structures, for example, turbine engine, depends on various issues, including how the measurement and processing of vibration signals was taken. Important in the further analysis is the fact that internal combustion engines in gas turbine propulsion ships do not run at a constant speed with compressor and turbine rotors.

This is the main reason for synchronizing the processing of selected displacements (of the signals) i.e. the rotational frequency of one or both of the engine rotors [2,3]. This method allows you to identify the most common groups of rotor systems, which allows you to identify their failure. Damages to operating gas turbine engines can be categorized as follows:

- damage or crushing of first-stage compressors' blades or power turbine blades (rare);
- the appearance of unbalance, originating from heating or salinity;

- cracks sealing systems and leakage of lubricating oil to the inside of the drum rotor;
- lack of alignment between the gas-dynamic gas generator and power turbine;
- thermal damage to the combustion chambers – torsion of power turbine rotor;
- damage to the auxiliary engine mechanism.

Some failures can be resolved in the recorded spectra as a change in vibration frequency of rotating engine components, hence the introduction of a synchronous sampling of the transient engine operation, eg in the boot process or in the run.

The occurrence of non-stationary effects, typical for residual unbalance may be due to small, incremental damage whose symptoms may be poorly recognized in the early stages of development. The results of the identification of such phenomena is exemplified in the article comparing the various methods of synchronous signal processing method such as PLD or Order Tracking [7]. The presented method for identification of defects can be introduced into the turbine engine monitoring systems as a tool for early identification of unbalance.

2 The Aim and Test Methods

Monitoring of vibration signals from rotating machinery is a well-known diagnostic procedure, known throughout the world [2,5,7]. Most of rotating machinery and marine gas turbine combustion engines are designed as a supercritical machines, hence, in steady states, are diagnostically limited.

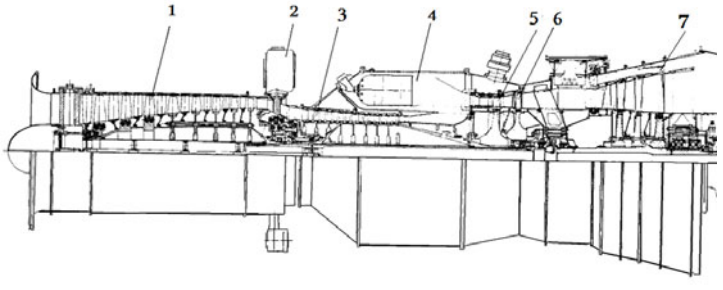

Fig. 1 Longitudinal section of rotor system gas turbine engine DR76 type, where: 1 – low pressure compressor (LPC), 2 – auxiliary drives, 3 – high pressure compressor (HPC), 4 – burning chambers, 5 –high pressure turbine (HPT), 6 – low pressure turbine (LPT), 7 – power turbine (PT)

Therefore it was decided to analyze the dynamics of rotors of gas turbine engines, using a method of off-line measurements of the unknown states It was expected that the results would yield information on the following areas: unbalance of rotors, lack of concentricity of the rotors, changes in their vibration frequency and changes in the speed of rotor system critical.

Marine gas turbine combustion engines mounted on a DR76 type of propulsion system for ships COGAG class Tarantula Polish Navy were studied using this method. Longitudinal cross section of rotor system is shown in Figure 1.

The study included analysis of the vibration parameters during start-up and run of rotors. Comparison of the results of modeling of dynamic loads using FEM (Final Elements Methods) and measurements of on the real object makes it possible to take correct decisions and give the proper diagnosis.

3 Model of the Unbalanced Rotor

Application of computer simulation to diagnose the condition of turbine engine rotors should be used already during the process of calculation and design, which it is currently implemented. The problem begins when the manufacturer does not provide this kind of know-how in the technical specification for the user. Such a situation arises in the case of exported warships equipped with turbine engines. While placing the engine, rotating parts are assembled with great care,. Main objective is to reduce unbalance in rotors. But even the best procedures are not able to prevent factors, such as the inadequacy of heat treatment or the difference of thermal expansion of materials which may cause slight unbalance in rotor, mentioned as residual. Problems in the dynamics of Marine Gas Turbine Engines (MGTE) are associated with the following elements of the engine: rotors, bearings, bearing brackets (bearing struts), engine block, the type of construction, the terms of hydro-meteorological and during sea trials and the aerodynamic parameters inside the engine. Proper and stable work of MGTE engine is mainly connected with these parameters. Loss of energy in rotating machinery is manifested in the form of loss of torque, a decrease in rotor speed, exhaust temperature increase or intensity in vibrations. Vibration energy dissipation is related to: unbalancing of rotors, oversize tolerated shaft misalignment, abrade of blade tips with the inner roller, wear of axis and radial bearings, asymmetry of elasticity and damping asymmetry of the rotor and the gas-dynamic processes anomaly. Emission of vibration yields a lot of information, including the ability to diagnose the technical condition of rotors. Vibration measurement, identification, classification, mathematical analysis, including the use of trend function, give information on the actual technical state and allow the prediction of the wear process in the future.

In the identification an important factor is to compare the results of modeling with the results of the measurements. Each rigid body has six degrees of freedom, whereas the deformable objects have an unlimited number of degrees of freedom. Rotating machinery such as MGTE have a number of degrees of freedom equal to the sum of all degrees of free parts of the engine, minus the number of rigid nodes connecting these elements. Each part of the engine can be described by physical characteristics such as stiffness and damping, obtained from vibration measurements the actual object or model or the modeling of the geometry and properties of materials (the use of rigidly connected structures). The use of a certain type of rigid object model allows the use of the motion ordinary differential equations. Deformable objects require the use of partial differential equations. This second assumption is much more complicated, but can help to achieve to the actual

object, especially when it's in a wide range of engine speeds. This was the reason for the choice of the second type of model turbine engine. Diagram of diagnosis using the MGTE model shown in Figure 2.

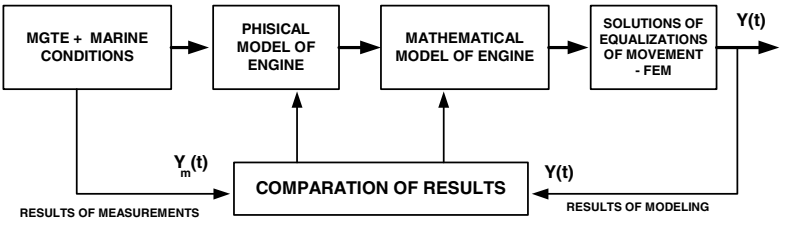

Fig. 2 Scheme of diagnostics model MGTE

Residual unbalance may appear in all sections of the rotor, however, two vectors of unbalance, at both ends of the shaft, may represent the replacement model. These vectors vary in values and phase shifts. Such an FE model allows for dynamic response to unbalance which in effect allows you to compare modeling results with the reports of vibration measurement. The most sensitive point in the unbalance of GT rotor, with respect to vibrations, is the measuring point on the front of the generator exhaust bracket bearing the vertical direction. This is the effect of the minimum thermal expansion of the rigid support used for measurement of radial vibrations at this point. The model is linear so it is clear that response is directly proportional to the value of unbalance The rotor is loaded dynamically and statically from various sources [4]. Identification of the sources and their calculations of the loads were a major problem during the modeling and evaluation of the actual object's vibration. Damage in the objects such as blades, have an impact on changes in the moments of inertia of rotating parts. This results in a shift of the main axis of inertia, which is not parallel to the axis of rotation. It is the main source of unbalance in the form of vibrations of rotor. Implementation of the mathematical model is difficult, mainly due to the problems of determining the stiffness and damping of supports and bearings at different temperatures - Figure 3.

Shape of the axis deflection is defined as discrete sets:

- Set of static deflections – u_s;
- Set of dynamic deflections – u_d.

Both sets depend on actual technical state of rotor and geometry, which can change through cracks and wanes of engine parts.

$$\mathbf{u}(\omega t) = \mathbf{u}_s + \mathbf{u}_d(\omega t) \tag{1}$$

1. This equation is a discrete set of points of axis movement of the rotor. Taking into account the damping and stiffness of the support bearings, we can demand that they are functions of temporary positions, namely:

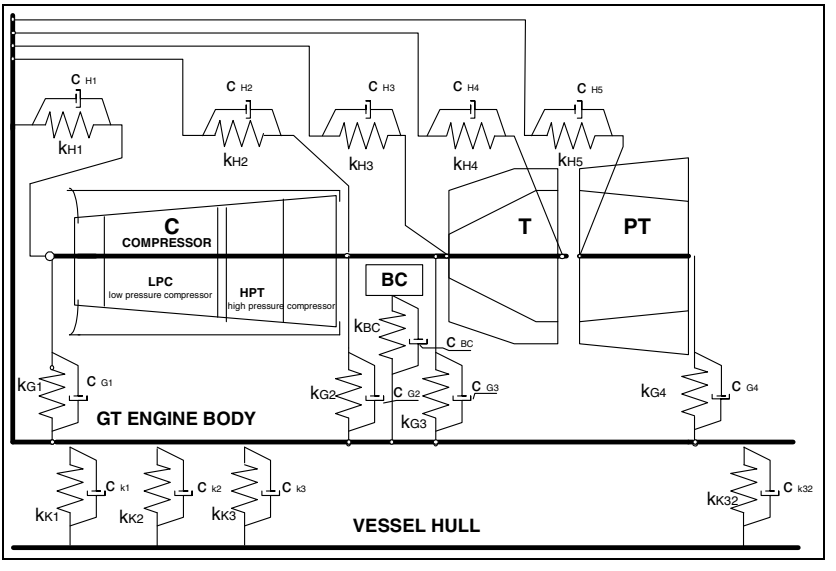

Fig. 3 Axi – symmetric lumped mass inertia model of the MGTE, where: LPC – low pressure compressor, HPT – high pressure compressor, T – turbines (low & high pressure), PT – power turbine, BC – burning chambers, k – stiffness, c – dumping.

$$k_{ik} = f(u) \qquad c_{ik} = f(u) \tag{2}$$

For the simplification it is assumed that, for a constant speed, these values are constant. Using FEM modeling can provide a three-dimensional discrete model. Rotors MGTE, in the circular symmetry, have been described by one-dimensional, two-beam bar having a symmetrical six degrees of freedom. All parts of the model have geometric and physical properties of the elements. Discrete model of traffic parameters have been obtained by solving the equation:

$$\mathbf{Ku} + \mathbf{C\dot{u}} + \mathbf{M\ddot{u}} = \mathbf{F}(t) \tag{3}$$

where: $\mathbf{K}$ – matrix of structure's stiffness
$\mathbf{C}$ – matrix of structure's damping
$\mathbf{M}$ – matrix of structure's inertia
$\mathbf{F}$ – vector of forces
$\mathbf{u}, \dot{\mathbf{u}}, \ddot{\mathbf{u}}$ – displacement and their derivatives (velocity and acceleration)

This can be solved as a linear problem, but in MGTE rotor must allow for changes in stiffness and damping, which are functions of motion parameters. In this case equation (3) should be expressed as:

$$\mathbf{K}(\mathbf{u}, \dot{\mathbf{u}})\mathbf{u} + \mathbf{C}(\mathbf{u}, \dot{\mathbf{u}})\dot{\mathbf{u}} + \mathbf{M\ddot{u}} = \mathbf{F}(t) \tag{4}$$

Equation (4) indicates that the rotor motion should be described as a nonlinear dynamic problem, and therefore should expect more than one harmonic in both measured and modeled spectrum. [8]

4 Non – Steady States Vibration Signals Analysis

To obtain the measurements of the real object Bruel & Kjaer 3560B analyzer was used. Namely, it was used during the collection and processing of measurement data using the PULSE(v.12). Two transducers (accelerometers ICP) have been fitted to the steel girders, situated on the flanges, on the front and on central pillar of the LPC. The fixing cantilevers are characterized by vibration resonance frequency value differing from harmonic frequencies due to rotation speed of the given rotors. Measurements were made perpendicular to the axis of rotation of the rotor. Such a choice was made on the basis of theoretical analysis of unbalance and as a result of analysis of the results of preliminary research on the subject.

Common assessment of the unbalance of rotors was developed through the concept of dimensionless coefficients of diagnosis. Using theoretical analysis of dynamic interactions, as well as using the results of initial diagnostic tests, the following symptoms were selected as the most sensitive to changes in balancing rotors [2]:

- First harmonic of amplitude of the corresponding velocity of the rotor,
- Second harmonic of amplitude of the corresponding velocity of the rotor,
- S 1 - the ratio of the average amplitude of vibration corresponding rotor speed (and harmonic) and the second harmonic of the corresponding rotor,
- S 2 ratio of the average amplitude of vibration corresponding rotor speed (and harmonics) corresponding and the third harmonic of the rotor.

These symptoms can confirm the theoretical assumption of nonlinear rotor dynamics.

5 Vibration Analysis of the Run-Up Process

The first test was to analyze the process of starting the engine. The characteristic changes in LPC rotor speed is shown in Figure 4. Synchronous signal measured by a tachometer connected with the auxiliary drive gear box where the transmission ratio averaged on i=0,125, so the LPC rotor was 8 times greater (in speed) than that shown in Figure 4 The main objective of the analysis of synchronous oscillations in the boot process was to determine the dynamics of the disorder. The impact of "other" signals is shown in Figure 5.

The boot process started at the point t = 7 seconds (see Figure 5), so all recorded vibration signals recorded from the start point contained the signals coming from other sources, i.e. non-rotating motor or frequency of its vibrations or a combination thereof. This allows to identify the main "other" signals, such as: f_1 = 305

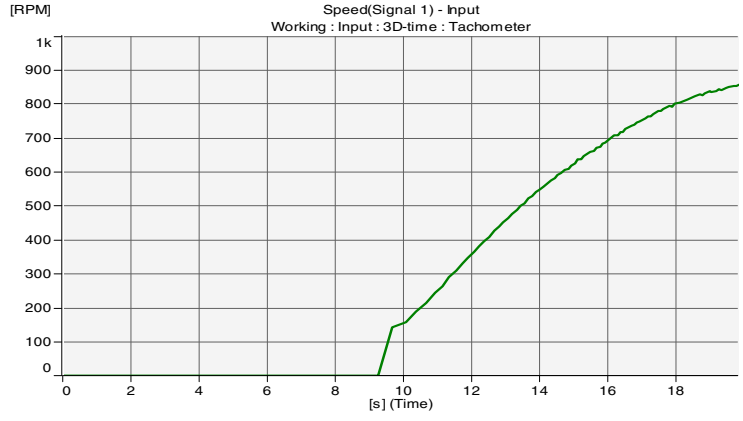

Fig. 4 Rotors LPC rotational speed characteristics during run-up process

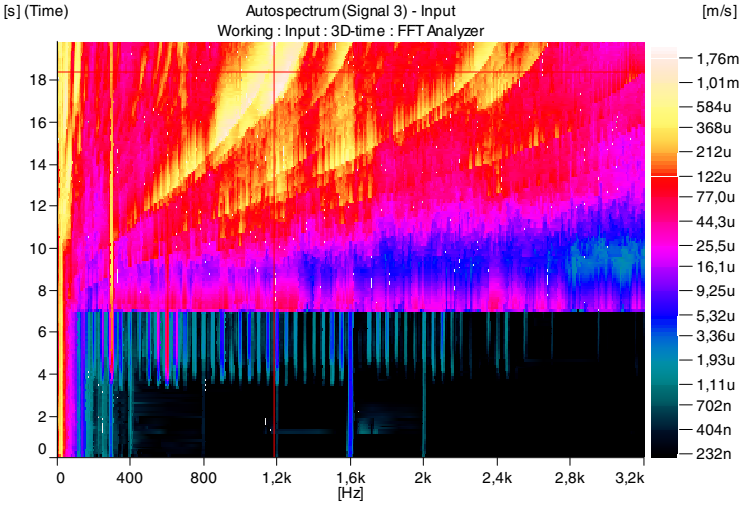

Fig. 5 Synchronous spectra of the velocity of vibration during run-up process with using the band – pass filter of 0,1Hz – 3,2 kHz range

Hz, f_2 = 600 Hz, f_3 = 1.6 kHz, and f_4 = 2 kHz. which are associated with sources outside the engine. The highest signal during the boot process is the rotor speed and harmonic vibrations, but in Figure 5 it is not clearly visible due to the lack of a synchronous signal tracking.

6 Vibration Analysis of the Shut-Down Process

Next test was associated with the analysis of vibration parameters and related to the process runs the motor rotor. Figure 6 shows autospectrum of the velocity measured over the middle LPC bearing using the order tracking procedure. Changes of parameters are presented in the domain of time function, in contrast to the boot process ,where the dominant energy range of vibration signal was 1/2 harmonic - seen as a 4th order. The pressure drop of the lubricating oil in the bearing caused an increase in values ranging from displacement and slope between the HPC and LPC rotor (rotating shafts each other, while the shaft rotates within the LPC HPC shaft - see Figure 1) and the typical dominance of the subharmonics .

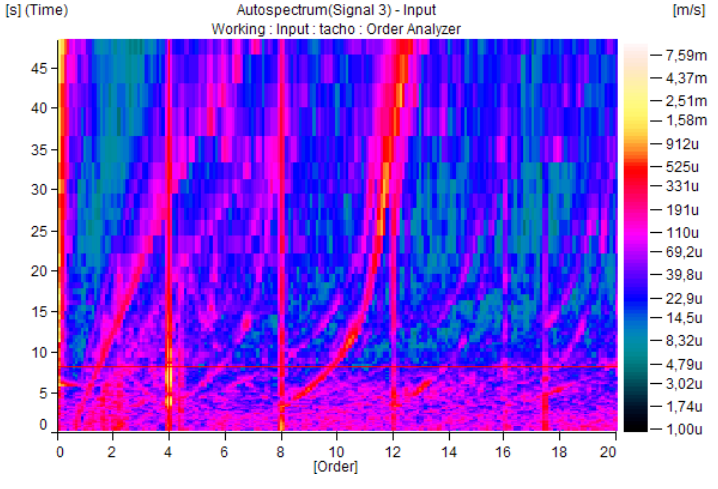

Fig. 6 Autospectrum of velocity of vibration in the shut-down process with the use of order tracking procedure, in the domain of time function

The increase in stiffness of the bearing system confirms the existence of the harmonic “right-hand branches” at the point where t (time) is equal to 4 seconds for the following rows: 4, 8 and 12, which is associated with a pressure drop of lubricating oil in the bearings.

Analysis of the dynamics of the turbine engine rotor in transient states of a system PULSE should be applied in both processes, ie start-up and run. The start-up process helpsto recognize the "other" signals, but the definition of dynamic functions is very difficult due to the significant acceleration of the rotors. Identifying characteristics of rotor system dynamics is much more recognizable in the process runs through the analysis of orders - Figure 7 and 8.

Analysis of the first harmonic (8th order) allows to observe changes in dynamics as trends. Application of the rotational speed function as a field of analysis is the most important factor in the study of the use of the Order Tracking procedure. This allows you to detect changes in the natural frequency, ignoring interference from the signals originating from the thermodynamics processes of turbine engines.

Subharmonics signal analysis is very useful in the diagnosis of rotating machinery. Autospectrum of 1 / 2 subharmonic's velocity range (considered in the LPC rotor) indicates the individual characteristics of particular rotors. The nature of changes in order values in the rotor speed can be thought of as an individual fingerprint of each rotor.

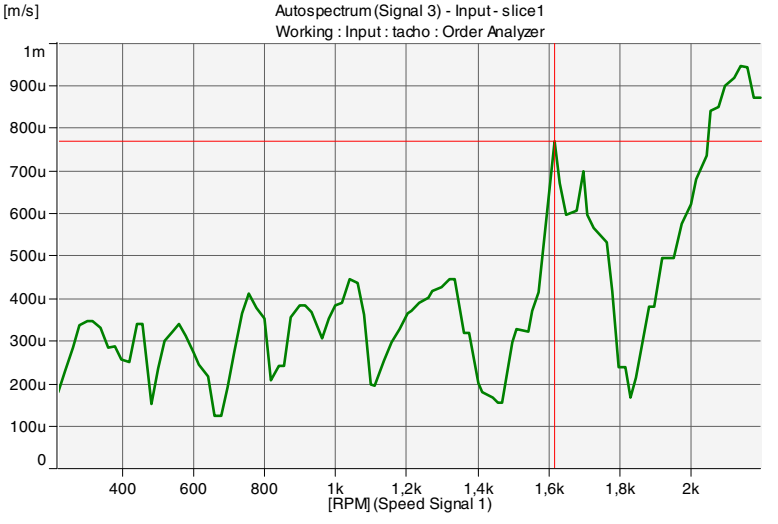

Fig. 7 Autospectrum of 8 order (I harmonic) of velocity of vibration in the shut-down process of LPC rotor stoppage.

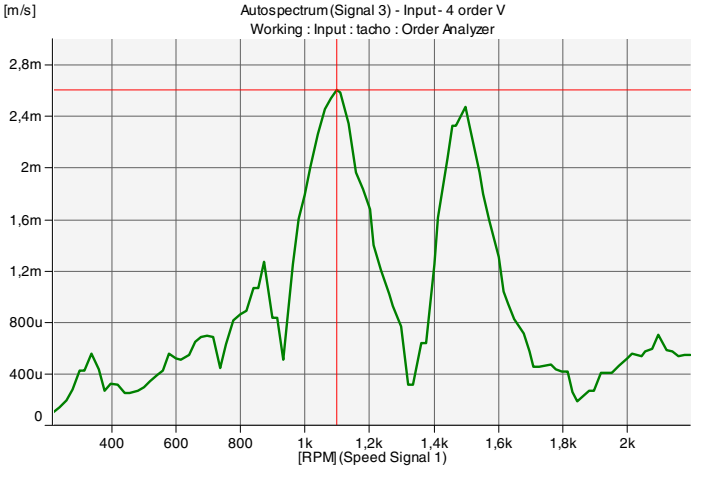

Fig. 8 Autospectrum of 4 order (subharmonic) of velocity of vibration in the shut-down process of LPC rotor stoppage.

All changes to the technical condition of rotor system, such as changes in stiffness and damping parameters of alignment, or unbalance result in changes in characteristics of subharmonics - Figures 7 and 8.

7 Conclusions

All statistical analysis performed on the available population of engines clearly show that the selected parameters analyzed in the non-stationary processes are the basis for predicting changes in the technical condition of rotor system. Implementation of this research turns out to be a credible verification of the technology. Conclusions presented below have been incorporated into operational diagnostics of marine gas turbine engines:

- Synchronous measurement of vibration signals during the boot and run processes enables us to recognize symptoms of damage, including the formation of resonance and changes in natural frequencies and unbalanced rotors
- symptoms of S1 and S2 do not have sufficient sensitivity for use in transient states due to the instability of the processes and the need for averaging the results,
- application of auto tracking and monitoring the turbine engine rotor systems can identify a wide range of typical damages, confirmed by the vibro-acoustic diagnostics.

Application of the proposed methods of analysis allows for the rational management of engine life time even in the developed processes of consumption. The analysis of test results obtained gives the following conclusions:

- the approach to the assess the technical condition of gas turbine engines rotor system allows to quickly detect changes in the permitted unbalance and the maintained database enables easier identification of the studied group of engines
- studies on trends in chosen parameters make it possible to reliably detect changes in the value of sensitive operational parameters during the operation of the engine and to evaluate its capabilities.

References

Journal Article

Charchalis, A., Grzadziela, A.: Diagnosing of naval gas turbine rotors with the use of vibroacoustic parameters. In: The 2001 International Congress and Exhibition on Noise Control Engineering, The Hague, The Netherands, p. 268 (2001)

Downham, E., Woods, R.: The rationale of monitoring vibration on rotating machinery. ASME Vibration Conference, Paper 71 - Vib - 96 (September 8 - 10, 1971)

Grządziela, A.: Vibroacoustic method of shafting coaxiality assessment of COGAG propulsion system of a vessel. Polish Maritime Researches (3), 29–30 (1999)

Grządziela, A.: Diagnosing of naval gas turbine rotors with the use of vibroacoustics parameters. Polish Maritime Researches (3), 14–17 (2000)

Book

Krzyworzeka, P., Adamczyk, J., Cioch, W., Jamro, E.: Monitoring of nonstationary states in rotation machinery. Biblioteka Problemów Eksploatacji, Wydawnictwo ITeE, Radom (2007)

Pedersen, T.F., Gade, S., Harlufsen, H., Konstantin-Hansen, H.: Order tracking in Vibroacoustic Measurements: A Novel Approach Eliminating the Tacho Probe. Technical Review (1) 15–28 (2006)

Rządkowski, R.: Dynamics of steam and gas turbines. IFFM Publishers, Gdańsk (2009)

Robust Fragmentation of Vibration Signals for Comparative Analysis in Signal Validation

Adam Jablonski and Tomasz Barszcz

AGH University of Science and Technology, 30-059 Krakow, Poland
ajab@agh.edu.pl, tbarszcz@agh.edu.pl

Abstract. The paper illustrates selected aspects of robust vibration signal fragmentation. Such fragmentation enables a comparison of vibration signal fragments, which gives additional information about a signal to its frequency contents. In particular, the paper illustrates how signal fragmentation followed by fragments' comparison may serve as an additional tool in data preprocessing, namely continuous selection of most suitable vibration data and rejection data with prohibited level of vibration level fluctuation. Presented techniques are especially applicable as a part of condition monitoring of machinery in non-stationary operational conditions.

Keywords: automatic signal validation, vibration signal fragmentation.

1 Introduction

In a typical vibration-based condition monitoring system, machine vibrations and paralelly acquired process parameters are sources of signals. These signals via data acquisition system enter various data analysis procedures. Currently applied procedures cover fundamental broadband analysis [1,2] as well as advanced modern techniques, which take advantage of *a priori* known machine characteristic components [3,4]. Next, methods' outputs give diagnostic information either in a scalar, vector or graphical form. On the basis of these information, possibly with the aid of predetermined values, e.g. norms [5,6], a maintenance decision is constructed. Such decisions are either executed automatically (i.e. automatic shutdown) or manually via human reasoning [7].

A simplified scheme of a machine monitoring system is illustrated in fig. 1. Within such common scheme, the data acquisition block may be considered as a subsystem consisting of equipment (sensors, cables, and data acquisition units, so-called DAQs), equipment installation quality (system connection, shielding, grounding, and hardware configuration), states definition, and finally configuration of data storage. The latter step, namely the issue of data storage procedures, is a general scope of this paper.

In last decade, the authors have extensively participated in designing and running systems of monitoring and diagnosis installed on various machinery,

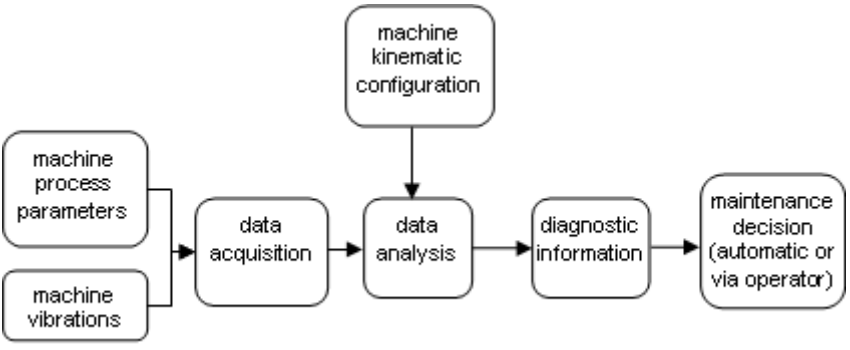

Fig. 1 Scheme of typical machine vibration-based diagnostics

including heavy duty machinery, which is generally characterized by a large size and strongly fluctuating operational parameters [8]. As it turned out, monitoring systems installed on such machinery are additionally prone to data acquisition errors due to electrical and electromagnetic disturbances, relatively short equipment duration, and even sabotage actions.

Therefore, implementation of standard systems of monitoring and diagnosis frequently failed causing large investments to become ineffective. After months of research, it turned out that one of major reasons for the lack of capability of fault detection were standard (so called fixed) data storage procedures. Basically, such procedures cause vibration data to be acquired in predefined, fixed time intervals, for instance one sample every 10 minutes. Such policy caused an extremely large number of stored samples to correspond to either highly fluctuating operational conditions or to data experiencing electrical disturbances.

In order to overcome these obstacles, authors have redesigned the data storage procedure, as illustrated in fig. 2.

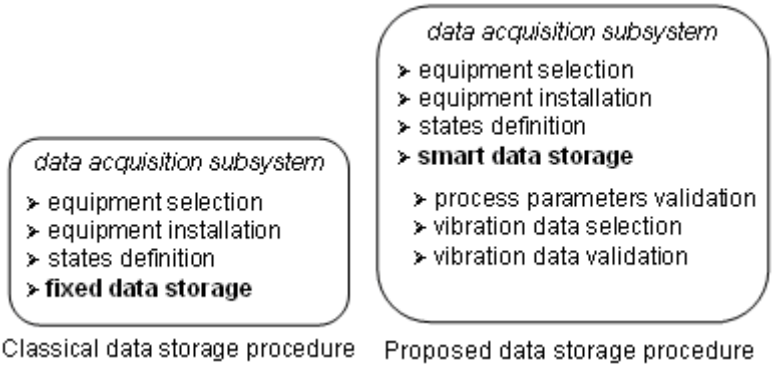

Fig. 2 Comparison of classical and proposed data storage procedure

In a proposed procedure, fixed data storage is replaced by three consecutive steps, namely validation of process parameters, selection of vibration data, and finally validation of vibration data. Current paper presents a selected fragment of vibration data validation module, namely signal validation via its comparative analysis.

2 Signal Correctness vs. Signal Validation

Reference [9] presents a number of methods for automatic detection of incorrectly recorded vibration signals. However, it is additionally preferable to reject some vibration signals, which do represent a machine's physical behavior correctly, yet they are unsuitable for data analysis due to unacceptable level of contents' change. In addition to defining signal as "correct" upon accurate description of vibrations, a signal may be defined as "valid" when it carries significant diagnostic information. In this sense, not every correct signal is valid.

For instance, noise recorded upon machine standstill is a perfectly correct signal, yet it brings no information about machine's technical state whatsoever. Likewise, sudden change of machine load consequent in one order of magnitude vibration level change restricts permissible data analysis techniques to ones tracking signal fragments, e.g. STFT (Short-Time Fourier Transform). Since these types of virtually image-oriented methods do not constitute mainstream analyses in distributed monitoring systems, signals with significant fluctuation of contents characteristics may be considered as unsuitable (referred to as "invalid") for frequency-domain analyses. It is important to emphasize that condition monitoring systems implemented on large installations are generally required to operate on scalar thresholds due to large number of independent data sets.

Therefore, most of data analysis algorithms produce time series of trend values, which are naturally calculated mostly in the frequency domain. Consequently, it is desirable to provide as stable signals as possible for frequency domain calculations.

3 Comparative Signal Validation Method

Taking into account stability constrains, after application of state definitions and stability limits to corresponding process data, further validity assessment of vibration signals might be also realized relatively via comparison of particular signal's consecutive fragments against each other and detection of prohibited level of alteration. Another words, change of operational parameters is not the only source of significant changes in vibration levels, and it is beneficial for a monitoring system to apply additional algorithms for detection of fluctuation of vibration data contents.

The key idea is that rotating machinery produces cyclostationary signals characterized by existence of at least one finite cycle with respect to which the machinery operation is periodic [10]. Fig. 3.a illustrates a vibration signal frequently encountered in heavy duty machinery, where such requirement is violated.

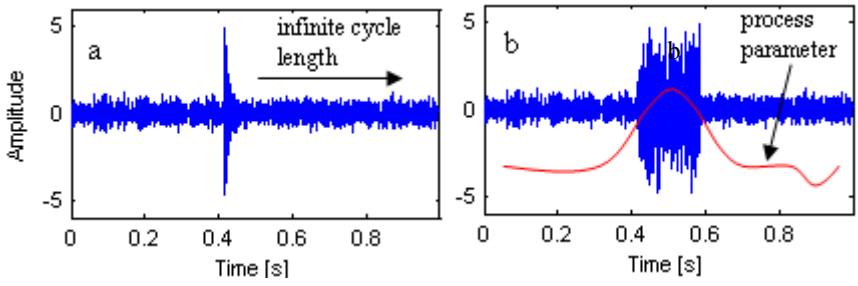

Fig. 3 Example of a non-stationary vibration signals violating fundamental assumptions of cyclostationarity

Since the visible impulse response in fig. 3.a may not be described by any finite cycle (although it may be a perfectly correct record), the signal is not suitable for general condition monitoring, scalar-oriented frequency analysis, and may be considered as invalid.

Although it is a common phenomenon to include some fragmented cycles within a vibration signal (for instance the least drive train common cycle in wind turbines with planetary gearboxes, which is to be measured in hours), these signals should be rejected if they significantly affect trend analyses, like for instance peak-to-peak value in case of signal illustrated in fig. 3.a.

It is important to notice that the issue of detection of such signals is different from impulse response (or transient signals) detection described in numerous autocorrelation-based works like [11,12] because significant signal change may be caused by rapid changes of operational parameters as well, as illustrated in fig. 3.b.

As it was mentioned, such invalid signals may be detected using simple comparison methods of signal fragments, as illustrated in fig. 4. Selected intervals of significantly different characteristics are marked with letters a, b, c, and d.

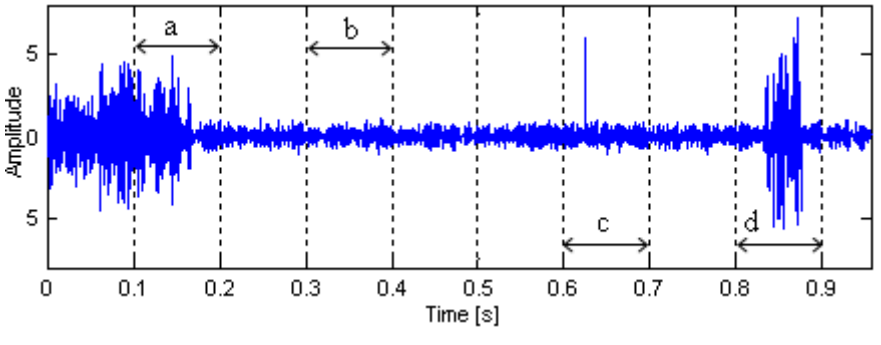

Fig. 4 Illustration of signal fragments' comparison

In the proposed approach, the comparison has two aspects: selection of signal fragments' length and selection of indicator to be compared. In case of the latter aspect, it is a natural choice to select a peak-to-peak[1] (PP) value as the indicator, because threshold value may be set intuitively on the basis of historical data with high accuracy.

Table 1 Selected methods of signal fragmentation

Method's Kernel	Main Advantages	Main Disadvantages
Fixed time	Easy programmable	Relatively low probability of success in drive trains with large transmission ratios
Fixed No. of fragments	Easy programmable	Provides relatively large fragments for long data and relatively short fragments for short data, which may significantly influence statistical operations
Cube root (time)	Suitable for number of statistics formulas; unparametrized	Typically, provides non-integer fragment lengths, which may be indistinguishable for signal of similar length
Lowest expected cyclic frequency	Handles widest scope of cyclic frequencies correctly	May require additional minimum number of signal fragments as well as additional programming effort; function of speed

Selection of fragments' length might be chosen in various ways, namely: signal division according to time, number of fragments, lowest expected characteristic frequency, root-based, and others. Table 1. illustrates main advantages and disadvantages of abovementioned methods. All four proposed methods are discussed below in consecutive order.

Time-based signal fragment is probably the easiest one to be realized. A given signal is divided according to a fixed time interval, e.g. 1 second. Next, from all fragments an indicator value is calculated and checked against threshold. This method is not suitable for large transmission ratios because characteristic frequencies are function of speed; therefore, actual time of desired, fault-generated signal components vary significantly and may be misinterpreted as undesired signal changes. Moreover, this approach may yield unexpected results when applied to data with relatively large difference in signals' duration. For instance, a 2-second signal would be assessed according to two indicator values; whereas 100-second signal would be assessed according to a statistical comparison from a set of hundred values.

[1] In case of vibration acceleration signal, a zero-peak (ZP) indicator might be accepted due to expected symmetry of a signal around mean zero value.

An extension to fragmentation is provided when exploring signals with fixed number of fragments. In this case, the length of fragment is a linear function of signal's length, therefore, it is again straightforward in implementation. Since fixed number of fragments delivers different fragments' length, this approach may be vulnerable to time-independent random signal deteriorations, e.g. falling rocks on mining conveyors. Another words, a comparison may be applied to fragments with different lengths subjected to a detrimental phenomenon with a constant probability.

Any of these two methods requires a priori parameter to be accepted, either a length or No. of intervals, which is sometimes inconvenient. Another approach to signal division is to use an unparametrized signal fragmentation, for instance a cube-root length of entire signal. Since this approach fits well to analysis of random time series, it enables additional statistical description. A major drawback of this approach is that a cube root produces insignificant values for inputs close to unity. Moreover, due to necessary rounding process (indexing), the same fragment length may be assigned to signals with slightly different lengths, which may cause some confusion.

Final, most advanced approach from methods listed in table 1. takes into account minimum expected frequency of signal contents, i.e. minimum characteristic frequency associated with machine's region covered by a particular sensor. An example of this approach is illustrated in fig. 5. This method requires significantly larger implementation effort (for instance adaptation to machine configuration change); however, it is not as error-prone as previous ones.

One of main disadvantages of this solutions is the fact that a reference maximum cycle length is a function of machine speed, so preferably this method requires recalculation of fragments' length for every signal.

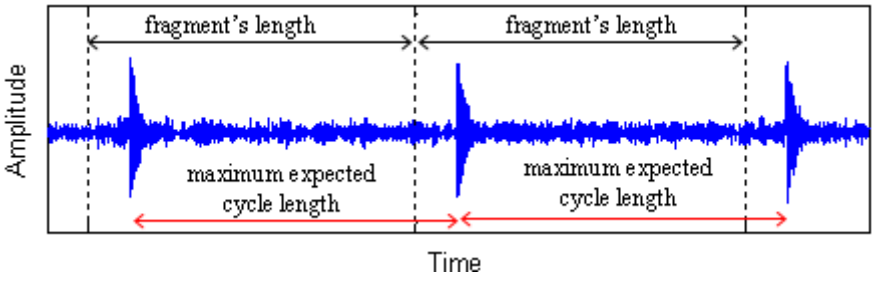

Fig. 5 Conditional signal fragmentation

For signals with equal number of samples per revolution (e.g. resampled signals), the length is to be calculated using a known ratio of the lowest characteristic frequency to the reference signal. For instance, if resampled signal has got 2000 samples per revolution, and the characteristic frequency is 0.05, fragments' length is to be set to 100 samples.

On the other hand, if a raw signal is to be analyzed, the length of each fragment needs to be calculated with respect to slowest machine cycle. This in turn may require recalculation of fragments' lengths for each sensor separately because generally vibration contents strongly depends on sensors' localization. This technique may be simplified for machines with clearly distinguishable machine speed levels. Having knowledge about nominal speed levels, these lengths may be calculated a priori as a function of detected machine state.

Final remark concerning application of proposed methods of signal assessment concerns realization of comparison. In any applied kernel, it is important to compare a fragment with a minimum indicator value vs. a fragment with a maximum indicator value rather than to compare consecutive fragments because significant signal change may be covered within a particular interval, as illustrated in fig. 4 (fragment a).

4 Case Study

Following section illustrates performance of presented methods of comparative analysis on the example of a real vibration signals recorded from a wind turbine experiencing faults within condition monitoring system installation. Fig. 6 illustrates a selected non-stationary vibration time signal.

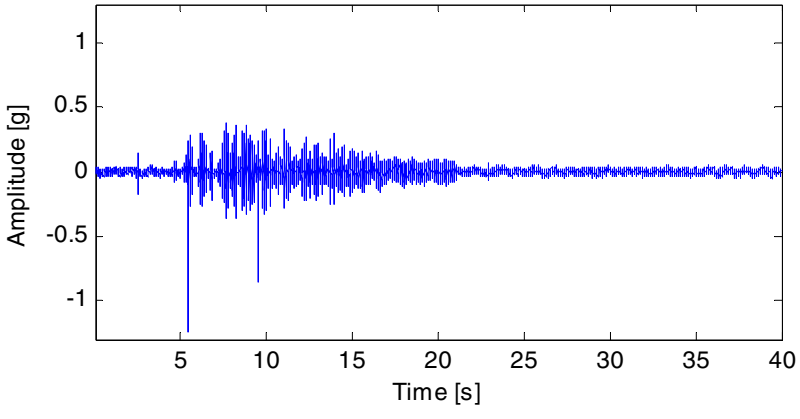

Fig. 6 Exemplary vibration time signal from a wind turbine

From fig. 6 it might be implied that unexpected results might be obtained when standard condition monitoring signal processing tools (dedicated to analysis of stationary signals) are to be applied to this signal.

However, before processing the data with comparative analysis, it is necessary to reject the possibility of variation of process parameters as a cause of signal non-stationarity.

Another words, before testing for signal invalidity, it is advisable to eliminate signal incorrectness. Fig. 7 illustrates a plot of instantaneous speed of the wind turbine recorded with a resolution of one impulse per rotation cycle sampled at signal sampling rate (24 kHz).

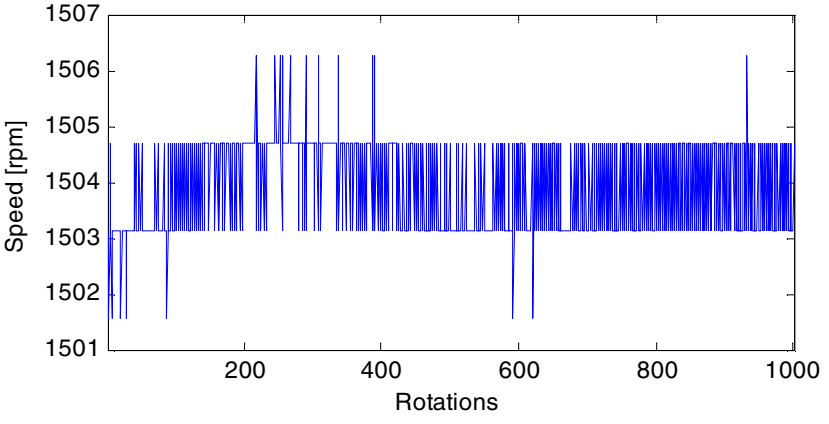

Fig. 7 Instantaneous speed corresponding to signal illustrated in fig. 6

Fig. 7 implies that during one thousand rotations of wind turbine's generator shaft, the wind turbine's speed was practically constant (apparent fluctuations are close to the accuracy of the measuring equipment, so they might be neglected). Therefore, according to the proposed method, the signal needs to be investigated in terms of signal's consecutive fragments. The goal of the study is to detect prohibited level of alteration.

As suggested in section 3, a simple choice of the PP (or ZP) indicator might be applied. Fig. 8 illustrates a comparative analysis of a 40-s signal illustrated in fig. 6.

The horizontal axis shows selected length for fragmentation, i.e. the signal fragmentation was investigated for fragments from length equal to 1[2] second to 20 seconds. Vertical axis shows a ratio of maximum ZP value to the minimum ZP value detected within the set of fragments for a given fragment's length.

From fig. 8 it is concluded that signal fragmentation into 1-second segments gives slightly better result than for larger segments; however, this advantage is at the cost of method vulnerability to any characteristic frequencies lower than 1 Hz possibly present in a signal. On the other hand, as implied by the figure, for this case study, selection of intervals from 2 seconds to 9 seconds produces practically

[2] Generally, rotating machinery vibration signals from industry are expected to have significant contents over 1 Hz, which includes possible cyclostationary components. Therefore, the authors find it impractical to fragment relatively long record into relatively short segments.

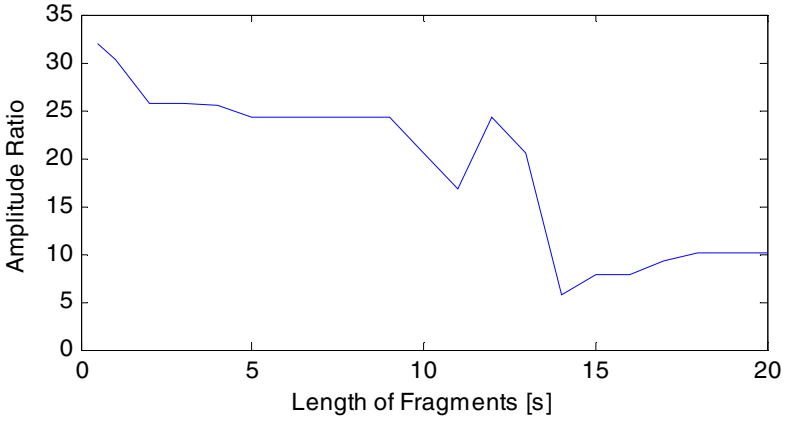

Fig. 8 Influence of selection of fragment's length to the result of comparative analysis

the same ratio around 25 (from author's research it is observed that a ratio of 2 is already alerting). Therefore, acceptance of relatively large fragment's length might combine the advantage of handling relatively low characteristic frequencies and detecting abnormal data.

Finally, fig. 8 shows that for relatively large fragments (about 20 % of total signal's length and higher), enlarging fragment's length might produce unexpected results, i.e. in some cases, larger fragments might produce greater ratio than smaller ones. This phenomenon is explained by the fact that comparative analysis may require signal truncation, for instance for a 40-second signal, fragmentation into 12-second fragments leaves 4 seconds out, fragmentation into 13-second fragments leaves 1 second out, while fragmentation into 14-second fragments leaves 2 seconds out, which might significantly influence overall results. Naturally, this phenomenon does not apply to relatively short fragments, where decreasing ratio trend is generally observed.

5 Summary

The paper illustrated robust methods for detection of vibration signals with abnormal level of fluctuation of amplitude level. As it was shown, due to large amplitude fluctuations, a correctly recorded vibration signal may be insignificant in terms of solely frequency-domain signal processing analyses, which constitute a fundament of distributed monitoring systems. The paper described various methods of signal division pointing out major pros and cons of each method. Practical remarks included in the paper based on authors' experience may serve as source of knowledge for researchers as well as software and diagnostic engineers.

Acknowledgements. This work is partially supported by the Polish Ministry of Science and Higher Education under the research grant no N504 670540.

References

1. Buscarello, R.T.: Practical Solutions to Machinery and Maintenance Vibration Problems, Lakewood, Colorado (1979)
2. Adams, M.L.: Rotating Machinery Vibration - From Analysis to Troubleshooting. Marcel Dekker, New York (2001)
3. Barszcz, T., Jabłoński, A.: A novel method for the optimal band selec-tion for vibration signal demodulation and comparison with the Kurtogram. Mechanical Systems and Signal Processing 25(1), 431–451 (2011)
4. Boustany, R., Antoni, J.: Blind extraction of a cyclostationary signal us-ing reduced-rank cyclic regression-A unifying approach. Mechanical Systems and Signal Processing 22(3), 520–541 (2008)
5. Steingröver, K., Dalhoff, P.: Richtlinien für die Zertifizierung von Con-dition Monitoring Systemen für Windenergieanlagen, Vorschriften und Richtlinien. Selbstverlag Germanischer Lloyd, Germany (2007) (in German)
6. Gellermann, T.: Requirements for Condition Monitoring Systems for Wind Turbines. AZT Expertentage, Allianz (2003)
7. Todd, M., et al.: The design of a decision support system for the vibration monitoring of turbine generators. In: Proceedings of 39th International Universities Power Engineering Conference - Conference , vol. 1, pp. 433–437 (2004)
8. Urbanek, J., et al.: Comparison of amplitude based and phase based methods for speed tracking in application to wind turbines. Metrology and Measurement Systems 18(2), 295–304 (2011)
9. Jabłoński, A., Barszcz, T., Bielecka, M.: Automatic validation of vibration signals in wind farm distributed monitoring systems. Measurement: Journal of the International Measurement Confederation 44(10), 1954–1967 (2011)
10. Antoni, J., et al.: Cyclostationary modelling of rotating machine vibra-tion signals. Mechanical Systems and Signal Processing 18(6), 1285–1314 (2004)
11. Angrisani, L., Daponte, P., D'Apuzzo, M.: A method for the automatic detection and measurement of transients – part I: the measurement method. Measurement 25(1), 19–30 (1999)
12. Angrisani, L., Daponte, P., D'Apuzzo, M.: A method for the automatic detection and measurement of transients – part II: applications. Measurement 25(1), 31–40 (1999)

Application of Vibration Monitoring for Mining Machinery in Varying Operational Conditions

Paweł Kępski[1] and Tomasz Barszcz[2]

[1] Famur Institute Sp. z o.o, ul. Armii Krajowej 51, 40-698 Katowice, Poland
pkepski@famur.com.pl
[2]AGH University of Science and Technology, Al. Mickiewicza 30,
30-059 Krakow, Poland
tbarszcz@agh.edu.pl

Abstract. The paper presents practical challenges in the process of implementation of vibration monitoring for the mining machinery. Advanced monitoring of critical components, especially gears and bearings, is presented. The proposed methods were implemented in an industrial system, called FAMAC VIBRO. The system was installed in two real coal mines and has the operational history of over one year. Interesting aspect of the proposed solution is operation in non statinary and very noisy environment as well as compliance with the explosive atmosphere requirement (ATEX).

The collected vibration and process data are subject to signal processing taking into account varying operational conditions and complex structure of monitored kinematics. The data are integrated at the next system level and then it is transferred to the highest level, i.e. the diagnostic center.

Keywords: condition monitoring system, drives of mining machines, coal mining machines monitoring.

1 Introduction

Nowadays there is a difficult challenge requested by customers from mining machines manufactures. It is important to provide machines that will have the availability at almost 100% level and ready to extract increasing amounts of coal in the same time. Moreover, big attention is paid to safety issues in underground mines. Taking into account the fact that geological conditions in polish mines are getting worse and price of the final product is very important when choosing suppliers, the manufactures are looking to the other forms of enhancing the availability and efficiency of machines, like using computer aided methods in the design process to improve the machining accuracy. But on the other hand, ontinuous monitoring systems are introduced to monitor the current state of machines (Jurdziak and Zimroz 2004),(FAMUR's Group Website), (Chroszcz et al. 2010).

In accordance with the adopted strategy, the FAMUR's GROUP spends a lot of time working on improving safety and efficiency in coal mines. In results of years of this effort is development and implementation of the **e-mine®** system by FAMUR INSTITUTE – the R&D Center of FAMUR's GROUP (FAMUR's Group Website), (Chroszcz et al. 2010). Part of this system – FAMAC VIBRO – is designed to the real time monitoring of gearboxes, conveyor drums and shearer loaders. This is a three-level diagnostic system:

- Underground visualization
- Surface visualization
- Service provided by FAMUR's Diagnostic Center

Machinery diagnostics with residual parameters such as vibration and temperature is becoming increasingly popular method of maintenance in coal mine industry (FAMUR's Group Website), (Chroszcz et al. 2010), (Zimroz 2008). Systems like FAMAC VIBRO are most useful in company, where unplanned shutdowns are very expensive and could disturb work of a large part of factory.

Vibration monitoring becomes more popular in coal industry due to high number of installed critical machines:

- Shearer loaders
- Belt and scrapper conveyors
- Main drainage pumps
- Main fans

There is a lot of important machines which according to global trend in machine conditioning should be continuously monitored, to preserve the safety of people underground and ensure continuous coal extraction process. Important novelty in the mining industry is the service of FAMUR's Diagnostics Center, which allows mines to benefit from the advanced vibrodiagnostics systems without hiring and training specialists.

2 Monitoring Methods

By creating the Diagnostic Center, FAMUR Group has opened a completely new quality of service for coal mine. In collaboration with the AGH University of Science and Technology and EC Systems (part of EC Group) – Polish company highly specialized in hardware and software for diagnostics – we implement fully ATEX compliant hardware for diagnostics in hazardous area (especially in coal mines). Nowadays we are developing methods and software for advanced vibration signal processing which were collected during varying operational conditions such as load, rotational speed, random impact noise and varying geological condition during coal extraction.

First level of FAMAC VIBRO system (underground visualization) allows crew underground to observe only a general vibration level (RMS, PP) and temperature. This information shows general problems in machines without any diagnostics. When RMS or PP level is too high miners underground see an alarm or warning.

On this level, they don't know what could be wrong, which element must to be replaced. This parameter is also sensitive to random impact noise (like flowing carbon on conveyors).

Due to the fact, that there are no specialists of machine conditioning and signal processing in the mine environment, FAMUR GROUP created Diagnostic Center. All the signals, which are collected by our systems underground, are continuously compressed, encrypted and sent through the secure internet connection to the Diagnostic Center where they are analyzed. All the data are stored on a dedicated secure database server which is protected against unauthorized access and hardware faults.

In Diagnostic Center specialists try to detect any information about the failure in an early stage. As soon as it's possible, right people are informed about any irregularities which give them time to arrange maintenance services. Once per an agreed period (e.g. quarterly) the Diagnostic Center sends reports describing current state of the machine park. In addition, all the time data are analyzed in terms of warning and alarm level. We set warning and alarm threshold rightly to current machine condition.

For understanding why the concept of a Diagnostic Center Service is so important, it's necessary to know how much signals are analyzed continuously. In our biggest installation (KWK Wieczorek coal mine) the sequence of 10 belt conveyors is monitored with the overall length of 3828m. We collect the data from 20 gear transmission and 50 drums. According to the kinematic model of monitored machines there are about 3200 vibration signal estimates related to bearings and gears fault (Figure 1).

Obviously Figure 1 shows only the scale of the problem, and there are numerous various analysis performed daily. Through line management and cooperation with EC Systems, we try to find optimal method for diagnostics of such a complex object. A lot of analysis are currently performed automatically, so we can work on further improvements of algorithms.

In recent times, more and more attention is paid to the quality of collected signals. The signal validation issue is very important in diagnostic systems (especially in system based on vibration) (Jablonski et al. 2011). Due to fact, that discussed systems are designed for machines which are working with very varying operational conditions and it is important to compare and analyze signals collected in a similar condition (load, speed), the methods proposed in (Jablonski et al. 2011) were implement in the FAMAC VIBRO system. Thanks to that, it is possible to write into a database only data with certain characteristics, suitable to further analysis.

One of the major difficulties in system is fact, that many of monitored machines are not new, and it is not possible in practice to determine their technical state and performed repairs at the start of monitoring process. Moreover, often there is a problem with installation of phase marker and additional sensors (i.e. current, load) when monitored machines were not produced by the FAMUR's

Group. Therefore, in cooperation with EC Systems, there was implemented algorithm of phase marker reconstruction in our system based on vibration signals. Thanks to this, it is possible to perform a variety of analysis which needs information about speeds (e.g. order analysis). Additionally, we have started work on an attempt to recover information about the load of monitored machines from vibration signals, which is the next step to eliminate additional sensors in our systems without losing important information.

Recently, there were a lot of publications about vibration conditioning machines working under varying operation conditions (Barszcz 2008) (Bartelmus and Zimroz 2009), (Barszcz and Jablonski 2011). Nowadays, in existing systems, following methods of signal analysis are used:

- Broadband estimates
- Narrowband estimates
- Spectrum analysis
- Envelope analysis

According to strong emphasis on development in Diagnostic Center, which will lead to increase efficiency of service, we have begun working on finding optimal methods of diagnostics machines covered by FAMAC VIBRO system.

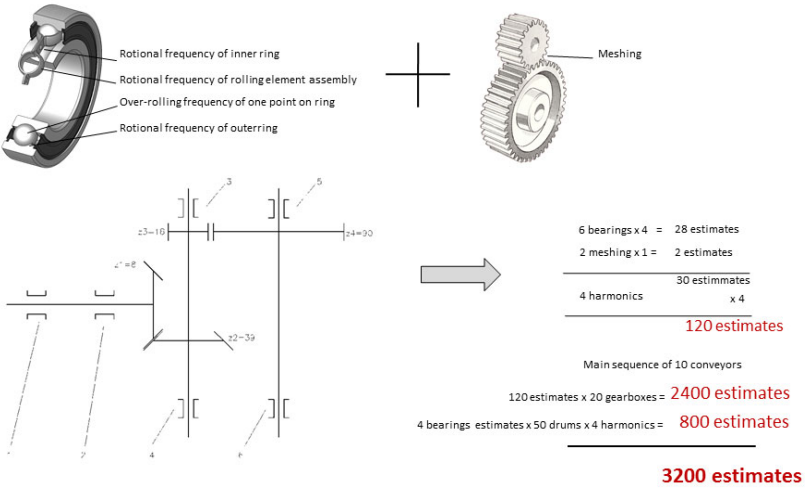

Fig. 1 Estimates observed in system on Wieczorek coal mine

3 Structure of the FAMAC VIBRO System

The FAMAC VIBRO is part of the supervisory system managing the coal extraction process – e-mine® (Figure 2). Main part of this system is the underground server – Green Diamond which is designed to coordinate processes

assigned to the local FAMAC LS station. Designed architecture allows to monitor machines very distant from each other which is necessary especially in the sequence of conveyors. Other parts of the system are:

- LS FAMAC VIBRO – underground local server which is used to collect, process and present the data. Local stations transfer data to Green Diamond and also to supervisory systems for adequate response in the case of a warning or alarm.
- LB FAMAC VIBRO is used in extended systems for collecting data and sending it to local station.
- RS/OPTO converter provides signal conversion to fiber optic.
- Intrinsically safe data hub
- Accelerometer compliant with the explosive atmosphere requirement
- Temperature sensor

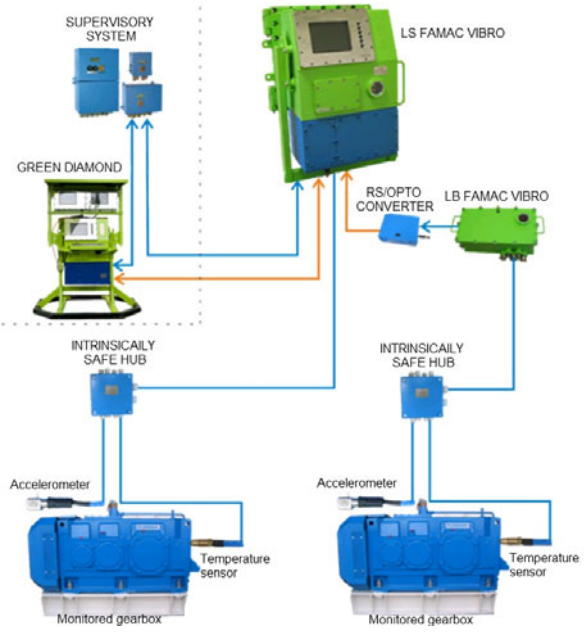

Fig. 2 Architecture of FAMAC VIBRO system

Collected signals (vibration and temperature) are transferred to the local station with the intrinsically safe optical fiber. This solution provides high data transfer rate which is very important for transferring large amounts of data, especially raw vibration records in system. In the proposed solution, there are collected several seconds time vibration signals with high sampling rate. Additionally, dedicated software module processes vibration signals using information about the

kinematics, calculates energies around main defect frequencies (i.e. BPFI, BPFO, MESH), and write its values to the database. Moreover basic estimates (i.e. RMS, P-P) are calculated more often and are displayed on the system visualization.

In addition we have proposed the solution for data transfer from the underground to the surface, where they are collected on a dedicated server. Thanks to this solution, supervision staff can observe the actual and historical data on their computers without going underground. With this solution there is a possibility for a fast reaction of right personnel in the case when a warning or alarm is detected by the system.

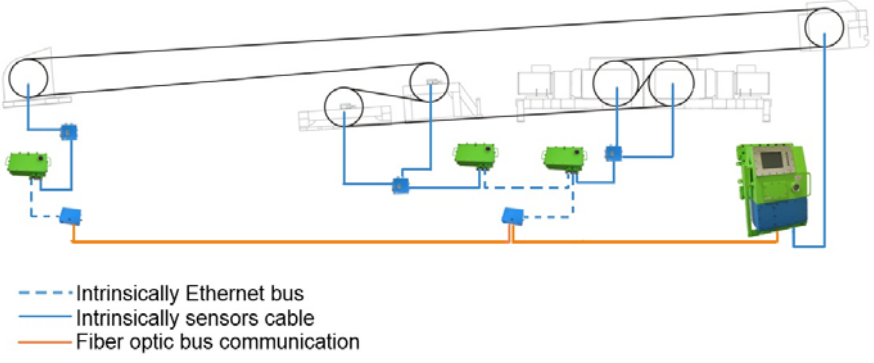

Fig. 3 Scheme of proposed architecture of underground system for belt conveyors monitoring

4 Operational Experience

Until now, the biggest installation of FAMAC VIBRO systems is implemented in KWK Wieczorek coal mine. There are 10 belt conveyors monitored which consist of 20 gearboxes and 50 drums. Each point is monitored with vibration and temperature, so there are over 200 sensors in the system. Because of high complexity of the system, it was a big challenge for the IT department to create transparent and user-friendly visualization. The Figure 4 presents a screen shot, which presents the sample screen from the system. The user can choose one of the belt conveyors from the sequence he is interested in and then he could observe the actual data. On the other hand it's also easy to present archive data from a defined period of time.

According to requirements, when the warning or alarm occurres in system, the point is highlighted in yellow (warning) or red (alarm). The same visualization is presented on underground local station (Figure 5) and on computers on the surface.

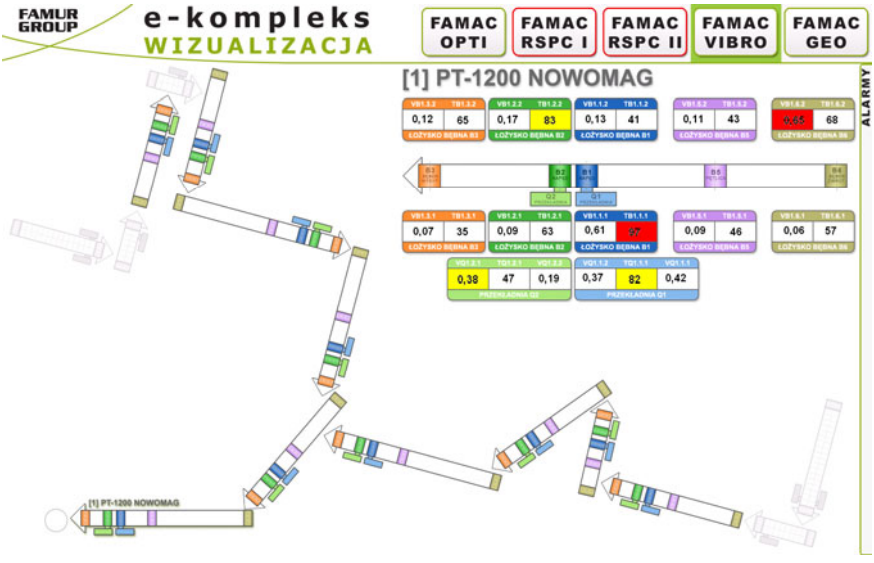

Fig. 4 Visualization of KWK Wieczorek system

Fig. 5 Underground visualisation on Local Station

5 Conclusions

The FAMAC VIBRO system is dedicated for vibration monitoring of heavy duty mining machinery and together with the Diagnostic Center it allows high performance signal processing and machine diagnostics. Thanks to the modular design of e-mine systems, it is easy to connect this system with the other diagnostics systems developed by the FAMUR Group.

The Diagnostic Center service allows our customer to reduce maintenance costs thanks to pursue the policy of planned machines' repairs, which increase availability of machines. End users can benefit from vibration diagnostics without employing specialists.

FAMAC VIBRO is easy to reconfigure with the possibility of change diagnostics points in the system which is especially important in such a specific company like a coal mine. On a regular basis there are many changes, e.g. length of the conveyors during the progress of mining operation.

Nowadays we could say, that a majority of problems in Polish minea are in the field of the maintenance of the system. There are many failures and mechanical damage in our system because of extremely hard environmental conditions underground (including the human factor). Obviously, first of all, the mines have to extract the coal, and in the first place they are repairing machines and equipment, which are directly needed in the coal extraction process and then it's the time to repair non-critical systems.

During the process of exploitation of this system in our customers, there was a lot of comments, that they see other uses of the FAMAC VIBRO especially in:

- Main fans
- Main drainage system

which perfectly fits to the design assumption and gives us a hope for further large system installations.

There is a lot of work behind us – especially in the field of hardware. Now we are focused on signal processing and searching for optimal methods in diagnostics machines with very complex structure, which work in extremely varying operational conditions.

References

[1] Jurdziak, L., Zimroz, R.: Dlaczego diagnostyka maszyn się opłaca i ile można na tym zaoszczędzić? Górnictwo i Geologia VII, Wrocław Oficyna Wydawnicza Politechniki Wrocławskiej, pp. 139–150 (2004)

[2] FAMUR's Group Website, http://www.famur.com.pl/page/index/59 (accessed December 20, 2011)

[3] Chrószcz, B., Gwiaździński, P., Kępski, P.: Nowoczesna diagnostyka napędów maszyn górniczych w KWK Wieczorek w oparciu o system FAMAC VIBRO. Napędy i Sterowanie 12 (7/8), 94–96 (2010)

[4] Bartelmus, W., Zimroz, R.: Diagnostyka uszkodzeń na podstawie sygnału drgań w maszynach górniczych. Górnictwo Odkrywkowe 47(4-5), 22–31 (2005)
[5] Zimroz, R.: Role of signal preprocessing in local damage detection in mining machines. Diagnostyka 2, 33–36 (2008)
[6] Jabłoński, A., Barszcz, T., Bielecka, M.: Automatic validation of vibration signals in wind farm distributed monitoring systems. Measurement 44(10), 1954–1967 (2011)
[7] Bartelmus, W., Zimroz, R.: Vibration condition monitoring of planetary gearbox under varying external load. Mechanical System and Signal Processing 23(1), 246–257 (2009)
[8] Barszcz, T.: Advanced methods for condition monitoring of machinery in distributed online monitoring and diagnostic systems. Wydawnictwo Naukowe Instytutu Technologii Eksploatacji (2008)
[9] Bartelmus, W., Zimroz, R.: A new feature for monitoring the condition of gearboxes in non-stationary operating condition. Mechanical System and Signal Processing 23(5), 1528–1534 (2009)
[10] Barszcz, T., Jabłoński, A.: A novel method for the optimal band selection for vibration signal demodulation and comparison with the Kurtogram. Mechanical System and Signal Processing 25 (1) 431–451 (2011)

Application of Time Descriptors to the Modified Hilbert Transform of Empirical Mode Decomposition for Early Detection of Gear Defects

Thameur Kidar[1,2], Marc Thomas[1], Mohamed Elbadaoui[2], and Raynald Guilbault[1]

[1] Department of Mechanical Engineering, École de Technologie Supérieure.
1100, Notre-Dame street West, Montreal, H3C 1K3, Quebec, Canada
thameur.kidar@univ-st-etienne.fr, marc.thomas@etsmtl.ca, raynald.guilbault@etsmtl.ca
[2] University of Lyon, University of Saint Etienne, LASPI EA-3059.
20 Av de Paris, 42334 Roanne Cedex, France
mohamed.elbadaoui@univ-st-etienne.fr

Abstract. Diagnosis and fault detection in mechanical systems during their time-varying non stationary operation is one of the most challenging tasks. The paper presents a method for the early detection of gearbox defects based on the empirical mode decomposition (EMD) algorithm and a proposed modified Hilbert transform. The EMD technique decomposes the measured signal into oscillatory functions called Intrinsic Mode Functions (IMF). A numerical model of damaged gears is used for generating a modulated vibratory signal with repetitive shocks. The application of time descriptors "Talaf" and "Thikat" to different IMF decomposition levels of the modified Hilbert envelope gives good results for early detection of defects in comparison with the IMF of the original time signal and its traditional Hilbert envelope or with the wavelet decomposition.

Keywords: Fault diagnosis, gearbox, Empirical Mode Decomposition, Modified Hilbert transform, Time descriptors, Talaf, Thikat, wavelet transform.

1 Introduction

Machines maintenance is conditioned to an adequate monitoring of potential failures. Machinery vibration consists essentially of three signal types: Periodic (unbalance, misalignment, blade pass), random (friction, noise, fluctuation, turbulence) and shocks (bearing faults, gear faults, etc.). The determination of each of these types of vibration constitutes in itself a powerful monitoring technique. One of the most involved mechanisms in rotating machines failures are the gearbox and numerical simulations of their vibratory behavior when damaged help to

understand the resultant signatures [Guilbault and Thomas 2008, Palaisi *et al* 2009]. The monitoring methods applied to gearboxes can be achieved in a number of ways. Some of these methods are simple to use while others require sophisticated signal processing techniques. In fact, a large number of defects generate shocks that can be analyzed in either time domain by scalar descriptors: RMS, Peak, Crest Factor (CF), Kurtosis (Ku), Impulse Factor, Shape Factor, etc, [Sassi *et al* 2008, Yadav and Wadhwani 2011] or in frequency domain: spectral analysis, frequency spectrum in the high frequency domain, Spike energy, enveloping, or time-frequency and wavelet analysis, etc. RMS and Max-Peak values are quite adequate when the fault is quite developed and the signal-to-noise is high. Unfortunately, when the fault is small and the signal-to-noise ratio is weak, these two descriptors are not enough efficient alone. The increase in size defect is usually observed more readily by the Peak rather than by the RMS value. Because of this, the crest factor, which is defined by the ratio of the Peak to RMS value, is better adapted for monitoring the evolution of shock phenomena (Badri *et al* 2011). This relationship between these two descriptors during the evolution of a fault is interesting, but it is easier to combine them in only one scalar descriptor such as the Crest Factor (CF) or the Kurtosis (Ku). Furthermore the fault detection and diagnosis in mechanical systems during their time-varying non stationary operation is one of the most challenging tasks and the techniques are not always efficient for the monitoring of machines with non stationary behavior [Vu *et al* 2011]. In order to improve the signal processing for an efficient monitoring, the empirical mode decomposition (EMD) technique [Pareya *et al* 2006, Ricci and Pennacchi 2011] has been proposed. The outputs of this adaptive approach are the intrinsic mode functions. The EMD method decomposes the measured signals into slow components (approximation) and fast components (detail) in a similar manner than a wavelet transform [Farag and Gaouda 2011]. We propose in this study to process the EMD signals with a modified Hilbert envelope and statistical temporal descriptors. A comparison between the proposed methods is carried out.

2 Empirical Mode Decomposition

The EMD method decomposes the time signal into a finite set of oscillatory functions called the intrinsic mode functions (IMF). An IMF is a function that checks the following conditions:

(1) The number of extrema and the number of zero crossings must either equal or differ at most by one;
(2) The value of the moving average envelope defined by local maxima and the envelope defined by local minima is zero.

An intrinsic mode is the embedded time scale in the signal. It is defined as the time between two successive extrema. It is not necessarily an harmonic function. In fact, it may include non-stationary amplitudes and modulated frequencies. The manner to decompose the signal in IMF is as follows:

- Firstly identify all the local extrema, and then connect all the local maxima by a cubic spline line as the upper envelope.
- Repeat the procedure for the local minima to produce the lower envelope.
- The upper and lower envelopes should cover all the data between them. The mean of upper and lower envelope values is defined as [Loutridis 2004]:

$$m_1(t) = \frac{u(t) + l(t)}{2} \tag{1}$$

- Then, the mean $m_1(t)$ is subtracted from the signal $s(t)$, obtaining the first component $h_1(t)$, i.e:

$$h_1(t) = s(t) - m_1(t) \tag{2}$$

Ideally, if $h_1(t)$ is an IMF, then $h_1(t)$ is the first component of $s(t)$.

- If $h_1(t)$ is not an IMF, $h_1(t)$ is treated as the original signal and repeat the previous steps.

$$h_{11}(t) = h_1(t) - m_{11}(t). \tag{3}$$

where $m_{11}(t)$ is the mean of the upper and lower envelopes of $h_1(t)$.

- After repeating the procedure, i.e. up to k times, $h_{1k}(t)$ becomes an IMF like:

$$h_{1k}(t) = h_{1(k-1)}(t) - m_{1k}(t) \tag{4}$$

then, it is designated like:

$$c_1(t) = h_{1k}(t) \tag{5}$$

the first component (IMF) of the original signal. $c_1(t)$ represents the shortest period of signal or the highest frequency band.

- By computing the difference between $c_1(t)$ and $s(t)$, we could get:

$$r_1(t) = s(t) - c_1(t) \tag{6}$$

where $r_1(t)$ may be considered as the original signal.

- Let's repeat the above process for n times, then n-IMFs of signal $s(t)$ could be got. Then :

$$\begin{cases} r_2(t) = r_1(t) - c_2(t) \\ \quad\quad\vdots \\ r_n(t) = r_{(n-1)}(t) - c_n(t) \end{cases} \tag{7}$$

- The process can be stopped when $r_n(t)$ becomes a monotonic function for which it is not possible to extract other IMFs.
- The signal $s(t)$ can then be written as:

$$s(t) = \sum_{k=1}^{n} c_k(t) + r_n(t) \tag{8}$$

where r_n is the mean trend of s(t).

The IMFs $\{c_1(t), c_2(t), \ldots, c_n(t)\}$ represent different frequency bands ranging from the high frequencies to low frequencies. Frequency components contained in each IMF relate changes with the signal itself.

3 Time Descriptors

Many time descriptors (Peak, RMS, crest factor, Kurtosis, etc.) of signal processing have been proposed in the literature for the early detection of fault. In this paper, Talaf and Thikat are used [Sassi *et al*, 2008]. The Kurtosis and the Crest factor are two particularly well adapted indicators for detecting the appearance of the default. However, after a certain stage of degradation, the use of these descriptors becomes not useful in monitoring of defects. The Talaf indicator is a combination between the traditional descriptors Kurtosis and RMS, as

$$TALAF = \log\left[kurtosis + \frac{RMS}{RMS_0} \right] \tag{9}$$

where RMS_0 is the root mean square value defined for healthy gears. If this value is not known or has not been recorded, the method may work by considering any initial value that can be obtained at the beginning of monitoring or from the ISO 10816 for healthy machines.

The parameter Thikat has been designed to incorporate data from several parameters (Kurtosis, RMS, Crest factor, Peak) into a single unit of information, as

$$THIKAT = \log\left[(kurtosis)^{cf} + \left(\frac{RMS}{RMS_0} \right)^{Peak} \right] \tag{10}$$

where cf is the Crest factor.

4 A Modified Hilbert Transform

For each IMF $c_i(t)$ in Eq. (8), we can express its Hilbert transform as:

$$H[c_i(t)] = \frac{1}{\pi} \int_{-\infty}^{+\infty} \frac{c_i(\tau)}{t - \tau} d\tau \cdot \tag{11}$$

With this definition, we can develop an analytic signal as follows:

$$Z_i(t) = c_i(t) + jH\left[c_i(t)\right] = A_i(t)e^{j\phi_i(t)}. \tag{12}$$

in which;

$$A_i(t) = \sqrt{c_i^2(t) + H^2\left[c_i(t)\right]}, \tag{13}$$

$$\phi_i(t) = \arctan\frac{H\left[c_i(t)\right]}{c_i(t)}. \tag{14}$$

For performing the Hilbert transform to each IMF component, the original signal can be expressed as the real part (RP) of the analytical signal in the following form:

$$s(t) = RP\sum_{i=1}^{n} A_i(t)e^{j\phi_i(t)}. \tag{15}$$

We have developed a new descriptor by adding the signal to the analytical signal in the imaginary part. We have called it the modified Hilbert transform:

$$Z_{m_i}(t) = c_i(t) + j\left[Z_i(t)\right] = c_i(t) + j\left[c_i(t) + jH\left[c_i(t)\right]\right] = A_{m_i}(t)e^{j\varphi_{m_i}(t)} \tag{16}$$

in which:

$$A_{m_i}(t) = \sqrt{(c_i(t) - H[c_i(t)])^2 + c_i^2(t)}, \tag{17}$$

$$\phi_{m_i}(t) = \arctan\frac{c_i(t)}{c_i(t) - H[c_i(t)]}. \tag{18}$$

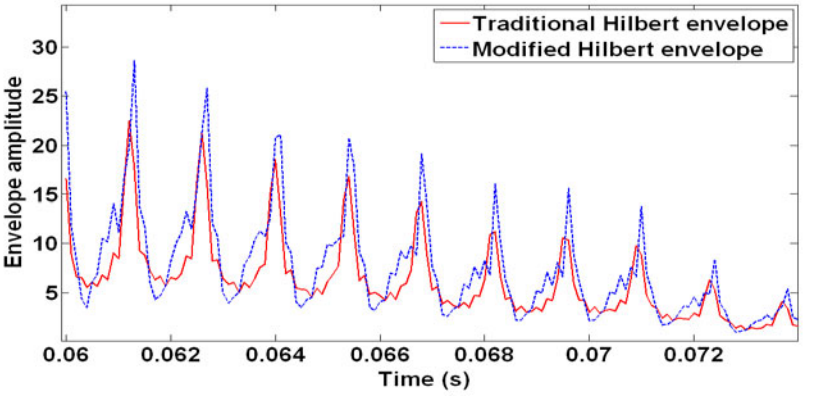

Fig. 1 Comparison of the Hilbert methods

The $A_{m_i}(t)$ offers a measure of the envelope contribution from each IMF, while the latter offer a measure of the phase or frequencies contribution from the measured signal. Fig 1 shows that the new Hilbert transform reveals more details in the envelope than the traditional method.

5 Wavelet Decomposition

This technique decomposes a signal $s(t)$ at different levels (Fig. 2) and presents it as series of approximate $a_j(t)$ and detail $d_j(t)$ expansion coefficients. The sets of expansion coefficients can be calculated as:

$$a_{i-1}(k) = \sum_p b_0(p-2k)a_i(p) \quad (19)$$

$$d_{i-1}(k) = \sum_p b_1(p-2k)a_i(p) \quad (20)$$

where $b_0(k)$ and $b_1(k)$ are the coefficients of the selected scaling and the wavelet functions, respectively.

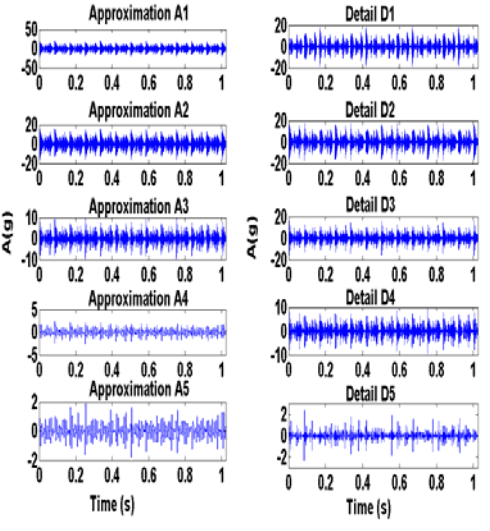

Fig. 2 Wavelet decomposition

6 Results Analysis and Applications

In order to simulate the vibratory signals of gearbox, a gear multiplicative model whose the meshing is modulated in amplitude has been used. To the gear model [El Badaoui 1999], repetitive shocks f(t) have been added to simulate the effect of damage (Fig 2):

$$s(t) = \left(\sum_{n=-\infty}^{+\infty} s_e(t-n\tau_e) \right) \left(1 + \sum_{m=-\infty}^{+\infty} s_{r1}(t-m\tau_{r1}) + \sum_{p=-\infty}^{+\infty} s_{r2}(t-p\tau_{r2}) \right) + f(t) \quad (24)$$

Wheel 1 Wheel 2

where τ_e, τ_{r1} and τ_{r2} represent the meshing period and the rotational periods of the two wheels, respectively. $s_e(t)$, $s_{r1}(t)$ and $s_{r2}(t)$ represent the meshing signal with its modulation, respectively. Fig3 shows the gear modulated signal, the added repetitive shocks and the IMF developed up to the 5th level.

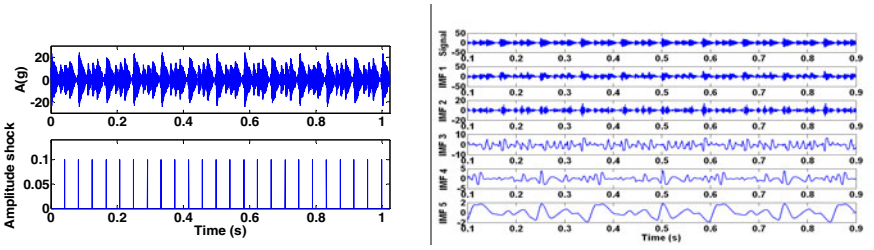

Fig. 3 Decomposition of the IMF

For different amplitudes of shocks, varying between 0.1 to 8, added to the numerical signal, the Talaf (Fig 4-a) and Thikat (Fig 4-b) descriptors have been computed for each IMF from the time signal, the traditional and the modified Hilbert envelopes. A comparison between the results is shown in Fig 4. The application of these descriptors to the wavelet decomposition has not really shown significant results for an early detection of damage.

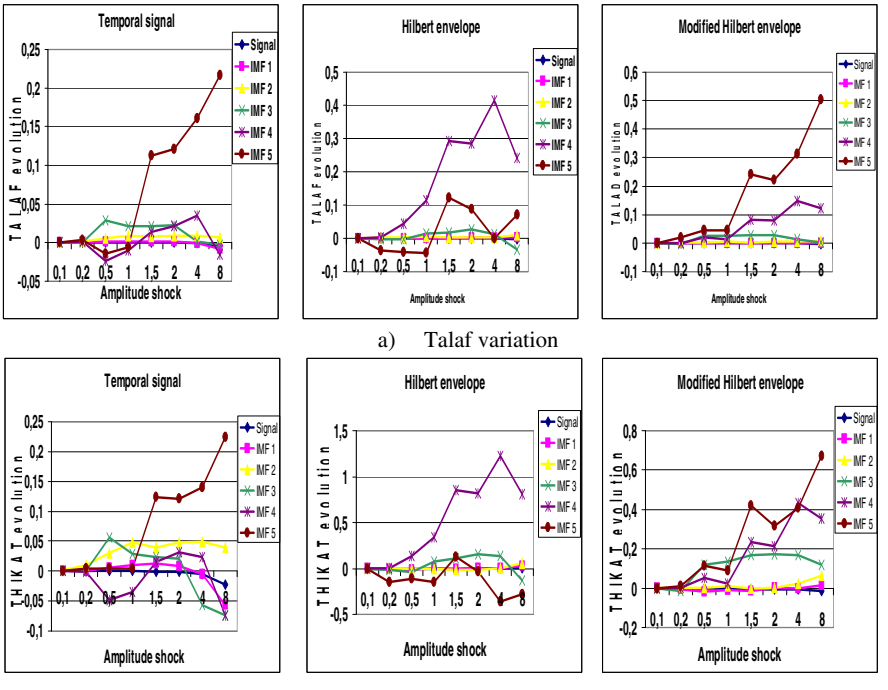

a) Talaf variation

b) Thikat variation

Fig. 4 Talaf and Thikat values of the IMF signals

The decomposition needs to go to the 5th level of the original time signal to detect a fault from shock amplitude of 1, while their application becomes to be sensitive from the 4th level of the Hilbert transform and even from the 3rd level when applied to the modified Hilbert transform. Furthermore, the detection becomes to be sensitive from shock amplitude of 0.2. Though the Thikat and Talaf values give similar trends, Thikat seems a better indicator as compared to Talaf with more sensitive amplitude for early detection of defects. The numerical results showed that the Thikat analysis of the modified Hilbert envelope with IMF could be a good indicator for early detection, characterization and monitoring the evolution of the defects.

7 Conclusion

This study showed the efficiency of the empirical mode decomposition method for the early detection of mechanical defects. This method revealed more significant variations than the wavelet decomposition for the studied case. A new modified Hilbert transform has been developed which shows more details in the envelope than the traditional method. Finally, the descriptors Talaf and Thikat have been found more sensitive to the defect amplitude than the Kurtosis or Crest factor. The application has been conducted on numerical signals of gear meshing perturbed by repetitive shocks produced by defects. The results show for the considered application that the Thikat descriptor can be used from the 3rd level of IMF decomposition of the modified Hilbert transform.

References

1. Badri, B., Thomas, M., Sassi, S.: A shock filter for bearing slipping detection and multiple damage diagnosis. International Journal of Mechanics 5(4), 318–326 (2011)
2. El Badaoui, M.: Contribution of vibratory diagnostic of gearbox by Cepstral analysis, Ph.D. thesis, Jean Monnet University of St Etienne (FR), p. 141 (1999) (in French)
3. Farag, K.O., Gaouda, A.M.: Dynamic wavelet-based tool for gearbox diagnosis. Mechanical Systems and Signal Processing 26, 190–204 (2011)
4. Guilbault, R., Thomas, M.: Prediction of Resonances of Thin-Rimmed Cylindrical Gears from a Sub-Structuring Approach. In: Proceedings of the CSME, Forum 2008, Ottawa, No. 1569100493, p. 8 (2008)
5. Loutridis, S.J.: Damage detection in gear systems using empirical mode decomposition. Engineering Structures 26, 1833–1841 (2004)
6. Palaisi, D., Guilbault, R., Thomas, M., Lakis, A., Mureithi, N.: Numerical simulation of vibratory behavior of damaged gearbox. In: Proceedings of the 27th Seminar on Machinery Vibration, p. 16. Canadian Machinery Vibration Association, Vancouver (2009) (in French)
7. Pareya, A., El Badaoui, M., Guillet, F., Tandona, N.: Dynamic modelling of spur gear pair and application of empirical mode decomposition-based statistical analysis for early detection of localized tooth defect. Journal of Sound and Vibration 294, 547–561 (2006)

8. Ricci, R., Pennacchi, P.: Diagnostics of gear faults based on EMD and automatic selection of intrinsic mode functions. Mechanical Systems and Signal Processing 25, 821–838 (2011)
9. Sassi, S., Badri, B., Thomas, M.: Tracking surface degradation of ball bearings by means of new time domain scalar descriptors. International Journal of COMADEM 11(3), 36–45 (2008); ISSN: 1363-7681
10. Vu, V.H., Thomas, M., Lakis, A.A., Marcouiller, L.: Operational modal analysis by updating autoregressive model. Mechanical Systems and Signal Processing 25, 1028–1044 (2011)
11. Yadav, M., Wadhwani, S.: Vibration analysis of bearing for fault detection using time domain features and neural network. International Journal of Applied Research in Mechanical Engineering 1(1), 69–74 (2011)

State Space Modeling Theory of Induction Motors for Sensorless Control and Motoring Purposes

Redha Meneceur[1], Abd-Razak Metatla[2], and Noureddine Meneceur[3]

Centre Universitaire D'El-Oued
Département de Géni Mécanique/Electromécanique
meneceurredha22@yahoo.fr
B. P.787 El-Oued Algeria
Tel :00213 770 92 13 10

Abstract. The purpose of this work is to investigate different models of the asynchronous machine in the state space representation for sensorless control purposes. The asynchronous machine is known as a complex non-linear system in which time–varying parameters entail an additional difficulty. Based on the fact that model can be significantly simplified if one applies the d-q Park transformation and that high dynamic performances are achieved by a field orientation technique also called vector control, different structures of the model are investigated and discussed. Each model merits and drawbacks are pointed out.

This work contributes to decrease of the number of sensors to be used at the machine without deteriorating the dynamic performance of the considered drive control system. With the development of parameter and state estimation techniques, mainly the observer technique such as Kalman filtering and Luenberger observer, one can, based on the available measurements, estimate the remaining parameters or state components. Thus allows us to increase the reliability and the robustness of drive systems and to decrease their cost.

Based on this point of view state feedback control of a linear state space model of the asynchronous machine involving the stator current and flux as state variables is experimented in a simulation study. The sensorless state feedback control uses the estimated stator flux and the measured stator current. The simulation permits also to estimated the remaining state variables of the asynchronous machine such as rotor current and flux.

The obtained results show that the state space technique is an efficient method for asynchronous machine modelling, state variables estimating and sensorless machine drives controlling. State space techniques are directly used by the observer-based as well as the Kalman filtering techniques for sensorless control and monitoring purposes.

1 Introduction

The induction motor is one of most widely used machine in industrial applications due to its high reliability, relatively low cost, and modest maintenance requirements. With the devlopment of power electronic technology, low cost digital processing (DSP) micro-controllers and estimation techniques the induction constitutes an attractive component for the future high performance drives [1],[2],[3].

The induction motor is known as a complex nonlinear sytem in which time-varying developing control strategies.Based on the fact that the model can be significantly simplified if one applies d-q Park transformation and field orientation technique also called vector, different structures of the model exist in the literature [3],[4]. The choice of a model structure depends on the problem at hand.Industrial applications involving inducton motors are subject to control and monitoring problems.

Sensorless control techniques focus on reducing the number of sensors. Observer- based state estimation algorithms are very helpful when the full state or some of the state variable measurements are unaviable. The well known state feedback control is a typical example of application when the full state variable vector is not measured.

The aim of a system monitoring is to control, through certain state variables that indicate the system health, its main functions and to compare the measured values of these state variables with their preset values[3],[4],[5].

Arother objective of a system monitoring is to decrease the rate of fault occurence and to increase the MTBF (Mean Time Between Failure).

In the case of sensorless control and system monitoring state space modeling of induction motors and observer – based state variabe estimation techniques are very helpful since induction motors are a very important part of any industrial electrically driven system and hence they must be controlled and carefully surveyed. Based on this point of view different structures of the induction motor model in the state space representation are investigated and discussed in this paper from the theoritical point of view.

2 State Space Modelling

In order to establish a state space mathematical model of the induction motor, the following classical hypotheses are used[2],[3],[4].

- The higher order harmonics of the magnetic field of stator and rotor are neglected.
- The ferromagnetic losses and effect of saturation are also neglected (for control design).
- The perfect electrical and maghetic circuit symmetry (uniform air gap and sinusoidal flux density ditribution), is assumed.

The dynamics of the induction motor are divided into two subsystems which are: the electromagnetic dynamics and the eleromechanical one.

The electromagnetic subsytem is, in its turn, divided into stator and rotor dynamics. The electromagnetic subsystem is represented, in an arbitrary rotating reference frame, by the following state space model:

$$\frac{d}{dt}\begin{pmatrix}\varphi_s\\ \varphi_r\end{pmatrix}=\begin{bmatrix}\Omega_a & 0\\ 0 & \Omega_{ar}\end{bmatrix}\begin{pmatrix}\varphi_s\\ \varphi_r\end{pmatrix}-\begin{bmatrix}R_s & 0\\ 0 & R_s\end{bmatrix}\begin{pmatrix}i_s\\ i_r\end{pmatrix}+\begin{bmatrix}I_2 & 0_2\\ 0_2 & 0_2\end{bmatrix}\begin{pmatrix}u_s\\ u_r\end{pmatrix} \tag{1}$$

Where $\varphi_s=[\varphi_{sd},\varphi_{sq}]$, $\varphi_r=[\varphi_{rd},\varphi_{rq}]$, $u_s=[u_{sd},u_{sq}]$, $u_r=[u_{rd},u_{rq}]$ stator flux, rotor flux linkage and stator terminal voltage and rotor voltage, respectively , $i_s=[i_{sd},i_{sq}]$,denotes stator current and, $i_r=[i_{rd},i_{rq}]$ denote rotor current, R_s stand for stator resistance. And I_2 is the identity matrix.

The electromechanical subsystem is represented by the following nonlinear differential equation called the motion equation.

$$\frac{d\omega_r}{dt}=\frac{1}{J}\frac{P}{2}(T_e-T_l) \tag{2}$$

P is the number of pole pairs, J denotes the moment of inertia of motor and T_l a load torque. The electromechanical torque and the flux linkage relations are respectively defined by:

$$T_e=P\varphi_s^T\begin{bmatrix}0 & 1\\ -1 & 0\end{bmatrix}i_s \tag{3}$$

$$\begin{pmatrix}\varphi_s\\ \varphi_r\end{pmatrix}=\begin{bmatrix}L_s & M\\ M & L_r\end{bmatrix}\begin{pmatrix}i_s\\ i_r\end{pmatrix} \tag{4}$$

The matrices $\Omega_a,\Omega_{ar},R_s,R_r,L_s,L_r,M$, and I_0 are defined as follows:

$$\Omega_a=\begin{bmatrix}0 & \omega_a\\ -\omega_a & 0\end{bmatrix},\ \Omega_{ar}=\begin{bmatrix}0 & (\omega_a-\omega_r)\\ -(\omega_a-\omega_r) & 0\end{bmatrix},\ R_s=\begin{bmatrix}r_s & 0_2\\ 0_2 & r_s\end{bmatrix},\ R_r=\begin{bmatrix}r_r & 0_2\\ 0_2 & r_r\end{bmatrix},$$

$$L_s=\begin{bmatrix}l_s & 0_2\\ 0_2 & l_s\end{bmatrix},\ L_r=\begin{bmatrix}l_r & 0_2\\ 0_2 & l_r\end{bmatrix},\ M=\begin{bmatrix}m & 0_2\\ 0_2 & m\end{bmatrix},\text{ and }\ I_0=\begin{bmatrix}I_2 & 0_2\\ 0_2 & 0_2\end{bmatrix}.$$

ω_r denotes the rotor electrical speed, m is the mutual inductance, l_s and l_r denote self inductance of stator and rotor respectively.

Usual notation for parameters and variables is used. The indexes s and r refer to the stator and rotor components respectively.

Analysis of the above induction motor model shows the complexity of the system. The nonlinearity of the model is introduced by the torque equation and the rotor angular velocity involved in the system evolution matrix. Based on the fact that the model can be significantly simplified if one the d-q Park transformation and field orientation technique also called vector control, different structures of the model can be obtained for sensorless control and monitoring purposes. Investigation result is not exhaustive. The motion equation, relation (2), is controlled via the torque equation, relation (3), does not change with the changing of the model structure.

Only relations (1),(3) and (4) are concerned with the changing of the selected state variable and the used reference frame. For futher model reduction one can add an appropriate field orintation technique taking into account the avialability of measurments (the number of sensors to be used).

The following matrix inversion lemma is used to make easy the transformation between the different structures of the induction motor model.

If $L_M = \begin{bmatrix} L_s & M \\ M & L_r \end{bmatrix}$ is a square matrix which involves square matrices then the inverse matrix L_M^{-1} is given by:

$$L_M^{-1} = \begin{bmatrix} (L_s - M L_r^{-1} M^T)^{-1} & -(L_s - M L_r^{-1} M^T)^{-1} M L_r^{-1} \\ -(L_r - M^T L_s^{-1} M)^{-1} M L_s^{-1} & (L_r - M^T L_s^{-1} M)^{-1} \end{bmatrix} \tag{5}$$

The particular diagonal form of the involved matrices leads to:

$$L^{-1}{}_M = \frac{1}{\sigma L_s l_r} \begin{bmatrix} L_s & M \\ M & L_r \end{bmatrix} \tag{6}$$

The selected state variable for a given model are a combination of the stator and the rotor state variable which are the flux and the current state variables. This leads to the following combinations.

A. Stator Flux and Rotor Flux as Selected State Variables

The first case takes into account the stator and the rotor flux as selected state variables. This leads to the elimination of the current vector from the state equation (1) by applying the matrix inversion lemma (5) to equation (4). The obtained model is then:

$$\frac{d}{dt}\begin{pmatrix} \varphi_s \\ \varphi_r \end{pmatrix} = \left[\Omega - R L_M^{-1}\right]\begin{pmatrix} \varphi_s \\ \varphi_r \end{pmatrix} + \begin{bmatrix} I_2 \\ 0_2 \end{bmatrix} u_s \tag{7}$$

$$\frac{d\omega_r}{dt} = \frac{1}{J}\frac{P}{2}(T_e - T_l) \tag{8}$$

$$T_e = \frac{P}{m}\frac{1-\sigma}{\sigma}\varphi_s^T \begin{bmatrix} 0 & -1 \\ 1 & 0 \end{bmatrix} \varphi_r \tag{9}$$

$$\begin{pmatrix} i_s \\ i_r \end{pmatrix} = L_M^{-1} \begin{pmatrix} \varphi_s \\ \varphi_r \end{pmatrix} \tag{10}$$

Where the matrix $\left[\Omega - RL_M^{-1}\right]$ stands for the dynamic evaluation matrix of the system with:

$$\Omega = \begin{bmatrix} \Omega_a & 0 \\ 0 & \Omega_{ar} \end{bmatrix} \text{ and } R = \begin{bmatrix} R_s & 0 \\ 0 & R_r \end{bmatrix}.$$

A simple calculus shows that:

$$\left[\Omega - RL_M^{-1}\right] = \frac{1}{\sigma L_s L_r}\begin{bmatrix} \Omega_a \sigma L_s L_r & R_s M \\ R_r M & \Omega_{ar}\sigma L_s L_r - R_r L_s \end{bmatrix} \tag{11}$$

The obtained model is a standard flux state space model which can be directly by the classical closed-loop state feedback control techniques, with some assunptions, if the full state flux vector is measured..

If the stator fixed reference frame is chosen one has to substitute in equation (11) Ω_a to 0_2 and Ω_{ar} to Ω_r. The stator sub-model is used to estimate the rotor flux linkage vector, without requiring a speed signal. It is therefore a preferred machine model for sensorless speed control applications. The rotor sub-model is used to estimate the rotor flux linkage vector based on the measured stator flux measurements and requires a speed signal. In order to reduce significantly the model one can use, in addition stator reference frame, the stator flux orientation technique known also as vector control. In this technique the direct component of the stator flux must be aligned with the real axis, thus leads to $\varphi_s = \varphi_{sd}$ and $\varphi_{sq} = 0.$ Rotor field orientation can be used. In this case the direct component of the rotor flux must be aligned the real axis, in consequence $\varphi_r = \varphi_{rdd}$ and $\varphi_{rq} = 0.$ The rotor angular vectory can be estimated as:

$$\omega_r = \frac{r_r}{m}\left(\frac{\sigma - 1}{\sigma}\right)\frac{\varphi_{sq}}{\varphi_r} \tag{12}$$

and the torque (9), becomes:

$$T_e = \frac{p}{m}\left(\frac{1-\sigma}{\sigma}\right)\varphi_{sq}\varphi_r \tag{13}$$

If the rotor fixed reference frame is used one has to substitute,in relation technique can be to reduce significantly the model. In this case the torque becomes proportional to the stator flux component since the rotor flux takes its maximum value as in relation (13). The decoupling between the stator and the rotor components is then obtained and the induction motor model becomes linear if the rotor angular velocity is assumed to be slowly varying or constant. The stator field orientation technique can also be used. In this case the rotor angular velocity can be estimated as:

$$\omega_r = \frac{r_s}{m}\left(\frac{\sigma - 1}{\sigma}\right)\frac{\varphi_{sq}}{\varphi_s} \tag{14}$$

and the torque relation becomes:

$$T_e = \frac{p}{m}\left(\frac{1-\sigma}{\sigma}\right)\varphi_{rq}\varphi_s \tag{15}$$

In the above both cases, the stator flux measurements are very helpful to design a rotor flux controlled system. The others state variables (i. e), the current state variable, The torque and the speed are then estimated via the relation (8) to (10) based on the measurements of the stator flux linkage vector. The drawback of this model is that the flux sensor is not accepted in industrial environment due to robustness and reliability problems. On the other hand, the flux sensor is not available. This problem can be solved by the use of an observer – based state variable estimation technique. A general observer – based state estimator is investigated for sensorless control and monitoring purposes I the third model.

B. Stator current and rotor current as selected variables

The second case consists of selecting stator and rotor current as variables. By a simple derivation of the second equation, relation (2), with the help of the matrix inversion lemma one obtains the following current state space model of the induction motor system.

$$\frac{d}{dt}\begin{pmatrix} i_s \\ i_r \end{pmatrix} = \left[L_M^{-1}(\Omega L_M - R)\right]\begin{pmatrix} i_s \\ i_r \end{pmatrix} + L_M^{-1}\begin{bmatrix} I_2 \\ 0_2 \end{bmatrix} u_s \tag{16}$$

$$\frac{d\omega_r}{dt} = \frac{1}{J}\frac{p}{2}(T_e - T_l) \tag{17}$$

$$T_e = pm_s^T i \begin{bmatrix} 0 & -1 \\ 1 & 0 \end{bmatrix} i_r \tag{18}$$

$$\begin{pmatrix} \varphi_s \\ \varphi_r \end{pmatrix} = L_M \begin{pmatrix} i_s \\ i_r \end{pmatrix} \tag{19}$$

In this case of model the system evolution matrix is $\left[L_M^{-1}(\Omega L_M - R)\right]$ and the system control matrix became:

$$L_M^{-1}\begin{bmatrix} I_2 \\ 0 \end{bmatrix} = \frac{1}{\sigma l_s l_r}\begin{bmatrix} L_r \\ -M \end{bmatrix} \tag{20}$$

The objective of the current state space model is to estimate the rotor current based on the stator current measurements. The rotor current is generally employed in procedures concerned with the condition based system maintenance and monitoring. In this case of application the stator current measurements are very helpful. The stator current must be exploited for this purpose since the control loop of major control drives incorporates a current loop. Reduced order current observer – based techniques can be used for monitoring purposes via the measurement of the stator current.

In the stator reference frame and with the help of stator field orientation technique the torque equation is reduced to:

$$T_e = p\varphi_{ds} i_{qs} \tag{21}$$

and the model order is then reduced since there exists a linear relation between the stator and rotor current components. Similar relations can be obtained in the rotor reference frame, with rotor field orientation technique.

The rotor angular velocity is estimated, with respect to the stator orientation hypothesis, by the following relation:

$$\omega_{isq} = -\left(\frac{d}{dt} + \frac{1}{\sigma\tau_s}\right) i_{sd} - \frac{r_r}{m}\frac{1-\sigma}{\sigma} i_{rd} - \frac{1}{\sigma l_s} u_{sd} \tag{22}$$

C. Stator current and stator flux as selected state variables

The third cases consist of stator current and flux as selected state. The method consists of eliminating the rotor current and flux state variables from equation (1) and (2). The induction motor is then:

$$\frac{d}{dt}\begin{pmatrix} i_s \\ \varphi_s \end{pmatrix} = \begin{bmatrix} a_{11} & a_{12} \\ -R_s & \Omega_a \end{bmatrix} \begin{pmatrix} i_s \\ \varphi_s \end{pmatrix} + \begin{bmatrix} b_{11} \\ I_2 \end{bmatrix} u_s \tag{23}$$

$$\frac{d\omega_r}{dt} = \frac{1}{J}\frac{p}{2}(T_e - T_l) \tag{24}$$

$$T_e = p i_s^T \begin{bmatrix} 0 & -1 \\ 1 & 0 \end{bmatrix} \varphi_s \tag{25}$$

$$\begin{pmatrix} i_r \\ \varphi_r \end{pmatrix} = \begin{bmatrix} -M^{-1}L_s & M^{-1} \\ (M - L_r M^{-1} L_s) & L_r M^{-1} \end{bmatrix} \begin{pmatrix} i_s \\ \varphi_s \end{pmatrix} \tag{26}$$

The evolution matrix parameters are:

$$a_{11} = \Omega_{ar} + (M - L_r M^{-1} L_s)^{-1}(R_r M^{-1} L_s + L_r M^{-1} R_s)$$
$$a_{12} = (M - L_r M^{-1} L_s)^{-1}\left[(\Omega_a L_r - R_r) M^{-1} - L_r M^{-1} \Omega_a\right]$$
$$a_{21} = -R_s, \qquad a_{22} = \Omega_a,$$
$$and\ b_{11} = -(M - L_r M^{-1} L_s)^{-1} L_r M^{-1}$$

The choice of the stator fixed reference frame and the stator field orientation technique are, in this case, imposed by the structure of the state space model of the induction motor. The model is linear at low speed operating and nonlinear at high speed operating. The advantage of this model is that it directly estimates the stator current using an open – loop as well as a closed – loop technique. The closed - loop technique uses a stator flux observer. Thus leads to say that control with stator field orientation is preferred in combination with the stator model. In this case torque relation becomes:

$$T_e = p i_{sq} \varphi_s \tag{27}$$

The rotor angular velocity is estimated with the respect to the stator orientation hypothesis, by the following relation:

$$\omega_r = \frac{1}{i_{sq}}\left[\frac{d}{dt} + \frac{1}{\sigma}\left(\frac{r_s}{l_s} + \frac{r_r}{l_r}\right)\right] i_{sd} + \frac{r_r}{\sigma l_s l_r}\frac{\varphi_{sd}}{i_{sq}} + \frac{1}{\sigma l_s}\frac{u_{sd}}{i_{sq}} \tag{28}$$

The resulting dynamic structure of the induction motor then significantly simplifies. However the rotor angular velocity depends on the stator and the rotor resistance which can be considered as time – varying parameters for high speed operating. The stator resistance or the rotor resistance can be estimated at the same time that the rotor angular velocity by using nonlinear estimation techniques. If the full stator current – flux state variable vector is not measured a reduced order observer can be then used for estimating the stator flux state variable based on the stator current measurements. Design of a stator flux controller or a stator flux – based induction motor monitoring is then possible by introducing some operating assumptions.

C. Stator current and rotor flux as selected state variable

The forth case consists of selecting the stator current and rotor flux as state variables. In this case the model becomes:

$$\frac{d}{dt}\begin{pmatrix} i_s \\ \varphi_r \end{pmatrix} = \begin{bmatrix} a_{11} & a_{12} \\ a_{21} & a_{22} \end{bmatrix} \begin{pmatrix} i_s \\ \varphi_r \end{pmatrix} + \begin{bmatrix} b_0 \\ 0_2 \end{bmatrix} u_s \tag{29}$$

$$\frac{d\omega_r}{dt} = \frac{1}{J}\frac{p}{2}(T_e - T_l) \tag{30}$$

$$T_e = p\frac{m}{l_r} i_s^T \begin{bmatrix} 0 & -1 \\ 1 & 0 \end{bmatrix} \varphi_r \tag{31}$$

$$\begin{pmatrix} i_r \\ \varphi_s \end{pmatrix} = \begin{bmatrix} -M^{-1}L_s & M^{-1} \\ (M - L_r M^{-1} L_s) & L_r M^{-1} \end{bmatrix} \begin{pmatrix} i_s \\ \varphi \end{pmatrix} \tag{32}$$

The evolution matrix parameters are:

$$a_{11} = (L_s - M\ L_r^{-1}M)^{-1}(R_s + ML_r^{-1}a_{11})$$
$$a_{12} = (L_s - ML_r^{-1}M)^{-1}(\Omega_a + ML_r^{-1}a_{22})$$
$$a_{21} = R_r L_r^{-1}M - \Omega_{ar}(L_s - ML_r^{-1}M)$$
$$a_{22} = (\Omega_{ar}M - R_r)L_r^{-1}$$
$$b_0 = (L_s - ML_r^{-1}M)^{-1}$$

The objective of this model is estimated by the rotor flux linkage state variable based on the stator current measurement using an observer – based technique. Once the rotor flux is estimated one can estimate the other state variables or the

mechanical variables mainly the rotor angular velocity and the torque. The stator reference frame can be used for this pupose in addition with the rotor field orientation technique. The signals that can be exploited for speed estimation are the stator voltage, the measured stator current and estimated rotor flux as:

$$\omega_r = \frac{\sigma L_s}{\varphi_{rd}}\left(\frac{di_{sq}}{dt} + \left(\frac{r_s}{\sigma L_s} + \frac{r_r}{\sigma L_r}\frac{1-\sigma}{m}\right) i_{sq}\right) - \frac{u_{sq}}{\varphi_{rd}} \tag{33}$$

The torque equation becomes:

$$T_e = p\frac{m}{l_r} i_{sq}\varphi_{ed} \tag{34}$$

Stator field orientation technique can also be used. The model order reduces in consequence and the induction motor system being only defined by the rotor model and the mecanical subsystem.

The choice of a model structure depends on the problem at hand. The fact that most drive systems have a stator current control loop incorporeted in thier control structure leads to select the stator current as the first state variable.

The second state variable is then either the stator flux linkage vector, the rotor flux linkage vector or the rotor current. The second state variable is estimated by using a closed – loop observer – based technique. In each case, the not selected state variables are then indirectly estimated based on the measured and the directly estimated state variables. Observer – based state estimation techniques are very helpful for closed – loop sensorless control application or for system monitoring. Linear models are obtained by considering the assumption that te mechanical velocity is slowty varying or constant and the parameters of the model are not time – varying. The first assumption is justified by the fact that electrical dynamics are in their turn very fast than the mechanical dynamics. Nonlinear models take into account that must be included in the model as well as the stator or the rotor resistance variation. The variation of the stator (the rotor) resistance can be modelled as a Gauss- Markov process. Other stochastic models can also be considered if the assumption of measurement noises is introduced.

3 Observer – Based State Estimation

In order to decrease the price of induction motor system and to increase its reliability, in consequence less maintenance requirements, ongoing research has concentrated on the minimization of the use of sensors without deteriorating the dynamic performance of the considered drive system. The devlopement of the estimation techniques and the availability of new low cost DSP- based (Digital Signal Processing) microcontrollers, have reinforced the industrial applications of this idea for sensorless control and monitoring purposes [2],[3].

The above models can be written in the following unified state space model:

$$\frac{dX(t)}{dt} = AX(t) + BU(t) \tag{35}$$

$$Y(t) = CX(t) \tag{36}$$

where $X(t)$ is the selected state variable vector and $Y(t)$ the measured output vector. A, B and C are the evolution, control and observation matrices respectively.

One of the most used technique for estimating the state variables of a system described in terms of state space model is observer technique. Observer – based state variables estimation uses an adaptive mechanical which involves as input, the error between the measured and estimated state variable values. The general from of the observer is [6],[7]:

$$\frac{d\hat{X}(t)}{dt} = A\hat{X}(t) + BU(t) + G[Y(t) - \hat{Y}(t)] \tag{37}$$

$$\hat{Y}(t) = C\hat{X}(t) \tag{38}$$

where $\hat{X}(t)$ is the estimated state variable vector of the unknown state variable vector $X(t)$ and $\hat{Y}(t)$ are the estimated output of the measured output signal $Y(t)$.

G is the observer gain matrix. It is constant if the observer system is linear varying if the observed system is nonlinear. Relation (37) and (38) can be written as:

$$\frac{d\hat{X}(t)}{dt} = [A - GC]\hat{X}(t) + BU(t) + GY(t) \tag{39}$$

This relation shows that the observer is a system in which the inputs are and the output of the system to be observed and the output is the estimsted state variable vector of the observer system. The dynamics the observer are determined by the eighen values of the evolution matrix $[A - GC]$. A practical choice of the gain matrix is based on the fact that the observer must be dynamically faster than the induction motor system. Thus not only assure stability of the observer but also to get an optimally filtered estimation in respect with the measurment and the eventual input noice. Pole placement technique is generally used in this case [7]. The error vector computed from the measured state variable and the observer estimated stat variable $\tilde{X}(t) = X(t) - \hat{X}(t)$ is not only used to generate the sensorless control law but also to monitor the operating condition of the induction motor drive system. The monitoring procedure is based on the analysis of the state variable estimation error and the covariance matrix of the error dynamics

computed from the difference between the dynamics of the induction motor system, relation (35), and the dynamics of the observer, relation(37), as:

$$\frac{d\tilde{X}(t)}{dt} = [A - GC]\tilde{X}(t) \tag{40}$$

The aim of a monitoring system is to control the main function of the considered system and to compare measured values of certain parameters or state variables with their preset values.

In the order case of a complete machine model including the mechanical subsystem a nonlinear observer technique must be applied since the obtained model is nonlinear. In this case the observer gain matrix depends on the rotor angular velocity.

In order to take into account the noise of the measured signals and the model parameter deviations nonlinear Kalman filtring technique must be used for estimating the selected state variables as well as the rotor angular velocity and the rotor (stator) resistance. Nonlinear techniques are generally avoided due to the high computational load required [6],[7].

4 Numerical Simulation

To highlight the performances of the technique of monitoring suggested we consider an engine with induction having the following characteristics:

$$f_r = 50\,Hz,\ U = 220\,V,\ \omega_m = 146.6\,rd/s,\ r_s = 0.63\,\Omega,\ r_r = 0.4\,\Omega,\ l_s = 0.097\,H,\ l_r = 0.091\,H,$$
$$m = 0.091\ H,\ \sigma = 1 - \frac{m^2}{l_s l_r} = 0.0682,\ T_r = 0.2275,\ T_s = .0.1539,\ f = 1\,Ns/rd,\ J = 0.22\,kgm^2.$$

The digital model having for vector of state the stator current and rotor flow is given by: Simulation consists of the study of the dynamic properties of the asynchronous machine in the space of state by using software MATLAB to see the possibilities of detection without sensor.

It is enough to make recordings of the variables of state estimated of the operational engine (on the figure the healthy state is represented in (noir continue and the failing recording is in noir discontinue clair and noir discontinue pas clair) and to make a comparison with the results estimated in the event of failure by using the analysis of the curves of Lissajou or the spectral analysis. In these results represents of them only the results obtained by the analysis of the current and estimated flow, it remains also the possibility of analyzing other variable as the electromagnetic couple. Figure 09 watch the signature of dephasing on the curve of lissajou, this signature which enables us to easily determine nature of defect and well on touts results obtained and estimated to ensure a diagnosis without sensors or at least of sensors.

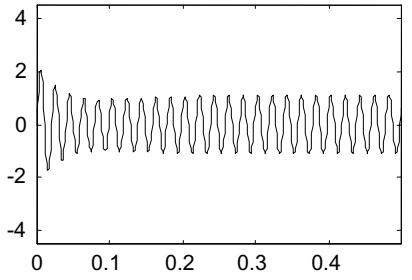

Fig. 1 Stator current isd

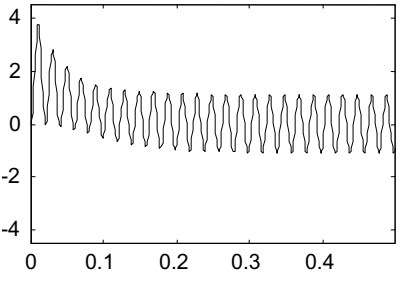

Fig. 2 Stator current isq

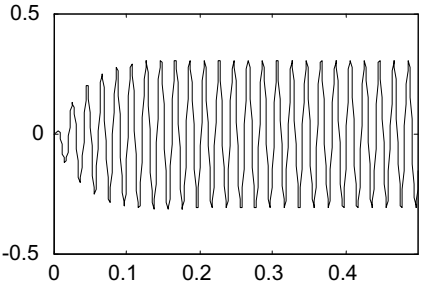

Fig. 3 Flow rotor fird

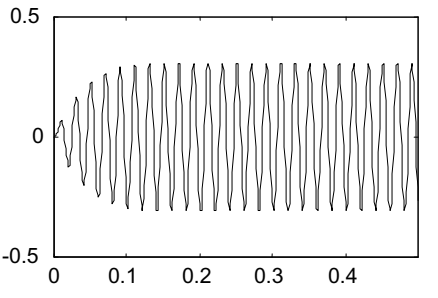

Fig. 4 Flow rotor firq

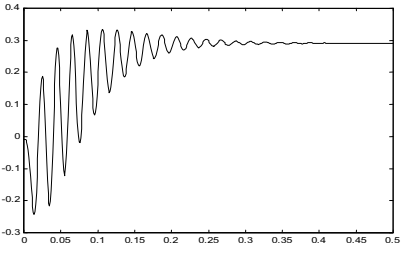

Fig. 5 Torque electromafgnetic

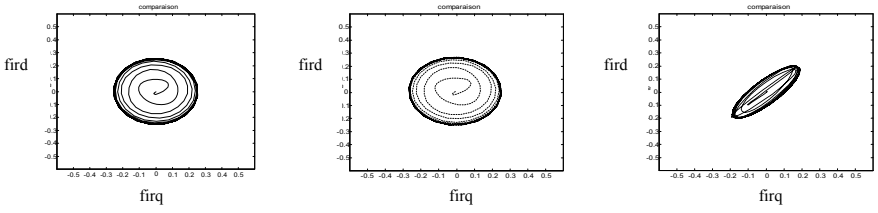

Fig. 6 Courbe de lissajou en régime complet

One little also to detect the rotor defects such as the break of the bars of the cage, figure 11 and 12 watch suonr a curve of lissajou the signature of this break (reduction in the intensity), here uses the estimated currents of them. Also, the defects stator can be detected by the same technique, here one has one on intensity. In little also to make an analysis spectral after the transform of furrier of each vector of state, which gives the spectrum in the healthy and failing case.

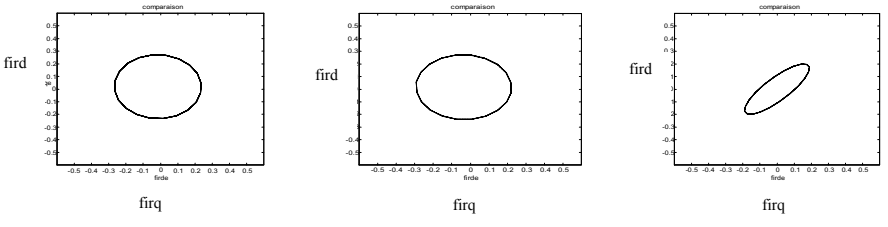

Fig. 7 Courbe de lissajou en régime permanent

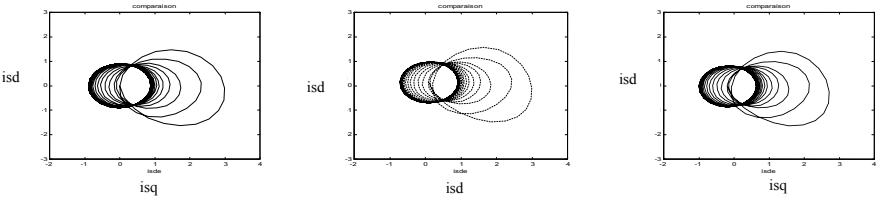

Fig. 8 Courbe de lissajou en régime permanent +5% R_r

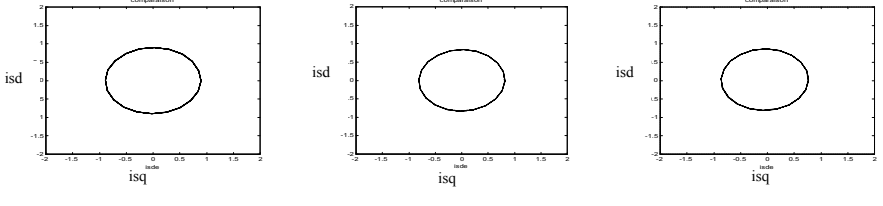

Fig. 9 Courbe de lissajou en regime complet +5% R_r

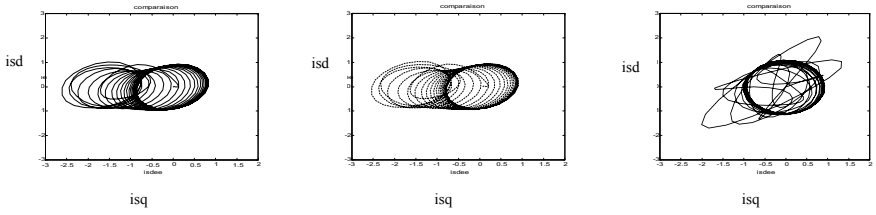

Fig. 9 Courbe de lissajou en regime complet-5% Rs

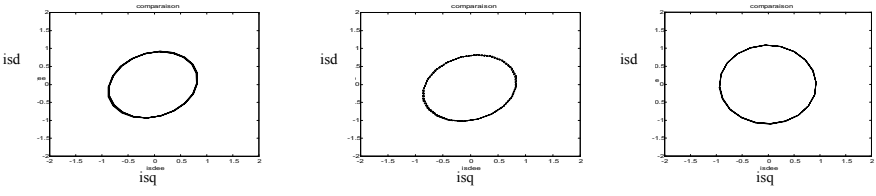

Fig. 10 Courbe de Lissajou en régime permanent -5% Rs

4 Conclusion

Finally we conclude that the state space technique is an efficient method for induction motor modelling, state variables estimating and induction motor drive monitoring. State space technique is directly used by the advanced control techniques such as the observer – based as well as the Kalman filtering.

This paper has investigated the state space modelling technique in order to implement a simultaneous observer – based sensorless control and monitoring induction motor driven systems.

References

[1] Holtz, J.: Sensorless control of induction motor drives. Proceeding of the IEEE 90(8), 1359–1394 (2002)

[2] Pana, T.: Speed sensorless induction drive system for direct driven electrical vehicle. In: Proceeding of 3rd Int. Symp. on Advanced Electromechanical Motion Systems, Partras Greece, pp. 829–834 (1999)

[3] Bodson, M., Chiasson, J.: A comparison of sensorless speed estimation methods for induction motor control. In: Proceeding of the American Control Conference, pp. 3076–3081 (2002)

[4] Wamkeue, R., Kamwa, I.: Generalized state space modelling of induction machines having multiple rotor circuits. In: Procceding of 3rd Int. Symp. on Advanced Electromechanical Motion Systems, Patras, Greece, pp. 61–66 (1999)

[5] Balan, H., Hedesiu, H., Timovan, R., Karaissus, P.: Electrical machines and equipment diagnosis using virtual instrumentation. In: Proceeding of 3rd Int. Symp. on Advanced Electromechanical Motion Systems, Patras, Greece, pp. 795–798 (1999)
[6] Maes, J., Melkbeek, J.: Improved adaptive flux observer for wide speed range sensorless induction motor drives. In: Proceeding of 3rd Int. Symp. on Advanced Electromechanical Motion Systems, Patras, Greece, pp. 379–384 (1999)
[7] Bostan, V., Cuibus, M., Ilas, C., Magureanu, R.: Comparison between Luenberger and Kalman observers for sensorless induction motor control. In: Proceeding of 3rd Int. Symp. on Advanced Electromechanical Motion Systems, Patras, Greece, pp. 335–340 (1999)

Some Remarks on Using Condition Monitoring for Spatially Distributed Mechanical System Belt Conveyor Network in Underground Mine – A Case Study

Pawel Stefaniak[1,2], Radoslaw Zimroz[1,2], Robert Krol[1], Justyna Gorniak-Zimroz[1], Walter Bartelmus[1,2], and Monika Hardygora[1]

[1] Institute of Mining Engineering
[2] Diagnostics and Vibro-Acoustics Science Laboratory,
Wroclaw University of Technology, Pl Teatralny 2, 50 051 Wroclaw, Poland
{pawel.stefaniak,radoslaw.zimroz,
robert.krol,justyna.gorniak-zimroz,
walter.bartelmus,monika.hardygora}@pwr.wroc.pl

Abstract. The paper deals with application of condition monitoring and information system to maintain of complex, spatially distributed machinery system, namely belt conveyor transportation network, which consists of hundreds of drive units located on mine territory. There is simple question: what managers/engineers should do to ensure safe and efficient work of transportation machines? It has appeared that number of objects, their spatial location, specific structure of mining company, harsh environment, diversity of machines etc make this problem really complicated. It is obvious that there is a need to use specialized equipment, software but first of all set of procedures of data acquisition, validation, processing, storage, visualization, decision making, reporting etc, so in other words maintenance management. All these stages, combined and implemented as maintenance management software called Diag Manager (CMMS class) is discussed here.

Keywords: maintenance, data bases, temporal GIS, analysis, information, data mining.

1 Introduction

Diagnosis of machines using vibration signals is very popular and many papers may be found in the literature. However, most of them concern new detection techniques using simulation/test rig data, rest of them is discussing application to real problems (in some cases even complex mechanical system). The issue discussed here is focused on completely different problem. Let's assume that we already have very powerful techniques for damage detection and diagnosis (Bartelmus2009,2006 Kruse 2006, Zimroz 2008,2010) and we want to apply them

to industrial problems, however, the difference is that “problems” here means not one machine (even complex one…) but hundreds of machines. To localize / visualize problem see example of such object shown on Fig 1. One can recognize two layers: in grey colour – map (structure) of mine with room and pillar technology and in colours elements of production lines.

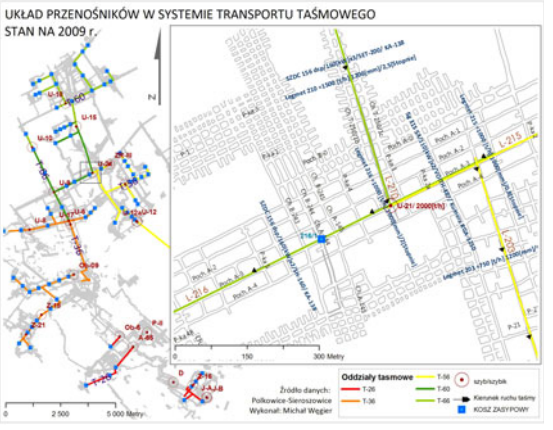

Fig. 1 Scheme o Belt Conveyor Network (BCN) for one mine

Drive units used in transportation network in general consist of electric motor, coupling, gearbox and drive pulley. However, their design (type/power), load/speed, control system etc may be different for given conveyor – depending on its function in the system (main or local transportation road, required power etc). In practice it means that diagnostic procedures should be ready to manage with different reality (design, operation conditions, environmental impact, human factors etc…) for given task. One should be aware that most of these machines work in series and stop of any conveyor in such production line will stop whole conveyor line (frequent start stop events). It makes extra difficulties and influences operation of machines and degradation processes. All these issues may be critical for final maintenance management result. Maintenance in such a case means integration of availability time, failure engineering, damage detection, diagnostics etc. The only reasonable solution is maximizing of number of automatic procedures and using advanced information system for machinery maintenance.

2 Maintenance of BCN – Example of Large Scale Spatial Systems

Huge work has been done to understand what should be taken into account during BCN maintenance [Swinderman 2002, Lodewijks 2004 Overmeyer 2007, Hardygora 2009 Zimroz 2011]. We here discus part of the system associated with “

gearbox" module. For other conveyor components one may study for example (Mazurkiewicz 2007, Kacprzak 2011) It has been found that a lot of information should be included to make diagnosis (Bartelmus 2006). One should get basic information about: design of gearbox (a several types of gearboxes are used in analyzed system), other elements of drive units (electric motor, coupling, speed control system), operating condition (exact value of load/speed condition, its nature, i.e. stationary, start up, some fluctuation, etc) and multidimensional set of diagnostic parameters (a few for each element of multistage gearbox). Obviously decision making should be automatic, without of any manual help of maintenance staff. Some information regarding failures analysis would be also helpful during decision making.

Such formula of maintenance requires automated computer aided decision making and database system to store, to maintain and to process data (Gorniak-Zimroz 2009). We deal with a spatial structure (conveyor network) and due to the fact that conveyors are in series, one may expect some interdependencies between conveyors.

These assumptions were a basis for information system platform selection. Natural solution for spatial data is Geographic Information System. Such class of information systems may store descriptive attributes (numbers, strings, logical values, etc), images, and spatial data related to location of objects. More information about GIS system, and its application to belt conveyor maintenance one may find in [Gorniak-Zimroz 2009]. In this paper, we would like emphasize that to build a data base system is not enough (it will not bring the expected profit), there is a need to provide very advanced data analysis algorithm for diagnostic data validation, classification (Cempel 2007, Bartelmus 2009a,b, Jablonski 2011,. Bartkowiak 2011, 2012) and searching the link between obtained clusters and condition of gearboxes, i.e. their diagnosis, reporting tools and other data base maintenance procedures.

3 Data Acquisition

Continuous transportation systems in mining company consists of network of conveyors. The purpose of this section is to provide brief description of conveyor and its drive unit. Fig 2 shows key elements of conveyor. From this work point of view crucial element is drive unit that may consist of 1-4 drive sets (motor, coupling, 2 or 3 stage gearbox and pulley.

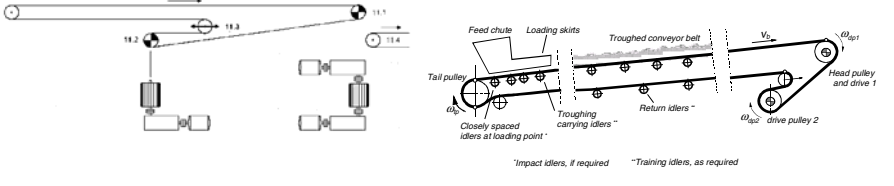

Fig. 2 Structure of belt conveyor.

Load of drive unit depends on material stream transported on the belt. It is easy to understand that there is a need to use multi-channel data acquisition system for measuring vibration and load/speed indicators

Failure Analysis Module

To minimize cost of maintenance, especially at the initiation phase, it was suggested to take advantage from failure analysis. By acquiring information about replacement events, their cost, time etc it is possible to select the most important, the most critical element that brings majority of looses. Fig 3 shows simple data base form that should be simply fill up when replacement event takes place.

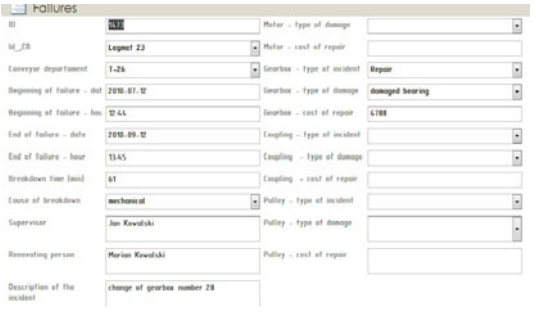

Fig. 3 User interface of module for failure analysis

Diagnostic Data Module

Due to number of drive units it was suggested to use portable data acquisition system that can simple measure, process and diagnose machine in quick time based on 120s vibration time series and speed profile. Fig 4 shows the idea of measurement (location of sensors) and main window for portable diagnostic system developed for such purpose.

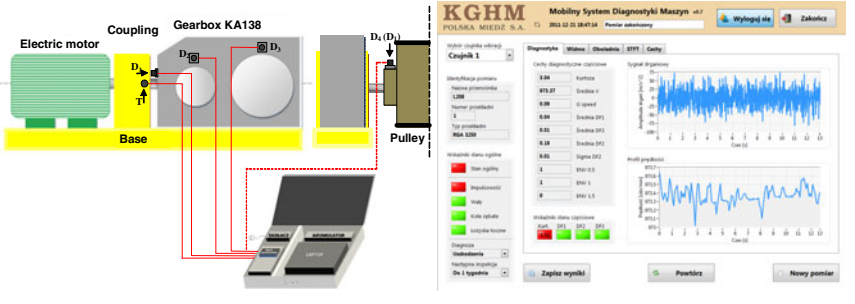

Fig. 4 An idea of measuring diagnostic signals for fault detection and diagnosis, main window for portable diagnostic system

Other Sources

It has appeared that mining company uses other systems for data/information acquisition, but they are used by different departments and information not integrated/fused). Such situation is very frequent in many companies, however structure of mining company, Mining Law etc makes this problem really serious.

However, it was possible to get some data from Enterprise Resource Planning (ERP) systems (cost of replacement) and from Supervisory Control and Data Acquisition (SCADA) systems (loading, downtime) already installed in the mine. All these information can be included in proposed Diag Manager system

2 Diag Manager – CMMS-Class Software for Conveyor Maintenance Management

Maintenance management often is supported by information systems. For Conveyor Maintenance Management it is proposed here to use Geographic Information System that contain different type of data (numeric, text, pictures, maps) related to aspects mentioned in previous sections. It is data based system supported by WEB environment (it is possible to explore data base via Internet browser). Structure of proposed information system is shown in Fig 5, In Fig 6 Main Window of Diag Manager software is presented.

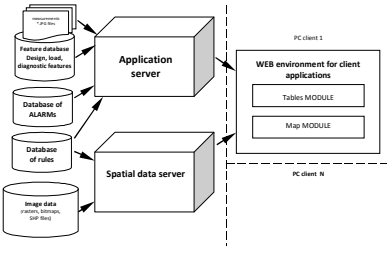

Fig. 5 Scheme of information system

Fig 6 Main Window of Diag Manager (right: table with decisions in colours, text/numeric data, right: scheme of transportation system referenced to map of the mine, bottom – examples of signal proc. results and photo for decision validation

3 Example of Results

Basic Analysis

From practical point of view, due to reporting policy in the mine, the most important are simple reports that should be prepared every month to manager of given department. It covers for example failure analysis, its cost, breakdown time and so on. The Diag Manager system allows to provide such reports thanks to the failure analysis module discussed above (see Fig. 7, 8).

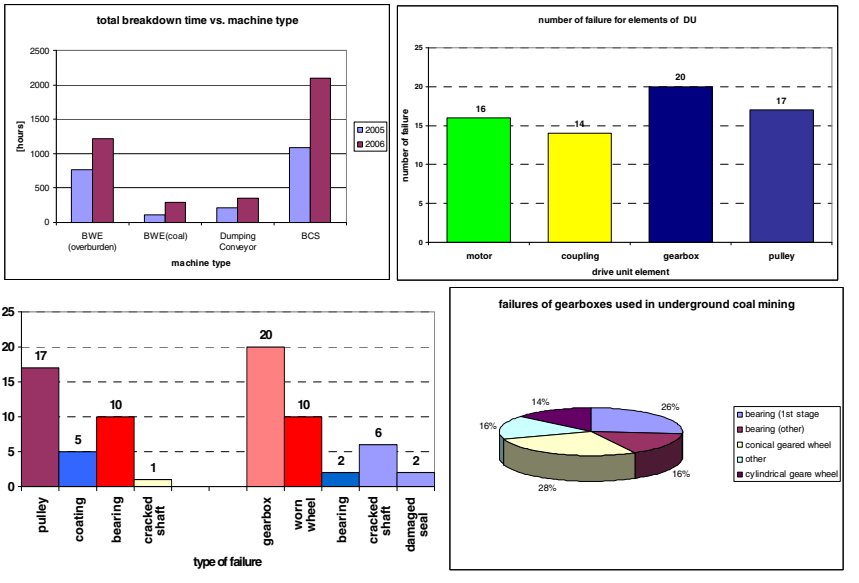

Fig. 7 Failure analysis for mining machines: a)Comparison of breakdown time for different machines (one mine), b) Number of failures related to elements of drive unit (motor-coupling-gearbox-pulley) c)The number of failures related to Driving Units elements with respect to type of type of event (motor and coupling), d) failures of gearboxes used in underground coal mining

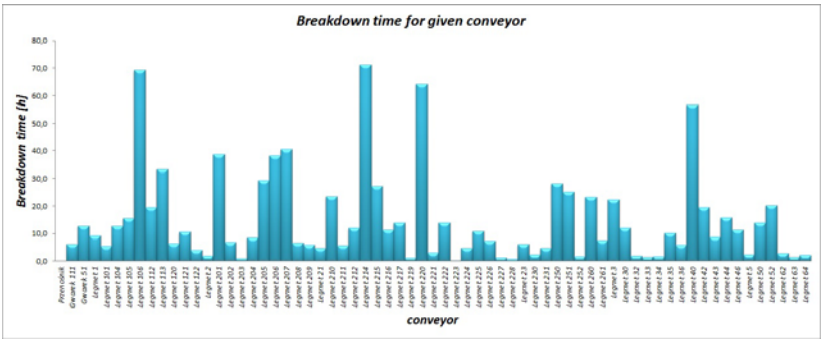

Fig. 8 Breakdown time for given conveyor for analyzed period of time.

Advanced Analysis

As it was proposed by Cempel (Cempel 2007), it is interesting to use multidimensional analysis for machine in non-stationary operations. There are many important issues in industrial application starting from data validation/selection, dimensionality reduction, classification, especially in unsupervised case (see Fig 9). It was said that transportation network consist of many types of machines. It is required to find thresholds (bad –good data separation value(s)) for every type of machine. Usually it is done during so called training process when data for good and bad condition are analyzed and relation between feature value and real condition of machine is examined (see fig 10left). Unfortunately, for some unique machines, there is no bad condition example, so there is a need to exploit so called one class classification (see Fig 10 right and Bartkowiak2011).

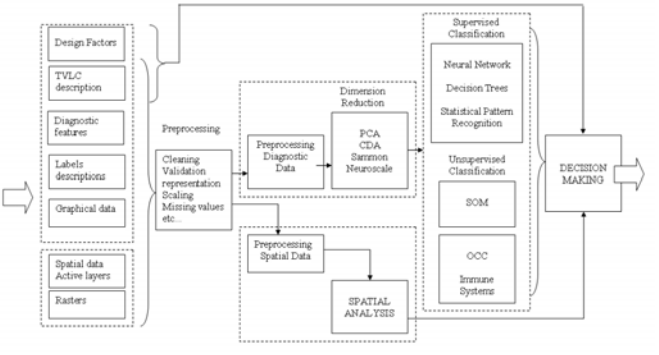

Fig. 9 The idea of maintenance system with advanced data analysis module

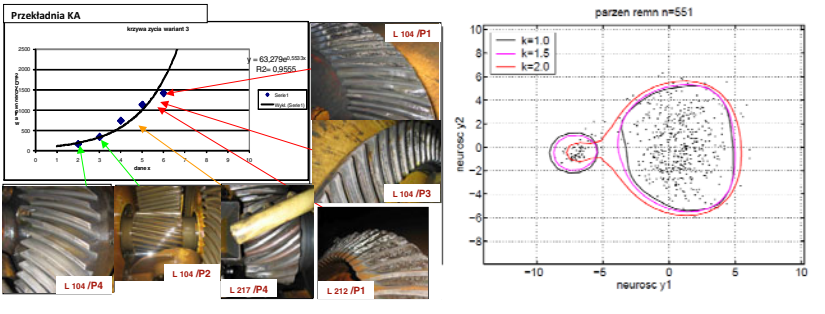

Fig. 10 Decision boundaries discovery: left – supervised case, right- OCC (see Bartkowiak&Zimroz 2011)

Spatial Analysis

Thanks to integration data from different sources (i.e. technical documentation) with thematic map, layers with individual elements of conveyors, it is possible to do complex, spatial analysis. The spatial analysis allow to study relationships and regularity between input data taking account of their attitude. The so called geo-processing (processing of spatial data related with their attributes data) generates new information which can be very important in the diagnostic and maintenance procedures. On the other hand, very advanced functionality of geo-informatics tools (i.e. tools of classification of data or presentation data, functions of quantities, charts or multiples attributes) allow to present output data of geo-processing in very clear form of presentation based on layout views such as: maps, graphs, reports, schemas etc. This can be very useful in processes of diagnostic conclusion. What's more very interesting are geo-statistical analyst tools which provides functions of (a) explore data such as: Histogram, Normal QQPlot, Trend Analysis, Voronoi Map, Semivariogram/Covawiance Cloud, General QQPlot, Crossvsariance Cloud and (b) geostatistical wizard connected with interpolation methods.

Analysis may relate both: failure analysis results, diagnostic data and other data such as data from measurements of temperature or humidity and so on. Following figures presented examples of maps generated based on discusses analysis. These

Fig. 11 Results of spatial visualization: Left: Spatial location of breakdown time individual conveyor belt of analyzed area of study in period January-August 2009. Right: Loss of transported ore for analyzed period of time.

selected examples concern: stops of mechanical system (Fig 11 left), value of loss of transported ore (Fig 11 right). Following figures show spatial distribution of temperature (Fig 12 left) and humidity (Fig 12 right) - they are estimated based on data with known values from hypothetical measurement points.

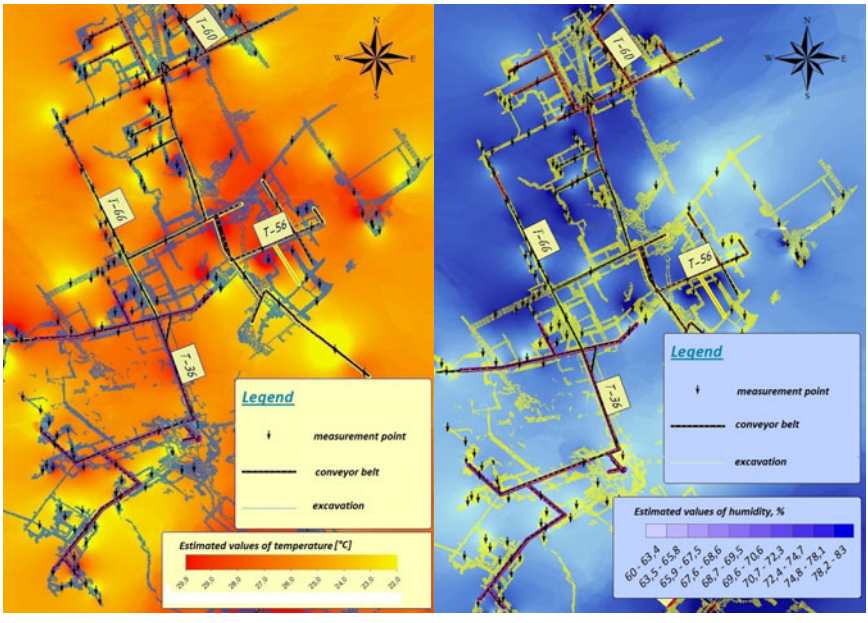

Fig. 12 Example of spatial analysis: Left Estimated values of temperature calculated based on interpolation method (IDW - Inverse Distance Weighted). Right Thematic map layers presented values of humidity in boundary of analyzed area.

5 Conclusion

An application of GIS information system and Data Mining techniques used for data stored in GIS have been discussed in the paper. We claim that for large scale spatial mechanical systems as conveyor network, selection of GIS data base is a good way. For hundreds object that should be diagnosed, in our data base we got a lot of data from different sources (SCADA systems, technical documentation, monitoring systems etc) and different structures. In order to extract diagnostic information we need advanced data analysis techniques and finally, when different information are fused (Data Fusion), one may got correct answer regarding diagnosis. Such a way may give information about machine condition, and it can be interpreted/validated using information stored in data base.

Our system is dedicated, optimized according to users expectation. From user' point of view it is very simple, however, as it was described in the paper, many advanced solutions have been implemented to get the final results (i.e. adaptive diagnostics including signal processing, feature extraction decision making, webGIS data base system etc.). The Diag Manager has been successfully deployed in the underground copper ore mine.

References

Bartelmus, W.: Monitoring, diagnostics, investigations of belt conveyors | [Monitorowanie, diagnostyka, badania przenośników taśmowych] Prace Naukowe Instytutu Gornictwa Politechniki Wroclawskiej 83, 23–32 (1998)

Bartelmus, W.: Condition monitoring of open cast mining machinery. Oficyna Wydawnicza Politechniki Wrocławskiej (2006)

Kruse, D.: Data acquisition techniques and measurement equipment for belt conveyors Bulk Solids Handling, vol. 26(2), pp. 116–122 (2006)

Zimroz, R.: Adaptive approaches for condition monitoring of mining machines. Gospodarka Surowcami Mineralnymi-Mineral Resources Management 24(4),103-116 (2008)

Swinderman, R.T., Tenzer, M.: Opportunities for improving conveying in lignite mines Prace Naukowe Instytutu Gornictwa Politechniki Wroclawskiej 98(34), 455-459 (2002)

Lodewijks, G.: Strategies for Automated Maintenance of Belt Conveyor Systems Bulk Solids Handling 24(1), pp. 16–22 (2004)

Overmeyer, L., Stock, A., Wennekamp, T.: RFID-supported maintenance planning for conveyor belts. Bulk Solids Handling 27(3), 174–178 (2007)

Müller, D., Uhlemann, S.: Open-cast mine optimization - Maintenance | [Tagebauprozessoptimierung - Instandhaltung]. World of Mining - Surface and Underground 59(2), 106–109 (2007)

Hardygora, M., et al.: Maintenance, diagnostics and safety of belt conveyors in the operations. Transport & Logistics (Belgrade) 6, 351–354 (2009)

Zimroz, R., et al.: A maintenance strategy for drive units used in belt conveyors network. In: Eskikaya, Ş. (ed.) 22nd World Mining Congress & Expo., Istanbul, September 11-16, vol. 1, pp. 433–440 (2011)

Mazurkiewicz, D.: Computer system for monitoring conveyor belt joints. Canadian Mining Journal 128(4), 24 (2007)

Gorniak-Zimroz, J., et al.: Decision making system based on GIS technology for supporting machinery maintenance. In: Sobczyk, E.J., Kicki, J., Saluga, P. (eds.) Deep Mining Challenges, pp. 179–189. Taylor & Francis (2009)

Kacprzak, M., Kulinowski, P., Wędrychowicz, D.: Computerized information system used for management of mining belt conveyors operation. Maintenance and Reliability 2 Eksploatacja i Niezawodnosc 50(2), 81–93 (2011)

Cempel, C.Z., Tabaszewski, M.: Multidimensional condition monitoring of machines in non-stationary operation. Mechanical Systems and Signal Processing 21(3), 1233–1241 (2007)

Bartelmus, W., Zimroz, R.: A new feature for monitoring the condition of gearboxes in non-stationary operating conditions. Mechanical Systems and Signal Processing 23, 1528–1534 (2009)

Bartelmus, W., Zimroz, R.: Vibration condition monitoring of planetary gearbox under varying external load. Mechanical Systems and Signal Processing 23, 246–257 (2009)

Bartkowiak, A., Zimroz, R.: Data dimension reduction and visualization of multidimensional data with application to gearbox diagnostics data: comparison of several methods. Solid State Phenomena 180, 177–184 (2012)

Bartkowiak, A., Zimroz, R.: Outliers analysis and one class classification approach for planetary gearbox diagnosis. J. Phys. Conf. Ser. 305, 012031

Jabłoński, A., Barszcz, T., Bielecka, M.: Automatic validation of vibration signals in wind farm distributed monitoring systems. Measurement: Journal of the International Measurement Confederation 44(10), 1954–1967 (2011)

Statistical Data Processing for Wind Turbine Generator Bearing Diagnostics

Radoslaw Zimroz[1], Walter Bartelmus[1],
Tomasz Barszcz[2], and Jacek Urbanek[2]

[1] Diagnostics and Vibro-Acoustics Science Laboratory,
Wroclaw University of Technology, Pl Teatralny 2, 50 051 Wroclaw, Poland
{radoslaw.zimroz,walter.bartelmus}@pwr.wroc.pl
[2] AGH University of Science and Technology 30-059 Kraków, Poland
{tbarszcz,urbanek}@agh.edu.pl

Abstract. Condition Monitoring of bearings used in Wind Turbines (WT) is an important issue and due to wide range of the operating conditions variations should be monitored online. Due to mentioned non-stationary load/speed conditions, signal processing and decision making for bearings diagnostics is still challenging issue. As a data source a professional monitoring system is used. Two kind of information have been acquired: RMS of vibration acceleration signal and generator power that is related to the operating conditions. The received data cover the period of several months, when the bearing has changed its condition significantly. Due to considerable variability of the mentioned data, an embedded decision making regarding the condition of bearings is difficult. The novel method proposed in the paper is based on statistical feature processing instead of just simple comparison of the value of the feature with threshold that is used in the system. Statistical data processing is done in two dimensional feature-load space in several sub-ranges of operating conditions. It has been found that for different load ranges behavior of data and effectiveness of bad-good data separation ability is different. Decomposition of data in several load sub-ranges has provided better recognition efficiency than for all data taken together.

Keywords: wind turbine, generator bearing, vibration analysis, diagnosis, non-stationary operation, load dependent processing.

1 Introduction

Wind turbines become widely used for the electric power generation and they are also frequently considered as an interesting object from condition monitoring perspective [1-9]. Indeed, it can be considered as compound and complex [10] mechanical system working in time varying conditions that classify the problem of diagnostics as a difficult one. The term complex in [10] is referred to a planetary gearbox. The planetary gearbox may be properly reduced to treat it as an element

of the compound gearbox. In this considered case the drive system of the generator is a multistage transmission system: planetary gearbox plus two-stage parallel gearbox. The system gives a multiplication of a rotor rotation to give the rotation of the generator. Time varying operating conditions are related to non-stationary wind behavior [11] that plays an important role and may be modeled as time varying excitation of the system. So, extracted feature are load dependent, and statistical data processing via time varying probability density functions analysis is not efficient. It has been proposed in [12-14] to use feature-load representation in order to extract distribution of features vs. operating conditions that gives better efficiency in classification than simple statistical feature processing. In this paper we propose further extension of such approach. It has been found that for different load ranges behavior of data and effectiveness of bad-good data separation ability is different. Decomposition of data in several load sub-ranges has provided better recognition efficiency than for all data taken together.

It should be clarified that, in general, one may easily find several interesting papers on bearings diagnostics using envelope analysis, wavelets, adaptive filters, exploiting cyclostationarity of vibration [15-20] etc. However, our idea was to use diagnostic data provided by the online monitoring system, not raw vibration signal so usage of such method is not possible. Using raw signals one needs to build advanced feature extracting module in online version that would be rather expensive. For offline processing it is not so problematic and as it was mentioned some techniques for multidimensional features extraction and further processing using, for example, SVD can be used. Some recent works [21-24] developed for similar problems shows ability of multidimensional data processing using Principal Component Analysis, data projection techniques, outliers analysis etc. However, it should be noted that in practical situation validation of data seems to be serious problem [25] so increasing of system complexity is not good idea.

2 Wind Turbine – Design, Operation and Data Stream Description

Fig.1 presents a typical layout of a wind turbine. The main rotor with three blades is supported by the main bearing and transmits the torque to the planetary gear. Second bearing supported the rotor is incorporated into the gearbox. The planetary gear has three planets, which are driven by the planet carrier. The planets transmit the torque to the sun gear, in the same time increasing the rotational speed. The sun shaft is the output of the planetary gear and drives the two-stage parallel gear. The parallel gear has three shafts: the slow shaft connected to the sun shaft, the intermediate shaft and the high speed shaft, which drives the generator. The generator produces AC current of a varying frequency. This current is converted first into DC power and then into AC current of frequency equal to the grid frequency. Electric transformations are performed by the controller at the base of the tower. The gearbox set-up changes the rotational speed from about 25 rpm on the main rotor to about 1500 rpm at the generator. In the considered case a diagnosed object is a bearing in electric power generator of a wind turbine.

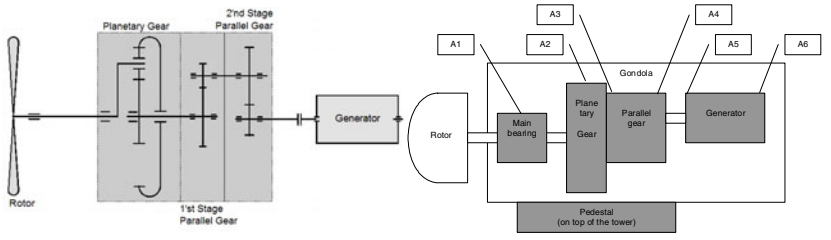

Fig. 1 Layout of a typical wind turbine and location of sensors (right)

Input data delivered from professional online monitoring system includes time series of peak to peak of vibration (P-P), RMS of vibration, instantaneous power of generator, wind speed, rotational velocity, kurtosis of vibration etc. In this work two data will be used: RMS value of vibration and power of generator. Data used in this paper are presented on Fig. 2 and 3 as data time series in monitoring system window, power variation and RMS long term trends, respectively. Data presented on Fig 2 and 3 have been exported from monitoring systems to Matlab workspace

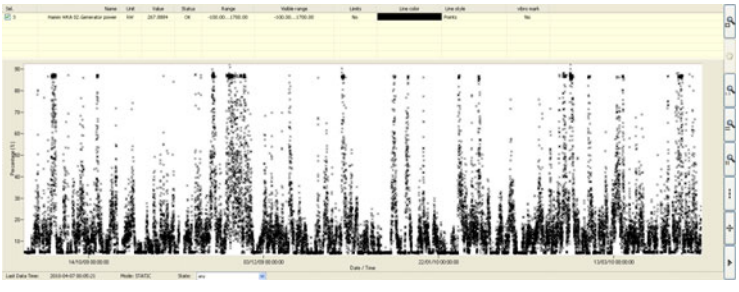

Fig. 2 Input data: generator power variation – a view from online monitoring system

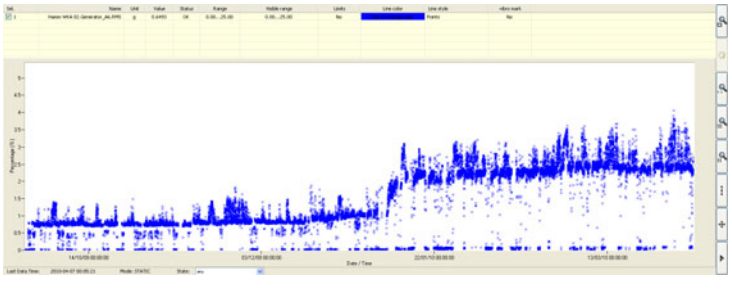

Fig. 3 Input data: long term trend of RMS of vibration data – a view from online monitoring system (RMS - percentage of visible range 0-5[g] vs. date from 14/10/09 to 13/03/10)

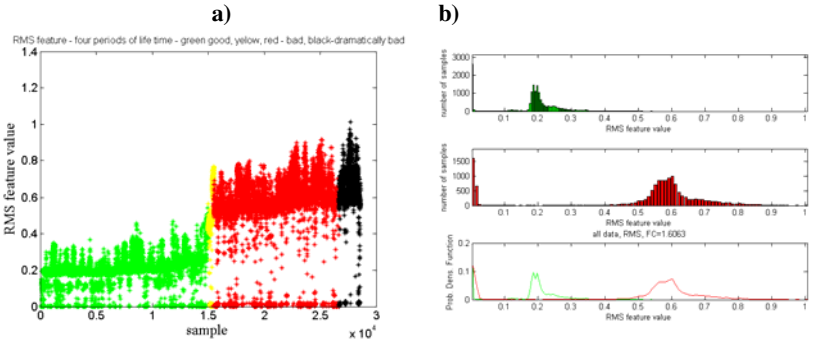

Fig. 4 a) Input data exported from online system and loaded to Matlab workspace with a priori pre-classification into 4 conditions (good, rapid change of condition, bad, very bad) b) Histograms for raw RMS data from the system: subplots are: top good condition, middle – bad condition, bottom – normalized histograms for two data sets on the same plot

and further processing has been done in Matlab environment. Some a-priori assumptions regarding feature-condition relationship have been used. Four periods of data are visible: green good condition, red bad condition, yellow – state between good and bad and finally black – very bad condition, Fig 4a. In the Fig 4b histograms obtained from good/bad data are presented. As it is clearly seen, there are some difficulties in the recognition of a bearing condition that is to separate data from good/bad data sets due to existing overlapping.

3 A Method of Data Processing

As it was mentioned the idea of data processing is to extend method proposed by the same team of authors, i.e. [12-13] to analyze data in feature-load space but in several load sub-ranges. The distribution of data vs. operating condition (power generator) is shown in Fig. 5a. The RMS data obtained from the system plotted as function of power (with colors assumed by authors) show measured value bit suspicious behavior for the lowest and the highest power, which at this stage we decided to reject them for further analysis. Fig 5b shows histograms for pre-selected ((features the lowest and the highest power are rejected) RMS data: subplots are: top good condition, middle – bad condition, bottom – normalized histograms on the same plot. It is easy to notice that such pre-filtering has improved efficiency of data clustering, but still there is an overlapping of data, see Fig 5b.

In this paper we will try to separate data from good/bad sets, but for some a priori pre-defined load range separately. It is easy to find that for some load ranges (Fig 5a) distance between green and red data clouds is different. We will use Fisher Criterion (FC) to compare effectiveness of classification [26]. So, the procedure is as follow:

- Plot features as function of operating conditions
- Divide load into sub-ranges (Lmax-Lmin)/N, where N is arbitrary integer value, Fig 6

- Calculate Fisher Criterion for each load sub-range
- Plot FC as function of load and compare with FC for raw data

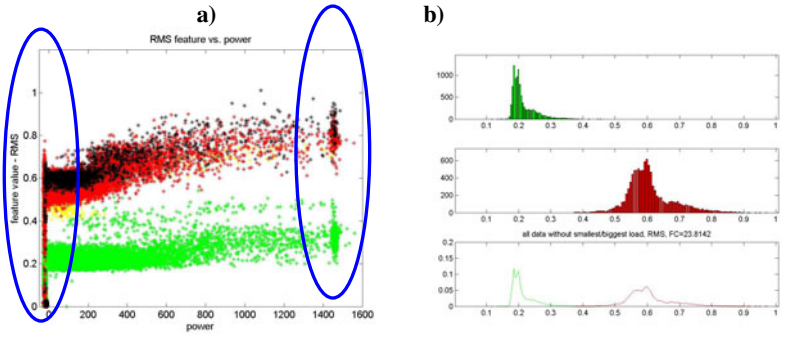

Fig. 5 a) RMS data from the system, but plotted as function of power (with colors from expert knowledge) b) Histograms for pre-selected ((features for the lowest and the highest power are rejected) RMS data: subplots are: top good condition, middle – bad condition, bottom – normalized histograms on the same plot

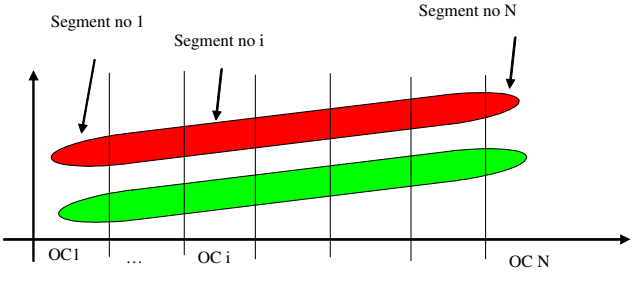

Fig. 6 The idea of novel approach

4 Results Wind Turbine Case study

Following the procedure defined in previous section data have been divided into 15 load ranges (every 100kW). Fig 7. shows data distribution in 15 subplots.

It is clear that separation ability for each subplot is different. To compare results, as an objective measure one may use Fisher Criterion [26]:

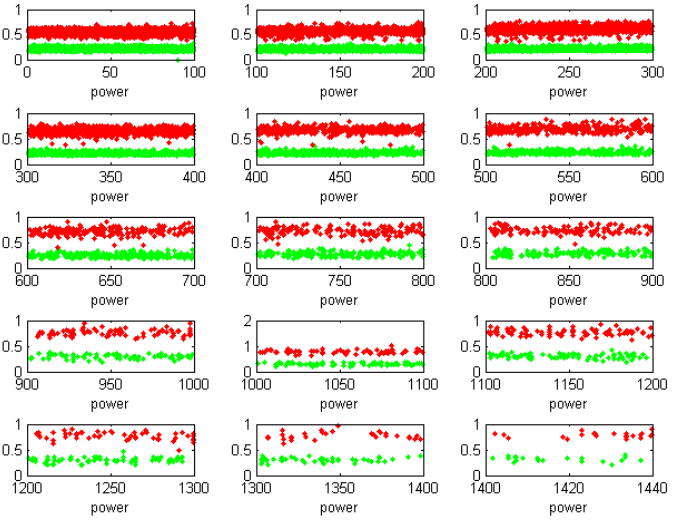

Fig. 7 Data distribution (RMS) in segments (power range 100kW)

$$FC = \frac{[m_1 - m_2]^2}{\sigma_1^{\,2} + \sigma_2^{\,2}}, \tag{1}$$

where:

m_1,σ_1^2 - denotes the mean and the variance of the first class data sample,

m_2,σ_2^2 - denotes the mean and the variance of the second class data sample respectively. Fig 8 shows probability density functions (PDFs) of good/bad data for each load sub-range separately. In a caption, for each plot, a value of FC is shown. Fig 9 presents comparison of FC value for each 100kW width range of power.

Fig 10 presents main conclusions of this work:

- FC of raw data is really not good due to mentioned overlapping of data
- FC for **pre-selected** data (after rejection of data for lowest and highest load, that can be associated with unloaded and overloaded machine [12]) is much higher (15 times better than for raw data)
- Proposed approach shows further improvement of classification efficiency: min. value of FC (for 750kW) is slightly better than overall FC for after selection, however, max. FC (for 150kW) is 45 times better. Averaged FC for novel approach is 20 times better than classification results for raw data.

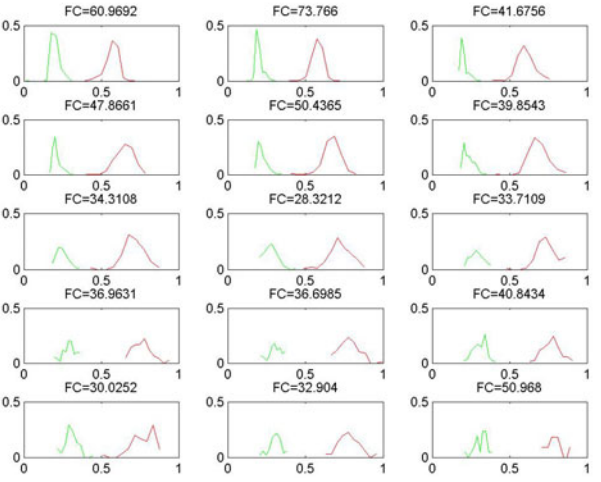

Fig. 8 Probability density functions good/bad data in segments (power range for each segment: 100kW), Fisher Criterion value in titles

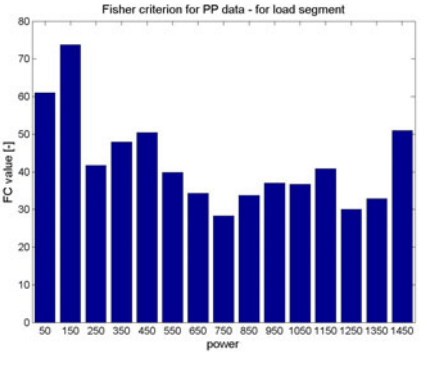

Fig. 9 Comparison of Fisher Criterion value for segments for RMS feature

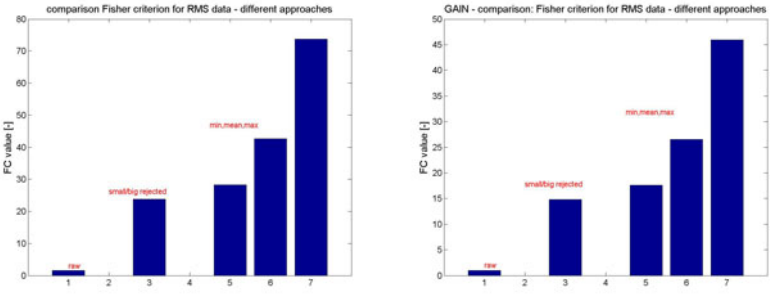

Fig. 10 Left: Comparison of Fisher' Criterion value obtained by analysis: raw data, selected data, selected and segmented RMS data Right: Comparison of Fisher' Criterion' GAIN obtained by analysis: raw data, selected data, selected and segmented data for RMS data

5 Conclusion

Novel classification technique for data acquired from online monitoring system is presented in the paper. Based on simple long term trends including RMS data of vibration signal and power variation we have shown that analysis of data in feature-load space separately for several sub-ranges of load is better than basic classification in feature-load space and much better than classical analysis. A clear evidence of influence to vibration based feature has been proposed (compare with [11], [26]). Additionally the research results highlight the importance of feature classification and the strong influence of operational condition on obtained diagnostic features. Operational states based classification, commonly used in industrial condition monitoring systems, may be inefficient or even give misleading results in object's technical condition evaluation. New approach proposed in the paper may allow to improve automatic decision making algorithms in vibration based condition monitoring systems and reduce the role of diagnostic engineers in the initial stage of fault recognition procedures.

Acknowledgements. This paper was financially supported by Polish State Committee for Scientific research 2010-2013 as research project no. N504 147838.

References

Hameed, Z., Hong, Y.S., Cho, Y.M., Ahn, S.H., Song, C.K.: Condition monitoring and fault detection of wind turbines and related algorithms: A review. Renewable and Sustainable Energy Reviews 13(1), 1–39 (2009); doi:10.1016/j.rser.2007.05.008

Amirat, Y., Benbouzid, M.E.H., Al-Ahmar, E., Bensaker, B., Turri, S.: A brief status on condition monitoring and fault diagnosis in wind energy conversion systems. Renewable and Sustainable Energy Reviews 13(9), 2629–2636 (2009)

Barszcz, T.: Application of diagnostic algorithms for wind turbines — Dobór algorytmów diagnostycznych dla turbin wiatrowych. Diagnostyka 2, 7–11 (2009)

Kusiak, A., Li, W.: The prediction and diagnosis of wind turbine faults. Renewable Energy 36(1), 16–23 (2011); doi: 10.1016/j.renene.2010.05.014

Barszcz, T., Urbanek, J., Uhl, T.: Comparison of advanced fault detection methods for rolling bearings fault in wind turbines. In: CM 2010/MFPT 2010 7th International Conference on Condition Monitoring and Machinery Failure Prevention Technologies 2010, June 22-24, pp. 1–12. Coxmoor Publishing, Co., England (2010)

Barszcz, T., Randall, R.B.: Application of spectral kurtosis for detection of a tooth crack in the planetary gear of a wind turbine. Mech. Syst. and Signal Proc. 23, 1352–1365 (2009)

Jiang, Y., Tang, B., Qin, Y., Liu, W.: Feature extraction method of wind turbine based on adaptive Morlet wavelet and SVD. Renewable Energy 36(8), 2146–2153 (2011)

Tang, B., Liu, W., Song, T.: Wind turbine fault diagnosis based on Morlet wavelet transformation and Wigner-Ville distribution. Renewable Energy 35(12), 2862–2866 (2010)

Barszcz, T., Bielecka, M., Bielecki, A., Wójcik, M.: Wind Turbines States Classification by a Fuzzy-ART Neural Network with a Stereographic Projection as a Signal Normalization. In: Dobnikar, A., Lotrič, U., Šter, B. (eds.) ICANNGA 2011, Part II. LNCS, vol. 6594, pp. 225–234. Springer, Heidelberg (2011)

Bartelmus, W., Zimroz, R.: Vibration spectra characteristic frequencies for condition monitoring of mining machinery compound and complex gearboxes. Scientific Papers of the Institute of Mining of the Wroclaw University of Technology 133, 17–34 (2011)

Barszcz, T., Bielecki, A., Wójcik, M.: ART-Type Artificial Neural Networks Applications for Classification of Operational States in Wind Turbines. In: Rutkowski, L., Scherer, R., Tadeusiewicz, R., Zadeh, L.A., Zurada, J.M. (eds.) ICAISC 2010, Part II. LNCS, vol. 6114, pp. 11–18. Springer, Heidelberg (2010)

Bartelmus, W., Zimroz, R.: A new feature for monitoring the condition of gearboxes in non-stationary operation conditions. Mech. Syst. and Signal Proc. 23(5), 1528–1534 (2009)

Bartelmus, W., Chaari, F., Zimroz, R., Haddar, M.: Modelling of gearbox dynamics under time varying non-stationary operation for distributed fault detection and diagnosis. European Journal of Mechanics - A/Solids 29(4), 637–646 (2010)

Zimroz, R., Bartelmus, W., Barszcz, T., Urbanek, J.: Wind turbine main bearing diagnosis - a proposal of data processing and decision making procedure under non stationary load condition. Presented at SHM 2011, Cracow Poland, to be published in Key Engineering Materials in 2012 (2012)

Rubini, R., Meneghetti, U.: Application of the envelope and wavelet transform analyses for the diagnosis of incipient faults in ball bearings. Mechanical Systems and Signal Processing 15(2), 287–302 (2001)

Randall, R.B., Antoni, J., Chobsaard, S.: The relationship between spectral correlation and envelope analysis in the diagnostics of bearing faults and other cyclostationary machine signals. Mechanical Systems and Signal Processing 15(5), 945–962 (2001)

Antoni, J.: Cyclostationarity by examples. Mechanical Systems and Signal Processing 23(4), 987–1036 (2009)

Makowski, R.A., Zimroz, R.: Adaptive Bearings Vibration Modelling for Diagnosis. In: Bouchachia, A. (ed.) ICAIS 2011. LNCS (LNAI), vol. 6943, pp. 248–259. Springer, Heidelberg (2011)

Barszcz, T.: Decomposition Of Vibration Signals Into Deterministic and Nondeterministic Components And Its Capabilities of Fault Detection And Identification. Int. J. Appl. Math. Comput. Sci. 19(2), 327–335 (2009)

Zimroz, R., Bartelmus, W.: Application of adaptive filtering for weak impulsive signal recovery for bearings local damage detection in complex mining mechanical systems working under condition of varying load. Solid State Phenomena 180, 250–257 (2012); doi:10.4028/www.scientific.net/SSP.180.250

Zimroz, R., Bartkowiak, A.: Investigation on spectral structure of gearbox vibration signals by principal component analysis for condition monitoring purposes. Journal of Physics: Conference Series 305(1), Article number 012075 (2011)

Bartkowiak, A., Zimroz, R.: Outliers analysis and one class classification approach for planetary gearbox diagnosis. Journal of Physics: Conference Series 305(1), Article number 012031 (2011)

Worden, K., Staszewski, W.J., Hensman, J.J.: Natural computing for mechanical systems research: A tutorial overview. Mechanical Systems and Signal Proc. 25(1), 4–111 (2010)

Bartkowiak, A., Zimroz, R.: Data dimension reduction and visualization of multidimensional data with application to gearbox diagnostics data: comparison of several methods. Solid State Phenomena 180, 177–184 (2012); doi:10.4028/www.scientific.net/SSP.180.177

Jabłonski, A., et al.: Automatic validation of vibration signals in wind farm distributed monitoring systems. Measurement (2011) (in Press); doi:10.1016/j.measurement.2011.08.017

Gelman, L., Zimroz, R., et al.: Adaptive vibration condition monitoring technology for local tooth damage in gearboxes. Insight: Non-Destructive Testing and Condition Monitoring 47(8), 461–464 (2005)

Bartelmus, W., Zimroz, R.: Vibration condition monitoring of planetary gearbox under varying external load. Mechanical Systems and Signal Proc. 23(1), 246–257 (2009)

Chapter 5
Noise and Vibration of Machines

Recent decades have seen the rise of noise and vibration problems associated with machinery which are more and more complex. Vibrations of machines are the results of the dynamic forces, due to moving parts which are related to the machine and its mechanical properties.

The understanding of the machine's noise and vibration signatures and their time dependent behavior are one of the main criteria for efficient condition monitoring.

In this section, where noise and vibration are discussed, different theoretical and practical methods are presented. The damping phenomenon is used for noise and vibration reduction. There are also given papers on more advanced techniques like: dynamic absorbers, floating supports, damper modeling and so on.

Seeded Damage Detection on Self-aligning Ball Bearings with Acoustic Emission

Sylvester A. Aye, Philippus S. Heyns, and Coenraad J.H. Thiart

Dynamic Systems Group, Department of Mechanical & Aeronautical Engineering, University of Pretoria, 0002, Pretoria, South Africa
sylvester.aye@up.ac.za, stephan.heyns@up.ac.za, coenie.thiart@up.ac.za

Abstract. Acoustic emission (AE) has evolved as one of the much used techniques for condition monitoring and diagnosis of rotating machinery. Major research has been carried out in the attempt to comprehend the prospects of AE in condition monitoring of bearings. However, this has been mainly applied to other types of bearings. This study investigates the usefulness of the AE approach in the seeded damage detection on self-aligning ball bearings.

Keywords: Acoustic emission, condition monitoring, self-aligning ball bearing.

1 Introduction

Acoustic emission (AE) could be defined as the range of phenomena that leads to the generation of structure-borne and fluid-borne (liquid, gas) propagating waves due to the rapid release of energy from localised sources within and/or on the surface of a material (ISO 22096, 2007). The use of the acoustic emission technology in research and industry is well-known (Mba and Rao, 2006). Few researchers have assessed the application of AE technology for diagnostic and prognostic purposes in self-aligning ball bearings. Others (Jamuludin and Mba (2002a), Jamuludin and Mba (2002b). Tandon 1994, Tandon and Choudhury, 1999, Barkov et al 1997, Tandon and Nakra, 1992, Kim et al., 2007,) applied AE in detecting damage on other types of bearings.

Elforjani and Mba presented the results of an investigation to assess the potential of the Acoustic Emission (AE) technology for detecting and locating natural defects in rolling element bearings. Rolling element bearings are the most common cause of rotating machinery failure. Over the past 20 years, Acoustic Emission (AE) technology has evolved as a significant opportunity to monitor and diagnose the mechanical integrity of rolling element bearings. The results from their investigation showed that the method of identifying the onset of crack propagation can be employed as a quality control tool for bearing manufacturers particularly for testing bearing material homogeneity (Elforjani and Mba 2010).

Elforjani and Mba demonstrated the use of AE measurements to detect, locate, and monitor natural defect initiation and propagation in a conventional rolling

element bearing. To facilitate the investigation they built a special purpose test rig to allow for accelerated natural degradation of a bearing race. They concluded that subsurface initiation and subsequent crack propagation can be detected with the AE technology. The study demonstrated that AE parameters such as RMS and energy are more reliable, robust, and sensitive to the detection of incipient cracks and surface spalls in slow speed bearing than vibration analysis (Elforjani and Mba 2008).

This study uses AE monitoring techniques to detect incipient damage at various torque loads and speeds for a self-aligning ball bearing.

2 Methodology

Incipient damage was artificially introduced to the outer race of the self-aligning ball bearing. The self-aligning ball bearing data was then obtained using acoustic emission sensors at various torque loads and varying speeds. The speed was varied by using a variable speed controller and a tachometer measured the speed. The acoustic emission sensor was connected to a SVAN958 data acquisition system. The data was obtained at a sampling rate of 48 kHz. Torque load was introduced by using a voltage controller which introduced torque loads corresponding to the voltage increase. The data obtained was then downloaded, processed and analyzed in the time domain using MATLAB based software. The statistical parameters of interest were peak value, Root Mean Square (RMS), Crest factor (CF) and Kurtosis (K). Kurtosis values above the value of three indicate the presence of damage whereas kurtosis values below three indicate the absence of damage.

3 Results

The data obtained at various torque loads and speeds was processed in MATLAB based environment and tabulated as shown below in tables 1. Table 1 shows the statistical parameters of peak value, Root Mean Square, Crest factor and Kurtosis at various torque loads of ‘no torque load’, ‘torque load 2’, ‘torque load 3’, ‘torque load 3’ and ‘maximum torque load’ and speeds of ‘156 RPM’, ‘360 RPM’, ‘500 RPM’, ‘810 RPM’ and ‘1100 RPM’.

Table 1 Statistical parameters at various torque loads.

Loads @156 RPM	Peak	RMS	CF	K
No Torque Load	1.3143	0.3671	4.0090	3.1354
Torque Load 2	1.3700	0.3677	4.1726	3.0913
Torque Load 3	1.2497	0.3669	3.8149	3.1145
Torque Load 4	1.3021	0.3697	3.9444	3.1352
Maximum Torque	1.2604	0.3470	4.0683	3.0727
Loads @ 360 RPM	Peak	RMS	CF	K
No Torque Load	1.7302	0.4157	4.6608	3.3438

Table 1 *(continued)*

Torque Load 2	1.7571	0.4254	4.6265	3.3428
Torque Load 3	1.5751	0.4169	4.2318	3.2249
Torque Load 4	1.5314	0.4211	4.0725	3.3103
Maximum Torque	1.1911	0.3536	3.7733	3.1314
Loads@ 500 RPM	Peak	RMS	CF	K
No Torque Load	1.6255	0.4558	3.9934	3.2586
Torque Load 2	1.8537	0.4773	4.3496	3.2930
Torque Load 3	1.6961	0.4736	4.0109	3.2315
Torque Load 4	1.8519	0.4818	4.3053	3.3089
Maximum Torque	0.4966	0.3528	3.9543	3.0770
Loads @ 810 RPM	Peak	RMS	CF	K
No Torque Load	1.6794	0.4820	3.9022	3.2506
Torque Load 2	1.8437	0.4891	4.2218	3.2014
Torque Load 3	1.8417	0.4966	4.1535	3.2762
Torque Load 4	1.7834	0.4949	4.0355	3.2842
Maximum Torque	1.1997	0.3594	3.7381	3.0178
Loads@1100 RPM	Peak	RMS	CF	K
No Torque Load	1.9373	0.4973	4.3633	3.3228
Torque Load 2	1.7065	0.4978	3.8397	3.2385
Torque Load 3	1.8328	0.4973	4.1278	3.2347
Torque Load 4	2.0306	0.5001	4.5476	3.2086
Maximum Torque	1.3206	0.3540	4.1774	3.1656

4 Discussion

Damage was artificially introduced to the outer race of the self-aligning ball bearing. The self aligning ball bearing data was then obtained using acoustic emission sensors at various torque loads and varying speeds. The speed was varied by using a controller and a tachometer measured the speed. Torque load was introduced by using a voltage controller which introduced torque loads corresponding to the voltage increase. The data obtained was then processed and analyzed in the time domain using MATLAB based software. The statistical parameters of interest were peak value, Root Mean Square (RMS), Crest factor (CF) and Kurtosis (K). Kurtosis values above the value of three indicate the presence of damage whereas kurtosis values below three indicate the absence of damage.

The self-aligning ball bearing data obtained at various torque loads and speeds was processed in MATLAB based environment and tabulated as shown below in table 1. Table 1 shows the statistical parameters at various torque loads of ‘no torque load’, ‘torque load 2’, ‘torque load 3’, ‘torque load 3’ and ‘maximum torque load’ and speeds of ‘156 RPM’, ‘360 RPM’, ‘500 RPM’, ‘810 RPM’ and ‘1100 RPM’.

It can be seen from table 1 that at a speed of 156RPM and no loading we have kurtosis values slightly above three which indicates the presence of incipient damage as we would expect. Also, at torque load 2, torque load 3, and torque load 4 the kurtosis value is slightly above 3 still indicating the presence of incipient damage. At a maximum torque load we still have a kurtosis value slightly above 3 even though it is lower in magnitude in comparison with previous values. It is still slightly higher than 3 and indicates the presence of incipient damage.

Furthermore, it can be seen from table 1 that at a speed of 360RPM and no loading we have kurtosis values slightly above three which indicates the presence of incipient damage as we would expect. Also, at torque load 2, torque load 3, and torque load 4 the kurtosis value is slightly above 3 still indicating the presence of incipient damage. At a maximum torque load we still have a kurtosis value slightly above 3 even though it is once again lower in magnitude in comparison to previous values obtained at the same speed. It is still slightly higher than 3 and indicates the presence of incipient damage.

Finally, it can be seen from table 1 that at a speeds of 500 RPM, 810 RPM and 1100 RPM and no loading we again have kurtosis values slightly above three which indicates the presence of incipient damage as we would expect. Also, at torque load 2, torque load 3, and torque load 4 the kurtosis value is still slightly above 3 still indicating the presence of incipient damage. At a maximum torque load we still have a kurtosis value slightly above 3 even though it is lower in magnitude in comparison to previous kurtosis values obtained at the same speeds respectively. The kurtosis values are still slightly higher than 3 and hence indicates the presence of incipient damage.

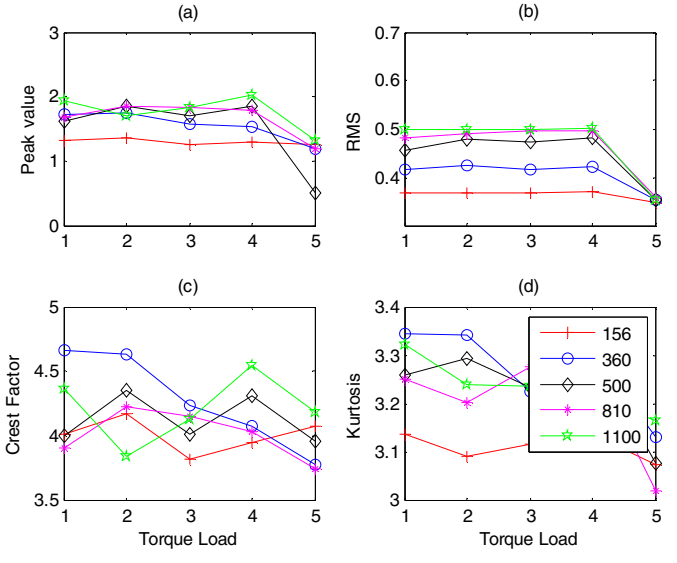

Fig. 1 Statistical parameters at various torque loads and speeds

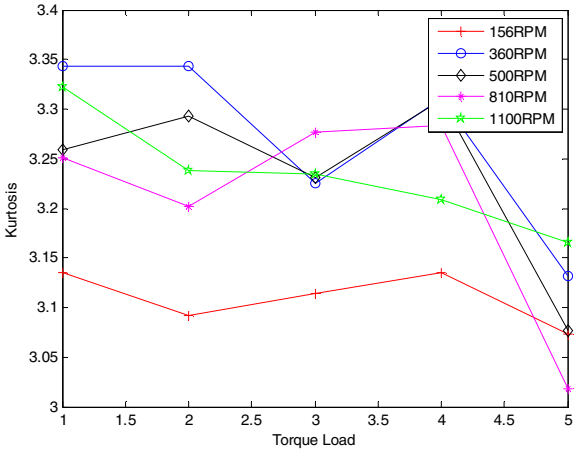

Fig. 2 Kurtosis at various torque loads and speeds

The statistical parameters of interest ie Peak value, RMS, crest factor and kurtosis tabulated in table 1 were plotted in figures 1 and 2. From figure 1a it can seen that the Peak value is constant for increasing torque value. However at maximum torque value the peak value is lower in magnitude than previous ones. From figure 1b it can equally be seen that the RMS value is constant for increasing torque value. However at maximum torque value the RMS value is lower in magnitude than previous ones. From figure 1c it can seen that the crest factor is generally decreasing gradually for increasing torque values. From figure 1d it can also be seen that the kurtosis is generally decreasing gradually for increasing torque values. From figure 2 it is clearly seen that the kurtosis value at all torque loads and speeds is slightly above 3 indicating the presence of incipient damage. It can also be seen that the kurtosis value generally decreases with increasing torque load.

5 Conclusion

Self-aligning ball bearing data was obtained and processed in MATLAB environment. From the results it can be seen that the kurtosis value at all torque values and speeds was slightly above 3 indicating the presence of incipient damage. It can equally be seen that for increasing torque loads the kurtosis value generally decreases. The acoustic emission technique was found to be useful in the condition monitoring of self-aligning ball bearings.

References

ISO 22096, Condition Monitoring and Diagnostics of Machines. Acoustic Emission (2007)

Mba, D., Rao, R.B.K.N.: Development of acoustic emission technology for condition monitoring and diagnosis of rotating machines: bearings, pumps, gearboxes, engines, and rotating structures. Shock Vib. Digest. 38(1), 3–16 (2006)

Jamuludin, N., Mba, D.: Monitoring extremely slow rolling element bearings: part I. NDT & E International 35, 349–358 (2002a)

Jamuludin, N., Mba, D.: Monitoring extremely slow rolling element bearings: part II. NDT & E International 35, 359–366 (2002b)

Tandon, N.: Measurement A comparison of some vibration parameters for the condition monitoring of rolling element bearings. Measurement 12, 285–289 (1994)

Tandon, N., Choudhury, A.: A review of vibration and acoustic measurement methods for the detection of defects in rolling element bearings. Tribology International 32, 469–480 (1999)

Barkov, A., Barkova, N., Azovtsev, A.: Peculiarities of slow rotating rolling element bearing condition diagnostics (1997), http://www.vibrotek.com/article.php?article=articles/bbmvi95/index.htm

Tandon, N., Nakra, B.C.: Comparison of vibration and acoustic measurement techniques for the condition monitoring of rolling element bearings. Tribology International 25(3), 205–212 (1992)

Kim, E.Y., Tan, A.C.C., Yang, B., Kosse, V.: Experimental Study on Condition Monitoring of Low Speed Bearings: Time Domain Analysis. In: 5th Australasian Congress on Applied Mechanics, ACAM, Brisbane, Australia, December 10-12 (2007)

Elforjani, M., Mba, D.: Accelerated natural fault diagnosis in slow speed bearings with Acoustic Emission. Engineering Fracture Mechanics 77(2010), 112–127 (2010)

Elforjani, M., Mba, D.: Monitoring the Onset and Propagation of Natural Degradation Process in a Slow Speed Rolling Element Bearing With Acoustic Emission. Journal of Vibration and Acoustics 130(2008), 1–14 (2008)

Effect of Uncertainties in Default Detection through the Wave Finite Elements

Mohamed Amine Ben Souf, Mohamed Ichchou,
Olivier Bareille, and Mohamed Haddar

[1] Ecole centrale de Lyon, 36 Avenue Guy de Collongue, F-69134 Ecully Cedex, France
(mohamed-amine.ben-souf, Mohamed.Ichchou,
Olivier.Bareille)@ec-lyon.fr
[2] Ecole nationale d'Ingénieurs de Sfax,
Unité de Mécanique, Modélisation et Productique, Tunisie
mohamed.haddar@enis.rnu.tn

Abstract. Wave propagation in coupled structure is investigated in this paper. When waves propagate through a media, they will encounter changes in geometry or material. At such discontinuities due to corrosion or cracks, some of waves will be reflected and transmitted. A hybrid numerical method called 'Wave Finite Element/Stochastic Finite Element Method' (WFE/SFEM) is been used to take into account the variation in propagation characteristics due to the variability in mechanical and geometrical properties of coupling element. The effect of uncertain discontinuities on the reflection and transmission coefficients is evaluated and validated for 3D multimodal waveguide vs Monte Carlo simulations.

1 Introduction

The safety of structures and damage detection are important tasks in many industrial applications such as civil engineering and petroleum engineering. The right diagnosis about default is a real challenge for engineers. Many industrial concept exist which helps to perform default detection. The non-destructive techniques like ultrasonic testing, magnetic particle testing and Thermal Infrared Testing, are often used to detect local defects and allows a precise information about inhomogeneities (size, distance, ...) that might be defects.

For connected element of structures, the diffusion coefficients can offer an idea about the dynamics of the global system. For that purpose, guided wave techniques are among the most useful non-destructive testing one. From the analysis of reflection coefficients, the location and the dimension of singularities can be evaluated. The presence of discontinuities (cracks, geometrical changes ...) in continuous structures causes a local flexibility and modify the dynamical behavior of the media. For an incident wave on this inhomogeneity, a reflected and transmitted waves are generated. The evaluation of the corresponding diffusion coefficients is an important preliminary task. It not only assesses the level of delectability of defects but also it serves as comparison signals to real measurements.

Diffusion properties have been obtained using different methods. Mace [1] investigated analytically the wave reflection and transmission in a beam. Mei *et al.* [2]

described the dynamical behavior of an axially loaded Timoshenko beam with discontinuities and offered an analytical expression for diffusion matrices. Wang *et al.* [3] extended an analytical approach using higher order plate theories to investigate the transmission and reflection coefficients in a damaged beam. Chondros *et al.* [4] used the Hu-Washizu-Barr variational formulation to develop a differential equation for the continuous cracked beam. Some researchers used also spectral formulations to describe, by mean of these coefficients, the dynamical behavior of coupled structures. Mencik *et al.* [5] and Ichchou *et al.* [6] used the Wave Finite Element (WFE) to evaluate the Diffusion Matrix Model (DMM) which predicts the diffusion matrix in low and mid-frequency. Zhou *et al.* [7] used the WFE to investigate the alterations in cylindrical pipes and extracted reflection coefficients for different cases.

This paper combine two different formulations: the wave finite element and the stochastic finite element method. An explicit form for statistics of reflection and transmission coefficients is proposed. Deterministic waveguides coupled by an uncertain media are more precisely considered. This method describes the mode conversion through local discontinuities. In the mid-frequency (MF) band, section's modes are strongly affected by singularities and the dynamic response of the whole structure can be modified. The WFE/SFEM leads to identify the effect of an uncertain coupling element on diffusion coefficients. In section 2, a brief introduction to the WFE method is presented. Section 3 deals with the statistics of kinematic diffusion matrix. Finally, numerical simulations are presented in section 4 and validated through the Monte Carlo simulations.

2 Brief Introduction of the Deterministic WFE

This section describes the principal of the wave finite element method (WFE). Since the goal is to describe the propagation in waveguide structures, the dynamic behavior of a straight elastic dissipative element is dealt with. The considered structure is composed by N identical element (Fig. 1) connected along the principal direction, say axis x. From a given cross-section along the x-axis, left and right parts are denoted as `L` and `R`, respectively. The length of each subsystem is denoted as d. The formulation is based on the finite element model of a typical subsystem, as illustrated in (Fig. 1), whose displacements and forces variables, are written **q** and **F** respectively. Mesh compatibility at coupling interfaces between subsystems

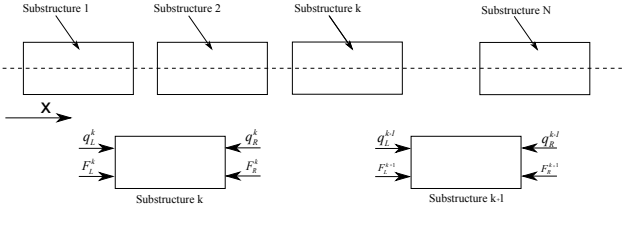

Fig. 1 Typical substructures waveguide.

is assumed. It's implies that the left and right cross-sections of the given subsystem contains the same number of degrees of freedom, say $\mathtt{n}$. The dynamic equilibrium equation of this subsystem, at frequency $\omega/2\pi$, can be stated as follows [8]:

$$\begin{pmatrix} \mathbf{D}_{\mathtt{LL}} & \mathbf{D}_{\mathtt{LR}} \\ \mathbf{D}_{\mathtt{RL}} & \mathbf{D}_{\mathtt{RR}} \end{pmatrix} \begin{pmatrix} \mathbf{q}_{\mathtt{L}} \\ \mathbf{q}_{\mathtt{R}} \end{pmatrix} = \begin{pmatrix} \mathbf{F}_{\mathtt{L}} \\ \mathbf{F}_{\mathtt{R}} \end{pmatrix} \tag{1}$$

where $(\mathtt{n} \times \mathtt{n})$ matrix $\mathbf{D}_{\mathtt{ij}} = \mathbf{K}_{\mathtt{ij}} - \omega^2 \mathbf{M}_{\mathtt{ij}}$ $(\{\mathtt{i},\mathtt{j}\} \in \{\mathtt{L},\mathtt{R}\})$ stands for the $\mathtt{ij}$ components of the dynamic stiffness operator $\mathbf{D}$ condensed on the left and right cross-sections [8]. Here, $\mathbf{K}$ and $\mathbf{M}$ stand for the stiffness and mass matrices, respectively. Dissipation can be considered through standard FEM models. According to Bloch's theorem, the dynamics of the global waveguide can be expanded on specific wave solutions of the form:

$$\mathbf{q}_{\mathtt{R}} = \mu \mathbf{q}_{\mathtt{L}} \tag{2}$$

and

$$\mathbf{F}_{\mathtt{R}} = -\mu \mathbf{F}_{\mathtt{L}} \tag{3}$$

where μ denotes the propagation coefficient. Indeed, inserting Eqs. (2) and (3) into Eq. (1) leads to the following spectral problem [9]:

$$\left(\mathbf{D}_{\mathtt{RL}} + \mu_{\mathtt{i}}(\mathbf{D}_{\mathtt{LL}} + \mathbf{D}_{\mathtt{RR}}) + \mu_{\mathtt{i}}^2 \mathbf{D}_{\mathtt{LR}}\right)(\phi_{\mathtt{q}})_{\mathtt{i}} = \mathbf{0} \tag{4}$$

where $(\mu_{\mathtt{i}}, (\phi_{\mathtt{q}})_{\mathtt{i}})_{\mathtt{i}=1,\ldots,2\mathtt{n}}$ stands for the wave modes of the global system. It is remarkable that $\mathbf{D}_{\mathtt{RL}}^{\mathtt{T}} = \mathbf{D}_{\mathtt{LR}}$ and $(\mathbf{D}_{\mathtt{LL}} + \mathbf{D}_{\mathtt{RR}})^{\mathtt{T}} = (\mathbf{D}_{\mathtt{LL}} + \mathbf{D}_{\mathtt{RR}})$. Using these properties, we can prove that $(\phi_{\mathtt{q}})_{\mathtt{i}}^{\mathtt{T}}$ is the eigenvector associated to the eigenvalue $\mu_{\mathtt{i}}^{-1}$ [5]. The frequency response of the global system can be expressed by expanding the kinematic variables of the considered subsystem on the eigenvectors basis:

$$\begin{pmatrix} \mathbf{q}_{\mathtt{L}} \\ -\mathbf{F}_{\mathtt{L}} \end{pmatrix} = \begin{bmatrix} \phi_{\mathtt{q}} \\ \phi_{\mathtt{F}} \end{bmatrix} \mathbf{Q}_{\mathtt{L}} \quad \text{and} \quad \begin{pmatrix} \mathbf{q}_{\mathtt{R}} \\ \mathbf{F}_{\mathtt{R}} \end{pmatrix} = \begin{bmatrix} \phi_{\mathtt{q}} \\ \phi_{\mathtt{F}} \end{bmatrix} \mathbf{Q}_{\mathtt{R}} \tag{5}$$

where $\phi_{\mathtt{q}}$ and $\phi_{\mathtt{F}}$ stand for the matrices of eigenvector $(\phi_{\mathtt{q}})_{\mathtt{i}}$ and $(\phi_{\mathtt{F}})_{\mathtt{i}}$, respectively, and where $\mathbf{Q}_{\mathtt{L}}$ and $\mathbf{Q}_{\mathtt{R}}$ stand for the $(2\mathtt{n} \times 1)$ generalized coordinates evaluated for the left and right boundaries of the subsystem. These eigensolutions serve as basic description for the propagative approach used in the WFEM for calculating the diffusion parameters.

3 Kinematic Diffusion Matrix for Random Coupled Elements

The hybrid (WFE/SFEM) method is used to establish the kinematic diffusion matrix of stochastic coupled structures. The deterministic formulation is developed using Lagrange multiplier [5, 6]. For this purpose, two deterministic periodic waveguide connected through a stochastic coupling element are considered (see Fig. 2). In this case, the Ghanem and Spanos' [10] SFEM based on polynomial chaos expansion, is used.

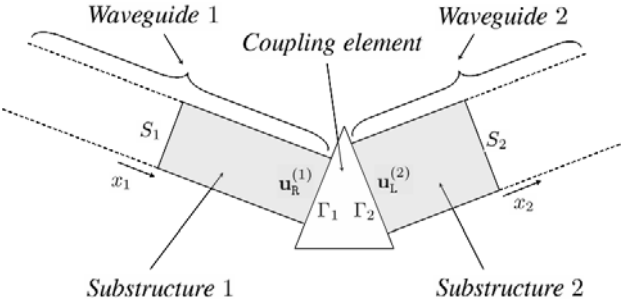

Fig. 2 Two coupled waveguides through a stochastic coupling element

The stochastic diffusion matrix is evaluated using one layer of element for each waveguide as well as for the uncertain coupled structure.

As described in the previous section, the dynamical behavior of coupled element is written as:

$$\tilde{\mathbf{K}}_{\mathtt{coup}} \begin{pmatrix} \tilde{\mathbf{q}}^{\mathtt{c}}_{\Gamma_1} \\ \tilde{\mathbf{q}}^{\mathtt{c}}_{\Gamma_2} \end{pmatrix} = \begin{pmatrix} \tilde{\mathbf{F}}^{\mathtt{c}}_{\Gamma_1} \\ \tilde{\mathbf{F}}^{\mathtt{c}}_{\Gamma_2} \end{pmatrix} \tag{6}$$

where $\tilde{\mathbf{K}}_{\mathtt{coup}}$ is the stochastic dynamical stiffness matrix condensed on the left and the right sides of each sections Γ_1 and Γ_2 and $\tilde{\mathbf{q}}^{\mathtt{c}}_{\Gamma_1}$ and $\tilde{\mathbf{q}}^{\mathtt{c}}_{\Gamma_2}$ (resp. $\tilde{\mathbf{F}}^{\mathtt{c}}_{\Gamma_1}$ and $\tilde{\mathbf{F}}^{\mathtt{c}}_{\Gamma_2}$) represent the stochastic displacement (resp. force) evaluated for the same sections. The continuity conditions can be expressed in matrix form as:

$$\begin{pmatrix} \tilde{\mathbf{q}}^{\mathtt{c}}_{\Gamma_1} \\ \tilde{\mathbf{q}}^{\mathtt{c}}_{\Gamma_2} \end{pmatrix} = \begin{pmatrix} \tilde{\mathbf{q}}^{(1)}_{\Gamma_1} \\ \tilde{\mathbf{q}}^{(2)}_{\Gamma_2} \end{pmatrix} \quad , \quad \begin{pmatrix} \tilde{\mathbf{F}}^{(1)}_{\Gamma_1} \\ \tilde{\mathbf{F}}^{(2)}_{\Gamma_2} \end{pmatrix} = - \begin{pmatrix} \tilde{\mathbf{F}}^{\mathtt{c}}_{\Gamma_1} \\ \tilde{\mathbf{F}}^{\mathtt{c}}_{\Gamma_2} \end{pmatrix} \tag{7}$$

where $\tilde{\mathbf{q}}^{(1)}_{\Gamma_1}$ and $\tilde{\mathbf{q}}^{(2)}_{\Gamma_2}$ (resp. $\tilde{\mathbf{F}}^{(1)}_{\Gamma_1}$ and $\tilde{\mathbf{F}}^{(2)}_{\Gamma_2}$) represent the stochastic displacements (resp. forces) evaluated in Γ_1 and Γ_2 for each waveguide. The variability of coupled mechanical characteristics affects directly the displacements and the forces in the whole system. The equations (6) and (7) lead to express the relation between stochastic kinematic variables on the left and on the right of substructure $\mathtt{1}$ and $\mathtt{2}$ using the stiffness matrix of coupled element as:

$$-\tilde{\mathbf{K}}_{\mathtt{coup}} \begin{pmatrix} \tilde{\mathbf{q}}^{(1)}_{\Gamma_1} \\ \tilde{\mathbf{q}}^{(2)}_{\Gamma_2} \end{pmatrix} = \begin{pmatrix} \tilde{\mathbf{F}}^{(1)}_{\Gamma_1} \\ \tilde{\mathbf{F}}^{(2)}_{\Gamma_2} \end{pmatrix} \tag{8}$$

From the eigensolutions of the equation (4), the stochastic kinematic variables for each waveguide $\mathtt{i}$ can be expanded on the wave base as:

$$\tilde{\mathbf{q}}^{(\mathtt{i})}_{\Gamma_{\mathtt{i}}} = \left(\phi_{\mathtt{q}}^{\mathtt{inc(i)}} \phi_{\mathtt{q}}^{\mathtt{ref(i)}}\right) \begin{pmatrix} \tilde{\mathbf{Q}}^{\mathtt{inc(i)}} \\ \tilde{\mathbf{Q}}^{\mathtt{ref(i)}} \end{pmatrix} \quad \text{and} \quad \tilde{\mathbf{F}}^{(\mathtt{i})}_{\Gamma_{\mathtt{i}}} = \left(\phi_{\mathtt{F}}^{\mathtt{inc(i)}} \phi_{\mathtt{F}}^{\mathtt{ref(i)}}\right) \begin{pmatrix} \tilde{\mathbf{Q}}^{\mathtt{inc(i)}} \\ \tilde{\mathbf{Q}}^{\mathtt{ref(i)}} \end{pmatrix} \quad \mathtt{i} = 1,2 \tag{9}$$

where $\tilde{\mathbf{Q}}^{(\mathtt{i})}$ are the stochastic mode amplitudes and $\phi^{(\mathtt{i})}$ are the deterministic wave shapes. The subscripts $\mathtt{q}$ and $\mathtt{F}$ refer respectively to the displacement and the force.

The stochastic equilibrium equation (8) can be expressed using equation (9) and it becomes the following diffusion matrix:

$$\underbrace{\left(\tilde{\mathbf{K}}_{\mathrm{coup}}\psi_{\mathbf{q}}^{\mathrm{inc}}+\psi_{\mathbf{F}}^{\mathrm{inc}}\right)}_{\tilde{\mathbf{A}}}\begin{pmatrix}\tilde{\mathbf{Q}}^{\mathrm{inc}(1)}\\ \tilde{\mathbf{Q}}^{\mathrm{inc}(2)}\end{pmatrix}=-\underbrace{\left(\tilde{\mathbf{K}}_{\mathrm{coup}}\psi_{\mathbf{q}}^{\mathrm{ref}}+\psi_{\mathbf{F}}^{\mathrm{ref}}\right)}_{\tilde{\mathbf{B}}}\begin{pmatrix}\tilde{\mathbf{Q}}^{\mathrm{ref}(1)}\\ \tilde{\mathbf{Q}}^{\mathrm{ref}(2)}\end{pmatrix} \tag{10}$$

In a condensed form:

$$\begin{pmatrix}\tilde{\mathbf{Q}}^{\mathrm{ref}(1)}\\ \tilde{\mathbf{Q}}^{\mathrm{ref}(2)}\end{pmatrix}=\tilde{\mathbf{C}}\begin{pmatrix}\tilde{\mathbf{Q}}^{\mathrm{inc}(1)}\\ \tilde{\mathbf{Q}}^{\mathrm{inc}(2)}\end{pmatrix} \tag{11}$$

where $\psi_{\mathbf{q}}^{\mathrm{inc}}$, $\psi_{\mathbf{q}}^{\mathrm{ref}}$, $\psi_{\mathbf{F}}^{\mathrm{inc}}$ and $\psi_{\mathbf{F}}^{\mathrm{ref}}$ are expressed as follows:

$$\begin{aligned}\psi_{\mathbf{q}}^{\mathrm{inc}}&=\begin{pmatrix}\phi_{\mathbf{q}}^{\mathrm{inc}(1)} & \mathbf{0}\\ \mathbf{0} & \phi_{\mathbf{q}}^{\mathrm{inc}(2)}\end{pmatrix}\quad,\quad \psi_{\mathbf{q}}^{\mathrm{ref}}=\begin{pmatrix}\phi_{\mathbf{q}}^{\mathrm{ref}(1)} & \mathbf{0}\\ \mathbf{0} & \phi_{\mathbf{q}}^{\mathrm{ref}(2)}\end{pmatrix}\\ \psi_{\mathbf{F}}^{\mathrm{inc}}&=\begin{pmatrix}\phi_{\mathbf{F}}^{\mathrm{inc}(1)} & \mathbf{0}\\ \mathbf{0} & \phi_{\mathbf{F}}^{\mathrm{inc}(2)}\end{pmatrix}\quad,\quad \psi_{\mathbf{F}}^{\mathrm{ref}}=\begin{pmatrix}\phi_{\mathbf{F}}^{\mathrm{ref}(1)} & \mathbf{0}\\ \mathbf{0} & \phi_{\mathbf{F}}^{\mathrm{ref}(2)}\end{pmatrix}\end{aligned} \tag{12}$$

The projection of the stochastic diffusion relation (10) leads to write the zero order term as:

$$\begin{pmatrix}\bar{\mathbf{Q}}^{\mathrm{ref}(1)}\\ \bar{\mathbf{Q}}^{\mathrm{ref}(2)}\end{pmatrix}=\bar{\mathbf{C}}\begin{pmatrix}\bar{\mathbf{Q}}^{\mathrm{inc}(1)}\\ \bar{\mathbf{Q}}^{\mathrm{inc}(2)}\end{pmatrix} \tag{13}$$

where

$$\bar{\mathbf{C}}=-\left[\bar{\mathbf{K}}\psi_{\mathbf{q}}^{\mathrm{ref}}+\psi_{\mathbf{F}}^{\mathrm{ref}}\right]^{+}\left[\bar{\mathbf{K}}\psi_{\mathbf{q}}^{\mathrm{inc}}+\psi_{\mathbf{F}}^{\mathrm{inc}}\right]=\bar{\mathbf{B}}^{+}\times\bar{\mathbf{A}} \tag{14}$$

where $^{+}$ is the pseudo-inverse.

$\bar{\mathbf{C}}$ represents the deterministic diffusion matrix which provides the mean of reflection and transmission coefficients. Both propagative and evanescent wave modes are considered in this formulation. In addition, the first-order projection of equation (10) is written as:

$$\bar{\mathbf{A}}\begin{pmatrix}\sigma_{\mathbf{Q}^{\mathrm{inc}(1)}}\\ \sigma_{\mathbf{Q}^{\mathrm{inc}(2)}}\end{pmatrix}+\sigma_{\mathbf{A}}\begin{pmatrix}\bar{\mathbf{Q}}^{\mathrm{inc}(1)}\\ \bar{\mathbf{Q}}^{\mathrm{inc}(2)}\end{pmatrix}=-\bar{\mathbf{B}}\begin{pmatrix}\sigma_{\mathbf{Q}^{\mathrm{ref}(1)}}\\ \sigma_{\mathbf{Q}^{\mathrm{ref}(2)}}\end{pmatrix}-\sigma_{\mathbf{B}}\begin{pmatrix}\bar{\mathbf{Q}}^{\mathrm{ref}(1)}\\ \bar{\mathbf{Q}}^{\mathrm{ref}(2)}\end{pmatrix} \tag{15}$$

The combination of equation (14) and (15) leads to express the standard deviation of the reflected and transmitted waves amplitudes as:

$$\begin{pmatrix}\sigma_{\mathbf{Q}^{\mathrm{ref}(1)}}\\ \sigma_{\mathbf{Q}^{\mathrm{ref}(2)}}\end{pmatrix}=\bar{\mathbf{C}}\begin{pmatrix}\sigma_{\mathbf{Q}^{\mathrm{inc}(1)}}\\ \sigma_{\mathbf{Q}^{\mathrm{inc}(2)}}\end{pmatrix}+\left(-\bar{\mathbf{B}}^{-1}\left[\sigma_{\mathbf{A}}+\sigma_{\mathbf{B}}\bar{\mathbf{C}}\right]\right)\begin{pmatrix}\bar{\mathbf{Q}}^{\mathrm{inc}(1)}\\ \bar{\mathbf{Q}}^{\mathrm{inc}(2)}\end{pmatrix} \tag{16}$$

where $\sigma_{\mathbf{A}}$ and $\sigma_{\mathbf{B}}$ represent the standard deviation of defined matrices in equation (10) and explicitly expressed as:

$$\begin{aligned}\sigma_{\mathbf{A}}&=\sigma_{\mathbf{K}}\psi_{\mathbf{q}}^{\mathrm{inc}}\\ \sigma_{\mathbf{B}}&=\sigma_{\mathbf{K}}\psi_{\mathbf{q}}^{\mathrm{ref}}\end{aligned} \tag{17}$$

where $\sigma_{\mathbf{K}}$ is the standard deviation of the dynamic equilibrium matrix for coupling element. Finally, with respect to the first-order expansion of equation (11), the standard deviation of kinematic diffusion matrix is expressed as:

$$\sigma_{\mathbf{C}} = -\bar{\mathbf{B}}^{-1}\left[\sigma_{\mathbf{A}} + \sigma_{\mathbf{B}}\bar{\mathbf{C}}\right] \tag{18}$$

This last equation provides the variability of the wave conversion on local inhomogeneities.

4 Numerical Validation

Using high frequency vibration causes many differences between experimental and numerical results. To deal with inspection of structures, the wavelength must be smaller then the size of the imperfection, so the high frequency excitation is required to detect all discontinuities in expected structure. In this validation case, the presented formulation is tested for a real case based problem.

Let's define an infinite pipeline containing a crack. This structure is modeled as two waveguides connected through a coupling element (small part of the pipeline containing the crack) (see Fig. 3). The two semi-infinite waveguides are modeled using only one layer directly related to the coupling element which is supposed to be an uncertain structure with 2% of variabilities in Young's modulus. The table 1 resumes the mechanical characteristics of the studied structure.

Table 1 Characteristics of studied structures

	E (Pa)	ρ (kg/m^3)	d (m)	$\eta(\%)$	*InnerRadius*(m)	*Outerradius*(m)
Waveguides	$2 \cdot 10^{11}$	7800	$1 \cdot 10^{-3}$	1	0.073	0.084
coupling element	$2 \cdot 10^{11}$	7800	$1 \cdot 10^{-2}$	1	0.073	0.084

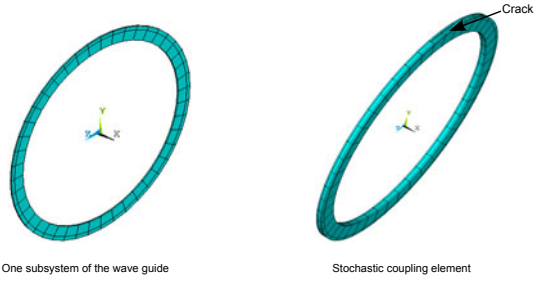

Fig. 3 Model of studied layer and coupling element

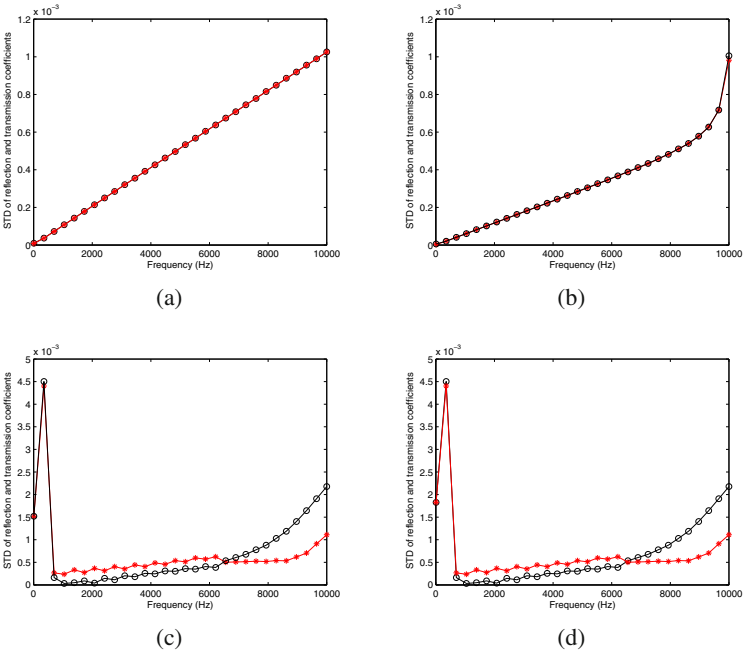

Fig. 4 Standard deviation of reflection and transmission coefficients for different waves: (- red): reflection, (- black): transmission , (∗): reflection Monte Carlo, (*o*):transmission Monte Carlo

Fig. 4 represents the standard deviation of diffusion coefficients respectively: (a)= Longitudinal, (b)= Torsion, (c)= Flexion 1, (d)= Flexion 2. The presented results shows the effects of variability of Young's modulus in the coupling element. This dispersion can be very useful in defect detection as it gives a clearer idea of the crack's dimension. The presented results are validated vs the Monte Carlo simulations with 2000 samples which proves its efficiency.

5 Conclusion

An explicit formulation to predict the dispersion of diffusion coefficients regarding uncertainties in the coupling element were presented in this paper. This presented formulation is based on the hybridization of a spectral formulation (WFE) and a stochastic representation (SWFE). In order to validate it, an example based on a real case was treated and compared to Monte Carlo simulations.In high-frequency, the energetic formulations are more accurate to describe the dynamical behavior of systems. In addition, the effect of uncertainties will be more and more significant. As a future work, the effects of the uncertainties on the energetic diffusion coefficients can be treated, as well as the investigation of the coupling loss factor sensitivity.

Acknowledgements. The authors gratefully acknowledge the ITN Marie Curie project GA-214909 'MID-FREQUENCY CAE Methodologies for Mid-Frequency Analysis in Vibration and Acoustics'

References

1. Mace, B.R.: Wave reflection and transmission in beams. Journal of Sound and Vibration 97(2), 237–246 (1984)
2. Mei, C., Karpenko, Y., Moody, S., Allen, D.: Analytical approach to free and forced vibrations of axially loaded cracked timoshenko beams. Journal of Sound and Vibration 291, 1041–1060 (2006)
3. Wang, C.H., Rose, L.R.F.: Wave reflection and transmission in beams containing delamination and inhomogeneity. Journal of Sound and Vibration 264, 851–872 (2003)
4. Chondros, T.G., Dimarogonas, A.D., Yao, J.: A continuous cracked beam vibration theory. Journal of Sound and Vibration 104(1), 6–23 (1998)
5. Mencik, J.M., Ichchou, M.N.: Multi-mode propagation and diffusion in structures through finite elements. European Journal of Mechanics - A/Solids 24(5), 877–898 (2005)
6. Ichchou, M.N., Mencik, J.-M., Zhou, W.J.: Wave finite elements for low and mid-frequency description of coupled structures with damage. Computer Methods in Applied Mechanics and Engineering 198(15-16), 1311–1326 (2009)
7. Zhou, W.J., Ichchou, M.N., Mencik, J.-M.: Analysis of wave propagation in cylindrical pipes with local inhomogeneities. Journal of Sound and Vibration 319(1-2), 335–354 (2009)
8. Zhong, W.X., Williams, F.W.: On the direct solution of wave propagation for repetitive structures. Journal of Sound and Vibration 181, 485–501 (1995)
9. Houillon, L., Ichchou, M.N., Jezequel, L.: Dispersion curves of fluid filled elastic pipes by standard fe models and eigenpath analysis. Journal of Sound and Vibration 281, 483–507 (2005)
10. Ghanem, R., Spanos, P.: Stochastic Finite Elements: A Spectral Approach. Springer, New York (1991)

Centralized and Decentralized Adaptive FTC of Interconnected and Networked Control System

Amina Challouf[1], Adel Tellili[2], Christophe Aubrun[3], and Mohamed Naceur Abdelkrim[1]

[1] Unité de Recherche: Modélisation, Analyse et Commande des Systèmes (MACS), Ecole Nationale d'Ingénieurs de Gabès, Tunisie
amina_chalouf@yahoo.fr, naceur.abdelkrim@enig.rnu.tn
[2] Institute Supérieure des Etudes Technologiques de Djerba, Tunisie
Adel_Tellili@Lycos.com
[3] Centre de Recherche en Automatique de Nancy(CRAN), Nancy-Université, CNRS UMR 7039, Facultés des Sciences et Techniques, France
christophe.Aubrun@cran.uhp-nancy.fr

Abstract. In this work, we focus on monitoring and reconfiguration of an Adaptive Model Reference (MRA) Fault-Tolerant Control (FTC) for large-scale system. This particular class presents an interconnected and networked control system (INCS). Moreover, the system can be decomposed into N-interconnected subsystems communicating with network. Then the global output of INCS and one or more outputs of N-interconnected and networked control subsystems are attacked by sensor faults. Therefore, an active Fault-Tolerant (FT) approach, say the model reference adaptive control of linear systems, is used in order to guarantee not only the stability of an overall INCS globally, but also all local stabilities of N-networked control subsystems with strong interactions, delay and additive faults. Moreover, two architectures: centralized and decentralized adaptive controllers are designed to compensate the sensor faults for different internal structures of systems which are subject of this paper. The law adaptations which make the different faulty systems stable are given. A simulation example of an overall INCS consisting of three interconnected and networked control subsystems and involving stabilization of unstable steady-states is used to demonstrate the efficiency of the proposed approach.

Keywords: Adaptive control, Centralized control, Decentralized control, Fault-tolerant control (FTC), Interconnected system, Networked control system (NCS), Reference model (RM), Sensor failure.

1 Introduction

The notion of Fault-Tolerant adaptive control has been an active area of research (Blanke et al 2003, Bodson and al1997, Patton 1997, Patton et al 1997, Patton et al

2007). The theory of large-scale systems is devoted to the problems that arise from some difficulties: dimensionality, information structure constraints, uncertainty and delays (Ioannou et al 1985, Mahmoud et al 1997, Huang and Nguang2010, Lina and Chen 2006, Patton et al 2010).

A system is considered large-scale if it is necessary to partition the given analysis or synthesis into manageable sub-problems. As a result, the overall system is no longer controlled by a centralized controller but by several independent controllers which all together represent a decentralized controller. This is the fundamental difference between feedback control of small and large systems. On one hand, the development in this direction has reached a level of important applications where adaptive controllers are used to enhance stability and improve operating conditions of defective systems (Bodson and Groszkiewicz1997, Ioannou and Kokotovic1985, Mahmoud1997, Tsai et al2009). On the other hand, her theory is developed to make a general practical use of adaptive controllers in both large-scale and networked control systems (Ioannou and Kokotovic1985, Mahmoud1997, Patton et al). In interconnected and networked control systems, there will be more adaptive controllers located at different, possibly distant units, and in control centers. Besides, the dynamic of each local subsystem is not known exactly and the local outputs are corrupted with noise disturbances and faults via network control. In this paper, centralized and decentralized adaptive FTC based on reference model is included in presence of all interactions and over medium of communication between each subsystem. Two structures of adaptive controllers for interconnected and networked system is proposed (Bakule 2008, Challouf et al, Hansheng2003, Hovakimyan and Ramachandra2006, Sundarapandian2005). Each adaptive controller is designed to compensate the additive faulty sensor. The stability of the overall adaptive control scheme is established.

The paper is organized as follows: Section 2 recalls the interconnected and networked control system modernization. Also, it represents the controller synthesis for LTI and continuous time systems. A simulation example of three interconnected and networked control subsystems subject to sensor faults is used in Section 3 to illustrate the effectiveness and performance of the two architectures (centralized and decentralized) active fault tolerant control system. Finally, a conclusion is included.

2 Problem Statement

2.1 Interconnected System

This class of the large-scale system can be composed of N-interconnected subsystems (Ioannou and Kokotovic1985, Mahmoud1997).

Consider an overall interconnected system which is given by the following state spaces:

$$\left(S_p\right)\begin{cases} X_p\left(t\right) = A_p X_p\left(t\right) + B_p U_p\left(t\right) + D_p w_p(t) \\ Y_p\left(t\right) = C_p X_p\left(t\right) + D_p U_p\left(t\right) + V_p v_p(t) \\ X_p\left(0\right) = \varphi(t) \end{cases} . \tag{1}$$

The index p designs the processus parameters.

A_p, B_p, C_p, D and V are the parameters system with appropriate dimensions.

On the other hand, $X_p\left(t\right) \in \mathbb{R}^n, U_p\left(t\right) \in \mathbb{R}^m, Y_p\left(t\right) \in \mathbb{R}^q$ and $W_p\left(t\right) \in \mathbb{R}^p and V_p\left(t\right) \in \mathbb{R}^p$ are the state vector, the control vector, the output vector and the external disturbance vectors respectively.

As black as this class of the large-scale system contains N-interconnected subsystems and based on equation (1), the partitioned matrix X_p, U_p and Y_p are:

So, we can write:

$$n = \sum_{i=1}^{N} n_i, m = \sum_{i=1}^{N} m_i, p = \sum_{i=1}^{N} p_i \; and \; q = \sum_{i=1}^{N} q_i . \tag{2}$$

$$\left(S_i\right): \begin{cases} \dot{X}_{pi}(s) = A_{pi} X_{pi}(s) + B_{pi} U_{pi}(s) + \sum_{j \neq i} \left(G_{pij} g_{pij}(s) + D_{pij} W_{pij}(s)\right) \\ Y_{pi}(s) = C_{pi} X_{pi}(s) + L_{pi} V_{pi}(s) \quad ; i, j = 1, ..., N \\ X_i(0) = \varphi_i(t) \end{cases} . \tag{3}$$

Where: $X_{pi} \in \mathbb{R}^{n_i}, U_{pi} \in \mathbb{R}^{m_i} and \, Y_{pi} \in \mathbb{R}^{q_i}$ are respectively the local states, the control and the output of the subsystems (S_i).

$A_{pi} \in \mathbb{R}^{n_i \times n_i}, B_{pi} \in \mathbb{R}^{n_i \times m_i} and \, C_{pi} \in \mathbb{R}^{q_i \times n_i}$ are respectively the parametric matrix of the local states, the control and the output of the i[th] processus coupled with j[th] subsystems (S_j).

2.2 NCS Model

The stage of modeling is rather significant at the time of the study of a process. The systems considered in this work belong to a particular class. They are the systems ordered by a medium of communication, they are known still by the systems

ordered in network (NCS) [Huang and Nguang 2010, Lina and Chen 2006, Patton et al 2007]. This class of the system presents the phenomenon of delay in their dynamic of which its structure is illustrated by the fig.1. Contrary to the ordinary systems whose temporal evolutions can be given starting from the value of state. Those of the systems ordered in network depend primarily on of the last values of the state X_p(t). Moreover, the latter present the phenomena of delay and the losses or duplications of the messages during the transmission of the data control/actuator: τ_{cA} and sensor/control: τ_{sc}.

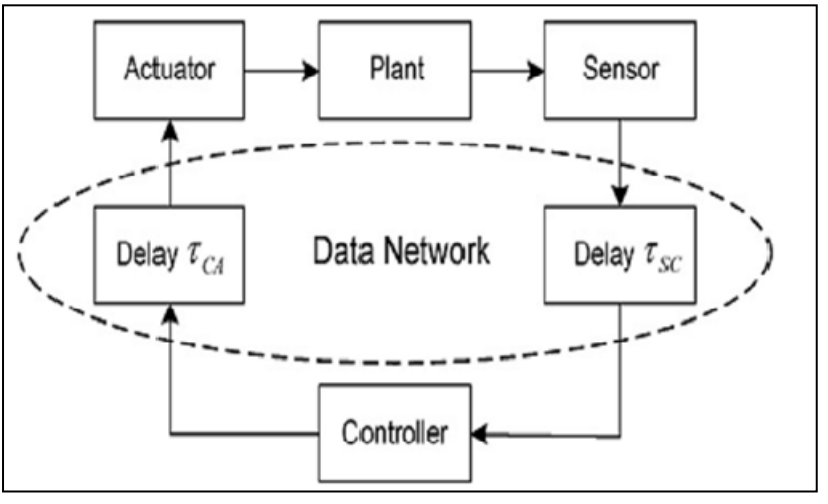

Fig. 1 Internal Structure of NCS

Generally, three working frameworks are used to represent a late system: models on ring, infinite models of dimension on operators and models in the form of differential equations. In this present work, concerning the stability on the one hand and the modeling of communication TCP on the other hand, we are interested in the effects of the delay in dynamics of the NCS. Plus precisely, we thus consider systems (eq.1) rewritten in the form:

$$\left(S_p\right)\begin{cases} X_p\left(t\right) = A_p X_p\left(t-\tau\right) + B_p U_p\left(t-\tau\right) + D_p w_p(t) \\ Y_p\left(t\right) = C_p X_p\left(t-\tau\right) \\ X_p\left(0\right) = \varphi(t) \end{cases} . \tag{4}$$

At the time of the phase of modeling, as well as the matrices defining a model, it is essential to determine the type of delay which affects the system (see fig 1). The delay can be between control/actuator and/or sensor/control that as (see fig.1):

$$\tau = \tau_{sc} + \tau_{cA} \quad ; 0 \le \tau_{\min} \le \tau \le \tau_{\max}. \tag{5}$$

τ_{min} and τ_{max} represent respectively the minimum and maximum values of delay. All MIMO transfer matrix representations have appropriate dimensions and are proper real-rational matrices, stabilisables and detectable. A state space rational proper transfer function is denoted by:

$$Sys_p = \frac{U_p}{Y_p} = \begin{bmatrix} A_p & B_p \\ C_p & D_p \end{bmatrix} = C_p \left(sI - A_p\right)^{-1} B_p + D_p \tag{6}$$

2.3 Model Reference Adaptive FTC Design

Consider a LTI system defined by eq.12. To accommodate the last system, we were implementing adaptive FTC. His principal is explained by fig.2 offering the structure of co-operative INCSs and FTC. The last method is based on reference model.

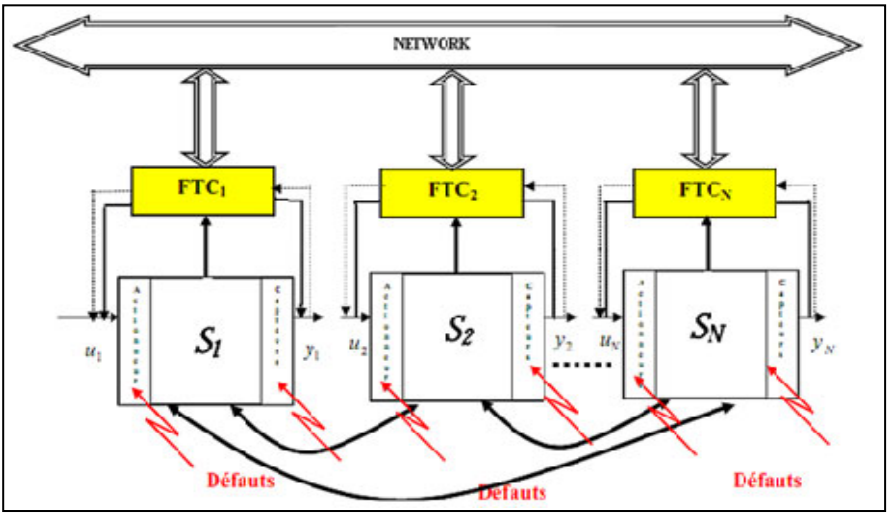

Fig. 2 Structure of co-operative Interconnected NCSs and FTC

This last figure proves the aptitude to reach the characteristics specified of control by the networked to communicate between N-interconnected subsystems in presence of faults (Bakule 2008, challouf et al 2009, Hansheng 2003, Sundarapandian 2005).

In the time domain, the overall reference model is described by the equation:

$$\dot{Y}_m(t) = A_m Y_m(t) + B_m r(t). \tag{7}$$

The index m designs the known reference model parameters.

In this part, we apply the direct method of the fault tolerant adaptive control. The control input is given by equation (8) as follow:

$$U_P(t) = (C_0(t)r(t)) + (G_0(t)Y_p(t)). \tag{8}$$

With C_0(t) and G_0(t) are the parameters of the adjustable controller.

The derivation of time response plant is given by:

$$\dot{Y}_p(t) = (C_p A_p + C_p B_p G_0) X_p(t) + C_p B_p C_0 r(t). \tag{9}$$

When $C_0(t) = C_0^*$ and $G_0(t) = C_0^*$

The motivation being that there exist nominal parameter values of the adaptive controller:

$$\begin{cases} C_0^* = \left(C_p B_p\right)^{-1} B_m \\ G_0^* = \left(C_p B_p\right)^{-1} \left(A_m C_p - C_p A_p\right) \end{cases} \tag{10}$$

The update laws are given by:

$$\dot{\phi} = \begin{bmatrix} \dot{\phi}_r(t) \\ \dot{\phi}_Y(t) \end{bmatrix} = \begin{cases} \dot{C}_0(t) = -g e_0(t) r(t) \\ \dot{G}_0(t) = -g e_0(t) Y(t) \end{cases} \tag{11}$$

Thus, the expression of the adaptive law control becomes:

$$U(t) = \left(\left(\phi_r(t) - C_0^*\right) r(t)\right) + \left(\left(\phi_Y(t) - C_0^*\right) Y_p(t)\right). \tag{12}$$

Since, the error dynamic equation between the plant time responses Y_{pf}(t) and reference model Y_m(t) with the adjustable parameters of the regulator is given by: $\dot{e}_0$

3 Three Interconnected and Networked Control Subsystems Example

In this simulation party, we interest at a numerical example where N=3 illustrated by fig. 3 in order to demonstrate the efficiency of the proposed control.

Consider the overall system (eq.1) consisting of three interconnected and networked control sub-systems (Sys_1), (Sys2) and (Sys_3) with unit reference input (r(t)=1). On one hand based on fig.2, the transfer function of overall interconnected networked control reference model (eq.17) is giving as follows:

$$Sys_m = \frac{Y_m(t)}{U_m(t)} = e^{-0.348s} \frac{3s^3 + 11.26s^2 + 13.14s + 4.703}{s^4 + 5.5s^3 + 11.06s^2 + 9.688s + 3.125}$$

But, the transfer function of overall interconnected networked control system without external disturbance is giving as follows:

$$Sys_p = e^{-0.348s} \frac{3s^3 + 11.26s^2 + 13.14s + 4.703}{s^4 + 5.5s^3 + 11.06s^2 + 9.688s - 3.125}$$

So reference to the last transfer function, the overall interconnected and networked control system Sys_p is unstable.

On the other hand, the interconnection vector functions are respectively: G_{12}=-0.5, G_{21}=0.5, g_{12}=-0.579 and the total delay is: τ= 0.348 where the delays into sensor/control and control/actuator are giving respectively: $\tau_{sc} = \tau_{cA} = 0.174$. The global Interconnected NCS (Sys_p) is unstable. Then as the fault f_s(t) is additive it can attack the total output Y_p(t)or one or more outputs Y_p(t) of the total system Sys_p. It is clearly, at the moment t = 20sec, we generate the offset fault with amplitude 1.

The time response Y_{pf}(t) of the plant becomes:

$$Y_{pf}(t) = Y_p(t) + f_s(t), i = 1,...,N. \tag{13}$$

We use the control law (18) for various types of faults. The figures 4 and 5 illustrate the trajectories of the overall INCS time responses Y_{pf}(t), the reference model Y_m(t) and the error e_0(t).

The fig.5 illustrates the dynamic global controls trajectories: U_p(t) were implemented on different interconnected and networked control Subsystems Sys_p to accommodate the defective overall interconnected and Networked control system.

4 Main Results and Interpretations

Here, to study the influence and the differences between centralized and decentralized architecturally adaptive controllers based on reference model, the fig.4 and fig.5 illustrate the various response trajectories. It is clearly that the accommodation of Interconnected NCS_f is realized by the proposed control laws such that are find simulation results. In addition, it is clearly that the adaptive FTC is implemented to three subsystems. They are LTI, continuous times, interconnected and networked control subsystems Sys_i,i=1,2,3. All constitute an overall interconnected NCS system Sys_p which his parameters depend essentially on all subsystems. Besides, the responses of defective plant Y_{pf}(t) are controlled by centralized

control: U(t) and decentralized controls: $u_1(t)$ and $u_2(t)$ in the presence of faulty sensor (see respectively fig.4 and 5). The global and distributed outputs respectively $Y_{pfg}(t)$ and $Y_{pf}(t)$ are reconfigured where a change then it recovers the desired output $Y_m(t)$ of reference model.

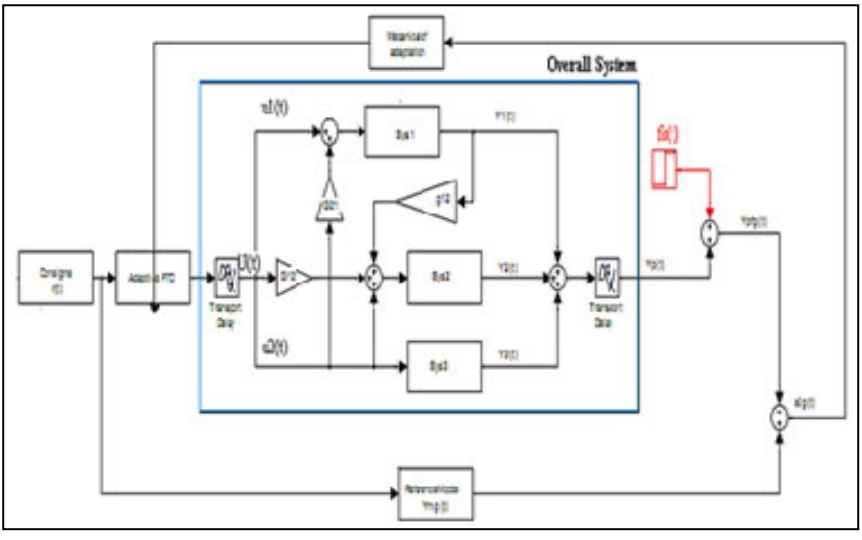

Fig. 3 Functional diagram of Interconnected NCS in presence of sensor faulty

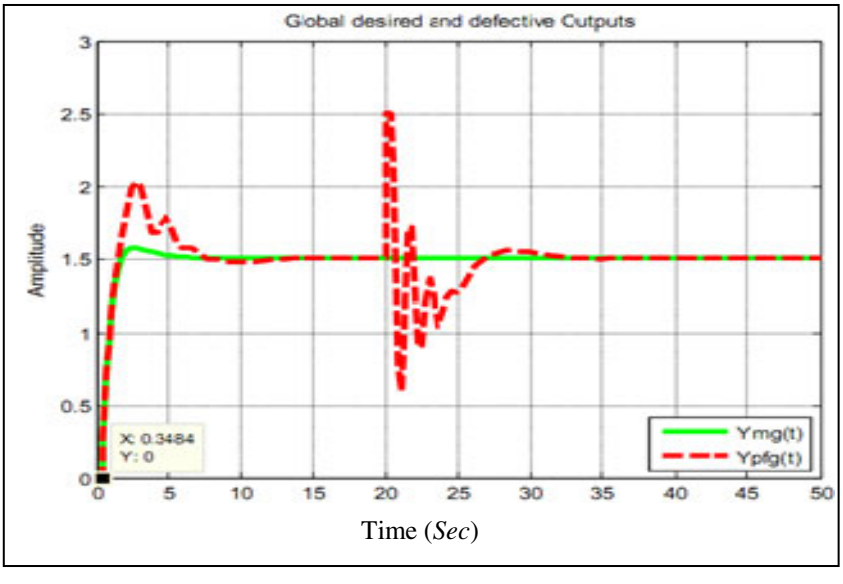

Fig. 4 Dynamic global output responses via MR Adaptive FTC.

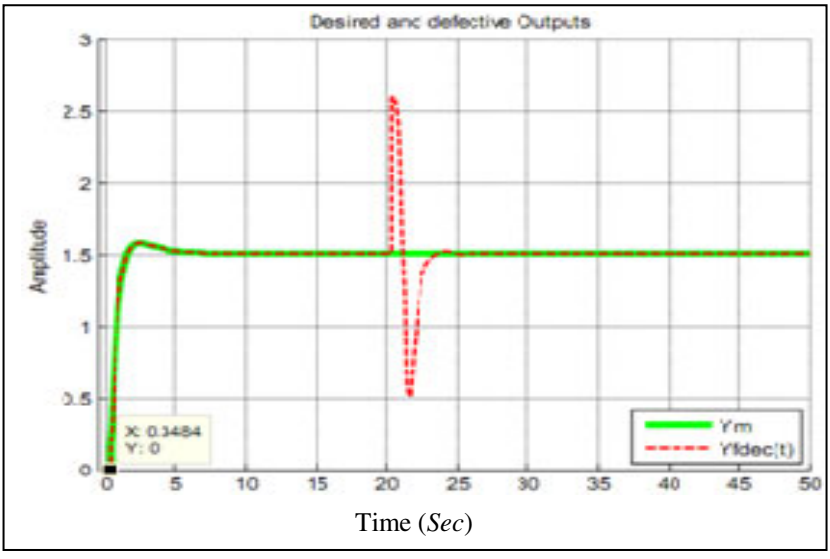

Fig. 5 Dynamic distributed output responses via MR Adaptive FTC

In fig.6, the errors between the outputs defective processus and his reference model towards zeros for centralized and decentralized adaptive controllers. In the presence of additive defects, the accommodation of the N-interconnected and networked control subsystems is assured by the fault tolerant adaptive control based

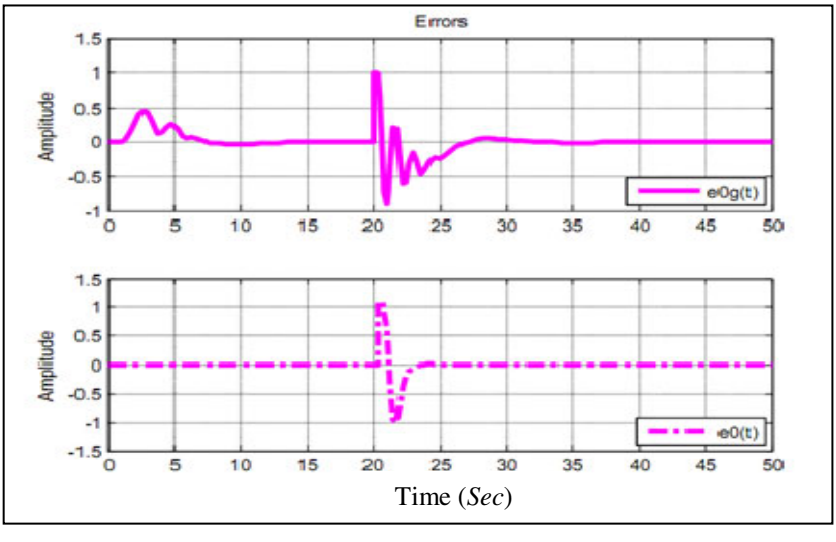

Fig. 6 State errors

on reference model. We can note that the decentralized architecture of adaptive FTC implanted of an overall interconnected networked control system permits to build high performances and marvelous accommodation. The actual class of system may be robust to change all delay parameters. If the totals delay τ overstepping the limited values, the processus cannot be stable.

The adaptive fault tolerant controllers are based on updated controller parameterizations C_0^* and G_0^*. They are updated by some adaptive laws and they are designed to minimize the deviation of output caused by the fault $f_s(t)$.

So, many strong points of the present fault tolerant adaptive control schemes in comparison with the existing techniques for two representations (centralized/decentralized) of INCSs are the following:

(i) they are two structures of large-scale system which differ from one another in the model used to represent the coupling between N-subsystems on which the controls are based;
(ii) sensor faulty dynamics are included in the adaptation loop and hence any online estimation parameters of overall system and N-interconnected subsystems will not cause significant of presence of sensor faults;
(iii) the present approach can be regarded as a generic one leading to different specific schemes that result from the choice of controller models of different degrees of complexity. There exists a tradeoff between models complexities and system performances for some tracking tasks. This can be used for the choice of appropriate fault tolerant adaptive control structures for desirable tasks;
(iv) the appropriate selection of decentralized techniques to be employed on N-interconnected subsystems distributed;
(v) a major point in the present development from the two architectures (centralized/decentralized) of controls that are high performances and marvelously reconfigurations of the distributed fault tolerant adaptive controls.

5 Conclusion

The paper addresses the adaptive stabilization problem of particular class of complex system: Interconnected and NCSs with time-invarying network-induced delay and without packet dropout. Various architectures: centralized and decentralized structures of adaptive MR control of objective systems in the presence of sensors failures were proposed. Simulation results are given to illustrate the efficacy of our design approach using two different structures of adaptive controllers. It is verified that, a major point in the present development from the two architectures (centralized/decentralized) of controls that are high performances and marvelously reconfigurations of the distributed adaptive FTC.

References

(Blanke et al 2003) Blanke, M., Kinneart, M., Lunze, J., Staroswiecki, M.: Diagnosis and fault tolerant control. Springer, Heidelberg (2003)

(Bodson and Groszkiewicz 1997) Bodson, M., Groszkiewicz, E.J.: Multivariable Adaptive Algorithms for Reconfigurable Flight Control. IEEE Transaction on Control Systems Technology 5(2) (1997)

(Patton1997) Patton, R.J.: Fault-tolerant control: The1997 situation. In: IFAC Fault Detection, Supervision and Safety for Technical Processes, Kingston Upon Hull, UK, pp. 1033–1055 (1997)

(Patton and Kilinkhieo2009) Patton, R.J., Klinkhieo: An Adaptive Approach to Active Fault-Tolerant Control. The Open Automation and Control Systems Journal 2(3), 54–61 (2009)

(Ioannou and kokotovic1985) Ioannou, P., Kokotovic, P.: Decentralized Adaptive Control of Interconnected Systems with Reduced-order Models. Ataomatica 21(4), 401–412 (1985)

(Hamoud1997) Mahmoud, M.S.: Adaptive Stabilization of a class of Interconnected Systems. Computers Elect. Engng. 23(4), 225–238 (1997)

(Huang and Nguan 2010) Huang, D., Ngguang, S.K.: Robust fault estimator design for uncertain networked control systems with random time delays: An ILMI approach. Information Sciences 180(3), 465–480 (2010)

(Lina and Chen2006) Lina, C., Chen, H.C.: Robust control of interconnected network schemes subject to random time varying communication delays. Int. J. Electron. Commun (AEÜ) 60(2), 647–658 (2006)

(Patton et al 2007) Patton, R.J., Kambhampati, C., Casavola, A., Zhang, P., Ding, S., Sauter, D.: A Generic Strategy for Fault-Tolerance in Control Systems Distributed Over a Network. European Journal of Control 12(4), 1–17 (2007)

(Tsai et al 2009) Tsai, Sue, N.C., Yang, C.: Integrated model reference adaptive control and time-varying angular rate estimation for micro-machined gyroscope. International Journal of Control (2009)

(Bakule 2008) Bakule, L.: Decentralized control: An overview. Annual Reviews in Control 32(3), 87–98 (2008)

(Challouf et al 2009) Challouf, A., Tellili, A., Abdelkrim, M.N.: Fault- Tolerant Adaptive control of linear Systems applied to A Robot H4. Le 3éme Colloque de Recherché Appliqué et deTtransfert de Technologie. In: 2éme Conférence Internationale, Nouvember 11-12, Tunisie (2009)

(Hansheng 2003) Hansheng, W.: Decentralized adaptive robust control for a class of large scale systems with uncertainties in the interconnections. International Journal of Control 76(3), 253–265 (2003)

(Hovakimyan and Ramachandra 2006) Hovakimyan, Ramachandra, A.: Decentralized adaptive output feedback control via input/output inversion. International Journal of Control 79(12), 1538–1551 (2006)

(Sundarapandian 2005) Sundarapandian, V.: Distributed Control Schemes for Large-Scale Interconnected Discrete-Time Linear Systems. Mathematical and Computer Modelling 41(2), 313–319 (2005)

Variable Drive Frequency Effect on Spindle Dynamic Behavior in High Speed Machining

Bechir Badri[1], Marc Thomas[1], and Sadok Sassi[2]

[1] Department of Mechanical Engineering, École de Technologie Supérieure.
1100, Notre-Dame street West, Montreal, H3C 1K3, Quebec, Canada
bechir.badri@gmail.com; marc.thomas@etsmtl.ca
[2] Sohar University, Sohar, Oman
s.sassi@soharuni.edu.om

Abstract. In high speed machining, the interaction between the variable drive frequencies and the excitation frequencies due to bearing defects of the spindle is studied in this paper. The interference between both phenomena causes an amplification of vibration, harmful for the machining stability and chatter, the surface quality, as well as the dynamic behavior of the spindle. Even if the implications of such interference highly affect the reliability of the machining process and the production by creating new critical speeds, this phenomenon has not been yet identified as the cause of the problem. The excited frequencies resulting from this interference imply new critical rotational speeds that should simply be prohibited while establishing cutting parameters. The observation of this phenomena help to diagnose bearing defects. Transient experimental results -conducted up to 30000 rpm- showed the interference phenomenon and pinpointed the critical speeds that can be avoided, after bearing maintenance.

Keywords: High speed machining, bearing spindle vibrations, variable drive frequencies, chatter.

1 Introduction

Surface quality (Fig 1) in high speed machining may be affected by many parameters. Specific combination of rotation speed and cutting depth can lead to the amplification of vibration (regenerative chatter) [Altintas, Y. and Budak, E., 1995; Gagnol, V. *et al*, 2007].

In fact, regenerative self-excited vibrations can occur under specific operating conditions [Gagnol, V. *et al*, 2007], causing waviness on the surface, basically related to the modulation of the cutting force, the chip thickness and the tool vibration (Fig.1).

In order to insure a good surface quality during the machining process, to prevent damaging the spindle, machining supervisors use stability lobes diagram [Altintas, Y. and Budak, E., 1995].

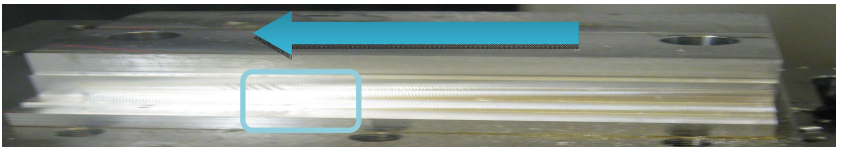

Fig. 1 Chatter during machining near the stability limit

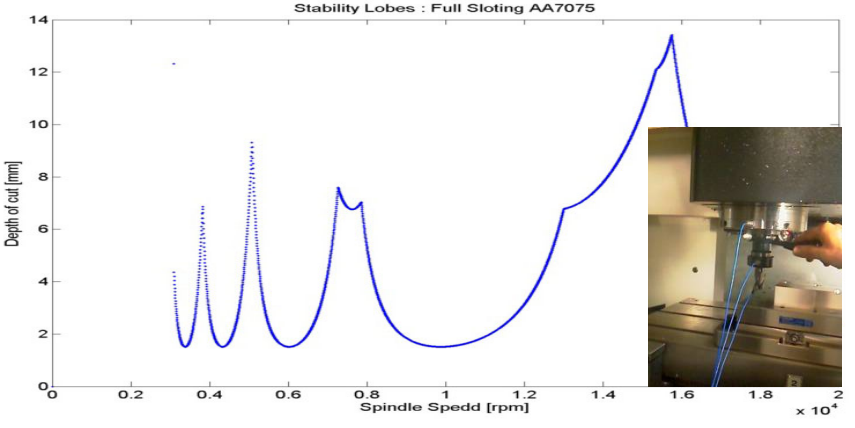

Fig. 2 Stability lobes and natural frequencies by impact

Stability diagrams are a graphical representation indicating stable cutting depth (underneath the curve) as a function of rotational speed and are dependent of the natural frequencies of the spindle-tool-workpiece system, measured by impact testing (fig 2).

2 High Speed Machining

Previous works [Badri *et al*, 2009] already proven that these direct stability lobes are not efficient, since they are calculated with natural frequencies measured in static, neglecting the drift of natural frequencies under the gyroscopic effect, occurring in high rotational speed [Swanson *et al*, 2005; Lacroix, 1988; Lalanne and Ferraris, 1996]. This phenomena will modify the system dynamic parameters according to the rotation speed, thus, the equation of motion becomes [Lalanne and Ferraris, 1990]:

$$[M].\{\ddot{y}\}+[C+G(\omega)].\{\dot{y}\}+[K].\{y\}=\{F\} \qquad (1)$$

The Campbell diagram is obtained by plotting, for each rotating speed, the eigenvalues of the following matrix:

$$A = \begin{pmatrix} \begin{pmatrix} 0 & \cdots & 0 \\ \vdots & \ddots & \vdots \\ 0 & \cdots & 0 \end{pmatrix} & \begin{pmatrix} 1 & \cdots & 0 \\ \vdots & \ddots & \vdots \\ 0. & \cdots & 1 \end{pmatrix} \\ (-M^{-1} \cdot K) & (-M^{-1} \cdot C) \end{pmatrix} \quad (2)$$

The Campbell diagram (fig 3) indicate the drift of the static natural frequencies (750Hz, 2010Hz and 4820 Hz when rpm=0), and the appearance of two new components corresponding to the Forward and the Backward mode in each frequency.

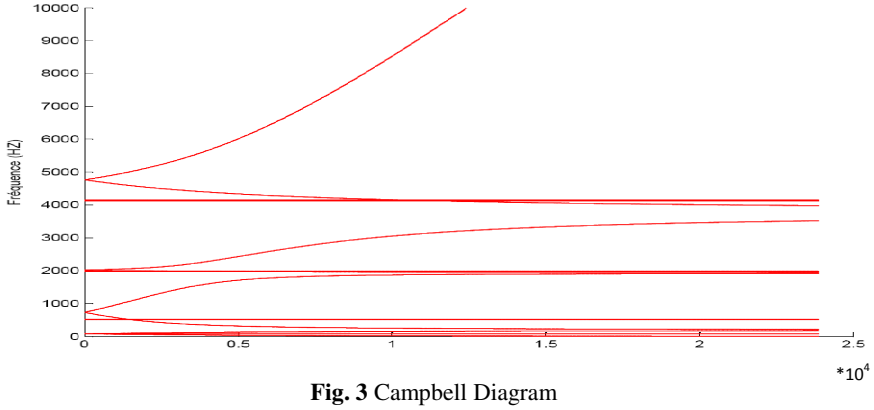

Fig. 3 Campbell Diagram

Using the modified natural frequencies (considering the gyroscopic effect), will lead to new stability lobes diagram indicating the maximum cutting rotational speed –for faster machining – and the maximum cutting depth allowed, all under stable machining [Badri *et al*, 2010].

This section already point out some prohibited rotational speeds for the cutting process. The following will investigate the appearance of new critical speeds due to the dynamic interaction of electrical phenomena induced by the Variable Frequency drive.

3 Spindle Model

In order to simulate the spindle dynamic behavior, a numerical simulation, based on a three-dimensional mechanical model with 20 degrees of freedom (Fig. 5), allows for generating the vibratory responses, affected by bearing defects, under variable rotating speed and including the gyroscopic effect. The spindle model is based on a simplified 3 d.o.f. bearing model [Sassi *et al*, 2007]. In order to integrate the directional XY coupling induced by the gyroscopic effect, the model has

to be bi-directional, and 2 bearing housings have been considered to support the shaft. The shaft was modeled using a discrete finite element model in order to consider its flexible modes. Equation of motion is built according the eq. (1), and all dynamic parameters of the model are calculated and detailed in [Badri *et al*, 2009].

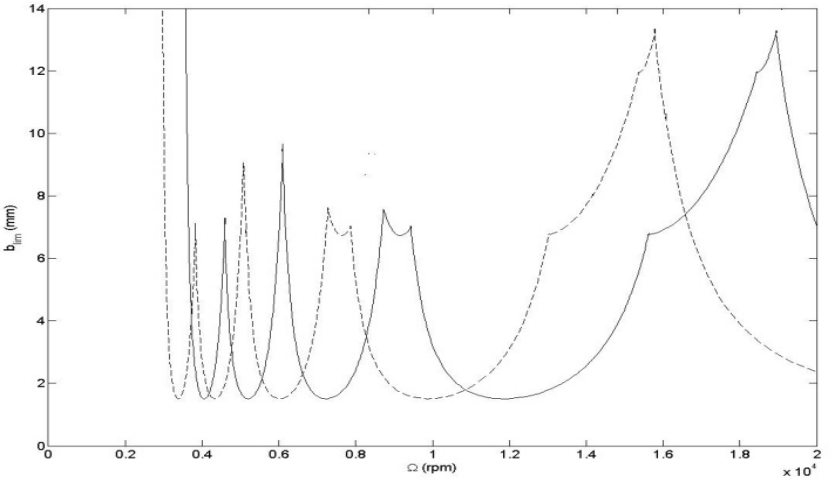

Fig. 4 Stability lobes diagram: Static Natural Frequencies (--) Including Gyroscopic Effect(-)

4 Variable Frequency Drive

In machining centers, when the rotational speed exceeds 16000 RPM, the most common spindle type is the built-in motorized spindles. The motor is literally built into the spindle. The speed variation is controlled by a VFD (fig. 6a).

To perform the speed variation, a pulse width modulation is performed on the input voltage sine wave (Fig. 6b), according the desired speed. The carrier frequency is the main pulse frequency –usually at high frequency: 5KHz and up-, and side bands modulation frequencies will appear with ΔF proportional to the rotating speed.

The technical specifications provided by the controller manufacturer -Siemens- indicate a carrier frequency located at 11 KHz, This value is confirmed by experimental vibration measurement on the spindle (fig 7).

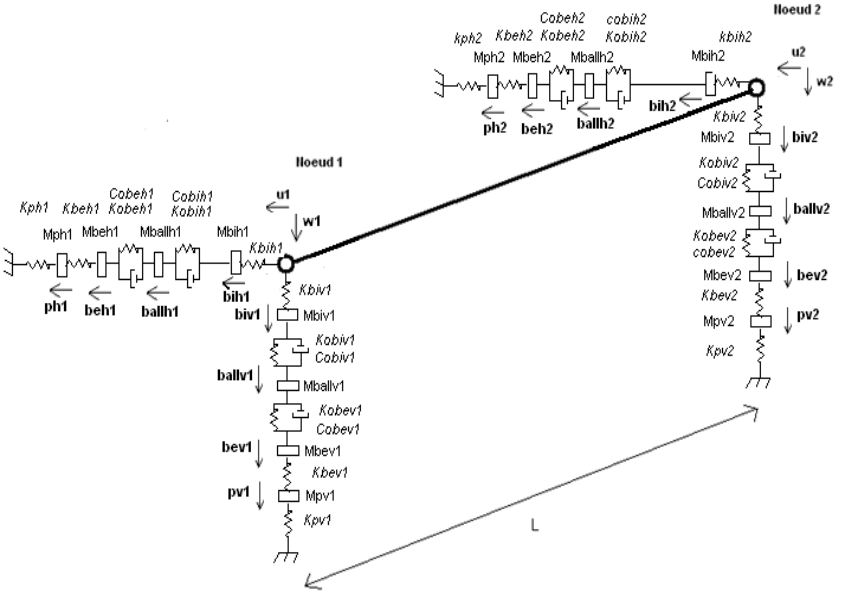

Fig. 5 20 d.o.f. Spindle Model

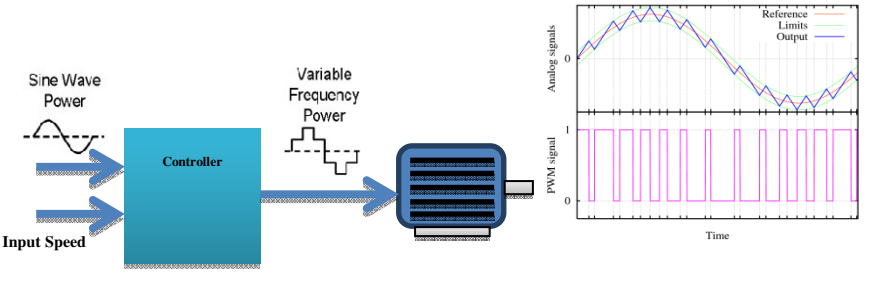

Fig. 6a VFD Principle; b: pulse width modulation

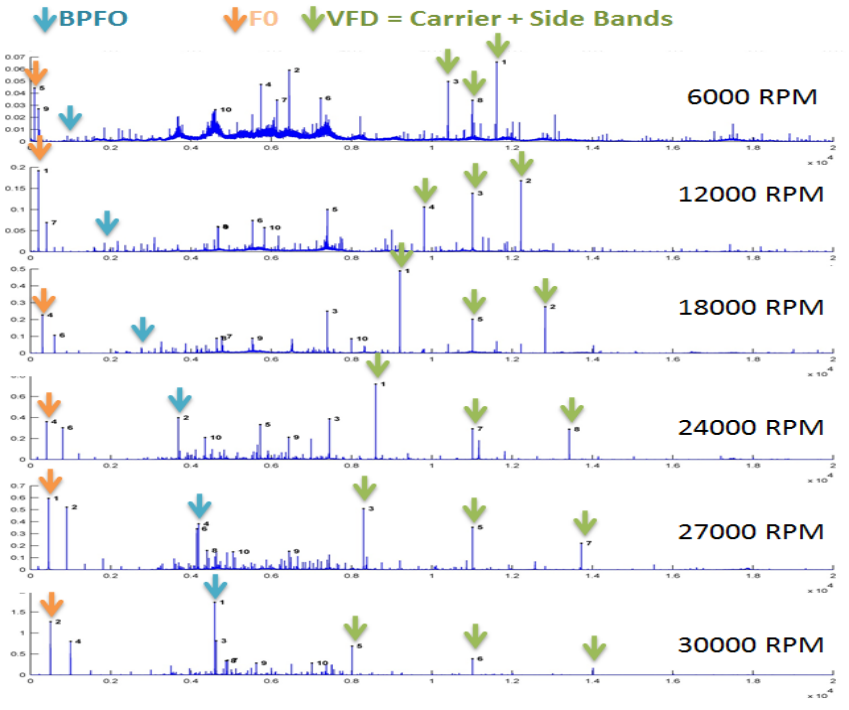

Fig. 7 Acceleration spectrum at different speeds

The wideband acceleration spectrums (20Khz) indicate the rotational speed F_0, an harmonic of the BPFO component due to a bearing defect –more perceptible in higher speed-, as well as the VDF carrier frequency at 11Khz and the corresponding side bands frequencies (varying with the rotational speed). The energy contribution of the variable drive frequency in the measured vibration levels is compiled in table 1. Between 18000 rpm and 24000 rpm, this contribution reaches 88% of the overall vibration energy, due to the interference with an harmonic of the bearing frequency BPFO. This harmonic was due to a spindle bearing defect on the outer race.

Table 1 VFD Energy Contribution in measured vibration levels

Speed(RPM)	RMS Overall (g)	VFD RMS (g)	%
6000	0,29	0,06	22,6 %
12000	0,32	0,17	54,3 %
18000	0,49	0,41	**84,5** %
24000	0,65	0,57	**88,8** %
27000	0,68	0,46	68,0 %
30000	1,19	0,55	46,6 %

In order to locate the critical rotational speed, the vibration signal (fig 8) is then recorded during linear run up, from 0 to 30 000 RPM (3 to 7 sec), followed by permanent regime (7 to 22.5 Sec), and then a shutdown (from 22.5 to 27 Sec). The signal has been filtered in the frequency domain to remove noise. Fig 8 shows the time-frequency representation. When the fourth harmonic of BPFO crosses the VFD lower side band, large vibration amplifications are noticed, that can be seen from both the time and time-frequency signals. This new critical frequency, very harmful for the spindle dynamic behavior as well as the surface quality, is located around 23 000rpm. For better results, it is recommended to operate at higher rotational speeds.

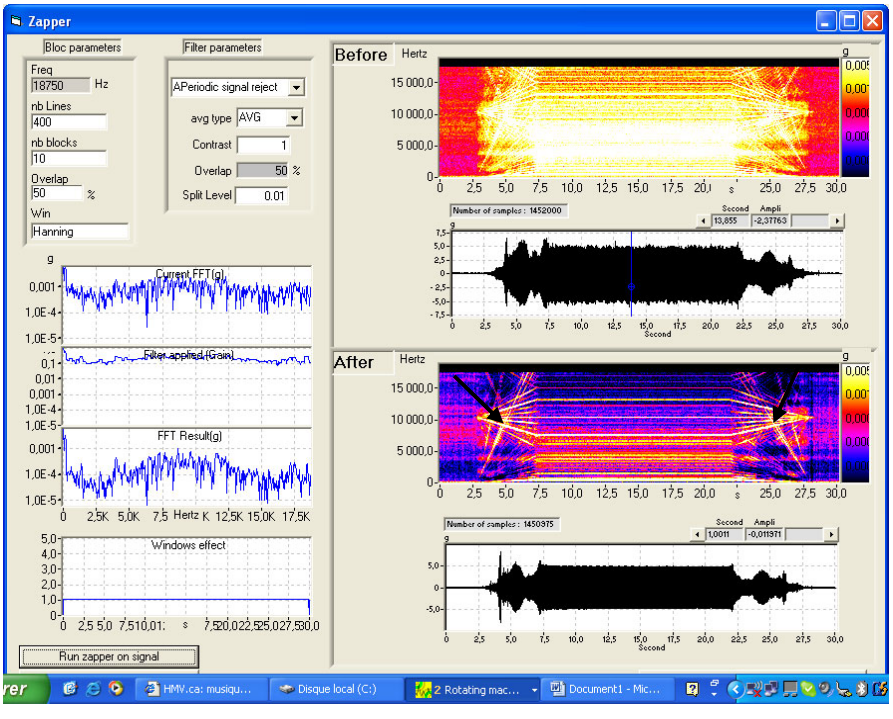

Fig. 8 STFT Spectrogram during run up and shut down measurements

5 Conclusion

Machining operators are already aware of prohibited rotating speed frequencies, as detected from the stability lobes diagram. Previous work already allowed adjusting the stability lobes according to the natural frequencies drift caused by the gyroscopic effect. This paper studied the effect of the variable drive frequencies (VDF) on the dynamic behavior of spindles in high speed machining. At specific rotational speeds, the energy contribution of the VDF can reach 88%

of the overall acceleration level, due to the interaction with a bearing defect frequency. The new critical frequency allows for detecting the bearing defect (here a BPFO from a defective bearing) and must be avoided if correction to the bearing is not immediately made.

Acknowledgements. This work is supported by : «Conseil de recherche en sciences naturelles et en génie du Canada (CRSNG), Bombardier aéronautique, Pratt & Whitney Canada and CRIAQ.

References

Sassi, S., Badri, B., Thomas, M.: A Numerical Model to Predict Damaged Bearing Vibrations. Journal of Vibration and Control 13(11), 1603–1628 (2007); doi:10.1177/1077546307080040

Badri, B., Thomas, M., Sassi, S., Zaghbani, I., Songméné, V., Lakis, A.A., Mureithi, N.: Étude du comportement des roulements dans les rotors tournant à haute vitesse. CIRI, Reims, paper CIRI013, 15 pages (Mai 2009)

Badri, B., Thomas, M., Sassi, S., Zaghbani, I., Songméné, V.: Surveillance des machines d'usinage à haute vitesse. In: Proceedings of the 28th CMVA, Québec, vol. 2, pp. 197–216 (October 2010)

Swanson, E., Powell, C.D., Weissman, S.: A Practical Review of Rotating Machinery Critical Speeds and Modes. Sound and Vibration Magazine, 10–17 (May 2005)

Lacroix, J.: Comportement dynamique d'un rotor au passage des vitesses critiques, thèse de doctorat de l'INSA de Lyon France (1988)

Lalanne, M., Ferraris, G.: Dynamique des rotors en flexion, Techniques de l'ingénieur, traité Génie mécanique, B5-110-1, B5110-39 (1996)

Lalanne, M., Ferraris, G.: Rotordynamics Prediction in Engineering, p. 198. J. Wiley, G.B (1990)

Altintas, Y., Budak, E.: Analytical Prediction of Stability Lobe in Milling. CIRP Ann. 44(1), 357–362 (1995)

Gagnol, V., Bouzgarrou, C.B., Ray, P., Barra, C.: Model-Based Chatter Stability Prediction for High-Speed Spindles. Int. J. Mach. Tools Manuf. 47(7-8), 1176–1186 (2007)

Gagnol, V., et al.: Stability-Based Spindle Design Optimization. Journal of Manufacturing Science and Engineering 127, 407–415 (2007)

Experimental Non-obstructive Particles Damping Approach for Passive Vibration

Manel Ben Romdhane[1], Moez Trigui[1], Emmanuel Foltête[2], Mohamed Haddar[1], and Noureddine Bouhaddi[2]

[1] Mechanics, Modelling and Manufacturing Research Unit,
National School of Engineers of Sfax BP 1173 – 3038 – Sfax – Tunisia
benromdhanemanel@yahoo.fr, moez.trigui@gmail.com,
mo hamed.haddar@enis.rnu.tn
[2] Department of Applied Mechanics, FEMTO-ST Institute,
UMR 6174, 24 Chemin de l'Epitaphe – 25000 Besançon – France
Emmanuel.Foltete@univ-fcomte.fr,
Noureddine.Bouhaddi@univ-fcomte.fr

Abstract. This paper presents an experimental study of energy dissipation in granular particles based on the shear frictional forces between layers of particles. This approach is known in the literature as a Non-obstructive particles damping technique (NOPD).The effects of the system parameters (sizes, materials and packing density of particles) on the evolution of specific damping capacity are determined in this work research.

Keywords: damping, friction, energy dissipation.

1 Introduction

Granular particles present significant advantages compared to traditional damping materials. The introduction of a granular material in a structure [1,2] is a passive damping technique, a relatively simple and low cost approach [3] to reduce vibration. Because of its extreme simplicity, some applications include granular materials such as shuttle space [4], turbine blades [5] and industrial machine [6]. In this paper, an experimental study of the dynamic behavior of granular passive damping is performed. The phenomena of damping due to frictional shear forces between layers of particles are used to reduce the vibration amplitude of a free-free beam. The influence of some system parameters such as particles size, material and packing density on the evolution of the specific damping capacity was experimentally examined.

2 Experimental Set Up

This section describes the experimental setup used for an elastic beam treated with particle damping for passive vibration reduction. The studied structure is a

free–free elastic beam with drilled damper holes filled with granular particles. The steel beam is specified with a mass density ρ = 7840 kg/m3, Young's modulus E = $2.04.10^{11}$Pa and Poisson ratio υ =0.33. The beam dimensions are length L = 500 mm, width h = 50 mm and thickness b = 15mm. The mass of the beam is 2.58 kg. The structure is excited perpendicular to the beam center line (z direction). It is suspended with elastic soft springs in order to realize free-free conditions (Fig.1). The external force is applied thanks to a voice-coil contactless exciter. A broad-band random excitation is applied to the beam with a maximum frequency of 10 kHz in order to reveal its dynamic behavior. The signals to be processed are the outputs from the two accelerometers mounted on the vibrating structure. The measurement points are chosen for two reasons: in order to detect all the bending modes of the beam and that the position of the accelerometer does not coincide with a vibration node. A schematic of the experimental set up is shown in figure 1.

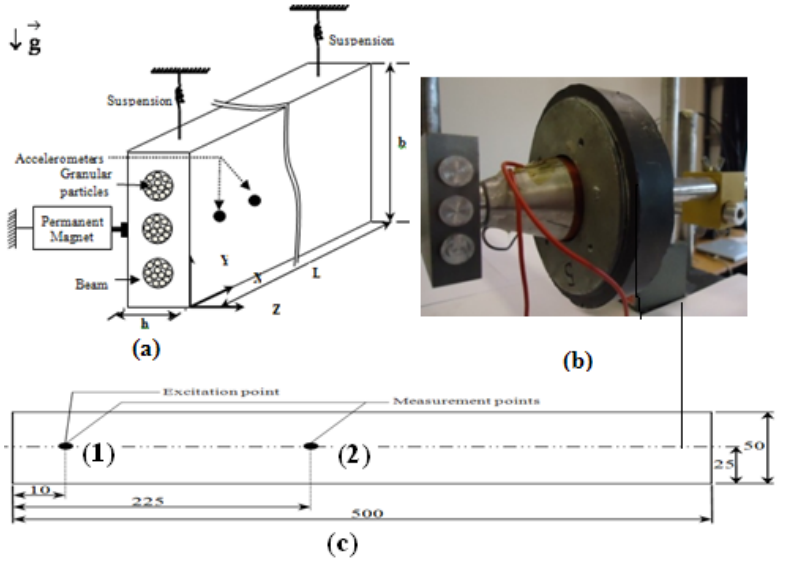

Fig. 1 (a) A schematic of experiment setup; (b) the voice-coil exciter; (c) **Distribution** of measurement points (1, 2) and excitation point (1)

The experimental procedure is as follow: In the first step, the modal characteristics of the solid beam with and without the damper holes are determined.

* The second step consists in introducing the granular particles in the holes. The frequency responses of the beam under a broadband random excitation are measured and analyzed.
* In the third step, the influence of some system parameters (particle size, material and packing density) on the evolution of the specific damping capacity is studied.

3 Modal Characteristics of the Beam

Fig. 2 shows the experimental frequency response function of the beam under random excitation. The presence of eight peaks corresponds to the eight first natural frequencies of the beam with and without the damper holes.

The modal frequencies were then identified by using Modan© software [7]. A finite element model of the beam was also built. The comparison between the experimental and numerical natural frequencies of the beam without the damper holes is summarized in Table 1.

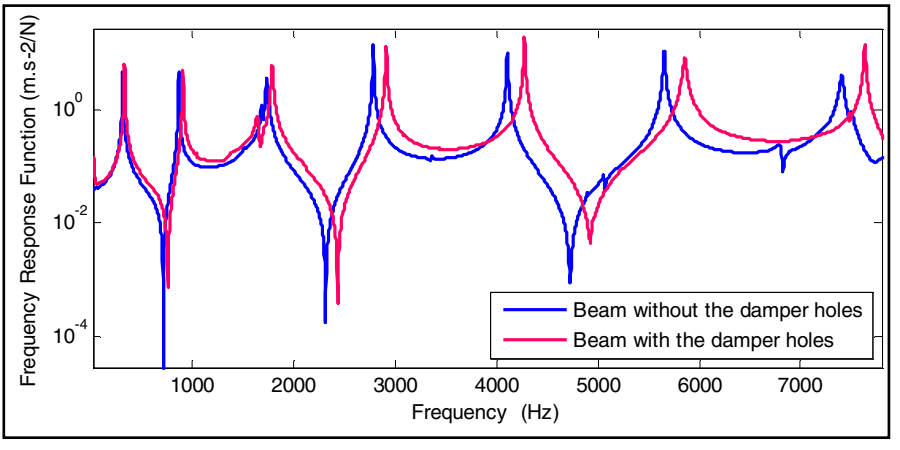

Fig. 2 Frequency response function of the beam with and without the damper holes under random excitation

Table 1 Modal eigenfrequencies of the beam without the damper holes

Method	Mode						
	1st	2nd	3rd	4th	5th	6th	7th
Experimental (Hz)	315.4	865.5	1732.9	2786.6	4107.4	5654.5	7402.3
Numerical (Hz)	314.58	863.57	1682.8	2759.8	4081.9	5634.5	7400.9
Error (%)	0.25	0.22	2.8	0.96	0.62	0.35	0.018

Table 1 shows a good correlation between the experimental and the numerical results.

Table 2 shows the effect of the damper holes on the experimental modal frequencies. For the first three modes the modal frequencies increase of about 30-40 Hz for the beam with holes. For the higher modes, the differences are much higher and reach more the 200 Hz.

Table 2 Modal eigenfrequencies of the beam with and without the damper holes

	Mode						
	1st	2nd	3rd	4th	5th	6th	7th
Without holes (Hz)	315.4	865.5	1732.9	2786.6	4107.4	5654.5	7402.3
With holes (Hz)	331.8	907.3	1786.7	2913.1	4273.7	5854.8	7630.7

4 Modal Characteristics of the Beam with Particles

Let us now introduce **steel particles** in the beam damper holes. Figure 3 shows a comparison of the beam response with and without the granular particles. In this test, filling holes requires a mass of 187.4 grams of particles of diameter 0.5 mm.

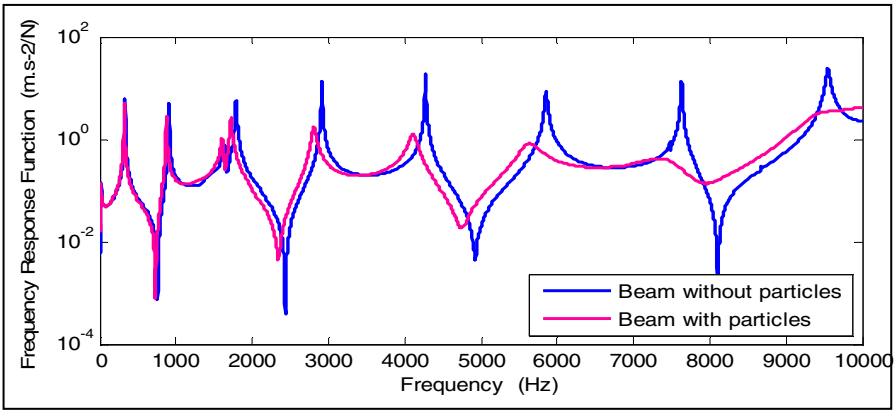

Fig. 3 Frequency response function of the beam with and without the steel particles under random excitation

From Table 3 and figure 3 we can estimate the performance of the granular particles for reducing the dynamic response of the beam. The effect of the particles is extremely high on the sixth, seventh and eighth modes. On the other hand, the level of damping is not very significant for the first three modes (low frequency modes). The explanation of this result is effected through an original experimental procedure to characterize the frictional damping rate in the second step of this project.

Table 3 Experimental modal damping of the beam with and without the particles (steel)

	Mode							
	1st	2nd	3rd	4th	5th	6th	7th	8th
Without particles (%)	0.36	0.15	0.47	0.11	0.077	0.24	0.79	0.22
With particles (%)	0.36	0.36	0.7	0.86	1.3	2.4	3.7	2.9

5 The Effects of Design Parameters

The influence of some design parameters (particles size, material and packing density) on the performance of NOPD procedure is now examined.

a. Damping effects for different particle sizes

To illustrate the effects of the particles size on the evolution of the specific damping capacity, some measurements were performed for the beam with two diameters of Zirblast particles:

* Size 1: diameter of the particles from 0.425 to 0.6 mm. The mass of particles to fill the three holes of the structure is 100.7 g.
* Size 2: diameter of the particles of 1 mm. The mass of particles necessary to fill the three holes of the structure is 91.1 g.

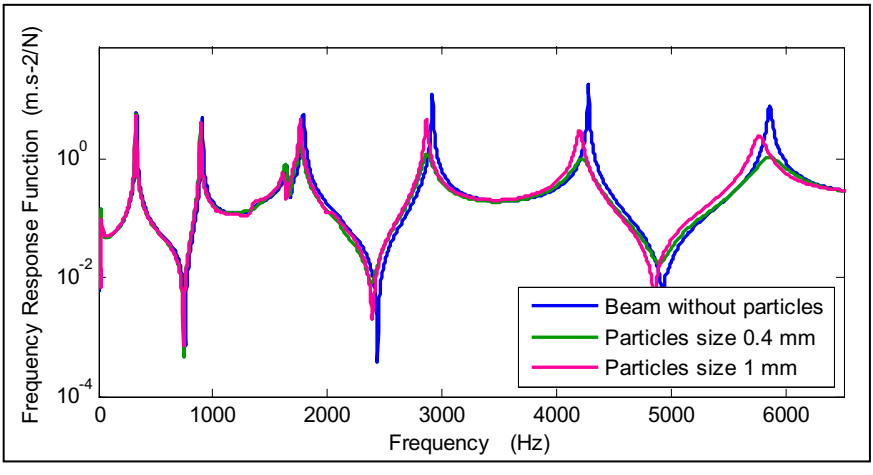

Fig. 4 Frequency response function of the beam

Fig. 4 shows the frequency response function of the system for two particle sizes with the same packing density. The figure indicates that the particle size have a direct influence on the frequency response function at resonance. For the larger diameter of the granular particles, the damping effect is less effective.

The Table 4 shows a comparison of the identified modal characteristics for the two sizes of particles. For example, for the fourth mode, the modal damping increases from 0.36 % to 1.3% while decreasing the particles size. By the way, the reduction in the response amplitude is approximately 3.5 dB.

It seems then that when the particle size is smaller, the number of contacts between particles and the wall of the damper hole increase. This would cause more friction energy dissipation.

Table 4 Experimental modal damping of the beam with different particles sizes

	Mode					
	1st	2nd	3rd	4th	5th	6th
Without particles(%)	0.36	0.15	0.47	0.11	0.077	0.24
Particles 1mm (%)	0.38	0.19	0.45	0.36	0.45	0.8
Particles 0.4 mm (%)	0.37	0.28	0.95	1.3	1.6	1.9

b. Effects of the mass density of the particles

Other parameters of studding the characteristic of particle damping is illustrate in this section. We tested two type of particle: lead and zirblast (ceramic: ZrO_2-S_iO_2) particles of 2 mm in size. We can consider:

* Lead particles: the mass of particles is 256.8 g; the density is 11320 Kg/m3 and the static friction coefficient 0.36.
* Zirblast particle (ceramic): the mass of particles is 88.7 g; the density is 3850 Kg/m3 and the static friction coefficient 0.15.

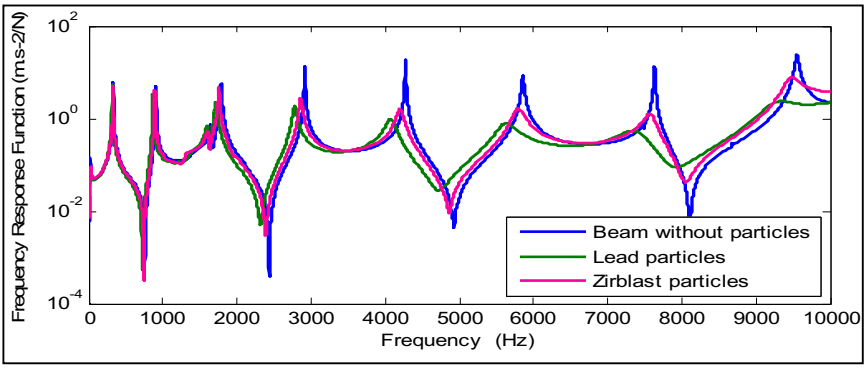

Fig. 5 Frequency responses function of the beam with lead and zirblast particles

Figure 5 shows the frequency responses function of the beam with two different types of particles: lead and ceramic. It is reported that a better damping performance is obtained with a particle material of a higher friction surface i.e. lead particles. The peak response amplitude for sixth, seventh and eighth resonance mode decrease of 1 dB by replacing ceramic particles with lead.

The comparison of the identified modal characteristics of lead and Zirblast particles is indicated in table 5.

Table 5 The modal damping of the beam with lead and zirblast particles

	Mode							
	1st	2nd	3rd	4th	5th	6th	7th	8th
Without particles (%)	0.36	0.15	0.47	0.11	0.077	0.24	0.79	0.22
Zirblast particles (%)	0.41	0.26	0.48	0.69	1.2	1.3	1	1.4
Lead particles (%)	0.38	0.24	0.93	0.89	1.7	2.4	2.7	2.9

c. Effects of the packing density of the particles

In order to highlight the effect of the compaction of granular materials on the evolution of specific damping capacity. We examined two different manners for the introduction of particles in the damper hole:

* Type 1: filling is done manually and the beam is in position angle about 45 degrees from horizontal. In this way, the distribution of the volume of the particles in the holes will may be uniform. Then, the mass of particles is 187.4 g
* Type 2: Also the filling is done manually, but we must use the hammer to realize a qualitative compaction of the granular particles. The mass of particles is 196.7 g.

We note that in both experiments we use steel particles of 0.5 mm in size.

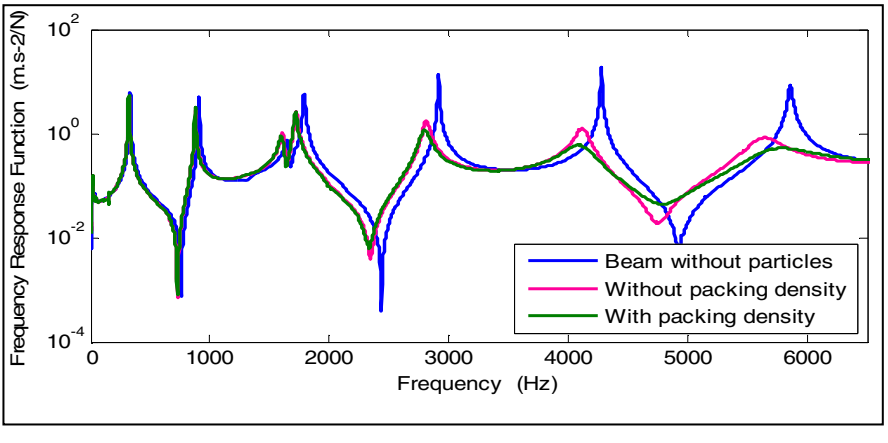

Fig. 6 Frequency responses function of the beam with two levels of compaction

As shown in Fig 6 the damping vibration is very sensitive to the effect of the compaction of granular materials. The difference in response amplitude is approximately 1.5 dB for the fifth and sixth mode. With the same modes, it is

observed (Table 6) that the modal damping increases from 2.4 % to 4.5% for sixth mode and from 1.5 % to 2.7% for fifth mode with growth of the mass of particles.

This result may be explicated by the increasing of the pressure P_v [2] between the layers of the particles. Then, the shear dissipation of energy becomes more important with the increasing of the volume fraction Φ [8].

Table 6 Experimental modal damping of the beam with and without packing density (steel particles)

	Mode					
	1st	2nd	3rd	4th	5th	6th
Without particles (%)	0.36	0.15	0.47	0.11	0.077	0.24
Without packing (%)	0.47	0.37	1.1	0.87	1.5	2.4
With packing density (%)	0.37	0.28	1.1	1.1	2.7	4.5

6 Conclusion

The focus of this investigation is on a Non-obstructive particle Damping (NOPD) technique recently introduced us a passive approach to absorb vibration energy in engineering applications. An elastic beam with damper holes embedded with metal particles is treated. The modal characteristics of the beam are determined and the modal damping is identified for original beam without damper holes and with damper holes. The NOPD is a means of passive damping vibrations, it is particularly efficient in an intermediate band frequency. In this experimental study, this band of frequency is between 2500 and 6500 Hz, which contains three bending modes. Based on shear friction energy, a numerical prediction model to confirm the experimental results is actually in progress.

References

Bourinet, J.M.: Approche numérique et expérimentale des vibrations amorties de tubes remplis de matériaux granulaires, thèse de doctorat, ECN (1996)

Liu, W., Tomlinson, G.R., Rongong, J.A.: The dynamic characterisation of disk geometry particle dampers. Journal of Sound and Vibration 280(3-5), 849–861 (2005)

Chettah, A.: Comportement vibroacoustique des structures élaborées à partir de poudrettes de pneus recyclés, thèse de doctorat, Université de Reims, ECL (2008)

Moore, J.J., Palazzolo, A.B., Gadangi, R., Nale, T.A., Klusman, S.A., Brown, G.V., Kascak, A.F.: A forced response analysis and application of impact dampers to rotor dynamic vibration suppression in a cryogenic environment. Transactions of the ASME. Journal of Vibration and Acoustics 117, 300–310 (1995)

Paget, A.L.: Vibration in steam turbine buckets and damping by impacts. Engineering 143, 305–307 (1937)

Xu, Z.W., Wang, M.Y., Chen, T.N.: A particle damper for vibration and noise reduction. Journal of Sound and Vibration 270(4-5), 1033–1040 (2004)

MODAN: MOdal ANalysis Software, Applied Mechanics Department, FEMTO-ST Institute, University of Franche-Comté, France

Fayed, M.E., Otten, L. (eds.): Handbook of Powder Science and Technology, 2nd edn. Chapman & Hall, New York (1997)

The Application of a First-Principle Damper Model for Tracking the Variation of Eigenvalues under Non-stationary Road Excitation

Piotr Czop, Grzegorz Wszołek, Dawid Jakubowski, and Wojciech Czaja

Silesian University of Technology,
Institute of Engineering Processes Automation and
Intgrated Manufacturing Systems, Konarksiego 18a, 44-100 Gliwice, Poland
piotr.czop@labmod.com

Abstract. The paper presents a method for analyzing and understanding the dynamics of prototype designs of hydraulic damper under non-stationary load conditions. In the method proposed in this paper, a high-frequency first-principle model of a damper is linearized around a series of operating points which are obtained from a preceding numerical simulation of the model. As a result of multiple repetitions of an elementary linearization, a series of linearized models and their respective eigenvalues are collected over a certain period of operation time, corresponding to the duration of a non-stationary excitation signal.

1 Introduction

Noise is the audible effect of structural and forced vibration, and its reduction is carried out at damper manufacturers as a product design and optimization activity. Noise and vibration evaluation is performed on the entire vehicle under road and laboratory conditions. However, it is quite frequently performed on isolated systems of gradually-increasing complexity in laboratory conditions, i.e. suspension or damper level. This approach allows the elimination of interactions with the vehicle body and then, in turn, enables more precise control test conditions. Laboratory experiments are more repeatable than on-road driving sessions. It is also easier to simulate typical road maneuvers and measure certain signals, such as tire forces, or use special measurement equipment (Vanhees, Maes 2000). On the other hand, laboratory-based tests allow costs to be reduced and tests to be performed faster.

The aim of this work is to develop a method for rapid model-based evaluation of natural frequency variations in excitation amplitude or operation time. An engineering approach requires a linearized model to obtain an understanding of eigenfrequencies and their dependency on the other system parameters, e.g. variable volumes above and below a damper piston. The eigenfrequencies are determined by means of instantaneous linearization at each sample instant around the current

operating point, determined from the simulation of a nonlinear damper model or its components for specific test signals (excitations), e.g. sinusoidal, step, and noise. In the results of multiple linearizations, a series of linearized models is collected for a longer operation time, e.g. typically within a few seconds. The method is presented in Fig. 1.

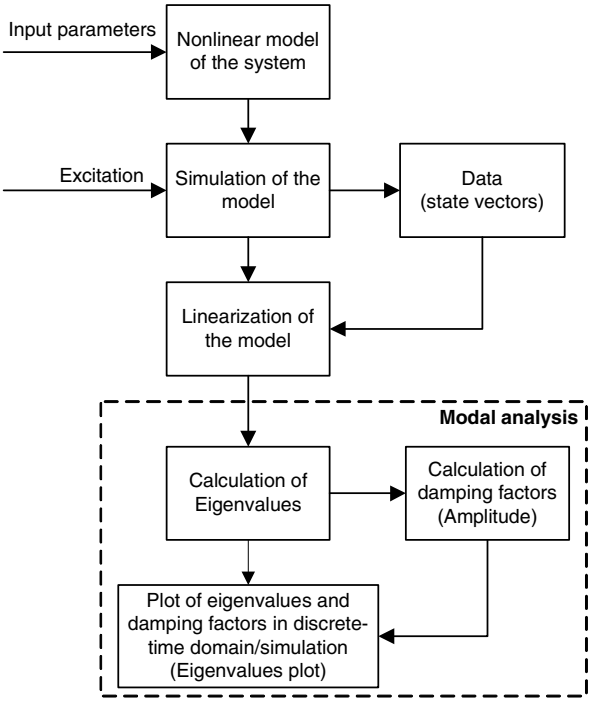

Fig. 1 Flowchart for calculation of the modal analysis technique (Eigenvalues plot)

A set of eigenvalues extracted from a linear first-principle damper model coupled with the servo-hydraulic tester model (Czop, Sławik 2011) allows natural frequency variations to be tracked under transient conditions, e.g. valve opening/closing sequence. This approach allows the influence of the model characteristics' nonlinearity on the eigenvalues variation to be investigated. The model enables the preparation of an amplification diagram, which presents the model response in the time-frequency domain where the height-coordinate is the damping ratio indicating the stability of the hydraulic damper. The amplification diagram indicates risk of amplification of vibrations for the specific excitation signal used to load the hydraulic damper. Fig. 2 shows an example of a such amplification diagram where a variable frequency component corresponding to a hydraulic stiffness of the damper (200-600Hz) and three other frequency components corresponding to structural vibrations of the test-rig system (25Hz: servovalve; 100Hz:hydraulic actuator; 1100Hz: fixation mount) are present.

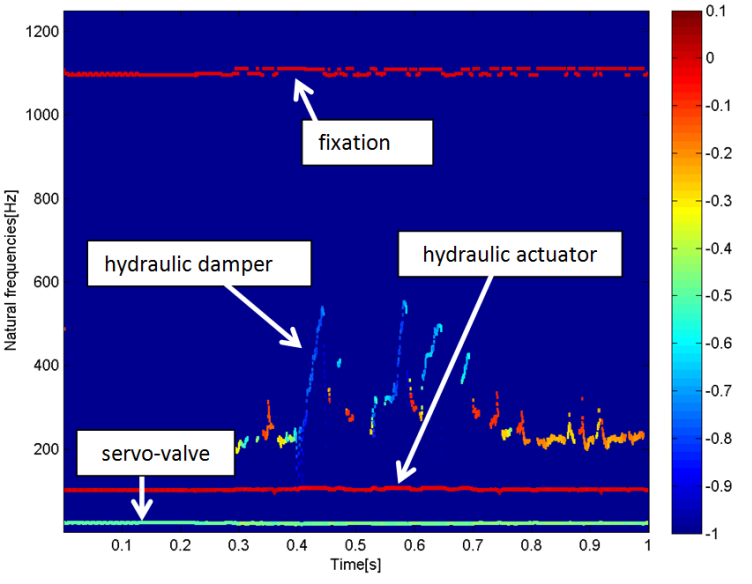

Fig. 2 Example of an amplification diagram

It is an essential problem in NVH (Noise, Vibration and Harshness) analysis (Czop, Sławik 2011), i.e. adjustment of the damper excitation range to the excitation range of interacting suspension components or internal components of a damper. The algorithm was developed, debugged and tuned within a Matlab/Simulink development environment. The linearization is performed with use of the linmodv5 function (MATLAB 1998). The proposed method can be supported by a frequency analysis, i.e. PSD (Power Spectrum Density), and time-frequency analysis, i.e. the spectrogram, for simulation and experimental data (obtained from measurements). The combined use of these techniques will allow an increase in the effectiveness of the development process and the robustness of prototype units.

2 Models of a Damper and Its Components

Damper models are widely presented in the literature. A first-principle dynamic model of a hydraulic damper was discussed by Lang in his early monograph (Lang 1977). This model was further simplified assuming massless valve systems (Kenneth, Morman 1984). The experimental results confirmed the correctness of the assumptions by providing accurate model response below 20Hz. A similar model has been created for a monotube damper, including a physical valve system model consisting of a disc stack giving a specific stiffness (Tallbot, Starkey 2002). Another monotube model is focused on the understanding of the hydraulic behavior of a piston valve. A model of the piston valve was developed using an advanced combined simulation/measurement approach (Beyer et al. 2002). A measurement setup

was equipped with a laser sensor and pressure sensors to evaluate the pressure drop across the valve assembly. A finite element method was used to simulate a valve stiffness characteristic (Beyer et al. 2002). A simplified static model was developed for the purpose of understanding the influence of a damper on the shake performance of body-on-frame vehicles (Subrabanian et al. 2003). A diagnostic model based on the first principle was created to understand and reduce the effect of self-exited vibration of a damper piston (Yamauchi et al.2003). The model was correlated to available measurement data including an experiment with the modified piston assembly. A model intended to optimize the structural dynamics of a damper was developed by Kruse (Kruse 2003). The grey-box models were developed by Duym (Duym et al. 1997) and Reybrouck (Reybrouck 1994). Those models were created to be valid for one configuration of a particular damper. They used a system identification approach to tune the set of parameters using a semi-physical valve system model based on the force-displacement characteristic.

The authors developed a damper model and servo-hydraulic tester which was described in (Czop, Sławik 2011). The FPDD model has free and fixed parameters, which can be adjusted to operational nonstationary data. The free parameters are adjusted based on an initial guess value in order to minimize the error function between the model response and operational data, while the fixed parameters are physical and geometrical properties. The procedure for adjusting a model consists of two in-a-loop phases:

- simulation of a model by solving differential equations numerically,
- numerical minimization in the parameter space with respect to an error-related criterion function.

The function describing the error has to be a positive and decreasing function of the differences between reference and modeled outputs which is the acceelration signal of the piston-rod assembly measured at the top-mount. A model to be adjusted to operational data is represented as a set of nonlinear first-prinicple state-space equations formulated in the continuous-time domain as follows:

$$\begin{aligned} &\frac{d}{dt}x(t) = f\left(t, x(t), u(t), w(t); \theta\right) \\ &y(t) = h\left(t, x(t), u(t), v(t); \theta\right) \\ &x(0) = x_0 \end{aligned} \tag{1}$$

where vector f(.) is a nonlinear, time-varying function of the state vector x(t) and the control vector u(t), while vector h(.) is a nonlinear measurement function; w(t) and v(t) are sequences of independent random variables and θ denotes a vector of unknown parameters. The details of the first-prinicple damper model and servo-hydraulic tester are given in (Czop, Sławik 2011). The sum of squared errors was used as the error criterion to evaluate the fit of the model to operational data in the frequency domain based on the rod damper acceleration. The power spectrum of the acceleration signals was obtained using the common logarithm function with base 10 applied to acceleration signal sampled at the rate of 2kHz and processed

with an FFT algorithm where the Hamming widow length is 512 samples and the overlap parameter is set to 50%. The objective function is defined as follows:

$$\varepsilon(\omega,\theta) = \log_{10}\left[y(\omega)\right] - \log_{10}\left[g(\omega;\theta)\right] \tag{2}$$

Three methods of minimizing the error function are feasible as following: (i) direct search, (ii) first-order, and (iii) second-order methods.

In addition, the hydraulic damper model requires a few physical parameters which are related to fluid (oil) properties affected by ambient conditions, e.g. oil density. Other physical parameters are provided in the form of parameters and characteristics, such as top mount stiffness or piston friction respectively. The fixed geometrical parameters are measured directly or taken from the customer specifications regarding the hydraulic actuator. The last category consists of the phenomenological parameters to which hydraulic leakages, gas/oil mass ratio, discharge and piston friction coefficients belong. These parameters are known only by their approximate values obtained at specific conditions, e.g. fixed ambient temperature.

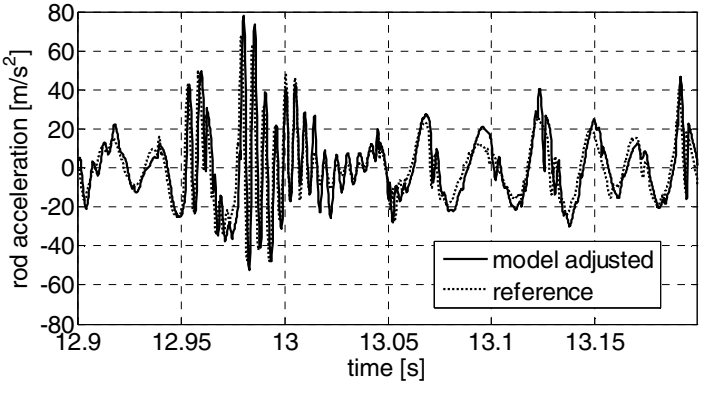

Fig. 3 Adjusted damper model in the time domain

The hydraulic leakages over the piston are difficult to obtain without precise measurements due to unknown tube-piston tolerances. The leakages over the piston-rod assembly in hydraulic dampers are tunable and controlled using valve discs with calibrated orifices. The gas-oil mass ratio was roughly calculated using Henry's equation (Dixon 2007) while the critical discharge coefficient of the servo-valve is the free parameter . A top-mount is the external component attached to the hydraulic damper which transfers the rod force to the suspension. Its stiffness is obtained on a static load frame machine as a force-displacement characteristic. In this model, the characteristic was linearized since the random signal used in NVH evaluation does not contain larger amplitudes, i.e. greater than 10mm. The damping of the top-mount is, however, difficult to obtain without specialized measurements, therefore this parameter is a free one. The servo-hydraulic tester model

uses a simplified model of a servo-valve reduced to the second-order transfer function representing the dynamics of the spool. The transfer function has two parameters, which are the natural frequency and damping ratio. The natural frequency is known, because the amplitude-phase-frequency characteristic of the servo-valve is available from the manufacturer, while the damping depends on usage of the valve and other factors (hydraulic forces), therefore it is a free parameter. The advantage of the first-principle approach is the possibility to apply physical boundaries to parameters to avoid local minimum regions during optimization. The PID settings are known as they are the test rig configuration parameters.

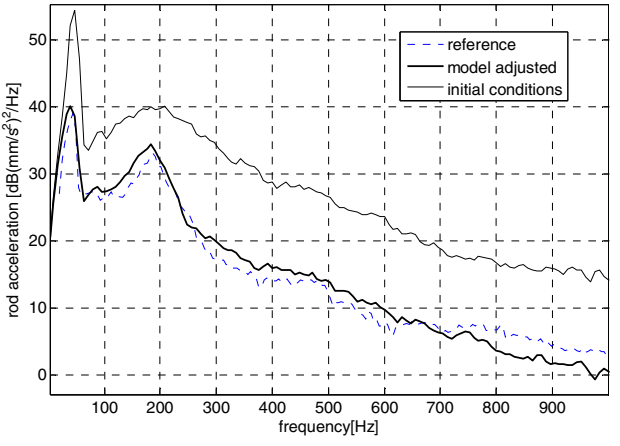

Fig. 4 Adjusted damper model in the frequecny domain

3 Results of the Analysis and Configuration Parameters

Eigenvectors were plotted in 2D-contour plots, where the height coordinate is related to the damping intensity, see Fig. 5. A frequency scale is plotted versus a time scale. Damping amplitudes are scaled in absolute values, relative decibel scale or rescaled to the dimensionless damping coefficients in the range (-1;1). The eigenvalues graphs are presented in the function of operational time. The imaginary part provides an insight into the frequency pattern. The real part provides an insight into the damping pattern related to model stability.

4 Discussion and Conclusions

The demonstrated case study supports the understanding of the model behavior over the considered frequency band, i.e. 0-1kHz. The analysis presented in this section identified top mount of a shock absorber as the major contributor to frequency response. During changes in top-mount stiffness, the eigenfrequencies and

spectrum density are changed in the wide range of frequencies. Additionally, one can notice that if the spring stiffness decreases and the amplitude of the excitation signal increases, the stability of the system deteriorates (Fig. 5).

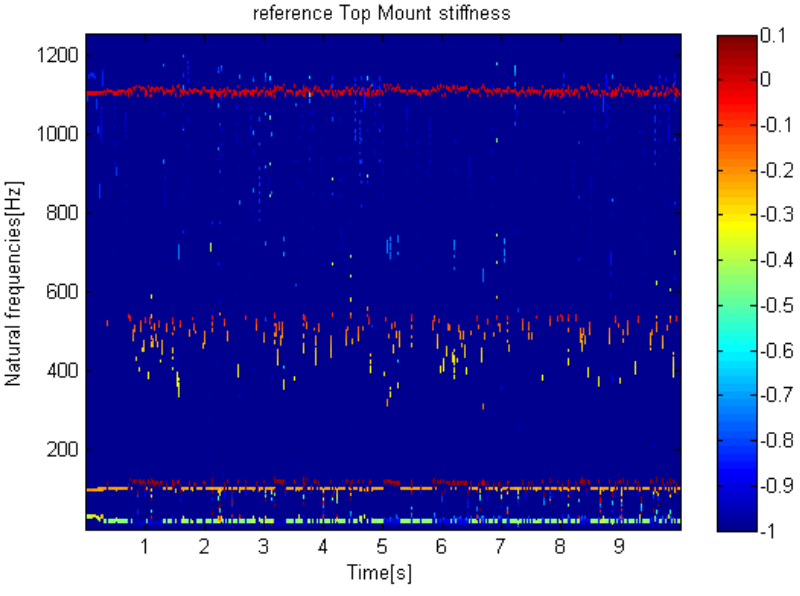

Fig. 5 Example of eigenvectors plotted in 2D-contour plot

The proposed method, i.e. diagram of the eigenvalues vs. time, can be an effective tool which enables natural frequency/damping variations of a system under development to be tracked. Nevertheless, one should realize that the accuracy of this method depends considerably on the model accuracy. Thus, the accurate characteristics of the damper are of paramount importance for a sufficiently-precise model of the damper for design purposes. High accuracy is provided by a damper model adjustment procedure. The proposed technique permits complex nonlinear systems, for which analytic solutions cannot be found, to be analyzed. The Eigenvalues plot represents a design chart enabling the selection of the optimum working range of the damper component. On the other hand, an experimental test can be conducted allowing the models to be compared/adjusted using operational measurements. However, the time-frequency analysis (i.e. spectrograms) has a compromised and limited time-frequency resolution. Other methods, such as wavelet representation, can be proposed. Nevertheless, operational signals do not provide such good resolution as the model-based analysis by means of instantaneous linearization.

Acknowledgements. The author gratefully acknowledges the financial support of the research project N N502 087838 funded by the Polish Ministry of Science (MNiI).

References

Vanhees, G., Maes, M.: Vehicle suspension characterization by using road simulation on a 4 poster test rig. In: Proceedings of ISMA, vol. 1, pp. 63–70 (2000)

Czop, P., Sławik, D.: A High-Frequency Model of a Shock Absorber and Servo-Hydraulic Tester. Mechanical Systems and Signal Processing 25(6), 1937–1955 (2011)

MATLAB. The Math Works Inc., Natick (1998)

Dixon, J.C.: The Damper Handbook. Wiley, England (2007)

Lang, H.: A study of the characteristics of automotive dampers at high stroking frequencies PhD thesis, Michigan (1977)

Kenneth, N., Morman Jr.: A modeling and identification procedure for the analysis and simulation of hydraulic damper performance. Ford Motor Company, Michigan (1984)

Tallbot, M.S., Starkey, J.: An experimentally Validated Physical Model of a High Performance Mono-Tube Damper. In: Proceedings of the 2002 SAE Motorsports Engineering Conference and Exhibition, US (2002)

Beyer, O., Becher, B., Stüwing, M., Zimmermann, G.: Measurement and simulation of the hydraulic behavior of the piston valve in a monotube damper. In: Proceeding of the 7th International Conference ATA, Italy (2002)

Subrabanian, S., Surampudi, R., Thomson, K.R.: Development of a nonlinear damper - model for low frequency NVH applications. In: SAE World Congress, Detroit, Michigan, US (2003)

Yamauchi, H., Sughara, T., Mishima, M., Noguschi, E.: 'Theoretical Analysis and Proposition to Reduce Self-Excited Vibrations of Automotive Damper'. In: Proceedings of Noise & Vibration Conference and Exhibition, Michigan, US (2003)

Kruse, A.: Characterizing and Reducing Structural Noises of Vehicle Damper Systems. In: SAE 2002 World Congress, Detroit, Michigan (2003)

Duym, S.W., Stiens, R., Baron, G.V., Reybrouck, K.G.: Physical Modeling of the Hysteresis Behaviour of Automotive Damper. In: International Congress and Exposition, Michigan, Detroit, pp. 125–137 (1997)

Reybrouck, K.: A non linear parametric model of an Automotive Damper. In: SAE International Congress, Michigan, Detroit, pp. 79–86 (1994)

Adjustment of a Feedwater Heater Model in Bi-stationary Load Conditions

Piotr Czop, Tomasz Barszcz, and Jarosław Bednarz

AGH University of Science and Technology, Department of Robotics and Mechatronics,
Al. Mickiewicza 30, 30-059 Cracow, Poland
piotr.czop@labmod.com

Abstract. Work related to the tuning of the first-principle model of a feedwater heater operating in a coal-fired power unit is presented. The objectives of this work is to find the most efficient and accurate process to tune the model parameters i.e. heat transfer coefficients under bi-stationary load conditions. The model variables (e.g. variability of the power rate of energy exchange) and estimated parameter values were used to formulate key performance indicators intended for a model-driven diagnostics approach. The computational process was organized in an iterative process of updating model parameters and indicators. The validation was successfully performed using operational data from a 225MW coal-fired power unit.

Keywords: power plant, feedwater heater, analytical modeling, system identification.

1 Introduction

According to the degree to which the a priori knowledge is available, then either a first-principle or a data-driven model, or a combination of both, can be applied (Fig. 1) (Bohlin 2006). First-principle (FP) models use understanding of the system underlying physics to derive its mathematical representation. FP models are expensive in development since expertise in the area of knowledge at the advanced level is required to derive equations from physical laws, while data-driven (DD) models use system test data to derive its mathematical representation. The advantage of the former approach is the depth of the insight into the behavior of the system and thus ability to predict the performance, while the advantage of the latter is the speed in which an accurate model can be constructed and confidence gained thanks to the use of the data obtained from the actual system. The difficulty of the former approach lies in the determination of the phenomenological parameters like the damping or the heat transfer coefficient. FP models are frequently adjusted by trial-and-error, which can lead to non-optimal results. On the other hand, the disadvantage of DD models is the need to handle multiple data sets in order to cover the range of system operation.

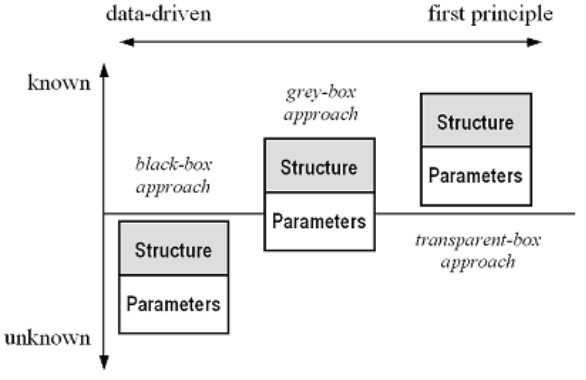

Fig. 1 Taxonomy of models representing a content of a priori and a posteriori knowledge

The goal is therefore to find a compromise and propose a combined first-principle data-driven (FPDD) model. FPDD models require a formal approach which allows the model parameters to be updated according to the operational data.

First-principle models are frequently adjusted by a trial-and-error approach manipulating the values of parameters as a result of performed sensitivity analysis with the model, i.e. a series of model responses corresponding to a combination of values of selected model parameters. Nevertheless, such an approach can lead to non-optimal and non-repeatable results due to a lack of any systematic approach in making changes to the parameter values. In order to avoid the deficiencies of the trial-and-error approach, a formalized mathematical method using optimization techniques to minimize the error criterion, and find optimal values of tunable model parameters of a heater model, was developed and is described in the second part of this work.

The approach proposed herein assumes that the number of tunable parameters is small compared to the number of known parameters. This, however, affects the correctness of the first-principle approach since, for example, the heat transfer process is treated using a combined coefficient which covers conduction, convection, and radiation phenomena. It is believed that the smaller the number of parameters, the more accurate the model and the faster the convergence of the algorithm used for model adjustment. In turn, the application scope of an FPDD model is wide-ranging, including the optimization and diagnostics of technical systems where a method of fast model update is essential.

2 Bi-stationary Load Conditions

Adjustment of FPDD models is the most general case of estimation theory where many assumptions regarding stochastic properties of the model variables and parameters cannot be stated. It implies that the quality criterion is the impli-cit function of the model parameters.

First-principle data-driven models have complicated structures based on sets of nonlinear and highly coupled equations (Barszcz and Czop 2007; Barszcz and Czop 2011a). The state variables and parameters are coupled within the structural interactions. For example, the inlet flow rate to the feedwater heater depends on the internal pressure, which is determined by the steam properties such as the steam saturation temperature (hard nonlinearity). The input data frequently has a bi- or multi-modal distribution depending on the current operating point to which the technical system is subjected. For example, a power unit operating point is affected by daily load demands as presented in Fig. 2 (Barszcz and Czop 2011b). As a consequence, there are two major operating points, representing output power around 155MW and 215MW. The operational measurements therefore have a bi-modal distribution as a mixture of Gaussian distributions corresponding to those operating points. Fig. 2 shows condensate temperature variation corresponding to 500 hours of feedwater heater operation.

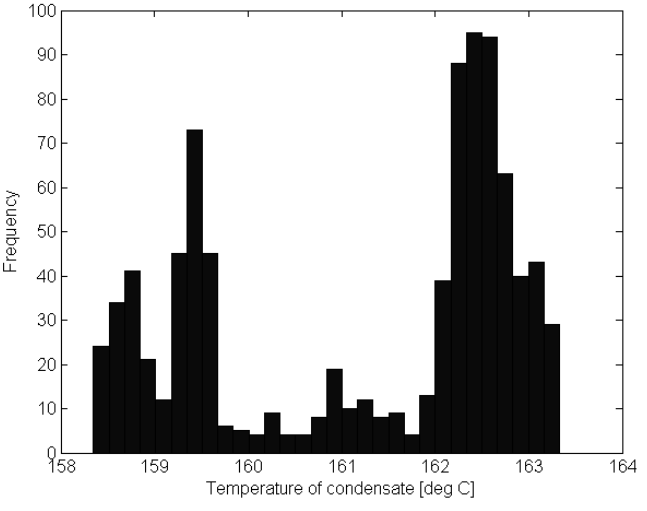

Fig. 2 Multi-modal distribution of an output signal of a heater model (temperature of a condensate leaving the heater)

3 Bi-stationary Load Conditions

The process of heater model calibration consists of (i) selection of representa-tive data sets, including a sufficiently broad operating range that the model proved could work correctly using a data fit measure and (ii) adjustment of model parameters to fit a model response to data (Barszcz and Czop 2011c). The model is represented as a set of non-linear state-space equations formulated in the continuous-time domain. The objective of the estimation is to minimize the error function between the measured signals and model responses by means of an iterative

numerical technique. The function describing the error has to be a positive and decreasing function. The procedure for updating model parameters consists of two in-a-loop phases: (i) simulation of a model by solving differential equations numerically in Simulink, and (ii) numerical minimization in the parameter space with respect to an error-related criterion function using the Matlab Optimization Toolbox (Matlab 1998). After each simulation of the model for fixed-length input signals, the simulated output data are sampled and the criterion function is re-evaluated to calculate a new set of model parameters.

Geometrical and physical parameters of the heater model were extracted from the operational documentation and were assumed to be known. A high-pressure heater was used as a reference system characterized by the operational and constructional data presented in (Barszcz and Czop 2011c). The heater is part of a feedwater regeneration flow path in which feed pumps pass the condensed steam (feedwater) from a condenser through heater banks, heated by the steam extracted from the high, intermediate and low-pressure sections of a steam turbine. The condensate is pumped to the deaerator, through the bank of low-pressure heaters, and further, from the deaerator to the steam generator (boiler) through the bank of high-pressure heaters. The draining system of the feedwater heater consists of a drain removal path from each heater. The normal drain flow path is cascaded to the next lower stage heater and the alternate path is diverted to the condenser.

Real-time assessment applications intended to be installed at power plant require an automated procedure of adjustment First-Principle Data-Driven models to operational data and updating model parameters. The automated procedure should be capable to evaluate the model quality and automatically reject the false models. The paper proposes such an automated procedure, which consists of a few in-loop stages as shown in Fig. 3.

The procedure of a model updating parameters process begins with a preprocessing stage, which allows to segment inputs and outputs signals. The signals are sequentially windowed to maintain a balance between a length of an n-th input-output sequence and time required to perform model adjustment process. In case of a feedwater heater considering herein, the sequence has a length of 180 samples corresponding to 180 minutes of operation time. Fig. 4 shows in the upper bar chart an average computation time corresponding to n-th data sequence versus available time marked with the dotted line. As expected, the model adjustment process consumes more time when the operating point of the feedwater heater changing (e.g. from 160 to 225MW) as presented in the bottom-diagram of the turboset power rate versus operational time.

Before every new n-th input-output data sequence, the model is initialized with the initial guess conditions (values of model state variables) obtained at the end of n-1 data sequence. Such numerical treatment allows to reduce the time of a complete tuning process of the model. In turn, the minimization algorithm has a better starting point and so a smaller number of iterations is required in each sequence.

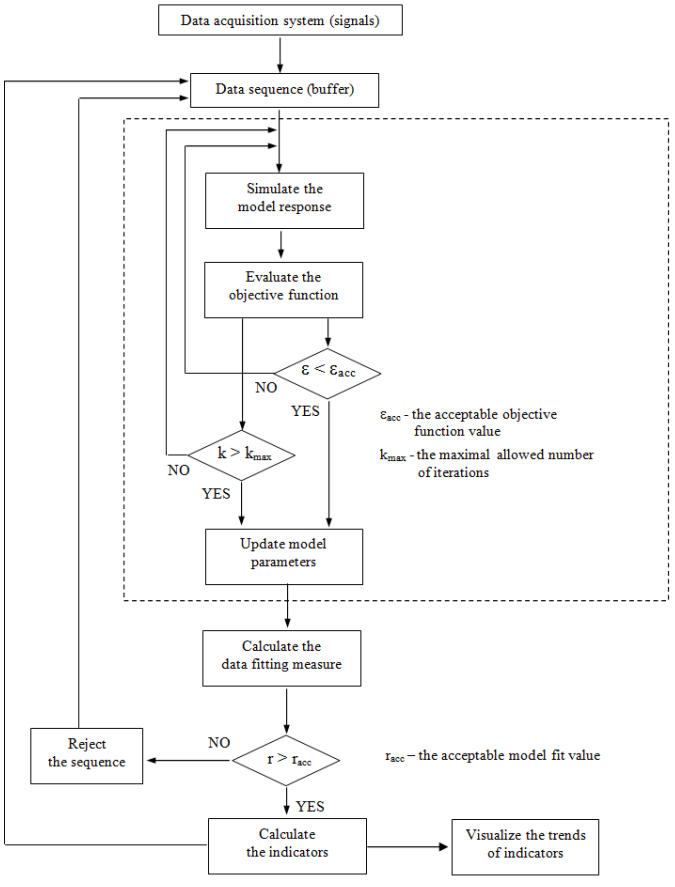

Fig. 3 Procedure of updating model parameters

The FPDD model is adjusted for every n-th data sequence independently. The tuning process for each sequence is stopped if the assumed number of iterations is exceeded kmax or the value of the objective function decreases below the specific value εacc. The quality of the model fit to operational data can deteriorate when a heater operate in exactly same operating point without any significant changes in an input-output data sequence. Such conditions do not allow to capture dynamics of a feedwater heater and should be rejected from the evaluation process as not relevant.

Execution of the procedure for numerical adjustment of FPDD heater model ensures the heater model that best fits the data is found. Parameters of the feedwater heater model were updated according to the flowchart presented in Fig. 3.

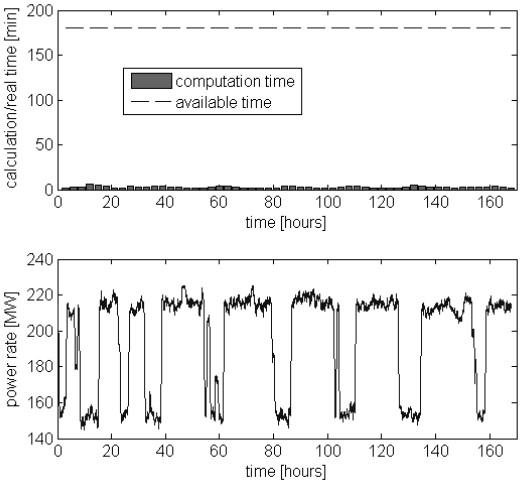

Fig. 4 Actual time vs. available real time (upper-plot) and the corresponding variation of the turboset operating point (bottom-plot) in the process of model parameters updating

The objective function arguments are the free (adjustable) model parameters. The function is evaluated by the chosen optimization algorithm to approach the global minimum of the function in a finite number of iterations (Matlab, 1998; Ljung, 1999). The value of the objective function error and the number of iterations are used as stopping criteria for the parameter updating process. Upon completion of a model parameters updating loop, the model parameters are passed to a post-process function which calculates the model fit to operational data based on the Pearson correlation coefficient. If the model quality is not satisfactory ($r<r_{acc}$) the model parameters corresponding to n-th input-output model sequence are rejected and the next sequence of the updating process is started for a new set of operational data. The calculations are not repeated for other algorithms or initial conditions since the number of parameters is enough high to plot the assessment trends and characteristics. It is less than 25% of sequences are rejected for the assumed $r_{acc}=0.6$.

A model quality fit is evaluated by analyzing the value of Pearson's product-moment correlation coefficient between the measured and simulated values of the N-sample-long output signals. For each output signal, the correlation coefficient is computed separately; in the particular case of the model discussed in this paper, the output signals were the temperature of the condensate and the temperature of the feedwater.

It can be observed that the fit indicator of the model response to data varies over input-output data sequences from very low values, which indicate a lack of correlation, to values that indicate acceptable to very good correlation. Long-term fluctuations in accuracy of the model are analyzed based on the plot of the model fit-quality indicator. Fig. 5 shows in the upper-diagram the collected values of the

fit-quality indicator for each elementary data sequence as a function of operational time. The values were also compared to the turboset power rate in the bottom-diagram in Fig 5. The model fit-quality indicator drops when operating conditions maintain stable for a longer time. Acceptable fit-quality values (above 0.65) are achievable when significant changes occur in input-output data sequence. In cases of low signal variation, low values of the fitting measure indicate that the model is not properly excited.

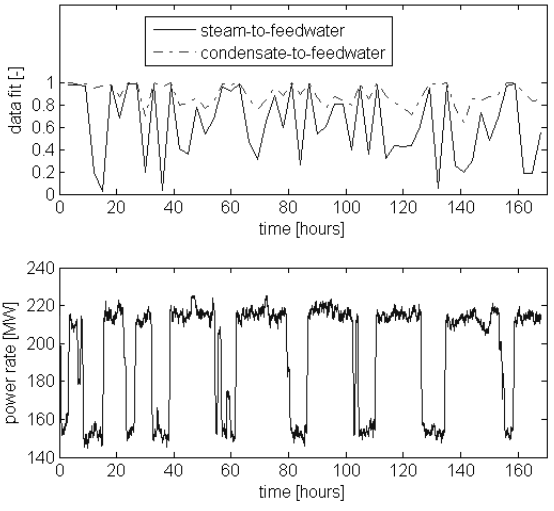

Fig. 5 Actual model fit indicator (upper-plot) and the corresponding variation of the turboset operating point (bottom-plot) in the process of model parameters updating

4 Discussion and Conclusions

This paper focuses on the tuning and validation process of the first-principle feedwater heater model intended for model-based diagnostics as part of the entire model of a power unit. The scope of the proposed methodology is limited to power plant systems with modern data acquisition systems. Such systems should be capable of gathering required input-output data with a sampling frequency to capture relevant heat transfer and fluid flow dynamics. This paper presents a representative case study where data are gathered with a sampling frequency of 60 seconds. This resolution is sufficient when compared to the normal operation of a power plant.

The objective of this study was to develop a tuning method for the moderately complex first-principle model developed in (Barszcz and Czop, 2007). Such a method is advocated for industrial conditions when the values of physical and geometrical parameters are known, while the values of phenomenological ones have to be adjusted as only their rough pre-calculated initial values are available.

Measurement data from a 225MW coal-fired unit were used to validate the model's accuracy. The validation process presented in the paper indicates that the performance in transient conditions is good, achieving a correlation between the simulations and measurements at a level of 0.7-0.9. This proves that the model can be used in further studies and the development of techniques related to model-driven evaluation and diagnostics.

Acknowledgements. The author gratefully acknowledges the financial support of the research project N N504 493239 funded by the Polish Ministry of Science (MNiI).

References

Bohlin, T.: Practical grey-box process identification, Theory and Applications (Advances in Industrial Control). Springer, London (2006)

Barszcz, T., Czop, P.: Methodologies and applications of virtual power plant – New environment for power plant elements modeling, Institute Sustainable Technologies, Radom (2007)

Barszcz, T., Czop, P.: Presentation of a Virtual Power Plant environment and its application with combined first-principle and data-driven models intended for the diagnostics of a power plant - part I & II. SIMULATION Transactions of The Society for Modeling and Simulation International (2011a), (published online before print March 17, 2011); doi:10.1177/0037549711398718

Barszcz, T., Czop, P.: A Feedwater Heater Model Intended for Model-Based Diagnostics of Power Plant Installations. Applied Thermal Engineering 31(8-9), 1357–1367 (2011b)

Barszcz, T., Czop, P.: Estimation of feedwater heater parameters based on a grey-box approach. International Journal of Applied Mathematics and Computer Science 21(4) (2011c)

MATLAB, The Math Works Inc., Natick (1998)

Ljung, L.: System identification - Theory for the User. Prentice-Hall, USA (1999)

Iterative Method for the Remote Identification of Impact Forces at Multiple Clearance Supports Using Few Vibratory Measurements

Vincent Debut and José Antunes

Instituto Tecnológico e Nuclear, 2686 Sacavém, Portugal
{vincentdebut,jantunes}@itn.pt

Abstract. Among the wear-prone components in industrial facilities, multi-supported tubes with clearances are particularly critical, as flow excitation may lead to vibro-impact wear between the tubes and their supports. Following our previous studies on remote impact identification using wave-propagation and modal techniques, the approach introduced in this paper consists on an iterative constrained-inversion procedure, using a modal representation of the system, to deal with simultaneous multiple identifications of impact forces, from a limited number of response measurement transducers. Preliminary identification results, based on numerical simulations, assert the satisfactory behaviour of the method to isolate the impact forces in multi-supported systems for realistic noise levels.

Keywords: Vibration, impact identification, constrained inversion, regularization.

1 Introduction

Identification techniques that enable the diagnostic of real-life industrial components, based on remote vibratory measurements, are quite valuable for validating predictive computations as well as for the control monitoring under real operating conditions. Among the wear-prone components in industrial facilities, gap-supported tubes are particularly critical as flow excitation may lead to vibro-impact wear between the tubes and their supports.Considerable efforts have been invested to enable the identification of impact forces at gap-supports using information from motion transducers located far from the impact locations. Pioneer works theoretical and experimental studies by Whiston [1], Jordan and Whiston [2], and Doyle [3]. They presented identifications for simple isolated impacts, achieved in the frequency domain, by using a wave-propagation approach. In a serie of papers [4, 5, 6], the present authors further extended such approach to deal with more complex vibro-impact motions, to move a step closer to realistic conditions. In particular, they achieved, using a pair of vibratory transducers, high quality force identifications for multi-supported tubes, as attested by the validation through laboratory experiments on a beam with three gap-supports.

Following our previous studies on remote impact identification using wave-propagation techniques, we recently applied modal methods to address similar problems [7, 8, 9] which provided quite satisfying identifications on both simulated and experimental data.

The approach introduced here is inspired by identification techniques previously developed by the authors. It consists on an iterative constrained-inversion procedure, based on a modal approach, in order to deal with simultaneous multiple-identifications of impact forces, from a limited number of response transducers. The identifications presented here are performed on numerical simulations of a multi-supported beam with clearances excited by a pulse force. The technique is tested numerically by comparing the identified dynamical impact forces with the actual values stemming from the original nonlinear computations. Preliminary identification results assert the satisfactory behaviour of the method to isolate the impact forces in multi-supported systems for realistic noise levels.

2 The Identification Problem and Procedure

The system addressed consists of a multi-supported beam with clearance supports which displays vibro-impact forces when subjected to a force field. As is typical in real field conditions, we assume a limited set of vibratory transducers to recover the details of the impact forces - less than the number of forces - which makes the problem ill-defined. However, using additional physically-based constraints, we will show that successfull identifications of impact forces can be achieved.

2.1 Modal Approach for the Force Identification

Based on a linear formulation in the frequency domain, the vibratory response $Y_m(\omega)$ of a beam measured at location x_m subjected to an excitation $F_s(\omega)$ located at x_s can be expressed simply as:

$$Y_m(\omega) = H(x_m, x_s, \omega)\, F_s(\omega) \tag{1}$$

where $H(x_m, x_s, \omega)$ is referred to as a transfer function. Adopting a modal representation of the beam and dealing with displacement signals, the *force-to displacement* function transfer can be built by modal superposition:

$$H^{(d)}(x_m, x_s, \omega) = H^{(d)}_{ms}(\omega) = \sum_{n=1}^{N} \frac{\varphi_n(x_m)\varphi_n(x_s)}{m_n(\omega_n^2 - \omega^2 + 2i\omega\omega_n\zeta_n)} \tag{2}$$

where m_n, ω_n, ζ_n and φ_n are the modal parameters, i.e. the modal mass, eigenfrequencies, damping values and mode shapes of the unconstrained beam. The velocity and acceleration responses can be computed similarly to the displacement, using Eq.(1), by replacing $H^{(d)}_{ms}(\omega)$ by the *force-to-velocity* transfer function and the *force-to-acceleration* transfer function given respectively by:

$$H_{ms}^{(v)}(\omega) = i\omega H_{ms}^{(d)}(\omega) \tag{3}$$

$$H_{ms}^{(a)}(\omega) = -\omega^2 H_{ms}^{(d)}(\omega) \tag{4}$$

In the case of a multi-supported beam, several impacts are usually generated at the various support locations. Consequently, the vibratory response measured at location x_m encapsulates the contributions of all the supports. Considering a beam supported at S clearance supports and a set of M vibratory transducers, Eq.(1) now reads in a matrix form as:

$$\begin{Bmatrix} Y_1(\omega) \\ Y_2(\omega) \\ \vdots \\ Y_M(\omega) \end{Bmatrix} = \begin{bmatrix} H_{11}(\omega) & H_{12}(\omega) & \dots & H_{1S}(\omega) \\ H_{21}(\omega) & H_{22}(\omega) & \dots & H_{2S}(\omega) \\ \vdots & \vdots & \ddots & \vdots \\ H_{M1}(\omega) & H_{M2}(\omega) & \dots & H_{MS}(\omega) \end{bmatrix} \begin{Bmatrix} F_1(\omega) \\ F_2(\omega) \\ \vdots \\ F_S(\omega) \end{Bmatrix} \tag{5}$$

While Eq.(5) refers to the direct dynamical problem formulated in the frequency domain, one notices that the inverse problem of finding the excitations $\{F_s(\omega)\}$ from a set of vibratory measurements $\{Y_m(\omega)\}$ is essentially a problem of response inversion. The process of computing the inverse solution appears quite straightforward, except from the fact that, when M<S, a straight inversion is obviously not possible. For the case M=S, the identification procedure starts by computing the frequency-domain vibratory responses by fast Fourier transforming all the measured time-domain signals. Then, one obtains the force estimates - in the frequency domain - from the product of the vibratory responses with the inverse of the transfer operator. Finally, the time-domain identified forces are obtained by inverse Fourier transform. Furthermore, in practice, an important issue is the proper inversion of the transfer operator which describes the phenomena. The ill-conditionning - physical or numerical - of the operator makes inverse problems extremely unstable in that small perturbations can lead to erroneous results and regularization methods are frequently essential to produce usable solutions [10]. Provided the inverse problem is determinate, the previously described basic procedure can be applied to more than one excitation and more than one response measurements using Eq.(5). However, because the number of forces to identifiy is usually higher than the number of response measurements (M<S), the inverse problem is ill-formulated and therefore should be solved differently.

2.2 *The Proposed Iterative Multiple-Force Identification Procedure*

To deal with the multiple identification inverse problem when M<S and overcome its ill-condition nature, an iterative constrained procedure is now proposed. It operates in an alternate fashion between the time and frequency domains, and enforces some additional physical knowledge for the solution. To be specific, the identification procedure is applied in the frequency domain while physical constraints are imposed to the force estimates in the time domain, at each iteration.

2.2.1 Iterative Procedure

Eq.(5) is used as a starting point. Using the information provided by a given vibratory transducer $Y_m(\omega)$, the inverse problem may be formulated in the form:

$$\begin{aligned} F_1(\omega) &= \frac{1}{H_{m1}(\omega)} Y_m(\omega) - \sum_{s\neq 1}^{S} \frac{H_{ms}(\omega)}{H_{m1}(\omega)} F_s(\omega) \\ F_2(\omega) &= \frac{1}{H_{m2}(\omega)} Y_m(\omega) - \sum_{s\neq 2}^{S} \frac{H_{ms}(\omega)}{H_{m2}(\omega)} F_s(\omega) \\ &\vdots \qquad\qquad\qquad\qquad \vdots \\ F_S(\omega) &= \frac{1}{H_{mS}(\omega)} Y_m(\omega) - \sum_{s\neq S}^{S} \frac{H_{ms}(\omega)}{H_{mS}(\omega)} F_s(\omega) \end{aligned} \tag{6}$$

which is valid for any measurement m and seems well-suited to generate a sequence of improving approximate solutions. One can compute successive approximations of the forces (in the left hand side) from the values obtained in the previous iteration (in the right hand side). By rewritting Eq.(6) in a matrix form and noting the forces to identify $\{F_m(\omega)\} = \{F_1(\omega), \ldots, F_S(\omega)\}^T$, the iterative procedure is governed by:

$$\{F_m(\omega)\}^{i+1} = \{C(\omega)\} Y_m(\omega) - [D_m(\omega)]\{F_m(\omega)\}^i, \quad \forall m = 1, \ldots, M \tag{7}$$

where

$$\{C(\omega)\} = \begin{Bmatrix} \dfrac{1}{H_{m1}(\omega)} \\ \dfrac{1}{H_{m2}(\omega)} \\ \vdots \\ \dfrac{1}{H_{mS}(\omega)} \end{Bmatrix}, \text{ and } \quad [D_m(\omega)] = \begin{bmatrix} 0 & \dfrac{H_{m2}(\omega)}{H_{m1}(\omega)} & \cdots & \dfrac{H_{mS}(\omega)}{H_{m1}(\omega)} \\ \dfrac{H_{m1}(\omega)}{H_{m2}(\omega)} & 0 & \cdots & \dfrac{H_{mS}(\omega)}{H_{m2}(\omega)} \\ \vdots & \vdots & \ddots & \vdots \\ \dfrac{H_{m1}(\omega)}{H_{mS}(\omega)} & \dfrac{H_{m2}(\omega)}{H_{mS}(\omega)} & \cdots & 0 \end{bmatrix} \tag{8}$$

If two or more response measurements are available, several estimates of the forces can be computed and then compared to isolate the impacts. Actually, when the number of vibratory sensors is equal or greater than the number of forces to identify, successful identifications can be achieved. However, as already mentioned, the problem is not so immediate when M<S.

2.2.2 Identification from the Comparison of Several Measurements

The basic ideas used here, and already discussed in [5] using a different representation formulation for the system dynamics, rely on the following observations: (a) the availability of several estimates of the impact forces; (b) the dispersive nature of the flexural waves. Considering a pair of vibration transducers and a support at a specific location, two estimates of the impact force - stemming from the two measurements - will obviously differ more or less due to the dispersion effect. Since the two

inversions are performed with respect to the same support, these estimates should correlate well when impacts arise there and very badly when they were generated elsewhere. It thus suggests that comparing estimates from various measurements is a convenient criterion to isolate impacts generated at distinct clearance supports.

In practice, a narrow moving-window is applied to the two estimates of the force $f_s^{(1)}(t)$ and $f_s^{(2)}(t)$ and then the cross-correlation $\gamma(t)$ is computed. A better estimate $f_s^{\star}(t)$ of the corresponding impact force is then given by:

$$f_s^{\star}(t) = \begin{cases} \dfrac{f_s^{(1)}(t) + f_s^{(2)}(t)}{2} & \text{if } \gamma(t) \geq \gamma_c \\ 0 & \text{if } \gamma(t) < \gamma_c \end{cases} \qquad \forall s = 1, \ldots, S \tag{9}$$

where γ_c is a parameter which acts as a lower boundary beyond which the constraint given by Eq.(9) is imposed. Obviously, the choice o the moving-window size and γ_c is open to discussion. Here, a value of 5 ms for the window size - which corresponds to the time scale of individual force spikes - works well in practice. As illustrated in [5, 6], the choice of γ_c can be completely automated, but here a fixed value of 0.7 proved to be well suited. Based on the preceeding arguments, the following iterative identification method is then proposed:

1. *Initial identification*
   a) Convert the M available response measurements $Y_m(t)$ to the frequency domain by Fourier transform,
   b) For each support s, compute initial estimates of the impact forces from the M vibratory measurements, each force at a time while ignoring the others, as:
   $$\{F_{s_m}(\omega)\} = \{C(\omega)\}Y_m(\omega)$$
   and convert them to the time domain by inverse Fourier transform,
2. *Identification loop*
   a) Improve the estimates of the impact forces $\{f_{s_m}(t)\}$ by applying the separation constraints according to Eq.(9),
   b) Compute new estimates of the force using Eq.(7) and convert them to the time domain by inverse Fourier transform,
   c) Loop iteratively between tasks 2-a and 2-b,
   d) Assert the convergence of successive iterations by comparing each iteration result with the preceeding identification time domain signals.

The preceeding algorithm seems logical, but an important question concerns the algorithm possible convergence (or not) to a solution. Indeed, problems of noise amplification can lead to instability of the process. However, adequate filtering - as namely SVD filtering or Tikhonov regularization - can overcome such difficulties and stabilize the solutions. Here, a Tikhonov-type regularization is applied to the transfer functions with a regularization parameter of 0.3.

3 Preliminary Identification Results

To provide a feel for the actual performance of the proposed approach, preliminary identification results are now presented. They are performed on numerical simulations of gap-supported tubes subjected to a pulse force.

Time-domain simulations of gap-supported tubes excited by a pulse were performed using the computational approach described in [8, 11] which has already proved to be adequate to obtain realistic vibro-impact regimes in an effective manner. The modeled beam has length L=6 m, with pinned boundary conditions at both extremities. Two point-supports with symmetrical gap of ±0.5 mm are considered at x_1=1.56 m and x_2=2.64 m. The excitation pulse, originated at t=0.3s, is treated as a third unknown impact force generated at x_3=2 m. The time-domain computations were performed using a modal basis of 9 flexural modes. Their lowest and highest frequencies are 10 and 810 Hz respectively. A constant modal damping of 0.5% was used for all modes. Here, because this paper focus on presenting the technique, the identifications are based on the true modal parameters, the study of the algorithm robustness being postponed to a future paper. The important topic of dealing with the imperfect knowledge of the modal parameters used to build the transfer functions was addressed in [12] where we showed that satisfactory estimates of the modal paramaters can be effectively obtained by optimization techniques.

Figure 1 shows the initial and final identified forces at the three locations, superimposed with the true results. One notices that the initial identifications, obtained after imposing the constraints, are already not so far from the true results even if additional uncorrect features are present. The final identications are, however, undoubtedly cleaner, illustrating the improvement of the identifications by the enforced constraints at each iteration. As can be seen, results compare very well with the computed signals and assert the satisfactory behaviour of the iterative process.

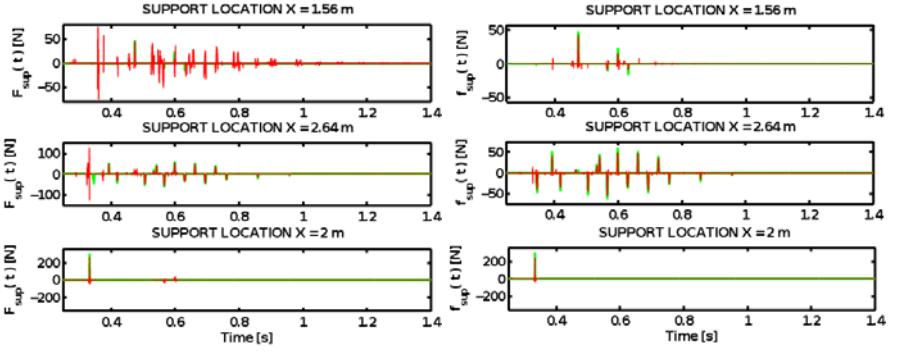

Fig. 1 Simulated (green) and identified (red) impact forces at the three supports obtained by the iterative technique. Left: initial estimates. Right: final identifications.

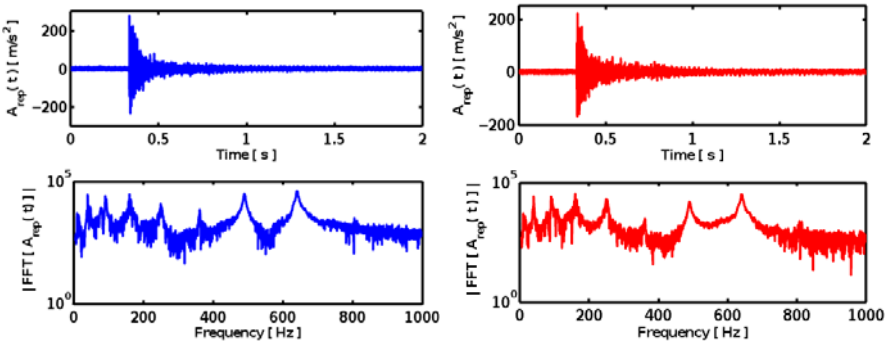

Fig. 2 Time-domain and spectra of the beam acceleration from the two response transducers with noise contamination of 20%. Left: at x =1.07 m. Right: at x =5.04 m.

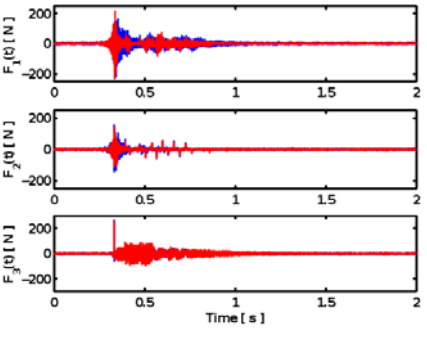

Fig. 3 Initial estimates of the impact forces at the three supports from measurements at x = 1.07 m (blue) and x = 5.04 m (red).

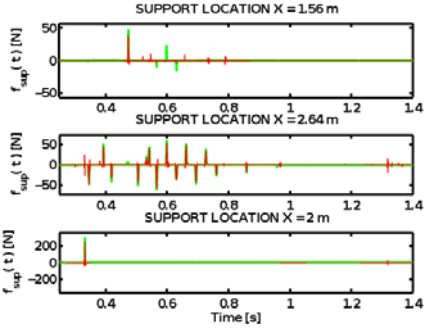

Fig. 4 Simulated (green) and identified (red) impact forces obtained after convergence, with noise contaminated measurement of 20%.

Figures 2, 3 and 4 pertain to identifications obtained from noisy measurements. Figure 2 shows the numerical simulated beam reponses, used as inputs for the identification procedure, "measured" at locations 1.07 m and 5.04 m, with noise contamination of about 20% of the RMS magnitude of the corresponding acceleration signals. Figure 3 presents the initial estimates at the three supports computed from each vibratory measurement, before imposing the constraints. For each support, one can notice the influence of the various impacts generated at other supports. From Figure 4, which displays the results after convergence, it is clear that comparing the identifications obtained from the various measurements enables a good discrimination of the impacts originated at different locations. Finally, in Figure 4, even if the true and identified forces are overall similar, significant details - including impacts - are missing in the identifications as the result of noise. Moreover, some residuals, which have not been effectively eliminated by the constraints procedure, are still present. There is therefore room for improvement of the proposed technique.

4 Conclusions

In this paper, we proposed an iterative-constrained inversion technique from a limited number of response transducers, based on a modal approach, to address the problem of simultaneous multiple impacts in a multi-supported beam. Illustrative identifications show that impact force can be attempted with success for a beam excited by a pulse force for realistic noise levels. Future work will address more difficult problems of practical interest, such as a multi-supported beam subjected to turbulence flow excitation as is typical of heat-exchangers.

References

1. Whiston, G.S.: Remote impact analysis by use of propagated acceleration signals: I - Theoretical methods. J. Sound Vib. 97, 35–51 (1984)
2. Jordan, R.W., Whiston, G.S.: Remote impact analysis by use of propagated acceleration signals: II - Comparison between theory and experiments. J. Sound Vib. 97, 53–63 (1984)
3. Doyle, J.: Wave propagation in structures: an FFT-based spectral analysis methodology. Springer, New York (1989)
4. De Aurajo, M., Antunes, J., Piteau, P.: Remote identification of impact forces on loosely supported tubes: Part 1 - basic theory and experiments. J. Sound Vib. 215, 1015–1041 (1998)
5. Antunes, J., Paulino, M., Piteau, P.: Remote identification of impact forces on loosely supported tubes: Part 2 - complex vibro-impact motions. J. Sound Vib. 215, 1043–1064 (1998)
6. Paulino, M., Antunes, J., Izquierdo, P.: Remote identification of impact forces on loosely supported tubes: analysis of multi-supported systems. J. Pressure Vessel Technol. 121, 61–69 (1999)
7. Debut, V., Delaune, X., Antunes, J.: Identification of the nonlinear excitation force acting on a bowed string using the dynamical responses at remote locations. International Journal of Mechanical Sciences 52, 1419–1436 (2010)
8. Delaune, X., Antunes, J., Debut, V., Piteau, P., Borsoi, L.: Modal techniques for remote identification of nonlinear reactions at gap-supported tubes under turbulent excitation. J. Pressure Vessel Technol. 132 (2011)
9. Delaune, X., Piteau, P., Debut, V., Antunes, J.: Experimental validation of inverse modal techniques for remote identification of impact forces in gap-supported systems subjected to local and flow turbulence excitations. J. Pressure Vessel Technol. 5 (2011)
10. Aster, R., Borchers, B., Thurber, C.: Parameter estimation and inverse problems. Elsevier Academic Press (2005)
11. Axisa, F., Antunes, J., Villard, B.: Overview on numerical methods for predicted flow-induced vibrations. J. Pressure Vessel Technol. 110, 7–14 (1998)
12. Debut, V., Delaune, X., Antunes, J.: Identification of nonlinear interaction forces acting on continuous systems using remote measurments of the vibratory responses. In: Proceedings of the 7th Euromech. Solids Mechanics Conference (ESMC 2009), Lisbon (2009)

Robust Optimization of Gear Tooth Modifications Using a Genetic Algorithm

Ghribi Dhafer[1,3], Bruyère Jérôme[1], Velex Philippe[1], Octrue Michel[2], and Mohamed Haddar[3]

[1] Université de Lyon, INSA Lyon, LaMCoS, UMR CNRS 5259, France
Philippe.Velex@insa-lyon.fr
[2] CETIM, Pôle d'Activités Mécatronique, Transmissions de Puissance et Capteurs (MEC) Senlis, France
[3] Université de Sfax, Ecole Nationale d'Ingénieurs de Sfax, U2MP, Tunisie

Abstract. Most studies in gear design analysis and optimization do not account for the presence of uncertainties inherent to the manufacturing and assembly precisions. In this paper, the issue of robustness of gear modifications with regard to transmission error fluctuations is addressed. An approach based on numerical integration (Gauss Quadrature) is adopted and a statistical optimization based on a genetic algorithm is used to determine the robust areas for tooth modifications. Finally, the influences of the gear quality grade and the probability law are analysed.

Keywords: gear, transmission error, tooth modifications, robustness.

1 Introduction

Over the last forty years, a large number of contributions on the behaviour of spur and helical gears have been presented and many authors have investigated the influence of tooth modifications on transmission errors [1-5]. It has been shown that suitably designed modifications or optimum modifications can significantly improve noise and vibrations. Most of the results stem from deterministic gear models which do not incorporate the influence of geometric variations and the possible scatter in terms of tooth modifications on the resulting stresses, transmission errors, etc. However, some stochastic approaches have been proposed leading to probabilistic results for static transmission error (*TEs)* and other design parameters such as root, contact stress, etc. [5, 6].

The main purpose of this study is to define "robust" tooth modifications such that the system can maintain the expected optimal behaviour even when submitted to variances.

2 Deterministic Optimization of Tooth Modifications

2.1 Definitions

It is widely accepted that gear tooth shapes can strongly influence gear system behaviour (noise, vibration, static and dynamic stress,..) [1-6] and that some suitable tooth profile and/or lead modifications can reduce vibration and noise characteristics significantly. Tooth modifications consist in introducing voluntary tooth shape deviations to produce quieter gears with smoother meshing conditions and more uniform load distributions. Profile relief correspond to correction patterns along the tooth profile mostly aimed at ensuring a quasi uniform motion transfer and avoiding corner contact at engagement [3]. Figure 1.a defines a symmetric linear tip relief (similar on the pinion and the gear) which is frequently used in spur and helical gear design. It is defined by a depth of modification at tooth tip E and an extent of modification measured on the base plane as $\Gamma\varepsilon_\alpha Pb_a$ which characterise the amount of material removed from the perfect involute profile. In what follows, E will be normalised with respect to δ_m, the average static mesh deflection for perfect gear and denoted E*.

Moreover, in order to compensate for mounting errors, misalignments and avoid overloads near the tooth edges (in the face width direction), lead modifications are frequently employed. As described in Figure1.b**,** such modifications can be introduced across the face width as lead crowns which, typically, are tangent to the involute surface in the gear mid-plane. In a number of cases, crowning is symmetric and can therefore be quantified by its amplitude Ap only.

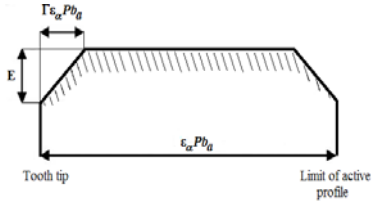

Fig. 1 a Profile modification

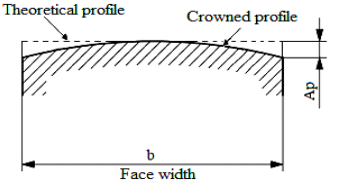

Fig. 1b Lead crown modification

Fig. 1 Tooth modifications

2.2 Objective Function

The classic approach to designing quiet gears relies on the reduction of the sources of vibration and noise which, as far as mesh excitations are concerned, are related to the fluctuations of the quasi-static transmission error under load *TEs* [3]. This parameter is defined as a measure of departure from perfect motion transfer at low

speeds [1] and, since the early works of Gregory et al. [2], it has been extensively used as a tool for assessing and improving gear noise quality. Tooth modifications also modify other functional parameters such as contact pressures, root stresses, power losses, etc. and designing optimum profile and lead relief often relies on a compromise between somewhat diverging constraints and conditions. In this paper, however, the objective function in the optimisation process will be the RMS of *TEs* only since the other relevant parameters vary monotonically with no optimum as opposed to what is observed for transmission error (Maatar and Velex [3]).

2.3 Optimization Methods

2.3.1 Overview

In the literature, many optimization techniques, either deterministic or stochastic, have been developed and used for design optimization in engineering problems [8]. Deterministic methods are effective when the evolutions of the objective function can be anticipated whereas stochastic methods involve the optimization of systems for which a relationship between the design variables and the objective function is not a priori known. Among the many stochastic optimization procedures, evolutionnary algorithms and especially genetic algorithms (GA) are amongst the most convenient and intuitive methods [8]. GA are less likely than conventional optimization techniques to get trapped in local optimal areas of the search space, and the GA's population structure makes it useful in exploring many candidate designs in parallel. Moreover, these techniques are hardly sensitive to the number of design variables.

2.3.2 Validation

Before extensive studies are performed, the accuracy of the approach is examined in the particular case of the helical gear described in Table 1 whose profiles are modified by symmetric linear relief (amplitude E* and dimensionless extent Γ) on the pinion and the gear. Figure 2 shows the contour plot of the RMS of TEs versus the dimensionless depth E* and extents Γ. Several series of results are compared which all indicate that there is a combination of depths and extents of modifications leading to minimal TEs fluctuations. The contour lines have been found based on the numerical solutions obtained by sweeping over a range of depths and length of relief [3] (analogous to what Houser at al. [1] coined a ‘run-all-the-cases’ methodology). The analytical results presented by Velex et al. [4] have been superimposed and they are materialised by the dotted curve which, actually, intersects the area of minimum RMS of TEs. Finally, the asterisks (*) in the graph represent the optimal individuals as found by the Genetic Algorithm which correlate very well with the other sets of results thus demonstrating the GA capability to find optimal profile modifications.

Table 1 Gear data for the study of the influence of profile modifications.

---	**Pinion/ Gear**	---	**Pinion/ Gear**
Tooth Number	28/56	Normal pressure angle (deg)	20
Face width (mm)	40/40	Profile contact ratio	1.48
Addendum coef.	1/1	Overlap contact ratio	1.34
Dedendum coef.	1.4/1.4	Helix angle (deg)	25
Module (mm)	40	Center distance (m)	No backlash
Pinion torque (Nm)	850	δ_m, average static mesh deflection	20µm

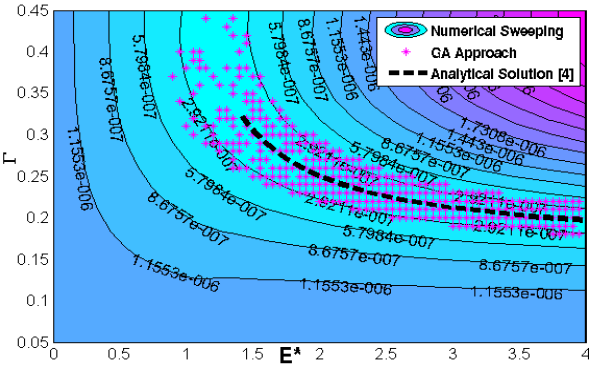

Fig. 2 RMS of TEs: Validation of the Genetic Algorithm (GA)

3 Design Optimization for Robustness

3.1 Concept of Robustness

The deterministic optimization presented in the previous section does not take into account the uncertainties in the design variables which, in general, cannot be completely eliminated thus leading to some geometry scatter which should be accounted for in the optimization process of tooth design. In this context, the concept of "robust" design is introduced which is defined as the combination of design parameters rendering the measures of design performance hardly sensitive to variances. Figure 3 illustrates this concept by introducing the range of variation of the design variable (X) and showing that, compared to the traditional optimisation (optimum solution), the robust optimization (robust solution) lead to a stable performance (Y) over a range of design variables [9,10].

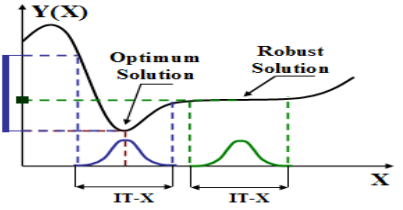

Fig. 3 Concept of robustness

The basic objective of robust design approaches is to optimize the mean and minimize the performance variance in a way that satisfies constraints such that any robust design problem can be considered as a bi-objective design optimization. With this objective in mind, Sundaresan et al. [5], Yu et al. [6] introduced a unique scalar objective function combining these two criteria under the form:

$$F_{\text{rob}}(\text{X}) = \mu_{\text{Y}} + \beta.\sigma_{\text{Y}} \quad ;\text{Y} = RMS(TEs) \tag{1}$$

where μ_Y is the mean of performance Y (Y=RMS(*TEs*) here) and σ_Y represents the standard deviation. The quality coefficient β in (1) can be interpreted as the contribution of the robustness in the optimized design since robustness becomes higher with larger values of β. Following Yu et al. [6], a quality coefficient of 2 has been retained in this paper.

3.2 Methods for Estimating Statistical Characteristics

Optimum robust design relies therefore on the mean value μ_Y and the standard deviation σ_Y of the objective function Y (multivariate yield) which are generally determined through statistical analyses based on Monte Carlo Simulations (MCS). Despite its simplicity, MCS method has the capability of handling practically every possible case regardless of its complexity; it requires, though, extensive computational effort. Motivated by the need for a more efficient methodology, and based on the concept of numerical integration, Taguchi [9], D'Errico and Zaino [11] proposed a "full factorial" discrete-point approximation procedure, later extended by Duffy et al [12] to non-normal distributions. Assuming that the design variables are independent, an approach based on the Cartesian product of univariate Gaussian Quadrature has been proposed. Because the distributions are sampled over the entire range of probable values, the number of samples required to adequately represent a distribution with a discrete-point approximation is less than for MCS, thus leading to a substantial reduction in the computational time for evaluating the multivariate yield. For various points dispersed within the research space (as defined in Table 2), it is shown in Figure 4 that the multivariate Gaussian Quadrature **(GQ)** with a few replications (the total number of points is $N=H^2$, H=3; 4 ..) can estimate the statistical variables as well as the more time-consuming MCS method (at least 300 iterations (SP=300) are needed to estimate the standard deviation of the response Y (Y=Rms of TEs) with a relative error <5%).

Table 2 Points of validation of Gauss Quadrature Method

Point (Pti)	Pt1	Pt2	Pt3	Pt4	Pt5	Pt6
(E*,Γ)	(0.25,0.1)	(0.25,0.4)	(1.2,0.1)	(1.2,0.4)	(3,0.1)	(3 ,0.4)

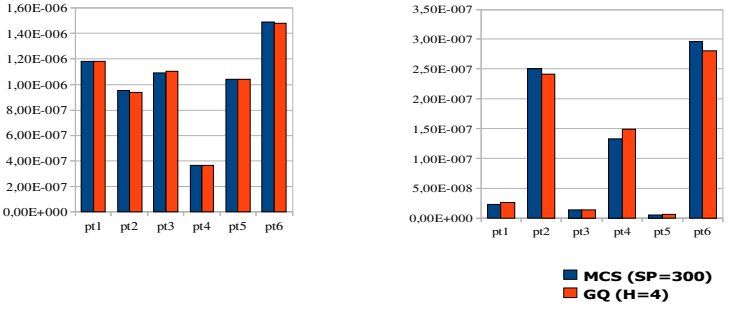

Fig. 4a μ_Y : Mean of RMS(*TEs*) **Fig. 4b** σ_Y: Standard deviation of RMS(*TEs*)

Fig. 4 Comparison between MCS and GQ Method

3.3 Robust Optimization for Gear Tooth Modifications

3.3.1 Quality Grade

In this section, the influence of the quality grade on transmission error is investigated. A parabolic crowning of normalized amplitude A_p* (with respect to δ_m) is superimposed on the symmetric profile relief characterized by E* and Γ for the helical gear defined in Table 1. The design variable vector comprises therefore E*, Γ and A_p* which are supposed to be independent and all attributed a nominal value along with a tolerance range IT-X. For a given quality class Q, the ranges IT-E* and IT-A_p* have been defined based on the NF-ISO 1328 standard [13] as opposed to IT-Γ (tolerance on the length of profile relief) not defined in [13] and expressed here as a percentage of the active profile (Table 3). A Genetic Algorithm combined with a Gaussian quadrature method is employed to evaluate the objective function (1) using only four discrete points to describe the probability distribution of each design variable (H=4). The corresponding limits of the robust areas for which the objective function is less than a given threshold Vs are plotted in Figure 5 for the 3 quality grades defined in Table 3 (in two different projection planes for clarity).

Table 3 Standard Gear Quality Grades [13].

Quality class (ISO)	IT-E*	IT-Γ	IT-Ap*
Q6	0.5	1.25 %	0.425
Q7	0.75	2.5 %	0.6
Q8	1.05	5 %	0.85

Examining these figures, it can be noticed that the location of the robust areas is almost the same for all the tested quality grades and that their surface area increase with the gear quality. As expected, the smallest robust area is associated with the ISO quality grade Q8. It can be observed that, regardless of the quality grade, robustness is essentially dependent on lead crowning Ap* and that a value of approximately 1.2 appears as optimal. Concerning profile relief, the amplitude at tooth tips E* has very little influence for the better quality grades since it can vary in the range 0.8<E*<2.2. On the other hand, the extent of modification seems far more influential and, generally speaking, robust solutions correspond to short relief with Γ<0.2.

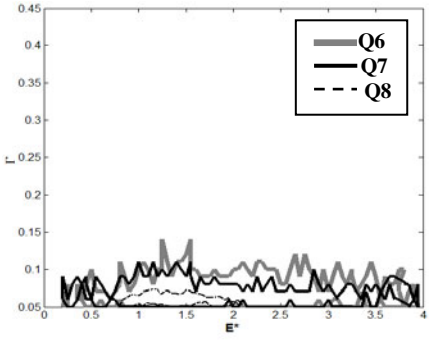

Fig. 5a Plane (E*, Γ)

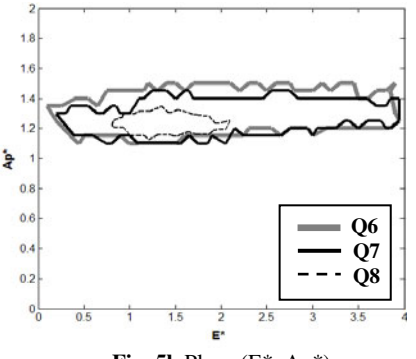

Fig. 5b Plane (E*, Ap*)

Fig. 5 Projections of robustness areas (F_{rob}<Vs; Vs=0.125μm)

3.3.2 Influence of Probability Law

The uncertainties or variability for tooth shapes are expressed in terms of probabilistic distributions which define the rule for describing the probability measures associated with the values of random (uncertain) variables. In this paper, two classic probability laws have been compared: the normal and uniform distributions.

The corresponding results described in figure 6 are the projections of the robust areas obtained for a quality grade 7 (Q7) which is considered as representative of usual industrial applications [13]. It can be observed that the magnitude of the objective function varies with the chosen probability distribution but, for both distributions, the robust areas in the design space are rather similar. Based on this finding, it is possible to conclude that the exact distribution has a secondary influence on the definition of robust tooth modifications.

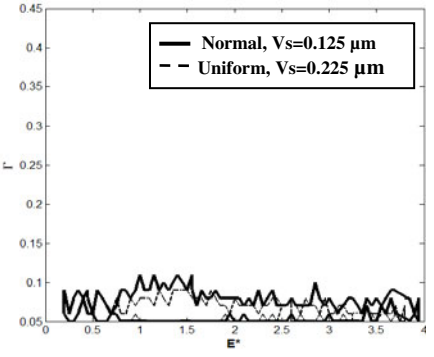

Fig. 6a Plane (E*,Γ)

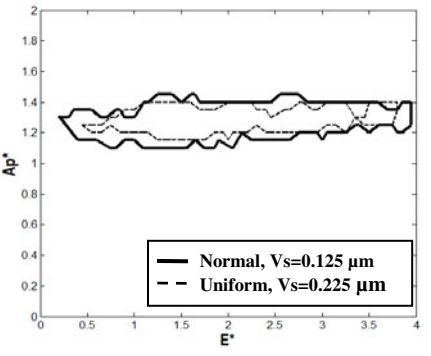

Fig. 6b Plane (E*,Ap*)

Fig. 6 Projections of robustness areas (F_{rob}<Vs)

4 Conclusion

The main objective of this paper was to present a method for the robust design of profile and lead modifications in helical gears based on a probabilistic optimization methodology. In order to estimate the relevant statistical parameters, the classic time-consuming Monte Carlo simulations have been replaced by a Gauss Quadrature method and combined with an optimization process using a genetic algorithm. The results reveal the presence of specific tooth modifications that are less sensitive to geometrical variances. For the example of helical gear treated, lead crowing appears as the most influent parameter and it is shown that, regardless of the quality grade, robust solutions correspond to short tip relief. Finally, it seems that the probability distribution is of secondary importance for the definition of robust tooth modification.

Acknowledgements. The support of the CETIM Foundation (M. Suquet) is gratefully acknowledged.

References

[1] Houser, D.R., Harianto, J., Iyer, N., Josephson, J., Chandrasekaren, B.: A multivariable approach to determining the 'best' gear design. In: Proc. 8th ASME International Power Transmission and Gearing Conference, Baltimore, September 10-13, 8 pages (2000)

[2] Gregory, R.W., Harris, S.L., Munro, R.G.: Dynamic Behavior of Spur Gears. In: Proc. IMechE Int. Conf. Gearing, vol. 178, pp. 261–266 (1963)

[3] Maatar, M., Velex, P.: Quasi-Static and Dynamic Analysis of Narrow-Faced Helical Gears With Profile and Lead Modifications. Loading of Spur Gears with Linear or Parabolic Tooth Profile Modifications. Trans ASME 119, 474–480 (1997)

[4] Velex, P., Bruyere, J., Houser, D.R.: Some Analytical Results on Transmission Errors in Narrow-Faced Spur and Helical Gears: Influence of Profile Modifications. J. Mech. Des. 133(3), 031010-1, 031010-11

[5] Sundaresan, S., Ishii, K., Houser, D.R.: A Procedure Using Manufacturing Variance to Design Gears With Minimum Transmission Error. J. Mech. Des. 113(3), 318–325 (1991)
[6] Yu, J.C.: Design Optimization for Robustness Using Quadrature Factorial Models. Engineering Optimzation 30, 203–225 (1998)
[7] Tavakoli, M., Houser, D.R.: Optimum Profile Modifications for the Minimization of Static Transmission Errors of Spur Gears. Journal of Mechanisms, Transmissions and Automation in Design 108, 86–95 (1986)
[8] Goldberg, D.E.: Genetic Algorithms in Search, Optimization and Machine Learning. Addison-Wesley (1989)
[9] Taguchi, G.: System of experimental design. Unipub/KrausInternational Publication, New York
[10] Phadke, M.: Quality Engineering using robust Design. Prentice Hall, Englewood Cliffs
[11] D'Errico, J.R., Zaino Jr., N.A.: Statistical Tolerancing using a Modification of Taguchi's Method. Technometrics 30(4), 397–405 (1988)
[12] Duffy, J., Liu, S., Moskowitz, H., Plante, R., Preckel, P.V.: Assessing multivariate process/product yield via discrete point approximation. IIE Transactions 30, 535–543 (1998)
[13] Norme française NF ISO 1328. Engrenages cylindriques – Système ISO de précision

Parametric Study on Energy Pumping of Mdof System Using Multiple Dynamic Absorbers

Kamel Khélifi[1], Mohamed-Lamjed Bouazizi[1], Emeline Sadoulet[2], Rachid Nasri [3], and Noureddine Bouhaddi[2]

[1] Unité de Recherche Dynamique des Structures,
l'Institut Préparatoire aux Études d'Ingénieur, de Nabeul,
Campus Universitaire, 8000 M'rezgua, Nabeul, Tunisie
khelifi_kamel72@yahoo.fr,
lamjed.bouazizi@ipein.run.tn
[2] Département de Mécanique Appliquée – Institut FEMTO-ST,
Université de Franche-Comté, 24 Chemin de l'Epitaphe,
25000 Besançon – France, France
noureddine.bouhaddi@univ-fcomte.fr,
emeline.sadoulet-reboul@univ-fcomte.fr
[3] Unité de recherche de Matériaux,
Ecole Nationale d'Ingénieurs de Tunis,
BP37, Le Belvédère, Tunis-Tunisie
rachid.nasri@enit.rnu.tn

Abstract. The concept of energy pumping is an innovative dynamic phenomenon. This phenomenon gives rise to a new generation of dynamic absorbers. Theoretical studies and feasibility tests are necessary for a better understanding of their dynamic behaviour and for them to be applied on real structures or machines.

In this paper, numerical evidence is firstly given for the passive and broadband targeted energy transfer in the case of a linear system (Machine for example) under shock excitation with Multiple Dynamic Absorbers (MDA). Secondly, it is shown that many MDA absorb shock energy in a one way irreversible fashion and dissipate this energy locally, without "spreading" it back to the linear system. Finally, numerical results in the case of MDA linked to a linear beam are compared to Tuned Mass Dampers (TMD absorbers) linked to the same linear beam.

Keywords: Energy pumping, Dynamic absorber, Cubic non-linearity, Nonlinear targeted energy transfer, Multiple Dynamic Absorbers.

1 Introduction

The phenomenon of energy pumping is the irreversible transfer of energy from a main structure, whose vibration levels are considered as critical in the frequency domain, to a secondary structure (Multiple Dynamic Absorbers (MDA)), just linked to the main structure. A strong nonlinearity in the design of the secondary structure is introduced. The problem is whether this phenomenon of energy

pumping can allow a passive attenuation of vibration in other words energy absorptions. This pumping concept is a dynamic innovation that has recently been introduced by the scientific community. The phenomenon of energy pumping leads to a significant and a rapid decrease in the amplitude of vibration of the main structure in a linear fashion compared to the classic case that decreases exponentially. Unlike their counterparts in linear case, the nonlinear absorbers have interesting features: they can automatically set the system frequency and they work in multiple requests (periodic or transient). In previous works ([F. Georgiades and al., 2007), it has been shown that essentially nonlinear oscillators attached to linear discrete structures can act as broadband passive absorbers of vibration energy. In particular, it has been shown that transient resonance captures of the transient dynamics may initiate one way, irreversible targeted energy transfer from a linear (main) subsystem to a local essentially nonlinear attachment, which acts, in essence, as nonlinear energy sink (NES) [F. Georgiades and A.F. Vakakis, 2007 , F. S. Samani, F. Pellicano, K. Khelfi and al., 2011].

In this work, the NES concept is demonstrated and extended to flexible systems. Specifically it is shown that an appropriately designed and placed essentially nonlinear local attachment may absorb a significant portion of shock induced vibration energy of a beam.

2 Dynamic Equations of Motion of Mdof Supported Beam

The structure chosen for the study consists of an impulsively forced simply supported damped linear beam, with multiple essentially nonlinear damped oscillators (Figure 1). This structure has been chosen because it has been addressed in [F.Georgiades 2007] with one NES but also because it was likely to be close to an experimental structure.

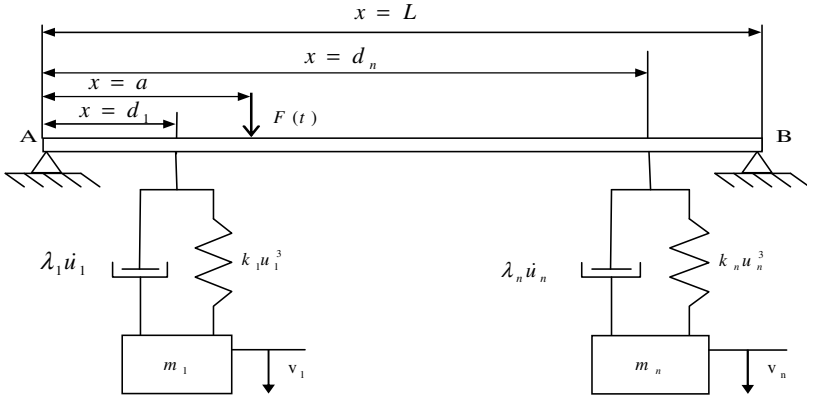

Fig. 1 Beam bi-supported with Multiple Dynamic Absorbers

- **System with Multiple Dynamic Absorbers (MDA)**

The beam model is based on the Euler-Bernoulli theory; the nonlinear equations of motion for the transverse displacement y of the beam and the vertical motion v_i of each oscillator $(1 \le i \le n)$ are given by:

$$\begin{cases} EI\frac{\partial^4 y(x,t)}{\partial x^4} + \lambda\frac{\partial y(x,t)}{\partial t} + \rho S\frac{\partial^2 y(x,t)}{\partial t^2} + \sum_{i=1}^{n}(\left\{k_i\left[y(d_i,t) - v_i(t)\right]^3 + \lambda_i(\frac{\partial y(d_i,t)}{\partial t} - \dot{v}_i(t))\right\}\delta(x-d_i)) = F(t)\delta(x-a) \\ \sum_{i=1}^{n}\left\{m_i\ddot{v}_i(t) + k_i\left[v_i(t) - y(d_i,t)\right]^3 + \lambda_i\left[\dot{v}_i(t) - \frac{\partial y(d_i,t)}{\partial t}\right]\right\} = 0 \end{cases} \quad (1)$$

E is the Young's modulus of the beam, I the moment of inertia, ρ the density, S the section and λ the damping. m_i, k_i, λ_i are respectively the mass, stiffness and damping for each oscillator. The portion of energy respectively dissipated by the MDA or the TMD noted η at time t are given by (equation 2):

$$\eta(t) = \frac{E_{NES/TMD}(t)}{E_{inj}} = \frac{\int_0^t \sum_{i=1}^{n} \lambda_i \left(\dot{v} - \dot{y}\right)^2_{x=d_i} d\tau}{\int_0^T F(t)\,\dot{y}_{(x=a)} dt} \quad (2)$$

Where T is the period of the mode and F the impulse force. This force is presented in the figure 2, respectively in the time and frequency domains, the five first modes of the beam are excited.

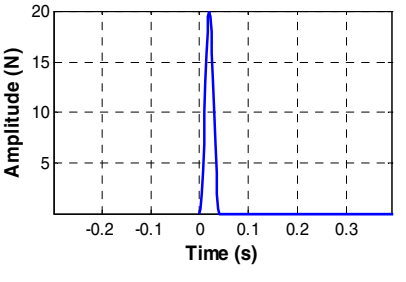

(a)

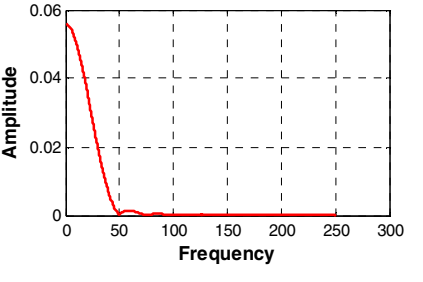

(b)

Fig. 2 Time and Frequency representation of the impulse force

3 Numerical Simulations

This section presents numerical simulations obtained for a bi-supported beam with one or more absorbers. The efficiency of the MDA is investigated through a parametric study.

3.1 Bi - supported Beam Coupled with Two NES

3.1.1 Reponses of the Beam and the Two NES in Time Domain

The same bi-supported linear beam is studied with MDA (two NES) and with the same parameters: k = 1322 N/m^3, λ = 0.05 N.s.m-1, m = 0.1 kg. The same impulse force $F(t)$ is applied to excite the beam at a distance a = 0.3 m (Figure 3). The positions of the two NES are respectively d_1 = 0.25 m and d_2 = 0.8 m. Only the results for d_2 = 0.8 m are presented in figures 3-a and 3-b. The transient responses are observed in the case before energy pumping.

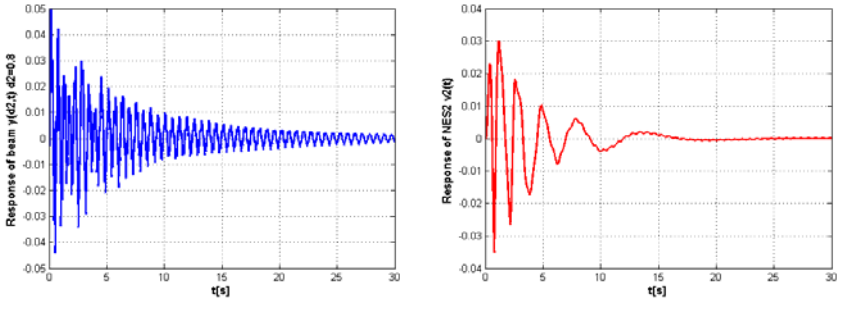

(a) (b)

Fig. 3 Responses of the beam with MDA (two NES) in the time domain - Phenomenon of pumping

3.1.2 Parametric Study of the Two Dynamic Absorbers

a- Effect of Nonlinear Stiffness

In this section, the influence of the nonlinear stiffness coefficient k, with the position of the two dynamic absorbers is studied. The figure 4-a shows that for a given position of the two dynamic absorbers, the highest amount of dissipated energy that can be achieved is η = 92.4% .The figures 4-b and 4-c illustrate the efficiency of two NES depending on their stiffness and on their position on the beam.

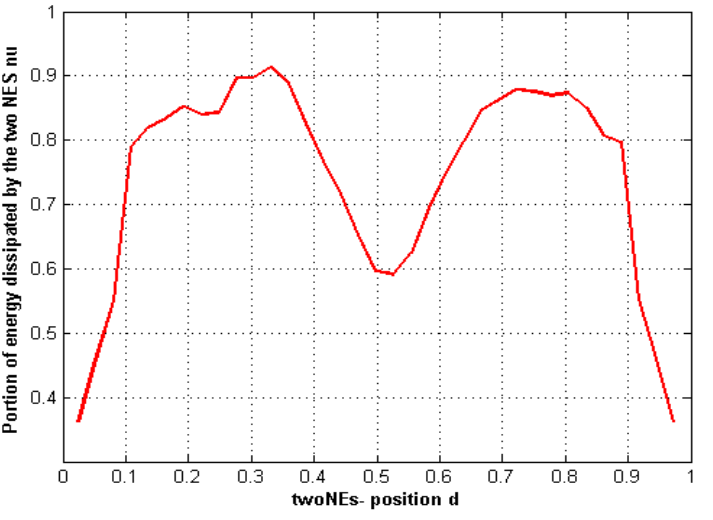

(a)

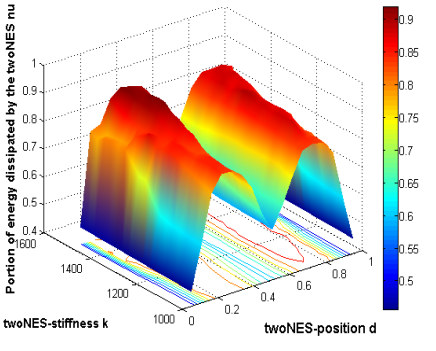

(b)

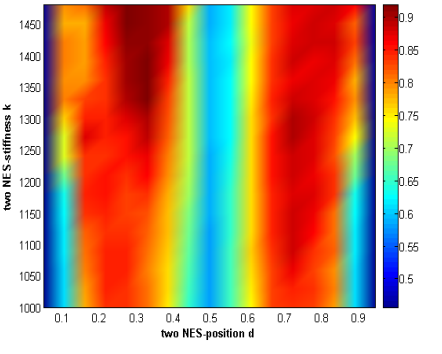

(c)

Fig. 4 Absorbed and dissipated energy by MDA based on the variation of the nonlinear stiffness and the position of the MDA: (b) 3D plot and (c) 2D projection plane (k, d)

b- Effect of the Linear Viscous Damping of Two Dynamic Absorbers

The influence of the damping of the two NES and their position on the linear beam is studied. Figure 5 shows that the quantity of dissipated energy is highest for $\lambda \geq 0.15$ ($\eta \sim 90\%$) for any position of the two NES that shows the robustness of the system. This robustness is influenced for $\lambda \leq 0.05$ N.s.m^{-1}.

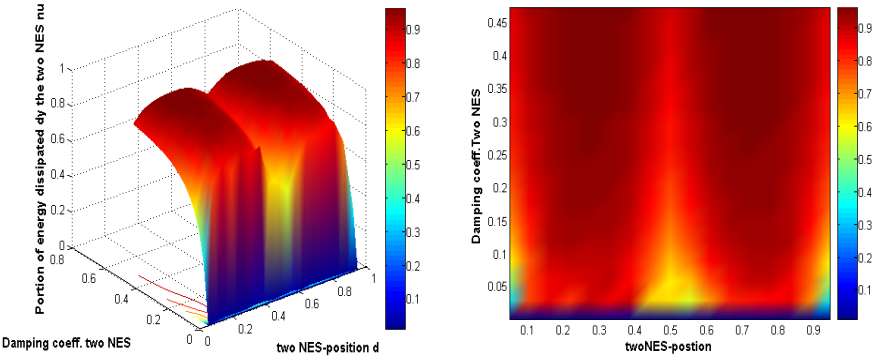

Fig. 5 Absorbed and dissipated energy by MDA based on the damper and the position of the two MDA: (b) 3D plot and (c) 2D projection plane

3.2 Bi - supported Beam Coupled with Two TMD

The response of the beam coupled to two TMD is computed in the time domain with the same parameters as the ones used in case of two NES. The efficiency and the quantity of dissipated energy are also studied. Two TMD are attached to the linear beam. They are placed at distance $d_2 = 0.8$ m. For this simulation, parametric studies for two TMD are performed with the same parameters as in section 3.3.2 and the same impulse force $F(t)$ to excite the beam at a distance $a = 0.3$ m. The influence of the linear stiffness coefficient k and with the position of the two TMD is studied. Figures 6-a and 6-b illustrate the amount of energy dissipated by the two TMD ($k \in$ [1000 1500]). The highest value is 65% at a position $d \in$ [0.2 0.4]) for the two TMD.

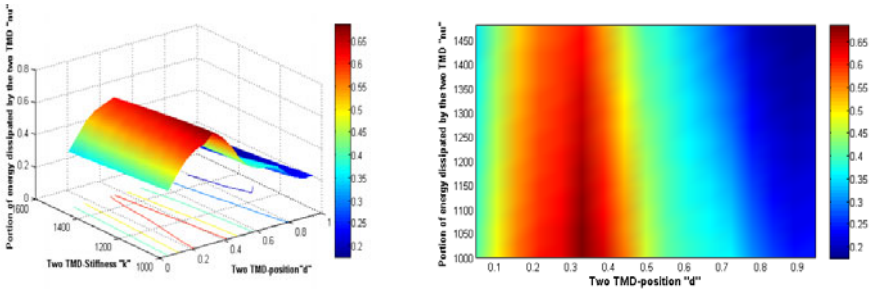

(a) (b)

Fig. 6 Absorbed and dissipated energy by the two TMD based on the variation of the linear stiffness and the position of the two TMD: (a) 3D plot and (b) 2D projection plane of (k, d)

4 Conclusion

This paper studies the portion of energy transferred from a linear beam excited by an impulse force to a secondary system. Dynamic absorbers such as MDA (two NES) or two TMD are linked to the same beam. A parametric study is carried out for all cases in order to evaluate the ability of the NES and the TMD to dissipate a portion of the injected energy under impulse force. The robustness of all configurations with variations of the design parameters is also studied.

Generally, the nonlinear attachment holds promise as an efficient, robust, lightweight and passive absorbing device for eliminating undesired shock-induced broadband disturbances in small or large scale flexible structures. Viewed in that context, the NES may be regarded as a passive, broadband boundary controller, and as such can find application in diverse problems in engineering.

In the part of the parametric study with two NES, it appears that the maximum value of dissipated energy is $\eta = 92.4\%$. The comparative study of the different configurations (single NES, two NES) shows that the robustness is improved with two NES. The main advantages of the proposed nonlinear design with one or two NES is its relative simplicity, its lightweightness, and its ability to be adaptive, its ability to resonantly interact with a set of structural modes of arbitrary frequency, extracting energy from all modes.

References

Georgiades, F., Vakakis, A.F.: Dynamics of a linear beam with an attached local nonlinear energy sink. Communications in Nonlinear Science and Numerical Simulation 12, 643–651 (2007)

Samani, F.S., Pellicano, F.: Vibration reduction on beams subjected to moving loads using linear and nonlinear dynamic absorbers. Journal of Sound and Vibration 325, 742–754 (2009)

Georgiades, F., Vakakis, A.F.: Passive targeted energy transfers and strong modal interactions in the dynamics of a thin plate with strongly nonlinear attachments. International Journal of Solids and Structures 46, 2330–2353 (2009)

Khélifi, K., Bouazizi, M.-L., Sadoulet Reboul, E., Nasri, R., Bouhaddi, N.: Etude paramétrique des conditions de pompage énergétique non linéaire. In: Quatrième Congrès International Conception et Modélisation des systems Mécanique, CMSM 2011, Hammamet-Tunisie (2011)

Chatter Recognition in Band Sawing Based on Feature Extraction and Discriminant Analysis

Tilen Thaler[1], Primož Potočnik[2], Peter Mužič[2], Ivan Bric[1], Rudi Bric[1], and Edvard Govekar[2]

[1] PETRA Machines d.o.o., Cesta Andreja Bitenca 68, 1000 Ljubljana, Slovenia
{tilen.thaler,ivan.bric,rudi.bric}@pe-tra.com
[2] University of Ljubljana, Faculty of Mech. Engineering,
Aškerčeva 6, 1000 Ljubljana, Slovenia
{primoz.potocnik,peter.muzic,edvard.govekar}@fs.uni-lj.si

Abstract. Tool damage due to chatter poses harmful economic impact in modern machining production therefore it is important to avoid or suppress chatter during the production process. In order to establish automated chatter-free cutting conditions, the methods for online recognition of chatter and chatter-free cutting should be developed. It this paper a band sawing cut-off process is considered where a combination of selected workpiece properties and cutting parameters result in chatter. A method for online chatter detection based on processing of acoustic signals is proposed. The method consists of pre-processing sound signals with Short-Time Fourier Transform (STFT), extracting frequency invariant features, and finally applying Quadratic Discriminant Analysis (QDA) for classification. The proposed method, tested with two-fold cross validation on experimental data, yields high recognition rate (over 96%).

Keywords: band sawing, chatter detection, short-time Fourier transform, feature extraction, discriminant analysis, cross-validation.

1 Introduction

Economy of machining depends on energy, time and material consumption as well as tool wear. Savings in material can be considerable if surface finish is adequate before the next production stage. Chatter significantly deteriorates surface quality and reduces tool life therefore considerable effort has been directed toward detecting and removing chatter phenomenon in different areas of machining.

In 1965 and 1967 Mote [1] reported on theoretical models for lateral and torsional moving band vibrations respectively which set milestones for theoretical chatter studies in band sawing. Work by Yang [2] and Le-Ngoc [3] was supported with theoretical models in 1981 and 1990 respectively. Okai [4] observed washboarding as a consequence of self-induced vibration with respect to workpiece thickness and its position in wood cutting in 2009. Several papers have been dedicated to chatter control in band sawing; Damaren [5] employed a force actuator to achieve robust active control of vibrations.

Chatter has been researched considerably more in other machining processes such as grinding, milling, turning and drilling. Methods for chatter detection in grinding were further employed by Inasaki [6], Govekar [7] and Altintas [8] in 2001, 2002 and 2004 respectively. In turning several methods were proposed for chatter detection. Stability lobe diagrams were presented in 1998 by Gradisek et al. [9], acoustic emission measurements were employed for chatter detection in 2000 [10].

Multisensory approach was reported in 2008 by Kuljanic [11] and concluded that sound signals alone provide sufficient information for chatter detection. For a complete review of chatter in machining processes reader should investigate paper by Quintana [12].

Chatter in band sawing causes low quality surface finish, increases tool wear and is a source of noise pollution, therefore it is crucial to detect and suppress this phenomena in band sawing as well. Objective of our research is to explore various signals such as sound, forces and vibrations in order to detect chatter produced by band sawing cut-off process. An industrial band sawing machine was equipped with multiple sensors for the purpose of chatter detection and based on recorded data several chatter detection methods were tested and compared.

2 Experimental Setup

Experiments were conducted on a true double column PE-TRA Toolmaster 300DC band saw of 300 mm maximum cutting width capacity. The blade Håkansson, type PCVII Commander, length 4150 mm and pitch 4-6 [teeth/inch] was used and tensioned at approximately 2.0 kN.

The band saw was equipped with a multi-sensory data acquisition system for a complete characterization of the band sawing process. Forces were measured by a Kistler 9257 dynamometer. Vibrations were recorded by a PCB piezo accelerometer (type 356A16) mounted on the left blade supporting arm. Sound was recorded by a Brüel & Kjaer microphone (type 4190). The microphone and preamplifier were mounted on a magnetic stand above the workpiece at distance approximately 32 cm away from the workpiece pointing directly towards the workpiece. Workpiece profiles covered in this research are presented in Figure 1. Workpieces were cut in 3-5 mm length from a 300-400 mm long tube. Material of the tested workpieces was mild easy-to-machine construction steel. Different geometries were selected to show generality of the methods for chatter detection. Cutting speed ranged from 56-77 m/min and down-feed ranged from 94.8-104.0 mm/min. Frequency of teeth entering the workpiece depends on blade pitch and cutting speed. In case of 4-6 teeth per inch (tpi) and above-mentioned cutting speeds two main frequencies can be determined. First results from the 4 tpi set and is in the range 147-202 Hz, the other results from 6 tpi and ranges from 220 to 303 Hz.

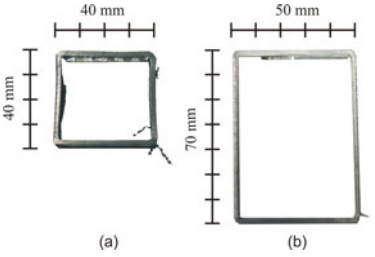

Fig. 1 Profiles of cut workpieces. Material of the tested profiles is easy-to-cut mild construction steel.

3 Measured Signals

Signals for chatter detection were provided by the multisensory experimental setup described in previous section. Figure 2 represents sound, cutting force and vibration signals and their average power spectra of chatter and chatter-free regions.

Comparison of the signals and corresponding power spectra reveals good discrimination of chatter and chatter-free regions by sound spectrum. Force and vibration signals are not informative for the recognition of chatter phenomena. Consequently, our subsequent analysis for chatter detection is based on sound signals. This is in accordance with multisensory chatter detection results in milling [11] confirming that sound signals alone provide sufficient information for chatter detection.

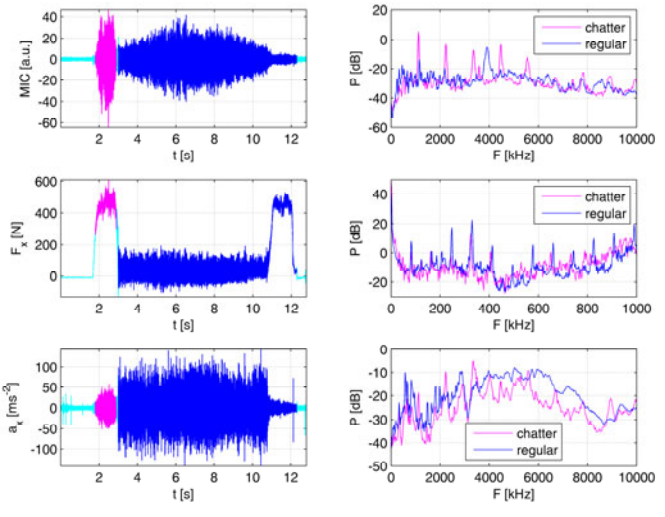

Fig. 2 Comparison of sound, force and vibration signals with the corresponding power spectra of regular and chatter band-sawing. Blue lines denote regular band sawing intervals, and magenta colour denotes chatter phenomena.

4 Solution Approach

As shown in previous section, the most informative signal for chatter detection was measured sound, acquired with sampling frequency f_s = 20 kHz. Preliminary power spectrum results shown in Figure 2 motivated application of spectral methods. In order to provide suitable temporal resolution for online chatter recognition, the Short-Time Fourier Transform (STFT) version was applied as a signal preprocessing method.

In our analysis, the reference for chatter and chatter-free signals was provided by expert operators who detected and recognized chatter based on their acoustic perception during the band-sawing process. Based on this reference, the acquired signals were segmented into chatter and chatter-free regions.

Based on STFT spectra, various features were extracted in order to provide frequency invariant information, and the following methods were tested with the objective of reliable chatter detection:

1. single feature with optimized decision threshold,
2. multiple feature combinations and *quadratic discriminant analysis* (QDA),
3. multiple feature combinations and *feed-forward artificial neural network* (FNN).

Chatter detection methods were tested based on 2-fold *Cross-Validation principle* (CV) where a complete set of signals was divided into training and testing sets as follows:

1. as first, training set was used to train the chatter detection method (setting decision threshold, etc.), then the method was tested on a test set,
2. in the next step, the training and test sets were swapped and the training/testing procedure repeated,
3. the result of the method was obtained as an average of both testing cross-validation results.

The objective for the chatter detection methods was defined by a percentage rate (R) of correctly classified samples. Two types of errors occur in chatter recognition: 1) chatter that occurred but is not detected and 2) normal signal is reported as chatter. In order to encompass both errors an objective function was defined by Eq. (1). Since the chatter-free regions are much more frequent compared to chatter regions, the equal probability of both regions was assumed and encoded into the objective function as follows:

$$R = \frac{1}{2} R_{ch} + \frac{1}{2} R_{reg} \tag{1}$$

The overall classification rate R is composed from equal contributions of chatter classification rate R_{ch} and chatter-free classification rate R_{reg}. Ignoring the proposed objective function the employed method would yield over 90% recognition rates already without detecting any chatter because the probability of chatter-free signal is significantly larger compared to chatter. The same objective function was also used by Kuljanic [11].

5 Feature Extraction Based on Frequency Domain

For real-time online chatter detection a fast routine should be employed for chatter characterization. Acquired signals of sound were analyzed in frequency domain where chatter is clearly separable from normal cutting therefore the Short-Time Fourier Transform (STFT) was applied as an initial signal pre-processing method. The method is also numerically very fast and thus appropriate for real-time application. The following parameters were applied in order to obtain suitable time/frequency resolution: window length = 1024, window type = *Hamming*, frequency resolution df = 20 Hz, time resolution dt = 25.6 ms, logarithmic scale. Such a combination of parameters provides a suitable basis also for online application of the method for real-time chatter detection on the band-sawing machine. Fig. 3 presents an example of a sound spectrogram based on STFT. Chatter interval shows clear characteristic stripes of amplified frequencies.

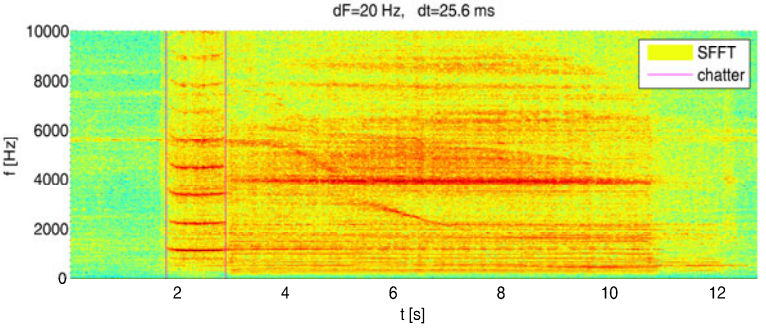

Fig. 3 Microphone STFT of regular and chatter band-sawing. The chatter interval is clearly marked between 1.8 s and 2.8 s.

Based on spectrogram observations (Fig. 3) a set of features was calculated from the STFT signal. At arbitrary workpieces and machine parameters presented in this paper, the chatter signal retains its characteristic shape however the peak locations vary depending on the geometry of the workpiece and machine parameters. The motivation of this paper was extraction of features that are independent of workpiece and machine parameters. Consequently, we propose the extraction of various frequency independent features (z_1, z_2, …, z_9) from STFT signals:

a) Simple features
   - z_1 max_1: amplitude of the 1st frequency peak in [0, 2] kHz range,
   - z_2 max_2: amplitude of the 2nd harmonic peak,
   - z_3 max_3: amplitude of the 3rd harmonic peak,
   - z_4 min_{12}: amplitude of the area between 1st and 2nd frequency peak,
   - z_5 min_{23}: amplitude of the area between 2nd and 3rd frequency peak,

b) Combined features (combination of simple features)
   - z_6 max_1+max_2
   - z_7 $max_1+max_2+max_3$,

z_8 $max_1+max_2\_2min_{12}$
z_9 $max_1+max_2+max_3\_min_{12}\_min_{23}$

The proposed features were extracted from logarithmic STFT that were also normalized with respect to average sound level at this time segment. With this step we provide invariance to the sound levels recorded and therefore a broader generality of the method. In the next section, the extracted features are tested as inputs to chatter detection methods.

6 Results of Chatter Detection

The proposed extracted features are tested as single chatter indicators, or as a combined input to discriminant analysis or neural network based chatter detection.

Single feature detection was accomplished by cross-validation method where the decision threshold was defined on the training set, and the feature tested on the test set. The chatter recognition testing results (classification rate R) are presented in Table 1.

Table 1 Chatter detection results by single extracted features. The best result is denoted in bold.

Feature:	z_1	z_2	z_3	z_4	z_5	z_6	z_7	z_8	z_9
R [%]	89.31	89.79	86.26	49.89	49.94	91.95	93.03	94.73	**95.95**

The best single feature result is obtained by feature z_9, which is composed from amplitudes of first three harmonic peaks with subtracted components of regions between harmonics. The result for feature z_9 based on cross-validation and optimal threshold yields $\underline{R = 95.95\%}$ recognition efficiency.

Multi-feature combinations were examined by a quadratic discriminant analysis method (QAD). All possible combinations of features (z_1, z_2, …, z_9) were tested and the best subset was determined based on cross-validation result. The winning overall combination of arbitrary features classified by quadratic discriminant analysis yields classification rate $\underline{R = 97.64\%}$. The winning combination of features is

$$z = [z_1, z_5, z_7, z_9].$$

The result means that adding several additional features can slightly improve the classification rate but the improvement is below 2%. For comparison, the best combination of two features was determined and the result is $\underline{R = 96.86\%}$ obtained by a combined input $z = [z_5, z_9]$. Cross-validation result for the best combination of two features is shown in Figure 4. Chatter and chatter-free samples are marked and discriminant analysis based on features z_5 and z_9 and quadratic polynomial is plotted. For both cross-validation runs, training and testing results are shown and the classification rate R is obtained as an average of testing results.

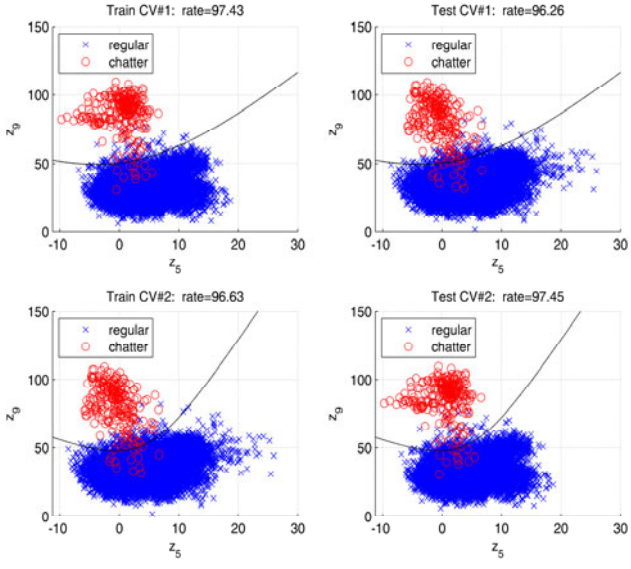

Fig. 4 Best discriminant analysis result $\underline{R = 96.86\%}$ based on quadratic method and the most informative two dimensional feature subspace (z_5, z_9).

Extracted features were applied as inputs also to the feed-forward artificial neural network with sigmoid transfer functions. The same cross-validation procedure was applied and the number of hidden neurons was explored from 2 to 20. Results of neural network testing could not improve the discriminant analysis results therefore we conclude that the best obtained QDA result is close to optimal classification rate that is obtainable with the proposed set of features. Classification rate is also limited by the prior selection of chatter / chatter-free regions based on expert knowledge. The transitions between chatter and regular cutting are sometimes difficult to determine therefore the obtained results can be considered as very good and similar to results reported by [11].

7 Conclusion

Force, vibrations, sound and energy consumption signals were acquired on industrial band saw machine. The signals were analysed and compared in order to find the most informative signals for machine chatter recognition. In accordance with previous research, sound is confirmed as the most informative signal in chatter detection. Frequency invariant features were extracted from sound signals, preprocessed by Short-Time Fourier Transform (STFT), and Quadratic discriminant analysis (QDA) was performed for feature classification. Good recognition rate was obtained already for a single extracted feature z_9 (r = 95.95%), and the best recognition was obtained by a combination of features z_1, z_5, z_7, z_9 (r = 97.64%).

The proposed method is very fast in execution therefore it is suitable also for fast online operation.

Further work will be dedicated to online integration of the proposed method in an industrial band saw machine and classification of chatter under time-varying conditions. Chatter depends on machining parameters, tribological properties, geometry and material of workpiece and tool properties. These time-dependent variables affect chatter occurrence hence detection methods for online chatter recognition have to be time-invariant. This paper addresses momentary loading of blade and workpiece under a range of arbitrary machine parameters and conditions. The extracted features are frequency invariant hence the method for detection could as well prove to be successful in all stages of tool life and for a wide arbitrary set of machining parameters, workpieces and conditions.

Unlike turning where controlled chatter experiments can be relatively easily carried out by varying depth of cut along the workpiece length, in band sawing chatter phenomenon is not that straightforward to achieve. We are expecting that chatter mostly occurs in workpiece due to its clamping system and rigidity however further experiments have to be carried out in order to systematically characterize chatter in band sawing.

Acknowledgements. Operation partly financed by the European Union, European Social Fund. Operation implemented in the framework of the Operational Program for Human Resources Development for the period 2007-2013, Priority axis 1: Promoting entrepreneurship and adaptability, Main type of activity 1.1.: Experts and researchers for competitive enterprises.

References

[1] Mote Jr., C.D.: A study of band saw vibrations. J. of the Franklin Institute 279, 430–444 (1965), doi:10.1016/0016-0032(65)90273-5

[2] Yang, B., Mote, C.D.: Vibration control of band saws: Theory and experiment. Wood Science and Technology 24, 355–373 (1990), doi:10.1007/BF00227056

[3] Le-Ngoc, L., McCallion, H.: Self-induced vibration of bandsaw blades during cutting. Proceedings of the Institution of Mechanical Engineers 213, 371–380 (1999), doi:10.1243/0954406991522329

[4] Okai, R.: Influence of vibration coupling between bandsaw frame and feed-carriage system on sawdust spillage and surface quality of workpiece during sawing. Eur. J. Wood Prod. 67, 189–195 (2009), doi:10.1007/s00107-009-0319-z

[5] Damaren, C.J., Le-Ngoc, L.: Robust active vibration control of a bandsaw blade. Journal of Vibration and Acoustics 122, 69–76 (2000)

[6] Inasaki, I., Karpuschewski, B., Lee, H.-S.: Grinding Chatter – Origin and Suppression. CIRP Annals – Manufacturing Technology 50, 515–534 (2001); doi:10.1016/S0007-8606(07)62992-8

[7] Govekar, E., Baus, A., Gradisek, J., Klocke, F., Grabec, I.: A new method for chatter detection in grinding. CIRP Annals – Manufacturing Technology 51, 267–270 (2002); doi:10.1016/S0007-8506(07)61514-5

[8] Altintas, Y., Weck, M.: Chatter stability of metal cutting and grinding. CIRP Annals – Manufacturing Technology 53, 619–642 (2004); doi:10.1016/S0007-8506(07)60032-8

[9] Gradisek, J., Govekar, E., Grabec, I.: Time series analysis in metal cutting: chatter versus chatter-free cutting. Mechanical Systems and Signal Processing 12, 839–854 (1998); doi:10.1006/mssp.1998.0174

[10] Chiou, R.Y., Liang, S.Y.: Analysis of acoustic emission in chatter vibration with tool wear effect in turning. Int. J. of Machine Tools and Manufacture 40, 927–941 (2000); doi:10.1016/S0890-6955(99)00093-0

[11] Kuljanic, E., Sortino, M., Totis, G.: Multisensor approaches for chatter detection in milling. J. of Sound and Vibration 312, 672–693 (2008); doi:10.1016/j.jsv.2007.11.006

[12] Quintana, G., Ciurana, J.: Chatter in machining processes: A review. Int. J. of Machine Tools and Manufacture 51, 363–376 (2011); doi:10.1016/j.ijmachtools.2011.01.001

Damping in Bolted Structures

Aymen Tleilia[1], Rachid Nasri[2], and Jamel Chakhari[3]

[1] Unité de Recherche Génie des Matériaux URGM – ENIT Tunisie
tlailia_aymen@yahoo.fr
[2] Unité de Recherche Génie des Matériaux URGM – ENIT Tunisie
Rachid.Nasri@enit.rnu.tn
[3] Unité de recherche de mécanique des solides,
de structures et de développement technologique (UR-MSSDT),
ESST de Tunis
ch_jamel@yahoo.ca

Abstract. In this study we were interested in bolted assemblies and their behaviour in response to harmonic excitations, their dynamic responses and their modelling in mass-spring model and finally validation with the finite element method.

Keywords: Damping, dynamic response, mass-spring model, finite element-model.

1 Introduction

Bolted structures are commonly used in complex industries and the most exposed to large loads, for this reason we re-fined this type of structure in the areas of transport namely aerospace, automotive, rail and ship. This type of fixing bolted and also riveted is classified up to now the most powerful and most resistible to large stresses due to fatigue and vibration (monotonous and sharp).

In the field of transport (cars, planes, ships), passenger comfort is becoming more and more a primary criteria in conception.

Therefore, the behaviour of structures at the design has become essential.

In general, the vibration quality of the structures depends primarily on three factors: the excitement, the modal characteristics and the damping of the structure. The last fundamental parameter is poorly controlled until now. In fact, the calculations of the dynamic response are often made by introducing arbitrary dumping values estimated from tests. Therefore, it is urgent to develop a methodology to understand and quantify the damping phenomena at the stage of conception.

This issue concerns mainly the automotive and aeronautics. Indeed, many parts are formed exclusively by the assembly of sub-structures made from thin stamped sheets assembled using electrical welding point. There are also other processes of the assembly of sub-structure (bolting and riveting).

The damping observed in the assembled structures is much higher than that intrinsic to the material. It is mainly due to energy loss caused by micro-slip between the surfaces in contact.

These phenomena are extremely complex because these energy losses depend on the contact pressure and the amplitude of vibration, leading to a nonlinear behaviour of structures. This work will form part of behaviour of dissipative structures meetings focused on the characterization and quantification of damping.

Then, the main motivation for studying the nonlinear behaviour of the junctions is strongly linked to their ability to absorb the energy so it is indeed a means of passive control of vibrations. Indeed, the energy dissipation leads to a decrease in the amplitude of vibration. The phenomena involved in a joint are extremely complex and several mechanisms of energy dissipation may be affected. I will begin by studying the damping of the friction.

Quick Bibliography; in 1985 [1] RM .EL ZAHRY have created procedure of resolution with simple mathematic model. In 1994 [2] S.Mourad A.Ghobarah and R.M.Korol concluded that the fasteners behave predictably. In 2002 [3] N.G.Pai and D.P.Hess presented and analyze vibrations generated by shear forces. In 2004 [4] S.S.Law, Z.M.Wu and S.L.Chan published a paper in which they invoke the analysis of the energy dissipated in bolted connection. In 2005 [5] R.A.IBRAHIM and C.L.PETTIT, took the same configuration (two plates and a bolt), but with the addition of piezoelectric discs to change the normal contact force between the two plates in question, they varied the contact force plates assembly to determine the eigenvalues of the random damping in the joints. In 2007 [6] H.JALALI, H.AHMADIAN, and J.E.MOTTERSHEAD simplified the complex phenomenon of energy dissipation bindings by using simple analytical model.

2 Choice of Model

2.1 Flowchart

In this flow chart we find the approach taken and considered in the choice of bolted model and digitization of CAD software and the mass-spring modelling.

This is a general flow chart because we find at the end the validation study between analytical and finite element simulation.

The choice of the CAO model is between two models sheet metal and machined. This choice is made by evaluating two criteria: (endurance to the excitement and strength compared with the type of use).

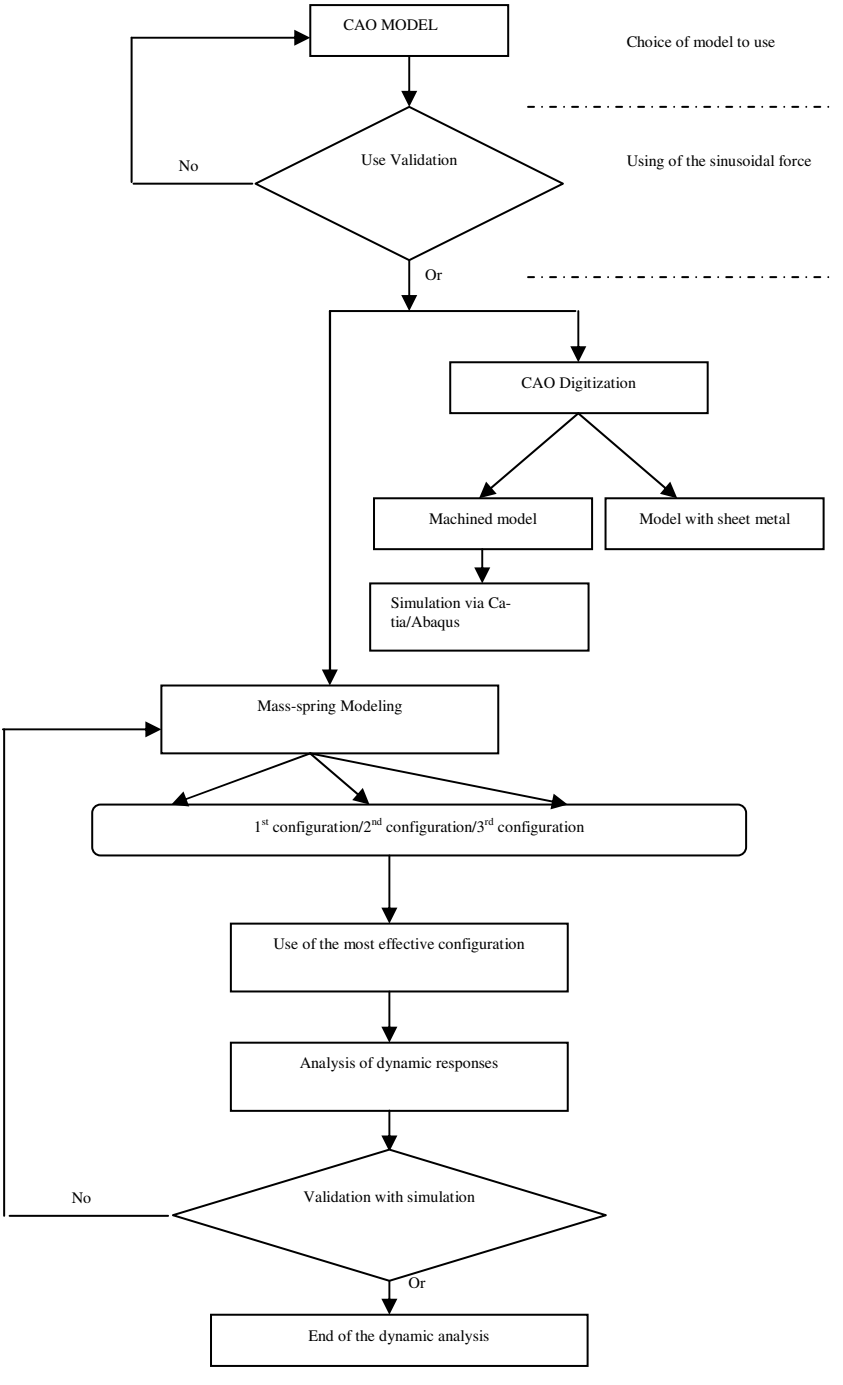
CAO MODEL
Choice of model to use
Use Validation
No
Using of the sinusoidal force
Or
CAO Digitization
Machined model
Model with sheet metal
Simulation via Ca-tia/Abaqus
Mass-spring Modeling
1st configuration/2nd configuration/3rd configuration
Use of the most effective configuration
Analysis of dynamic responses
Validation with simulation
No
Or
End of the dynamic analysis

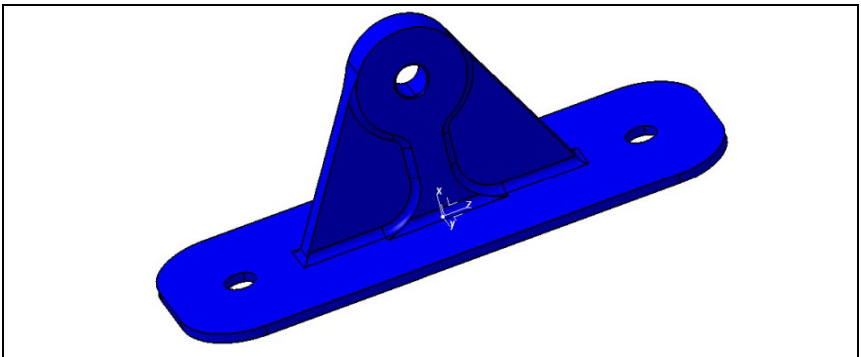
machined bracket in reality (after optimization)

2.2 *Stratification and Modelling*

When all mesh nodes belonging to the representative surface of contact will be connected to a master node. The boundary conditions and loads appropriate will be imposed manually.

The modelling of contact prints is through the construction of a representative area of contact (see figure below). This surface is then sewn to the fixed bracket.

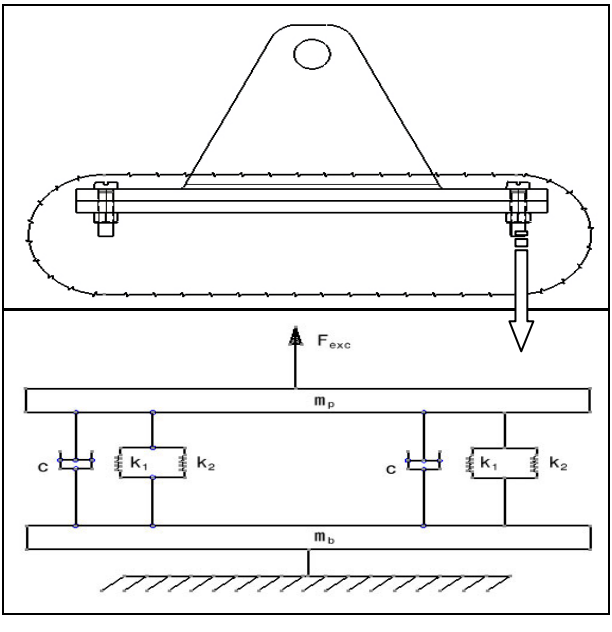

Fig. 1 Complete model

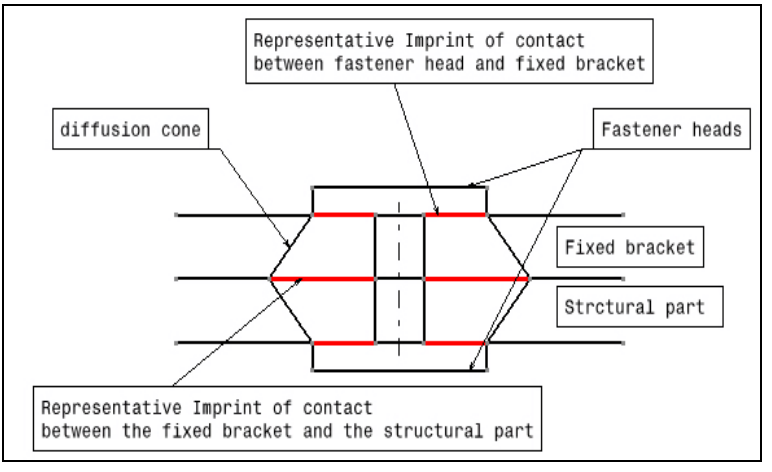

Fig. 2 Imprint of contact

3 Equations and Figures

Lagrange Equation:

$$\begin{cases} m_p X_1'' + 2c X_1' + 2(k_1 + k_2) X_1 + k(X_1 - X_2) = 0 \\ M . X_2'' + k(X_2 - X_1) = F_0 \cos(\beta t) \end{cases} \quad (1)$$

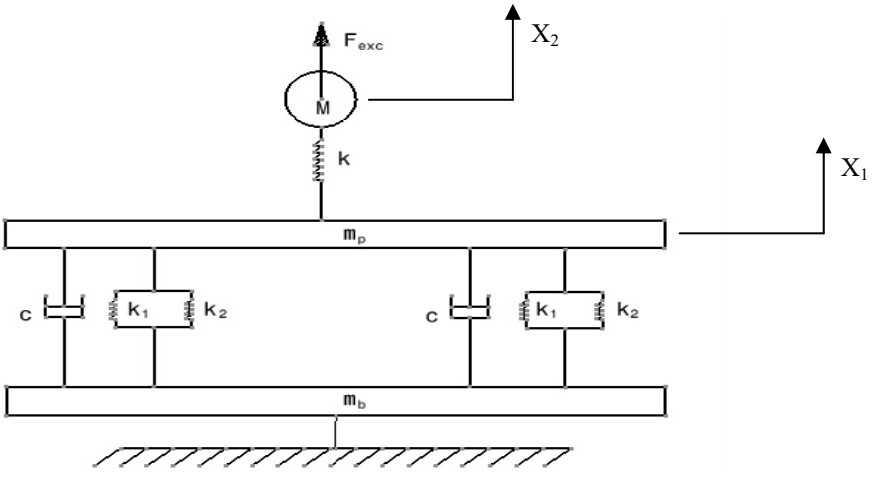

Fig. 3 Stratified model

$$\begin{cases} X_1'' + \dfrac{2c}{m_p} X_1' + 2\dfrac{(k_1 + k_2)}{m_p} X_1 + \dfrac{k}{m_p}(X_1 - X_2) = 0 \\ X_2'' + \dfrac{k}{M}(X_2 - X_1) = \dfrac{F_0}{M}\cos(\beta t) \end{cases} \tag{2}$$

We Set:

$$\omega = \sqrt{\frac{k}{M}} \quad , \quad \omega' = \sqrt{\frac{k}{m_p}} \quad , \quad \omega_2 = \sqrt{\frac{k_2}{m_p}} \quad , \quad \omega_1 = \sqrt{\frac{k_1}{m_p}}$$

$$\alpha' = \frac{c}{2.m_p.\omega'} \quad , \quad \alpha_1 = \frac{c}{2.m_p.\omega_1} \quad , \quad \alpha_2 = \frac{c}{2.m_p.\omega_2}$$

$$P_0 = \frac{F_0}{M}$$

We will have:

$$\begin{cases} X_1'' + \alpha'.\omega' X_1' + 2(\omega_1^2 + \omega_2^2) X_1 + \omega'^2 (X_1 - X_2) = 0 \\ X_2'' + \omega^2 (X_2 - X_1) = P_0 \cos(\beta t) \end{cases} \tag{3}$$

We set the following parameter:

$$X_{exct} = \frac{F_0}{k}$$

Whether: $\bar{X}_1 = \dfrac{X_1}{X_{exct}}$, $\bar{X}_2 = \dfrac{X_2}{X_{exct}}$ (Terms dimensionless)

Now we divide the equations by ($X_{exct}.\omega^2$), we obtain the following dimensionless equations:

$$\begin{cases} \dfrac{\bar{X}_1''}{\omega^2} + \alpha'.\omega' \dfrac{\bar{X}_1'}{\omega^2} + 2((\dfrac{\omega_1}{\omega})^2 + (\dfrac{\omega_2}{\omega})^2)\bar{X}_1 + (\dfrac{\omega'}{\omega})^2 (\bar{X}_1 - \bar{X}_2) = 0 \\ \dfrac{\bar{X}_2''}{\omega^2} + (\bar{X}_2 - \bar{X}_1) = \cos(\beta t) \end{cases} \tag{4}$$

It is assumed that:

$$\{u\} = \begin{Bmatrix} X_1 \\ X_2 \end{Bmatrix} \quad , \quad \{u'\} = \begin{Bmatrix} X_1' \\ X_2' \end{Bmatrix} \quad , \quad \{u''\} = \begin{Bmatrix} X_1'' \\ X_2'' \end{Bmatrix}$$

This gives the following dimensionless equation:

$$\left[\bar{M}\right].\{\bar{u}''\}+\left[\bar{c}(\bar{u}')\right].\{\bar{u}'\}+\left[\bar{k}(\bar{u})\right].\{\bar{u}\}=\{\bar{F}\} \quad (5)$$

Where $\{\bar{u}\}=\begin{Bmatrix}\bar{X}_1\\ \bar{X}_2\end{Bmatrix}$ Displacement vector.

$\{\bar{u}'\}=\frac{1}{\omega}\begin{Bmatrix}\bar{X}_1'\\ \bar{X}_2'\end{Bmatrix}$ Velocity vector.

$\{u''\}=\frac{1}{\omega^2}\begin{Bmatrix}\bar{X}_1''\\ \bar{X}_2''\end{Bmatrix}$ Acceleration vector.

$\{\bar{F}\}=\begin{Bmatrix}0\\ \cos(\beta t)\end{Bmatrix}$ Force vector.

$\{\bar{M}\}=\begin{pmatrix}1 & 0\\ 0 & 1\end{pmatrix}$ Mass matrix

$\{\bar{c}(\bar{u}')\}=\begin{pmatrix}\frac{\alpha'\omega'}{\omega} & 0\\ 0 & 0\end{pmatrix}$ Damping matrix.

$\{\bar{k}(\bar{u})\}=\begin{pmatrix}\frac{2}{\omega^2}\left[\omega^2{}_1+\omega^2{}_2\right]+\frac{\omega'^2}{\omega^2} & -1\\ -\frac{\omega'^2}{\omega^2} & 1\end{pmatrix}$ Stiffness matrix

k=50000N/m; k_1=50000N/m; k_2=50000N/m; c=2N.s/m; F_0=500 N;

Boundary conditions are:

Initial displacement X_1= 0,005 m and X_2= 0,025 m Initial velocity V_1=0 m/s V_2= 15 m/s

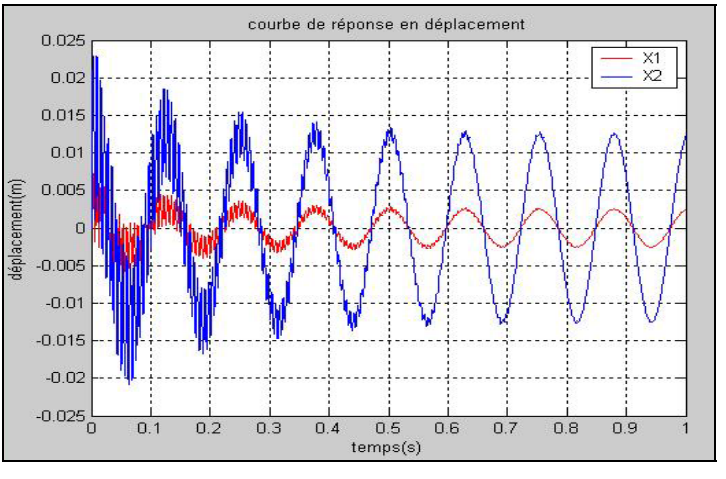

Fig. 4 Displacement curve

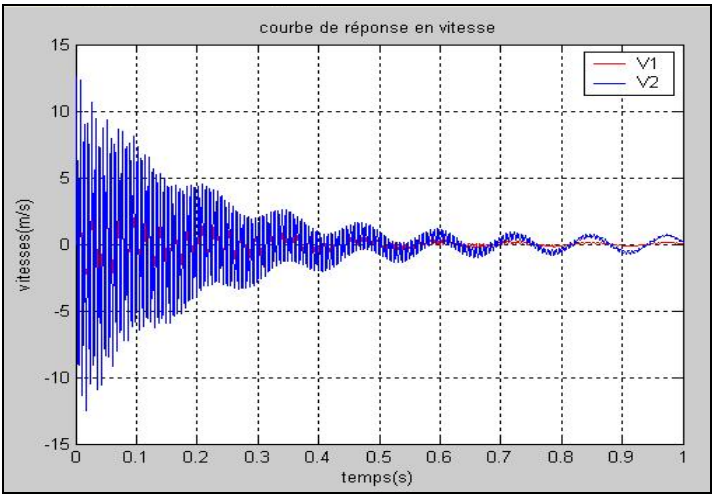

Fig. 5 Velocity curve

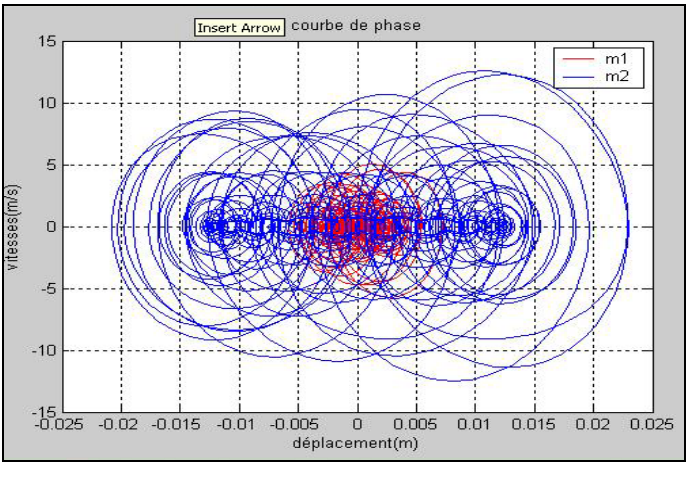

Fig. 6 Phase Curve

Figure 4 shows the evolution of the movement of two masses M and mp as a function of time with an initial condition of the second movement of the mass equal to 0,025 m. There is a very rapid reduction which explains the phenomenon of vibration damping.

Figure 5 shows the evolution of the velocities of two masses m1 and m2 over time. The velocity response of the system diminishes rapidly away from the origin of time. There is a phenomenon of damping in the bolted fixation.

Figure 6 shows the evolution of the velocity and displacement in phase space, it shows two fixed attractors that model the damping of the system to excitation forces.

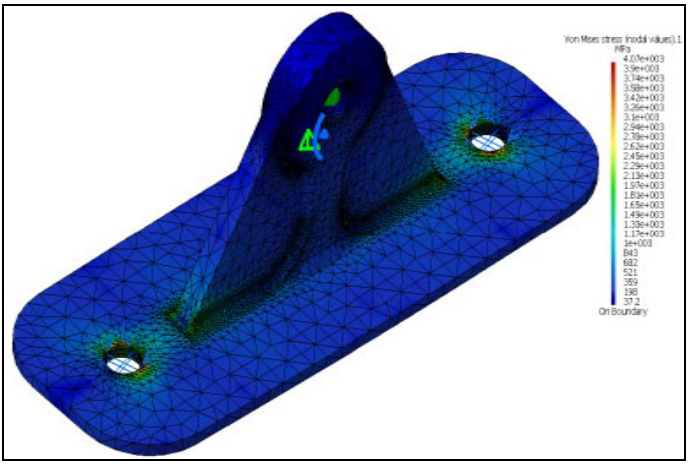

Fig. 7 SFX bolted in dynamic

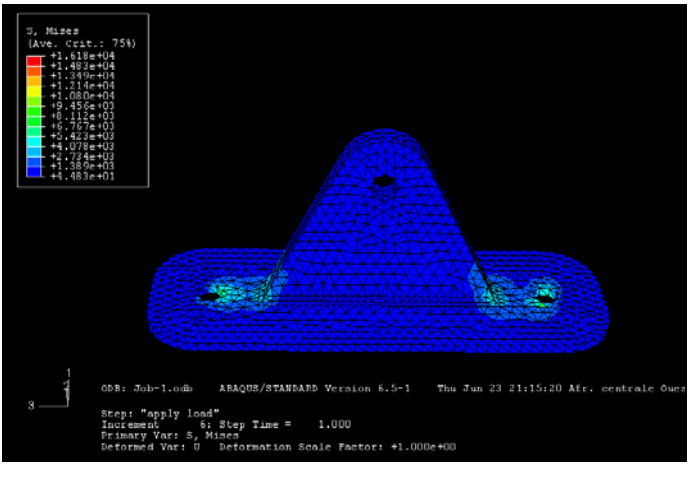

Fig. 8 Result of “Von Mises” in Abaqus

5 Conclusion

In this study, two types of assembly brackets for rods are considered, but only one was chosen for industrial reasons that there is "machined brackets".

The analysis of the behaviour of the bracket in question highlighted the following conclusions:

- According to the response curves of displacement and velocity, there is always the absorption of vibrations in the dynamic state of the system and this explains the phenomenon of damping in the fasteners.
- By viewing the phase curve, there are indeed two attractors and therefore our system about to dampen the motion and converge to the steady state and repetitive. (This focuses on two very different concepts [First our system cannot well be chaotic and it trends to stabilize and dampen vibrations linearly] [second system and chaotic dynamics and we should study all aspects stochastic and random].
- Based on the finite element analysis, we find that our vibration absorption phenomenon is concentrated at the bolted fasteners in the case of bolted assembly with support and these both in static and dynamic study. This interpretation leads us directly important to refine our study and go further up the study of threads.

In the end, it remains the party validation between analytical calculations and finite element for the validation of our model and then generalizing this type of modelling for bolted joints correctly identified analytically.

Acknowledgements. My special thanks go to Nasri Rachid and Chakhari Jamel, without their helps and support the continuity of work in my thesis would be more painful.

References

El-Zahry, R.M.: Optimum design of preloaded bolted joint under harmonic excitation. Journal of Sound and vibration 108(3), 455–470 (1985)

Mourad, S., Ghobarah, A., Korol, R.M.: Dynamic response of hollow section frames with bolted moment connections. Engineering Structures 17(10), 737–748 (1994)

Pai, N.G., Hess, D.P.: Three-dimensional finite element analysis of threaded fastener loosening due to dynamic shear load. Engineering Failure Analysis 9, 383–402 (2002)

Law, S.S., Wu, Z.M., Chan, S.L.: Vibration control study of a suspension footbridge using hybrid slotted bolted connection elements. Engineering Structures 26, 107–116 (2004)

Ibrahim, R.A., Pettit, C.L.: Uncertainties and dynamic problems of bolted joints and other fasteners. Journal of Sound and Vibration 279, 857–936 (2005)

Jalali, H., Ahmadian, H., Mottershead, J.E.: Identification of nonlinear bolted lap-joint parameters by force-state mapping. Solids and Structures 44, 8087–8105 (2007)

Dynamic Analysis of an Offshore Wind Turbine Drivetrain on a Floating Support

Fernando Viadero[1], Alfonso Fernandez del Rincon[1], Emilio Liaño[1], Miguel Angel Serna[1], and Manuel Angel Diaz[2]

[1] Department of Structural and Mechanical Engineering, University of Cantabria, Avenida de los Castros s/n 39005-Santander, Spain
{viaderof,fernandra,miguelangel.serna}@unican.es, emiliolianolopez@gmail.com
[2] APIA XXI. Avenida Albert Einstein, 6, 39011-Santander, Spain
MDiaz@apiaxxi.es

Abstract. This paper presents a multi-body model for the study of the non stationary dynamic behaviour of an off-shore wind turbine power train. The problem studied is an off-shore implementation with seafloor depths around a thousand metres, making it necessary to use a floating platform. Special attention is paid to combining the characteristics of the buoy's off-shore support with a detailed model of the power train in order to assess the consequences of buoy movement in the forces that appear in gears and bearings. A multi-body analysis code was used to develop the model and a conventional wind turbine set up was implemented as an example. Gearbox dynamic behaviour is simulated for common manoeuvres of start-up and emergency stop and the results obtained are presented.

Keywords: Wind Turbine, Off-Shore, Gear Dynamics, Meshing Stiffness.

1 Introduction

The development of wind energy development has been of great importance in the last decade. This means that there are now many wind farms located at sea, but all of them near the coast where the low water depth allows the anchoring of wind turbines on the seabed. The alternative in deep sea areas is to use floating structures that support the wind turbine which usually consist of a float that gives vertical stability to the wind turbine and chains that limit the horizontal displacements. These conditions represent a new engineering challenge not only from the point of view of the structural elements but also the gearbox design as the dynamic loads are more complex than those corresponding to conventional ground facilities.

The gearbox is one of the most critical components on the operation of wind turbines, being responsible for most of the downtime and as a consequence of the

increment in operational costs [1]. This fact has received the attention of several researchers and increasingly accurate and advanced models have been developed in recent years to understand the dynamic loads involved [2], [3]. Furthermore, offshore applications increase the complexity of dynamic loads and therefore the uncertainty related to the design process.

Although various studies have addressed the dynamic modeling of floating offshore wind turbines [4], none has focused on the consequences on the operation of the gearbox. This work presents a study of the behavior of the power train of a wind turbine on a floating structure that has free movements in all displacements and rotations with the structural constraints due to the floating structure. With this aim, a model has been developed by mean of a Multibody System (MBS) code because this approach enables the whole system to be handled. Moreover, the MBS approach provides more flexibility to include additional phenomena such as the excitations coming from aerodynamic blade loads or the flexibility of different components (shafts, tower, etc.) although in this work the attention is focused on the dynamics of the gear train.

The model developed includes a planetary stage and two ordinary stages with variable meshing compliance as well as bearing flexibility. Special attention is given to the run up and emergency stop as dynamic forces are critical in these maneuvers. Information about the behavior of loads induced by the dynamic interactions is analyzed.

2 MBS Model

The whole MBS model developed in MSC-ADAMS, is presented in Fig. 1 with details of the gearbox and kinematics scheme. The blades with the hub are considered as a rigid body with lumped mass and inertia. Wind loads are included as external forces on the rotor hub neglecting aerodynamic loads due to the structural behaviour of blades and the aero-elastic coupling. Buoy restoring forces are included at the base of the tower using specific Single Forces defined in the MBS code environment.

Regarding gearbox, shafts and gears are lumped and assumed to be rigid bodies while gear meshing forces are modelled by a variable stiffness spring following the approach described later. The rotor hub is connected thorough the main shaft to the carrier of the planetary stage (see Fig 1). The carrier moves planets and transmits the power by the fixed ring and the sun to the low-speed shaft. Then, two ordinary stages are used to increase the rotational speed, up to the desired value at the generator side which is included by means a representative mass.

In order to simplify, all shafts have been considered as rigid and the main shaft is the only one supported by flexible bearings, while rotational joints are used for the others. Flexible bearings are included in the MBS model as bushing joints defining the corresponding stiffness and damping values neglecting cross terms.

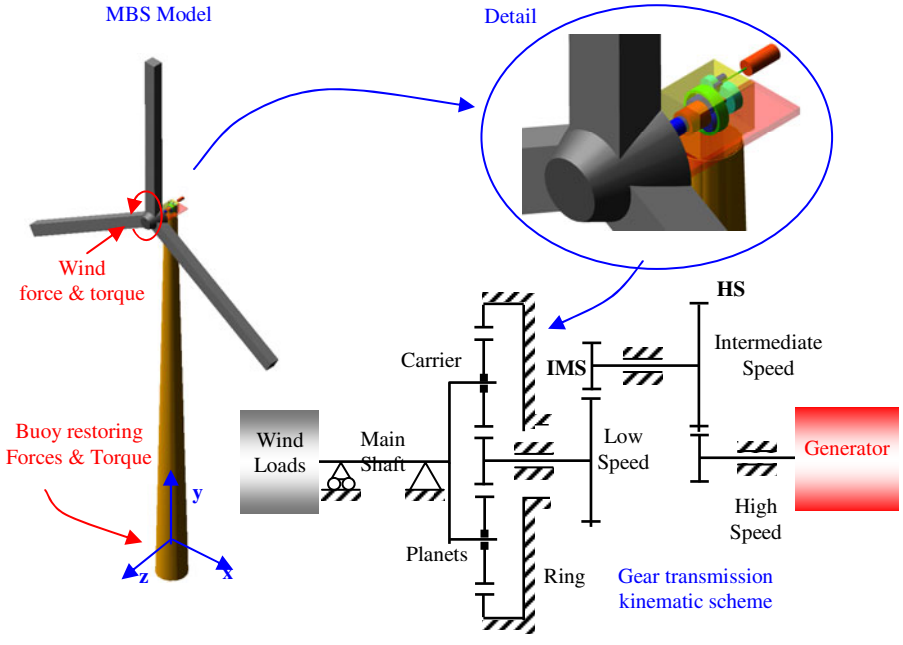

Fig. 1 MBS model and details of the drive train

The torque load due to the generator (T_G) has been approached by a simple induction generator model according to the expression

$$T_G = R_T(\omega_S - \omega) \tag{1}$$

Where ω is the actual generator speed, ω_S is the synchronous generator speed corresponding to zero torque and R_T is a constant defined in order to balance the nominal wind torque at the desired operation speed ω_G. This model is connected when the generator rotational speed reaches a certain value defined by the user. In this way the coupling can be done even with the generator working as a motor when the generator speed is lower than the synchronous one.

Meshing forces have been included as user functions (GFORCE) defined following the approach in previous work by the same authors for a low-speed ordinary transmission [5]. Tooth contacting forces are assumed to be contained in the transmission plane, perpendicular to the tooth surface. Thus, tooth deflection can be obtained from the relative displacements of each gear center $x_i, y_i, z_i, \theta_{xi}, \theta_{yi}, \theta_{zi}$, using the following expression (see Figure 2):

$$\delta ij=(x_i\cdot\cos\varphi_{ij}+y_i\cdot\sin\varphi_{ij}+\rho_i\cdot\theta_{zi}-x_j\cdot\cos\varphi_{ij}-y_j\cdot\sin\varphi_{ij}+\rho_j\cdot\theta_{zi})\cdot\cos\beta_{ij} \\ +(z_i-\rho_i\cdot\theta_{xi}\cdot\cos\varphi_{ij}-\rho_i\cdot\theta_{yi}\cdot\sin\varphi_{ij}-z_j-\rho_j\cdot\theta_{xj}\cdot\cos\varphi_{ij}-\rho_j\cdot\theta_{yj}\cdot\sin\varphi_{ij})\cdot\sin\beta_{ij}+e_{ij}(t) \quad (2)$$

Where $e_{ij}(t)$ represents the periodic static transmission error due to profile errors, β_{ij} is the helix angle on the pitch cylinder and φ_{ij} the normal pressure angle.

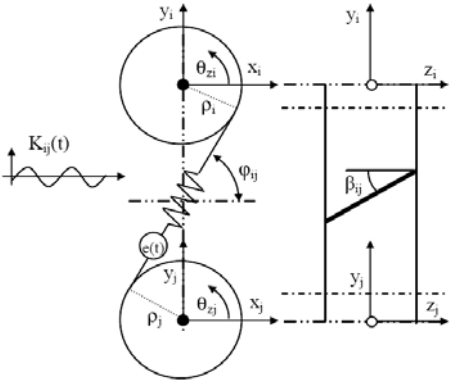

Fig. 2 Tooth meshing deflections

Once tooth deflections are known, meshing force is obtained by multiplying the resulting deflection by the gear pair stiffness. There are several works about the stiffness variation along the contact point, also taking into account the number of couples in contact for each position. In this case, due to the high contact ratio, there is a large overlap of tooth couples and therefore the stiffness is described by a simple expression defined by a mean value and a harmonic term [5]. Thus, forces on gear centres are defined from deflection by the force projection vector.

The floating support platform is a spar-buoy concept which achieves static stability locating the center of gravity below the center of buoyancy by means of ballast. Three catenary mooring lines in a delta connection are used to attach the buoy to the sea floor restricting horizontal movement of the turbine to keep it within a certain area. The placement of the chains around the floating platform defines the yaw stiffness which is one of the most critical features in the design of this kind of supports. A preliminary analysis of the hydrostatic buoyancy behaviour provides rotational stiffness as well as the translational one in the vertical direction. These features are defined in the MBS model by a GFORCE element where the damping associated with each translational and rotational degree of freedom is included. Mooring lines are also analysed in a previous stage and then included in the model as three non linear springs arranged in the xz plane (see Fig 2) every 120 degrees.

3 Example

The MBS model described previously has been applied to a known 750 kW wind turbine drive train, the NREL 750 GRC [6]. No details are presented in this work about the parameters and data related to the example except those not appearing in the cited reference. In Table 1 the data corresponding to the meshing stiffness of each gear pair are presented. These data have been obtained following the approach proposed in [5]. Bearings for the main shaft are modelled as BUSHING joints and only present supported by the main shaft bearing closest to the carrier and the planets themselves. The axial stiffness for this bearing adopts the same value used for the radial direction of 10^9 N/m.

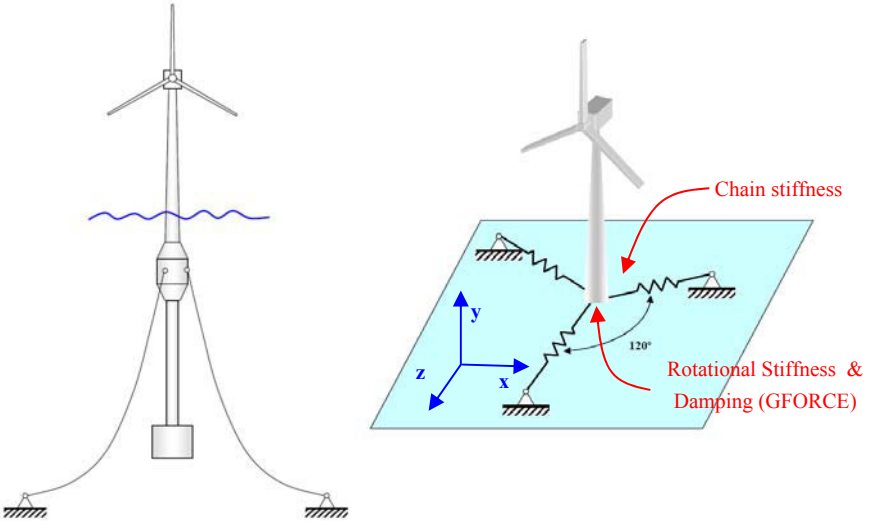

Fig. 3 MBS model of the buoy's restoring forces

Table 1 Transmission gear data

	Transversal Contact ratio	*Axial Contact ratio*	*Average Stiffness (N/m)*	*Variable Stiffness (N/m)*
Planet / Ring	1.5847	1.2456	$5.7605\ 10^9$	$6.287\ 10^8$
Planet / Sun	1.5456	1.2456	$6.0827\ 10^9$	$7.276\ 10^8$
IMS Gear Pair	1.5208	1.8668	$2.9956\ 10^9$	$3.468\ 10^8$
HS Gear Pair	1.4538	2.1562	$1.7947\ 10^9$	$1.809\ 10^8$

Regarding the model of the floating structure, the vertical translation stiffness due to gravitational forces and flotation at the equilibrium point is 96.74 kN/m.

The horizontal stiffness due to the tension of the mooring lines is non-linear according the values shown in Table 1. To simplify the model, the same value has been used for roll, pitch and yaw rotational stiffness. Moreover, linear viscous damping has been considered for all the buoy's degrees of freedom (see Table 2).

Table 2 Parameters of the wind turbine

	Stiffness (15 m)	Stiffness (20 m)	Stiffness (25 m)	Damping
Horizontal translation (for 15m, 20m, 25m)	16.34 kN/m	23.52 kN/m	39.2 kN/m	40 kN/m/s
Vertical translation	96.74 GN/m			40 kN/m/s
Roll / Pitch / Yaw	1.14 GNm/rd			1 MNm/rd/s

The results that will be presented correspond to the previously described model under several transitory loads. Initially, with the generator disengaged, the model was subjected to wind loads on the blades which are represented as a torque and a thrust in the hub rotor. These loads increment their magnitude progressively from zero to the maximum value over a time period from 0.1 to 5 seconds. As a consequence the drive train starts up and simultaneously the floating support begins its horizontal movement as well as pitch oscillation due to the wind thrust load. Later, when the rotational speed of the high-speed shaft has exceeded 157 rad/s, the generator is connected progressively achieving the maximum power when the speed exceeds 160 rad/s. Then, after a short period of time the turbine reaches its stationary working conditions of torque load and rotational speed. Afterwards, the next step was to simulate an emergency stop maneuver due to an electrical failure. The objective sought was to study the phenomenon of unexpected shutdown of the machine and evaluate the contact stresses in the gears, bearings, as well as the dynamic behavior of the entire machine. This event was carried out by disconnecting the generator (at 20 seconds) with a sudden drop in the resistant torque. As a consequence the drive train lost the pretension in the meshing contacts, increasing their speed. After 0.1 seconds (at 20.1 seconds), the control system reacts activating the aerodynamic brake by pitching the blades. Then, until 25 seconds the torque and thrust due to the wind are progressively reduced and simultaneously a rotational damper representing the aerodynamic brake torque is connected at the hub. Furthermore, at the same time (20.1), the mechanical brake is activated on the generator side increasing its value up to the maximum in 0.5 seconds (20.6 seconds). Finally the torque of the mechanical brake is progressively reduced depending on the generator speed from 10 rad/s to 1 rad/s when it is deactivated.

Next some results are presented, which are considered representative of the behavior of the transmission analysed on a floating support in the conditions described above.

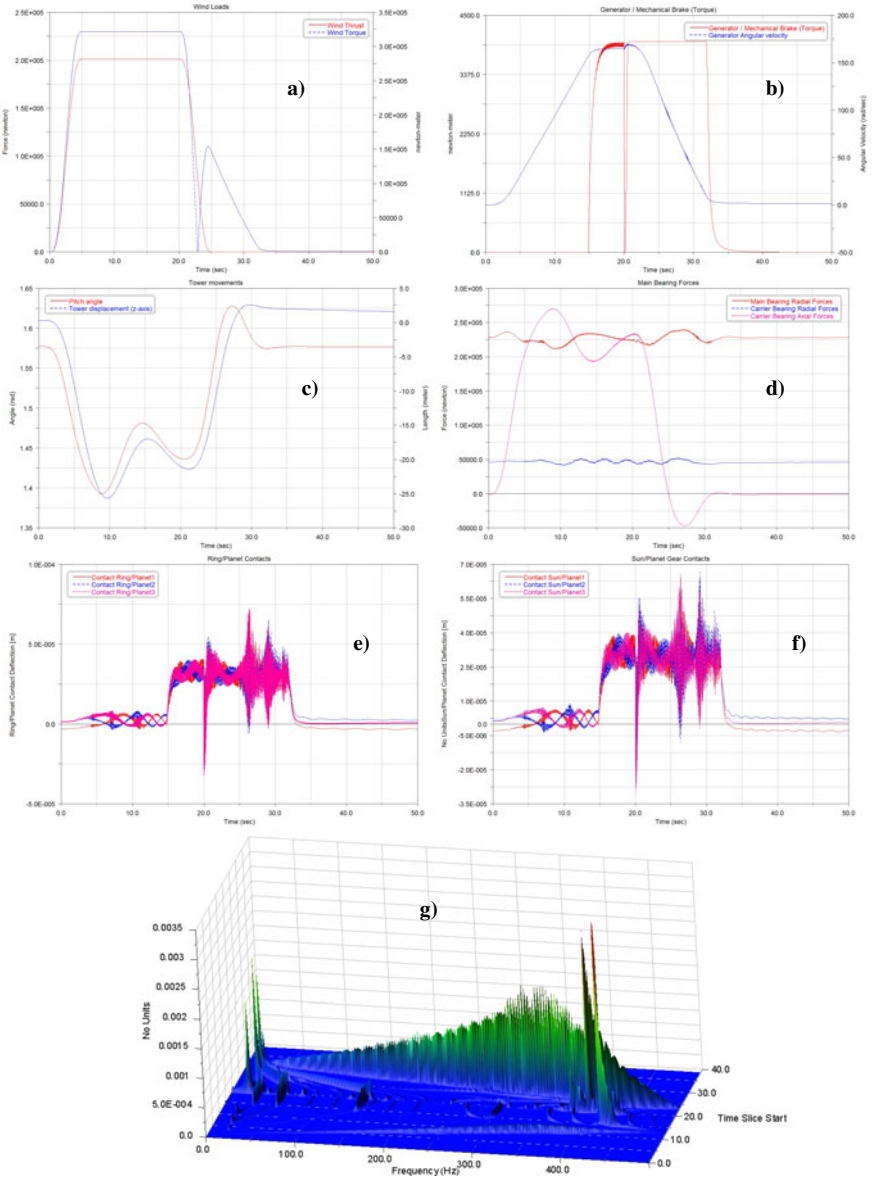

Fig. 4 Simulation results: a) Wind loads (Thurst and Torque); b) Generator torque and rotational speed; c) Tower movement (displacement and pitch angle); d) Main Shaft Bearing forces; e) Ring/Planet contact deflection; f) Sun/Planet contact deflection; g) Waterfall spectra of High-Speed gear stage deflection derivative

4 Conclusions

This work presents the dynamic behaviour of an offshore wind turbine power train. The system has been anlysed considering two common non-stationary maneouvers, start-up and emergency stop. The results show the influence of variable meshing stiffness in a rotational model of a power train. These aspects have a strong influence on the performance of the transmission resulting in oscillations related to the load and velocity-related operating conditions.

The influence of the buoy displacements on the operation of the offshore wind turbine power train has been also considered. Although these effects are difficult to assess, they are important in the main bearing and planetary components as a consequence of gyroscopic effects.

Reversing contact appears in the planetary stage at rest (time 0 sec) as a consequence of the main shaft support deflection. Moreover, during run up unloaded period (generator disengaged) and particularly during the emergency stop reversal, contacts are also observed in all the gear pairs. Maximun meshing deflections appear during the braking period due to the excitation of geartrain resonances.

Acknowledgements. The authors would like to thank the company Apia XXI for supporting part of the research presented through the Project DINAER. Moreover, some parts of the developments presented have been achieved in the framework of Project DPI2006-14348 funded by the Spanish Ministry of Science and Technology.

References

Oyague, F.: Gearbox Modeling and Load Simulation of a Baseline 750-kW Wind Turbine Using State-of-the-Art Simulation Codes NREL/ TP-500-41160 (2009)

Peeters, J.: Simulation of Dynamic Drive Train Loads in a Wind Turbine. Dissertation. Katholieke Universiteit Leuven (2006)

Helsen, J., Vanhollebeke, F., Marrant, B., Vandepitte, D., Desmet, W.: Multibody modelling of varying complexity for modal behaviour analysis of wind turbine gearboxes. Renewable Energy 36(11), 3098–3113 (2011)

Jonkman, J.M.: Dynamics of offshore floating wind turbines-model development and verification. Wind Energy 12(5), 459–492 (2009)

Fernández del Rincón, A., Viadero, F., Pascual, J., García, P., Sancibrian, R.: Vibration Behaviour Modelling for a Low-Speed Gearbox. In: ISMA 2002 (2002)

Oyague, F.: GRC Drive Train Round Robin GRC 750 / 48.2 Loading Document (IEC 61400-1 Class IIB) (2008)

Author Index